AD-A157 608

THIN FILM RESEARCH

VOL. 1

Contract: N60530-81-C-0158
Effective date of contract: 1 August 1981
Expiration date of contract: 31 July 1984

Final Report

Principal Investigator: H. Angus Macleod
(602-621-2449)

Optical Sciences Center
University of Arizona
Tucson, AZ 85721

Sponsored by:
Defense Advanced Research Projects Agency (DoD)
ARPA Order No.: 3343

Monitored by Dr. James L. Stanford
under Contract N60530-81-C-0158

DTIC
ELECTE
AUG 9 1985
S A D

The views and conclusions contained in this document are those of the authors and should not be interpreted as representing the official policies, either expressed or implied, of the Defense Advanced Research Projects Agency of the US Government.

May 30, 1985

DTIC FILE COPY

This document has been approved for public release and sale; its distribution is unlimited.

85 7 18 091

REPRODUCED AT GOVERNMENT EXPENSE

UNCLASSIFIED
SECURITY CLASSIFICATION OF THIS PAGE

AD A 157 608

REPORT DOCUMENTATION PAGE

1a. REPORT SECURITY CLASSIFICATION UNCLASSIFIED	1b. RESTRICTIVE MARKINGS
2a. SECURITY CLASSIFICATION AUTHORITY	3. DISTRIBUTION/AVAILABILITY OF REPORT Approved for public release; distribution unlimited.
2b. DECLASSIFICATION/DOWNGRADING SCHEDULE	
4. PERFORMING ORGANIZATION REPORT NUMBER(S)	5. MONITORING ORGANIZATION REPORT NUMBER(S)
6a. NAME OF PERFORMING ORGANIZATION Optical Sciences Center University of Arizona 6b. OFFICE SYMBOL (If applicable)	7a. NAME OF MONITORING ORGANIZATION Naval Weapons Center
6c. ADDRESS (City, State and ZIP Code) Optical Sciences Center University of Arizona Tucson, AZ 85721	7b. ADDRESS (City, State and ZIP Code) China Lake, California 93555
8a. NAME OF FUNDING/SPONSORING ORGANIZATION DARPA 8b. OFFICE SYMBOL (If applicable)	9. PROCUREMENT INSTRUMENT IDENTIFICATION NUMBER N60530-81-C-0158
8c. ADDRESS (City, State and ZIP Code) 1400 Wilson Blvd Arlington, Virginia 22204	10. SOURCE OF FUNDING NOS. PROGRAM ELEMENT NO. / PROJECT NO. / TASK NO. / WORK UNIT NO.
11. TITLE (Include Security Classification) Thin Film Research, Vols. 1 and 2	
12. PERSONAL AUTHOR(S) H. Angus Macleod	
13a. TYPE OF REPORT Final 13b. TIME COVERED FROM 1/8/81 TO 7/31/84	14. DATE OF REPORT (Yr., Mo., Day) May 30, 1985 15. PAGE COUNT 77 + Appendices
16. SUPPLEMENTARY NOTATION	

17. COSATI CODES		
FIELD	GROUP	SUB. GR.

18. SUBJECT TERMS (Continue on reverse if necessary and identify by block number)
Thin films, coatings, physical vapor deposition, PVD, ion-assisted deposition, IAD, ion bombardment, electron-assisted deposition, electron bombardment, optical thickness monitor,

19. ABSTRACT (Continue on reverse if necessary and identify by block number)

Optical thin films are critical components in a broad range of technologies, ranging from energy conversion to information storage. In response to the demand for increasingly specialized and durable coatings, enquiry into the basic nature of these coatings has intensified. Such efforts are necessary because assumptions that thin films were similar to nominally identical bulk materials have proven unreliable. For example, while most bulk materials show a high degree of isotropy, thin films display pronounced anisotropy. Another distinction between bulk and thin film materials is the lower density of the latter, with the resulting porosity. Both anisotropy and porosity often contribute to the unpredictable performance and durability of optical coatings. This report covers three years of fruitful research aimed at better understanding and modifying film microstructure in the direction of greater isotropy and density through novel deposition techniques. We have supported this effort with an array of analysis techniques and with a major effort in film growth simulation and in the theoretical description of anisotropic films. Our

20. DISTRIBUTION/AVAILABILITY OF ABSTRACT UNCLASSIFIED/UNLIMITED ☒ SAME AS RPT. ☐ DTIC USERS ☐	21. ABSTRACT SECURITY CLASSIFICATION Unclassified	
22a. NAME OF RESPONSIBLE INDIVIDUAL H. Angus Macleod	22b. TELEPHONE NUMBER (Include Area Code) (602) 621-2449	22c. OFFICE SYMBOL

DD FORM 1473, 83 APR EDITION OF 1 JAN 73 IS OBSOLETE.

UNCLASSIFIED
SECURITY CLASSIFICATION OF THIS PAGE

REPRODUCED AT GOVERNMENT EXPENSE

18. Subject Terms (Continued)

scanning optical monitor, surface plasmons, narrowband filters, moisture adsorption, columnar growth, anisotropic structure, optical constants, inhomogeneities.

19. Abstract (Continued)

program also included development of a scanning monochromator for our Balzers 760 evaporation system, which covers a 400 to 800 nm bandwidth by dispersing the beam with a holographic grating and detecting it with a linear array.

Accession For
NTIS GRA&I
DTIC TAB
Unannounced
Justification
By
Distribution/
Availability Codes
Dist | Avail and/or Special
A-1

ACKNOWLEDGMENTS

The success of this project owes much to the encouragement and help of Dr. James L. Stanford of the Naval Weapons Center, China Lake, and of Dr. E. Joseph Friebele of the Defense Advanced Research Projects Agency.

The people at the Optical Sciences Center who have been involved to more than a minor degree in the project are in the following list. Their contributions are gratefully acknowledged.

FACULTY AND STAFF

B. Bovard	Postdoctoral Associate on an AFOSR Grant
J. Henry	Research Assistant
M. R. Jacobson	Research Specialist
H. A. Macleod	Principal Investigator
J. M. Mueller	Electronics Specialist
R. H. Potoff	Thin-Film Specialist
R. W. Sprague	Thin-Film Technician
R. Swenson	Research Assistant

GRADUATE STUDENTS

S. D. Browning	
L. DeSandre	Naval Weapons Center Scholarship
F. Horowitz	Brazilian Government Scholarship
C. C. Lee	
M. Messerly	
F. Van Milligen	
N. A. Raouf	Supported by Joint Services Optical Program
S. Saxe	Army Research Office Scholarship
J. J. Wharton	Air Force Major

VISITING PROFESSORS

I. J. Hodgkinson	University of Otago, New Zealand
B. J. Liao	Institute of Instrumentation Technology, Shenyang, PRC
J. Q. Miao	Institute of Optics and Electronics, Chengdu, PRC
M. Sikkens	University of Groningen, The Netherlands
J. F. Tang	Zhejiang University, PRC

CONTENTS

INTRODUCTION 1

PART I. REVIEW OF RESEARCH ACTIVITIES 3

A. LABORATORY DEVELOPMENT 3

1. Deposition Equipment: Balzers 760 Box Coater 3
   a. Acquisition and Installation 3
   b. Modification and Improvement 4
   c. Scanning Monochromator Development 6
2. Spectrophotometry 11
   a. Cary 14 UV-Vis-NIR Spectrophotometer Developments 11
   b. Analect FX-6200 FTIR Acquisition 11
3. Summary 12

B. DEPOSITION PROCESSES 13

1. Introduction 13
2. Electron-Assisted Deposition 14
3. Ion-Assisted Deposition 16
4. Ultraviolet-Assisted Deposition 17
5. Summary 18

C. CHARACTERIZATION TECHNIQUES 19

1. Introduction 19
2. Optical Methods 19
   a. Narrowband Filter Shifts 19
   b. Surface Plasmon Detection 19
   c. Ellipsometry 20
   d. Fringes of Equal Chromatic Order (FECO) 23
3. X-Ray Diffraction 26
4. Transmission Electron Microscopy (TEM) 26
5. Summary 26

D. DEGRADATION PROCESSES 28

1. Introduction 28
2. Moisture Damage 28
3. Laser Damage 29

E. SIMULATIONS OF THIN FILM GROWTH 32

1. Two-Dimensional Hard Sphere Model 32
2. Relaxation and Mobility 33
3. Extensions of the Program 34

F. PUBLICATIONS 35

PART II. DETAILED ACCOUNT OF THE SCIENTIFIC RESULTS

A. INTRODUCTION 37

B. THEORETICAL STRUCTURE MODELING 39

C. ANISOTROPY 56

D. MOISTURE ADSORPTION 60

1. Introduction 60
2. Surface Plasmon Resonances 63
3. Moisture Adsorption and Optical Instability in Thin Film Coatings 63
4. Anisotropic Moisture Penetration 63
5. Effect of Ion Bombardment on Moisture Adsorption 70

E. OPTICAL INHOMOGENEITY 70

F. ULTRAVIOLET AND ION BOMBARDMENT 71

G. ELECTRON BOMBARDMENT 73

1. Antimony trioxide 73
2. Potassium hexafluorozirconate 73
3. Silicon oxide 73
4. Magnesium fluoride 73
5. Zinc sulfide 74

H. LASER DAMAGE 74

I. CONCLUSION 75

REFERENCES 75

APPENDIX A. STRUCTURE-INDUCED OPTICAL ANISOTROPY IN THIN FILMS

APPENDIX B. MOISTURE ADSORPTION AND OPTICAL INSTABILITY IN THIN FILM COATINGS

APPENDIX C. ION BOMBARDMENT-INDUCED RETARDED MOISTURE ADSORPTION IN OPTICAL THIN FILMS

APPENDIX D. DEVELOPMENT OF AN AUTOMATED SCANNING MONOCHROMATOR FOR MONITORING THIN FILMS

APPENDIX E. OPTICAL CONSTANTS DERIVATION FOR AN INHOMOGENEOUS THIN FILM FROM IN SITU TRANSMISSION MEASUREMENTS

APPENDIX F. MICROSTRUCTURE RELATED PROPERTIES OF OPTICAL THIN FILMS

APPENDIX G. ELECTRON BOMBARDMENT OF CERTAIN THIN FILMS DURING DEPOSITION

APPENDIX H. LASER DAMAGE MEASUREMENTS ON ALL-DIELECTRIC NARROW-BAND FILTERS

INTRODUCTION

Optical thin films have become critical components in a broad range of technologies, ranging from energy conversion to information storage. In response to the resulting demand for increasingly specialized and durable coatings, inquiry into the basic nature of these coatings has intensified. Such efforts have been necessary because earlier assumptions that thin films were similar to nominally identical bulk materials have been proved unreliable. For example, while most bulk materials show a high degree of isotropy, whether they are crystalline or amorphous, thin films display pronounced anisotropy. Another distinction between bulk and thin film materials is the lower density of the latter, with the concomitant porosity. Both anisotropy and porosity often contribute to the unpredictable performance and durability of optical coatings. Efforts to modify film microstructure in the direction of greater isotropy and density have been made by a number of researchers in recent years.

In August 1984, three years of fruitful research on the fundamental microstructural properties of optical thin films, generously supported by the Defense Advanced Research Projects Agency of the Department of Defense, were completed. During this period, our Thin Films Laboratory made significant progress in the three areas just described (characterizing film anisotropy, understanding film porosity, and modifying these features) and established a strong basis for further advances in these areas. In this final report, the progress is described by presenting the experimental details of our work in the five sections of Part I, equipment acquisition and modification, deposition processes, measurement techniques, degradation processes, and computer simulations. Progress in each of these areas depended on support from the others; the encouragement of our sponsors to interpret the domain of our contract in the broad sense required by basic research contributed to the beneficial interaction that resulted. Part II places these experiments in the context of the three basic issues addressed by this program: anisotropy, porosity, and modification. The reader who is interested in conclusions might begin here, referring back to Part I for further information on equipment and procedures. The final chapters contain a list of the publications and doctoral dissertations supported by this contract and include some reprints of published material.

This research has not only contributed to our understanding of thin films, but also supported four excellent graduate students through parts of their studies and/or research-related equipment. Their work appears in very abridged form throughout this final report; those interested should obtain copies of their dissertations. Cheng-Cheung Lee investigated water adsorption of thin films; Steve Browning experimented with electron-assisted deposition, Flavio Horowitz devised an optical measurement technique for the indices of birefringent materials, and John Wharton explored ion- and electron-assisted deposition. Other students involved in this research will be receiving degrees in the next year or two. Since the Optical Sciences Center is

one of very few institutions granting optical science degrees, this support of students has a valuable and unique impact on the level of American optics.

PART I

REVIEW OF RESEARCH ACTIVITIES

A. LABORATORY DEVELOPMENT

1. Deposition Equipment: Balzers 760 Box Coater

a. Acquisition and Installation

At the outset of this three-year project, our laboratory was extremely limited by size, age, and sophistication. Our largest plants were a Balzers 510 coater (510 mm, or 20 in.) and an Edwards 18-in. bell jar coater. Both were diffusion pumped, with manual vacuum control systems and very few possibilities for upgrading. Further references to these two plants can be found in the next section on deposition processes and in several doctoral dissertations. Despite their age, both of these plants performed well for certain aspects of the research conducted under this contract, but it was realized that to perform the experiments central to our proposal, a larger, cleaner, system would be needed. Consideration of our objectives led to several requirements on the new system:

(1) Cryopumping, inherently cleaner than diffusion pumping, was necessary to achieve extremely low levels of contamination of residual gases, especially for activated processes.

(2) Residual gas analysis, both to monitor unwanted contaminants and the concentration of working or reactive gases, was specified.

(3) Capacity similar to production systems was important, so that successful process technology could be transferred to other laboratories without problems of scaling. Adequate chamber capacity was also needed to accommodate the many internal modifications implicit in process development. It was concluded that a box coater roughly 30 in. in each dimension was appropriate.

(4) Substrate rotation and heating arrangements were obviously desired.

(5) Optical and quartz crystal monitoring, for data on both optical and mass thickness, were ordered, with the intention to construct a more elaborate scanning monochromator unavailable at the time.

(6) Resistance and electron beam sources were included to provide the two basic evaporation processes.

(7) Flexibility was also critical, since our experimental program envisioned the need for considerable and continual changes in the plant's internal configuration.

After competitive bidding, the Balzers 760 was selected, not only because it met all our requirements, but also because previous experience of the Principal Investigator and of the significant thin-films group in Marseille indicated that this system was the best available at the time. This box coater's performance since its arrival in 1982 has not disappointed us.

Moving and installing such a box coater is a formidable job. Fortunately, communication between us and Balzers as to the delivered dimensions of the plant was accurate: The uncrated main coating module, which incorporates the chamber, its base, and the cryopump, and the three electronics modules, or racks, fit through all the doors on its route from the truck to the "clean room" with a few precious inches to spare. For the next several months, our thin films specialist, Ross Potoff, performed and supervised the connection of roughing vacuum lines, electricity, hot water, and chilled water, to the plant. Of these services, the most problematic was the volume of chilled water required. Existing supplies were inadequate, so the University's Physical Resources Department designed a new system around a large heat exchanger located several floors below. After numerous delays which affected our program during parts of the first and second years, the chilled water system has worked without unusual problems up to the present.

b. Modification and Improvement

Once the plant was operational, modifications and additions were initiated. A large number of ports were specified in the system, including 20 at the base of the chamber and one on each side. These ports provide the means of adding new components. A list of important changes follows. Some are mentioned only here; the scanning monochromator and ion and electron beam guns are of such importance that individual sections cover them in more detail. Once again, Ross Potoff deserves most of the credit for designing and machining the majority of the mechanical parts in this system.

(1) External Superstructure - The scanning monochromator and ultraviolet source had to be physically located, for optical reasons, on the top and side of the coating chamber, respectively. Since no extra space was available in the three supplied electronic racks, ultraviolet source and ion gun power supplies also needed a home. To this end, a framework of brazed 2-in.-square tubing was erected over the top and left side (facing the door) of the large module that included the main coating plant. The framework incorporated a sturdy optical baseplate, drilled and tapped on 1-in. centers, for the monochromator.

(2) Ultraviolet Source - One possible means of increasing adatom mobility on the growing film surface is irradiation by ultraviolet light. Toward this end, a 1000-W mercury-xenon lamp was installed in the superstructure so that it could be projected into the chamber through a

side port. This project required careful work to couple the lamphouse to an ultraviolet-transmitting viewport and to direct the beam up to the substrate with internal reflective optics. To remove the ozone generated by the lamp, a separate exhaust and cooling duct extending to fixed fume hood ductwork was built.

(3) Scanning Monochromator Input Optics - The scanning monochromator required numerous modifications to the plant. The original lamphouse under the coating chamber was removed and replaced with a more powerful unit containing a chopper and a 500-W tungsten-halogen lamp. Within the chamber, the beam had to be laterally translated with a pair of flat mirrors to align better with the witness samples, and improved fixturing for the witness samples to insure centering was required. Above the chamber, the original photomultiplier was removed, and the mount was modified to accommodate a turning mirror, which steers the beam into the scanning monochromator. A description of the scanning monochromator, which is mounted on the external superstructure, follows below.

(4) Gas Cylinder Rack - A rack for the secure, horizontal storage of four compressed gas cylinders was built to reside under the external superstructure already described, which allows quick access to the associated regulators. The gases are used in a variety of thin film deposition processes.

(5) Internal Superstructure - The wide range of experiments that were to be performed suggested that the limited number of options be increased for mounting equipment such as heaters, guns, and sensors in the coating chamber. To implement this, an internal structure made of 1-in.-square stainless tubing was fabricated. It fits against the top and side walls of the chamber and can be easily removed. Without this structure, every internal change would require major modifications and long, complex supports for each new device.

(6) Quartz Lamp Heaters - The quartz lamps were moved to the top of the chamber for three reasons. First, they occupied much critical space above the baseplate, while space above the substrates was wasted. Second, they were removed from the vicinity of the main stream of evaporant material. Third, by heating the substrates in close proximity from above, heating was more localized and temperature control was more accurate. This helpful change required use of the internal superstructure and the procurement of stainless cable armor to extend the existing flexible conduits.

(7) Ion Guns - An ion gun from Denton Vacuum were positioned in the coating chamber in 1984. Appropriate power and cooling water lines had to be fed through to supply the device internally.

(8) Second Electron Beam Gun - A second Balzers electron beam gun was purchased on another contract and installed at the factory before shipment.

(9) Multipoint Thermocouple System - To provide critical temperature data, thermocouple system sampling temperatures in five different chamber locations was installed recently.

(10) Domed Fixtures - A set of four spun 22-in.-diameter domed aluminum plates was ordered to serve as rotating substrate holders, or fixtures. These have been machined in-house to accommodate a variety of substrate shapes of maximum dimensions in the 4- to 5.75-in. range. The domed shape holds the substrates roughly equidistant from the sources below. Coating uniformity is improved by allowing for critical adjustment to compensate for the positions of the resistive and electron beam sources.

(11) Computer Control - The Balzers 760 was delivered with its own computer system for overseeing vacuum conditions and valve positions and for displaying this information with a light board in the middle electronics module. As part of an overall plan to monitor the progress of film growth, our own computer was added, first a Southwest Technical Products system based on the 6809, which was later replaced by an IBM-PC. Interfaces with both the scanning monochromator and the quartz crystal monitor were built. While the full anticipated diagnostic potential was not completely realized during the three years of the contract, we feel that the effort will pay off handsomely in the future. More on this computer will follow in the section on the scanning monochromator.

c. Scanning Monochromator Development

To produce an evaporated coating that conforms to a specified design, it is necessary to control numerous parameters. Starting materials of the form and purity appropriate for the chosen evaporation process must be selected. The coating environment--the partial pressures of the residual gases, the temperature of the substrate, the electromagnetic fields and ionization, if any, in the chamber, and other parameters--must be monitored. Finally, the deposition rate must be directly controlled by manipulating the operation of the hot sources and the position of the shutters. This entire effort is aimed at depositing films of predetermined thicknesses and optical constants. These film characteristics are normally measured by crystal monitors, which measure the mass-dependent frequency of a piezoelectrically driven quartz crystal, and by optical monitors, which gauge optical thickness by following the fringes generated by interference effects in the growing film. The Balzers 760 evaporation system was supplied with both types of systems. Quartz crystal monitors are often used as controllers to maintain a constant deposition rate until the desired thickness is reached; this was originally implemented in the 760. Even with such monitors, however, several runs are still required to understand the effect of each of the parameters on a coating process. Our interest in experiment rather than production made the existing systems inadequate.

To augment the capabilities of the original process controller, the simple, single wavelength optical monitor was replaced with our own

scanning monochromator and was connected to an IBM PC. The same computer is interfaced with the existing quartz crystal monitor. The scanning monochromator required a new, brighter source, to deliver sufficient signal to the detector through a more complex, dispersive optical train. The optical path in the chamber had to be adjusted. Above the chamber, the narrowband filter and the photomultiplier were removed, to be replaced by a flat mirror that diverted the beam horizontally into the scanning monochromator detection system. The beam passed first through a telescope-slit configuration, which sent it on to the Jobin Yvon holographic grating, built to disperse the 400 to 800-nm band, of which about 360 nm is used. This reflective grating sends the converging beam on to another turning mirror and to a Fairchild 1728 element CCD array, which consists of 1728 elements that are added in tens in the interface electronics to define 173 data points. Given that 360 nm are observed, this allows the CCD to resolve about 2 nm. From here, data acquisition and interface electronics read and send the data points to an IBM PC. Figures 1, 2, and 3 show side and top views of the Balzers 760, emphasizing the modifications made to accommodate the scanning system.

The IBM PC, incorporating a Tecmar A/D board, accepts data from both the quartz crystal and the scanning optical transmission monitors. Although the system could record data at a frequency of 4 Hz, data are actually recorded more slowly, once every 6 seconds, due largely to the lack of adequate storage or use for this potential torrent of data. This is adequate, since in 6 seconds, the manageable, typical thickness of 20 to 40 Å is deposited.

Although the results obtained with the scanning monochromator will be mentioned in connection with some of the studies reported in later chapters, examples of its capabilities follow:

(1) A sequence of transmission spectra for each run can be stored for later analysis of the effects of various process parameter effects. A 360K double-density 5 1/4 in. disk can accommodate about 50 minutes of continuous monitoring data.

(2) The wideband transmission spectra that appear on the monitor provide the plant operator with a much broader view of coating progress. Should problems arise, the operator can base decisions during deposition on a larger data base.

(3) Monitoring done in situ permits the execution of many different tests on samples without removing them from the system. For example, the effects of residual water vapor in the evacuated coating chamber can be monitored continuously both during and after deposition.

(4) The larger data base available to the computer permits better characterization of a film's optical constants and their associated dispersion. These measurements can be performed as a function of film thickness as well.

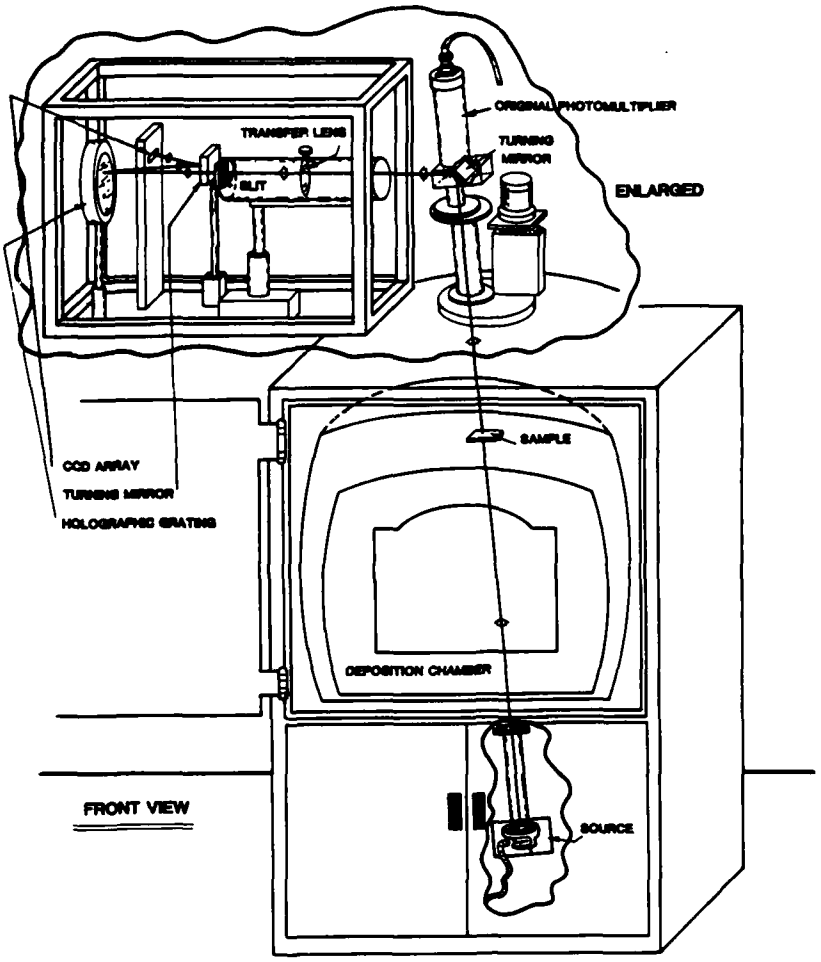


Fig. 1. Balzers 760 coating plant with scanning monochromator modification.

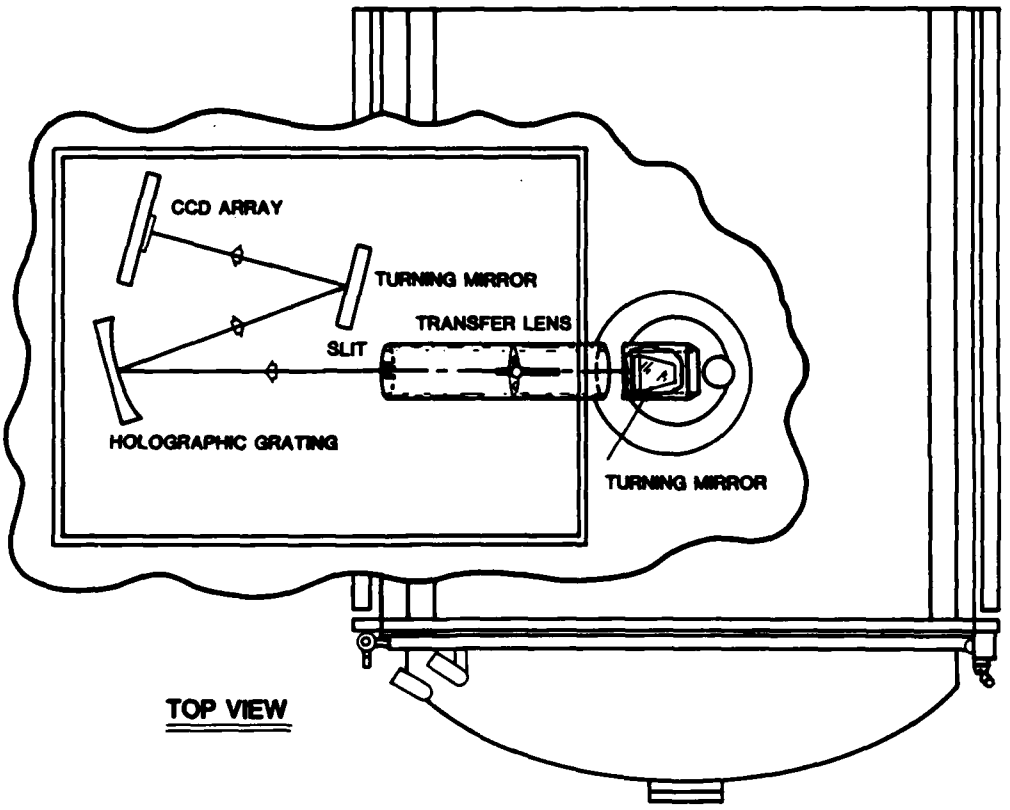


Fig. 2. Balzers 760 with scanning monochromator modification.

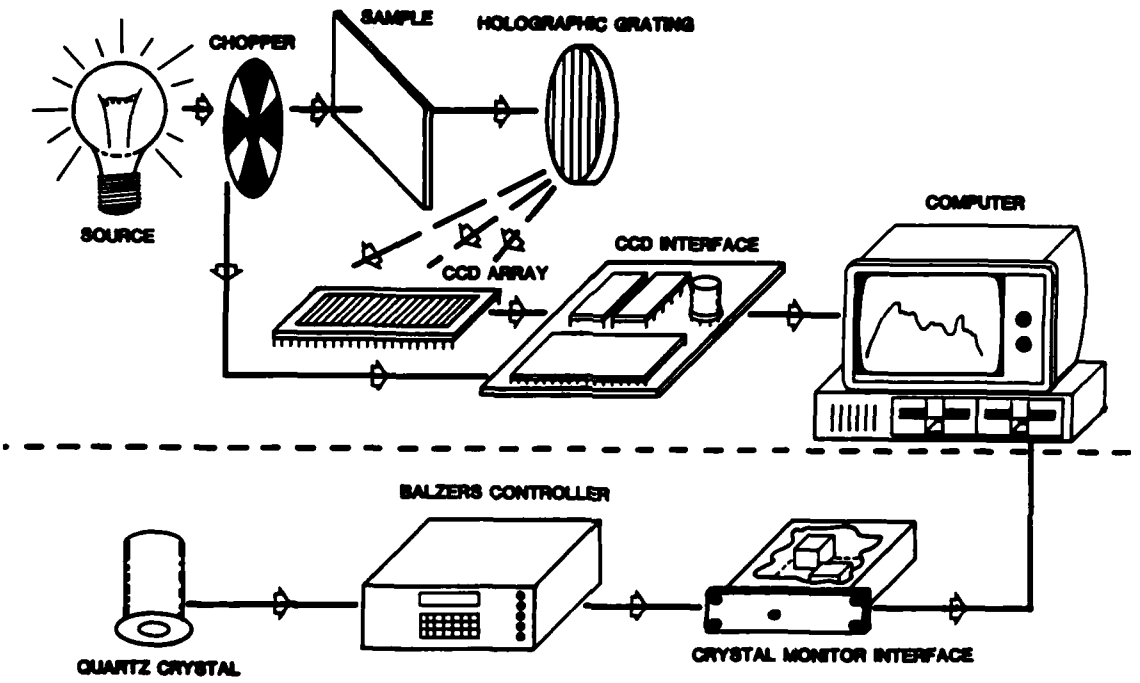


Fig. 3. Scanning monochromator flow diagram.

The development of our scanning monochromator system was inspired by a pioneering system constructed at the Laboratoire d'Optique de l'Ecole Nationale Supérieure de Physique in Marseille, France, led by E. Pelletier and including F. Flory, A. Fornier, and R. Richier (Vidal, Fornier, and Pelletier, 1979; Lerner et al., 1980; Bousquet and Pelletier, 1981; Pelletier, 1983). One other member of that group is among the authors of this paper. We were fortunate enough to have B. Bovard as a post-doctoral scientist for one year at the Optical Sciences Center. His visit had an extremely stimulating influence on the construction and completion of the instrument. The Air Force Office of Scientific Research (AFOSR) provided salary support for his year in Arizona. Ross Potoff was primarily responsible for the design and fabrication of most of the mechanical components of the scanning monochromator. We express equal thanks to Jim Meuller for constructing the electronics and interfacing them with the Balzers 760 and the IBM-PC (Bovard et al., 1984; Van Milligen et al., 1984).

2. Spectrophotometry

a. Cary 14 UV-Vis-NIR Spectrophotometer Upgrading

Since 1980, a later model Cary 14 spectrophotometer has been the main source of transmittance and reflectance measurements in our Optical Measurement Laboratory, which serves the Thin Films and other groups at the Center. When properly calibrated and maintained, this instrument is capable of very high accuracy and precision. However, production of the Cary 14 stopped in 1969, and even its successor, the Cary 17, is now out of production. As a result, spare parts are increasingly difficult and expensive to obtain. To protect ourselves, a used Cary 14 was purchased for $3,000 in 1983 to serve as a source of spare parts. The compensator was incorporated from the used system in our working unit in a subsystem that allows the operator to switch between compensators optimized for reflectance and transmittance. When the chopper motor failed, a replacement was at hand and the equipment was operational again in a few hours. The used Cary 14 has already paid for itself.

b. Analect FX-6200 FTIR Acquisition

Another major instrument purchased through this contract was an Analect FX-6200 FTIR spectrophotometer. This system was needed by the Optical Measurement Laboratory to replace a Perkin-Elmer 137 NaCl Prism Spectrophotometer. As with the large coater, the instruments available for under the budgeted figure of $35,000 were scrutinized until a request for bids could be prepared. Systems from Analect and Nicolet competed for selection. The former was chosen on the basis of speed, lack of noise, satisfaction of other owners, ruggedness, maintainability, and overall customer support. The FTIR instrument arrived in our laboratory and was installed and accepted in the spring of 1982 and has continued to operate with no major problems.

3. Summary

The support provided by this contract has been carefully used to build a powerful and versatile capability to deposit and characterize thin films. The equipment of the Thin Film and Measurement Laboratories has enabled us to pursue several lines of research and to contribute to the understanding of thin film microstructure.

B. DEPOSITION PROCESSES

1. Introduction

A major objective of this program is to improve thin film performance by devising a more durable microstructure. Many severe problems of optical coatings could be solved if the films had bulk-like properties. Instead of an isotropic, void-free continuum, equivalent to a packing density very close to unity, conventional physical vapor deposition produces a columnar microstructure with a large void volume and extensive internal surface area. This has several problematic consequences: (1) Film surfaces and interfaces are rough, due in part to the intersection of the columns with the interface plane. In multilayers of more than a few layers on critically smooth substrates, the intrinsic surface roughness of the films dominates the optical scattering. (2) These rough interfaces have also been identified as a source of absorption losses in multilayers. (3) Films are frequently in a state of considerable stress. The associated strain energy is often high enough to drive adhesion failures or to contribute to damage caused by high flux irradiation.

The pores also allow gases to enter the film and permit water vapor to condense. Water in a film has important optical and structural consequences; most of them are harmful. Liquid water's refractive index differs from that of the gases it displaces, affecting the optical performance. The same moisture weakens interlayer attractive forces, promoting the delamination tendency already present in many films. Therefore, the porous, columnar structure assumed by most conventionally deposited films is not desirable. Modifying the deposition process to encourage a more isotropic configuration is a principal goal of our research.

Extensive experimental evidence verifies the indications of computer simulations and demonstrates that increasing the mobility of adatoms in the growing film leads to a denser, less porous, structure for many materials. Presumably, this leads to more stable optical properties. The empirical relationship between substrate temperature and the film microstructure was presented by Movchan and Demchishin (1969) and Thornton (1974). This can be interpreted as a connection between microstructure and adatom mobility. Movchan and Demchishin showed that for some metals and oxides, the structure was a function of the substrate temperature, T_s, as a fraction of the film material's melting point. Thornton added a second axis representing residual pressure, inversely related to adatom kinetic energy in a sputtering system. On this basis, other workers have attempted different means of increasing adatom mobility beyond that provided by the heat of the substrate.

Energy to increase mobility can be supplied either by increasing the energy with which the source material arrives at the surface or by delivering energy to the growing film by other means. Sputtering and its variants use the first approach, where a plasma is set up in which ions are accelerated and target atoms are provided with considerably

more energy than thermally evaporated species. The second approach is the one we investigated. The film material is delivered to and adsorbed on the substrate by standard evaporation techniques, but the surface is under simultaneous bombardment by energetic electrons, ions, or photons, which mobilize the adatoms.

We have focused on the refractory oxides, an important class of thin film materials because of their durability and their range of refractive indices. However, when conventionally deposited, they suffer from the above defects and also may be deficient in oxygen, which tends to reduce the refractive index and shift optical performance. This oxygen deficiency can sometimes be corrected by deposition in a residual oxygen atmosphere, but even then, a slight oxygen deficiency normally remains. We have attempted to rectify these problems with electron, ion, and ultraviolet photon bombardment, all of which are intended to increase the mobility of adsorbed atoms, or adatoms, on the substrate. The following sections describe our experiments. In Chapter III we place these investigations in the context of film modification of anisotropy and porosity.

2. Electron-Assisted Deposition

Although electron-assisted deposition (EAD) was patented by Rice (1947), the actual mechanism by which electrons interact with the growing films of various thin film materials is still not completely understood. In work documented in a doctoral dissertation by Browning (1983), an Edwards EC-18 evaporation system was modified with a tungsten filament as an electron source and a nichrome loop as a positively charged grid to direct electrons to the positively charged substrate holders (see Fig. 4). The estimated current of 420 μA at the substrates is equivalent to an arrival rate of about 25 electrons for every molecule of a typical film material at normal rates of deposition. By varying parameters, this ratio can be adjusted downward to zero.

Only thermally evaporated materials were used, due to limitations of the equipment and concern that stray electrons would complicate the analysis of electron beam effects. The five materials studied were antimony trioxide (Sb_2O_3), silicon monoxide (SiO), zinc sulfide (ZnS), magnesium fluoride (MgF_2), and potassium hexafluorozirconate [$2KF(ZrF_4)$]. Brief results follow:

(1) SiO remained amorphous after bombardment, as evidenced by X-ray diffraction, and showed no other changes.

(2) For Sb_2O_3, the crystallite size was reduced, another lattice plane was preferentially oriented parallel to the substrate, and the packing density may have increased slightly. None of these changes has any major influence on macrostructural or optical performance.

(3) On the other hand, $2KF(ZrF_4)$ strongly responded to electron bombardment, in that crystallinity could be entirely eliminated

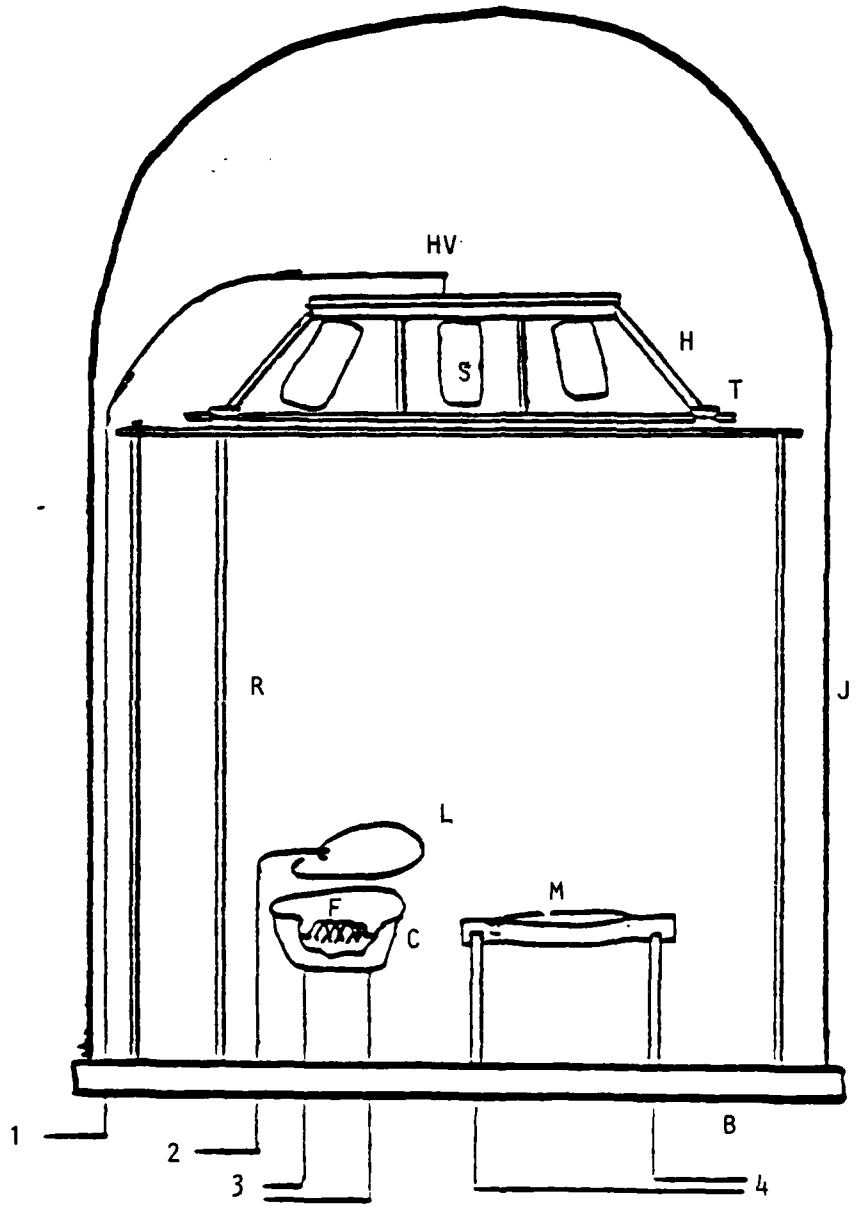


Fig. 4. Coating plant diagram. F - filament, C - crucible (cutaway view), L - accelerating loop, M - evaporant material source, B - baseplate, J - bell jar, R - rotary drive rod, HV - high voltage lead, S - substrate, H - substrate holder, T - teflon roller, 1 - to high voltage supply, 2 - to another high voltage supply, 3 - to grounded secondary of filament transformer, 4 - to source transformer secondary.

by electron/molecule ratios of 0.5 on a heated substrate. A slight increase in blue-UV absorption was observed, but effects on durability were not significant.

(4) Normally evaporated ZnS includes some of the hexagonal-close-packed (HCP) form that is stable at high temperatures. Later relaxation to the cubic form disrupts the film. Electron bombardment encourages the formation of cubic ZnS during deposition, eliminating the destructive stabilization phenomenon and improving durability, without affecting the optical properties.

(5) Electron bombardment's main effect on MgF_2 was the reduction in crystallite size. The films were too thin for meaningful x-ray diffraction analysis. Durability and transmittance of the films suffered.

X-ray diffraction revealed that all of the materials except SiO underwent some changes in crystal structure. No general effects of electron bombardment were identified other than the observations that multiple electron collisions are probable, that crystallites seem to be reduced, and that the effects are roughly linear with electron number and energy. The influence of the technique depends on the individual materials. Further discussion follows in Chapter III.

3. Ion-Assisted Deposition

In contrast to the limited work in electron-assisted processes, numerous ion-assisted deposition (IAD) processes have emerged in recent years. This activity has taken place in the broader context of processes that involve ions in other ways, such as RF sputtering, ion-beam sputtering, ion plating, and reactive evaporation. Ion-assisted deposition is distinguished by its emphasis on employing ions to deliver additional energy to the growing film surface to enhance adatom mobility. In the other processes, ions are the projectiles that sputter coating material or are themselves a component of the coating material. More on these distinctions appears in Part II. In IAD, the energizing ions are generated by various types of ion guns. The important process parameters are the values of and spreads in ion energies and the total beam currents. One common watershed is placed at ion energies of 100 eV. Ions above and below this point are thus utilized in high- and low-energy processes, respectively.

Ion-assisted deposition is compatible with existing thermal evaporation techniques and equipment, which is a great advantage. Its implementation, therefore, does not involve the abandonment of all the skills and procedures that have been accumulated around the conventional processes. Existing plants can be modified by the addition of ion guns and alterations of similar magnitude to the installation of electron beam evaporation sources. This approach was followed in coating plants at two widely separated laboratories. In one case, the Principal Investigator worked with a group led by R. Netterfield at the CSIRO

Division of Applied Physics in Australia. In the other, the modification was carried out at the Optical Sciences Center.

The Australian work is described in a paper by Martin et al. (1983). The oil-diffusion-pumped 28-in. bell jar coater reached base pressures of 10-4 Pa, and an electron beam gun evaporated the source material. The substrates were held 420 mm directly above the centrally located source. A Kaufman ion gun bombarded the growing film at an angle of 30 degrees from the normal and at a distance of about 350 mm. Representative 02+ ion beam parameters ranged from energies of 600 to 750 eV and currents of 16 to 48 $\mu A/cm^2$. The experiments carried out at the Optical Sciences Center took place in the Balzers 760 box coater described above. A rotating turret sample holder carried test and reference samples for alternating illumination by the monitor beam. A water-cooled inverted magnetron Kaufman ion gun, manufactured by Denton Vacuum, bombarded the test sample with 3-keV 02+ ions with an estimated flux of 1 $\mu A/cm^2$. In Australia, single-layers coatings of ZrO_2, TiO_2, and SiO_2 were prepared, along with multilayers incorporating these three materials. Narrow-band filters (NBFs) made of the same materials were deposited in Arizona. As we shall discuss more fully in Part II, the IAD films made in Australia demonstrated that bombardment during deposition has a beneficial effect on films of these oxides, as packing density rises to the degree that no measurable change in performance is observed on exposure to atmospheric moisture.

Wharton (1983) reported on evaporation of the same materials in our Balzers 760 coating plant at the University of Arizona. In different experiments, oxygen or argon ions from the Denton Vacuum ion gun were directed on growing ZrO_2 and TiO_2 2 films. For ZrO_2, the higher tetragonal [111] peak corresponded to an increase in crystallinity, while the TiO_2 became completely amorphous under even slight bombardment. For both oxides, argon bombardment increased absorption, apparently due to the removal of oxygen. Bombardment by oxygen ions mitigates this effect. Also, bombardment tends to increase refractive indices for both oxides.

Work in Arizona has also included post-deposition bombardment of titania and zirconia films, with the result that films containing titania show reduced adsorption and desorption of moisture, while films with a high index layer of zirconia show no improvement. This opens a new, simplified approach to the porosity problem. For some materials, ion bombardment apparently converts the porous, open surface zone into a dense layer that seals the film against moisture penetration.

4. Ultraviolet-Assisted Deposition

The irradiation of thin films after deposition by ultraviolet light has been performed by a number of workers. In his doctoral dissertation, Wharton (1983) summarizes these experiments. At the Optical Sciences Center we have investigated the influence of irradiation during deposition. A Kratos LH-151 lamphouse was mounted in the superstructure outside of a port on the left side of our Balzers 760 box

coater. Ultraviolet radiation from the 1000-W mercury-xenon arc lamp passed through a Schott UG-5 filter, which blocked the visible and infrared spectrum, and a sapphire high-vacuum window. Inside the plant, the beam was defined by a mask with a slit and was directed by two flat mirrors onto a stationary substrate. Roughly 25 photons were calculated to arrive at the substrate with each evaporant molecule. An alternative UV source, wholly inside the chamber, consisted of a 160-W mercury lamp, modified by removal of the outer glass envelope. It was connected to line and starting voltages through two electrical feedthroughs. Single layer coatings and multilayer filters with 17 or 21 layers were again made from silica, zirconia, and titania. Effects of UV on the high index layers were generally small, with less absorption and a slight increase in index for ZrO_4 and less crystallinity and more stability with time for TiO_2.

5. Summary

Work on three types of deposition modification, involving electron, ion, and ultraviolet photon bombardment, has been pursued under this basic research contract. For the materials studied, impinging ions have had the greater impact than electrons or energetic photons. The implications of this effort will be discussed more fully in Part II. In our next section on measurements, a description of both general and specialized techniques of thin film characterization will be presented.

C. CHARACTERIZATION TECHNIQUES

1. Introduction

In the course of investigating anisotropy and porosity in thin films, we have employed a wide variety of analytical techniques. Some techniques involve optical photons as probes to be reflected, transmitted, or scattered and then detected. These approaches are primarily aimed at determining optical constants. Others methods involve x-rays, electrons, and ions as probes for elucidating structure and composition. The equipment, procedures, and some results follow below. The results will be discussed in terms of the broader issues of anisotropy and porosity in Part II.

2. Optical Methods

a. Narrowband Filter Shifts

Spectrophotometric measurements of films, especially those incorporated in narrowband multilayer filters, can detect absorption and birefringence. Birefringence is often a consequence of anisotropy in thin films. Two examples of such measurements, both made in a Cary 14 spectrophotometer, follow. First, three ZrO_2/SiO_2 filters were deposited and irradiated over part of their surfaces by a UV source mounted within the chamber. In two of the three cases, the irradiated regions showed less absorption, and in the third case, the absorption was unchanged. For ion bombarded films, the reverse held, with increased absorption, due perhaps to the preferential removal of oxygen in both ZrO_2/SiO_2 and TiO_2/SiO_2 filters. Much of this work was carried out in our laboratory by Prof. Ian Hodgkinson (1983) during his sabbatical year from the University of Otago in New Zealand.

Second, a series of narrowband filters deposited early in the program displayed a double, rather than the expected single, peak. By using a matched pair of polarizers mounted in the Cary 14, this double peak was shown to be an effect of birefringence. The amount was determined by noting the maximum shift in wavelength while rotating the polarizer. An additional, more qualitative experiment was performed with the filters still in the vacuum chamber by using the optical monitor beam, a turning mirror, a polarizer, and a monochromator. Rotating the polarizer and watching the monochromator, the transmission peak shift decreased from 45° in vacuum to 25° after air was admitted. The latter agrees with the hypothesis that intercolumnar voids are partially filled with airborne water vapor, reducing the contrast in refractive index between columns and voids (Wharton, 1983).

b. Surface Plasmon Detection

One technique developed under the Joint Services Optical Program contributed significantly to our work on film porosity. A surface wave, or plasmon, can be generated on the metal coated hypotenuse of a prism which is internally illuminated by p-polarized light beyond the critical

angle (see Fig. 5). The coupling of the light into the plasmon is observed as a sharp dip in the internal reflectance, which can theoretically be zero under the correct conditions. This p-polarized resonance is one of a family of resonances for both s- and p-polarized light that occur when the metal is overcoated with one or more dielectric layers. The resonances all show a marked sensitivity to conditions either at the metal surface or within the dielectric overcoating layers. We have employed this plasmon resonance to investigate the stability of dielectric layers and and the anisotropy of both metal and dielectric layers.

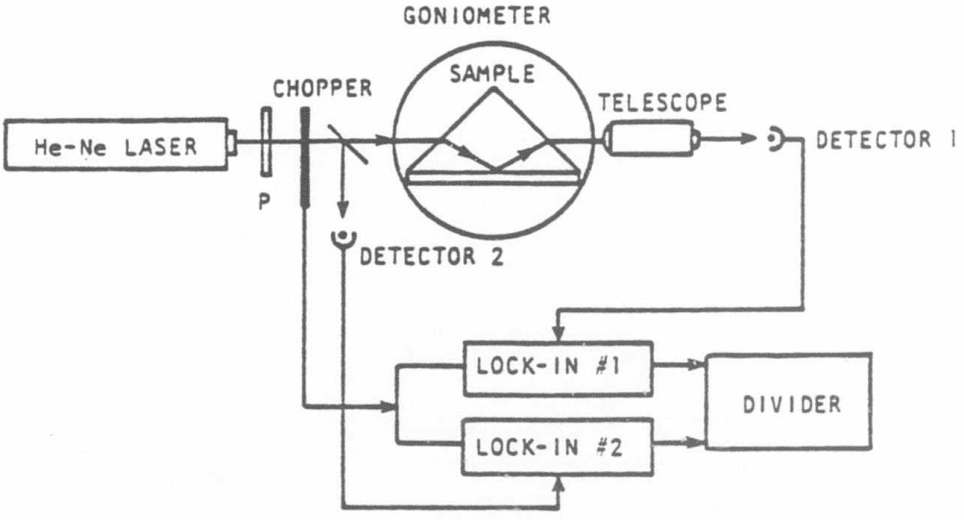
For example, obliquely deposited silver films with strong anisotropies have been examined, but only shifts in resonance smaller than the uncertainties in the measurement have been observed. Another measurement involved computing the adsorption isotherms of cryolite films. The prisms were first coated with silver and the resonance angle for p-polarized light was measured. This allows us to determine the thickness and optical constants for the silver layer. Then, the dielectric film (in this instance, cryolite) is added. For a p-polarized resonance, the thickness of the dielectric should be around one halfwave at the appropriate angle of incidence, while for s-polarized resonance, the thickness should be an odd number of quarterwaves. Measurements of the resonance, together with the knowledge of the thickness and the optical constants of the silver film, permit the derivation of the same quantities for the dielectric. When the assembly is exposed to atmospheres with varying degrees of humidity, changes in thickness or refractive index can be tracked by repeatedly measuring the resonance.

For cryolite, the changes in the index were consistent with a reasonable value of the packing density. The thickness apparently grew slightly, near the measurement limit of a few tenths of a nanometer, with most increases in relative humidity. Changes in refractive index were similarly small, until a critical value of around 80% relative humidity above the cryolite took place. Around this point, the humidity jumps from 1.315 to 1.52, which is equivalent to a packing density of 0.38 and an index of the solid film of 1.82. Both of these figures are outside the range of what could be considered possible, so that some chemical reaction seems to be the only feasible explanation. Desorption of water from porous films shows considerable hysteresis, indicating that much of the chemical change was irreversible (see Fig. 6).

c. Ellipsometry

The form birefringence of non-normally deposited, anisotropic films is of particular interest to us. The differing amounts of columnar film material presented to waves of orthogonal polarizations provides a means of quantifying this birefringence. Measurements of this anisotropy in ZrO_2 films have been performed by Horowitz (1983) and by Horowitz and Macleod (1983), as described in the following paragraphs.

In this discussion of anisotropy measurements, we will employ a set of axes oriented as shown in Fig. 3.1 of Horowitz's dissertation.



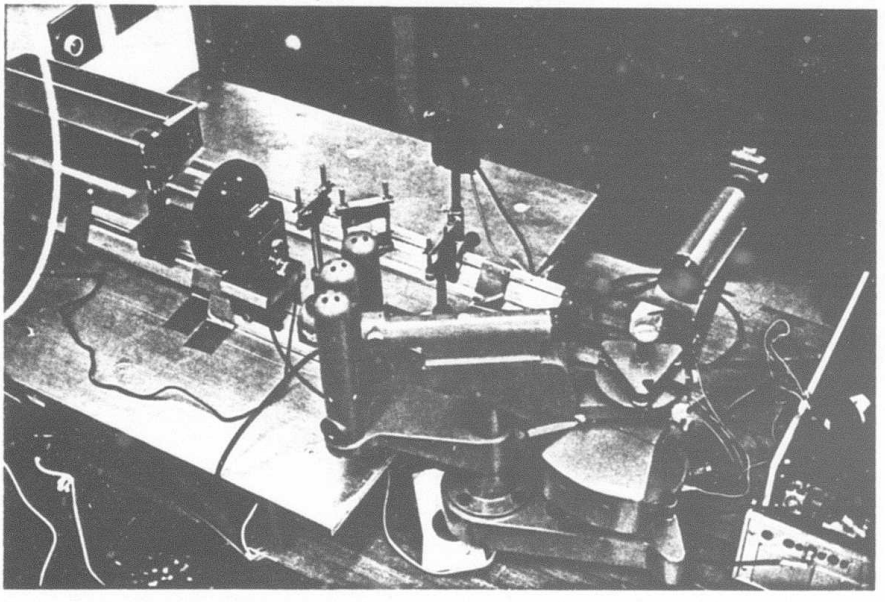


Fig. 5. Apparatus used for measuring surface plasmon. (a) Schematic drawing). (b) Actual machine.

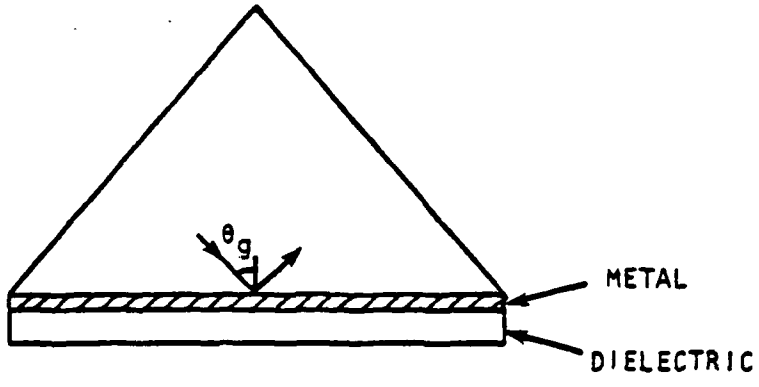


Fig. 6. Schematic of a dielectric overcoat on a metal for observing the surface plasmon, halfwave thickness for p-polarized light and quarterwave thickness for s-polarized light.

Obviously, for films deposited at normal incidence, no unique plane of incidence can be defined, and birefringence cannot be detected by measurements at normal incidence. However, if films are obliquely deposited, biaxial birefringence will be observable with optical axes parallel to n_3 and n_2, since maximum and minimum amounts of material will be encountered along those respective axes, as shown in Fig. 7.

The anisotropy in index was measured with a modified ellipsometer, as shown in Fig. 8. A HeNe laser with a stability of better than 0.5% served as a source, followed by a chopper and a quarterwave plate to produce circularly polarized light from the linearly polarized laser input. Glan-Thompson prisms, part of the Gaertner ellipsometer, polarized and analyzed the light. A Babinet-Soleil compensator, mounted on the polarizer arm of the ellipsometer, determined optical path differences on the order of 10 Å after careful calibration. A photomultiplier on the analyzer arm of the ellipsometer was preceded by a diffuser to diminish the effects of small lateral shifts in the beam on the photocathode. In the center, the Gaertner ellipsometer included a smaller rotating specimen table, coaxial with the motion of the analyzer arm. The accuracy of the measurement was critically dependent on the exact positioning of a point on the surface of the specimen substrate at the center of rotation for both the inner and outer tables. Special procedures (Zeidler, Kohles, and Bashara, 1973) insured this alignment.

Since film thickness and the three refractive indices for the three axes of the sample had to be determined (d, n_1, n_2, n_3), four measurements were necessary. Details of this method are described by Horowitz (1983). With the four data in hand, algebraic manipulation yielded the three indices and the thickness. However, the system as devised, though successful, was very difficult to use, due to its great vulnerability to vibration and disturbance and its essentially manual operation. We have proposed the construction of a dedicated, automated instrument.

d. Fringes of Equal Chromatic Order (FECO)

The computed thickness was checked by aluminizing a sample and performing a FECO measurement. Results were within 20%, which is quite reasonable, considering the nonuniformity of film thickness and phase changes due to reflection. Indices were estimated from models by Sikkens et al. (1984) at the appropriate angles of vapor incidence, which yield columns of elliptical cross section. If a bulk value of index is used and one of the three indices is assumed, a value of packing density can be derived and used, with the estimate of column ellipticity, to compute the other two indices, based on an adaptation of an expression due to Wiener (Bragg and Pippard, 1953). The results are within 2% of those computed from the anisotropy measurement.

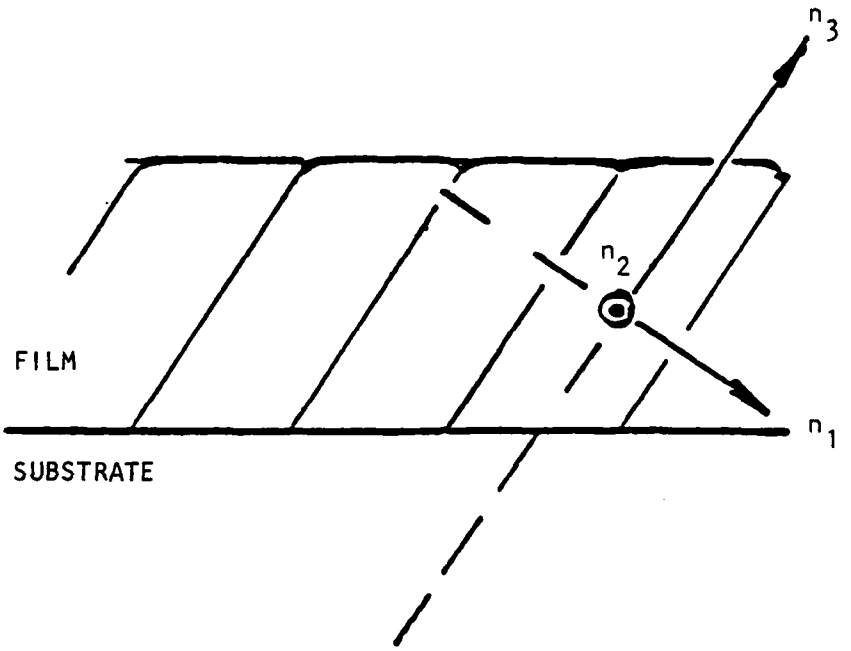


Fig. 7. Orientation of the principal directions and the associated indices for a film with oblique columns.

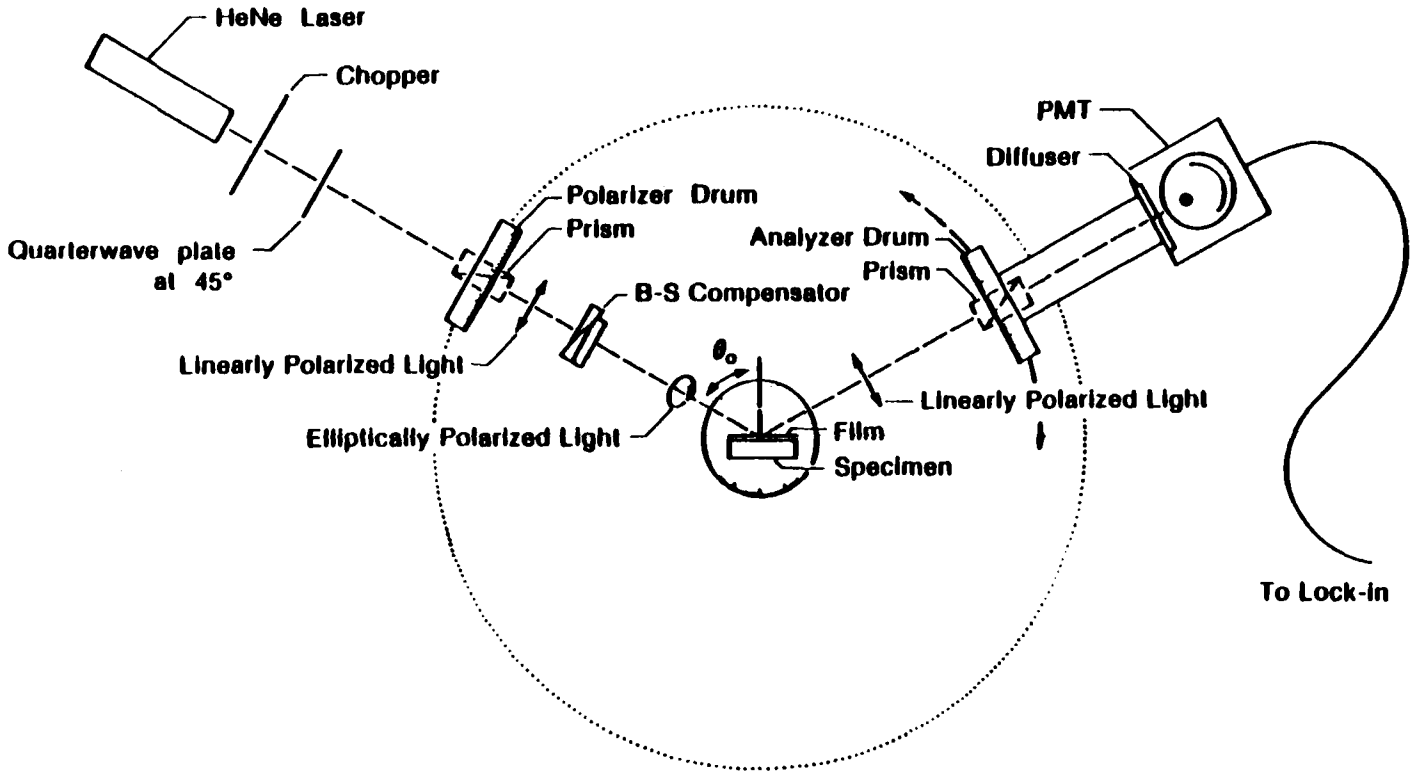


Fig. 8. Schematic diagram of experimental setup.

3. X-Ray Diffraction

On a truly microscopic level, crystal structure in thin films or bulk materials can be detected through x-ray diffraction. Bragg diffractometers operated by other University departments compared the UV irradiated and ion bombarded SiO_2, TiO_2, and ZrO_2 films to the materials before evaporation. The SiO_2 remained amorphous throughout, while effects on crystal structure were observed for the latter two materials. The Ti_2O_3 source material for TiO_2 had the expected x-ray signature, while thin single layers of TiO_2 lacked x-ray lines altogether, due either to their thinness or to an amorphous structure. On the other hand, multilayers of SiO_2 and TiO_2 revealed a crystalline, anatase structure for the TiO_2 where the crystallinity was reduced by UV irradiation. The crystalline structure vanishes completely for ion bombarded SiO_2-TiO_2 multilayers, providing additional evidence that increasing adatom mobility promotes amorphous, uniform, noncolumnar growth. For ZrO_2, strong lines indicate polycrystallinity before deposition that is clearly retained in monolayers. Ultraviolet irradiation and ion bombardment either preserve or enhance the crystallinity.

Returning to SiO_2/TiO_2 multilayers, if such samples are rotated 90 degrees in their own plane in the diffractometer sample holders, the pattern changes. This anisotropy is more pronounced for UV irradiated films, so much so that they appear almost amorphous at some orientations. Two explanations have been advanced: One argues that the tilted columns have elliptical cross sections, so that observation along the long axes results in more consistent crystal order and stronger x-ray lines. Another possibility is that the crystal planes are not exactly parallel to the substrate, so that rotation of the substrate changes the line strengths. If the former explanation holds, x-ray diffraction provides another sensitive probe to birefringence and columnar structure (Wharton, 1983).

4. Transmission Electron Microscopy (TEM)

Other means of observing birefringence involve imaging film surfaces or cross sections obtained by fracture of the substrate. The imaging can be either direct, as in scanning electron microscopy (SEM), or indirect with higher resolution, through carbon replicas, as in conventional TEM. Using the facilities available in other University of Arizona departments, replicas of conventionally deposited, UV irradiated, and ion bombarded ZrO_2-SiO_2 multilayers, were examined in a TEM. A distinction between conventional and UV irradiated layers was found, in that the latter did not show a distinctive "plateau" texture common in the normally deposited and fractured SiO_2 layers (Wharton, 1983).

5. Summary

The conclusions that can be drawn from the techniques and results described above include the superiority of ion-assisted deposition over other processes with respect to the improvement of film structure, the

importance of birefringence as a probe of columnar structure and as a possible means of producing films with specialized functions, and the need to refine measurement techniques to characterize our films more completely.

D. DEGRADATION PROCESSES

1. Introduction

Degradation of thin films under a range of environmental conditions, from high and/or variable humidities to intense photon fluxes, is now the major problem in their application. At one time, design of a coating to fill an optical need in the first place was a severe challenge, but powerful and readily available computers have eased this difficulty. Even the best designs for as-deposited optical performance, however, do not directly address the material problems that affect coating durability. In our research program, we have considered the influence of microstructure on two agents of coating damage--moisture and lasers. Of course, laser damage may be aggravated by the presence of moisture, so the subjects are related.

2. Moisture Damage

The transmittance of a narrowband filter is extremely sensitive to slight changes in the optical properties of its layers. By incorporating the material in question into a filter, this phenomenon can be used to reveal small optical changes caused by the adsorption of moisture in a multilayer coating. If the film is then monochromatically illuminated at the design wavelength, the areas of the film that transmit the beam as intended will be bright. In areas where the layer properties have changed, the monochromator must be tuned to the new passband at that point. By observing the film with a microscope or projecting portions of the filter into a camera, the pattern of defects can be studied with respect to the direction and degree of the shifts in transmission wavelength.

In our laboratory, this procedure was implemented by Lee (1983) with a simple system on a single optical bench. A tungsten-halogen lamp in a Bausch and Lomb lamphouse and a small, high-intensity Model 33-86-76 monochromator, also by Bausch and Lomb, illuminated a small, aluminum environmental chamber that contained the sample. The chamber was physically connected to one of many adjacent vessels that contained saturated salt solutions, over which constant humidities can be maintained. Entrance and exit windows permitted sample illumination and observation by either a small microscope or by Polaroid photography.

Metal-dielectric filters, a simple glass/metal/dielectric/metal/air design, can isolate the properties of the dielectric if a metal relatively impervious to the effects of water is used. Silver serves well, since it has a high packing density and is stable in humid atmospheres, as evidenced by other work we have done on silver with the surface plasmon technique. Several such filters were used in this program, but these filters had several disadvantages. Their transmittances are low, and tuning the filter to the correct peak wavelength is difficult. All-dielectric filters avoid these problems.

The narrowness of the bandwidth is proportional to the number of layers, which is limited in practice by the tedium of the evaporation process and the cumulative effects of small amounts of absorption.

The multilayer design used most often has 19 layers, with high (H) and low (L) index quarterwaves in the following sequence:

$$\text{Glass}/(HL)^4HLLH(LH)^4/\text{Air}$$

The superscript refers to a fourfold repetition of the (HL) period. In some films, the high index material was ZnS, which has a high packing density and is relatively unaffected by water, allowing us to assume that the main effect of water adsorption is on the low index cryolite. Other films studied used ZrO_2 and TiO_2 as the high-index layers and SiO_2 as the low-index layers.

Study of water adsorption by these films led to significant quantitative results, which will be included and reviewed in Chapter III. In brief, the appearance, as well as the number, of moist patches observed is significant. For example, patches in zirconia/silica filters have much less definite boundaries than do zinc sulfide/cryolite filters. It is clear that zirconia is much more porous than silica, but the comparison between zirconia and cryolite is more difficult. The films were baked to desorb the water, and it was found that although much water was driven off, some remained. Further exposure to water enlarged the patches again, but boundaries were blurred and/or different, indicating subtle, permanent changes caused by liquid water.

3. Laser Damage

We hypothesized that many defects associated with laser damage in dielectric coatings may be a result of their columnar, porous microstructure, and that these defects limit the optical performance of coatings at high laser powers. The objective of this experiment was to investigate the hypothesis with respect to three types of film defects. Narrowband dielectric filters were chosen as the test specimens because one can view, with a microscope, film defects in monochromatic light. Multilayer filters of ZnS/Cryolite and ZrO_2/SiO_2 were deposited and examined by Desandre (1984) for moisture patches, penetration sites, and pits.

Examples of these defects and adjacent intact portions of the film were irradiated with a continual-wave (cw) 514-nm Coherent Innova argon laser (Model 90-4). The beam was focused onto the test sample with a microscope. The same microscope was used for inspecting the sample before and after laser exposure. Damage was revealed in the same way as in the moisture damage experiment described above, in that a monochromatic beam was tuned to the passband of the filter and projected through the filter from the back. Damaged areas no longer transmitted as well and were easily distinguished. At the sample, output powers as high as 2.5 W were produced. Using pinholes, scans across the beam in its focal plane revealed a Gaussian profile with a

$1/e^2$ waist diameter of 115 μm. The experimental procedure began with centering the defect to be irradiated in the field of the microscope. Next the laser beam was directed through the microscope to the sample for a range of times and at a range of power levels.

Evaluation of the data in terms of the damage frequency was made and compared to theoretical damage probability distributions from a degenerate defect ensemble model, which treats every defect as capable of inducing laser damage at an identical nonprobabilistic onset value (Porteus and Seitel, 1984) (see Table 1). Laser damage onset values were approximated for the three types of defects and for nondefective areas that were examined. Because time and resources for the experiment were limited, we had to compromise between the number of tests and the exhaustiveness of the diagnostics. We do not believe that the errors resulting from the restricted sample size and diagnostic measurements are large enough to invalidate the findings.

Four conclusions can be drawn

(1) From the values at the 50% damage threshold, and for the defect types investigated, the ZrO_2/SiO_2 film is more susceptible to laser damage.
(2) Penetration site defects have the lowest 50% damage threshold and damage onset values for both filter designs.

(3) For the ZrO_2/SiO_2 filter, the onset values for both the clear areas and moisture patches were nearly equal and were larger than those of penetration site defects. However, the steep slope in the moisture patch damage frequency curve indicates a greater number of defects per unit area than in the clear portions of the film.

(4) Results of the measurements on the ZnS/cryolite filter are even more inconclusive than those on the ZrO_2/SiO_2 sample. However, adsorption site defects do show less laser damage resistance than clear areas or other defects present in the film.

In summary, certain defects influence laser damage in the dielectric narrowband filters tested. Moisture penetration sites appear to be most responsible for lowering the damage threshold. Although the influence of other defects on laser damage is not clear, moisture patch areas may contain a greater number of defects.

Table 1

Summary of Damage Onset Values and Damage Defect Models

Defects	ZrO_2/SiO_2 Damage Onset (10^3 W/cm^2)	Damage Model	ZnS/Cryolite Damage Onset (10^3 W/cm^2)	Damage Model
Clean area	1.0	Degenerate $N \approx 1$	4.0	?
Adsorption sites	0.5	Degenerate $1 < N < 2$	0.5	Nondegenerate
Moisture patches	1.0	Degenerate $N > 6$	2.0	?
Pit defects			6.0	?

E. SIMULATIONS OF THIN FILM GROWTH

1. Two-Dimensional Hard Sphere Model

The advent of rapid scientific progress several hundred years ago can be correlated with the addition of controlled experiments to the largely theoretical approach of ancient and medieval philosophers. With the arrival of powerful and accessible computers, a third avenue of enquiry has been opened, that of simulation. By reproducing certain conditions in a mathematical model and writing a computer program, the implications of those conditions can be investigated to a degree that depends mainly on the speed and memory of the computer. The growth of thin film structures from individual atoms is difficult to predict from a purely theoretical basis, and is not easily controlled or observed in real time with existing techniques. Computer simulation of this process, however, has been implemented and continues to be an instructive means of elucidating film microstructures.

A notable early effort in modeling thin film growth was made when Henderson and others (1974) modeled a gas with individual hard spheres, directed them at random on the growing surface, and permitted them to move to the nearest triangular pocket formed by three other spheres. For normally incident particles, such simulations reproduce the columnar structure that frequently dominates thin films. When the spheres are obliquely incident, tilted columns are reproduced, with the column angle with respect to the film normal, β, always less than the angle of vapor incidence, α. Niewenhuizen and Haanstra (1966), first noted that these angles were related by the expression: $2\tan\beta = \tan\alpha a$. Qualitatively, "shadowing" by particles already present, combined with limited mobility, are responsible for the structure. Further efforts by Dirks, Leamy, and Gilmer (1977, 1980) presented a more detailed picture of the columnar growth process.

With the essential features of these models confirmed, more sophisticated programs have been written to simulate more realistic structures. At the Optical Sciences Center in early 1983, Sikkens (1983) developed two- and three-dimensional modeling programs for microcomputers in BASIC and later in PASCAL. One of his concerns was film porosity--the structure and topology of the intercolumnar voids, often filled or lined with water, that permeate the film. When multilayer filters evaporated over a range of angles were simulated, the models began to deal with anisotropy as well.

Late in 1983, Bangjun Liao, a Visiting Scholar from the Peoples Republic of China, arrived with a strong interest in thin films and in simulation. He extended Sikkens programs through and beyond the end of the contract period. A recent paper of his (Liao and Macleod, 1985) includes this work. The program can be adjusted to accommodate varying numbers of unit adatoms. The resulting matrix cells are dimensioned so that no more than one disk can reside in each cell. The film cross section is organized as an NY by NX matrix, where NY and NX are the total numbers of cells perpendicular to and in the plane of the substrate,

respectively. Each cell has unit size. The row at the bottom represents the substrate. The y and x coordinates of a disk are stored in cell [i,j], where i = trunc(y), j = trunc(x). In all but one special version of the program, the coordinates are truncated to save space in memory, where they are held in two separate integer arrays, containing i and j values. In the epitaxial version, the original [y,x] values remain real to improve calculation accuracy. Of course, with the truncating versions, transformations back from "cell" space to "coordinate" space will contain small displacements from the original positions. A typical model is 85 disks wide and 52 disks high. Disks are incident at random lateral positions at a angle fixed by the program.

The disk diameters must be greater than $\sqrt{2}$ so that one cell cannot be occupied by two particle centers. Also, to satisfy the periodic boundary conditions, the diameters of the particles must be chosen so that the number of particles required to span a horizontal layer is close to an integer. Otherwise, the modeled part of a film could not be extended indefinitely without leaving gaps between the modeled segments.

Disks are projected toward the substrate from random positions along a plane above the film. The angle at which the disks are directed toward the growing film can be set anywhere from normal to grazing incidence. When the vapor stream is obliquely incident, tilted columns appear, just as observed in real films. The columnar tilt follows the tangent rule given above, $2\tan\beta = \tan\alpha$. This relationship has been extensively explored in our work, since it is central to the understanding of film anisotropy.

2. Relaxation and Mobility

A critical set of assumptions involves the mobility of the disks after their arrival at the growing film surface. We have presumed that if the adatoms retain sufficient mobility to minimize their surface energies, the film will tend toward a smooth, dense configuration. On the other hand, if the adatoms are assumed to have only limited mobility, so that shadowing is important, a more open matrix will grow. These hypotheses have been borne out by simulations. Liao improved the two-dimensional hard-disk model by elaborating the important relaxation process.

The sticking coefficient is assumed to be unity. However, after impact, an incident disk may move from one adsorption site to another until certain relaxation conditions are obtained, such as contact with two other disks. The average distance traveled by disks, $\mathbf{x}$, is normalized by their diameters, d, to yield the parameter $\mathbf{x/d}$, which is regarded as a quantitative measure of their mobility. An approximate expression for this parameter is

$$\frac{x}{d} = 0.6R_1 + 1.6(R_2-R_1) + 2.6(R_3-R_2) + 3.6(R_4-R_3) + 4.6(1-R_4). \quad (2)$$

The values [R1, ($R - R_1$), ..., ($1 - R_4$)] represent the rates of the number of disks jumping (1, ..., 5) times from the point of impact, respectively. The factors (0.6, 1.6, ..., 4.)] are the average distances traveled by these disks. The jumping time of each disk is determined randomly, and the maximum number of jumps, 5 in this version, can be easily changed to another value. By appropriately selecting the numbers (R_1, ..., R_4), the disk mobility can be controlled. In one of the modified versions the disks moving left and right may have different sets of jumping rates to simulate the anisotropic relaxation processes having anisotropic relaxation. The first jump of a disk determines the direction of subsequent jumps.

As the computation proceeds, some "process parameters" are calculated and stored in another file: the total number of deposited disks, the number of disks moving left and right, the average distance x/d traveled by the disks, and the distributions of disk jumping rates and relaxation distances. An auxiliary program also computes the packing density of the deposited film by counting the occupied cells in the [i,j] array, the column angle, and the angular autocorrelation function.

3. Extensions of the Program

When the contract ended in August 1984, Liao was engaged in further extensions of the program. One aspect included the effects of changing disk size to simulate "two-layer" systems, a factor in substrate quality, since the earlier systems assumed perfectly smooth substrates. Attempts to reproduce the effects of substrate irregularity have been made by superposing rectangular depressions and elevations on flat substrates. The effects of multiple sources and substrate rotation have also been modeled in this program. Aside from such elaborations on the model during simulation, software is being developed to characterize the resulting models in terms of packing density, column angle, and anisotropy. These extensions are contained in specialized modules that can be called from the main program to simulate certain facets of film growth. To summarize, the two-dimensional hard sphere model has attempted to simulate nodule formation, substrate defects, two incident angles due to two-source vaporization, multiple incident angles due to substrate rotation, anisotropic relaxation, oblique incidence (mentioned above), and epitaxial growth.

F. PUBLICATIONS

During the three years of the contract, a number of papers, talks, and dissertations were presented to the optical community. The references are listed in two sections to reflect this contribution. Papers by faculty, staff, students, and visitors at the Optical Sciences Center during the period 1981-1985 are presented here. Specific citations from the text, including those listed in this section, are found in Part III at the end of this report.

Bovard, B., Saxe, S. G., Messerly, M. J., Van Milligen, F. J., and Macleod, H. A., "Techniques for Thin Film Optical Constants Derivation from In-Situ Transmission Measurements," Paper presented at the 1984 Annual Meeting of the Optical Society of America, San Diego, California, October 29-November 2, 1984. Abstract appears in J. Opt. Soc. Am. A, **1**, (December, 1984).

Bovard, B., Van Milligen, F. J., Messerly, M. J., Saxe, S. G., and Macleod, H. A., "Optical Constants Derivation for Inhomogeneous Thin Films from In Situ Transmission Measurements," submitted to Applied Optics.

Borgogno, J. P., Flory, F., Roche, P., Schmitt, B., Albrand, G., Pelletier, E., and Macleod, H. A., "Refractive Index and Inhomogeneity of Thin Films," Applied Optics, **2**, 3567-70 (15 October 1984).

DeSandre, L., Hodgkinson, I. J., Macleod, H. A., Messerly, M. J., Saxe, S. G., and Wharton, J. J., "Ion-Induced Desorption of Moisture in Optical Coatings," Technical Digest on Optical Interference Coatings, Topical Meeting on Optical Interference Coatings, Monterey, CA, April 17-19, 1984, Optical Society of America.

Flory, F., Schmitt, B., Pelletier, E., and Macleod, H. A., "Interpretation of Wide Band Scans of Growing Optical Thin Films in Terms of Layer Microstructure," Proc. SPIE **401**, 109-16 (1983).

Hodgkinson, I. J., Jacobson, M. R., Lee, C. C., Macleod, H. A., Potoff, R. H., Sikkens, M., and Sprague, R., "Anisotropic Moisture Penetration in Optical Coatings," presented at the 1983 Annual Meeting of the American Optical Society, New Orleans, Louisiana, October 17-20, 1983.

Hodgkinson, I. J., Horowitz, F., Jacobson, M. R., Lee, C. C., Macleod, H. A., Sikkens, M., and Wharton, J. J., "Deposition, Characterization, and Simulation of Thin Films with Form Birefringence," Technical Digest on Optical Interference Coatings, Topical Meeting on Optical Interference Coatings, Monterey, CA, April 17-19, 1984, Optical Society of America.

Horowitz, F., and Macleod, H.A., "Form Birefringence in Thin Films," Los Alamos Conference on Optics, 1983, and Proc. SPIE **380** (1983).

Jacobson, M. R., Horowitz, F., and Liao, B., "Deposition, Characterization, and Simulation of Thin Films with Form Birefringence," Proc. SPIE **505** (1984).

Liao, B. J., and Macleod, H. A., "Thin Film Microstructure Modeling," presented at the Southwest Conference on Optics, Albuquerque, NM, March 4-8, 1985.

Martin, P. J., Macleod, H. A., Netterfield, R. P., Pacey, C. G., and Sainty, W. G., "Ion-Beam Assisted Deposition of Thin Films," Appl. Opt. **22**, 178-184 (1983).

Saxe, S. G., Messerly, M. J., DeSandre, L., and Macleod, H. A., "The Effect of Ion Bombardment on Moisture Sensitivity of Optical Thin Films," Conference Paper, Arizona Chapter, American Vacuum Society Fourth Annual Symposium, Tucson, AZ, March 1, 1984.

Saxe, S. G., Messerly, M. J., Bovard, B., DeSandre, L., Van Milligen, F. J., and Macleod, H. A., "Ion Bombardment-Induced Retarded Moisture Adsorption in Optical Thin Films," Applied Optics, **23**, 3633-3637 (15 October 1984).

Sikkens, M., Hodgkinson, I. J., Horowitz, F., Macleod, H. A., and Wharton, J. J., "Computer Simulation of Thin Film Growth: Applying the Results to Optical Coatings," Proc. SPIE **505** (1984).

Van Milligen, F. J., Bovard, B., Jacobson, M. R., Mueller, J., Potoff, R., Macleod, H. A., and Shoemaker, R., "Development of an Automated Scanning Monochromator for a Balzers 760 Evaporation System," Poster presented at the 1984 Annual Meeting of the American Optical Society, San Diego, California, October 29-November 2, 1984. Abstract appears in J. Opt. Soc. Am. A **1** (December, 1984). Submitted to Applied Optics.

Thesis

DeSandre, L., 1984, Laser Damage Measurements on All Dielectric Narrow Band Filters.

Dissertations

Browning, S. D., 1983, Electron Bombardment of Certain Thin Films during Deposition.

Horowitz, F., 1983, Structure-Induced Anisotropy in Thin Films.

Lee, C.C., 1983, Moisture Adsorption and Optical Instability in Thin Film Coatings.

Wharton, J.J, Jr., 1984, Microstructure Related Properties of Optical Thin Films.

PART II

DETAILED ACCOUNT OF THE SCIENTIFIC RESULTS

Part I of this report contains a summary of the project, its objectives, and the progress made toward fulfilling them. Part II contains a more detailed account of the scientific achievements including those parts that were sufficiently well developed to warrant publication. Wherever possible, the published accounts are used and included as appendices. Short commentaries have been added in order to connect these various parts together and to explain the way in which they fit into the overall goals of the project. So that it should not be necessary to refer to Part I in order to read Part II, some material in Part I is repeated.

A. INTRODUCTION

This report describes the scientific results of a three-year fundamental study supported by the Defense Advanced Projects Agency, and administered and monitored by the Naval Weapons Center, China Lake. The objectives of the study were broad and gave us considerable freedom to pursue what was perceived as fruitful research topics in the general area of vapor-deposited optical thin films. Several broad topics were addressed in the study, ranging from the measurement of fundamental film properties to details of the deposition process. The thread that runs through all of them is film microstructure.

Thin films are often considered to be like bulk material with one very small dimension. This is the ideal model that is commonly used for the calculation of their optical properties and for coating design. Real thin films differ from this model in a number of respects, and the differences are responsible for most of their problems (Macleod, 1982). In particular, there is almost invariably a disappointing gap between the performance of real thin film multilayers and ideal predictions. Thin film performance rarely, if ever, exceeds what we might expect from bulk material of the same dimensions.

The reason for the unfortunate deficiencies are largely connected with film microstructure. Evaporated thin films have a columnar microstructure that includes a large internal surface area around the columns and a large internal void volume between them. An important parameter directly associated with this microstructure is packing density, p, defined as:

$$p = \frac{\text{volume of the solid part of the film}}{\text{total volume of the film}} .$$

or

$$p = \frac{\text{columns}}{\text{solid plus voids}} .$$

It is normally in the range 0.7 to 1.0 and most frequently between 0.8 and 0.9. The lower the packing density, the more the film departs from ideal bulk-like material. The columnar microstructure has enormous repercussions on film properties of all kinds: It (1) reduces film density below bulk values; (2) induces considerable internal stress; (3) reduces film durability; (4) lowers the refractive index of dielectrics and increases losses in metal films; (5) permits the adsorption and desorption of atmospheric constituents, especially water, which renders the films unstable both optically and mechanically; (6) induces anisotropy and inhomogeneity of all film properties particularly optical; and (7) makes film performance sensitive to preparation conditions. Not only is the regular microstructure far from ideal, but related defects such as nodules cause further problems. It is not an exaggeration to state that 90% of the troubles with thin film coatings are traceable to microstructure-induced effects.

The structure is columnar, but although the columns in a given film are of similar size, they appear to vary with film thickness. Thick films have larger columnar diameters than thin films. The reason for this phenomenon has been given by Messier (1981). The basic building unit is of small dimensions. The structure of very thin films consists of a close-packed array of features some 2 or 3 nm in diameter. As the film grows in thickness, the length of these dendritic features increases until gradually they are pulled into contact by attractive forces to form units of larger diameter. As the film thickness increases, these larger units are combined into still larger units, and so on. Since the columnar structure exists in virtually all evaporated thin films, it must have a physical rather than a chemical origin. The primary causes of columnar growth are shadowing of parts of the film by material that has already been deposited, and the limited mobility of condensing atoms or molecules, which make it difficult for them to enter the shadows once they have condensed. Mechanical models of film growth that include these two effects reproduce well many of the features seen in real thin films.

The account that follows begins with the modeling of film growth using a mechanical model but implemented on a computer. It then considers some aspects of microstructure-induced thin film behavior, in particular optical anisotropy, optical inhomogeneity, and moisture adsorption. Finally, techniques for the modification of film microstructure are considered. The order is chosen to be logical rather than chronological.

B. THEORETICAL STRUCTURE MODELING

Much can be learned about layer microstructure and its origins from computer models of film growth. Perhaps the most successful published model to date is the two-dimensional approximation of Dirks and Leamy (1977) in which the molecules are represented by hard disks that arrive at the growing film at random lateral positions from a fixed direction corresponding to the source direction. The molecules either have zero mobility, so that they stick where they land, or limited mobility, in which case they can roll into the nearest position where they are supported on two points (three if they were spheres in a three-dimensional model). The results support the theory that the columnar structure of the films is due to self-shadowing within the growing film (a molecule being unable to reach the area shadowed from the evaporation source by previously deposited molecules) combined with the limited mobility of the condensing evaporant on the substrate, which prevents later molecules from migrating into the shadows of previous ones. The zero-mobility case produces long thread-like growths with low packing density, but the limited-mobility case reproduces a dendritic growth that is similar to what is seen in practice. At first sight there are some immediate problems of scale. The dendritic features of the model are an order of magnitude smaller than the columns that are seen in films of normal thickness. Messier (1981), however, has shown that the real structure of thin films is a hierarchical one in which there is a continual clustering of smaller units into larger ones as film thickness increases. The basic units are of a size comparable to those of Dirks and Leamy. The rigid disk model has been successful particularly in reproducing an empirical law of deposition that relates the angle of inclination of the columns, β, to the angle of incidence of the vapor, α, by a simple expression,

$$2 \tan\beta = \tan\alpha$$

known as the tangent law.

The model used by Dirks and Leamy in their original publication was mechanical and operated by hand, but the principles can readily be programmed for computer calculation. As a first step it was decided to use one of our small laboratory computers to reproduce the Dirks and Leamy model and repeat some of their results. Although the existing model confirmed the tangent law and the general appearance of the film microstructure, the packing densities achieved were well below values for normal optical thin films. All the published models used a fixed direction of incidence unlike the conditions in an optical thin-film coating plant where rotating substrates are subjected to a range of angles of incidence. It was not immediately obvious that shadowing would be as effective in the presence of varying incidence angles. We hoped also to examine the generation of defects in the films.

The first computer-implemented model assumed a featureless flat plane for the substrate just as the Dirks and Leamy version did. This was almost immediately changed to a regular array of close-packed disks.

The first runs of this modified model gave the expected dendritic outgrowths from the substrate, but the growth was perfectly epitaxial. Every molecule was in perfect register with all other molecules in the film and substrate. Nevertheless, the usual void structure was present and, except for the long-range order, the film was normal. This result emphasizes the fact that epitaxial growth does not necessarily imply the absence of voids. To make the growth more realistic, the first layer deposited on the substrate was assumed to have zero mobility, and this broke up the epitaxy. Dendrites were still often single crystals, but the orientation varied from one dendrite to another, and the typical voids were also present. In the Dirks and Leamy work, the epitaxial growth was prevented by including a small quantity of molecules of different size in the evaporant. Later versions of the computer model assumed a different size for the substrate molecules and normal mobility for those of the condensing evaporant, and this too gave polycrystalline columns.

Using the model, films have been deposited at various angles of incidence. Some of these results are shown in Fig. 9. The results have been analyzed in terms of film density, column orientation, and column size.

Packing density is calculated with reference to perfect hexagonal packing, which has the highest possible density and is therefore designated as unity. There are difficulties in making density measurements because of the uncertainty in measurement of film thickness. The density is therefore determined in thin strips across the film parallel to the substrate. There is usually a disturbance next to the substrate and next to the outer surface, so only 29 inner strips are used for density calculations in each film. Figure 10 shows the variation of density as a function of the tangent of the angle of incidence, α, of the vapor during deposition, the error bars representing the variation of density in the various strips of each film. According to Dirks and Leamy, the relative density should vary linearly with $\tan\alpha$. It is difficult to say what the relationship is in Fig. 10. Possibly, a straight line could be drawn through the points up to $\tan\alpha = 4.5$, but points beyond that are certainly off the line. Note the rapid fall in density with oblique incidence of the vapor. There is no suggestion in Fig. 10 of a plateau at angles around normal.

Measurement of the column angles presents some problems, so it was decided to make the procedure as automatic as possible and to avoid subjective judgment, although some subjective element remained. An orientation function was defined, which measures the mean deviation of density along a line swept across the film inclined at a set angle to the substrate. Variations in density show variations that are a maximum when the line is parallel to the columns. For infinitely thick films and perfectly aligned columns, the normalized orientation function should be unity if the line tilt is equal to the column orientation. Any other tilt will give zero. Some results are shown in Fig. 11. The orientation function shows a wide spread with little definite sign of orientation for $\alpha = 0$ but for oblique vapor incidence the orientation is much more

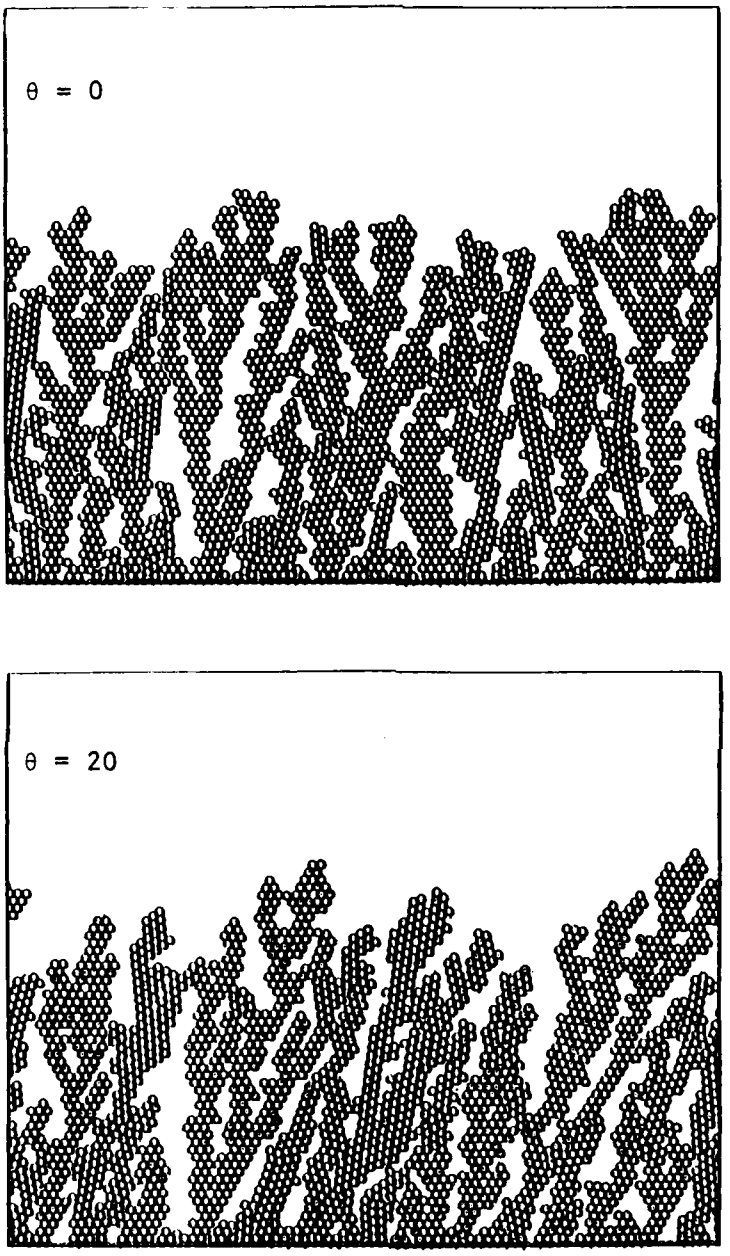


Fig. 9. Thin-film growth simulations. Theta is the angle of incidence of the vapor, NX and NY are the approximate dimensions of the film segments in terms of the molecular diameters. NX = 120, NY = 65.

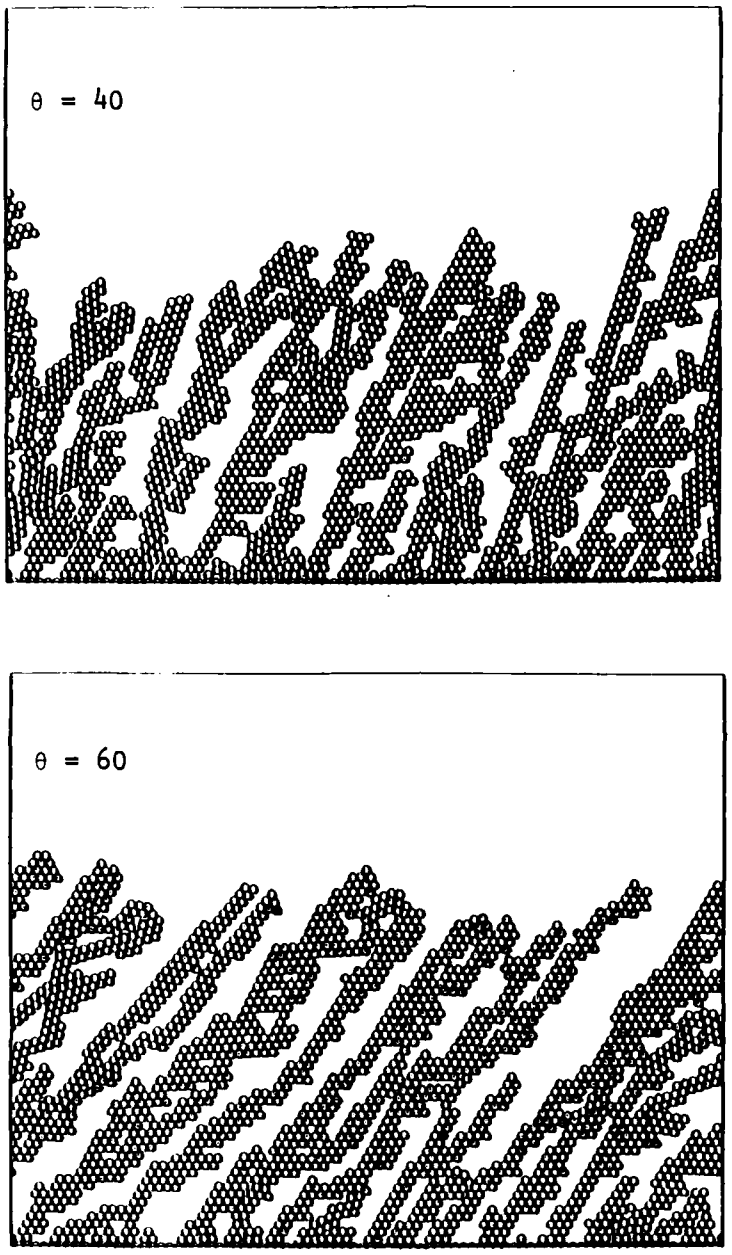


Fig. 9. (Continued) Thin-film growth simulations. Theta is the angle of incidence of the vapor, NX and NY are the approximate dimensions of the film segments in terms of the molecular diameters. NX = 120, NY = 65.

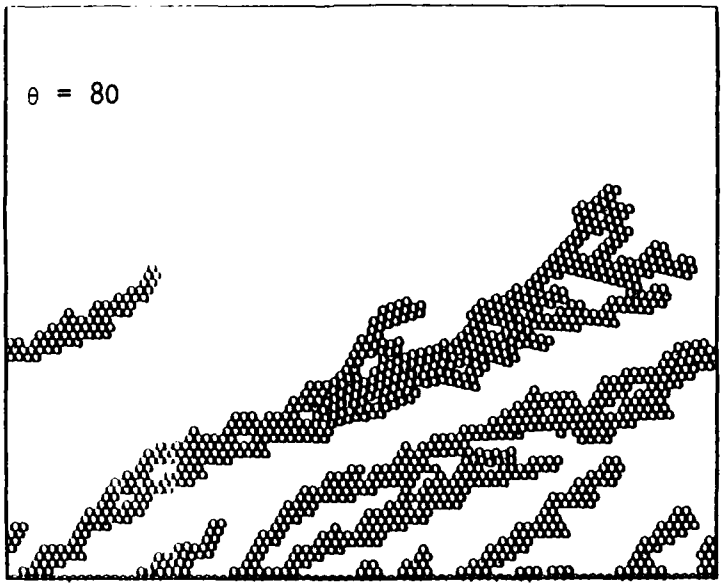


Fig. 9. (Continued) Thin-film growth simulations. Theta is the angle of incidence of the vapor, NX and NY are the approximate dimensions of the film segments in terms of the molecular diameters. NX = 120, NY = 65.

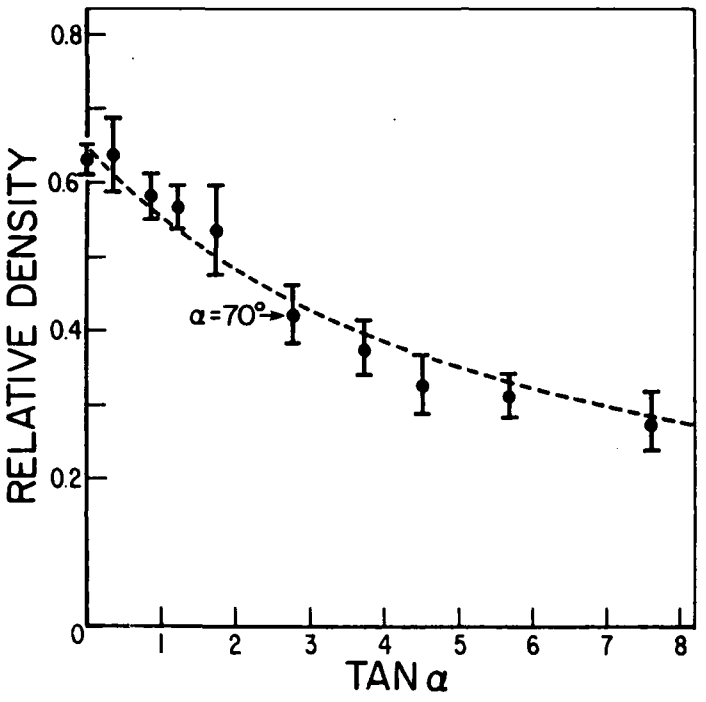


Fig. 10. Variation of calculated relative or packing density versus tanα where α is the angle of incidence of the vapor. The error bars are explained in the text.

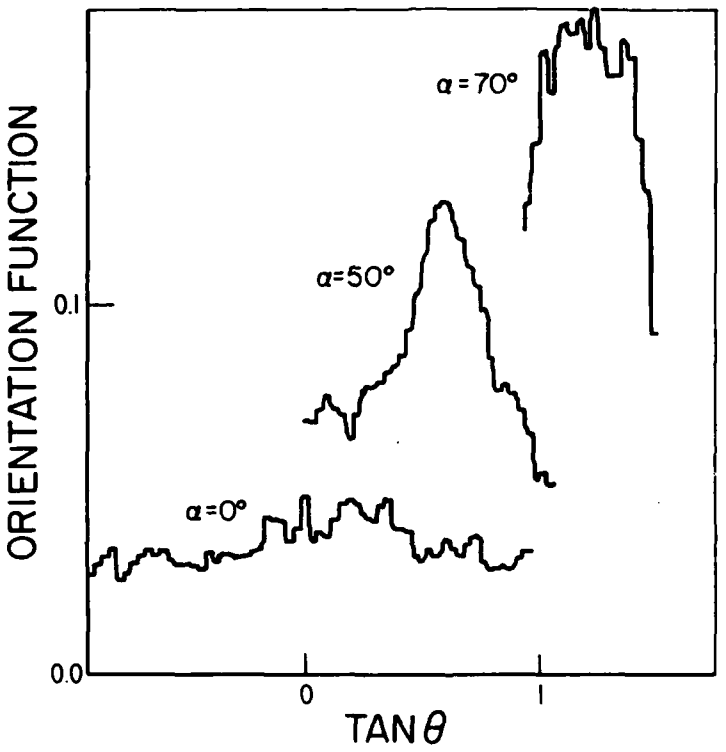


Fig. 11. Variation of the orientation function as a function of tanα, where is the angle of the reference line generating the function. Curves are drawn for three values of α, the angle of incidence of vapor, 0°, 50°, and 70°.

pronounced. The results of measurement of the range of films produced are plotted as tanβ against tanα in Fig. 12. The error bars are estimates of the error in reading the peak of the orientation function. The tangent rule

$$2 \tan\beta = \tan\alpha$$

is plotted as a straight line and is reasonably well satisfied up to $\alpha = 70°$. For greater values of α, β is too small. This may be an artifact of the periodic boundary conditions associated with the film segment, which may force orientations different from those expected in an infinite film. These angles are, of course, much larger than those in optical coatings of normal manufacture. Note that in the Dirks and Leamy paper, the periodic boundary conditions were found necessary for the tangent rule to be obeyed. However, in that paper the column orientation was subjectively compared with the tangent rule and the highest value of α for which the results are actually reproduced is 60°.

The size of the dendrites relative to the molecular size can be measured by the periodicity of the structure. The technique consists of sweeping a line parallel to the columns across the film and calculating the autocorrelation function of the density measured along the line. The form of the autocorrelation function gives the period. A typical plot is shown in Fig. 13, and a plot of the mean period against vapor angle α is given in Fig. 14. The error bars in this case are estimates of the likely errors in reading the results from the autocorrelation function plots. The limited size of the film segment could force a periodicity. The allowed values of such periodicities are shown in the diagram.

The concept of mobility of the adatoms or molecules can be represented by the parameter λ, defined here as the ratio of the average relaxation distance to the diameter of the particle. The average relaxation distance is the mean distance traveled by a condensing particle after impingement. For the zero mobility case, λ is zero and the simulations show that λ is approximately 0.6 for the limited mobility case. The packing density for $\lambda = 0.6$ is, as we have already seen, around 0.63 at normal incidence and therefore unrealistically low in comparison with normal optical thin films. The mean distance between pockets is roughly the diameter of an adsorbed atom or molecule, which can be referred to as an addisk. We can introduce the idea of an increased mobility by arranging that only a certain fraction, R_1, of the arriving addisks remain at the nearest stable position while a fraction R_2 continues to the next nearest, R_3 to the next again, and so on. The sum, ΣR is unity, and λ is given approximately by

$$\lambda = 0.6R_1 + 1.6R_2 + 2.6R_3 + \ldots + A_nR_n \ .$$

The set of R is chosen to give the desired value of λ using the above relationship, but the actual value achieved is calculated after each simulation run. Slight variations from one run to the next with exactly the same set of R values are found.

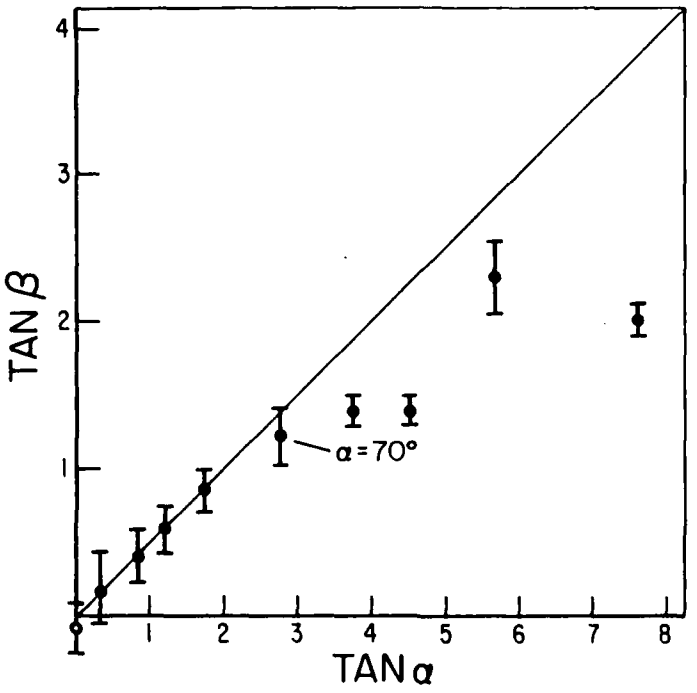


Fig. 12. The relationship between column angle β and vapor incidence α calculated from orientation function plots as in Fig. 11.

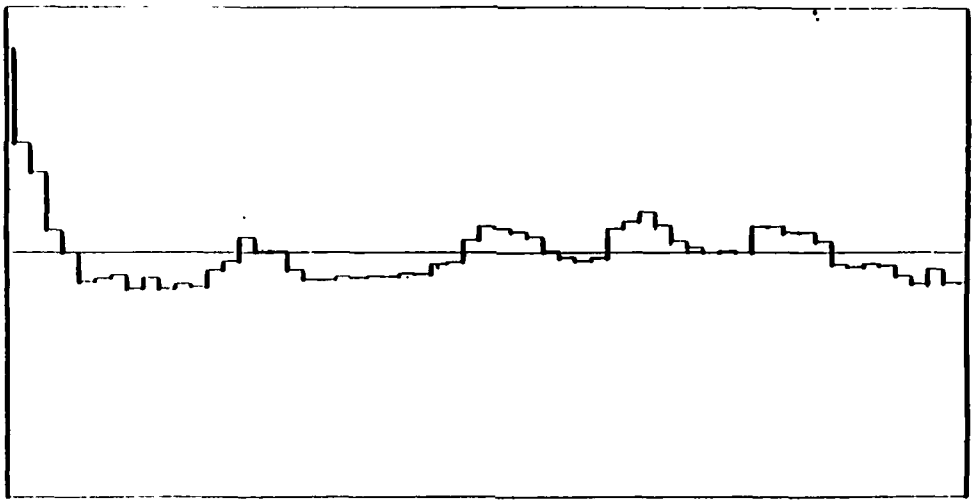


Fig. 13. Typical plot of the autocorrelation function of density measured along a line parallel to the columns. This example is for a vapor incident angle of 60°. The abscissa is the displacement of the density function in molecular units.

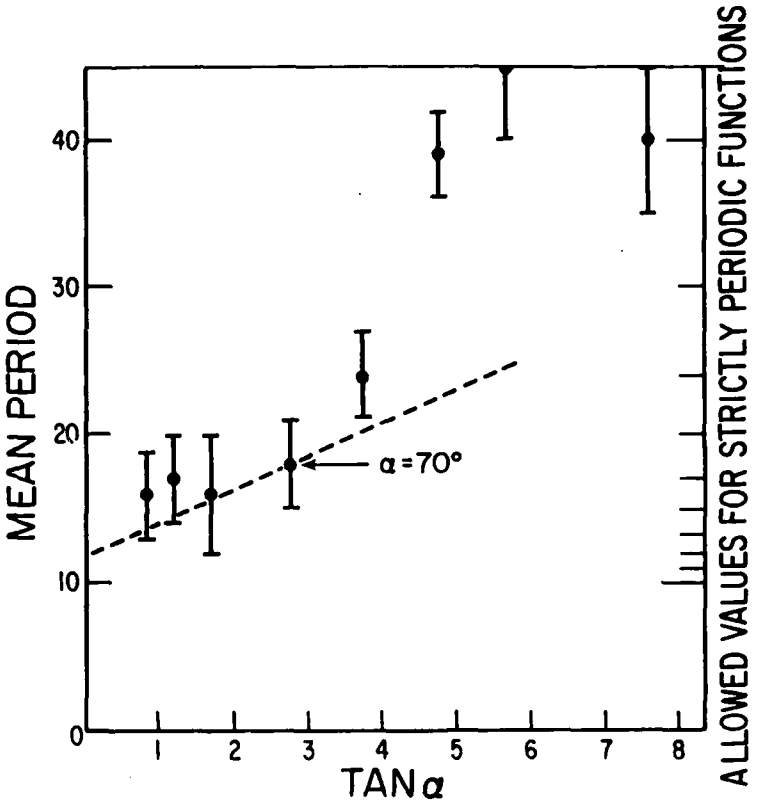


Fig. 14. Mean period in molecular units against tanα, where α is the angle of vapor incidence. The plots of autocorrelation function for $\alpha = 0^{\circ}$ and $\alpha = 20^{\circ}$ are very difficult to interpret and their values are shown as dotted circles. In the others the error bars represent likely errors in interpretation of the autocorrelation plots as in Fig. 13. The finite size of film segment and the periodic boundary conditons may force periodicities. Possible values are shown to the side of the diagram.

With an angle of incidence of 40° the relaxation parameter λ was varied from the 0.6 corresponding to the simple limited mobility to just over 3.0. The packing density of the films produced was measured along with the columnar orientation. The results are shown in Table 2.

Table 2

Packing Density and Columnar Angle
as a Function of Relaxation Distance

Incident Angle 40°		
Average Relaxation Distance (λ=X/D)	Density	Columnar Angle (Degrees)
0.590	0.593	26.9
1.106	0.666	32.4
1.506	0.725	26.9
1.794	0.777	28.4
2.065	0.780	34.9
2.686	0.780	32.4
3.117	0.806	38.4

The value of 2.065 for λ appears fairly realistic with a packing density of 0.780. This is selected as the standard value in what follows.

Note that the columnar orientation in Table 2 is now departing from the tangent law. This is not considered in any way a defect of the model.

There are many accounts in the literature of violations of the tangent law, and this modification of mobility gives us the opportunity of studying such violations. From the model it appears that the tangent law applies to the class of depositions where the mobility of the condensing adatoms or molecules is quite small.

Next, the relaxation parameter, λ, was held constant while the angle of incidence of the vapor, α, was varied. Film packing density and column orientation angle, β, were calculated. Results are shown in Table 3.

Table 3

Effect of Angles of Incidence on
Packing Density and Column Orientation

α	Average Relaxation Distance (X/D)	Density	β	ϕ	$\tan^{-1}(1/2 \tan\alpha)$
0°	2.073	0.810	3.0°	0.0°	0.0°
20°	2.075	0.773	17.6°	18.3°	10.3°
30°				26.2°	16.1°
40°	2.065	0.780	34.9°	33.3°	22.8°
50°	2.111	0.735	41.6°	39.7°	30.8°
60°	2.075	0.720	46.3°	45.5°	40.9°
70°	2.118	0.583	54.4°	50.8°	53.9°
75°	1.911	0.519	63.4°	53.2°	61.8°

$$\phi = \alpha - \sin^{-1}\left[\sin^2\left(\frac{\alpha}{2}\right)\right]$$

The column orientation is clearly violating the tangent law. An attempt to fit the results to a better law is shown in the column marked ϕ. This is based on the idea of a mean pair orientation. That is, the direction defined by the angle of inclination ϕ is normal to the line joining the centers of addisks in the two extreme positions around an already condensed addisk on a flat surface. Figure 15 illustrates this case. The density does fall with increasing angle of incidence of the vapor but not as rapidly as was indicated in the earlier limited mobility studies. Now the packing density remains fairly high until angles of incidence of around 45°. This is consistent with studies of the variation of film durability with increasing angle of incidence by Holland and van Dam (1956), for example.

Figure 16 shows a simulation of the effect of a small scratch or indentation in the surface of the substrate. The angle of incidence in this case was 40°, and the effect of the scratch propagates to the surface in the form of a column. There seems to be no suggestion of nodular growth in this case, and although there is a corresponding depression in the upper surface of the film, it tends to be lost in the intrinsic roughness of the film itself. Could rotation of the substrate during deposition help to eliminate the effects of such a scratch altogether? The effect of substrate rotation in which the angle of incidence oscillates through a range of 50° on either side of the normal is shown in Fig. 17. The depression due to this somewhat smaller pit is

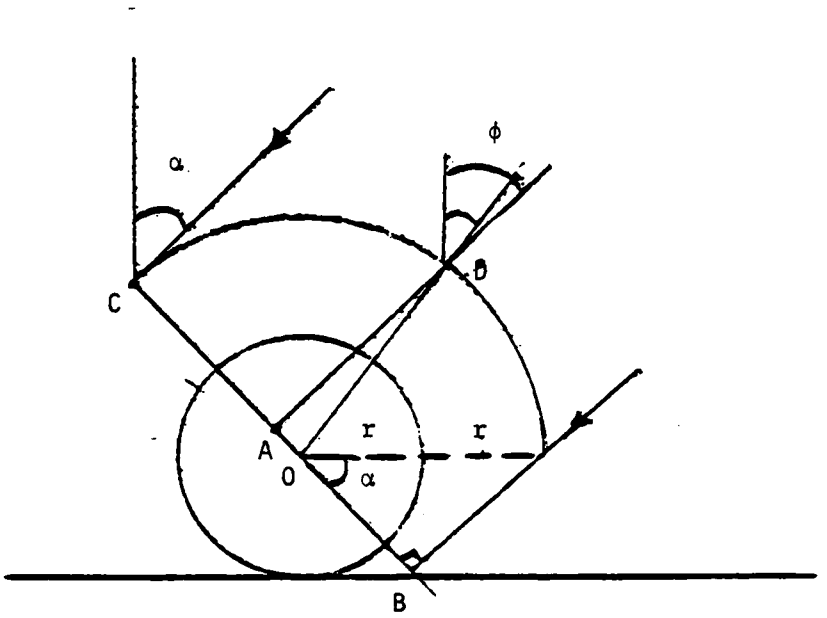


Fig. 15. O is the center of an addisk already on the substrate surface. α is the vapor incidence. Lines inclined at angle α passing through B and C represent the extreme tracks of addisks that will make contact with O. A is the midpoint of BC and D therefore represents the mean of the range of positions possible for incoming addisks that make contact with O. The idea of mean pair orientation is derived from Dirks and Leamy (1977).

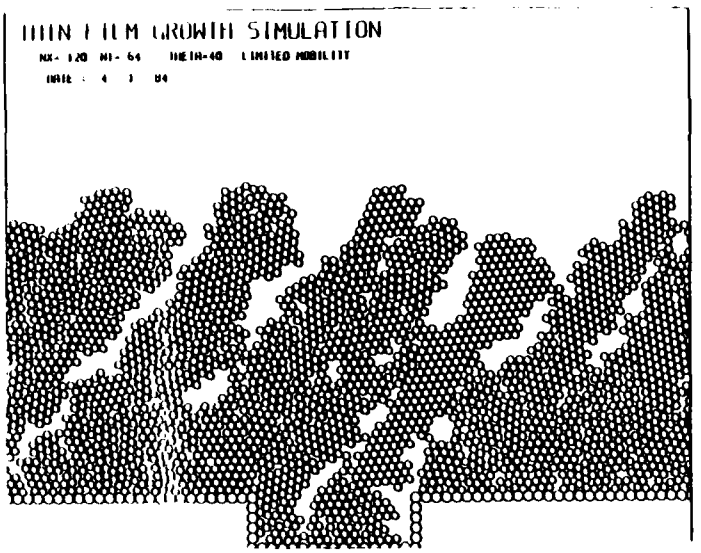


Fig. 16. Simulation of film growth over a scratch in the substrate. The angle of major incidence is 40°.

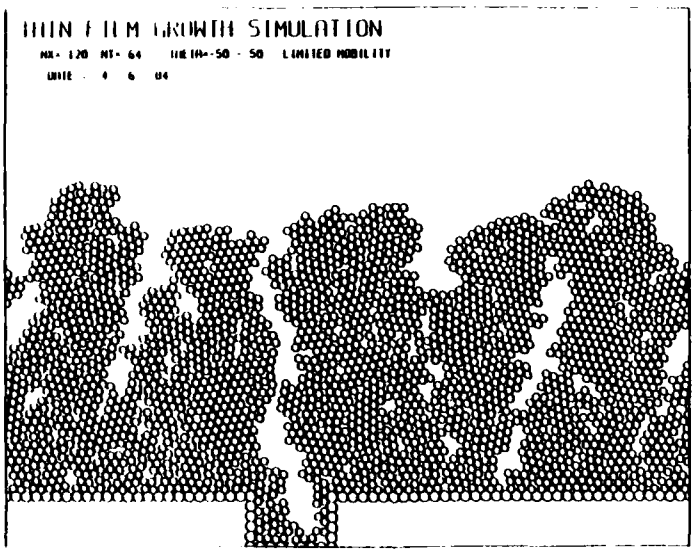


Fig. 17. Effect of substrate rotation in which the angle of incidence of the vapor varies from -50° to +50°. Note the fissure propagating upwards from the small scratch.

almost completely lost, but there is a fissure extending through the film from the substrate to the outer surface. Investigations, using the model, of density variations in films over such substrate defects shows virtually no effect. Table 4 summarizes the findings.

Table 4

Simulation of Scratch

	α	Density With Scratch	Density Without Scratch
Large Scratch	40°	0.785	0.780
	-50°+50°	0.756	0.766
Small Scratch	40°	0.776	--
	-50°+50°	0.768	--

Density variations are, however, definite in the case of projections from the substrate. These are summarized in Table 5. When the substrate is subjected to a range of angles of incidence of the arriving vapor, as in the case of substrate rotation, nodular projections tend to form. These are not as obvious when only one angle of incidence is involved.

Table 5

Simulation of Nodular Growth

	α	Density With Bump	Density Without Bump
Large Bump	0°	0.778	0.810
	40°	0.728	0.780
	-30°+30°	0.776	
	-20°+70°	0.702	
	-50°+50°	0.754	
Small Bump	0°	0.776	
	40°	0.764	
	-50°+50°	0.779	

Finally growth was simulated with dust particles on the substrate in Figs. 18 and 19. Here, with substrate rotation, there are unmistakable indications of nodular growth.

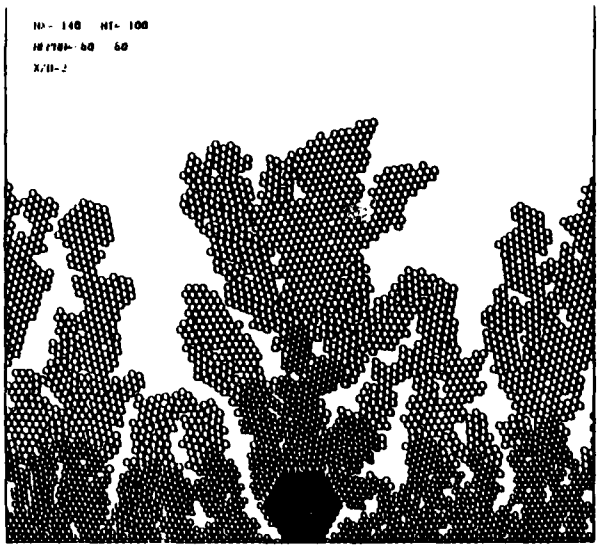


Fig. 18. Nodular growth in a bilayer above a dust particle on the substrate. Substrate rotation is assumed.

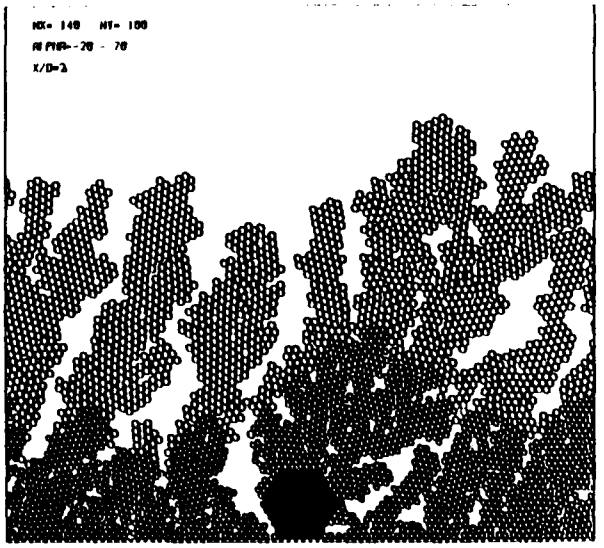


Fig. 19. Nodular growth above a dust particle. Substrate rotation is assumed but the angle of incidence varies from -70° to $+70^{\circ}$ so that the columns are inclined.

C. ANISOTROPY

Form birefringence in thin films has long been a subject of some interest. Bousquet (1957a) published an analytical treatment of the calculation of the optical properties of an anisotropic thin film. In the same year he reported (1957b) the detection of birefringence in calcium fluoride films that were uniaxial with optic axes perpendicular to the film surfaces and with $(n_o - n_e) = 2.5 \times 10^{-3}$. In a review written with Rouard in 1960 he warned of the problems caused by birefringence in the measurement of optical constants involving obliquely incident light. Rouard (1956) had already pointed out that provided the axes of the grains in the films were normal to the boundaries, then methods of measurement of optical constants that employ only normal incidence would not be perturbed. Recently King and Talim (1981) carried out a series of comparisons between various techniques of optical constant determination. Guided wave techniques showed a significant difference between indices measured for TE modes, 1.9887, from those for TM, 2.0015, at 632.8 nm in zirconium dioxide.

The columnar nature of the films strongly suggests that they should be birefringent with the principal axes of the dielectric tensor along the columnar direction (n_3), and normal to the columns both in the plane of incidence of the vapor (n_1) and normal to that plane of vapor incidence (n_2), Fig. 7. For films that are evaporated at normal incidence one would expect the birefringence to be uniaxial with the optic axis normal to the film surface and not detectable by purely normal incidence measurements. Normal incidence measurements would, however, permit us to infer the presence of birefringence in obliquely deposited films where biaxial birefringence could be expected with the optic axes in the plane of incidence of the vapor. Because obliquely deposited columns are less closely spaced in the plane of vapor incidence than normal to the plane, the birefringence could be expected to be characterized by a maximum index along the columns and by a minimum normal to the columns in the plane of incidence. The optic axes for a biaxial film would therefore be in the plane of vapor incidence.

Some measurements of anisotropic behavior in dielectric films have been made. In preliminary experiments, zirconium dioxide films evaporated at very high angles of incidence were found to be anisotropic with an effective $D_n = 0.042$ for propagation through the film at normal incidence. The transmittance of a film 4.6-mm thick is shown in Fig. 2.3 of the second part of this section taken from Horowitz's PhD dissertation. It acts almost as a halfwave plate. For a perfect halfwave plate, the transmittance at an orientation of 45° in 2.3(a) would be zero.

Two techniques have been pursued for the measurement of the principal indices of refraction of the films. One involved measurements on single layers and the other the construction and examination of multilayer narrowband filters. Both included normal and oblique incidence measurements, the single-layer measurements being rather more difficult and demanding, and both assumed that the orientation of the

columns in the films was known and used the tangent rule for this purpose. The tangent rule, discussed in section 1, gives the relationship between the angle of vapor incidence, α, and the column orientation angle, β, both measured with respect to the substrate normal:

$$\tan\alpha = 2\tan\beta.$$

The most detailed study of anisotropy in thin films was performed by Horowitz and Appendix A reproduces the central part of his PhD dissertation. Part of the study involved the development of techniques for the calculation of the optical properties of anisotropic multilayers. These were based on an original paper by Teitler and Henvis (1970). Some measurements were made on metal films, silver and aluminum evaporated at extremely oblique angles of incidence, which demonstrated that these metals acted as polarizers under such conditions. The high reflectance of wire grids when the electric vector is along the wires and high transmittance when the electric vector is normal to the wires is known as the Hertz effect. At first sight the results on metal films seem to be the opposite of the Hertz effect since the orientation of greatest transmittance corresponds to electric vector along the columnar direction in the films. However, the structural models dealt with in another section of this report show that the metal is much more closely packed in the direction normal to the columns and so the behavior is, in fact, consistent with the Hertz effect.

The bulk of the work under this heading dealt with the biaxial birefringence of dielectric films evaporated at oblique incidence, and in particular zirconium dioxide. The techniques developed for the measurement of the optical constants of single films used four measurements made using a converted ellipsometer. First, reference axes labelled s- and p-polarization were established for normal incidence, p-polarization corresponding to incident light with electric vector in the plane of vapor incidence and s-polarization normal to that plane. S-polarization was therefore along the n_2 axis. Next, a portion of the film was found that corresponded to a thickness for s-polarized light of an integral number of either quarter or half waves. Since the films were evaporated obliquely, they exhibited considerable thickness variations, and so this operation was not a problem. The second measurement was of the relative retardation of the sample at normal incidence for s- and p-polarizations. The third measurement was the ratio of the transmittances for s- and p-polarized light. Finally the Brewster angle of the film/air interface was found by the Abelès technique. These quantities are:

Λ_S = optical thickness for s-polarization = $m(\lambda/2)$ or $m(\lambda/4)$

$\Lambda_\Delta = (n_{po} - n_s)d$

$\psi_t = \arctan|t_{pp}/t_{ss}|$

θ_B = Brewster angle between film and air

Added to these measurements is the orientation of the principal axes of the film found from the tangent rule. The ellipsometer was set up with a HeNe laser; all measurements made were at 632.8 nm. The results for ZrO_2 films deposited at an angle of incidence of 65° are listed in Table 6.

The filters for the multilayer measurements had a $(HL)^4HHHH(LH)^4$ configuration in each case with a peak wavelength in the red around 630 nm. The high-index layers were either zirconium dioxide or titanium dioxide, and the low-index layers were silicon dioxide. Here, four measurements were made. These consisted of the peak wavelength of the filter for p- and s-polarized light, with the planes defined as above, at normal incidence and at 30° angle of incidence. Again, assuming the orientation of the columns in the films is known and assuming further that the birefringence is confined to the high index layers, the refractive indices can be found by fitting calculated transmittances to the measured results. Table 6 includes results found by this method for titanium dioxide and zirconium dioxide evaporated at an angle of incidence of 30°.

The measurements were made in air after deposition, so the films must have contained moisture. Since form birefringence is being dealt with (any strain birefringence has been estimated to be an order of magnitude lower), the raising of the index of the voids from a dry value of 1.00 to a wet value of 1.33 must reduce the birefringence. It is difficult to measure the principal indices in vacuo but possible to determine the wavelength shift between s- and p-polarization peaks at normal incidence. For filters having a peak wavelength of around 630 nm, the shift for zirconium oxide deposited at a vapor incidence of 30° was reduced from 4.0 nm to 2.3 nm on air admittance, while titanium dioxide deposited at 30° showed a reduction from 4.5 nm to 2.5 nm.

Silicon oxide deposited at 30° in a metal dielectric filter gave a shift in air of 0.8 nm suggesting birefringence of around one quarter of that found in the high-index materials. Figure 20 shows some of these results.

Samples that have been rotated during deposition for uniformity should, it is hoped, possess columnar axes normal to the substrate and to the film interfaces. In such cases one would not expect to detect any birefringent effects at normal incidence. Yet zirconium oxide/silicon oxide filters deposited under such conditions in the BAK760 plant exhibited shifts of 0.3 to 0.4 nm at normal incidence, showing that the columnar axes were not quite normal to the film interfaces and the films were probably slightly biaxial.

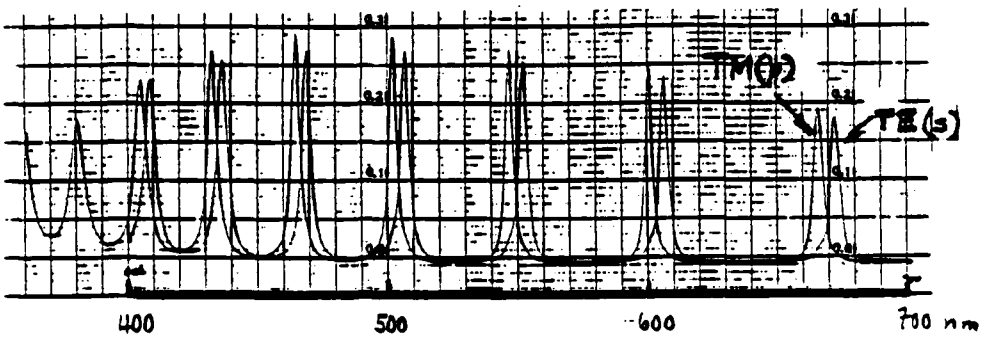
Comparisons of measured results, other than those used for the calculation of refractive index, and calculated results using the derived figures for refractive index show good agreement and are listed in Appendix A.

Table 6

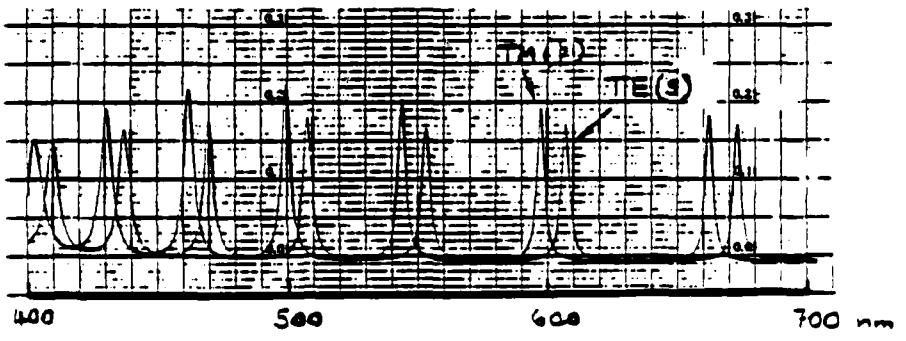
Comparison of Measured Results

Material	α	β	n_1	n_2	n_3
Zirconium oxide	30°	16.1°	1.948	1.966	2.033
Zirconium oxide	65°	47.0°	1.502	1.575	1.788
Titanium oxide	30°	16.1°	2.437	2.452	2.552

Note:
n_1 corresponds to E in plane of vapor incidence normal to column axis
n_2 corresponds to E normal to vapor incidence plane - s-polarization
n_3 corresponds to E along column axis.



(a)



(b)

Fig. 20. Birefringence in SiO_2 deposited at angles of incidence of vapor of 60° (a) and 70° (b) shown by measurements of $Ag/SiO_2/Ag$ filters in normally incident polarized light. The p-polarization indicates light parallel to the dire-tion of vapor incidence. The silver layers were deposited at normal incidence.

D. MOISTURE ADSORPTION

1. Introduction

The study of moisture adsorption by optical coatings is important because of its role in coating degradation and its utility as a vehicle for the study of film microstructure. Optical techniques were used to investigate moisture adsorption because they are straightforward, nondestructive, and reveal the early degradation of filter performance by moisture adsorption.

The microstructure of vapor-deposited optical thin films was discussed earlier. Briefly, the columnar microstructure contains considerable void volume in the form of pores between the columns. The voids and the large surface area of the columns are accessible from the atmosphere. Any fresh surface that is exposed to the atmosphere will adsorb atmospheric moisture. At virtually any relative humidity, a surface will acquire about one monolayer of water, although some multilayer coverage will be present to an extent that varies with the ambient relative humidity. When thin films are exposed to the atmosphere, they adsorb atmospheric moisture (Koch, 1965; Pulker and Jung, 1971; Ogura, 1975; Ogura and Macleod, 1976; Macleod and Richmond, 1976; Harris et al., 1979; Gibson and Lissberger, 1983). At low values of relative humidity the principal effect is the formation of a layer (essentially a monolayer) over the entire inner surface, that is, the internal surfaces of the columnar grains. The quantity of moisture adsorbed in this way has a significant effect on the optical properties. The immediate result is an increase in film refractive index since the moisture increases the index of the space it occupies. The optical thickness, which is the product of film refractive index and geometrical thickness, will also be increased. The film mechanical properties are affected because the moisture blocks the bonds across the gaps between the columns. The tensile stress falls and may occasionally become compressive. At higher values of relative humidity, the pores in the films fill with liquid water by capillary condensation (Ogura, 1975), increasing still further the refractive index. If the relative humidity falls, the liquid water tends to desorb, although there may be considerable hysteresis. The materials used in optical coatings are almost entirely high-surface-energy materials with strong bonds. In such materials the bonds that link the water monolayer to the surface are very strong so that the water is tightly bound and desorption is inhibited even if the relative humidity falls to low values. The tightly bound water is often called "irreversible" water because it does not desorb under vacuum. Pulker and Jung (1971) have shown that its volume can be calculated on the basis of a monolayer over the entire surface of the columnar grains. Because of the weakening of the forces between the columns, the film durability falls.

In multilayers, the behavior is more complicated than in single layers because the interfaces between the layers obstruct the pores. Ogura (1975) has shown that a temporary halt in evaporation without altering material can cause trapped pores. This obstruction slows down the rate of moisture penetration. The behavior in any particular case

iepends greatly on the materials. In zinc sulfide/cryolite multilayers the high packing density of the zinc sulfide effectively seals off the nultilayer so that the formation of the initial monolayer of moisture is inhibited. In such a case, the moisture tends to enter at isolated penetration sites passing through to deeper layers and spreading laterally in circular patches that gradually expand with time. In nultilayers made up of titanium dioxide or zirconium dioxide as high index and silicon dioxide as low index, the pores tend to have some connection to the outside environment, and the formation of the initial monolayer together with at least some multilayer coverage of the inner surface can be exceedingly rapid. As relative humidity rises, the intrinsic pore system tends to saturate, and isolated defects become relatively more important. Then we see the formation of the spreading circular patches centered on the isolated penetration sites in the same way as the zinc sulfide/cryolite system. The rate of spreading depends on the relative humidity and on the characteristics of the particular materials. It may take a matter of minutes or of months, even years, to reach equilibrium.

The effect of moisture penetration on coating performance depends on the particular design. The wet areas of narrowband Fabry-Perot (that is single-cavity) filters simply exhibit a shift toward longer wavelengths as the depth of penetration increases. The wet patches can be observed by illuminating the filter with monochromatic light. Depending on the relationship between the wavelengths of the illuminating light and the peak of the filter, the patches will appear as dark against a bright background or as bright against a dark background. Narrowband Fabry-Perot filters have therefore been used widely in the study of moisture penetration. The illuminated area of the filter will normally be great enough to include a number of moisture penetration patches. At an early stage of adsorption the wet patches will be small and surrounded by relatively large areas of dry material that will gradually decrease as the adsorption proceeds. The overall performance of the filter will be a combination of the characteristics of the individual elements of area, which depend both on the stage reached in the adsorption process and on the filter design. Narrowband Fabry-Perot filters have passbands shifted more or less toward longer wavelengths, often broadened and curiously misshapen.

Much of the work on moisture adsorption under this contract was aimed at a better understanding of its mechanism. A full description of this part is given in an extract from the PhD Dissertation of C. C. Lee (see Appendix B). A large part of the investigation of moisture adsorption concerned multilayers of zinc sulfide and cryolite. These materials are normally combined in narrowband filter construction for the visible region of the spectrum. Zinc sulfide is also a common material in infrared coatings, and cryolite is finding increasing application in the ultraviolet. A principal reason for the choice, however, was simply that the BAK760 plant was not available in the early stages of the contract, and the equipment that was operational had no electron beam source and could not attain the power levels required to evaporate titania and silica from directly heated boat sources. Once the

BAK760 was installed, multilayers of silicon dioxide and either titanium dioxide or zirconium dioxide became possible.

An interesting series of experiments was aimed at identifying the origin of the penetration sites that exist at the center of each moisture patch. Deliberate defects were introduced on otherwise normal substrates, and the number of patches were observed. The defects consisted of contamination, introduced simply by omitting the usual glow discharge cleaning step in the deposition process, dust, scratches, and small pits produced by a light sandblasting of the substrates. In every case, many more patches were seen than with unaltered substrates. In a further experiment superpolished substrates were used instead of the usual microsheet glass and the number of patches in a given area was reduced by a factor of around four. It seems clear that the penetration sites can be caused by virtually any departure from substrate perfection. The presence of patches on the superpolished substrates is probably due to imperfect processing. Our laboratory is not a clean room, and it is impossible to completely prevent dust or other minor contamination on the surface before the coating operation.

The fact that there is no single specific defect that can be associated with the production of a moisture penetration site reinforces our suspicion that the penetration sites are in fact nodules. A nodule is an inverted conical structure in a film that results in the appearance of a small dome at the surface. Nodules are the result of a different growth mechanism. The material of the nodule is exactly that of the remainder of the film. Nodules are presumed to originate from disturbances at the substrate surface, and they are rarely if ever seen to originate at any other level in the film. Once nodular growth begins, it propagates through the film system to the outermost surface, even in multilayers.

Our identification of the nodules as the defects that admit water into the patches is further strengthened by Lee's investigation of the kinetics of the process. The central defect must supply the water that is needed by the patch in its lateral propagation across the layers. We believe that this liquid water has to form at the penetration site itself which must therefore have dimensions that encourage capillary condensation at values of relative humidity around 50%, corresponding to a pore radius of around 25 Å. A single cylindrical pore of this radius could never supply enough water for even a very small patch, so we are driven to the conclusion that either a very large number of such pores exists in a cluster at the central site or the defect cross section is long as well as narrow. In this way capillary condensation could take place at the required level of relative humidity, but the volume of water produced would depend on the defect length. The crack or fissure that frequently surrounds a nodule would be an ideal candidate.

Another matter that is of some interest is the nature of the transport of moisture across the layers. Does the propagation of moisture simply occur through undisturbed film material with its intrinsically columnar structure in much the same way as ink across

blotting paper or is there something else? It seems clear that the propagation is essentially a capillary effect where the fluid is carried along by the surface tension forces at the meniscus but is restrained by the viscous drag in the channels linking the advancing moisture front with the central source of supply. The intrinsic film material can be considered as a network of small interlinked channels that continually divide into further similar channels as the distance from the supply source increases. The observed rate of expansion of the patches, which does not fall off rapidly with increasing radius, seems inconsistent with such a model. The results appear more characteristic of transport through a set of channels, which falls off in density as the distance from the central site increases. This is consistent with a defect from which radiates a series of cracks or fissures, and suggests that the central defect exerts an influence over a much wider area of the film than might otherwise be suspected.

2. Surface Plasmon Resonances

A technique that was devised during the course of the project for investigating small instabilities in thin films involves the tracking of a coupling resonance associated with surface plasmon propagation. The Kretschmann coupling technique is used, in which a thin metal film is first deposited on the base of a prism. Then, provided the thickness of the metal film is correctly chosen, p-polarized light incident internally on the prism base will exhibit a sharp dip in reflectance over a narrow range of angles of incidence associated with the coupling of the light into a surface plasmon on the outer surface of the metal. The shape of the resonance and its position are a function of the optical constants and thickness of the metal layer. In the visible region, silver has the highest performance of any metal and the silver resonance is the narrowest. The resonance is still obtained when the metal is overcoated with a dielectric layer of correctly chosen thickness. Now the parameters of the resonance are also sensitive functions of both films and can be used to track small changes in the dielectric layer. Depending on the thickness of the dielectric layer, it is possible to have resonances either with s- or p-polarized light, but the p-resonances are narrower and hence more useful. Some limited experiments using this measurement technique are described in Chapter 3 of Lee's dissertation (see Appendix B).

3. Moisture Adsorption and Optical Instability in Thin Film Coatings

(See Chapters 3 to the end of the PhD dissertation of C. C. Lee in Appendix B.)

4. Anisotropic Moisture Penetration

The optical anisotropy of films, especially those that have been deposited at oblique incidence, is considered in a separate chapter in this report. However, oblique incidence of the condensing vapor leads to other forms of anisotropy as well. Some experiments have been carried

out on a series of metal-dielectric filters with SiO_2 as high-order spacer and silver films as reflectors that demonstrate an anisotropy of moisture penetration in such films. The silver was deposited at normal incidence but the SiO_2 was deposited at a series of angles of incidence from zero to 70°. Moisture penetration patches were rapidly detected in those films with angles of incidence up to 45°, but 60° and 70° samples showed no patches although spectral shifts were detected. Since it is unlikely that these two samples were devoid of moisture, the most plausible explanation is that the adsorption process on atmospheric exposure was too rapid for normal detection. Patches in the other samples are shown in Fig. 21. In samples deposited at 23° or higher, the moisture penetration patches have a markedly elliptical shape with the ratio of major to minor axes varying from approximately 1.4 to 1.9. There is a slight scatter in the ratio for each individual film and a tendency for the ratio to be greater at greater angles of incidence. The major axes of the ellipses are normal in all cases to the direction of incidence of the vapor. Although patches could not be detected in the samples deposited at 60° and 70°, strong anisotropy was detected in both.

A simple theory is proposed to explain the patterns. We can suppose from the two-dimensional simulation of film growth that the width of voids, measured in the plane of incidence, is given by B_0 for normal incidence of the vapor and that at oblique incidence there is an extra contribution that depends on $\tan\alpha$, so that the total width is given by

$$B = B_0 + B_1 \tan\alpha. \tag{1}$$

Extending the two-dimensional ideas to three dimensions, we can suppose that the voids will have some significant length and random orientation θ with respect to the vapor plane of incidence. Those running normal to the plane of incidence will have width given by the above expression, but those parallel to the plane of incidence will have width B_0 similar to normal vapor incidence. We can therefore express the randomly oriented width as

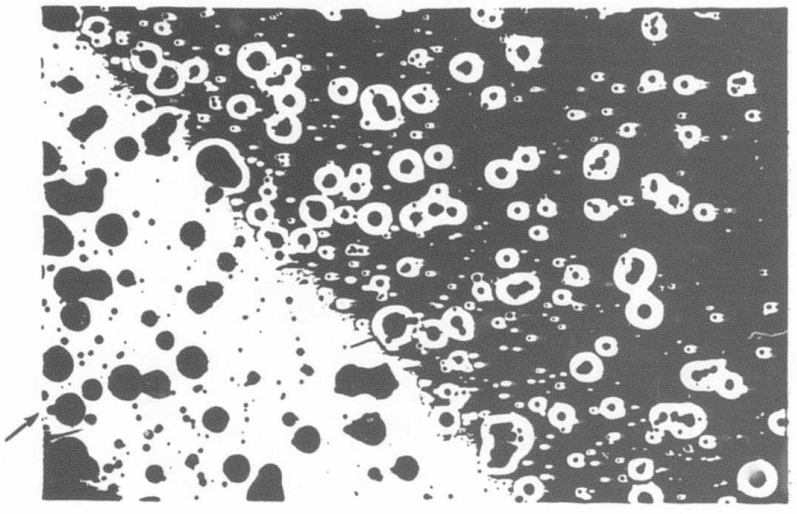
$$B = B_0 + B_1 \tan\alpha \cos\theta.$$

If we consider B_0 as so small that it can always be neglected and $B_1 \tan\alpha$ as large, then we have for the width

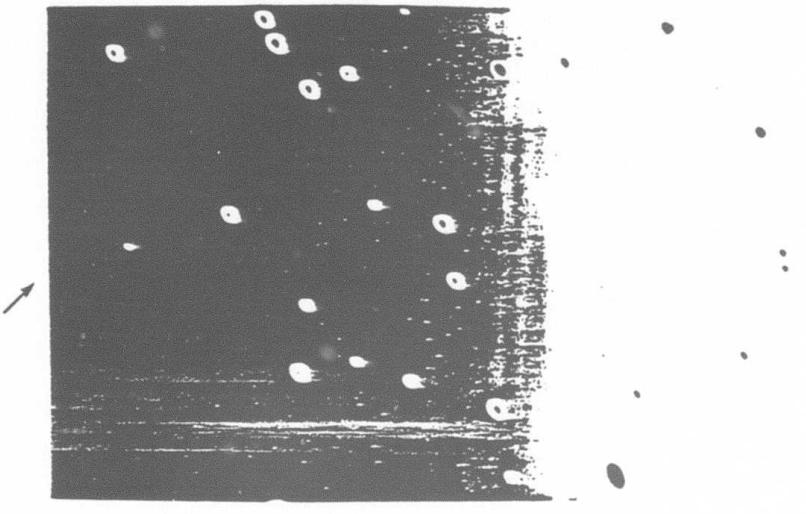
$$B = B_1 \tan\alpha \cos\theta = B\alpha \cos\theta.$$

We can suppose that the time taken for the water to propagate along a given length of void, parallel to the film interfaces, is inversely proportional to the void width. Now we consider the two directions x and y normal to and along the vapor incidence respectively, indicated in Fig. 22, that is

$$t = k \frac{L}{B},$$



(a)



(b)

Fig. 21. Elliptical moisture penetration patches in filters of construction $Ag/SiO_2/Ag$. The silver reflecting layers were deposited at normal incidence but the SiO_2 layers were deposited at a range of angles of vapor incidence: (a) 7°, (b) 23°, (c) 30°, (d) 38°, (e) 45°. In each case the direction of vapor incidence, marked with an arrow, is parallel to the minor axes of the ellipses.

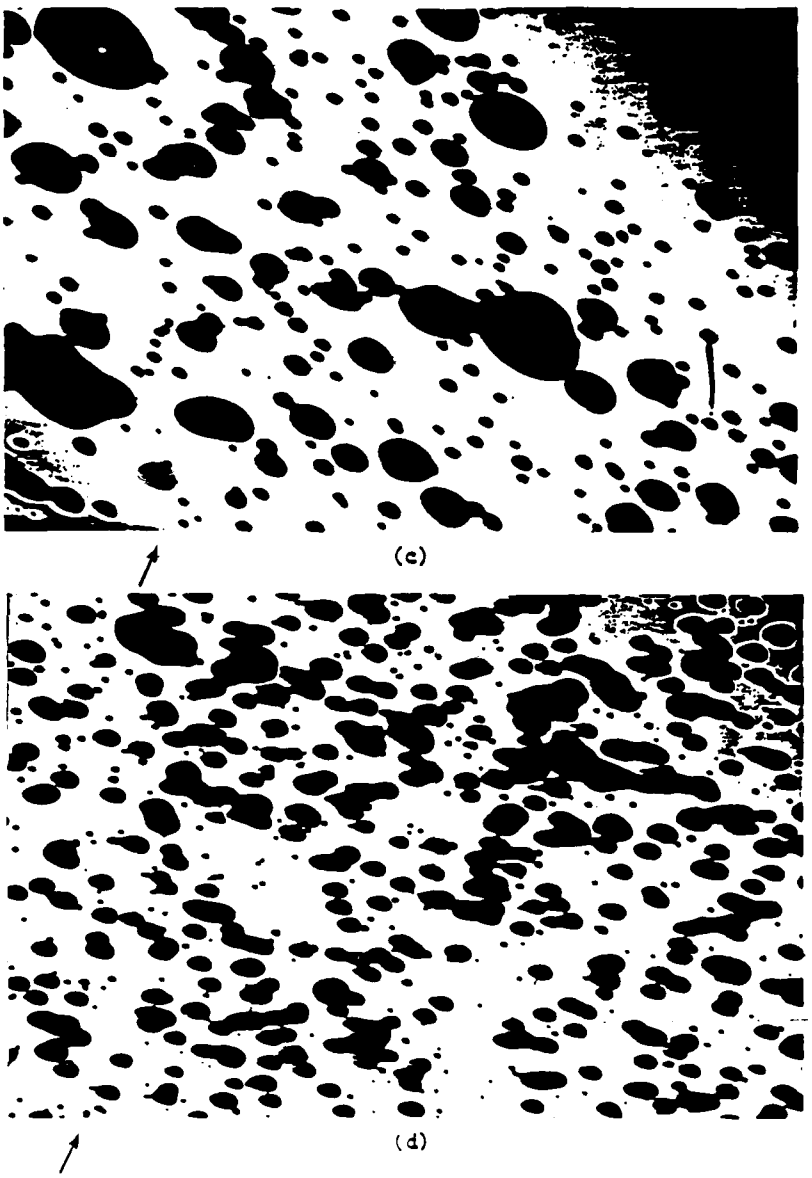
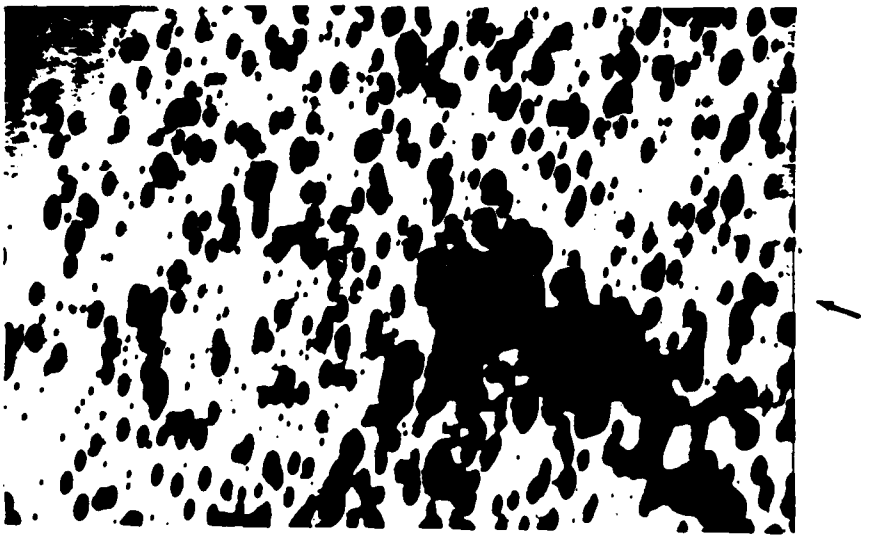


Fig. 21. (Continued) Elliptical moisture penetration patches in filters of construction $Ag/SiO_2/Ag$. The silver reflecting layers were deposited at normal incidence but the SiO_2 layers were deposited at a range of angles of vapor incidence: (a) 7°, (b) 23°, (c) 30°, (d) 38°, (e) 45°. In each case the direction of vapor incidence, marked with an arrow, is parallel to the minor axes of the ellipses.



(e)

Fig. 21. (Continued) Elliptical moisture penetration patches in filters of construction $Ag/SiO_2/Ag$. The silver reflecting layers were deposited at normal incidence but the SiO_2 layers were deposited at a range of angles of vapor incidence: (a) 7°, (b) 23°, (c) 30°, (d) 38°, (e) 45°. In each case the direction of vapor incidence, marked with an arrow, is parallel to the minor axes of the ellipses.

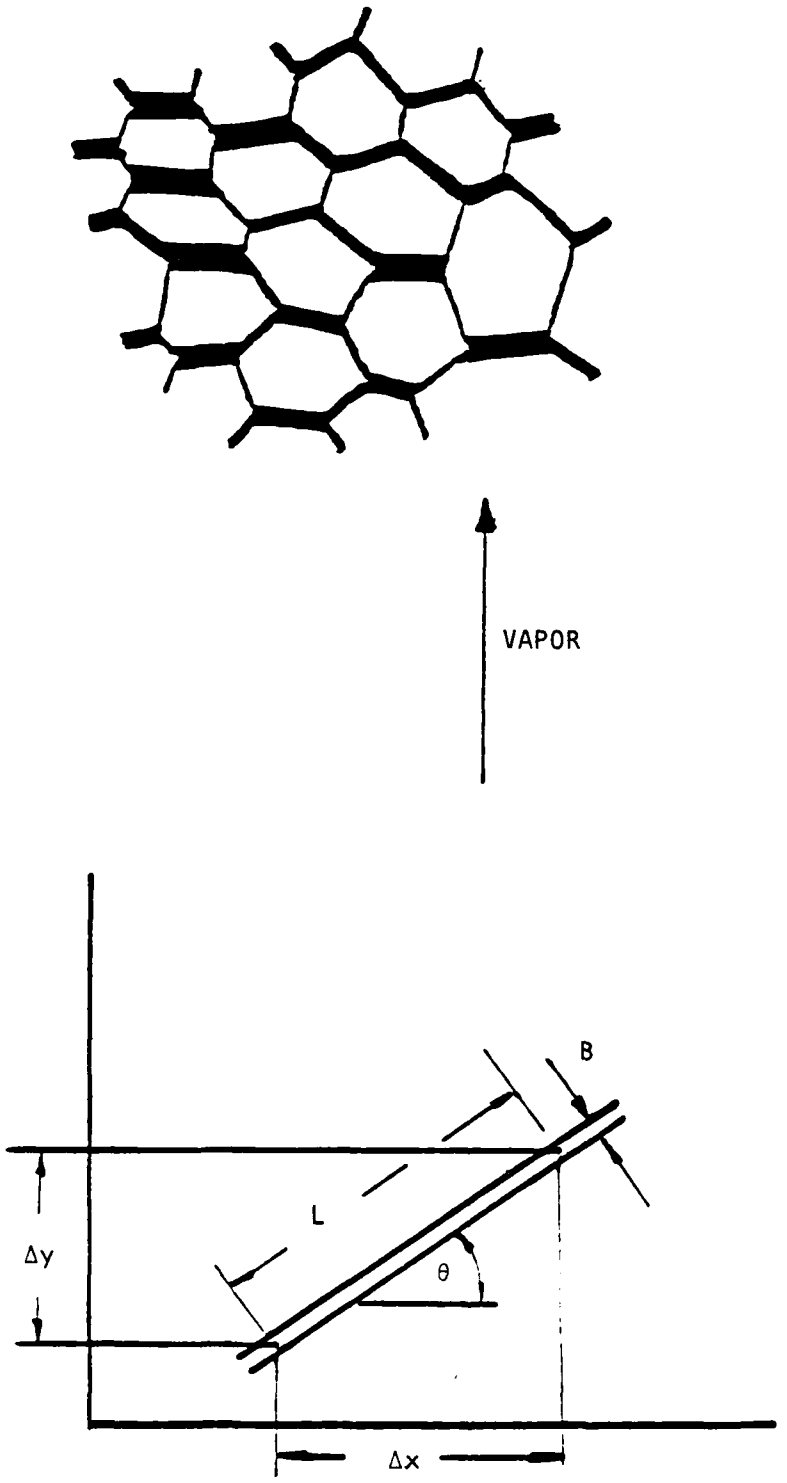


Fig. 22. Postulated void network in a deposited film looking downward onto the film normal to the substrate. The quantities used in the analysis of penetration rate are sketched in the lower diagram.

i.e.,

$$t = k \frac{\Delta x}{\cos\theta \; B_\alpha \cos\theta} = k \frac{\Delta x}{B_a \cos^2\theta}$$

and

$$V_x = \frac{\Delta x}{t} = (B_a/k)\cos^2\theta = k' \cos^2\theta.$$

If we average over randomly oriented voids, then the velocity V_x, perpendicular to the plane of incidence, is given by

$$V_x = \frac{k'}{\pi} \int_{-\pi/2}^{\pi/2} \cos^2\theta \; d\theta = \frac{k'}{2} .$$

Similarly the velocity parallel to the direction of incidence is

$$V_x = \frac{k'}{\pi} \int_{-\pi/2}^{\pi/2} \cos\theta \; \sin\theta \; d\theta = \frac{k'}{\pi} .$$

Then the ratio of the major and minor axes of the ellipse is given by the ratio of the velocities, that is

$$\frac{V_x}{V_y} = \frac{\pi}{2} = 1.57,$$

which is independent of α.

The theory is doubtless an oversimplification and is really only a starting point for a more rigorous analysis, but it is surprising that such simple assumptions can result in a figure that is close to the actual measurements.

Silicon dioxide is an amorphous material by the usual tests of x-ray diffraction and electron microscopy exhibiting a glassy fracture in fractographs. This result illustrates that in spite of its amorphous nature, a silicon dioxide film possesses a microstructure that is revealed in these adsorption observations. It is impossible to say at this stage whether or not the structure of the film around the defect possesses the radial cracks postulated for the normal incidence films discussed earlier. The explanation simply considers the intrinsic structure of the films. However, the variation of packing with direction around the defect, which was discussed, could be reflected in the width and distribution of any radial cracks that might form, and so the explanation of the effect is not inconsistent with such a model. It is also relevant that a small amount of optical anisotropy was detected in obliquely deposited silicon dioxide layers.

5. Effect of Ion Bombardment on Moisture Adsorption

The effects of ion bombardment on moisture adsorption and desorption of completed filters has been a further area of investigation. This resulted from some observations made during testing of a cold-cathode ion gun which was to be used in ion-assisted deposition experiments. In order to optimize the parameters, the gun was being used to sputter etch some existing coatings. An effect that was initially thought to be an ion-induced desorption effect was observed at ion fluxes that were quite low so that sputtering rates were small. The suspected desorption was in fact found to be an inhibition of readsorption. The experiment is described in some detail in Appendix C, the text of a paper in Applied Optics.

E. OPTICAL INHOMOGENEITY

We have seen how thin films almost invariably have optical properties that differ significantly from those of similar materials in bulk form. Film microstructure is largely responsible. So far we have considered microstructure as constant in character throughout the thickness of the films under study. However, any variation of microstructure as a function of film thickness will result in inhomogeneity of optical constants. Inhomogeneity is found to some degree in almost all thin films and the development of techniques for its measurement was therefore considered as an important part of the study. Although inhomogeneity of optical constants can be inferred from post-deposition measurements, it is almost impossible to obtain the actual profile of the optical constants within the layer. The reason is the insensitivity of the reflectance and transmittance of the layer to the profile. Provided the variation in optical constants is smooth, then reflectance and transmittance are largely determined by the extreme values. This implies that any detailed study of inhomogeneity must include measurements made during the deposition of the layer. An important part of the project, therefore, was the design and development of a rapid-scanning spectrometer for the continuous measurement and recording of film properties during deposition. The effort involved in this part of the project occupied the better part of the three-year program, and so results were obtained only through the latter part of the final year of the project. Additional support was also obtained through a DARPA/NOSC contract for the development of special filters and through an AFOSR grant that permitted the employment for one year of a post-doctoral research associate from the Ecole Nationale Supérieure de Physique in Marseille where layer-thickness monitoring systems involving rapid scanning systems have been under development since the mid 1970's.

The results have been described in two publications included in Appendix D and E. The results reported on post-deposition bombardment of multilayers were obtained using this system.

F. ULTRAVIOLET AND ION BOMBARDMENT

A series of films has been deposited with and without ultraviolet irradiation and ion bombardment during deposition. Measurements were made of optical constants during deposition, of x-ray diffraction after deposition, of the performance of multilayers containing the irradiated layers, and of moisture sensitivity of these multilayers. The ultraviolet flux was calculated roughly as 25 photons for each condensing molecule, which should be adequate for effects to be revealed. The results are detailed in an extract from J. J. Wharton's PhD dissertation (see Appendix F).

Results of x-ray diffraction measurements on films of zirconium oxide, titanium dioxide, and silicon oxide, with and without bombardment, are detailed in the dissertation. Silicon oxide appeared to be amorphous, exhibiting no x-ray peaks at any time, consistent with the observations of others. Single layers of zirconium oxide showed only weak peaks, the principal one being the (111) tetragonal peak. Ion bombardment of zirconium dioxide resulted in a strong enhancement of the (111) peak while ultraviolet irradiation appeared to have little effect. Titanium dioxide films showed only exceedingly weak peaks and in single layers it was virtually impossible to recognize any structure at all. However, multilayers of titanium oxide and silicon oxide did show weak peaks that were due to the titanium oxide. These peaks were reduced in intensity by both ultraviolet irradiation and ion bombardment, the latter removing them completely. The ion bombardment results are consistent with the findings of Martin et al. (1983). The effects of ultraviolet irradiation were similar but less intense.

Optical measurements made on zirconium oxide and titanium oxide consisted first of optical constant determination from measurements of transmittance made on the films during deposition. A modification of the envelope method of Manifacier et al. (1976) was used to derive measures of both n and k from transmittance results. Further work is required on the topic of interpretation of in situ measurements, but there are clear indications from the results so far of changes induced by both ultraviolet irradiation and ion bombardment. Table 7 summarizes the results.

Here the ultraviolet irradiation tends to decrease the absorption in the layers, increasing the index of the zirconium oxide at the same time but slightly reducing that of the titanium oxide. This reduction in index may be due to the decrease in absorption and not an effect of changes in packing density.

These results were of course obtained on single layers, and the measurements were made in situ. Every precaution was taken to try to keep all conditions except uv irradiation and ion bombardment exactly the same so that the comparisons should be valid. However, it is possible that slight differences in temperature could have been responsible for the changes rather than the irradiation. In an attempt to reduce the possibility of such effects, narrowband filters were

constructed with only part of their surface treated. Comparison was made of the treated and untreated parts.

Table 7

Results of Optical Measurements on ZrO_2 and TiO_2

Material		Normal Evaporation	Ultraviolet Irradiation	Ion bombardment Argon	Oxygen
ZrO_2	n:	1.91	1.96	2.07	
	k:	3.3×10^{-3}	2.9×10^{-3}	5.6×10^{-3}	
TiO_2	n:	2.19	2.12	2.35	2.22
	k:	16.0×10^{-3}	8.8×10^{-3}	59.0×10^{-3}	13.0×10^{-3}

Zirconium oxide/silicon oxide filters showed clear evidence of higher transmittance and lower absorption under uv irradiation. The higher transmittance was present over the sidebands as well as the peak of the filter, reinforcing the suggestion that the increase in transmittance is indeed a reduction in absorption and not simply a thickness effect related to monitoring.

The results of irradiation of titanium oxide and silicon oxide filters are less clear, with apparently increased absorption in some cases and reduced in others. However, there are indications that the irradiated parts are more stable in the atmosphere after deposition. After baking in air at 125°C for 72 hours to remove moisture, the parts of filters treated with ultraviolet during deposition remained stable while the untreated parts drifted in the usual way. The x-ray diffraction measurements indicated that uv irradiated titanium dioxide tended to become amorphous although not in as pronounced a way as with ion bombardment. In the discussion of post-deposition ion bombardment, this crystalline-amorphous transition is postulated as causing a swelling of the titanium dioxide which inhibits adsorption of moisture. It is likely that a similar, though less pronounced, effect is produced by the uv irradiation. The uv irradiation during deposition therefore produces beneficial effects, but they are less marked that those of ion bombardment. Argon ion bombardment leads to higher absorption because oxygen is preferentially sputtered from the condensing material, but bombardment with oxygen ions rather than argon removes this problem. (See Appendix F, pages 29 through 146.)

G. ELECTRON BOMBARDMENT

An old trick to improve the durability of zinc sulfide is to bombard the growing film with electrons. This prompted an investigation of the effects of electron bombardment on a series of films of various and different materials, the objective being to determine whether or not there is any general benefit to be gained from electron bombardment during growth. The results are described in detail in the excerpt from the PhD dissertation of S. D. Browning (Appendix G).

Briefly, he found that there was no general effect common to all film types. The results were exceedingly material-dependent. This section of the study was begun well in advance of the installation of the BAK760 and since no electron gun was available in the plant that had to be used, it was necessary that the materials examined could be thermally evaporated from boat sources. They included zinc sulfide, potassium fluorozirconate ($2KF.ZrF_4$, potentially useful in the blue and near uv), antimony trioxide, silicon oxide, and magnesium fluoride. Characterization techniques were principally x-ray diffraction and electron microscopy.

1. Antimony trioxide

X-ray diffraction of films deposited conventionally with no bombardment shows a preponderance of (222) planes parallel to the substrate. The (222) planes are less prominent in electron-bombarded samples and the (400) planes predominate. Thus there is a reorientation of the lattice planes. Crystallite size is reduced, especially in films deposited at room temperature. The appearance of electron micrographs suggests a somewhat higher packing density for the bombarded films.

2. Potassium hexafluorozirconate

The structure tended toward a more amorphous form under electron bombardment with little evidence from electron micrographs of the prominent columnar structure of unbombarded films. There was a very slight increase in absorption in the blue and uv.

3. Silicon oxide

Virtually no effect of the electron bombardment could be detected in these films. Silicon oxide films are amorphous in structure under normal conditions and this continued to be the case with electron bombardment. The durability of the films appeared completely unaffected.

4. Magnesium fluoride

Magnesium fluoride films showed increased heights of x-ray diffraction peaks, especially the (111) peak. Gross details of the structure as revealed by electron microscopy showed little change, but the durability of the films was adversely affected.

. Zinc sulfide

Thermally evaporated zinc sulfide is usually a mixture of two orms, a cubic form, stable at room temperatures, and a hexagonal form, table only at elevated temperatures. Lack of stability of zinc sulfide ilms after deposition has been attributed to a gradual conversion of he hexagonal form into the cubic. X-ray diffraction peaks in bombarded ilms show a reduced fraction of the hexagonal form, which indicates otentially greater stability. This is in accord with the published indings of Bangert and Pfefferkorn (1980).

This has been, admittedly, a somewhat limited investigation, but here is certainly no indication of any great general benefit to be ained from electron bombardment. In zinc sulfide a definite change can e recognized, and experience over the years has shown that there is a erceptible advantage. Changes in the other materials studied were mall and not necessarily beneficial and in the case of magnesium luoride definitely detrimental. Zinc sulfide is a material that eparates almost completely into its atomic constituents in the vapor hase. It is possible that the electrons might play some part in the ecombination of the components on the substrate. (See Appendix G for a etailed discussion.)

H. LASER DAMAGE

A very limited series of experiments on the damage sensitivity of lfferent defects was carried out on narrow-band filters toward the end f this program. An argon laser became available to us for just a few eeks and the opportunity was taken to make a short series of easurements. These should be taken purely as an indication of the nterest in continuing this work in a more extended set of tests without he tight time constraint. Details are given in Appendix H extracted rom the thesis of L. DeSandre.

I. CONCLUSION

The research has confirmed the importance of microstructure in etermining the properties of thin films and especially those ways in hich films differ from corresponding bulk materials. Usually these roperties result in inferior performance, but this is not inevitable. ome of the special behavior of thin films might be used to advantage. his is the case with the very large form birefringence that exists and hat can be enhanced by oblique deposition. Possible additions to the acuum evaporation process for thin film deposition, and electron, hoton, and ion bombardment, have been examined to assess their otential for modification of microstructure. Here there is no doubt hat the process of ion bombardment of the growing film has the largest ffect on microstructure. Electron bombardment was found to be ependent on the particular material involved, sometimes leading to nprovements, sometimes to deterioration, and sometimes having no pparent effect at all. Ultraviolet irradiation appeared to give results imilar to those of ion bombardment but weaker.

REFERENCES

ngert, H., and Pfefferkorn, H., "Condensation and stability of ZnS thin films on glass substrates," Appl. Opt. **19**, 3878 (1980).

usquet, P., and Pelletier, E., "Optical thin film monitoring--recent advances and limitations," Thin Solid Films **77**, 165 (1981).

vard, B., Saxe, S. G., Messerly, M. J., Van Milligen, F. J., and Macleod, H. A., "Techniques for thin film optical constants derivation from in-situ transmission measurements," paper presented at the 1984 Annual Meeting of the Optical Society of America, San Diego, California, October 29-November 2, 1984. Abstract appears in J. Opt. Soc. Am. A **1** (December, 1984).

agg, W. L., and Pippard, A. B., Acta Cryst. **6**, 865 (1953).

owning, S. D., "Electron bombardment of certain thin films during deposition," PhD dissertation, University of Arizona (1983).

sandre, L., "Laser damage measurements on all dielectric narrow band filters," MS thesis, University of Arizona (1985).

bson, D. R., and Lissberger, P. H., "Optical properties and narrowband spectral filter coatings related to layer structure and preparation," Appl. Opt. **22**, 269 (1983).

irris, M., Macleod, H. A., Ogura, S., Pelletier, E., and Vidal, B., "The relationship between optical inhomogeneity and film structure," Thin Solid Films **57**, 173 (1979).

nderson, D., Brodsky, M. H., and Chaudhari, P., Appl. Phys. Lett. **25** (1974).

dgkinson, I. J., Jacobson, M. R., Lee, C. C., Macleod, H. A., Potoff, R. H., Sikkens, M., and Sprague, R., "Anisotropic moisture penetration in optical coatings," presented at the 1983 Annual Meeting of the American Optical Society, New Orleans, Louisiana, October 17-20, 1983.

owowitz, F., "Structure-induced anisotropy in thin films," PhD dissertation, University of Arizona, 1983.

rowitz, F., and Macleod, H.A., "Form birefringence in thin films," Los Alamos Conference on Optics, 1983, and Proc. SPIE **380**.

ch, H., "Optische Untersuchungen Zur Wasserdampfsorption in Aufdampfschichten (inbesondere in MgF2 Schichten)," Phys. Stat. Sol. **12**, 533-543 (1965).

Leamy, H. J., Gilmer, G. H., and Dirks, A. G., "The microstructure of vapor deposited thin films," pp. 1002-1004 in Current Topics in Materials Science, Vol. 6, E. Kaldis, ed. (North-Holland, 1980).

Lee, C. C., "Moisture adsorption and optical instability in thin film coatings," PhD dissertation, University of Arizona (1983).

Lerner, J. M., Flamand, J., Laude, J. P., Passereau, G., and Thevenon, A., "Diffraction gratings ruled and holographic--a review," Proc. SPIE **240**, 82 (1980).

Liao, B. J., and Macleod, H. A., "Thin film microstructure modeling," presented at the Southwest Conference on Optics, Albuquerque, NM, March 4-8, 1985.

Macleod, H. A., and Richmond, D., "Moisture penetration patterns in thin films," Thin Solid Films **37**, 163 (1976).

Manifacier, J. C., Gasiot, J., and Fillard, J. P., "A simple method for the determination of the optical constants n, k, and the thickness of a weakly absorbing thin film," J. Phys. E: Sci. Instrum. **9**, 1002 (1976).

Martin, P. J., Macleod, H. A., Netterfield, R. P., Pacey, C. G., and Sainty, W. G., "Ion-beam assisted deposition of thin films," Appl. Opt. **22**, 178 (1983).

Movchan, B. A., and Demchishin, A. V., "Investigation of the structure and properties of thick vacuum deposited films of nickel, titanium, tungsten, alumina, and zirconium dioxide," Fizica Metall. **28**, 83 (1969).

Niewenhuizen, J. M., and Haanstra, H. B., Phillips Tech. Rev. **27**, 87 (1966).

Ogura, S., "Some features of the behavior of optical thin films," Doctoral Dissertation, Newcastle upon Tyne Polytechnic (1975).

Ogura, S., and Macleod, H. A., "Water Sorption Phenomena in Optical Thin Films," Thin Solid Films **34**, 371 (1976).

Porteus, J. O., and Seitel, S. C., "Absolute onset of optical surface damage using distributed defect ensembles," Appl. Opt. **23**, 3796 (1984).

Pulker, H. K. and Jung, E., "Correlation between film structure and sorption behavior of vapor deposited ZnS, cryolite, and MgF_2 films," Thin Solid Films **9**, 57 (1971).

Rice, R. M., "Method of deposition of thin films of material," U.S. Patent 2,420,724 (1947).

Pelletier, E., "Monitoring of optical thin films during deposition," Proc. SPIE **401**, 74 (1983).

Sikkens, M., Hodgkinson, I. J., Horowitz, F., Macleod, H. A., and Wharton, J. J., "Computer simulation of thin film growth: applying the results to optical coatings," Proc. SPIE **505** (1984).

Thornton, J. A., "Influence of apparatus geometry and deposition conditions on the structure and topography of thick sputtered coatings," J. Vac. Sci. Tech. **11**, 666 (1974).

Van Milligen, F. J., Bovard, B., Jacobson, M. R., Mueller, J., Potoff, R., Macleod, H. A., and Shoemaker, R., "Development of an automated scanning monochromator for a Balzers 760 evaporation system," Poster presented at the 1984 Annual Meeting of the American Optical Society, San Diego, California, October 29-November 2, 1984. Abstract appears in J. Opt. Soc. Am. A **1** (December, 1984). Submitted to Applied Optics.

Vidal, B., Fornier, A., and Pelletier, E., "Wideband Optical Monitoring of Non-Quarterwave Multilayer Filters," Appl. Opt. **18**, 3851-3856 (1979).

Wharton, Jr., J. J., "Microstructure related properties of optical thin films," University of Arizona (1983).

Ziedler, J. R., Kohles, R. B., and Bashara, N. M., Appl. Opt. **13**, 1115 (1974).

APPENDIX A

STRUCTURE-INDUCED OPTICAL ANISOTROPY IN THIN FILMS

PhD Dissertation by Flavio Horowitz

TABLE OF CONTENTS

LIST OF ILLUSTRATIONS x

LIST OF TABLES xii

ABSTRACT xiii

1. INTRODUCTION 1

Background and Contents 3

2. POLARIZATION EFFECTS IN METAL AND DIELECTRIC FILMS 13

Sample Preparation and Characterization 13
Results and Discussion 14
Structural Origin 20

3. A UNIFIED MATRIX FORMULATION FOR ANISOTROPIC MULTILAYER SYSTEMS 23

The Propagation Matrix 24
The Reflectance and Transmittance Matrices 28
Homogeneous Anisotropic Medium 31
CASE ZERO: The Isotropic Limit 32
CASE 1: Linear Polarization Modes 36
Generalization 41
Discussion 44
CASE 2: Elliptical Polarization Modes 45
Discussion 50

4. MEASUREMENT OF PRINCIPAL REFRACTIVE INDICES OF BIREFRINGENT THIN FILMS 52

Setup Description and Operation 53
Method 57
Measurements in Transmission at Normal Incidence (Steps 1 to 3) 59
Measurement at Oblique Incidence 60
Data Analysis 61
Theory of the Measurement 62
On Relations (4.3): First-Order Approximation 63
On Relations (4.4): Absentee Layer and Admittance Matching 65
Discussion 66

TABLE OF CONTENTS--Continued

Example 69
Interpretation 75

5. OPTICAL PROPERTIES: THEORY AND EXPERIMENT 79

The ANTF Program 79
Experimental Evidence 82
$T \times \theta_0$ 82
$T \times \alpha$ 90
$T \times \lambda_0$ 95
A Hypothetical Metal Film 100

6. CONCLUSION 103

Summary 103
Potential Applications 105
Polarizers 105
Retarders 106
FTR Filters 106
Bifocal Elements 107
Birefringent Narrowband Filters 107
Compact Birefringent Filters 108
Understanding the Human Eye 108
Toward Real Films 108

APPENDIX A. COMPOSING THE L-MATRIX WITH A VECTOR BASIS 110

APPENDIX B. COORDINATE AXES REPRESENTATION OF THE ϵ TENSOR 112

SELECTED BIBLIOGRAPHY 114

LIST OF ILLUSTRATIONS

Figure		Page
1.1.	Cross Section of a ZnS/ThF_4 Quarterwave Multilayer	2
1.2.	The Tangent Rule is Illustrated with Data from Several Investigators and a Variety of Film Materials.	9
1.3.	A Simplified Map of Our Approach	12
2.1.	Characterization Setup	15
2.2.	Relative Transmittances Measured as Functions of the Sample Rotation Angle for an Aluminum Sample Al, AN 0326-85)	16
2.3.	Relative Transmittances Measured as Functions of the Sample Rotation Angle for a Zirconium Oxide Sample (Zr Oxide, El 0124t-70).	19
2.4.	Scattering in (a) Reflection and (b) Transmission from an Anisotropic Silver Film	21
3.1.	Geometry for Refraction in Anisotropic Media	25
3.2.	Conventions and Schematic for the Determination of the Reflectance and Transmittance Amplitude Coefficients	29
3.3.	Possible CASE 1 Columnar Structure Configuration	37
4.1.	Schematic Diagram of Experimental Setup	54
4.2.	Sideview of the Ellipsometer	56
4.3.	Closeup of the Ellipsometer.	58
4.4.	Brewster Reflection for Anisotropic Media	68
4.5	Deposition Geometry and Sample Holder	70
4.6.	Experimental Data for the Determination of the Refractive Index of a 2 in. x 2 in. Glass Slide	72

LIST OF ILLUSTRATIONS--Continued

Figure		Page
4.7.	Closeup of Figure 4.6.	73
4.8.	Experimental Data for the Determination of Brewster's Angle for a Zirconium Oxide Sample	74
4.9.	Film Structure Resulting from the Simulated Deposition Process at (a) v = 60° and (b) v = 0°	77
5.1	Overall Structure of the ANTF Program	81
5.2	Noncrossed Transmittauces versus Angle of Incidence (Zirconium Oxide Sample)	83
5.3.	Corrected Noncrossed Transmittances versus Angle of Incidence (Zirconium Oxide Sample).	88
5.4.	Noncrossed s-Polarization Transmittance versus Azimuth Angle	91
5.5.	Crossed Transmittances versus Azimuth Angle	92
5.6.	Spectral Data in the Visible Region for the Noncrossed Transmittance of a Birefringent Narrowband Filter with 21 Layers	96
5.7.	Spectral Data for Noncrossed Transmittances at Normal Incidence	98
5.8.	Spectral Data for Noncrossed Transmittances at 30°	99
5.9.	Noncrossed and Crossed Transmittances versus Azimuth Angle as Predicted from the Theory for the Hypothetical Metal Film Specified in (5.6).	.101
5.10.	Noncrossed and Crossed Reflectances versus Azimuth Angle as Predicted from the Theory for the Hypothetical Metal Film Specified in (5.6)	.102

LIST OF TABLES

Table		Page
5.1.	Values of T_{pp} and T_{ss} for Various Angles of Incidence . .	87
5.2.	Values of T_{sp} and T_{ss} for Various Angles of Incidence . .	93

ABSTRACT

We consider in this work the contribution of anisotropic microstructure to polarization effects in thin films. The microstructure is pictured by a simple model as composed of identical columns with elliptical cross section elongated in a direction perpendicular to that of the vapor incidence. The asymmetry in columnar structure that results from oblique deposition is identified as the common source for the significant dichroism and birefringence observed in metal and dielectric films, respectively. A four-dimensional theory for multilayer systems is presented that starts from first principles, unifies previous treatments for particular cases of film anisotropy, and properly handles the most general case of elliptically polarized mode propagation. In this framework and from a set of polarimetric measurements, a simple method is devised, with explicit consideration of the anisotropic microstructure, for the determination of the physical thickness and principal refractive indices of a single dielectric film. A sequence of transmittance measurements is performed with a zirconium oxide film deposited at 65° and, substrate role and instrumental errors considered, good agreement is obtained between theory and experiment. Spectrophotometer data for a narrowband filter with 21 layers deposited at 30° is shown to confirm theoretical predictions of peak positions with Angstrom resolution. A hyptothetical metal film is discussed that reproduces the essential features observed in the optical behavior of an

aluminum film deposited at 85°. Potential applications and suggestions for future work are included.

CHAPTER 1

INTRODUCTION

In contrast with the conventional assumption in current multilayer design techniques, virtually all vacuum-deposited thin films are anisotropic. (See Figure 1.1.)

Would such a porous, discontinuous material, with its evident preferential orientations, produce under proper conditions a significant amount of optical anisotropy? By optical anisotropy we mean a behavior exhibited during the interaction with light that depends on the direction of the incident electric field. Its relation to film microstructure is the general theme of this dissertation.

We could well have entitled it "Form Birefringence in Thin Films," as long as this is understood in a wide sense to include dichroism, or direction-dependent absorption, especially for metal films. According to Born and Wolf (1975, p. 705), form birefringence "...arise(s) from a scale much larger than molecular, namely when there is an ordered arrangement of similar particles of optically isotropic material whose size is large compared with the dimensions of molecules, but small compared to the wavelength of light."

Crystalline orientation and anisotropic stress have also been known as sources of birefringence in dielectric coatings, although the reported extent of their effect (Burgers and Dippel, 1934; Turner and

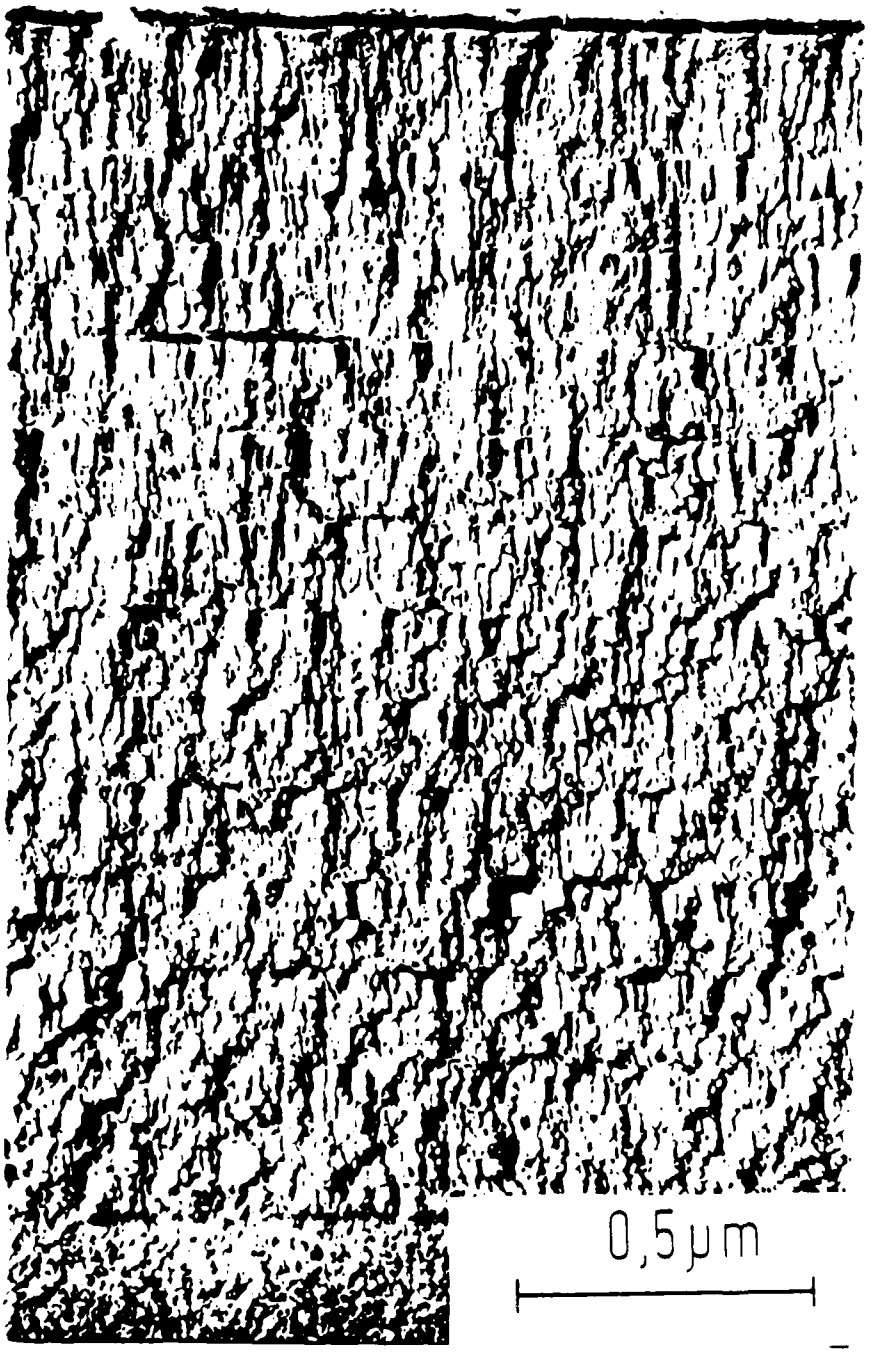


Figure 1.1. Cross Section of a ZnS/ThF_4 Quarterwave Multilayer.

Substrate temperature was approximately 30°C. Transmission micrograph of a preshadowed carbon replica. Columnar crystals with large diameters are ZnS layers, smaller columns indicate ThF_4 layers. (From Guenther and Fulker, 1976)

Ulbrich, 1947; Bousquet and Delcourt, 1957; Lichtenstein, 1980) is at least one order of magnitude smaller than the one we will be considering.

We now proceed to place our study in its proper historical context, while briefly outlining its main contents.

Background and Contents

This work is at the intersection between two main historical trends in the science of thin films, one primarily phenomenological, the other predicated on rigorous electromagnetic principles.

The first trend probably started when Kundt (1886) observed polarization effects in several metal films by placing them between Nicol prisms at orthogonal orientations. Supporting reports by Braun (1905), Bergholm (1914), Cau (1928), and later by Coper, Frommer and Zocher (1931), followed.

From that time, when thin film technology was in its early stages of evolution, we often find peculiar expressions such as "film deflagration" and "exploding wires" in the description of deposition procedures (sputtering was also used). It seems that the proximity of sources to substrates initially required by such processes, by inducing the deposition to occur at high angles in some regions, was the triggering cause for those early observations.

Another wave of interest, mainly in obliquely deposited metal films, emerged in the 1950's with investigations by Holland (1953) and Heimer (1957). In 1959, Thiessen and Broglia came across an unwelcomed

larization effect at the edges of their thermally-aluminized tronomical mirror.

It should also be mentioned that a magnetic counterpart of the tical anisotropy considered here was noticed in evaporated Permalloy .ms (Smith, 1959; Smith, Cohen and Weiss, 1960).

In the last few years, apart from its use for metal polarizers the near-infrared (Slocum, 1981) and as a rather small birefringence tected in a few waveguiding dielectric films deposited at low angles incidence (King and Talim, 1981), the polarization effect attracted ttle attention.

More recently, a significant retarder-like behavior was observed a zirconium oxide film deposited at a high angle of incidence. Its ount of birefringence, as well as that of dichroism for a mitransparent aluminum film deposited in similar conditions, were antitatively estimated at the HeNe wavelength by analyzing their ansmittance variations with azimuth angle in a conveniently adapted lipsometer. This work (Horowitz and Macleod, 1983) is reproduced in apter 2 of this dissertation with some extensions. It is still along e first trend, essentially characterized by a (semi)phenomenological proach.

As to the second trend, it probably acquired its initial well-fined forms in the classic article published by Abelés (1950), which esents the following three particularly attractive aspects. (1) The

theory starts directly from Maxwell Equations. (2) Interference effects are taken into account without need to explicitly consider multiple traversals of traveling waves within the medium. (3) The resulting 2x2 matrix treatment is a powerful and simple tool for multilayer calculations.

The problem then arose of finding a similar treatment which would apply equally well for arbitrary anisotropic thin films. Early theories by Schopper (1952) and by Bousquet (1957a) provide valuable predictions but lack items (2) and (3) above, and are only valid when one of the principal axes lies normal to the plane of the film (see also Heavens, 1965, p. 92).

Goncharenko and Fedorov (1963) considered the problem of an arbitrary absorbing crystal of arbitrary orientation in plane-parallel plate form at normal incidence. However, their approach lacks item (3) and cannot be extended to an arbitrary angle of incidence.

A useful 2x2 matrix technique was developed by Holmes and Feucht (1966) for the case in which one principal axis is perpendicular to the plane of incidence. Schesser and Eichmann (1972) proposed a general theory for wave propagation in layered anisotropic media, although their method lacks the simplicity mentioned in (3).

All three requirements are potentially fulfilled, with a high degree of generality, by a 4x4 matrix formulation developed in the following different contexts. In 1970 Teitler and Henvis extended the traditional two-dimensional approach to handle the case of refraction

under magnetically induced anisotropy in an otherwise isotropic semiconductor. Later Berreman (1972) announced a solution to the problem of reflection and transmission by cholesteric and other liquid crystals with continuously varying but planar ordering, in which he utilized a 4 x 4 differential-matrix technique. More recently, Yeh (1979) presented a similar formalism in a solid state physics context, and applied it to the Solc birefringent layered media, to the exchange Bragg scattering, and for a mode dispersion relation in guided waves.

It was hinted by Berning (1963, p. 71) that if a procedure were to be found for anisotropic films that would lead to the results obtained by several authors through different methods, each appropriate for a particular case, then such a procedure should arise from fundamental principles based on electromagnetic theory.

In Chapter 3 of this dissertation we begin from Maxwell's equations and recreate the Teitler and Henvis formalism, with its potential application for thin films in mind. Their approach is particularly suited to our purposes because it retains a close resemblance to the original Abelès method. Once the 4 x 4 propagation matrix of a system is known, transmittances and reflectances are obtainable in a straightforward manner.

It is not made clear in their formalism, however, how the elements of the propagation matrix are to be determined for applications other than the particular one they were studying. Additional insight is

required to fully enable the theory to handle problems on thin-film multilayer design.

We have interpreted the propagation matrix as an operator that maps one vector basis onto another, each corresponding to one of the film surfaces. With this understanding, we show that in the isotropic limit the matrix, properly inverted, is composed of a pair of independently operating submatrices, and these are identified as the 2 x 2 Abelès matrices connected to the s and p-polarization modes. When the same procedure is systematically applied for different anisotropic cases, the results attained by Schopper (1952), Bousquet (1957a), and Holmes and Feucht (1966) arise quite naturally.

In principle, apart from a few mathematical singularities, the theory is capable of producing the results of all treatments previously mentioned. At the end of Chapter 3 we go beyond them and consider the interaction of normally incident light with a stratified system composed of anisotropic layers, each with an arbitrary orientation of its optical axes (here a convenient vector operation is defined to greatly simplify the formalism).

A computer program was developed to turn the above considerations into a practical tool. It is briefly described in the beginning of Chapter 5. To determine reflectances and transmittances corresponding to an anisotropic multilayer system, each of its component layers (biaxial in the most general case) is specified by three pairs of principal optical constants, a physical thickness, and the direction of

columnar growth (which represents the average preferential orientation in the film microstructure).

The last of these is easily obtained from the so-called tangent rule

$$tg\phi = \frac{1}{2} tg\nu, \tag{1.1}$$

where ϕ is the columnar orientation angle and ν is the angle of vapor incidence, both with respect to the substrate normal. This identity was first experimentally determined by Nieuwenhuizen and Haanstra (1966) and its universality has been confirmed for a large number of film materials, as shown in Figure 1.2 with data from several investigators collected by Leamy, Gilmer, and Dirks (1980). The observation that the columns are oriented closer to the substrate normal than the vapor beam dates back to 1950. At that time, König and Helwig also stated that the anisotropic structures they observed with an electron microscope in obliquely deposited films was apparently due to shadowing of the impinging molecules by molecules already settled within the growing film. This idea has been recently supported by computer simulations of thin film growth (Dirks and Leamy, 1977), and the tangent rule statistically interpreted in terms of a stochastic process. The geometrical nature of the "self-shadowing" effect, as it is called, is evidenced by the fact that the models utilized for the simulated growth are able to reproduce the main structural features of the films without

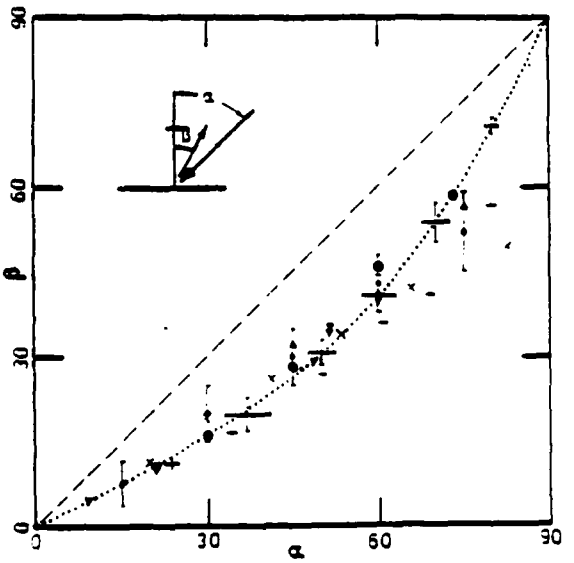


Figure 1.2. The Tangent Rule is Illustrated with Data from Several Investigators and a Variety of Film Materials.

The rule is obeyed well for all situations except for the data shown at + and x, which has been traced to a geometrical artifact of that particular experiment. Here α is the vapor angle of incidence and β is the columnar orientation angle. (From Leamy, Gilmer, and Dirks, 1980.)

taking into account crystalline texture, oxygen adsorption, momentum, or facet formation (Dirks, Leamy, and Gilmer, 1980).

With respect to the physical thickness, it can be determined by the observation of fringes of equal chromatic order (FECO) or by a stylographic measurement, as well as by simply counting repeated patterns of colored fringes with the simple technique we used for the obliquely deposited film we consider in Chapter 4.

On the optical constants of such anisotropic films, however, quantitative information is extremely scarce, if not absent, in the literature. For that reason we present a method that interprets ellipsometric measurements in light of the film columnar microstructure, and whose calculations can be performed with a simple pocket calculator.

In 1960, Bousquet and Rouard, reviewing experiments performed for a decade involving the determination of optical constants in thin films and their theoretical framework, concluded "...it well seems that the granular structure of the films remains the main cause for the anomalies observed in the optical constants...." (our translation)

We hope our method will facilitate the understanding of these anomalies during the course of the vast amount of work that lies ahead in this area.

Following the description of the method, a simple model of the microstructure is considered. The columns are taken as solid rods of infinite length with elliptical cross section and refractive index of the bulk material randomly distributed in an air matrix. A plausibility

argument is then presented that shows reasonable agreement between model predictions and measured values of the principal refractive indices.

Another clear realization that arises from the interpretation of the experiment, in the framework of the theory we have developed, is that Brewster's law does not hold for anisotropic media, films deposited at normal incidence included. A simple explanation for this is discussed, and a more general expression attained through the more fundamental "admittance-matching" between the two media involved. For practical reasons, this expression is derived for the case in which one principal axis is perpendicular to the plane of incidence so that it still retains some of the simplicity of Brewster's law, while reducing to it in the isotropic limit.

With the above considerations, we finally arrive at a stage in which the intersection between the two trends can be undertaken. In Chapter 5 we compare theory and experiment of transmittance measurements with variations of angle of incidence and azimuth angle for a simple dielectric film, as well as with respect to the spectral behavior of a narrowband filter with 21 layers. The properties of a hypothetical metal film are discussed at the end, in parallel with the aluminum sample deposited at 85° described in Chapter 2.

In the last chapter we summarize the results from this work and their possible extensions, followed by potential applications and further suggestions for future work.

A simplified map of our approach, as it was initially idealized, is shown in Figure 1.3.

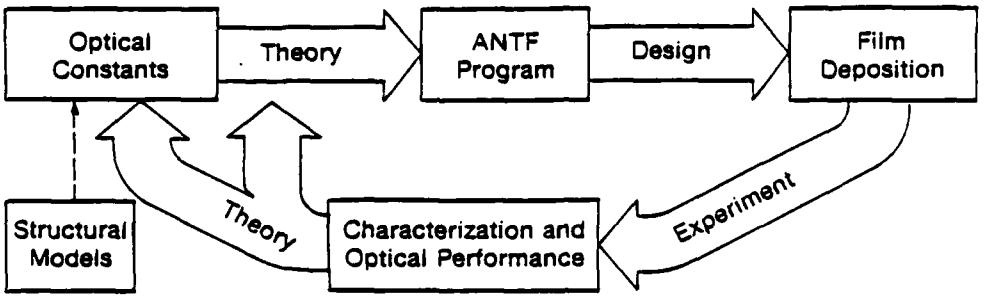


Figure 1.3. A Simplified Map of Our Approach.

CHAPTER 2

POLARIZATION EFFECTS IN METAL AND DIELECTRIC FILMS

We consider in this chapter the major features of the anisotropic microstructure contribution to the polarization effect in thin films deposited at high angles of vapor incidence. Previous reports that metal films mainly respond as polarizers under such conditions are confirmed. Structural anisotropy in dielectric films, rather than affecting the extinction coefficient values differently along different directions, seems to induce significant asymmetry in the refractive index values that enables us to find a retarder-like behavior. Quantitative analysis of the effect under normal incidence light at 632.8 nm is presented for aluminum and zirconium oxide films, and its structural origin is discussed.

Sample Preparation and Characterization

The films were vapor deposited by thermal evaporation in vacuo on glass substrates at room temperature and pressures of the order of 10^{-6} Torr. Prior to the deposition of the semitransparent aluminum and zirconium oxide films, the substrates were positioned to allow average vapor angles of incidence of 85° and 70° respectively. The distance between sources and substrates was approximately 250 mm. A directly heated tungsten spiral was used as the aluminum source. An electron-beam source with water-cooled copper hearth was used for the zirconium oxide.

An ellipsometer with Glan-Thompson polarizers that provided extinction ratios of at most one part in 10^6 was adapted to function as a polarimeter (Figure 2.1). The source was a single-mode HeNe laser, followed by a neutral density filter and a quarterwave plate that converted the plane polarized laser output to circularly polarized light. The neutral density filter and quarterwave plate together ensured that the signal was processed in the linear region of the photomultiplier whatever the orientation of the polarizer (a more detailed description of the apparatus is presented in Chapter 4).

Film thicknesses were determined with a profilometer, as well as with the fringes of equal chromatic order (FECO) technique.

Results and Discussion

Figures 2.2(a), (b) and (c) show the observed polarization response of an aluminum film as it was rotated around an axis defined by a normally incident light beam. The p-polarization was arbitrarily chosen to be horizontal. All measured values are relative to a direct signal obtained in the absence of the sample. In the following, the transmittance is indicated by the symbols T_{pp}, T_{ss}, T_{ps}, and T_{sp} where the first subscript indicates polarizer orientation and the second that of the analyzer. The initial angular position of the film was set so that the projection of its optical axis, determined by the direction of columnar growth,[5] along the glass-film interface was vertical.

Figures 2.2(a) and (b) show a significant difference between the ordinary and projected extraordinary direction transmittances. Slocum has presented a plausible explanation for this effect based on the idea

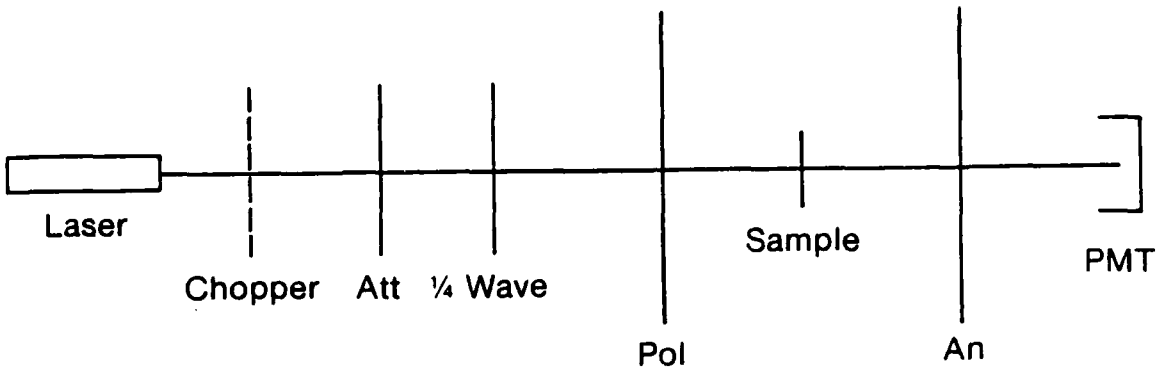


Figure 2.1. Characterization Setup.

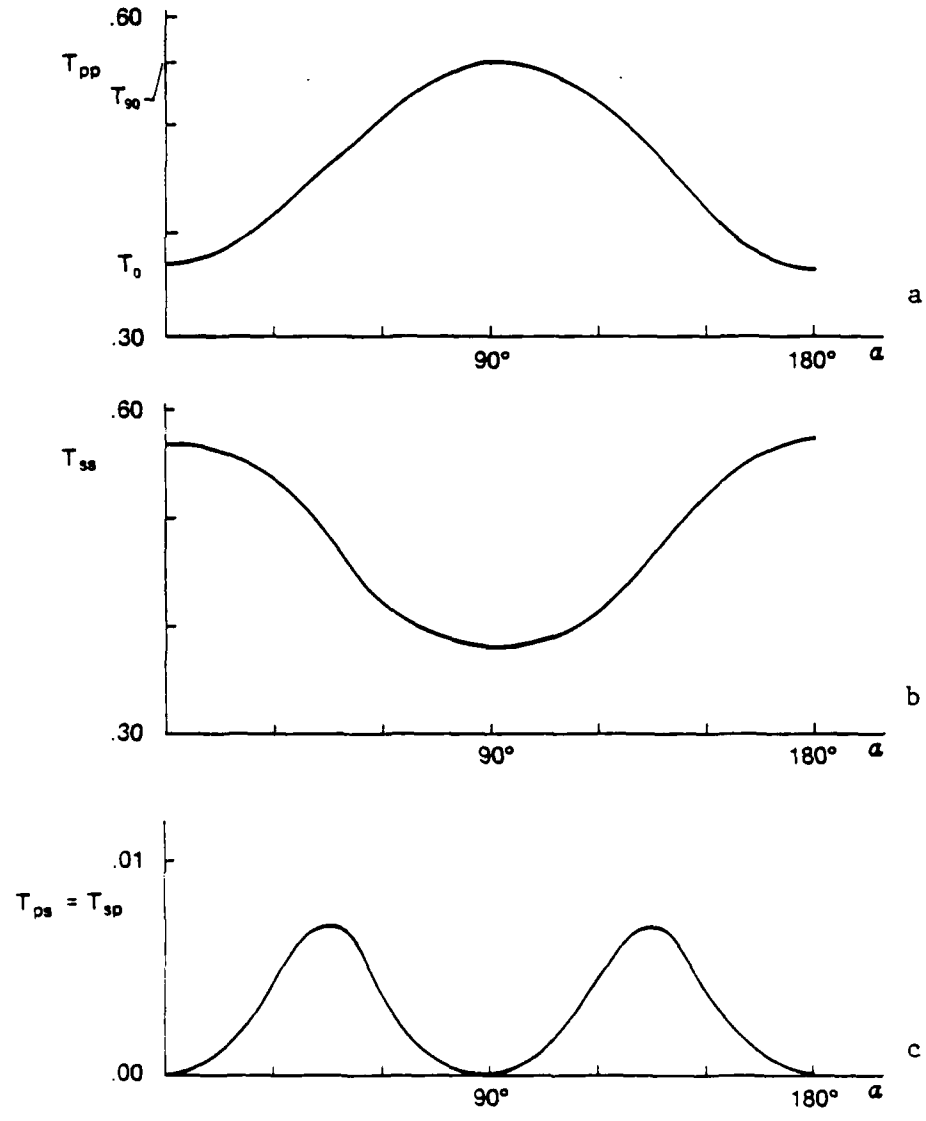


Figure 2.2. Relative Transmittances Measured as Functions of the Sample Rotation Angle for an Aluminum Sample (Al, AN 0326-85).

Error = ±0.01 for (a) and (b) and ±0.001 for (c). Since curve (b) should simply be curve (a) shifted by 90°, their equality can be used to confirm the alignment of the equipment and as a check of consistency.

of a wire grid Hertzian polarizer,[3] but the film seems to be most transmissive along the columnar direction. This property seems to be peculiar to the much smaller dimensions of the columns and their relative closeness.

It is well known that metals have extinction coefficients much larger than refractive indices in the visible. This allows us to approximately describe our aluminum film as a polarizer, based on the following reasoning. If we decompose an incident field at 45° into its components along the ordinary and projected extraordinary coordinates, each experiencing a different attenuation as indicated by T_o and T_{ee} in Figure 2a, and project the resulting fields along the direction coplanar and orthogonal to the original one, we will obtain the resulting transmittance:

$$T_{ps}^{(45°)} = \frac{1}{4} [T_{90}^{1/2} - T_0^{1/2}]^2 \approx 0.005, \quad (1)$$

which roughly reproduces the observed value in Figure 2c.

This allows us to easily estimate the effective extinction coefficient difference:

$$\Delta k \approx \frac{\lambda}{4\pi d} \ln \left(\frac{T_{90}}{T_0}\right) = 1.44, \quad (2)$$

where d = 14.5 nm is the measured thickness of the film.

To observe the birefringence effect in a dielectric, we deposited a 4.6-μm thick layer of zirconium oxide. The resulting data are shown in Figures 2.3(a) and (b). The polarization effect here, as opposed to that for aluminum, is due mainly to a refractive index variation. From a retarder point of view, we can estimate the effective amount of birefringence with the aid of Figure 2.3(a). We define a potential transmittance at 45°, indicated by $\psi_{pp}(45°)$, as

$$\psi_{pp}^{(45°)} = \frac{T_{45}}{T_0} , \tag{3}$$

where T_0 and T_{45} are the transmittances at $\alpha = 0°$ and 45° respectively in Figure 2.3(a). The decomposition of an incident p-polarized field at 45° into its ordinary and projected extraordinary components, which become phase-separated by $\Delta\phi$ as they travel along the material, and their subsequent projection back to the p-polarization direction yield

$$\psi_{pp}^{(45°)} = \cos^2 \left(\frac{\Delta\phi}{2}\right) . \tag{4}$$

From Equations (3) and (4) we obtain the effective amount of birefringence

$$\Delta n = \frac{\lambda}{\pi d} \cos^{-1} \left(\frac{T_{45}}{T_0}\right)^{1/2} = 0.042. \tag{5}$$

This actually sets a lower limit to Δn since there are many possible

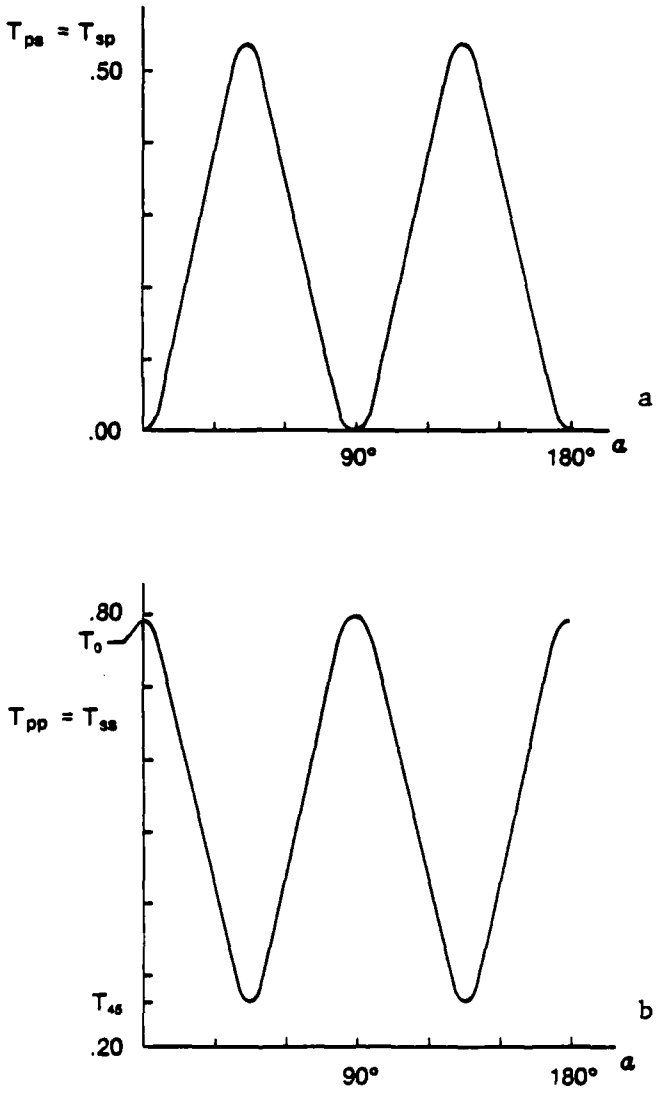


Figure 2.3. Relative Transmittances Measured as Functions of the Sample Rotation Angle for a Zirconium Oxide Sample (Zr oxide, EL 0124t-70).

Error = ±0.01. The 90° period permits us to write $T_{pp} = T_{ss}$ in curve (a).

values of $\Delta\phi$ that satisfy identity (4). The samples we have observed so far apparently point toward this lower value, but we are still intending to look at more samples over a wide thickness range to make this result more conclusive.

Structural Origin

There are many reports in the literature of thin film characterization by transmission electron microscopy of shadowed direct carbon replicas. Particularly relevant to the present study are the works by Guenter and Pulker (1976) and Nieuwenhuizen and Haanstra (1966) (where micrographs of excellent quality are reproduced. Our own measurements were similar and quite consistent with these earlier results. Column dimensions in each sample showed a spread in sizes but almost all were in the range of 30 to 100 μm diameter. These results, as well as the directional character of the polarization effect we have discussed, indicate the columnar growth origin of the effect.

Although the results that have been quoted refer to either aluminum or zirconium oxide films, these effects have also been observed in preliminary work on silver, copper, and titanium oxide films, all of which have a pronounced columnar structure. In addition, scattering measurements made on some of our samples at the Center for Thin-Film Studies in Marseille (Flory, 1978; Bousquet, Fory and Roche, 1981) have shown anisotropy related to a narrow range of sizes only. This behavior is particularly pronounced in Figures 2.4(a) and 2.4(b) for a silver film.

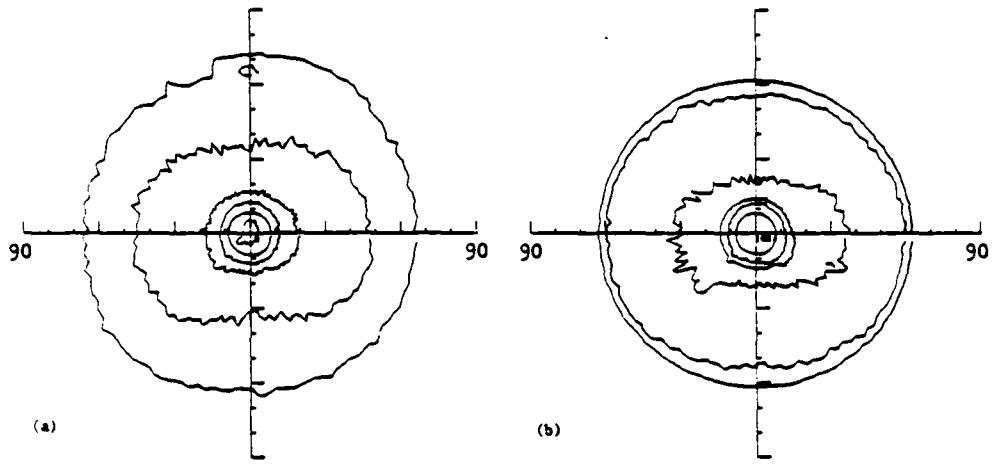


Figure 2.4. Scattering in (a) Reflection and (b) Transmission from an Anisotropic Silver Film.

Note the marked anisotropy of the third contour in (b) while the others are circular. The receiver analyzer is parallel to the plane of polarization of the incident light. The lines are constant intensity contours. Relative intensities, outer to inner, are 5×10^{-6}, 1×10^{-5}, 2×10^{-5}, 4×10^{-5}, 1×10^{-4}, and 1×10^{-3}. (Sample AG10A90)

The almost universal columnar structure of vacuum-deposited films[5] suggests strongly that behavior similar to that which we have reported should be observed in films of virtually any material.

Up to this point we have assumed a uniaxial film microstructure, with the optical axis along the columnar direction. However, experimental evidence, obtained from transmission electron microscopy observations with the electron beam parallel to the columnar orientation (Leamy, Gilmer and Dirks, 1980), has shown that for a more detailed study columns should be taken with an elliptical cross section elongated in a perpendicular direction to that of the vapor incidence. For that reason, in the theoretical analysis that follows, the microstructure is considered in the most general biaxial configuration.

CHAPTER 3

A UNIFIED MATRIX FORMULATION FOR ANISOTROPIC MULTILAYER SYSTEMS

In this chapter we consider a general theory for stratified anisotropic media with the purpose of understanding the anisotropic optical behavior reported in Chapter 2 from electromagnetic principles. This understanding will later allow us to present a computer program developed as a test for anisotropic multilayer design.

Starting from Maxwell equations, we recreate the Teitler and Henvis formalism (1970), with homogeneous thin film multilayer systems in mind. We specialize to isotropic media (CASE 0), anisotropic media with linear polarization modes (CASE 1), and later to anisotropic media with elliptical polarization modes (CASE 2). In CASE 0, we show that the formalism can be reduced to Abelés treatment (1950) traditionally used for isotropic multilayer films. In CASE 1, we reproduce the results previously obtained by several authors for particular configurations, and form the basic framework for the experimental determination of the principal refractive indices of a biaxial dielectric film (see Chapter 4). With those indices as ad hoc parameters, the optical properties predicted from CASE 1 and CASE 2 treatments will ultimately be compared with the corresponding experimental results in Chapter 5.

The Propagation Matrix

We begin by recalling the curl Maxwell equations in a linear, nonmagnetic and polarizable medium in the Gaussian system

$$\nabla \times \mathbf{E} = -\frac{1}{c}\frac{\partial \mathbf{B}}{\partial t} \tag{3.1}$$

$$\nabla \times \mathbf{H} = \frac{1}{c}\frac{\partial \mathbf{D}}{\partial t} + \frac{4\pi}{c}\mathbf{J}, \tag{3.2a}$$

where

$$\mathbf{B} = \mu_0 \mathbf{H}, \qquad \mu_0 = 1 \tag{3.3}$$

$$\mathbf{D} = \epsilon\, \mathbf{E}, \qquad \mathbf{J} = \sigma\, \mathbf{E}. \tag{3.4}$$

From (3.4), (3.2a) can be rewritten

$$\nabla \times \mathbf{H} = \frac{1}{c}\epsilon_{eff}\frac{\partial \mathbf{E}}{\partial t}, \qquad \epsilon_{eff} = \epsilon + 4\pi\sigma . \tag{3.2b}$$

For simplicity we will refer to the effective "dielectric" tensor ϵ_{eff} as ϵ, while still allowing it to be nonreal, asymmetric, or non-Hermitian as a result of current contributions.

We assume that the electromagnetic fields propagate within the medium as attenuated plane waves,

$$\begin{aligned} \mathbf{E} &= \mathbf{E}(z)\exp\left[-i\left(\frac{S\omega}{c}x - \omega t\right)\right] \\ \mathbf{H} &= \mathbf{H}(z)\exp\left[-i\left(\frac{S\omega}{c}x - \omega t\right)\right], \end{aligned} \tag{3.5}$$

where $S = n_0 \sin\theta_0$, and the geometry shown in Figure 3.1 is understood.

Expansion of the field amplitude vectors into their components along the coordinate axes,

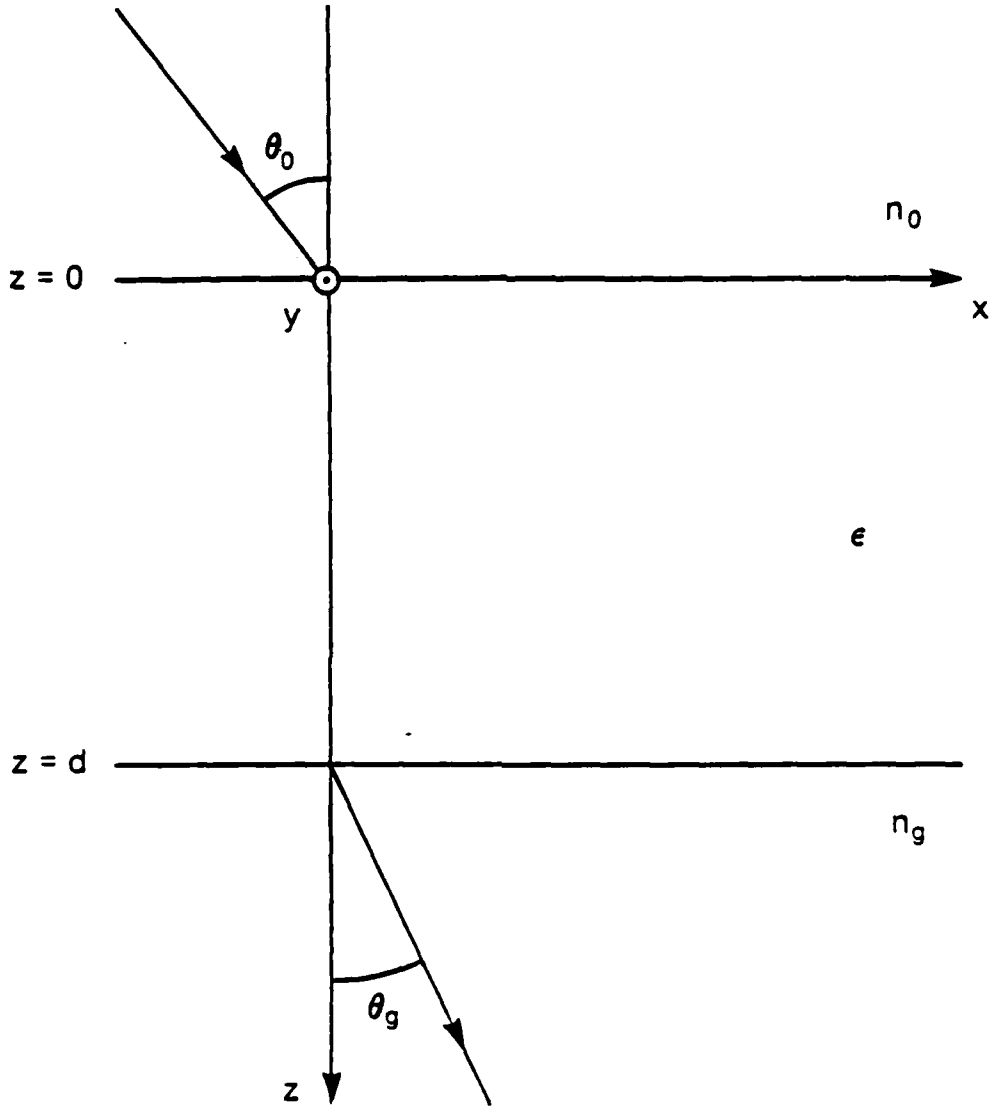


Figure 3.1. Geometry for Refraction in Anisotropic Media.

$$\mathbf{E}(z) = \sum_{j=1}^{3} E_j(z)\,\hat{e}_j$$

$$\mathbf{H}(z) = \sum_{j=1}^{3} H_j(z)\,\hat{e}_j \;; \qquad (\hat{e}_1,\hat{e}_2,\hat{e}_3) \equiv (\hat{x},\hat{y},\hat{z}), \tag{3.6}$$

followed by direct substitution into (3.1) and (3.2b), leads to six component equations which for $\epsilon_{33} \neq 0$ allow us to eliminate $E_3(z)$ and $H_3(z)$. If we simplify our notation through the identities,

$$u_n \equiv E_n(z),\; u_{n+2} \equiv H_n(z) \;; \quad n = 1,2$$

and

$$D \equiv \frac{c}{i\omega}\,\frac{d}{dz} \;,$$

the remaining four equations become

$$\begin{aligned} Du_1 &= c_{11}u_1 + c_{12}u_2 + c_{14}u_4 \\ Du_2 &= u_3 \\ Du_3 &= c_{31}u_1 + c_{32}u_2 + c_{34}u_4 \\ Du_4 &= c_{41}u_1 + c_{42}u_2 + c_{44}u_4 \;, \end{aligned} \tag{3.7}$$

where

$$\begin{aligned} c_{11} &= \frac{S}{\epsilon_{33}}\,\epsilon_{31} & c_{12} &= \frac{S}{\epsilon_{33}}\,\epsilon_{32} & c_{14} &= \left(\frac{S}{\epsilon_{33}}\,S\right) - 1 \\ c_{31} &= \epsilon_{21} - \epsilon_{31}\,\frac{\epsilon_{23}}{\epsilon_{33}} & c_{32} &= \epsilon_{22} - S^2 - \epsilon_{32}\,\frac{\epsilon_{23}}{\epsilon_{33}} & c_{34} &= -S\frac{\epsilon_{23}}{\epsilon_{33}} \\ c_{41} &= \epsilon_{31}\,\frac{\epsilon_{13}}{\epsilon_{33}} - \epsilon_{11} & c_{42} &= \epsilon_{32}\,\frac{\epsilon_{13}}{\epsilon_{33}} - \epsilon_{12} & c_{44} &= -S\frac{\epsilon_{13}}{\epsilon_{33}} \;. \end{aligned} \tag{3.8}$$

Any solution of the system of four linear equations (3.7) can be expressed as a linear combination of four independent solutions. Teitler and Henvis (1970) suggest we choose these, called u^{α} (α=a,b,c,d), with components $u_{\beta}{}^{\alpha}$ (β=1,2,3,4) that satisfy the boundary conditions

$$u_{\beta}{}^{\alpha}(z=0) = \delta_{\alpha\beta}, \tag{3.9}$$

where $\delta(\alpha\beta)$ is the Kronecker delta function, and collect them to form the matrix

$$L(z) = \begin{bmatrix} u_1{}^a(z) & u_1{}^b(z) & u_1{}^c(z) & u_1{}^d(z) \\ u_2{}^a(z) & u_2{}^b(z) & u_2{}^c(z) & u_2{}^d(z) \\ u_3{}^a(z) & u_3{}^b(z) & u_3{}^c(z) & u_3{}^d(z) \\ u_4{}^a(z) & u_4{}^b(z) & u_4{}^c(z) & u_4{}^d(z) \end{bmatrix} . \tag{3.10}$$

This matrix has the property of mapping the tangential field component $u_{\beta}{}^{0}$ at the interface $z = 0$ onto the corresponding components $u_{\beta}(z)$ at $z \geq 0$ within the same medium:

$$\begin{bmatrix} u_1 \\ u_2 \\ u_3 \\ u_4 \end{bmatrix} = L(z) \begin{bmatrix} u_1{}^0 \\ u_2{}^0 \\ u_3{}^0 \\ u_4{}^0 \end{bmatrix} . \tag{3.11}$$

For that reason, we refer to $\mathbf{L}(z)$ as the propagation matrix for one layer. Formally its two-dimensional analog is the inverse of the Abelès (1950) characteristic matrix traditionally used for the isotropic case, as will be shown later.

If N layers are present between 0 and z, (3.11) can be simply extended to

$$u(z) = \left[\prod_{j=1}^{N} L_j(z)\right] u^0 , \tag{3.12}$$

which makes the propagation matrix particularly useful for multilayer systems.

Our interpretation of the Teitler and Henvis prescription can be found in Appendix A. This understanding will later enable us to apply the propagation matrix technique to some cases of practical interest.

The Reflectance and Transmittance Matrices

We now proceed to determine the reflectance and transmittance matrices. We assume that the incident electric field E_o^+ consists of two plane-wave components, i.e.,

$$E_o^+ = \begin{bmatrix} E_{op}^+ \\ \\ E_{os}^+ \end{bmatrix} \exp\left[-i\left(\frac{S\omega}{c}\, x-\omega t\right)\right] \tag{3.13}$$

polarized parallel and perpendicular to the plane of incidence, respectively. Similar conventions for the reflected and transmitted electromagnetic fields are shown in Figure 3.2.

Using the boundary conditions provided by the continuity of the tangential components of the **E** and **H** fields at the interfaces $z = 0$ and $z = d$, and connecting the tangential fields within the anisotropic layer through the L-matrix, we obtain the expressions:

$$a_p^- E_{op}^- + a_s^- E_{os}^- + a_p^+ E_{op}^+ + a_s^+ E_{os}^+ = 0 \tag{3.14}$$

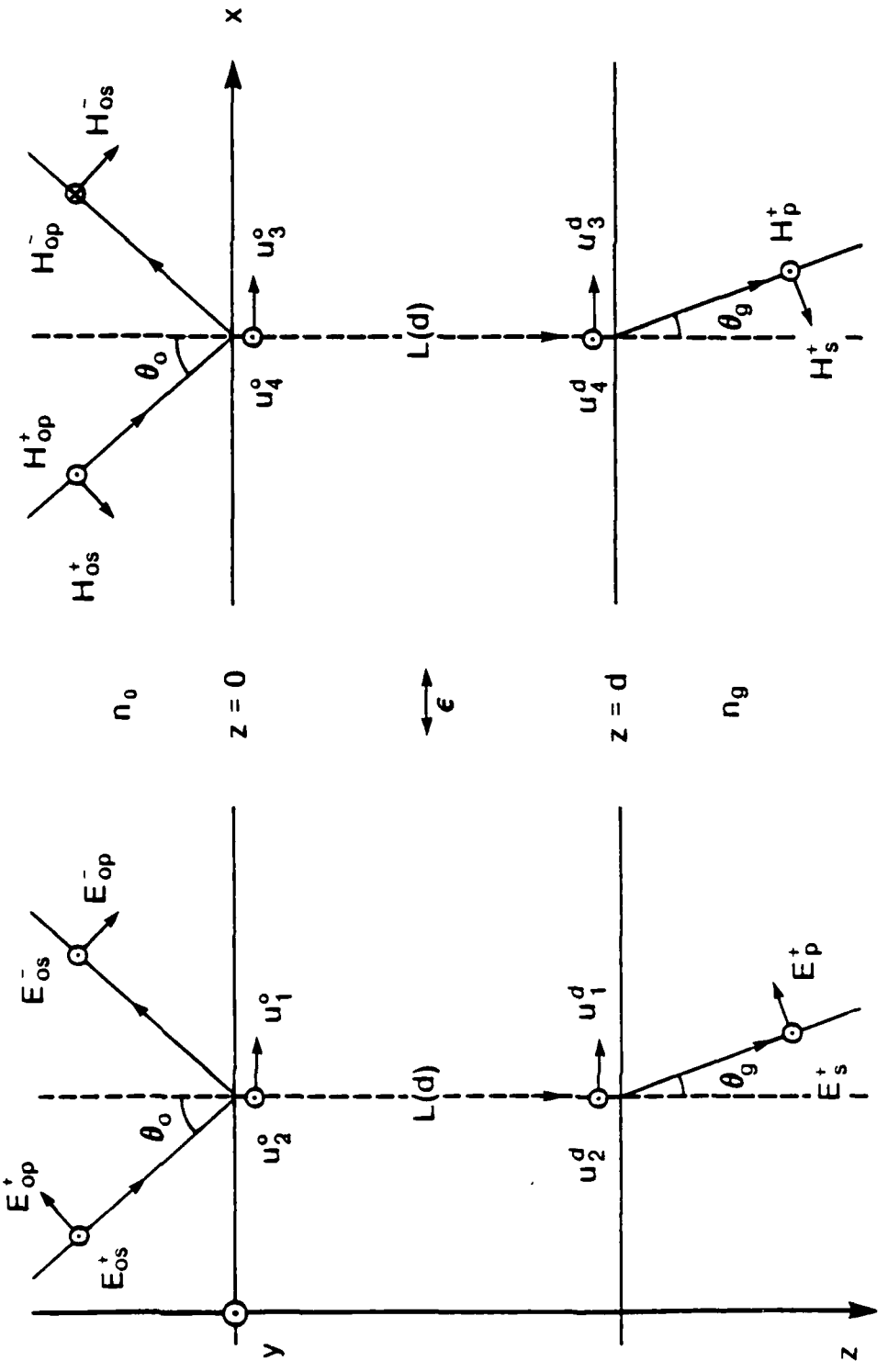


Figure 3.2. Conventions and Schematic for the Determination of the Reflectance and Transmittance Amplitude Coefficients.

$$b_p^- E_{op}^- + b_s^- E_{os}^- + b_p^+ E_{op}^+ + b_s^+ E_{os}^+ = 0,$$

where

$$\begin{aligned} a_p^{\pm} &= (\ell_{11}\cos\theta_0 \pm \ell_{14} n_0) n_g - (\ell_{41}\cos\theta_0 \pm \ell_{44} n_0)\cos\theta_g \\ a_s^{\pm} &= (\ell_{12} \mp \ell_{13} N_0) n_g - (\ell_{42} \mp \ell_{43} N_0)\cos\theta_g \\ b_p^{\pm} &= (\ell_{21}\cos\theta_0 \pm \ell_{24} n_0) N_g + (\ell_{31}\cos\theta_0 \pm \ell_{34} n_0) \\ b_s^{\pm} &= (\ell_{22} \mp \ell_{23} N_0) N_g + (\ell_{32} \mp \ell_{33} N_0), \end{aligned} \tag{3.15}$$

with $N_0 = n_0 \cos\theta_0$, $N_g = n_g \cos\theta_g$, and ℓ_{ij} is the ijth element of the L-matrix at $z = d$.

We define amplitude reflectance and transmittance matrices by

$$\begin{aligned} E_o^- &= [r]\, E_o^+ \\ E^+ &= [t]\, E_o^+ , \end{aligned} \tag{3.16}$$

and through (3.14) determine their elements. We get

$$\begin{bmatrix} r_{pp} & r_{ps} \\ r_{sp} & r_{ss} \end{bmatrix} = (a_s^- b_p^- - a_p^- b_s^-)^{-1} \begin{bmatrix} a_p^+ b_s^- - a_s^- b_p^+ & a_s^+ b_s^- - a_s^- b_s^+ \\ a_p^- b_p^+ - a_p^+ b_p^- & a_p^- b_s^+ - a_s^+ b_p^- \end{bmatrix}$$

$$\begin{bmatrix} t_{pp} & t_{ps} \\ t_{sp} & t_{ss} \end{bmatrix} = N_g^{-1} \begin{bmatrix} a_{p_1}^- & a_{s_1}^- \\ b_{p_1}^- & b_{s_1}^- \end{bmatrix} \begin{bmatrix} r_{pp} & r_{ps} \\ r_{sp} & r_{ss} \end{bmatrix} + N_g^{-1} \begin{bmatrix} a_{p_1}^+ & a_{s_1}^+ \\ b_{p_1}^+ & b_{s_1}^+ \end{bmatrix}, \tag{3.17}$$

where the subscript $_1$ (e.g. $\alpha_{p_1}^-$) refers to the first term of the corresponding quantity in (3.15) (e.g. a_p^-). Note that the last

contribution in the expression above is the amplitude potential transmittance matrix. (Potential transmittance is the maximum transmittance achievable in a system as allowed by material constraints.)

From (3.17) we finally obtain the corresponding reflectance and transmittance matrices

$$[R] = [r^*.r] \tag{3.18}$$

$$[T] = \frac{N_g}{N_0} [t^*.t] ,$$

where the symbol * denotes the complex conjugate.

Homogeneous Anisotropic Medium

The treatment we have considered up to now is valid for general, inhomogeneous (layered) anisotropic media. Let us apply it to the simpler homogeneous anisotropic case.

Consider a solution basis set consisting of vectors with components

$$u_j(z) = A_j \exp(-ik_0 \eta z), \qquad k_0 \equiv \frac{\omega}{c} = \frac{2\pi}{\lambda_0} \tag{3.19}$$

where the A_j's are the constant coefficients, λ_0 is the light wavelength in vacuum and η is a parameter that will be determined later.

Equations (3.7) then take the form

$$\begin{aligned} (\eta + c_{11})u_1 + c_{12}u_2 + c_{14}u_4 &= 0 \\ \eta u_2 + u_3 &= 0 \end{aligned} \tag{3.20}$$

$$c_{31}u_1 + c_{32}u_2 + \eta u_3 + c_{34}u_4 = 0$$

$$c_{41}u_1 + c_{42}u_2 + (\eta + c_{44})u_4 = 0.$$

Nontrivial solutions exist for (3.20) provided they satisfy the corresponding secular equation

$$\eta^4 + G_3\eta^3 + G_2\eta^2 + G_1\eta + G_0 = 0, \tag{3.21}$$

where

$$G_3 = c_{11} + c_{44}$$

$$G_2 = c_{11}c_{44} - c_{32} - c_{14}c_{41}$$

$$G_1 = c_{34}c_{42} + c_{12}c_{31} - c_{32}c_{44} - c_{11}c_{32}$$

$$G_0 = c_{11}c_{34}c_{42} + c_{12}c_{31}c_{44} + c_{14}c_{32}c_{41} - c_{11}c_{32}c_{44} - c_{12}c_{34}c_{41} - c_{14}c_{31}c_{42}.$$

The quartic equation above becomes a simpler biquadratic when $G_3 = G_1 = 0$. With identities (3.8) in mind, this occurs whenever the ϵ tensor is diagonal, which characterizes the cases we consider next.

CASE ZERO: The Isotropic Limit

Consider a homogeneous isotropic layer with thickness d, associated with an ϵ tensor expressed as

$$\begin{bmatrix} \epsilon & 0 & 0 \\ 0 & \epsilon & 0 \\ 0 & 0 & \epsilon \end{bmatrix} . \tag{3.23}$$

From (3.8) it follows that

$$c_{11} = 0 \qquad c_{12} = 0 \qquad c_{14} = \frac{S^2}{\epsilon} - 1$$

$$c_{31} = 0 \qquad c_{32} = \epsilon - S^2 \qquad c_{34} = 0 \tag{3.24}$$

$$c_{41} = -\epsilon \qquad c_{42} = 0 \qquad c_{44} = 0 \ ,$$

and the secular equation (3.21) becomes

$$\eta^4 + 2(S^2-\epsilon)\eta^2 + (S^2-\epsilon)^2 = 0, \tag{3.25}$$

leading to the allowed η-values

$$\eta\mp \equiv \pm\eta = \pm (\epsilon-S^2)^{1/2}. \tag{3.26}$$

The four component equations (3.20) take the form

$$\begin{aligned} \pm\eta u_1 - \frac{1}{\epsilon}\eta^2 u_4 &= 0 \\ \pm\eta u_2 + u_3 &= 0 \\ \eta^2 u_2 \pm \eta u_3 &= 0 \\ -\epsilon u_1 \pm \eta u_4 &= 0. \end{aligned} \tag{3.27}$$

This is clearly an undetermined equation system that can provide only the ratios

$$\frac{u_4}{u_1} = \pm\frac{\epsilon}{\eta} \qquad \frac{u_3}{u_2} = \pm\eta \ , \tag{3.28}$$

unless $u_1 = u_4 = 0$ or $u_2 = u_3 = 0$.

We thus form the plane-wave component solutions from

$$\begin{aligned} u_1 &= A_1 \exp(\mp ik_0\eta z) \quad u_2 = A_2 \exp(\mp ik_0\eta z) \\ u_4 &= \pm A_1 \frac{\epsilon}{\eta} \exp(\mp ik_0\eta z) \quad u_3 = \pm A_2\eta \exp(\mp ik_0\eta z) \end{aligned} \tag{3.29}$$

and the above pairs of trivial values.

We take linear combinations of these solutions in such a way that boundary conditions (3.9) are satisfied. For example, take two independent solutions

$$\left[A_1 \exp(-ik_0\eta z),\ 0,\ 0,\ A_1 \frac{\epsilon}{\eta} \exp(-ik_0\eta z)\right] \tag{3.30}$$

$$\left[A_1 \exp(+ik_0\eta z),\ 0,\ 0,\ -A_1 \frac{\epsilon}{\eta} \exp(+ik_0\eta z)\right],$$

add them up and choose $A_1 = 1/2$ to obtain

$$u^a = \left[\cos(k_0\eta z),\ 0,\ 0,\ -i \frac{\epsilon}{\eta} \sin(k_0\eta z)\right], \tag{3.31a}$$

so that $u^a(z=0) = [1,0,0,0]$, as required. (We are here interchangeably expressing the "column vectors" in Appendix A as "line vectors.)

Similarly,

$$u^b = [0,\ \cos(k_0\eta z),\ -i\eta \sin(k_0\eta z),0] \tag{3.31b}$$

$$u^c = \left[0,\ \frac{-i}{\eta} \sin(k_0\eta z),\ \cos(k_0\eta z),\ 0\right] \tag{3.31c}$$

$$u^d = \left[-i \frac{\eta}{\epsilon} \sin(k_0\eta z),\ 0,\ 0,\ \cos(k_0\eta z)\right] \tag{3.31d}$$

We are now able to construct the L-matrix representing the propagation of the tangential fields from the $z = 0$ to the $z = d$ interfaces

$$L(z=d) = \begin{bmatrix} \cos\delta & 0 & 0 & -i \frac{\eta}{\epsilon} \sin\delta \\ 0 & \cos\delta & -\frac{i}{\eta} \sin\delta & 0 \\ 0 & -i\eta \sin\delta & \cos\delta & 0 \\ -i \frac{\epsilon}{\eta} \sin\delta & 0 & 0 & \cos\delta \end{bmatrix} \tag{3.32}$$

where

$$\delta \equiv \frac{2\pi}{\lambda_0} \eta d.$$

For simplicity let us examine the case of a single dielectric layer with refractive index n. With $\epsilon = n^2$ and from (3.26):

$$\eta = (n^2 - S^2)^{1/2} = n \cos\theta\ , \tag{3.33}$$

where Snell's law was used and θ is the angle of refraction within the

medium. We conveniently reorder the tangential field components to get from (3.32)

$$\begin{bmatrix} u_1^d \\ u_4^d \\ u_2^d \\ u_3^d \end{bmatrix} \begin{bmatrix} \cos\delta & -i\frac{\cos\theta}{n}\sin\delta & 0 & 0 \\ -i\frac{n}{\cos\theta}\sin\delta & \cos\delta & 0 & 0 \\ 0 & 0 & \cos\delta & -i\frac{\sin\delta}{n\cos\theta} \\ 0 & 0 & -in\cos\theta\sin\delta & \cos\delta \end{bmatrix} \begin{bmatrix} u_1^0 \\ u_4^0 \\ u_2^0 \\ u_3^0 \end{bmatrix} \tag{3.34}$$

If we recall the convention $[u_1,u_2,u_3,u_4] \equiv [E_x,E_y,H_x,H_y]$ and split the 4×4 propagation matrix above into its 2×2 submatrices, their inverses will provide

$$\begin{bmatrix} E_x^0 \\ H_y^0 \end{bmatrix} = \begin{bmatrix} \cos\delta & \frac{i}{n_p}\sin\delta \\ in_p\sin\delta & \cos\delta \end{bmatrix} \begin{bmatrix} E_x^d \\ H_y^d \end{bmatrix}$$

$$\begin{bmatrix} E_y^0 \\ H_x^0 \end{bmatrix} = \begin{bmatrix} \cos\delta & \frac{i}{n_s}\sin\delta \\ in_s\sin\delta & \cos\delta \end{bmatrix} \begin{bmatrix} E_y^d \\ H_y^d \end{bmatrix} \tag{3.35}$$

where

$$n_p = \frac{n}{\cos\theta}$$

$$n_s = n\cos\theta$$

and

$$\delta = \frac{2\pi}{\lambda_0} nd \cos\theta.$$

We have just obtained the traditional Abelès (1950) characteristic matrices.

CASE 1: Linear Polarization Modes

Consider a homogeneous anisotropic layer with thickness d whose principal axes, or axes of electrical symmetry, coincide with the coordinate axes defined previously. See Figure 3.3(a) for the corresponding columnar structure configurations. Such a material is associated with an ϵ tensor expressed as

$$\begin{bmatrix} \epsilon_{11} & 0 & 0 \\ 0 & \epsilon_{22} & 0 \\ 0 & 0 & \epsilon_{33} \end{bmatrix} \quad ; \quad \epsilon_{jj} = n_j^2 \ (j=1,2,3). \tag{3.36}$$

From (3.8) we get the coefficients

$$\begin{aligned} c_{11} &= 0 & c_{12} &= 0 & c_{14} &= \frac{S^2}{\epsilon_{33}} - 1 \\ c_{31} &= 0 & c_{32} &= \epsilon_{22} - S^2 & c_{34} &= 0 \\ c_{41} &= -\epsilon_{11} & c_{42} &= 0 & c_{44} &= 0 \ , \end{aligned} \tag{3.37}$$

and component equations (3.20) become

$$\begin{aligned} \eta u_1 + c_{14} u_4 &= 0 \\ \eta u_2 + u_3 &= 0 \\ c_{32} u_2 + \eta u_3 &= 0 \\ c_{41} u_1 + \eta u_4 &= 0 \ , \end{aligned} \tag{3.38}$$

from which we determine the allowed η-values

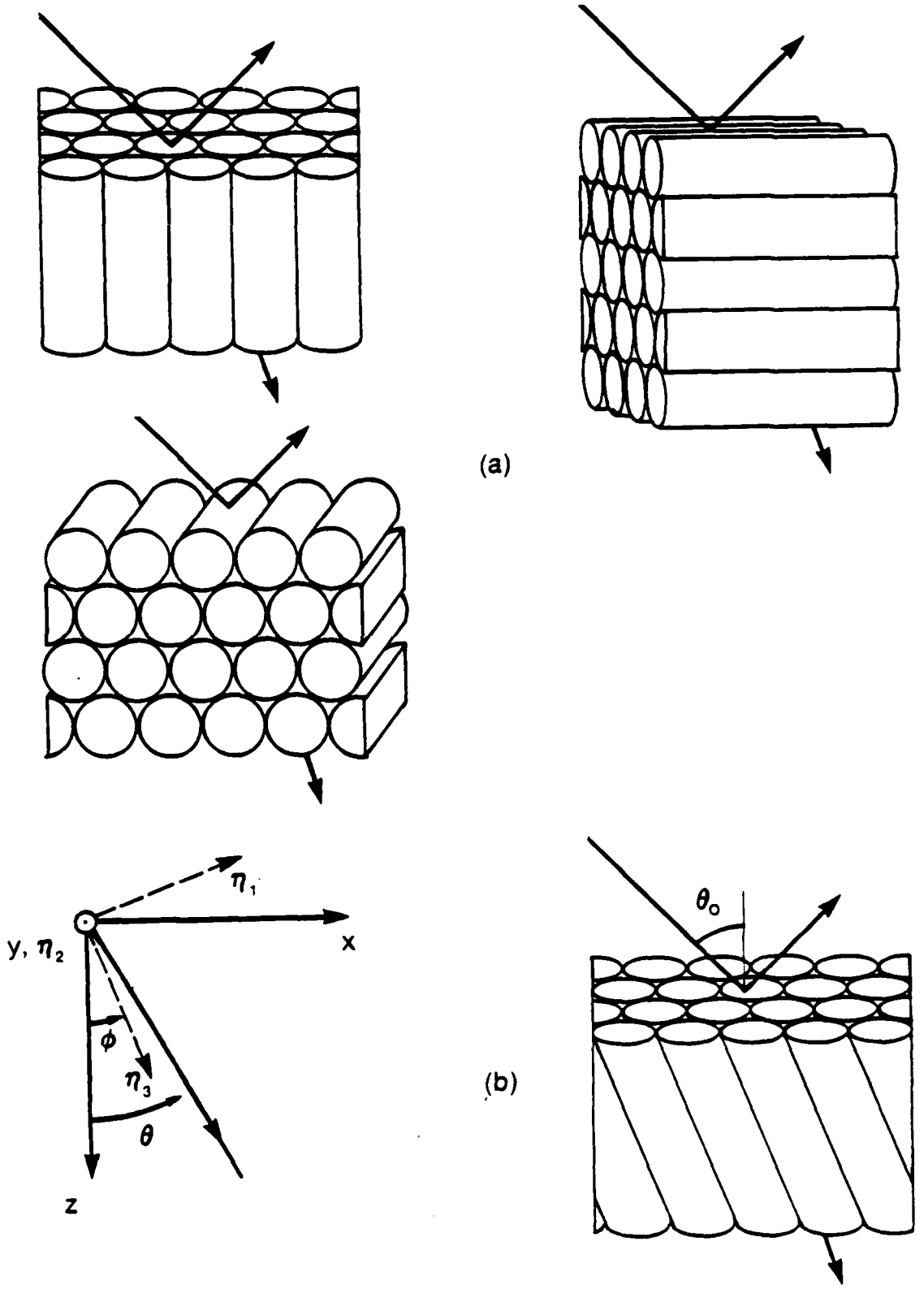


Figure 3.3. Possible CASE 1 Columnar Structure Configurations.

$$\eta_s^{\pm} \equiv \pm\eta_s = \pm(c_{32})^{1/2}$$
$$\eta_p^{\pm} \equiv \pm\eta_p = \pm(c_{14}c_{41})^{1/2}. \tag{3.39}$$

We have already labeled these two pairs of solutions as s and p because they are independently attached to $\{u_2,u_3\}$ and $\{u_1,u_4\}$, in that order.

The corresponding two pairs of nontrivial component solutions are

$$u_2 = A_2 \exp(\mp ik_0\eta_s)\ u_1 = A_1 \exp(\mp ik_0\eta_p) \tag{3.40}$$
$$u_3 = \pm\eta_s A_2 \exp(\mp ik_0\eta_s)\ u_4 = \pm \frac{\epsilon_{11}}{\eta_p} A_1 \exp(\mp ik_0\eta_p).$$

We take convenient linear combinations of the basis vectors composed of these and of trivial components, in a manner similar to that shown in the isotropic case, to obtain

$$u^a = \left[\cos(k_0\eta_p z),\ 0,\ 0,\ -i\ \frac{\epsilon_{11}}{\eta_p}\ \sin(k_0\eta_p z)\right]$$
$$u^b = [0,\ \cos(k_0\eta_s z),\ -i\eta_s\ \sin(k_0\eta_s z),\ 0] \tag{3.41}$$
$$u^c = \left[0,\ -\frac{i}{\eta_s}\ \sin(k_0\eta_s z),\ \cos(k_0\eta_s z),\ 0\right]$$
$$u^d = \left[-i\ \frac{\eta_p}{E_{11}}\ \sin(k_0\eta_p{}^2),\ 0,\ 0,\ \cos(k_0\eta_p{}^2)\right],$$

which satisfy boundary conditions (3.9), as required.

The following propagation matrix at z=d results

$$L(z=d) = \begin{bmatrix} \cos\delta_p & 0 & 0 & -i\,\frac{\eta_p}{\eta_1^2}\,\sin\delta_p \\ 0 & \cos\delta_s & -\frac{i}{\eta_s}\,\sin\delta_s & 0 \\ 0 & -i\eta_s\,\sin\delta_s & \cos\delta_s & 0 \\ -i\,\frac{\eta_1^2}{\eta_p}\,\sin\delta_p & 0 & 0 & \cos\delta_p \end{bmatrix}, \tag{3.42}$$

where

$$\delta_s = \frac{2\pi}{\lambda_0}\,\eta_s d$$

$$\delta_p = \frac{2\pi}{\lambda_0}\,\eta_p d \tag{3.43}$$

and

$$\eta_s^2 = \eta_2^2 - \eta_0^2\,\sin^2\theta_0\,, \quad \eta_p^2 = \frac{\eta^2}{\eta_3^2}\,(\eta_3^2 - \eta_0^2\,\sin^2\theta_0);$$

$$\eta_j^2 \equiv \epsilon_{jj}\ (j=1,2,3).$$

Identities (3.43) are consistent with the results presented by Bousquet (1957a) in the theory he developed for this particular case.

The matrix above is easily split into its two-dimensional submatrices, and by taking their inverses we can write

$$\begin{bmatrix} E_y^0 \\ H_x^0 \end{bmatrix} = \begin{bmatrix} \cos\delta_s & \frac{i}{\eta_s}\sin\delta_s \\ i\eta_s\sin\delta_s & \cos\delta_s \end{bmatrix} \begin{bmatrix} E_y^d \\ H_x^d \end{bmatrix} \qquad (3.44)$$

$$\begin{bmatrix} E_x^0 \\ H_y^0 \end{bmatrix} = \begin{bmatrix} \cos\delta_p & i\frac{\eta_p}{\eta_1^2}\sin\delta_p \\ i\frac{\eta_1^2}{\eta_p}\sin\delta_p & \cos\delta_p \end{bmatrix} \begin{bmatrix} E_x^d \\ H_y^d \end{bmatrix} .$$

Note the similarity between these and matrices (3.35) for the isotropic case. They are the same for $\eta_1 = \eta_2 = \eta_3$, as expected. At normal incidence we get $\eta_s = \eta_2$ and $\eta_p = \eta_1$, and each of the matrices above is still formally equivalent to (3.35). This implies that in this situation the anisotropic layer behaves as if it were isotropic for each polarization mode separately. In other words, the concept of "equivalent (isotropic) admittance" still applies, as long as we think in terms of two "equivalent isotropic layers," one for each polarization mode.

These are the same when $\eta_1 = \eta_2$ ($\neq \eta_3$), which supports the validity of optical measurements performed with normally vapor-deposited films under normal light incidence while still disregarding the anisotropy of the films. However, care must be taken in oblique light incidence measurements, since it is clear from identities (3.43) that anisotropy can significantly influence optical behavior in some cases.

Generalization

An important point to be realized is that a 2×2 matrix treatment is valid if and only if the s- and p-polarized fields are uncoupled. In terms of equations (3.20), for an arbitrary angle of incidence, that means

$$c_{12} = c_{31} = c_{34} = c_{42} = 0, \tag{3.45a}$$

or, from (3.8)

$$\varepsilon_{12} = \varepsilon_{21} = \varepsilon_{23} = \varepsilon_{32} = 0. \tag{3.45b}$$

Whenever these conditions are satisfied, the s- and p-polarized fields will travel independently along the medium. This is always the case when one of them vibrates along one of the principal axes of the material.

Consider the geometry shown in Figure 3.3(b). The principal axis along which an electric field experiences an admittance η_3 is at an arbitrary angle ϕ from the z axis, but still in the plane of incidence. This implies that the s-polarized field is always at another principal axis and thus propagates independently from the p field.

This configuration is still associated with the diagonal ε matrix (3.36) in the principal axes representation. Since these axes are obtainable from the coordinate axes system through a counterclockwise rotation by ϕ around the y axis, as considered in Appendix B, the following coordinate axes representation will result:

$$\begin{bmatrix} \varepsilon_{11}\cos^2\phi + \varepsilon_{33}\sin^2\phi & 0 & (\varepsilon_{11}-\varepsilon_{33})\sin\phi\cos\phi \\ 0 & \varepsilon_{22} & 0 \\ (\varepsilon_{11}-\varepsilon_{33})\sin\phi\cos\phi & 0 & \varepsilon_{11}\sin^2\phi + \varepsilon_{33}\cos^2\phi \end{bmatrix}, \quad (3.46)$$

and the (3.8) coefficients become

$$\begin{aligned} c_{11} &= S\,\frac{\varepsilon'_{31}}{\varepsilon'_{33}} & c_{12} &= 0 & c_{14} &= \frac{S^2}{\varepsilon'_{33}} \\ c_{31} &= 0 & c_{32} &= \varepsilon'_{22} - S^2 & c_{34} &= 0 \\ c_{41} &= \frac{\varepsilon'_{13}\varepsilon_{31}}{\varepsilon_{33}} - \varepsilon'_{11} & c_{42} &= 0 & c_{44} &= S\,\frac{\varepsilon'_{13}}{\varepsilon'_{33}} \end{aligned} \quad (3.47)$$

where the ε'_{ij}'s (i,j=1,3) refer to the elements of matrix (3.46).

The component equations (3.20) related to the s-polarization mode take the form

$$\begin{aligned} \eta u_2 + u_3 &= 0 \\ (\varepsilon_{22}-S^2)u_2 + \eta u_3 &= 0, \end{aligned} \quad (3.48)$$

from which we obtain

$$\eta_s^2 = \eta_2^2 - S^2 ; \qquad S = n_0 \sin\theta_0 . \quad (3.49)$$

In the p-polarization case the equations are

$$\begin{aligned} (\eta+c_{11})u_1 + c_{14}u_4 &= 0 \\ c_{41}u_1 + (\eta+c_{44})u_4 &= 0, \end{aligned} \quad (3.50)$$

which combined with (3.46) and (3.47) allow us to write the resulting η-solutions in a concise way as

$$\eta_p^{\pm} = -c_{11} \pm g , \quad (3.51)$$

where g is such that

$$g^2 = c_{14}c_{41} = \left(1 - \frac{S^2}{\varepsilon'_{33}}\right) \eta^2_{po} .$$

For this last identity we have defined the quantity η_{po} so that

$$\frac{1}{\eta^2_{po}} \equiv \frac{1}{c_{41}} = \frac{\cos^2\phi}{\eta_1^2} + \frac{\sin^2\phi}{\eta_3^2} . \tag{3.52}$$

Since at normal incidence S = 0, it is easy to see from (3.51) and (3.47) that

$$\eta_p^{\pm} (\theta_0=0) = \pm \eta_{po} . \tag{3.53}$$

From (3.48) and (3.50) we get the nontrivial component solutions

$$u_2 = A_2 \exp(\mp ik_0 \eta_s^2)$$

$$u_3 = \pm \eta_s u_2 \tag{3.54}$$

and

$$u_1 = A_1 \exp(iK_0 c_{11} z) \exp(\mp ik_0 g z)$$

$$u_4 = \pm\gamma u_1 ; \quad \gamma = -\frac{c_{41}}{g} , \tag{3.55}$$

where (3.51) was used.

Proceeding exactly as we did following (3.40), we obtain the propagation matrix at z = d

$$\begin{bmatrix} \Phi \cos\delta_p' & 0 & 0 & -\frac{i\Phi}{\gamma}\sin\delta_p' \\ 0 & \cos\delta_s & -\frac{i}{\eta_s}\sin\delta_s & 0 \\ 0 & -i\eta_s \sin\delta_s & \cos\delta_s & 0 \\ -i\gamma\Phi \sin\delta_p^2 & 0 & 0 & \Phi\cos\delta_p' \end{bmatrix} \tag{3.56}$$

where

$$\delta_s = \frac{2\pi}{\lambda_0} n_s d, \qquad \delta_p' = \frac{2\pi}{\lambda_0} g d$$

$$n_s^2 = n_2^2 - S^2, \qquad g^2 = \left(1 - \frac{S^2}{\varepsilon_{33}'}\right) n^2 po \tag{3.57}$$

$$\phi = \exp\left(i \frac{2\pi}{\lambda_0} dS \frac{\varepsilon_{31}'}{\varepsilon_{33}'}\right), \qquad \gamma = \frac{n^2 po}{g} .$$

The inverse of the s-submatrix is identical to that in (3.44). As for the p-submatrix, we take its inverse and get

$$\begin{bmatrix} E_x^0 \\ H_y^0 \end{bmatrix} = \phi^* \begin{bmatrix} \cos\delta_p' & \frac{i}{\gamma} \sin\delta_p' \\ i\gamma \sin\delta_p' & \cos\delta_p' \end{bmatrix} \begin{bmatrix} E_x^d \\ H_y^d \end{bmatrix} . \tag{3.58}$$

Careful examination of the results (3.57) and (3.58) shows that they are in agreement with (3.43) and (3.44) in the $\phi = 0$ limit, as expected. They are also consistent with an independent calculation performed by Ian Hodgkinson in connection with the two-dimensional matrix treatment by Holmes and Feucht (1966).

Discussion

We now consider the results we have attained so far for the simple case of a dielectric single layer.

Bearing in mind our comments following (3.44), let n_{eq} be an "equivalent (isotropic) refractive index" that allows us to use Snell's law

$$S \equiv n_0 \sin\theta_0 = n_{eq} \sin\theta. \tag{3.59}$$

For the s-polarization mode, obviously $n_{eq} = n_2$ at any angle of incidence. This is confirmed by direct comparison between (3.33) and (3.57), Snell's law considered.

To determine n_{eq} for the p-mode we use (3.33) and Snell's law, combined with (3.51) and its auxiliary relations (3.47), (3.46) and (3.52). After a laborious but straightforward algebraic exercise we obtain

$$\frac{1}{n^2_{eq}} = \frac{\cos^2(\theta-\phi)}{n_1^2} + \frac{\sin^2(\theta-\phi)}{n_3^2} . \tag{3.60}$$

In the isotropic limit $n_{eq} = n_1 = n_3$, as expected. This expression is consistent with (3.52) at normal incidence. It also agrees with (3.43) in the $\phi = 0$ limit.

The dependence of n_{eq} on the angle between the wavevector inside the medium and the n_3-axis (see Fig. 3.3(b)) leads us to a simple physical interpretation of (3.60). From it we derive the phase-velocity relation

$$v^2_{eq} = v_1^2 + v_3^2 , \tag{3.61}$$

where $v_{eq} = c/n_{eq}$; v_1 and v_3 are the phase velocities, in the plane of incidence, respectively perpendicular to the n_1 and n_3 axes. In other words, Snell's law can be used as if for an isotropic dielectric layer provided we decompose the "equivalent (isotropic) phase velocity vector" v_{eq} into its components along the principal axes, whose contributions account for the angular dependence of n_{eq} according to expression (3.60).

CASE 2: Elliptical Polarization Modes

Consider a homogeneous anisotropic layer with thickness d whose principal axes system is at an arbitrary orientation. A general ε tensor, expressed in the coordinate axes representation by the matrix

$$\begin{bmatrix} \varepsilon'_{11} & \varepsilon'_{12} & \varepsilon'_{13} \\ \varepsilon'_{21} & \varepsilon'_{22} & \varepsilon'_{23} \\ \varepsilon'_{31} & \varepsilon'_{32} & \varepsilon'_{33} \end{bmatrix} \tag{3.62}$$

can be easily obtained from the principal axes diagonal representation as shown in Appendix B.

Identities (3.22) and (3.8) in mind, the quartic equation (3.21) simplifies to a biquadratic whenever S = 0. It is fortunate that we can still find an analytical solution for all normal incidence configurations, which constitute most circumstances of practical interest.

For S = 0 the (3.8) coefficients become

$$\begin{aligned} c_{11} &= 0 & c_{12} &= 0 & c_{14} &= -1 \\ c_{31} &= \varepsilon'_{21} - \varepsilon'_{31}\frac{\varepsilon'_{23}}{\varepsilon'_{33}} & c_{32} &= \varepsilon'_{22} - \varepsilon'_{32}\frac{\varepsilon'_{23}}{\varepsilon'_{33}} & c_{34} &= 0 \\ c_{41} &= \varepsilon'_{31}\frac{\varepsilon'_{13}}{\varepsilon'_{33}} - \varepsilon'_{11} & c_{42} &= \varepsilon'_{32} - \frac{\varepsilon'_{13}}{\varepsilon'_{33}} - \varepsilon'_{12} & c_{44} &= 0 , \end{aligned} \tag{3.63}$$

so that the secular equation (3.21) can be written

$$\eta^4 + G_2\eta^2 + G_0 = 0,$$

where

$$\begin{aligned} G_2 &= -c_{32} - c_{14}c_{41} \\ G_0 &= c_{14}(c_{32}c_{41} - c_{31}c_{42}). \end{aligned} \tag{3.64}$$

We then obtain two pairs of allowed η-values

$$\eta_1^{\pm} \equiv \pm\eta_1 = \pm \left(\frac{-G_2+F}{2}\right)^{1/2} \qquad (3.65)$$

$$\eta_2^{\pm} \equiv \pm\eta_2 = \pm \left(\frac{-G_2-F}{2}\right)^{1/2}$$

where

$$F = ((G_2)^2 - 4G_0)^{1/2} .$$

The nontrivial component solutions to equations (3.20) associated with the first pair of η-values are

$$\begin{aligned} u_1(\eta_1) &= A_1 \exp(-ik_0\eta_1 z) \\ u_2(\eta_1) &= r_{21}(\eta_1)\cdot u_1 \; ; \quad r_{21}(\eta_1) = (\eta_1^2 - c_{14}c_{41})/c_{14}c_{42} \\ u_3(\eta_1) &= r_{31}(\eta_1)\cdot u_1 \; ; \quad r_{31}(\eta_1) = -\eta_1 r_{21}(\eta_1) \\ u_4(\eta_1) &= r_{41}(\eta_1)\cdot u_1 \; ; \quad r_{41}(\eta_1) = -(c_{41}+c_{42}r_{21}(\eta_1))/\eta_1 . \end{aligned} \qquad (3.66)$$

(The last of identities (3.66) is not in agreement with the corresponding expression for r_{41} presented by Teitler and Henvis (1970), which, as printed in p. 832 of their article, requires a sign correction.) Similar nontrivial component solutions hold in connection with the second pair of admittances. They are directly obtained from (3.66) by performing the changes $A_1 \to A_2$ and $\eta_1 \to \eta_2$.

At this point we note that r_{21}, r_{31}, and r_{41} are functions with well-defined parity with respect to the η-values. This allows us to follow naturally the procedure used in previous cases to determine the propagation matrix.

We take the first two independent solutions

$$\mathbf{u}_1 = [\, u_1(\eta_1),\ r_{21}(\eta_1)u_1(\eta_1),\ r_{31}(\eta_1)u_1(\eta_1),\ r_{41}(\eta_1)u_1(\eta_1) \,] \qquad (3.67)$$

$$\omega_2 = \omega_1(-\eta_1)$$

$$= [u_1(-\eta_1),\ r_{21}(\eta_1)u_1(-\eta_1),\ -r_{31}(\eta_1)u_1(-\eta_1),\ -r_{41}(\eta_1)u_1(-\eta_1)]$$

and sum them up at z = d to get

$$\omega_{12} = 2A_1[\ \cos\delta_1,\ r_{21}(\eta_1)\cos\delta_1,\ -ir_{31}(\eta_1)\sin\delta_1,\ -ir_{41}(\eta_1)\sin\delta_1\ ], \tag{3.68a}$$

where we have used the identity

$$\delta_i \equiv \frac{2\pi}{\lambda_0} n_i d\ ; \qquad i = 1,2. \tag{3.69}$$

Similarly we obtain from the second pair of independent solutions

$$\omega_{34} = 2A_2[\ \cos\delta_2,\ r_{21}(\eta_2)\cos\delta_2,\ -ir_{31}(\eta_2)\sin\delta_2,\ -ir_{41}(\eta_2)\sin\delta_2\ ]. \tag{3.70a}$$

To simplify the notation, let us define the "direct vector product" operation @ such that, given two arbitrary vectors

$$\mathbf{a} \equiv [a_1,a_2,a_3,a_4]$$

and

$$\mathbf{b} \equiv [b_1,b_2,b_3,b_4]\ ,$$

$$\mathbf{a} \,@\, \mathbf{b} \equiv [a_1b_1,\ a_2b_2,\ a_3b_3,\ a_4b_4]. \tag{3.71}$$

With this in mind, we can rewrite (3.68a) and (3.70a) as

$$\omega_{12} = 2A_1\ p(\delta_1) \,@\, r(\eta_1) \tag{3.68b}$$

$$\omega_{34} = 2A_2\ p(\delta_2) \,@\, r(\eta_2), \tag{3.70b}$$

where

$$p(\delta_i) \equiv [\cos\delta_i,\ \cos\delta_i,\ -i\ \sin\delta_i,\ -i\ \sin\delta_i] \tag{3.72}$$

$$r(\eta_i) \equiv [1,\ r_{21}(\eta_i),\ r_{31}(\eta_i),\ r_{41}(\eta_i)];\quad i=1,2. \tag{3.73}$$

We now take the difference

$$u^a = w_{12} - w_{34} = 2A_1\ p(\delta_1) \ @\ r(\eta_1) - 2A_2\ p(\delta_2) \ @\ r(\eta_2), \tag{3.74}$$

and choose

$$2A_2 = \frac{r_{21}(\eta_1)}{r_{21}(\eta_2)-r_{21}(\eta_1)}\ , \qquad 2A_1 = \frac{r_{21}(\eta_2)}{r_{21}(\eta_1)}\ 2A_2 \tag{3.74a}$$

so that $u^a(d=0) = [1,0,0,0]$, as required by (3.9).

In a similar way we get

$$u^b = u^a \text{ (formally)},$$

where now the choice is

$$2A_1 = 2A_2 = [r_{21}(\eta_1) - r_{21}(\eta_2)]^{-1}. \tag{3.74b}$$

The other two solution vectors are

$$u^{c \text{ or } d} = 2A_1\ q(\delta_1) \ @\ r(\eta_1) - 2A_2\ q(\delta_2) \ @\ r(\eta_2), \tag{3.75}$$

where

$$q(\delta_i) = [-i\ \sin\delta_i,\ -i\ \sin\delta_i,\ \cos\delta_i,\ \cos\delta_i]; \quad i=1,2$$

and u^c:

$$2A_1 = \frac{r_{41}(\eta_2)}{r_{31}(\eta_1)r_{41}(\eta_2)-r_{41}(\eta_1)r_{31}(\eta_2)}\ , \qquad 2A_2 = \frac{r_{41}(\eta_1)}{r_{41}(\eta_2)}\ 2A_1 \tag{3.75a}$$

for u^d

$$2A_1 = \frac{-r_{31}(\eta_2)}{r_{31}(\eta_1)r_{41}(\eta_2)-r_{41}(\eta_1)r_{31}(\eta_2)}\ , \qquad 2A_2 = \frac{r_{31}(\eta_1)}{r_{31}(\eta_2)}\ 2A_1. \tag{3.75b}$$

The usual construction of the L-matrix follows, with its elements l_{jk} given by the components u_j of the solution vectors

$$l_{j1} = u_j^a,\ l_{j2} = u_j^b,\ l_{j3} = u_j^c,\ l_{j4} = u_j^d\ ;\quad j = 1,2,3,4. \tag{3.76}$$

Discussion

The detailed final structure of the l_{jk} elements is of no practical interest to us because the above recurrence relations already allow for a compact and systematic calculation in the ANTF program, which will be introduced later. All general expressions (3.12) to (3.18) follow, leading to the determination of the reflectance and transmittance of multilayer systems.

A novel feature that arises in this case is that the cross terms in the amplitude reflectance and transmittance matrices are generally nonzero. When this happens linearly polarized light may become elliptically polarized after interaction with the anisotropic system. Also the p and s-polarizations lose their traditional roles as eigenmodes since, as already evident from equations (3.20) with coefficients (3.63), their corresponding fields may propagate in a coupled manner along the medium, and this is the physical cause for the appearance of the nonzero amplitude cross terms.

It should be mentioned that this problem was also tackled by Goncharenko and Fedorov (1963). However, their treatment applies for normal incidence only and, far from a matrix formulation, is not appropriate for multilayer system calculations. It seems impractical to compare their results with ours.

With regard to expression (3.66), we have implicitly assumed in our treatment that $c_{42} \neq 0$. When $c_{42} = 0$ and $c_{31} = 0$ (also $c_{12} = c_{34} = 0$ for normal incidence), equations (3.20) split into two independent pairs, the s and p-polarized fields travel uncoupled along the medium and we are back to CASE 1. $c_{42} = 0$ implies $c_{31} = 0$ for any lossless medium since, (3.63) considered, no energy loss in the system implies that the ϵ tensor is symmetrical, as elegantly demonstrated in Born and Wolf (1975, p. 666). Consequently the actual restriction in our formulation occurs when $c_{42} = 0$ and $c_{31} \neq 0$ for lossy media (or eventually when one denominator in identities (3.74a) or (3.75) becomes zero).

The method is potentially extendable to arbitrary principal axes orientation under arbitrary oblique incidence situations. This would involve solving the quartic equation (3.21) with the aid of numerical techniques like, for example, the algorithm for complex polynomials by Jenkins and Traub (1972).

CHAPTER 4

MEASUREMENT OF PRINCIPAL REFRACTIVE INDICES OF BIREFRINGENT THIN FILMS

An arbitrary, biaxial dielectric film is ideally specified by its physical thickness d and a set of three refractive indices $\{n_1,n_2,n_3\}$, each along one of the principal axes of the material. Therefore at least four independent observations are required for its complete characterization.

It should be clear from our considerations in the previous chapter that a conveniently simple configuration involving a single-layer film, vapor-deposited at an arbitrary angle, consists of allowing the so-formed columnar axis to lie in the plane of incidence. In other words, one of the principal dielectric axes is perpendicular to that plane, and thus the s and p-polarized fields travel independently along the material.

Also for simplicity, we turn to advantage the nonuniform thickness distribution produced by oblique deposition. We carefully scan the sample position until the light beam interacts with an area of the film where the optical thickness is an integer number of quarterwaves (STEP 1). This will ultimately enable us to obtain explicit expressions for the refractive indices in terms of the experimental observables.

In what follows, we will be using two standard procedures in ellipsometry (Winterbottom, 1948; Azzam and Bashara, 1977; Bennett and Bennett, 1978), although in a different context from that in which the usual Fresnel equations or identities involving Airy functions are assumed to be valid (STEPS 2 and 3). These procedures have the advantage of high accuracy inherent in null measurements.

The fourth observation will utilize the Abelès technique (1949) for its extreme simplicity, although the Brewster angle will be located photoelectrically rather than visually only (Kelly and Heavens, 1959). The polarimetric extension of the technique as proposed by Hacskaylo (1964) will be incorporated to increase further the accuracy of the measurement (STEP 4).

These four experimental steps will be described in some detail in our exposition of the measurement method.

Setup Description and Operation

The arrangement of the ellipsometer is shown in Figure 4.1. The source is a single-mode HeNe laser whose output power varies by less than half of a percent over extended periods of time. It is followed by a chopper operating in tune with a lock-in amplifier at the receiver end of the apparatus. A quarterwave retarder converts the linearly polarized laser output to circularly polarized light, and is followed by a neutral density filter to ensure that the signal is processed in the linear region of the photomultiplier response whatever the orientation of the polarizer.

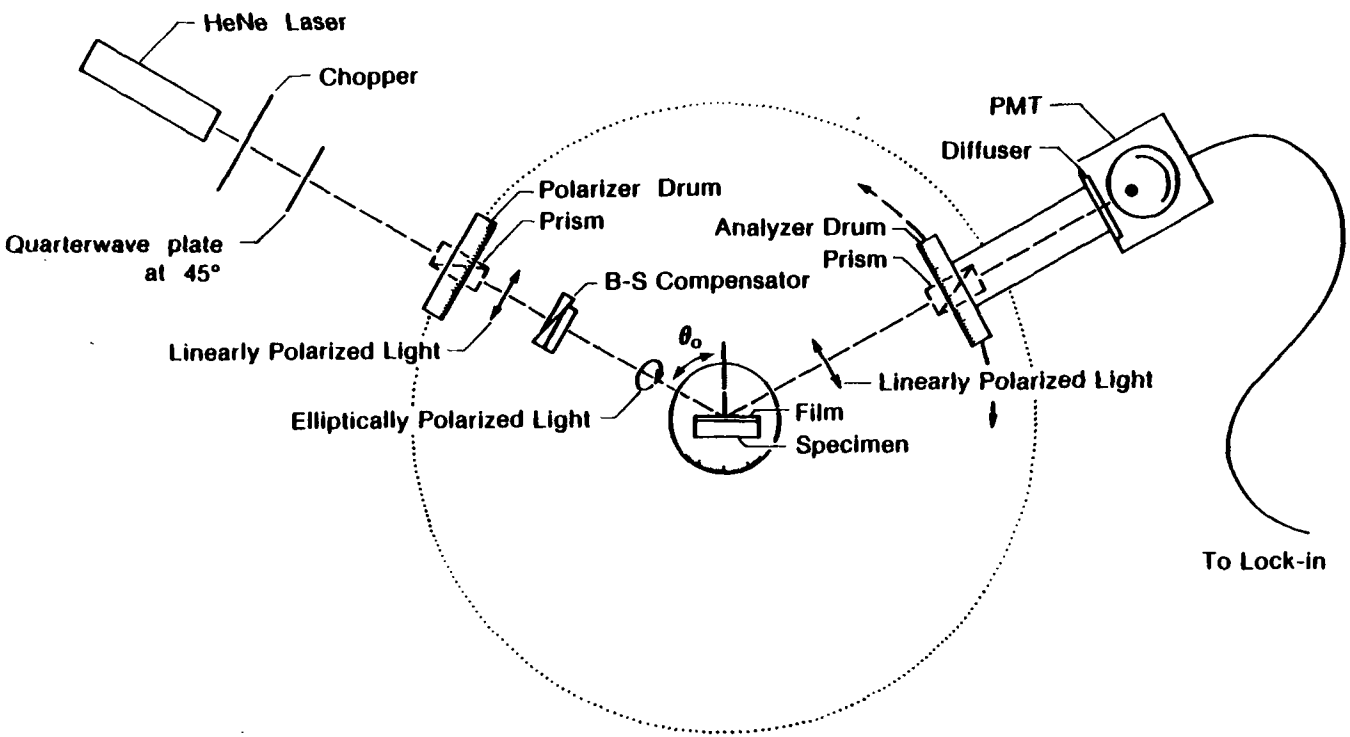


Figure 4.1. Schematic Diagram of Experimental Setup.

The polarizer and analyzer are Glan-Thompson prisms which provide extinction ratios of at most one part in 10^6. Their angular position can be read at their respective drums to an accuracy of 0.01° of arc.

A Babinet-Soleil compensator, preceding the sample, makes possible the determination of optical path differences smaller than 0.2% of the HeNe wavelength. Its calibration was performed with a high-quality quarterwave retarder at that wavelength, and later its zero position was checked by producing a dark field with the polarizer and analyzer crossed.

The sample holder is positioned on a rotating table surrounded by a horizontal master circle scaled to an accuracy of 20 sec of arc.

A critical feature of the ellipsometer (see Figure 4.2) is that the rotation of the specimen table and that of the analyzer-receiver arm must share the same central axis. At the intersection between this axis and the laser beam, centered in both arms of the instrument, lies the spot under observation. This spot is to remain ideally in the same location on the specimen as the table is rotated.

To ensure that those conditions were reasonably fulfilled, the various alignment stages of the ellipsometer were performed in accordance with the high precision procedure described by Zeidler, Kohles, and Bashara (1974) except for the following point. Since our interest was on a thin film coating rather than on a slab of material, only one surface of a glass slide was partially aluminized for the

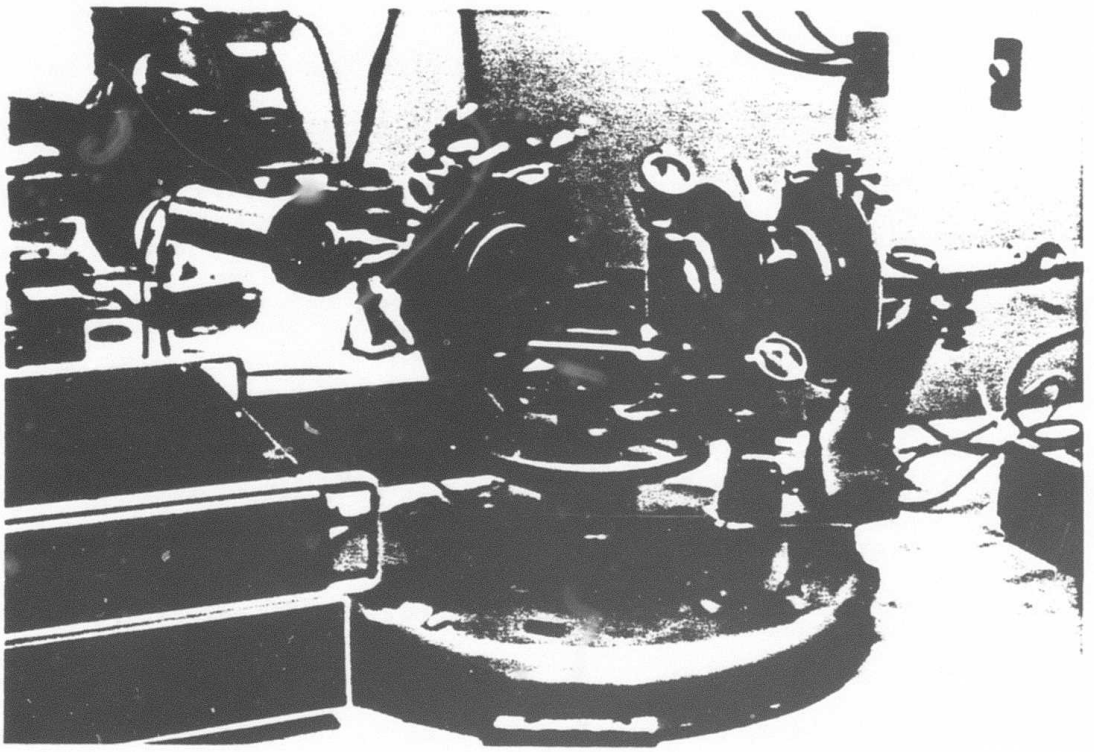


Figure 4.2. Sideview of the Ellipsometer.

alignment procedure. This ensured that the film, not the substrate, contained the central axis of rotation, and furthermore eliminated the strict requirement of parallelism between two aluminized surfaces encountered by the above authors.

A slight lateral shift of the beam over the photocathode surface occurs when a transmittance measurement is in operation at oblique angles of incidence. The consequent variation in detector sensitivity was minimized by placing a diffuser at the entrance of the photomultiplier.

Another difficulty appeared when the data showed significant dependence on touch pressure as a sample was manually scanned during the Brewster angle measurement between its coated and uncoated parts. This was circumvented by attaching a metal rod to the substrate holder (see Figure 4.3). The rod, always in contact with two fixed bolts, allowed for a smooth sliding of the holder while keeping a uniform pressure against a fixed mount. A clamp marker always ensured that the same location on the coated portion of the sample was illuminated during the iterative procedure. Reproducible results were then finally achieved.

Method

The method consists of determining $\{n_1, n_2, n_3, d\}$ from the observables $\{\Lambda_S, \Lambda_\Delta, \psi_t, \theta_B\}$, as defined in the steps below. Prior to observation, the dielectric film is obliquely deposited at a known angle ν of vapor incidence on a partly masked substrate of known refractive

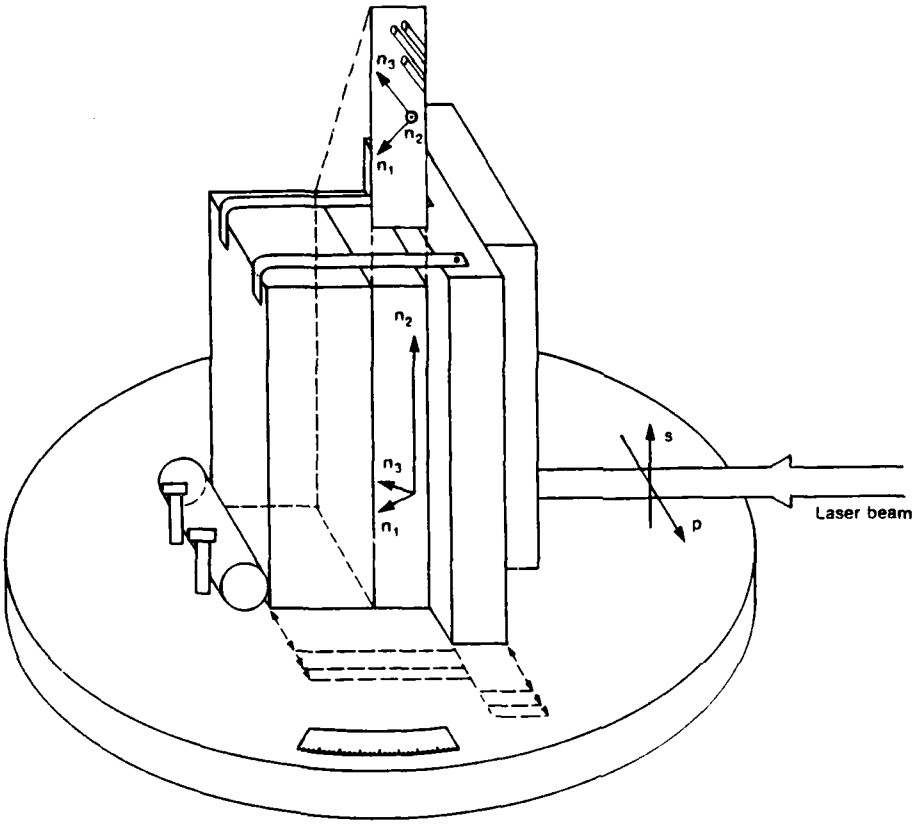


Figure 4.3. Closeup of the Ellipsometer.

index n_g. The resultant specimen is placed in the ellipsometer holder so that the columnar axis of the film microstructure lies in the horizontal plane of incidence. This can be checked with the colored fringes of constant thickness seen by reflection under fluorescent light illumination. The fringes are perpendicular to the columnar axis.

Measurements in Transmission at Normal Incidence (Steps 1 to 3)

1. With the polarizer and analyzer transmission axes vertical, the specimen is scanned across the laser beam until a region is located where the transmittance value is an extremum. At this region Λ_s, the optical path length for s-polarized light, is given by

$$\Lambda_s \equiv n_s d = \left(\frac{\lambda_0}{4} \text{ or } \frac{\lambda_0}{2}\right) + m\,\frac{\lambda_0}{2}\,, \tag{4.1}$$

corresponding to a minimum or a maximum in transmittance, respectively ($n_s > n_g$ assumed). A convenient way of determining the integer number m is by simply counting the number of repeated patterns of colored fringes at a film wedge whose thickness varies from zero to that of the spot under observation. When the deposition is to occur at high angles, this wedge can be formed by placing a small obstacle under the substrate, so that a portion of the latter is partially vapor-shadowed. Another alternative is to combine a FECO or a stylograph measurement of d with a rough estimate for n_s.

For steps 2 and 3, the transmission axis of the polarizer is positioned at a 45° azimuth angle. The compensator phase retardation is varied until it is equal and opposite to that produced by the specimen.

Proper analyzer orientation is then able to bring the resultant plane polarized light to nearly total extinction. In practice extinction is achieved after a very quick iteration.

2. From the compensator reading we directly obtain Λ_Δ, the optical path difference between the p and s-polarized modes,

$$\Lambda_\Delta \equiv \Delta d = (n_{po}-n_s)d \, . \tag{4.2}$$

3. The angular displacement of the analyzer transmission axis from the horizontal position, here represented by ψ_t after reduction to the first quadrant, leads to the amplitude transmittance ratio through the identity

$$\text{tg}\psi_t = \left|\frac{t_{pp}}{t_{ss}}\right| \approx \begin{cases} \dfrac{n_{po}}{n_s}\left(\dfrac{n_s^2+n_g}{n_{po}^2+n_g}\right), & \text{for a quarterwave} \\ \\ n_{po}\left(\dfrac{1+n_g}{n_{po}^2+n_g}\right), & \text{for a halfwave.} \end{cases} \tag{4.3}$$

The last relation is shown in the next section to be a reasonable approximation arising from the theory developed in Chapter 3.

Measurement at Oblique Incidence

4a. Preliminary. A lens is introduced right after the polarizer, set with its transmission axis horizontal, to diverge the laser beam into a bright spot containing parts of the specimen coated and uncoated regions. The angle of incidence is scanned by rotating the central table. As the reflected spot is viewed from a screen, the angular range over which a nearly uniform field can be visualized is then determined.

4b. Accurate. The observation proceeds over this angular range with the polarizer transmission axis now oriented at about 1° off the horizontal position. At each chosen angle of incidence, the specimen coated and uncoated portions are illuminated alternately while the output from the photomultiplier collecting the reflected light is examined for modulation. The analyzer orientation angle θ_M, with its origin when the transmission axis lies along the horizontal position, is varied until the modulation is zero. A set of values for $|\theta_M|$ is then plotted as a function of angle of incidence. Properly evaluated, this function is seen to converge quickly to the $\theta_M = 0$ limit corresponding to the Brewster angle (or to the absentee-layer condition, as will be explained later). An accurate result is then obtained by straightforward graphic interpolation, and the following relations among the refractive indices hold:

$$tg^2\theta_B = \frac{1-n_{po}^{-2}}{n_{po}^{-2}-(n_1 n_3)^{-2}} \text{ , for Brewster's angle,}$$

or (4.4)

$$\left[1 - \left(\frac{n_{po}}{n_1 n_3}\right)^2 \sin^2\theta_{abs}\right]^{1/2} n_{po}d = m\,\frac{\lambda_0}{2} \text{ , for absentee-layer.}$$

These two alternatives will be considered in the next section.

Data Analysis

5. From expressions (4.1) through (4.4) the physical thickness and three refractive indices of the film are obtained as follows:

$$d = \Lambda_s/n_s$$

$$n_s = n_{po}/\sigma; \quad \sigma = \frac{\Lambda_\Delta}{\Lambda_s} + 1$$

$$\text{quarterwave:} \quad n_{po} = \left(\frac{\sigma^2-\sigma tg\psi_t}{\sigma tg\psi_t-1}\, n_g\right)^{1/2} \tag{4.5}$$

$$\text{halfwave:} \quad n_{po} = \rho \pm (\rho^2-n_g)^{1/2}; \quad \rho = \frac{1+n_g}{2tg\psi_t}$$

$$\text{Brewster:} \quad (n_1n_3)^{-2} = n_{po}^{-2}csc^2\theta_B - ctg^2\theta_B$$

$$\text{absentee:} \quad (n_1n_3)^{-2} = \frac{1-(g/n_{po})^2}{n_{po}^2\sin^2\theta_{abs}}; \quad g = \frac{m'\lambda_0}{2d}.$$

These relations are easily translated into the three principal refractive indices by use of the "equivalent (isotropic) refractive index" concept discussed in Chapter 3 leading to (3.60):

$$n_s = n_2$$

$$\frac{1}{n_{po}^2} = \frac{\cos^2\phi}{n_1^2} + \frac{\sin^2\phi}{n_3^2}, \tag{4.6}$$

where ϕ defines the columnar orientation in accordance with the tangent rule (1.1)

$$tg\,\phi = \frac{1}{2}\, tg\,\nu. \tag{4.7}$$

Theory of the Measurement

We now apply the theory from Chapter 3 to substantiate the two arguments leading to expressions (4.3) and (4.4) left open in the description of our method.

On Relations (4.3): First-Order Approximation

Consider the particular situation for which the following conditions between the impinging light and the dielectric thin film are satisfied:

1. The s-polarization direction lies along one of the principal axes as shown in Figure 3.3(b).
2. The light beam is normally incident.
3. At least in the area where it is hit by the light beam, the film has a quarterwave optical thickness with respect to the s-polarized mode.

In the context of Chapter 3, these conditions imply that expressions (3.56) and (3.57) can be used with $S = 0$ and $\delta_s = \pi/2$, so that the propagation matrix becomes

$$\begin{bmatrix} \cos\delta_{po} & 0 & 0 & -\frac{i}{n_{po}}\sin\delta_{po} \\ 0 & 0 & -\frac{i}{n_s} & 0 \\ 0 & -in_s & 0 & 0 \\ -in_{po}\sin\delta_{po} & 0 & 0 & \cos\delta_{po} \end{bmatrix} \tag{4.8}$$

where now, (3.52) considered,

$$\delta_{po} = \frac{2\pi}{\lambda_0} n_{po} d \,, \qquad \delta_s = \frac{2\pi}{\lambda_0} n_s d$$
$$\frac{1}{n_{po}^2} = \frac{\cos^2\phi}{n_1^2} + \frac{\sin^2\phi}{n_3^2} \,, \qquad n_s = n_2 \,. \tag{4.9}$$

Let

$$\Delta \equiv n_{po} - n_s , \qquad \delta \equiv \delta_{po} - \delta_s . \tag{4.10}$$

By hypothesis $\delta_s = \pi/2$. In addition, we expect δ to be in practice sufficiently small to allow us to write in first order approximation

$$\cos\delta_{po} \approx -\delta, \qquad \sin\delta_{po} \approx 1. \tag{4.11}$$

The coefficients (3.15) can then be written

$$\begin{aligned} a_p^{\pm} &\approx (-\delta \mp i/n_{po})n_g + in_{po} \pm \delta \\ a_s^{\pm} &= b_p^{\pm} = 0 \\ b_s^{\pm} &\approx \pm i\, n_g/n_s - in_s , \end{aligned} \tag{4.12}$$

where air was taken as the incident medium.

It follows that the nontrivial amplitude reflectance coefficients from (3.17) become

$$\begin{aligned} r_{pp} &= -\frac{a_p^+}{a_p^-} \approx -\frac{(n_{po}^2-n_g) + i\delta n_{po}(n_g-1)}{(n_{po}^2-n_g) + i\delta n_{po}(n_g+1)} \\ r_{ss} &= -\frac{b_s^+}{b_s^-} \approx -\frac{n_s^2-n_g}{n_s^2+n_g} , \end{aligned} \tag{4.13}$$

which are easily seen to coincide with their counterparts for an isotropic quarterwave layer in the $\delta = 0$ limit.

From the above, neglecting terms in δ^2,

$$\left| \frac{r_{pp}}{r_{ss}} \right| \approx \left| \frac{n_{po}^2-n_g}{n_s^2-n_g} \right| \cdot \frac{n_s^2+n_g}{n_{po}^2+n_g} . \tag{4.14}$$

Also from (3.17), we similarly get

$$\begin{aligned} |t_{pp}| &\approx |i(1-r_{pp})/n_{po} + \delta(1+r_{pp})| \approx 2n_{po}/(n_{po}^2+n_g) \\ |t_{ss}| &\approx |i(1-r_{ss})/n_s| \approx 2n_s/(n_s^2+n_g), \end{aligned} \tag{4.15}$$

where (4.13) and first order approximation were used.

It is interesting to note that this approximation allows conservation of energy to be valid in its exact form, i.e., the approximate amplitude coefficients expressed above, (3.18) considered, are still such that in first order $R_{pp} + T_{pp} = R_{ss} + T_{ss} = 1$.

From (4.15) we get

$$\left| \frac{t_{pp}}{t_{ss}} \right| = \frac{n_{po}}{n_s} \cdot \frac{n_s^2+n_g}{n_{po}^2+n_g} , \tag{4.16}$$

which is the quarterwave expression in (4.3).

A similar procedure, involving a calculation even simpler than the above, leads to its halfwave counterpart in (4.3).

On Relations (4.4): Absentee Layer and Admittance Matching

Consider the configuration shown in Figure 3.3(b), the s-polarized electric field experiences a refractive index n_2 as it oscillates along the y axis, for which the propagation matrix (3.56) applies.

From the elements of this matrix, through coefficients (3.15) we determine the amplitude reflectance r_{pp} as expressed in (3.17). The corresponding reflectance can then be written

$$\begin{aligned} R_{pp} &= |a_p^+/a_p^-|^2 \\ &= \frac{(\gamma_g-\gamma_0)^2 \cos^2\delta_p' + (\gamma-\gamma_0\gamma_g/\gamma)^2 \sin^2\delta_p'}{(\gamma_g+\gamma_0)^2 \cos^2\delta_p' + (\gamma+\gamma_0\gamma_g/\gamma)^2 \sin^2\delta_p'} , \end{aligned} \tag{4.17}$$

where γ, $\gamma_g = n_g/\cos\theta_g$ and $\gamma_0 = n_0/\cos\theta_0$ are the admittances of the film, substrate, and incident medium, respectively, for p-polarized light.

It is easy to see from (4.17) that R_{pp} becomes identical to the reflectance of the bare substrate,

$$R_{pp}^{g} = \left| \frac{\gamma_g - \gamma_0}{\gamma_g + \gamma_0} \right|^2 , \tag{4.18}$$

when one out of two conditions is satisfied.

The first occurs when δ_p' is a multiple of π or, from (3.57), with the aid of (3.46), (3.52), and (3.59), at $\theta_0 = \theta_{abs}$:

$$\left[1 - \frac{n_0 n_{po}}{n_1 n_3}^2 \sin^2\theta_{abs}\right]^{1/2} n_{po} d = m' \frac{\lambda_0}{2} ; \; m' = 1,2,.... \tag{4.19}$$

With regard to traditional thin film theory, noting that when this identity holds the effective optical path traversed by p-polarized light is an integer number of halfwaves, we refer to (4.19) as the "absentee-layer" condition. It becomes the first of expressions (4.4) for air as the incident medium.

The second condition occurs when $\gamma = \pm\gamma_0$, to which we refer as "admittance-matching." With (3.57), (3.46), and (3.59), this implies that at $\theta = \theta_B$

$$\frac{1}{\gamma^2} = \frac{1}{n_{po}^2} - \frac{n_0 \sin^2\theta_M}{n_1^2 n_3^2} = \frac{\cos^2\theta_B}{n_0^2} , \tag{4.20}$$

which after a straightforward manipulation leads to

$$tg^2\theta_B = \frac{n_0^{-2} - n_{po}^{-2}}{n_{po}^{-2} - n_0^2 (n_1 n_3)^{-2}} . \tag{4.21}$$

For $n_0 = 1$ we obtain the second of expressions (4.4).

Discussion

In the isotropic limit, $n_{po} = n_1 = n_3$, (4.21) takes the form

$$tg\theta_B = \pm \frac{n_3}{n_0}, \qquad (4.22)$$

from which it becomes evident that Brewster's law is a particular consequence of the admittance-matching condition.

It is interesting to note that, even under the presence of a strongly asymmetric microstructure, (4.21) still allows for the existance of a pair of angles θ_B symmetrically located with respect to the surface normal. This is consistent with the periodicity of the T_{pp} versus θ_0 curve shown in Chapter 2.

Why does Brewster's law become invalid for anisotropic media?

A way of looking at this question is as follows. In the isotropic case, Brewster's law is derivable from Snell's law and by taking the refracted ray in a direction orthogonal to that of the reflected ray (virtual, if light is p-polarized only). This last ingredient is physically attributed to the well known radiation pattern that results from dipole oscillations along the refracted electric field $\mathbf{E}_p^+$ direction. In the anisotropic case, however, the refracted ray is perpendicular to the displacement vector $\mathbf{D}_p^+$, and <u>not</u> to $\mathbf{E}_p^+$, as shown in Figure 4.4. Therefore, for the dipole oscillations to occur perpendicularly to the reflected ray direction, the refracted ray must <u>not</u> be orthogonal to that direction and Brewster's law does not apply (although we keep calling θ_B by "Brewster's angle" for convenience).

Very significantly, that is still the case for films deposited at normal vapor incidence. Here $\phi = 0$, from (3.52) $n_{po} = n_1$, and thus (4.21) becomes

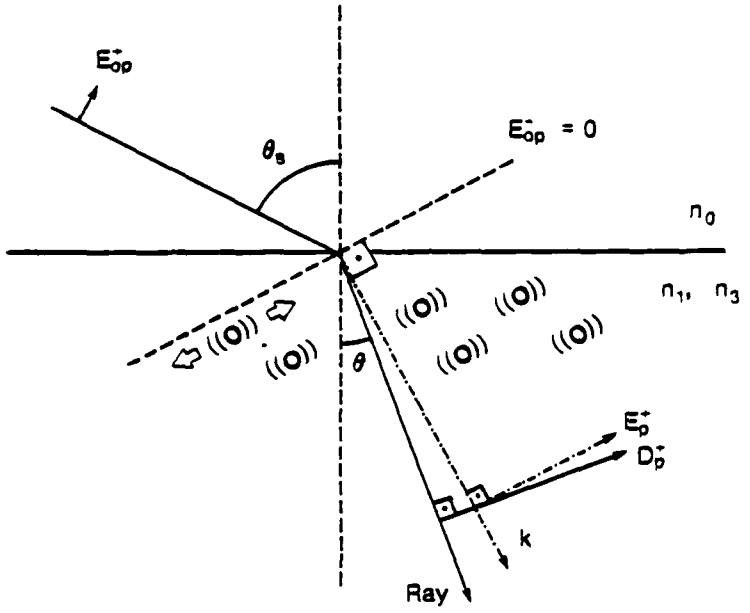


Figure 4.4. Brewster Reflection for Anisotropic Media.

$$tg^2\theta_B = \left(\frac{n_3}{n_0}\right)^2 \cdot \frac{n_1^2-n_0^2}{n_3^2-n_0^2} \quad . \tag{4.23}$$

This result alone is good reason for careful interpretation of thin film measurements at the Brewster angle.

For $\phi = 90°$ we reobtain (4.23) with the permutation $n_1 \leftrightarrow n_3$.

These two particular cases were reported by Malleman and Suhner (1944), and their results are in perfect agreement with ours.

Example

For illustration we now apply our method to the determination of the principal refractive indices of a zirconium oxide film deposited at 65° onto a glass substrate (sample ZO 0808-65), corresponding to a columnar orientation angle $\phi = 46.997°$ in accordance with (4.7).

Prior to deposition, the substrate is masked in two regions, as shown in Figure 4.5. The horizontal mask allows for the measurement at oblique incidence, step 4 in the exposition of the method, involving the alternate illumination of the specimen's coated and uncoated portions. The vertical mask is elongated perpendicularly to the loci of constant thickness. It produces a sharp step which, properly aluminized, will later enable the determination of the physical thickness of the film through a FECO observation at, or in the neighborhood of, the locus of constant thickness where the ellipsometer measurements are carried.

These measurements start with the determination of n_g, the refractive index of the glass substrate. Here we utilize the Abelès technique with photoelectric detection and the Hacskaylo polarimetric

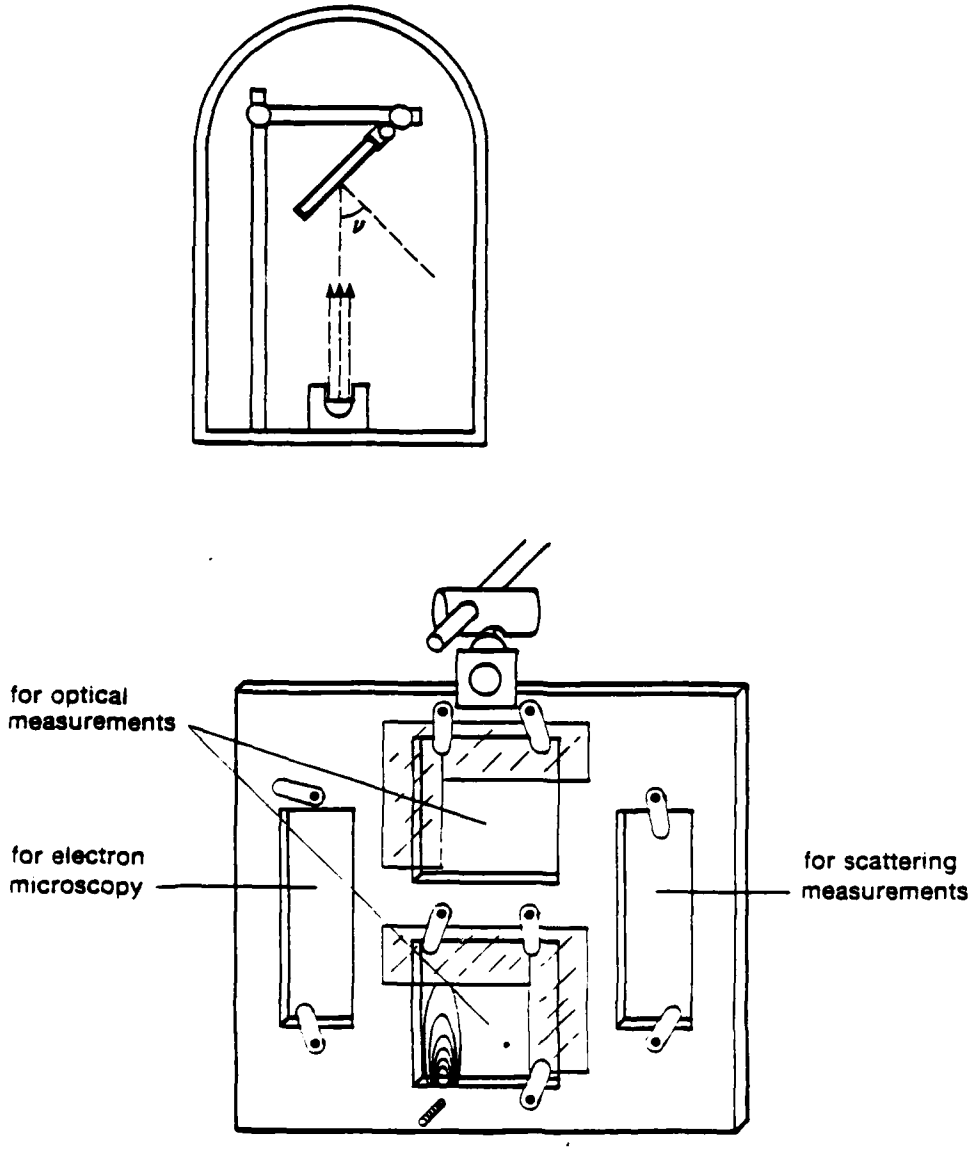


Figure 4.5. Deposition Geometry and Sample Holder.

At the bottom, the colored fringes seen under fluorescent light on the wedge produced by the partial vapor-shadow of a bolt are represented.

extension, as described in step 4b, with the only difference that we now look for a null rather than a matching reflectance. Figure 4.6 shows the outcome of this observation, followed by a close-up in Figure 4.7. The resulting refractive index value is

$$n_g = 1.5131\ (\pm\ 0.0005). \tag{4.24}$$

Our error estimate is slightly more conservative than that reported by Hacskaylo (1964) because in our understanding the error contribution from the graphical interpolation process should be taken into account.

We now proceed with the characterization of the specimen through the steps outlined in the exposition of the method. The resulting data are as follows:

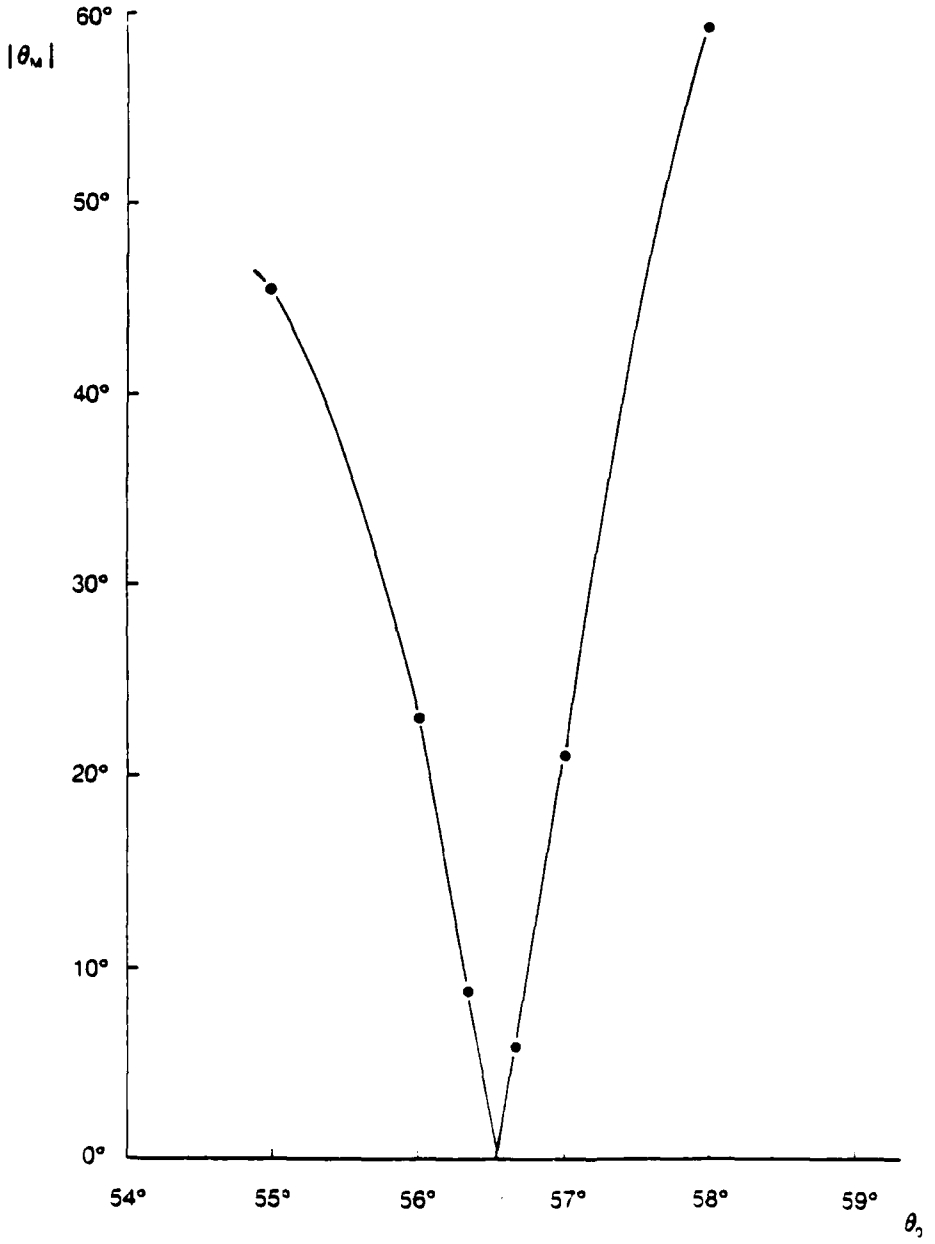
$$\begin{aligned} \Lambda_s &= 3/2\ \lambda_0 \\ \Lambda_\Delta &= 0.05783\ (\pm 0.00010)\ \lambda_0 \\ \psi_t &= 44.460^\circ\ (\pm 0.005^\circ) \\ \theta_B &= 58^\circ 31' 12''\ (\pm 30'') = 58.520^\circ\ (\pm 0.008^\circ). \end{aligned} \tag{4.25}$$

The graphical determination of Brewster's angle is shown in Figure 4.8.

Analysis of these data, with $\phi = 46.997^\circ$, $h_g = 1.5131$, and $h_0 = 1.0000$, leads to the four characterization parameters

$$\begin{aligned} n_1 &= 1.502\ (\pm 0.009) \\ n_2 &= 1.575\ (\pm 0.001) \\ n_3 &= 1.788\ (\pm 0.015) \\ d &= 0.952\ (\pm 0.001)\ \lambda_0 = 602.5\ (\pm 0.6)\ \text{nm}, \end{aligned} \tag{4.26}$$

while the "equivalent refractive index" at normal incidence for p-polarized light (see discussion following (3.59))



igure 4.6. Experimental Data for the Determination of the Refractive Index of a 2 in. x 2 in. Glass Slide.

θ_n is the azimuth angle of the analyzer transmission axis, with origin at the horizontal position, for which the reflectance is extinguished at a given angle of incidence θ_0.

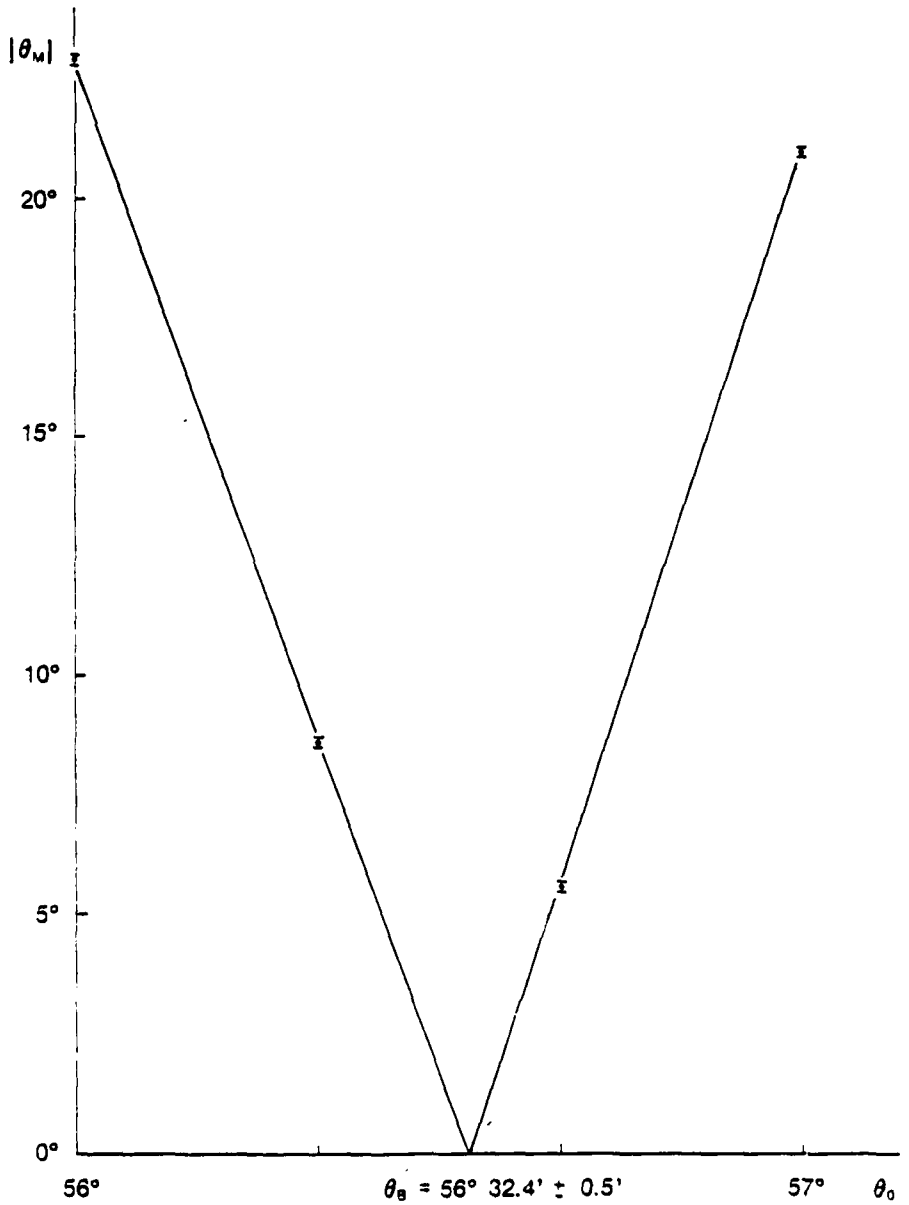


Figure 4.7. Closeup of Figure 4.6.

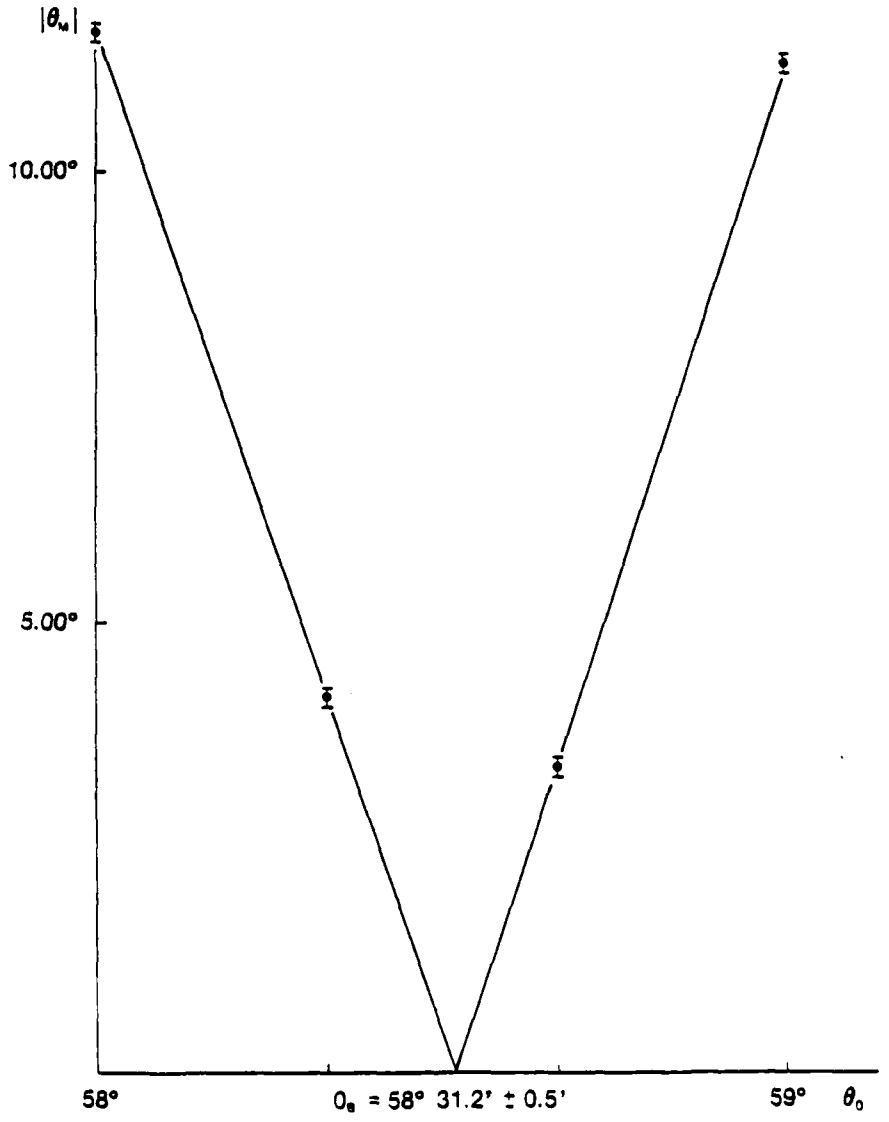


Figure 4.8. Experimental Data for the Determination of Brewster's Angle for a Zirconium Oxide Sample.

θ_M is the azimuth angle of the analyzer transmission axis, with the origin at the horizontal position, for which the reflectances of the coated and uncoated parts of the specimen are matched at a given angle of incidence θ_0.

$$n_{po} = 1.636\ (\pm 0.001), \tag{4.27}$$

so that the effective amount of birefringence at normal incidence results as

$$n_{po} - n_s = 0.061\ (\pm 0.002). \tag{4.28}$$

The numbers indicated in parentheses are rough error estimates originated in the measurement process and magnified as they propagated through the calculation.

Interpretation

Do parameters (4.26) make sense? Given the literature omission on quantitative information about form birefringence in thin films, we now resort to some other evidence that is available to us. The considerations that follow are not to be taken rigorously, but rather as constituting a plausibility argument.

We performed a FECO measurement at, or in the neighborhood of, the locus of constant thickness where the ellipsometer measurements were made. The observed physical thickness is of the order of 530 nm, which indicates that the value for d obtained in (4.26) is not unreasonable. Their difference may be partly due to the strong nonuniformity in film thickness we have observed, which makes the FECO measurement extremely dependent on position. It may also be due to dissimilar phase changes by reflection on the aluminized film and (much smoother) aluminized glass surfaces.

As to the refractive indices, we now consider a simple columnar structure model in connection with the thin film growth simulation

performed by Marten Sikkens. His two-dimensional results for 60° and normal incidence are shown in Figure 4.9.

In a three-dimensional situation we can imagine those pictures, in that order, as representing the projected film microstructure in a plane parallel and perpendicular to the plane defined by the vapor beam and the substrate normal.

The perpendicular plane clearly presents a larger amount of solid material per unit area. Therefore, if we are to model the three-dimensional microstructure as a sequence of identical columns, each column must have an elliptical cross section elongated in the perpendicular direction. In fact, experimental evidence for this elongation was found by Leamy, Gilmer, and Dirks (1980) through a transmission electron microscopy observation with the electron beam parallel to the columnar orientation.

Howe elongated should it be in our case? A crude estimate can be made by counting the number of solid disks along a typical horizontal section AB in Figures 4.9(a) and (b), and taking their ratio. The ellipticity that follows is

$$b/a = 58/40 = 1.45. \tag{4.29}$$

The microstructure of the film can then be modeled as consisting of solid rods with an elliptical cross section, infinite length, and refractive index n, randomly distributed in an air matrix. A simple adaptation of Wiener's expression (Bragg and Pippard, 1953) leads to the effective refractive indices along the principal axes

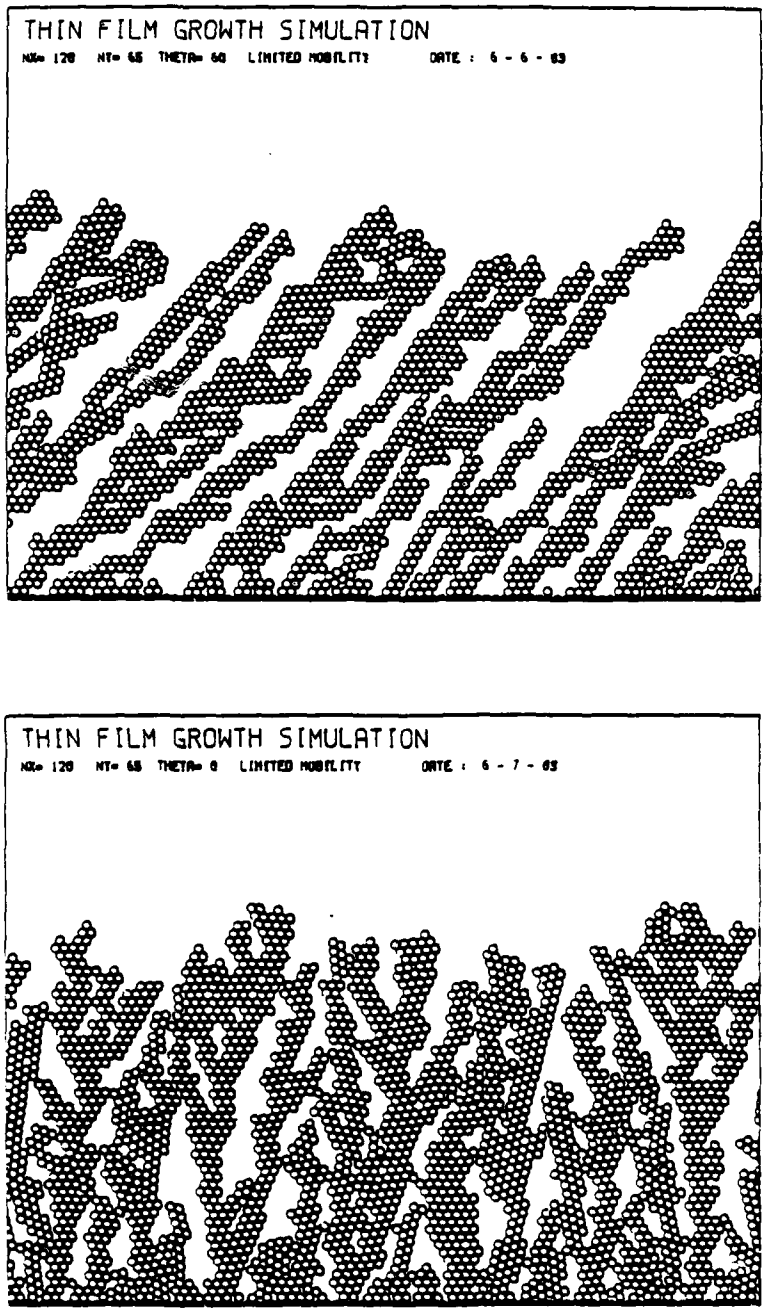


Figure 4.9. Film Structure Resulting from the Simulated Deposition Process at (a) $v = 60°$ and (b) $v = 0°$.

Each impinging molecule, represented by a hard disk, was allowed to "move" randomly until contact with other two was reached (by Marten Sikkens).

$$n_j^2 = 1 + \frac{p(n^2-1)}{1 + (1-p)(n^2-1)L_j} ; \qquad j = 1,2,3 , \tag{4.30}$$

where p is the packing density, or fractional volume of solid material in the medium, and the depolarization factors are

$$L_1 = \frac{b}{a+b} , \qquad L_2 = \frac{a}{a+b} , \qquad L_3 = 0. \tag{4.31}$$

From the CRC Handbook (Weast, 1980, p. B-166) we know that zirconium dioxide in bulk form has an average refractive index of 2.17. We use this value for n.

Now we set the packing density value so that $n_3 = 1.80$, say, and from (4.30) and (4.31) get $p = 0.60$. Identity (4.30) is not strictly valid for this packing density value, but can reasonably be used for our rough estimation.

The above considerations result in the following set of principal refractive indices:

$$\begin{aligned} n_1 &= 1.48 \\ n_2 &= 1.55 \\ n_3 &= 1.80, \end{aligned} \tag{4.32}$$

which are less than 2% off their corresponding measured values in (4.26). This seems to indicate that our measurement does indeed make sense, as well as in the simple model we have used.

CHAPTER 5

OPTICAL PROPERTIES: THEORY AND EXPERIMENT

Our task here is to collect experimental evidence on the optical properties of an anisotropic thin film and compare it with the predictions of the theory developed in Chapter 3. To do this quantitatively, we need the optical constants and physical thicknesses that specify the film under study. That was our concern in Chapter 4. In practice we connect these characterization parameters to optical properties through a computer program developed directly from the theory. We call it the "anisotropic thin film (ANTF) program," and begin with a brief description of its main features.

The ANTF Program

The program applies for CASES 0, 1, and 2 of homogeneous, biaxial thin films (see Chapter 3). Absorption is allowed for all media but the incident. Although it was devised with the columnar model in mind, it is valid as well for any other source of optical anisotropy, as long as principal axes are still definable. From a user's point of view, the program can be specified as follows:

Input:

Refractive index for the incident medium and optical constants for the substrate.

Initial and final values of variable, and variable interval

(variable = wavelength, angle of incidence, or azimuth angle).

Values of the two fixed variables.

For each layer: principal optical constants, two angles defining the columnar orientation and physical thickness.

Vertical scaling defined by minimum and maximum ordinate values.

Output:

Required vapor angle of incidence for each layer.

Reflectance, reflectance phase and transmittance for s, p, and crossed polarizations at chosen angle of incidence, wavelength, or azimuth angle ranges.

The overall structure of the program is shown in Figure 5.1. MAIN PROGRAM is a direct consequence of our theory without any specific particularization. SIMLAR performs a similarity transformation that allows for rotations of the principal axes (see Appendix B). MATMUL provides the product of any two square matrices (3x3 for SIMLAR and 4x4 for MAIN PROGRAM). BIQUAD particularizes the problem to situations for which the secular equation becomes biquadratic or for which the s and p-modes can be treated separately, and addresses the program to CASE1 or CASE2 after testing for a few mathematical restrictions. VECMUL performs the "direct vector product" operation, as defined in Chapter 3. PLOT plots.

The program was initially tested in the isotropic limit through a few multilayer design problems by comparing its results to those of

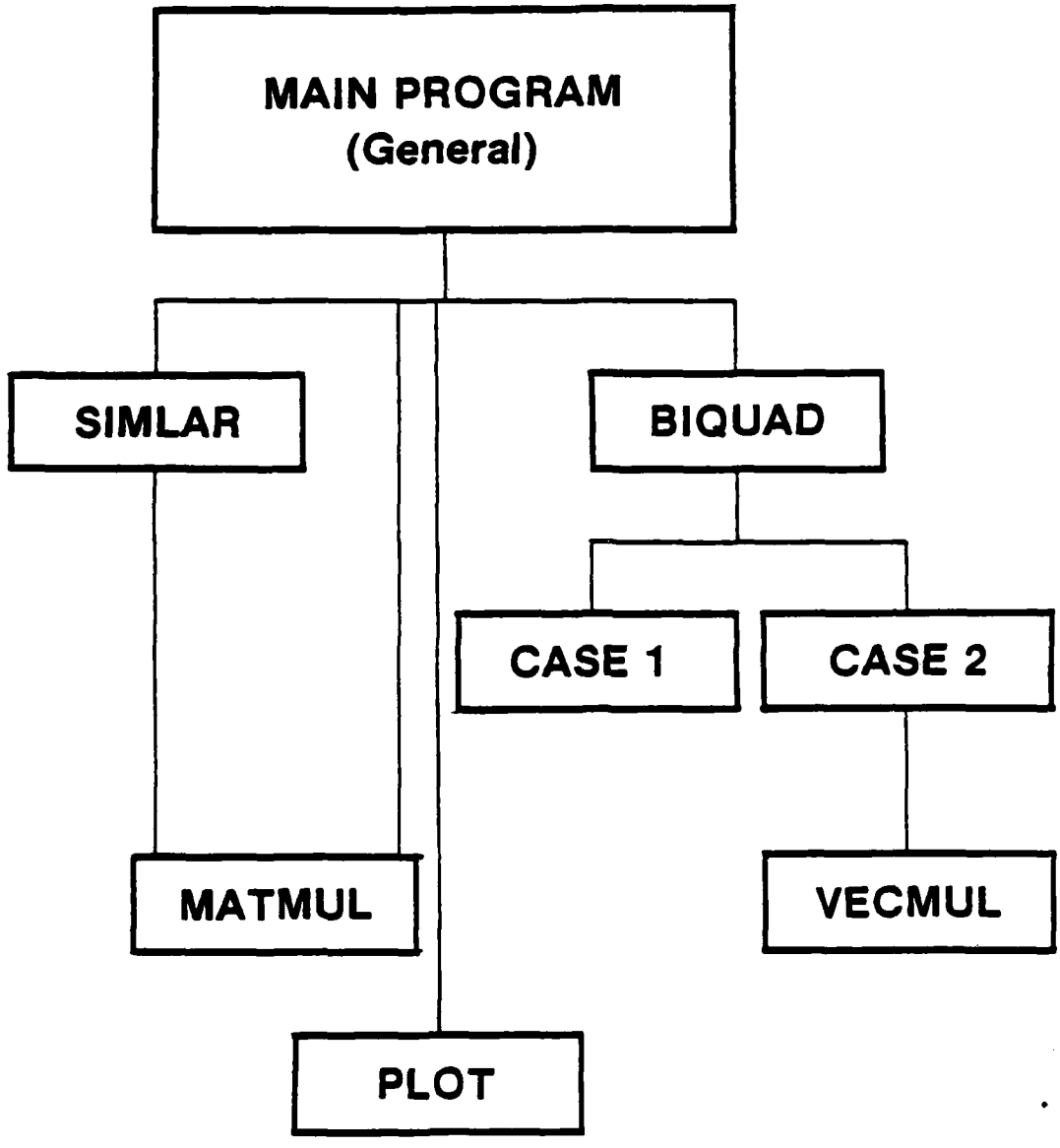


Figure 5.1. Overall Structure of the ANTF Program.

Prof. Angus Macleod's OPTF. The agreement was complete, at least up to the six-decimal digits provided by the output of the two programs, in all cases considered.

The decisive tests for the ANTF program, however, are in its main purpose of dealing with anisotropic films. In the process of allowing us to place the consequences of the theory side by side with the experimental data, which we describe next, one should bear in mind that the validity of the program itself is also under question.

Experimental Evidence

We start from the measurements of transmittance versus angle of incidence ($T \times \theta_0$), which are not intended for the direct observation of optical anisotropy, but rather as a preparation for the transmittance measurements with variation of azimuth angle ($T \times \alpha$) in which the effect is much more pronounced. All those were performed with the setup and the zirconium oxide sample considered in the previous chapter. Later we present spectral data ($T \times \lambda_0$) obtained from a Cary 14 spectrophotometer for a dielectric multilayer system.

$T \times \theta_0$

The results of the measurement are shown in Figure 5.2. The experimental procedure is as follows. The polarizer and analyzer transmission axes are rotated to the chosen polarization mode, horizontal for p, and the gain of the lock-in amplifier (and/or that of the voltage across the photomultiplier) is set for a digital reading of 100.0. The

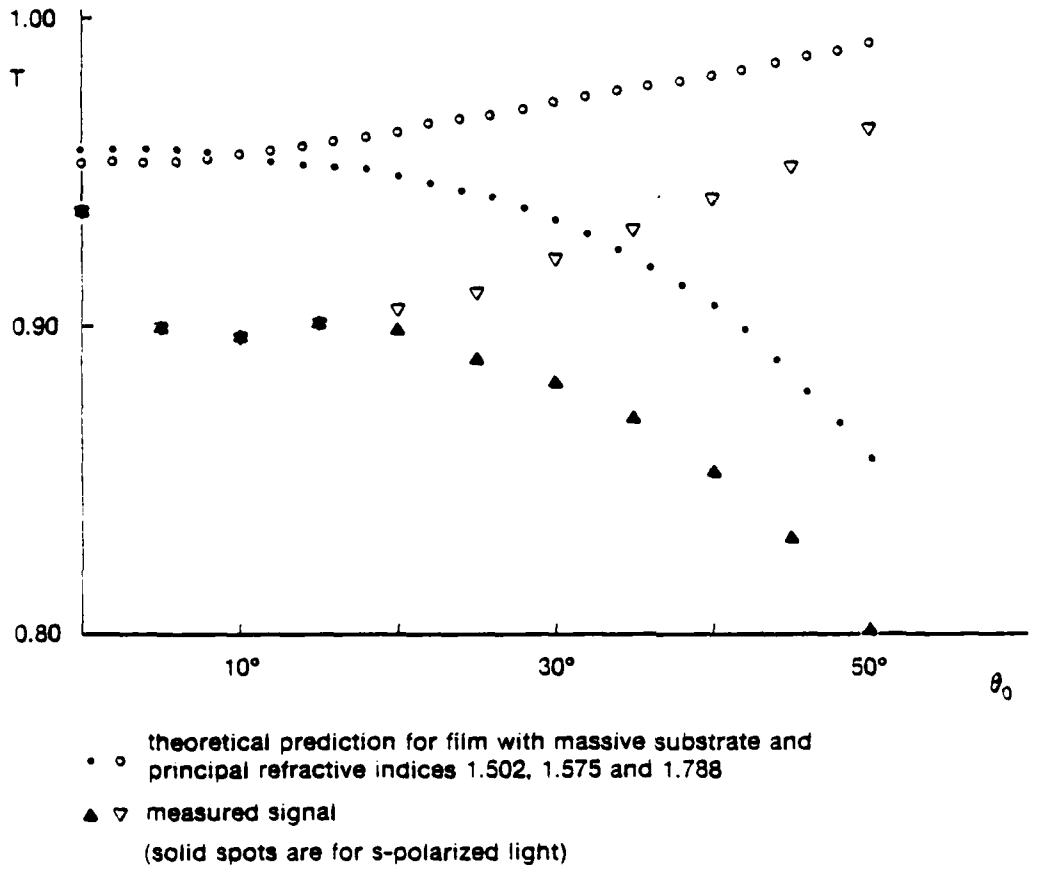


Figure 5.2. Noncrossed Transmittances versus Angle of Incidence (Zirconium Oxide Sample).

sample is then properly attached to the holder for the starting, normal incidence data point.

The positioning of the Z00808-65 sample is critical because we try to reproduce the conditions present during its characterization (see Chapter 4) as accurately as possible. This also means that the whole set of observations for an individual specimen should be performed in the period of a few days, since films deposited at high angles of vapor incidence are very porous and thus extremely susceptible to water adsorption from the atmosphere.

The laser fluctuations, up to 0.5% in intensity, are another important source of error. Their influence is minimized, as the specimen table is rotated for each data point in Figure 5.2, by resetting the 100.0 reading in the absence of the sample whenever a signal discontinuity by more than 0.3% is noticed under otherwise unchanged conditions.

Also present in Figure 5.2 is the prediction from the theory, which assumes a massive substrate medium. If it is to be compared with the measured results, then the substrate back-reflectance must be taken into account (the glass substrate absorption is negligible for our purposes).

A rigorous treatment would require an integration of the interference fringe intensities, originated from the near-parallel surfaces of the substrate, over the detector aperture for each angle of incidence. Another alternative is to pick a similar glass slide, subject it to the same measurement conditions as that of the sample, and from

its optical behavior establish the amount of back-reflectance from the glass-air interface.

We started from this second alternative without much success because, as different portions of the slide were illuminated at low angles of incidence, we observed dramatic fluctuations in transmittance that precluded determining a typical value. Such fluctuations are clearly connected to those involving relative orientation between the two surfaces of the slide, as well as to irregularities at each surface.

We then decided to approach the problem with the simplifying assumption that the sum of the individual fringe contributions to the detector intensity signal, each resulting from a mostly coherent effect, would ultimately come close to the outcome of an incoherent formulation as many fringes were taken into account.

Multiple-beam internal reflections in a nonabsorbing slab of material, treated as incoherent contributions to its total transmittance T, lead to the well known identity

$$\frac{1}{T} = \frac{1}{T_f} + \frac{1}{T_g} - 1, \tag{5.1}$$

where T_f and T_g are the intensity transmittances of the two opposite surfaces of the material.

In our case, $T_g(\theta_0)$, referring to the glass-air interface, is determined from

$$T_g = 1 - \left| \frac{\gamma_g - \gamma_a}{\gamma_g + \gamma_a} \right|^2, \tag{5.2}$$

where $\gamma_g(\theta)$ and $\gamma_a(\theta_0)$ are the admittances of glass and air,

espectively, at a given angle of incidence θ_0 (to which θ is connected hrough Snell's law) and at a given polarization mode (see (3.35)).

Several values of T_g are shown in the first column of Table 5.1 a) and (b), for which the refractive index of the glass substrate was aken as $n_g = 1.5131$ in accordance with our previous measurement (see igure 4.6). Those values and the data shown in Figure 5.2 for T_f, the heoretical film transmittance, are used in (5.1) to produce the redicted transmittance curves with back-reflectance correction in igure 5.3.

Also shown in Table 5.1 is the correction for the residual letector nonlinearity noticed after the experiment was completed. This orrection was established by exact reproduction of the range of setup rrangements and settings utilized during all stages of the experiment, nd by detailed observation of the signal when the laser beam was ubjected to different amounts of attenuation under those conditions. he input to the detector was taken as a function of the corresponding ignal in the quadratic form

$$I(S) = aS + bS^2. \tag{5.3}$$

onstants a and b were determined by taking a common origin and a ommon reference maximum, i.e., $I(0) = 0$ and $I(100) = 100$, combined with the observation of an arbitrary signal for the conditions of minimum and aximum nonlinearity. A signal reading of 91.70 corresponded to a relative input of 91.22 and 90.55 (checked in linear, very low-intensity onditions), respectively, leading to the values:

Table 5.1. Values of T_{pp} and T_{ss} for Various Angles of Incidence

	T_{pp} (%)+					T_{ss} (%)+				
θ_0 (Deg)	T_g(TH)	T(BR)	S	I_1(NL)	I_2(NL)	T_g(TH)	T(BR)	S	I_1(NL)	I_2(NL)
0	95.831	91.512	93.7	92.808	93.329	95.831	91.914	93.8	92.921	93.435
5	95.873	91.624	89.9	88.528	89.330	95.789	91.833	90.0	88.640	89.435
10	96.000	91.942	89.8	88.416	89.225	96.660	91.591	89.7	88.304	89.120
15	96.211	92.499	90.2	88.864	89.645	95.435	91.157	90.2	88.864	89.645
20	96.508	93.284	90.5	89.201	89.960	95.101	90.486	89.8	88.416	89.225
25	96.891	93.899	91.0	89.762	90.486	94.632	89.514	88.9	87.409	88.281
30	97.356	94.763	92.0	90.888	91.538	93.997	88.174	88.2	86.627	87.547
35	97.895	95.693	93.0	92.016	92.591	93.146	85.954	87.1	85.402	86.395
40	98.488	96.694	94.1	93.261	93.752	92.010	83.966	85.2	83.295	84.409
45	99.095	97.768	95.2	94.509	94.913	90.489	80.472	83.2	81.088	82.323
50	99.639	98.849	96.3	95.762	96.076	88.445	77.058	80.1	77.691	79.100

+Explanation of symbols:

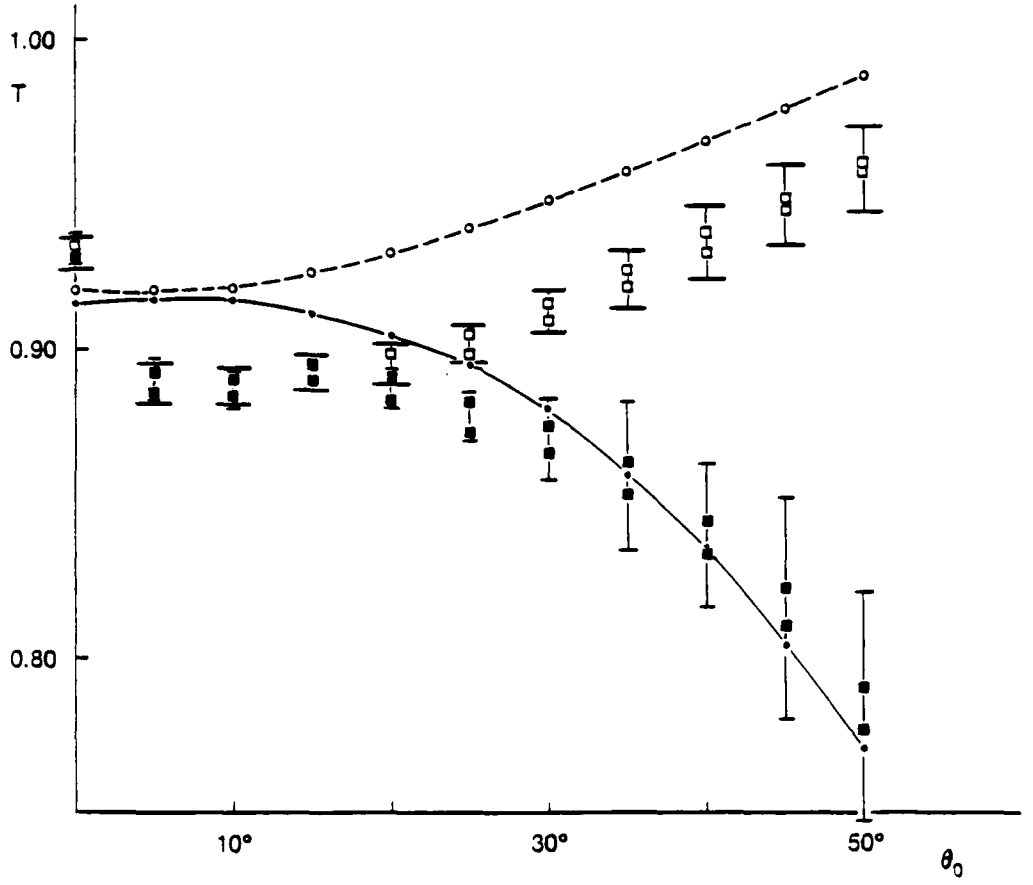
θ_0 Angle of incidence

T_g(TH) Glass transmittance from theoretical calculations

BR Substrate back-reflectance considered (theory)

S Measured signal

NL Detector nonlinearity corrected



• ○ theoretical curves with back-reflectance

■ □ experimental data with detector nonlinearity correction

(solid spots are for s-polarized light)

Figure 5.3. Corrected Noncrossed Transmittances versus Angle of Incidence (Zirconium Oxide Sample).

I_2 (min. NL): $a = 9.372 \times 10^{-1}$, $b = 6.276 \times 10^{-4}$

I_1 (max. NL): $a = 8.489 \times 10^{-1}$, $b = 1.511 \times 10^{-3}$,

utilized for obtaining the last two columns in Table 5.1 (a) and (b).

The experimental data shown in Figure 5.3 are the result of the above correction applied to the measured signal in Figure 5.2. Note that the general shapes of the experimental and theoretical curves for p-polarized light, as well as those for s-polarization up to around 30°, are in reasonable agreement.

We could easily select extinction coefficients that would optimize the fitting between corresponding curves but, instead, decided to keep the comparison free from adjustable parameters, bearing in mind that the differences may be partly caused by inhomogeneity or scattering losses. The experimental results for s-polarization over 30° are relatively poor in information content due to increasing transmitted beam walkoff and elongation of the illuminated spot with increasing angle of incidence. In addition, the pronounced steepness of the curve at that region magnifies small deviations in alignment and other imperfections of the ellipsometer. Nevertheless, those results are presented here for completeness.

One problem remains in the comparison between theory and experiment: why is there such a discrepancy at normal incidence?

We got an answer to this question only after we carefully looked at the intensity-structure of the beam reflected by the sample as its supporting table was slowly rotated toward low angles of incidence.

Following the beam in this manner, we readily noticed that the number of fringes gradually decreased until essentially only one was observed at near-normal incidence. In other words, at that angle and at the particular region of the sample we picked for our measurements, the substrate happens to partially behave like a Fabry-Perot cavity!

For that reason, the normal-incidence experiments we describe next must have their results corrected accordingly.

T x α

The transmittance versus azimuth angle curves are shown in Figures 5.4 and 5.5. The substrate interference effect we have just discussed is taken into account through Table 5.2 when we multiply the measured signal by the ratio between the measured transmittances at 5° and at normal incidence shown in Figure 5.2. This simple correction is supported by the fact that the transmittance curves are expected to be nearly flat between zero and 15°.

In Figure 5.4, it is interesting to note that the theory predicts an asymmetry in the transmittance curve that could hardly be noticed during the experiment (or even later with the nonlinear correction). The asymmetry is due to the variation of the effective refractive index when the columnar orientation changes with respect to the normally incident electric field. The magnitude of this variation is well within the experimental error.

Looking at the good agreement in general shape between the theoretical and experimental curves, one may be tempted to use

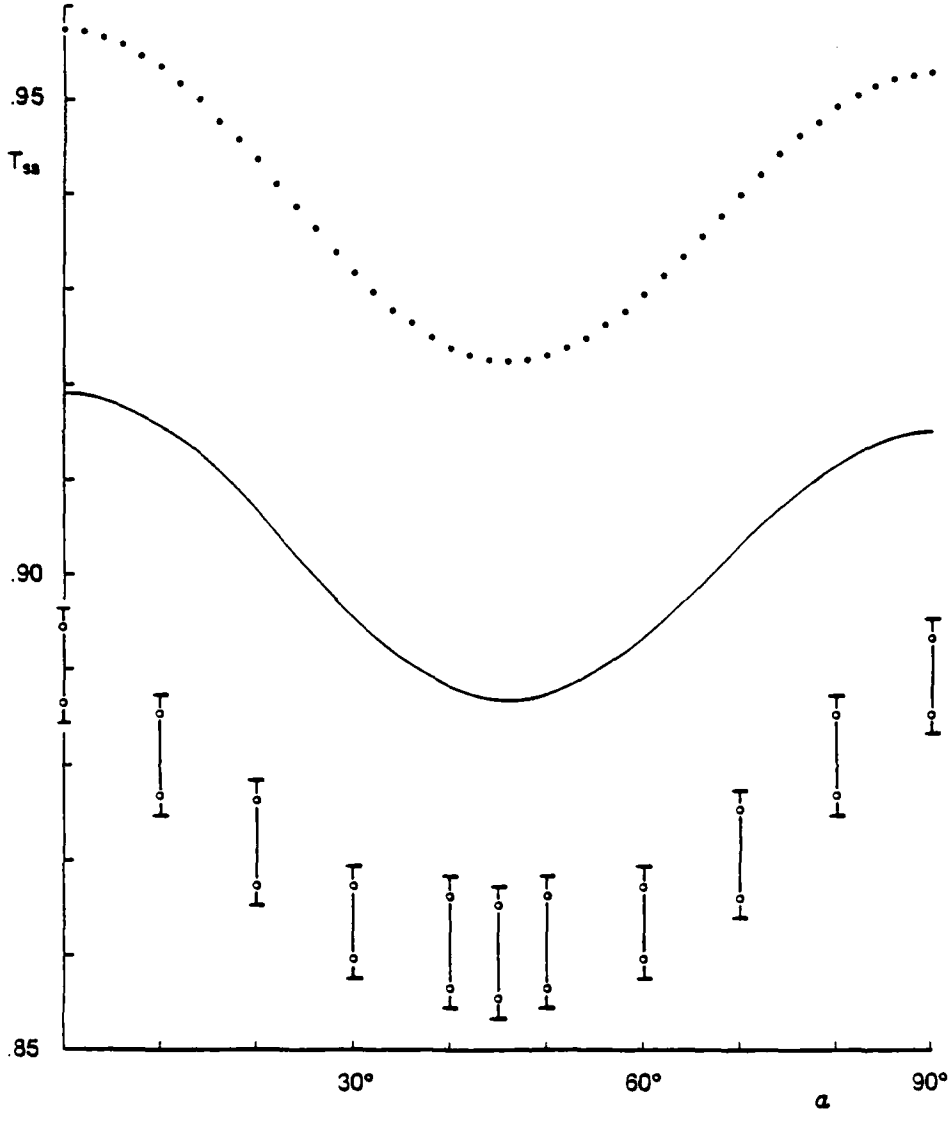


Figure 5.4. Noncrossed s-Polarization Transmittance versus Azimuth Angle.

The corresponding T_{pp} curves can be visualized by the mirror image of this figure. Columnar orientation is horizontal at the origin (zirconium oxide sample).

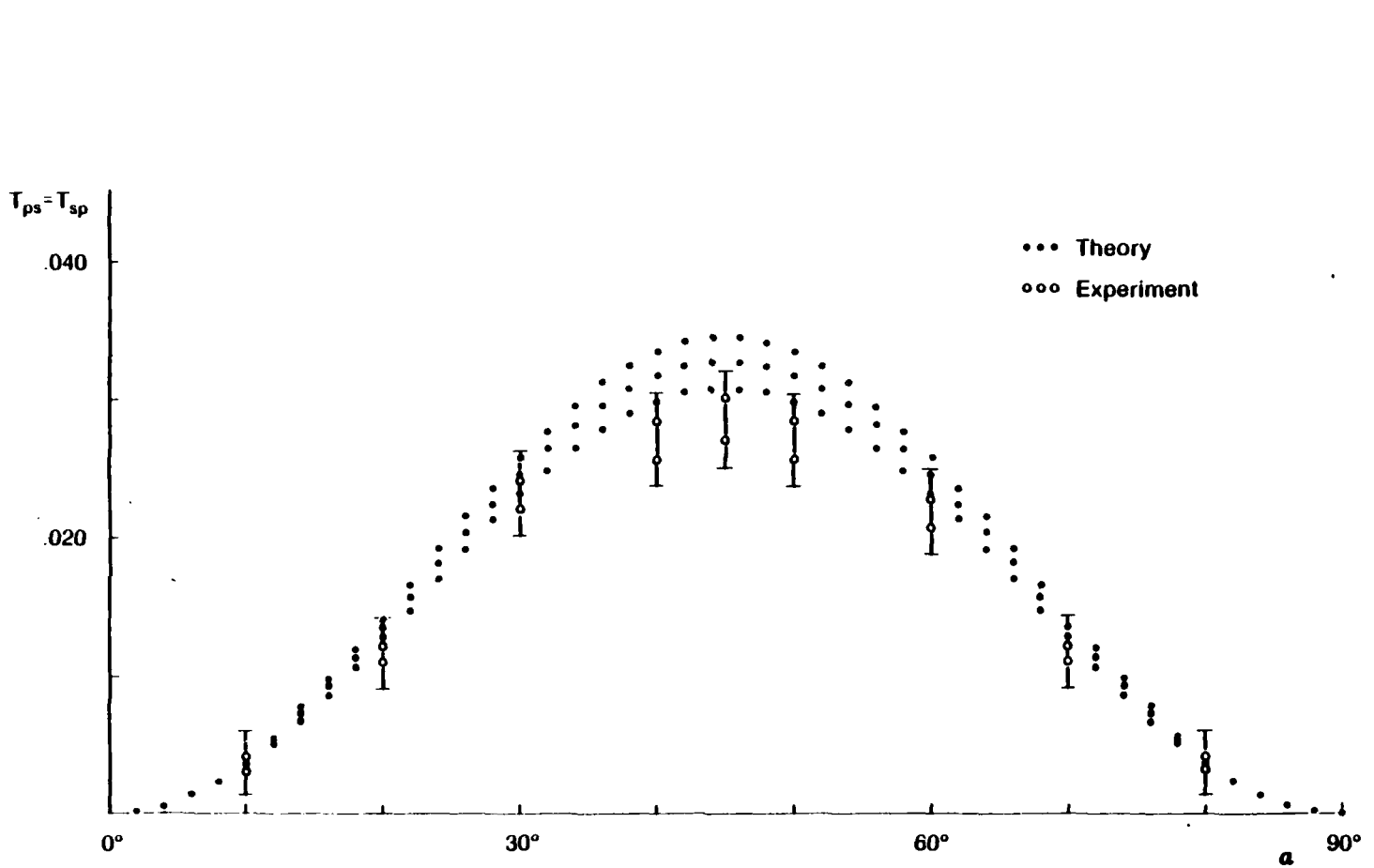


Figure 5.5. Crossed Transmittances versus Azimuth Angle.

Sets of principal refractive indices assumed for the theoretical curves are, in descending order: [1.493, 1.574, 1.803], [1.502, 1.575, 1.788], and [1.511, 1.576, 1.773] (zirconium oxide sample).

Table 5.2. Values of T_{sp} and T_{ss} for Various Angles of Incidence

	T_{sp} (%)+					T_{ss} (%)+				
θ_0(Deg)	S	xSI	xP	T_1 (NL)	T_2 (NL)	S	xSI	T (NL)	T_1 (NL)	T_2 (BR)
0	0.0	0.000	0.000	0.00	0.00	93.8	90.000	88.64	89.43	9o.91
10	0.3	0.288	0.430	0.36	0.40	92.9	89.136	87.67	88.53	91.55
20	0.9	0.863	1.289	1.10	1.21	92.0	88.273	86.71	87.62	90.63
30	1.8	1.727	2.578	2.20	2.42	91.3	87.601	85.96	86.92	89.54
40	2.1	2.015	3.007	2.57	2.82	91.0	87.313	85.64	86.62	88.81
45	2.2	2.111	3.151	2.69	3.00	90.9	87.217	85.53	86.52	88.69
50	2.1	2.015	3.000	2.57	2.82	91.0	87.313	86.64	86.62	88.74
60	1.7	1.631	2.434	2.07	2.28	91.3	87.601	85.96	86.92	89.33
70	0.9	0.863	1.289	1.10	1.21	91.9	88.177	86.60	87.52	90.31
80	0.3	0.288	0.430	0.36	0.40	92.9	89.136	87.67	88.53	91.16
90	0.0	0.000	0.000	0.00	0.00	93.7	89.904	88.53	89.33	91.51

+Explanation of symbols:

α Azimuth angle
S Measured signal
P Polarizer correction factor = 1.4925
NL Detector nonlinearity corrected
SI Substrate interference correction factor = 0.9595
BR Substrate back-reflection considered (theory)

convenient extinction coefficients to overlap them. We again choose to keep the comparison free from adjustable parameters and to leave their 2 to 4% gap for future work on inhomogeneity and scattering losses in thin films deposited at high angles of vapor incidence. Furthermore, we would expect the amount of absorption to be slightly different for different columnar orientations with respect to the electric field.

When we corrected the crossed transmittance experimental curve in the same manner as we did for the noncrossed, it would fall about 1% under the theoretical prediction. That was too large a difference (about 30% of the predicted value at $\alpha = 45°$), as can be seen from the second column in Table 5.2 (a). The substrate back-reflectance correction for such small transmittance values is negligible, and similarly minute amounts of loss were to be expected.

We then searched for another source for the disagreement and found it.

The polarizer was set (with its transmission axis) at 45°, while no other optical component was allowed to be in the beam trajectory to the analyzer. We first checked for extinction with the analyzer at 135°, and the ellipsometer performed satisfactorily. Next we oriented the analyzer transmission axis parallel to that of the polarizer and set the signal reading to 100.0, as usual in the experiment. When we turned the analyzer to 0° (horizontal position), however, the signal was 33.5. That is a pronounced departure from the expected 50% intensity transmittance and is probably due to displacement of the Glan-Thompson prisms, if not

to imperfections in the prisms themselves (about the same signal was observed with the analyzer at 180°). A polarizer correction factor is then in order, as shown in the third column in Table 5.2 (a).

Also due to the extreme sensibility of the crossed transmittance measurement, we present in Figure 5.5 theoretical curves not only for the set of principal refractive indices [1.502, 1.575, 1.788] reported in Chapter 4, but also for [1.493, 1.574, 1.803], and [1.511, 1,5767, 1733], corresponding to the upper and lower limits for the expected signal without losses. Those two additional sets are consistent with the errors estimated in (4.26) from the determination of the principal refractive indices.

The agreement in Figure 5.5 seems good supporting evidence not only to theory and experiment on the optical properties of our single dielectric film, but to the measurement of its refractive indices as well.

$T \times \lambda_0$

Figure 5.6 shows the spectral data in the visible region for a birefringent narrowband filter in the form

$$(HL)^5\ HHHH\ (LH)^5, \tag{5.4}$$

where H stands for the zirconium oxide, high index layer and L for the silicon oxide, low index layer. Both H and L are quarterwaves at $\lambda_0 = 627.8$ nm.

The film was deposited at nearly 30° with a fixed substrate (Hodgkinson et al., 1983). Hodgkinson independently measured in

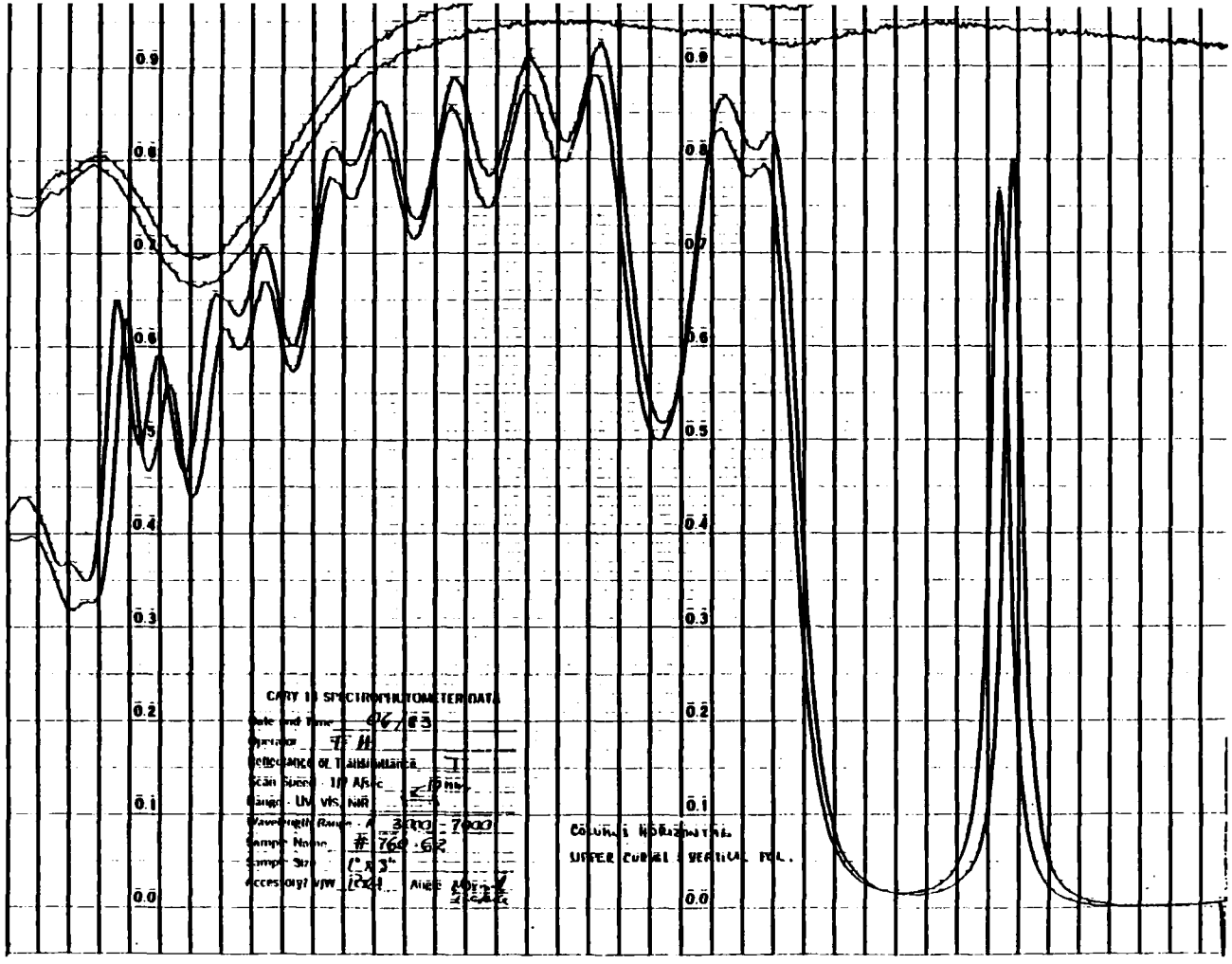


Figure 5.6. Spectral Data in the Visible Region for the Noncrossed Transmittances of a Birefringent Narrowband Filter with 21 Layers.

The upper pair of curves is a reference to the lower pair, and corresponds to the detected signal in the absence of the sample.

transmission the two pairs of peaks for s and p-polarized light at normal and 30° incidence shown in the close-up Figures 5.7 and 5.8. Assuming that the silicon oxide layers (structurally much more amorphous and thus with negligible birefringence as compared to those of zirconium oxide) were specified by their typical refractive index value of 1.46, and by analyzing the peaks in their highly resolved positions, he was able to provide us the following principal refractive indices for the zirconium oxide layers:

$$h_1 = 1.9476$$
$$h_2 = 1.9664 \qquad (5.5)$$
$$h_3 = 2.0332$$

The theoretical curves produced by the ANTF program with these refractive indices are shown in the upper portion of Figures 5.7 and 5.8.

The dissimilarity in predicted and measured lineshapes can be attributed to several factors. From the theoretical side, absorption or any other losses, as well as inhomogeneity, were not considered, thus producing higher and sharper peaks than otherwise expected. As to the experimental side, the rectangular cross section of the spectrophotometer beam, combined with a strong film nonuniformity, resulted in an integration over a range of different thicknesses that lowered and broadened the observed lineshape.

Still, agreement in peak position between theory and experiment is achieved within a resolution of Angstroms.

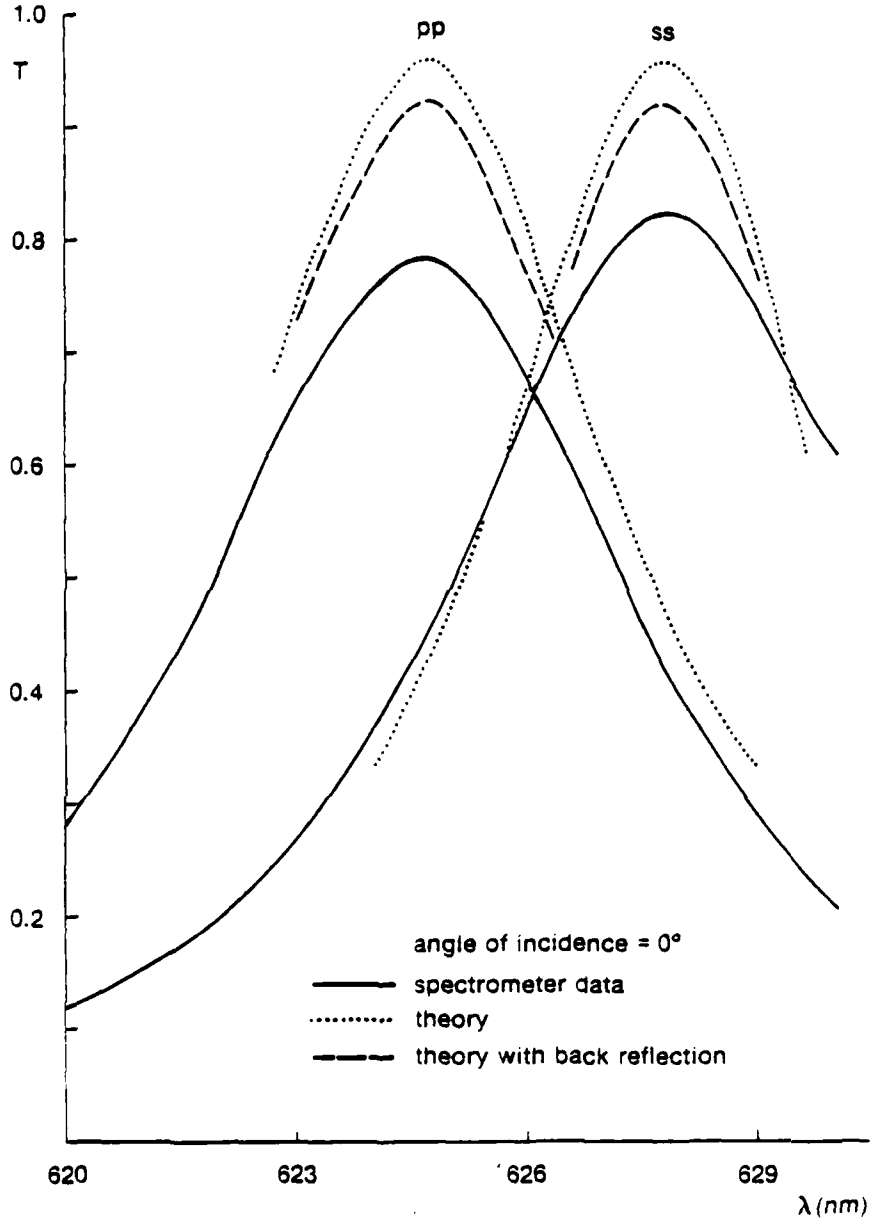


Figure 5.7. Spectral Data for Noncrossed Transmittances at Normal Incidence.

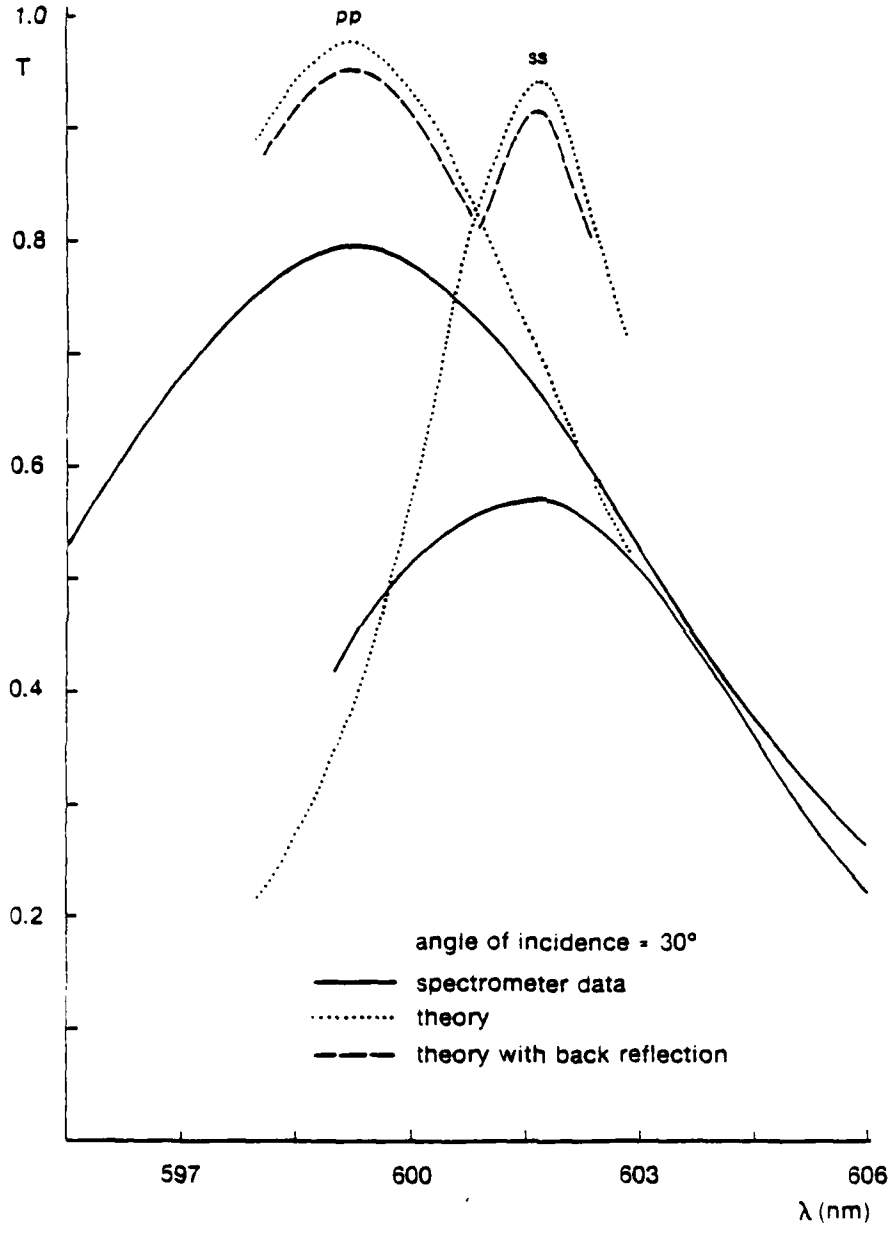


Figure 5.8. Spectral Data for Noncrossed Transmittances at 30°.

A Hypothetical Metal Film

Although we have not measured the optical constants of an isotropic metal film, we conclude this chapter with a brief esentation on what its optical properties might be.

We imagine a single metal film, 14.5 nm thick (semitransparent), ıich was vapor-deposited at 85°, corresponding to a columnar orientation ıgle $\phi = 80.07°$. Note the similarities in preparation conditions between ır hypothetical film and those for the Al sample considered in Chapter for which an effective extinction coefficient difference $\Delta k = 1.44$, lentity (2.2), was experimentally determined.

For our imaginary film, we pick $\Delta k = 1.5$, disregard any slight .fference in refractive indices, and choose for these a typical value in ıe visible region (Hass, 1965), thus generating the following optical ɔnstants:

$$\begin{aligned} n_1 - ik_1 &= 1.3 - i\,2.5 \\ n_2 - ik_2 &= 1.3 - i\,2.5 \\ n_3 - ik_3 &= 1.3 - i\,4.0. \end{aligned} \tag{5.6}$$

The resulting curves of transmittance versus azimuth angle, btained from the theory through the ANTF program, are shown in Figure .9. It is interesting to notice their similarities with those in Figure .2.

We present in Figure 5.10 the reflectance curves for our ypothetical film and stop at this point, in the hope that this peculiar ehavior will be more fully pursued in future work.

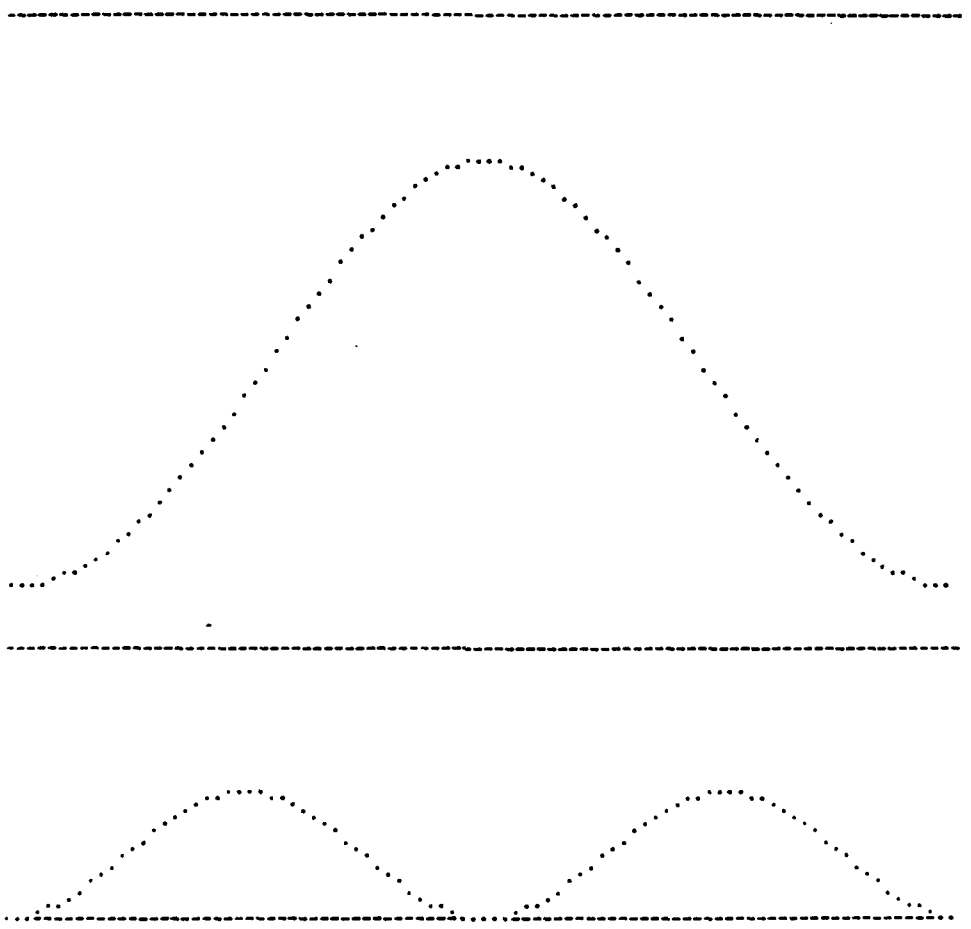


Figure 5.9. Noncrossed and Crossed Transmittances versus Azimuth Angle as Predicted from the Theory for the Hypothetical Metal Film Specified in (5.6).

Peak and valley ordinates (in percent) are 46.72 and 27.02 for (a), 1.22 and 0.00 for (b). Projection of the columnar orientation axis along the glass-film interface is vertical at the origin.

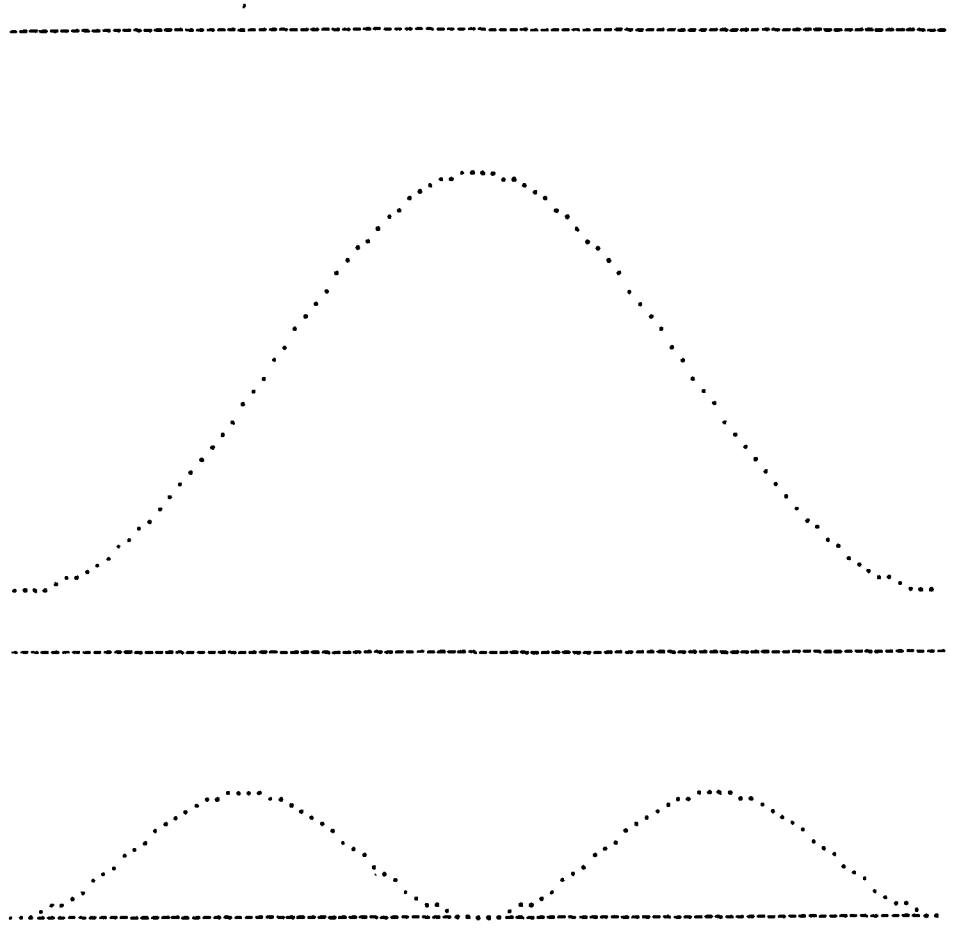


Figure 5.10. Noncrossed and Crossed Reflectances versus Azimuth Angle as Predicted from the Theory for the Hypothetical Metal Film Specified in (5.6).

Peak and valley ordinates (in percent) are 43.14 and 22.95 for (a), 0.79 and 0.00 for (b). Projection of the columnar orientation axis along the glass-film interface is vertical at the origin.

CHAPTER 6

CONCLUSION

We now conclude with a brief summary of the results attained and their possible extensions, followed by some potential applications and further suggestions for future work.

Summary

The relationship between the departure from optical isotropic behavior and the microstructure of thin films was the main concern of this dissertation.

In Chapter 2, quantitative analysis of aluminum and zirconium oxide films deposited at high angles of vapor incidence indicated that metals and dielectrics present two different and analogous manifestations of the structure-induced optical anisotropy observed under normal incidence light at 632.8 nm. Such metal and dielectric films tend to behave mostly as polarizers and retarders because of significant asymmetries in extinction coefficients and refractive index values, respectively.

The almost universal columnar structure of vacuum-deposited films suggests strongly that similar behavior should be observed in films of virtually any material.

The essential thrust of this work was to grasp the fundamental reasons for this behavior beyond the phenomenological level. With

multilayer systems in mind, a four-dimensional theory was presented in Chapter 3 that starts from first principles, unifies previous treatments developed by several investigators for particular cases of film anisotropy, and properly handles the most general case of coupled mode propagation. Although it was built with the columnar model in mind, the theory is also valid for other sources of optical anisotropy, as long as principal axes are still definable.

In Chapter 4, the insights obtained from the theory allowed us to establish an experimental method for the determination of the three principal refractive indices and physical thickness of a single dielectric film with explicit consideration of its microstructure. The procedure is essentially straightforward, and intricate iterative calculations, common in this area, unnecessary.

All measurements in transmission can alternatively be performed in reflection, a requirement for opaque samples, and their results interpreted with an analogous outcome from the theory. The method can eventually be extended for metal films by, for example, additional retardation measurements at nonnormal incidence, although at the expense of its simplicity.

Experiment and theory were placed side by side in Chapter 5. Here the goal was to test the theoretical predictions, as well as the values previously determined for the refractive indices, against transmittance curves obtained from the ellipsometer, with the same zirconium oxide sample and under similar conditions. Although the

ellipsometer performed well in extinction measurements, detailed examination of the instrument disclosed the need for corrections in the transmittance data. After instrumental errors were identified, and the substrate role was also taken into account, the experimental curves with varying angle of incidence or azimuth angle exhibited good agreement with the corresponding predictions. A similar comparison involving a zirconium oxide/silicon oxide narrowband filter with 21 layers deposited at 30° resulted in an agreement in peak position within a resolution of Angstroms. Finally, optical properties were considered through the ANTF program for a hypothetical metal film, and similarities were pointed out between its crossed and noncrossed transmittance curves with those reported in Chapter 2 for an aluminum sample deposited at 85°.

Potential Applications

We indicate the potential usefulness of the polarization effects we have considered through examples that come to mind as these lines are being written. Some of these examples may become viable applications as control is gained over film properties.

Polarizers

Slocum (1981) has reported a metal film polarizer for the 0.8 to 1.1 μm region with transmission higher than 0.40 and a degree of polarization in excess of 0.88. This element could be used in electro-optical systems, lasers, and other devices requiring a thermally stable polarizer (the common HR Polaroid sheet degrades when subjected to

temperatures above 55°C for extended periods of time). Figures 5.9(a) and 5.10(a), combined with the 90° shift in those curves from one polarization state to the other, suggest a simple and inexpensive polarizing beamsplitter. It is especially promising for the infrared, where efficiencies are expected to be higher.

Retarders

It is well known that crystal retarders require a delicate cleavage process in their manufacture and become excessively costly for large-aperture configurations, while being extremely fragile. In addition, materials like calcite, exhibiting large amounts of birefringence, can hardly be used for single-piece retarders due to prohibitive physical thickness requirements. Birefringent films of zirconium oxide, as well as of other dielectric materials, involve a much simpler fabrication process and can be easily deposited onto large areas. Tunable retarders, with different calibrations for different wavelengths, could be made by turning to advantage the gradual thickness variations of those films.

FTR Filters

Dr. Phillip Baumeister called to our attention the paper by Billings (1950), in which the use of a birefringent layer in the Turner frustrated total reflection filter (Leurgans and Turner, 1947) is proposed to induce an overlap of the otherwise separated transmission bands corresponding to the s- and p-polarizations. By using organic

birefringent films composed of benzene rings (see for example Barr and West, 1945), Billings was able to produce a single band, although without effective gain in transmission and with a much larger halfwidth. The use of our inorganic dielectric films instead would possibly provide more flexibility in design with varying deposition angles, but their discontinuous microstructure constitutes a serious source of waveguide scattering that would preclude obtaining efficient performances from the device (Burke, 1983). Nevertheless, we present it here as an illustration of the principle.

Bifocal Elements

Coating lenses or mirrors with birefringent films may induce them to exhibit two foci in distinct locations. An application for this effect was devised by Shack (1983) when he used one of the foci from a specially made quartz lens as a focusing aid for a scanning microscope. Birefringent films could be applied to existing glass elements, as well as provide more design flexibility.

Birefringent Narrowband Filters

The performance of such filters is shown in Figures 5.6 to 5.8 (Hodgkinson et al., 1983). They may find some application in information processing, for example.

Compact Birefringent Filters

Conventional Solc and Lyot filters (Evans, 1958), consisting of different combinations of birefringent crystal plates and polarizers, may have a good chance of being totally or partly translated into properly designed multilayer films composed of obliquely deposited components.

Understanding the Human Eye

It has been shown (Laties, Liebman, and Campbell, 1968) that cones in primate eyes are not perpendicular to the retina, pointing toward the center of the pupil. Hochheimer and Kues (1982) report the observation of retinal polarization effects as a clinical tool for diagnosing diaseases affecting the macula. The polarized-light retinal pattern is attributed to birefringence in cone-photoreceptor outer segments. Haidinger's brushes, a manifestation of a weak sensitivity of the human eye to polarization (Minnaert, 1954), are probably due to birefringence dispersion and dichoism of those segments.

Toward Real Films

Real films are not only anisotropic, but are inhomogeneous and scatter light. Also, their interfaces with other media are not well defined plane-parallel surfaces.

Although we were able to support qualitatively the measured results for the refractive indices with a model for the anisotropy alone,

the challenge remains for a simple effective index theory that would be valid for the whole range of film packing densities.

In principle, inhomogeneity can be treated with the matrix formulation by dividing each layer of a system into sublayers as thin as required. Similarly, interface imperfections can be taken into account by postulating the so-called "couches de passage" (transition layers), although increasing the complexity of the problem.

Analytical theories and measurement techniques have been developed for inhomogeneity and scattering problems. Perhaps the final goal toward real films will be achieved when all those departures from isotropic behavior are integrated in a common framework.

Current efforts to modify film microstructures may provide important clues in this direction. Conversely, a better understanding of those microstructures as they are, a context where this dissertation belongs, may stand as a valuable tool for monitoring such efforts.

APPENDIX A

COMPOSING THE L-MATRIX WITH A VECTOR BASIS

Let an arbitrary vector $\mathbf{v}(z)$ in the solution-space of equations (3.7) be represented by

$$\begin{bmatrix} v_1(z) \\ v_2(z) \\ v_3(z) \\ v_4(z) \end{bmatrix}$$

Let $\mathbf{u}^1(z)$, $\mathbf{u}^2(z)$, $\mathbf{u}^3(z)$, and $\mathbf{u}^4(z)$ be four independent solutions of (3.7) that have the following property at the $z = 0$ boundary:

$$\mathbf{u}^1(0) = \begin{bmatrix} 1 \\ 0 \\ 0 \\ 0 \end{bmatrix}, \quad \mathbf{u}^2(0) = \begin{bmatrix} 0 \\ 1 \\ 0 \\ 0 \end{bmatrix}, \quad \mathbf{u}^3(0) = \begin{bmatrix} 0 \\ 0 \\ 1 \\ 0 \end{bmatrix}, \quad \mathbf{u}^4(0) = \begin{bmatrix} 0 \\ 0 \\ 0 \\ 1 \end{bmatrix}. \tag{A.1}$$

Let $\mathbf{u}(z)$ be a solution of (3.7) such that $\mathbf{u}(0) = \mathbf{u}_0$. It can be expressed in terms of the basis set $\{\mathbf{u}^1(z), \mathbf{u}^2(z), \mathbf{u}^3(z), \mathbf{u}^4(z)\}$ as

$$\mathbf{u}(z) = u_1^0 \mathbf{u}^1(z) + u_2^0 \mathbf{u}^2(z) + u_3^0 \mathbf{u}^3(z) + u_4^0 \mathbf{u}^4(z) \tag{A.2}$$

or, in component form,

$$u_\beta(z) = \sum_{\alpha=1}^{4} u_\beta^\alpha(z)\, u_\alpha^0; \qquad \beta = 1,2,3,4. \tag{A.3}$$

This is equivalent to writing

$$\begin{bmatrix} u_1(z) \\ u_2(z) \\ u_3(z) \\ u_4(z) \end{bmatrix} = \begin{bmatrix} u_1^{1}(z) & u_1^{2}(z) & u_1^{3}(z) & u_1^{4}(z) \\ u_2^{1}(z) & u_2^{2}(z) & u_2^{3}(z) & u_2^{4}(z) \\ u_3^{1}(z) & u_3^{2}(z) & u_3^{3}(z) & u_3^{4}(z) \\ u_4^{1}(z) & u_4^{2}(z) & u_4^{3}(z) & u_4^{4}(z) \end{bmatrix} \begin{bmatrix} u_1^{0} \\ u_2^{0} \\ u_3^{0} \\ u_4^{0} \end{bmatrix}, \qquad (A.4)$$

which reproduces identities (3.10) and (3.11) in the text. Note also that boundary conditions (A.1) consistently allow the L-matrix to become the identity matrix at $z = 0$.

APPENDIX B

COORDINATE AXES REPRESENTATION OF THE ϵ TENSOR

By definition the ϵ tensor is represented in the principal axes system $P \equiv (n_1, n_2, n_3)$ by a diagonal matrix in the form

$$\epsilon_P \equiv \begin{matrix} \epsilon_{11} & 0 & 0 \\ 0 & \epsilon_{22} & 0 \\ 0 & 0 & \epsilon_{33} \end{matrix} . \tag{B.1}$$

Let P be obtainable from the coordinate axes system $C \equiv (x,y,z)$ shown in Figure 3.1 through a counterclockwise rotation around the y-axis, say, by an arbitrary angle ϕ. We represent this operation by the well known rotation matrix

$$R \equiv \begin{matrix} \cos\phi & 0 & -\sin\phi \\ 0 & 1 & 0 \\ \sin\phi & 0 & \cos\phi \end{matrix} . \tag{B.2}$$

Therefore, the identity connecting the displacement and the electric field vectors can be shifted from the P-representation to the C-representation through the following steps:

$$\begin{aligned} D_P &= \epsilon_P E_P \\ R^{-1} D_C &= \epsilon_P (R^{-1} E_C) \\ D_C &= (R \epsilon_P R^{-1}) E_C , \end{aligned} \tag{B.3}$$

from where it becomes clear that

$$\epsilon_C = R \epsilon_P R^{-1} . \tag{B.4}$$

We have also considered in this work situations in which P is obtainable from C through the R-rotation, followed by a counterclockwise rotation around the z-axis by an arbitrary angle ξ represented by

$$S \equiv \begin{matrix} \cos\xi & -\sin\xi & 0 \\ \sin\xi & \cos\xi & 0 \\ 0 & 0 & 1 \end{matrix} \qquad \text{(B.5)}$$

With the same reasoning that led to (B.4), we can promptly write

$$\epsilon_C = SR\epsilon_p R^{-1} S^{-1}. \qquad \text{(B.6)}$$

In the most general case we perform one more rotation in a similar fashion.

SELECTED BIBLIOGRAPHY

Abeles, Florin, C. R. Acad. Schi. Paris 228, 553 (1949.

Abeles, Florin, Ann. Phys. (Paris), 12th series, 5, 596 (1950).

Azzam, R. M. A., and Bashara, N. M., Chapter 4 in Ellipsometry and Polarized Light (North-Holland, Amsterdam, New York, 1977).

Barr, E. E., and West, C. D., U.S. Patent No. 2447790 (1945).

Bennett, Jean M., and Bennett, Harold E., Section 10 in Handbook of Optics, W. G. Driscoll, ed. (McGraw-Hill, New York, 1978).

Bergholm, Carl, Ann. Phys. 43, 1 (1914).

Berning, Peter H., Chapter 2 in Physics of Thin Films, 1, 71 (1963).

Berreman, Dwight W., J. Opt. Soc. Am. 62, 502 (1972).

Billings, B. H., and Pittman, M. A., J. Opt. Soc. Am. 39, 978 (1949).

Born, Max, and Wolf, Emil, Chapter 14 in Principles of Optics, 5th ed., (Pergamon, Oxford, New York, 1975).

Bousquet, Paul, Optica Acta 3, 1 (1956).

Bousquet, Paul, Ann. Phys. (Paris), 2, 5 (1957a).

Bousquet, Paul, PhD Dissertation (Masson et Cie., Paris, 1957b).

Bousquet, Paul, and Delcourt, Y., J. Phys. Radium 18, 447 (1957).

Bousquet, Paul, Flory, Francois, and Roche, P., J. Opt. Soc. Am. 71, 1115 (1981).

Bousquet, Paul, and Rouard, P., J. Phys. Radium 21, 873 (1960).

Bradford, A. P., Hass, G., McFarland, M., and Ritter, E., Appl. Opt. 4, 971 (1965).

Bragg, W. L., and Pippard, A. B., Acta Cryst. 6, 865 (1953).

Braun, Ferdinand, Ann. Physik 16, 1 (1905).

Browning, Stephen Douglas, PhD Dissertation, Optical Sciences Center, University of Arizona (1983).

Burgers, W. G., and Dippel, C. J., Physica 1, 549 (1934).

Burke, James J., Optical Sciences Center, University of Arizona, personal communication (1983).

Cau, Marcel, Comtes Rendues 186, 1293 (1928).

Coper, H. K., Frommer, L., and Zocher, H., Ztschr. Elektrochem. 37, 571 (1931).

Dirks, A. G., and Leamy, H. J., Thin Solid Films 47, 219 (1977).

Evans, John W., J. Opt. Soc. Am. 48, 142 (1958).

Faraday, M., Phil. Trans. 147, 145 (1857).

Flory, Francois, PhD Dissertation, Universite de Droit d'Economie et des Sciences d'Aix-Marseille (1978).

Goncharenko, A. M., and Fedorov, F. I., Optics and Spectroscopy 14, 48 (1963).

Guenter, K. H., and Pulker, H. K., Appl. Opt. 15, 2992 (1976).

Hacskaylo, Michael, J. Opt. Soc. Am. 54, 198 (1964).

Hass, Georg, in Applied Optics and Optical Engineering, Vol. 3, R. Kingslake, ed. (Academic, New York, 1965).

Heavens, O. S., Chapter 4 in Optical Properties of Thin Solid Films (Dover, New York, 1965), 2nd ed.

Hochheimer, B. F., and Kues, H. A., Appl. Opt. 21, 3811 (1982).

Hodgkinson, Ian, Horowitz, Flavio, Macleod, H. Angus, Sikkens, Marten, and Wharton, John, paper to be presented at the Optical Society of America Annual Meeting, San Diego, California (1983); to be published in J. Opt. Soc. Am.

Holland, L., J. Opt. Soc. Am. 43, 376 (1953).

Holmes, D. A., and Feucht, D. L., J. Opt. Soc. Am. 56, 1763 (1966).

Horowitz, Flavio, and Macleod, H. Angus, paper presented at the Los Alamos Conference on Optics, Santa Fe, New Mexico (1983); to be published in Proc. SPIE.

Jenkins, M. A., and Traub, J. F., Comm. ACM 15, 97 (1972).

Kelly, J. C., and Heavens, O. S., Optica Acta 6, 339 (1959).

King, R. J., and S. P. Talim, Optica Acta 28, 1107 (1981).

Konig, Von H., and Helwig, G., Optik 6, 111 (1950).

Koch, H., Phys. Stat. Sol. 12, 553 (1965).

Kundt, A., Ann. Physik 27, 59 (1886).

Laties, A. M., Liebman, P. A., and Campbell, C. E., Nature (London) 218, 172 (1968).

Leamy, H. J., Gilmer, G. H., and Dirks, A. G., Chapter 4 in Current Topics in Material Science, Vol. 6 E. Kaldis, ed. (North-Holland, Amsterdam, 1980).

Leurgans, P., and Turner, A. F., J. Opt. Soc. Am. 37, 983 (1947).

Lichtenstein, Terri L., MsC Thesis, Institute of Optics, University of Rochester (1980).

Macleod, H. Angus, Proc. SPIE 325, 21 (1982).

Malleman, R., and Suhner, F., Rev. Opt. 23, 20 (1944).

Martin, P. J., Macleod, H. A., Netterfield, R. P., Pacey, C. G., and Sainty, W. G., Appl. Opt. 22, 178 (1983).

Meaburn, J., Appl. Opt. 5, 1757 (1966).

Metzdorf, W., and Wiehl, H. E., Phys. Stat. Sol. 17, 285 (1966).

Minnaert, M., The Nature of Light and Colour in the Open Air (Dover, New York, 1954).

Movchan, B. A., and Demchishin, A. V., Fiz. Metal. Metalloved 28, 653 (1969).

Nieuwenhuizen, J. M., and Haanstra, H. B., Philips Tech. Rev. 27, 87 (1966).

Pearson, J. M., Thin Solid Films 6, 349 (1970).

Pocza, E. F., Acta Phys. (Acad. Sci. Hung.) 15, 1 (1962).

Reimer, Von L., Optik 14, 83 (1957).

Schesser, Joel, and Eichman, George, J. Opt. Soc. Am. 62, 786 (1972).

Schopper, Herwig, Z. Phys. 132, 146 (1952).

Shack, Roland, Optical Sciences Center, University of Arizona, personal communication (1983).

Slocum, R. E., Proc. SPIE 307, 25 (1981).

Smith, D. O., J. Appl. Phys. 30, 264S (1959).

Smith, D. O., Cohen, M. J., and Weiss, G. P., J. Appl. Phys. 31, pp. (1960).

Teitler, S., and Henvis, B. W., J. Opt. Soc. Am. 60, 830 (1970).

Thiessen, G., and Broglia, P., Z. Astrophys. 48, 81 (1959).

Thornton, John A., J. Vac. Sci. Technol. 11, 666 (1974).

Turner, A. F., and Ullrich, O. A., J. Opt. Soc. Am. 37, 521 (1947).

Weast, Robert C., ed., Section B in CRC Handbook of Chemistry and Physics (CRC Press, Florida, 1980).

Winterbottom, A. B., J. Opt. Soc. Am. 38, 1074 (1948).

Yeh, Pochi, J. Opt. Soc. Am. 69, 742 (1979).

Zeidler, J. R., Kohles, R. B., and Bashara, N. M., Appl. Opt. 13, 1115 (1974).

APPENDIX B

MOISTURE ADSORPTION AND OPTICAL INSTABILITY IN THIN FILM COATINGS

PhD Dissertation by C. C. Lee

TABLE OF CONTENTS

		Page
	LIST OF ILLUSTRATIONS	ix
	LIST OF TABLES	xvi
	ABSTRACT	xvii
1.	INTRODUCTION	1
2.	ADSORPTION	5
	Adsorption in General	5
	BET Classification	6
	Adsorption in Optical Coatings	9
	Control of Relative Humidity	17
3.	SURFACE PLASMONS	19
	Admittance Loci on an Argand Diagram	19
	Tilted Films	32
	Surface Plasmon Resonance in Single Layers	37
	Surface Plasmon Resonance in Single Layers	40
	Surface Plasmon Resonance in Multilayers	44
4.	MOISTURE ADSORPTION IN METAL-DIELECTRIC NARROWBAND FILTERS	54
	Metal-dielectric Narrowband Filter	54
	Wavelength Shift due to Water Adsorption	59
	Adsorption Isotherm	63
	Packing Density	69
	Baking Effect	73
	Moisture and Adhesion Failure	77
5.	MOISTURE ADSORPTION IN ALL-DIELECTRIC NARROWBAND FILTERS	79
	All-Dielectric Narrowband Filters	79
	Adsorption Isotherm	82
	Adsorption in Different Layers	85
	High Index Spacer and Low Index Spacer	95
	Desorption	102
	Narrowband Filters of Oxide Materials	105
	Moisture and Adhesion Failure	126

TABLE OF CONTENTS--Continued

Page

6. PREVENTION OF ADSORPTION IN COATING FILMS 128

Dust, Substrate Surface Defects and Adsorption . . . 128
Computer Simulation of Film Growth 129
Glow-Discharge Cleaning 144
Energy Activation for Condensing Molecules 149
Protective Layer or Cover Plates over Coating 158
Summary 160

7. MODELS FOR WATER PENETRATION IN THIN FILMS 163

Single Pore 163
Multipores with Assumption of Constant Rate of Supply from the Cental Pore 166
Multipores with Capillary Forces 168

8. CONCLUSION 173
Further Questions and Suggestions for Future Work 181

REFERENCES 183

LIST OF ILLUSTRATIONS

Figure		Page
2.1	Adsorption isotherms	7
2.2	TEM photograph of glass/ZnS (3/4 λ_0) cryolite (1/2 λ_0)/air	10
2.3	Two-inch coating unit for making TEM replicas	12
2.4	Fiber-like appearance of thin film coating	13
2.5	Edwards 18-inch coating plant	14
3.1	Loci of admittance and constant phase thickness	20
3.2	Isoreflectance and isophase contours	21
3.3	Admittance loci for ideal and real metal	22
3.4	Electric field distribution in Argand diagram	23
3.5	Sign convention for positive direction of electric field	24
3.6	Modified p- and s-admittance, η, of materials of 10, 1.35, 1.52, 2.0, and 2.5 for an incident medium of index 1.52	25
3.7	The variation of s- and p-polarized modified admittance .	26
3.8	Angular sensitivity of surface plasmon	27
3.9	Reflectance as a function of incident angle for system of Fig. 3.8(a)	39
3.10	Experimental measurements of the shift in resonance angle due to water adsorption for a system similar to Fig. 3.8(a) subjected to 100% RH. N = 0.0569-i4.1985, d = 50 nm calculated from the Δt = 0 curve	41
3.11	Apparatus used for measuring surface plasmon	42
3.12	Schematic of a dielectric overcoat on a metal for observing the surface plasmon, halfwave thickness for p-polarized light and quarterwave thickness for s-polarized light	43

LIST OF ILLUSTRATIONS--Continued

Figure		Page
3.13	Reflectance as a function of angle of incidence for system of Fig. 3.12	45
3.14	Electric field distribution of p-polarized surface plasmon in multilayer system	46
3.15	Illumination of a screen by the light reflected from the films at resonance. The electro-magnetic wave is scattered mainly in the dielectric layer of Fig. 3.14 and emerges as part of a cone of light	47
3.16	Adsorption and desorption in cryolite	49
3.17	Adsorption isotherm of cryolite	50
3.18	Change of refractive index after water adsorption measured in an Abelés refractometer	52
3.19	Degradation of cryolite film in humid atmosphere above NaCl solution	53
4.1	The schematic structure of a metal-dielectric narrowband filter	55
4.2	Measurement of transmittance of a growing filter	58
4.3	Schematic showing peak wavelength shift	60
4.4	Apparatus for observing water adsorption in the coating filter	61
4.5	Water adsorption in silver/cryolite filter	62
4.6	Computer simulation of water adsorption in metal-dielectric-metal narrowband filter, assuming a packing density of Na_3AlF_6 is 0.82	64
4.7	Measured shifts due to water adsorption	65
4.8	Water adsorption of metal-dielectric-metal narrowband filter air/Ag/Na_3AlF_6/Ag/glass	66
4.9	Adsorption isotherm giving the growth rate of patches	67

LIST OF ILLUSTRATIONS--Continued

Figure		Page
4.10	Wavelength shift due to water adsorption within four hours, where $\Delta\lambda_{rm}$ is the wavelength shift when the filter is exposed to air after opening the coater.	68
4.11	Texture of the filter surface by scanning electron microscope; water adsorption in Ag-Na_3AlF_6Ag filter . . .	70
4.12	Network of channels in a metal-dielectric-metal filter .	71
4.13	Baking effect of silver-cryolite filter baked at 120°F for two hours	74
4.14	Water adsorption in Ag/Na_3AlF_6 filter	75
4.15	Result of baking Ag/Na_3AlF_6 filter	76
5.1	Calculated performance of silver-cryolite narrowband filter with thickness errors. Mean = 1%, standard deviation = 1%	80
5.2	Computer simulation of water adsorption in all-dielectric narrowband filter. Assume that the packing density of Na_3AlF_6 is 0.82 and that of ZnS is 1.0	81
5.3	Shift of characteristic of narrowband filter due to moisture adsorption	83
5.4	Water adsorption in ZnS/Na_3AlF_6 filter 4 days after coating, RH = 47%.	84
5.5	Water adsorption in ZnS/Na_3AlF_6 filter 5 days after coating, RH = 47%	86
5.6	Water adsorption in ZnS/Na_3AlF_6 filter six days after coating	87
5.7	Water adsorption in ZnS/Na_3AlF_6 filter eight days after coating	88
5.8	The filter of Fig. 5.7 a few days later	89
5.9	Water adsorption of all-dielectric narrowband filter (ZnS/Na_3AlF_6)	90
5.10	The patch growth rate in filter versus relative humidity	91

LIST OF ILLUSTRATIONS--Continued

Figure		Page
5.11	The patch growth rate in filters versus relative humidity	92
5.12	The wavelength difference between different circles in the same patch of ZnS/Cryolite $[(HL)^5 4H(LH)^5]$ versus relative humidity	93
5.13	The wavelength difference between different circles in the same patch of ZnS/Cryolite $[(HL)^5 2L(LH)^5]$ versus relative humidity	94
5.14	The wavelength shift of ZnS/Cryolite $[(HL)^5 4H(LH)^5]$ filters due to water adsorption in different relative humidities	96
5.15	The wavelength shift of ZnS/Cryolite $A[(HL)^5 2L(LH)^5]G$ filters due to water adsorption in different relative humidities	97
5.16	The time taken for the circles in the same patch to reach a given size versus relative humidity	98
5.17	The growth of patch size in filter due to water adsorption (100% RH)	101
5.18	The wavelength shift of ZnS/Cryolite $A[(HL)^5 4H(LH)^5]G$ filter due to water desorption after being taken out of the cell at different relative humidities	103
5.19	The wavelength shift of ZnS/Cryolite $[(HL)^5 2L(LH)^5]$ filter due to water desorption after being taken out of the cell at different relative humidities	104
5.20	Dust, defects and patch on filter shown by scanning electron micrograph at different magnification	106
5.21	Shift of characteristics of narrowband filter after exposure to 81% RH for 10 hours after baking	108

LIST OF ILLUSTRATIONS--Continued

Figure		Page
5.22	Shift of characteristics of narrowband filter after exposure to 66% RH for five days and after baking. Note the appearance of a slight double peak after moisture adsorption	109
5.23	Shift of characteristics of narrowband filter after exposure to 100% RH for three hours and after baking. Note the very distorted peak shapes which result	110
5.24	Water adsorption in ZrO_2/SiO_2 filter. Sample 760-17-3 immediately after removal from the coater	111
5.25	Balzers BAK760 coating plant	112
5.26	Micrograph (TEM) of single-layer film	114
5.27	Micrograph (TEM) of thin-film multilayer of $ZrO_2(H)$ and $SiO_2(L)$	115
5.28	Water adsorption in ZrO_2/SiO_2 filter. Sample 760-17-3. New patches appeared one month after the first patches had appeared and then disappeared	116
5.29	The wavelength shift of ZrO_2/SiO_2 filter due to water adsorption (Sample 760-21-4, Air/$(HL)^5(6H)(2H)^5$/Glass)	118
5.30	Adsorption () and desorption (---) isotherms of ZrO_2/SiO_2 narrowband filter of design $(HL)^5 6H(LH)^5$	119
5.31	Water adsorbed filters after baking. Sample 760-17-3 after baking at 370° for 1.5 hr in vacuum. The patches disappeared and reappeared when exposed to air. $\Delta\lambda_{ad}$ = 50 Å, $\Delta\lambda_{bk}$ =-25 Å	120
5.32	Water adsorption in ZrO_2/SiO_2 filter. Sample 760-23-9 a few days after coating and before baking	121
5.33	Baking of filter after water adsorption. Sample 760-23-9 after baking at 370° for 1.5 hr in vacuum. $\Delta\lambda_{ad}$ = 40 Å. $\Delta\lambda_{bk}$ = -20 Å	122
5.34	Effect of baking on filter. Sample 760-26-1B shows non-uniformity after baking at 370° for 1.5 hr in vacuum	123

LIST OF ILLUSTRATIONS--Continued

Figure		Page
5.35	Effect of baking on filter. Sample 760-21-5 after sitting in 66% RH for 45 hr, $\Delta\Lambda_{ad}$ = 25 Å. After baking at 370° for 1.5 hr in vacuum, $\Delta\lambda_{bk}$ = -337 Å. After baking, the patches grew much faster. RH_{air} = 41%	124
5.36	Effect of baking on filter	125
5.37	Cracking and recrystallization of ZnS/Na_3AlF_6 filter	127
6.1	Water adsorption in ZnS/Na_3AlF_6 for sandblasted substrate (very rough surface)	130
6.2	Water adsorption in ZnS/Na_3AlF_6 filter. Left side of photos is with sandblasted substrate, right side is without sandblasting. (a) λ_d = 471 nm, (b) λ_b = 494 nm	131
6.3	Water adsorption in ZnS/Na_3AlF_6 filter. Left side of photographs is with sandblasted substrate and right side is without sandblasting. (a) After 50 minutes, (b) after 150 minutes	132
6.4	SEM photograph of sandblasted substrate	133
6.5	Sandblasted substrate	134
6.6	Water adsorption in ZnS/Na_3AlF_6 filter. Substrate scratched by sandpaper before coating. Any defect in the substrate will apepar at the center of the patch	135
6.7	Water adsorption in filter, RH = 43%	136
6.8	Scattered light shows the positional relation between dust and patch	137
6.9	Aluminum oxide intentionally dusted on substrate (by scanning electron micrscope, tilt 30°, 80X/800X)	138
6.10	Sample D-23-1. Superpolished substrate	139
6.11	Sample D-23-3. Superpolished substrate	140

LIST OF ILLUSTRATIONS--Continued

Figure		Page
6.12	Sample D-23-3. Superpolished substrate 1 day after removal from the desiccator where the sample was stored for 6 months	141
6.13	Sample D-3-1. Moisture adsorption in a filter on a regular microscope slide substrate	142
6.14	Computer simulation of thin film growth on different types of substrate (evaporation angle = 20°, with substrate holder not rotating)	145
6.15	Computer simulation of thin film growth on different types of substrate (evaporation angle = 20°, with substrate holder rotating)	146
6.16	Water adsorption in filter in air without glow discharge	147
6.17	Sample ML-12-3 without glow-discharge cleaning before coating	148
6.18	The mass spectrum of the residual gas in the BAK-760 coating plant	150
6.19	Structural zones in condensates (after Movchan and Demchishin)	152
6.20	Structural zones in condensates (after Thornton)	152
6.21	The increased packing density of ZrO_2 films produced by ion bombardment during deposition is indicated by the absence of a wavelength shift on exposure to atmospheric humidity	155
6.22	Silicon oxide films deposited over an ion-bombarded zirconium oxide film to increase fringe contrast	156
6.23	Comparison of sensitivity to moisture of narrowband filters constructed from ion-bombarded films (right) and conventionally deposited (left)	157
6.24	TEM photograph of G/ZnS($3/4\lambda_0$)/cryolite ($7/4\lambda_0$)/a	159
6.25	Filter damaged by an argon ion laser beam	161
7.1	Three possible models for porous films	164

LIST OF TABLES

Table		Page
2.1	Relative Humidity Over Saturated-Salt Solutions	18
5.1	Multilayer Water Adsorption	99
5.2	Multilayer Water Adsorption of $A\|(HL)^5 2L(LH)^5\|G$	100
5.3	Water Adsorption and Baking Effect of ZnS/Cryolite Filter	107

ABSTRACT

Materials in the form of thin films that have been deposited from the vapor phase are significantly different from similar bulk materials, both optically and mechanically, because of their columnar structure and consequent porosity. Their porosity has been verified in different ways. The effects of the pores on optical and mechanical performance and, in particular, the influence of water adsorption, have also been demonstrated.

Three techniques used for investigating optical instabilities in thin films are given. They all involve sharp resonances. The resonances are associated either with surface plasmons, metal-dielectric narrowband filters, or all dielectric narrowband filters. These resonances are very sensitive functions of layer properties and hence can be used to detect and measure changes in the layers, particularly those that are induced by adsorption of moisture. Moisture adsorption in thin films is a complex process that occurs unevenly in patches. Using resonance techniques, the adsorption isotherms of change in refractive index, of growth rate in patch size, and of peak wavelength shift, which are all important in characterizing the porosity of films, have been measured.

Some effects that locally increase film porosity and create central pores that permit water to penetrate into multilayer

structures have been investigated. Based on these results, some suggestions for preventing water adsorption in films are then made.

Moisture penetration into thin film structures is the major source of optical coating instability and it is therefore very important that the mechanisms of penetration be understood. Some deductions of the mechanisms are made from the experimental results.

CHAPTER 1

INTRODUCTION

Bottlenecks in optical thin-film technology are no longer attributable just to the design and monitoring of optical coatings, but are also much more related to materials; particularly with the fundamental effects of structure and composition on the properties of thin films. It is recognized that data concerning bulk materials cannot be applied blindly to thin films. Instead, research shows that thin films differ from similar bulk materials with respect to measured physical properties and to durability under exposure to humidity, radiation, and abrasion. A principal reason for the distinct differences between thin films and bulk is the structure of the films, which directly affects their properties and also renders them more vulnerable to be attacked by elements in the operating environment.

Electron microscope studies show that, with only a few exceptions, the structure of vacuum-deposited thin films is strongly columnar. The radii of the columns are often in the range of 10 to 30 nm depending on evaporation conditions, although they can be much larger. An important feature of the structure is that voids exist between the columns, taking the form of pores stretching through the film. The refractive index of those voids will differ from that of the material making up the columns. The pores have a major influence

on the adsorption behavior of the films. It is this adsorption that makes the refractive index of the film increase or decrease when environmental conditions change. The magnitude of the change in refractive index also depends on the materials which the films have adsorbed, but under normal conditions, the adsorbate is water vapor.

Research in nonoptical adsorption is already well-developed, and a general review will be given at the beginning of Chapter 2. The milestones of water adsorption in thin film coating will then be surveyed. A cell with accurate control of relative humidity is necessary and will be introduced at the end of Chapter 2.

Good work needs good tools. Three techniques for studying small instabilities of coating films are presented in the following three chapters. A surface plasmon technique will be given in Chapter 3. Its great sensitivity to a small change in optical constant allows us to investigate water adsorption of coating films. Chapter 3 begins with an introduction of admittance loci on an Argand diagram, which has been well developed by Macleod. It is a very handy graphical technique which provides a quick way of looking at the optical performance of a coating. Both single layer and multilayer surface plasmons are predicted by this graphical method and confirmed by experiments. The optical constants of silver and cryolite have been calculated. An adsorption isotherm of a cryolite film will then be discussed.

Another possible technique for observing optical instability due to water adsorption is to manufacture a narrowband filter using

the material in question. This technique was used by Richmond (1976). Metal-dielectric filters are the simplest type of narrowband filter and they are described in Chapter 4. Peak wavelength shift due to water adsorption has been predicted by computer simulation and verified by experiments. Adsorption isotherms and packing density of cryolite film, which relate to the film's porous nature are also discussed in this chapter. The chapter then ends with a discussion of desorption and adhesion failure caused by moisture.

Chapter 5 deals with the dynamic processes of water adsorption in multilayer coatings that are all-dielectric narrowband filters. Two very popular materials, zinc sulfide and cryolite, are used here as examples. Again, the adsorption study consists of computer simulation followed by experimental observation. Visible shifts of peak wavelength through each layer can be seen in each patch of moisture in the filters. The relation between adsorption and porosity of materials has been demonstrated by looking at both high and low index spacers. The influence on peak transmittance and on half peak width by adsorption is also discussed. The refractory oxide materials are more interesting nowadays because of their low loss and high durability under high-power radiation. Chapter 5 ends with an investigation of two oxide materials: ZrO_2 and SiO_2.

It would be very useful if one could stop water adsorption in films. The search for reasons which make coating films porous is described in Chapter 6. Limited mobility of condensing atoms (molecules) is the main reason. This will be demonstrated by computer

simulation of film growth. Surface defects of substrate, dust, spitting of sources, and impurities will then exaggerate the porosity of the coatings and this is shown by experiments described in this chapter. Some means of stopping adsorption in films are proposed.

Chapter 7 outlines three models for interpreting water adsorption in porous films. Water is assumed to go through central pores and to spread laterally. Rather than simply plotting the pore size distribution and void density of the films, the models give a mechanism for water penetration inside the films, which could be valuable information in the search for methods of preventing water adsorption.

CHAPTER 2

ADSORPTION

Adsorption in General

From the phenomenological point of view, one observes, upon mechanically separating solid and gas phases, that there is a certain distribution of adsorbate between them. This may be expressed, for example, as X, the volume at STP adsorbed per gram of solid versus the pressure P. The distribution, in general, depends on the temperature T, and also on the natures of the gas and the solid, so that the complete empirical description would be in terms of an adsorption function $X=f(P,T,gas,solid)$.

For a given gas adsorbed on a given solid, maintained at a fixed temperature, the adsorption function simplifies to $X=f(P)_{T,gas,solid}$ and is referred to as an adsorption isotherm.

If the gas is below its critical temperature, i.e., if it is a vapor, the alternative form $X=f(p/P_0)_{T,gas,solid}$ is more useful, P_0 being the saturation vapor pressure of the adsorbate. P/P_0 is then called the relative humidity (RH).

It is customary to divide adsorption into two broad classes, namely, physical adsorption and chemisorption. Physical adsorption equilibrium is very rapid in attainment and is reversible, except within some of the porous absorbents. Physical adsorption is usually

important only for gases below their critical temperature, i.e., vapor, as a result of general van der Waals interaction with the solid surface.

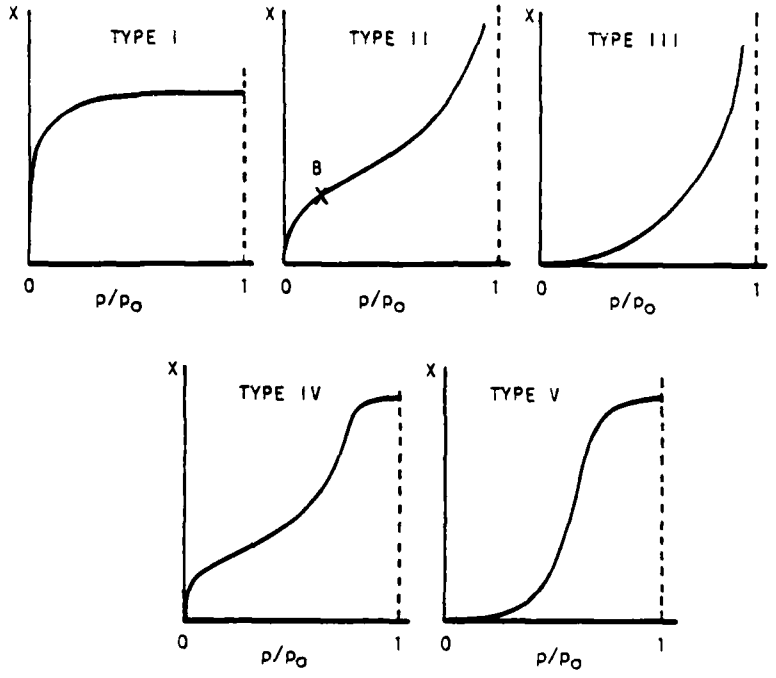
Chemisorption may be rapid or slow and may occur above or below the critical temperature of the adsorbate. It is distinguishable, qualitatively, from physical adsorption in that chemical specificity is higher and the energy of adsorption is large enough to suggest that full chemical bonding has occurred. Gas that is chemisorbed may be difficult to remove, and desorption may be accompanied by chemical changes. The rate of behavior of chemisorption is indicative of the presence of an activation energy.

It may, in fact, be possible for a gas to be physically adsorbed at first and then enter into some chemical reaction with the solid surface while the physical adsorption is still in process.

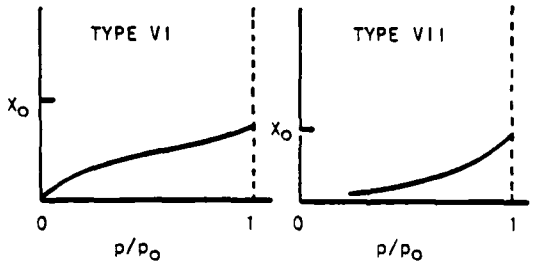
BET Classification

There are tens of thousands of adsorption isotherms reported. They include adsorbents such as nonporous solids like mica, glass, quartz, metal, etc., or porous solids like charcoal, silica, alumina, dielectric, polymers, etc., and adsorbates such as organic compounds like benzene, ethylchloride, hexane, heptane, etc., or water vapor or inert gases like nitrogen, argon, etc.

In 1940, Brunauer, Deming, Deming, and Teller classified isothermal physical adsorption into five principal forms, nowadays known as the BET classification. This classification is shown in Fig 2.1(a).



(a)



(b)

Figure 2.1. Adsorption isotherms.

(a) BET five classifications, (b) two additional types of adsorption isotherm expected for nonwetting adsorbate-adsorbent systems.

Type I depicts monolayer adsorption. Type II is very common in the case of physical adsorption and corresponds to multilayer formation. Point B at the knee of the curve is considered as the point of completion of a monolayer. Type III is adsorption characterized by heat adsorption equal to or less than the heat of liquifaction of the adsorbate, for example the adsorption of nitrogen on ice (Adamson and Dormant, 1966). Type IV and Type V are considered to reflect capillary condensation phenomena in that they level off before the saturation pressure, P_0, is reached and may show hysteresis effects.

The description above is traditional and some further comment is in order. The flat region of the type I isotherm has never been observed up to pressures approaching P_0; this type typically is observed in chemisorption at pressures far below P_0. Type II and Type III approach the P_0 line asymptotically and are typical of adsorption on powdered samples. The approach towards infinite layers is actually due to interparticle condensation (Wade and Whalen, 1968). Types IV and V specifically refer to porous solids with Type II and Type III behavior, respectively.

There are two additional isotherm types shown in Fig. 2.1(b). There are two simple types possible for adsorption on a flat surface for the case where bulk liquid adsorbate rests on the adsorbent with a finite contact angle (Tadros, Hu, and Adamson, 1974).

A number of techniques for finding the surface area and/or pore size distributions or volume of the pores from experimental

adsorption isotherms are given by Arthur W. Adamson (1976) and by S. J. Gregg and K. S. W. Sing (1967). They also give a complete theoretical derivation of the adsorption isotherms. However, not all of the experimental adsorption isotherms are as simple as can be classified into one of the standard types. This is because real adsorbents are not as simple as the models represent. The detailed pore structure, which is our interest, departs from the ideal models. Some of the examples they give show hysteresis characteristics which could be due to ink-bottle type pores that can trap adsorbate and/or to irreversible changes that may occur in the pore structure on adsorption.

One of the important features of adsorption is the adsorption rate. In the capillary model, J. Stone and H. E. Earl (1973) verified that the rate of filling in capillaries is governed by Poiseuille's law, which predicts the filled length to be proportional to the square root of the filling time. The pores in most porous materials are linked by many short, bent capillaries. The bends slow down the filling rate. Even more, if there are barriers between the capillaries, i.e., pores, it will take a much longer time to fill up all the pores. This may happen in multilayer optical coatings.

Adsorption in Optical Coatings

Transmission electron microscopy (TEM) allows us to look at the microstructure of a porous material. Figure 2.2 is a photograph of a replica of an optical coating with cryolite on top of zinc sulfide supported by glass. The replica was made in the two inch-

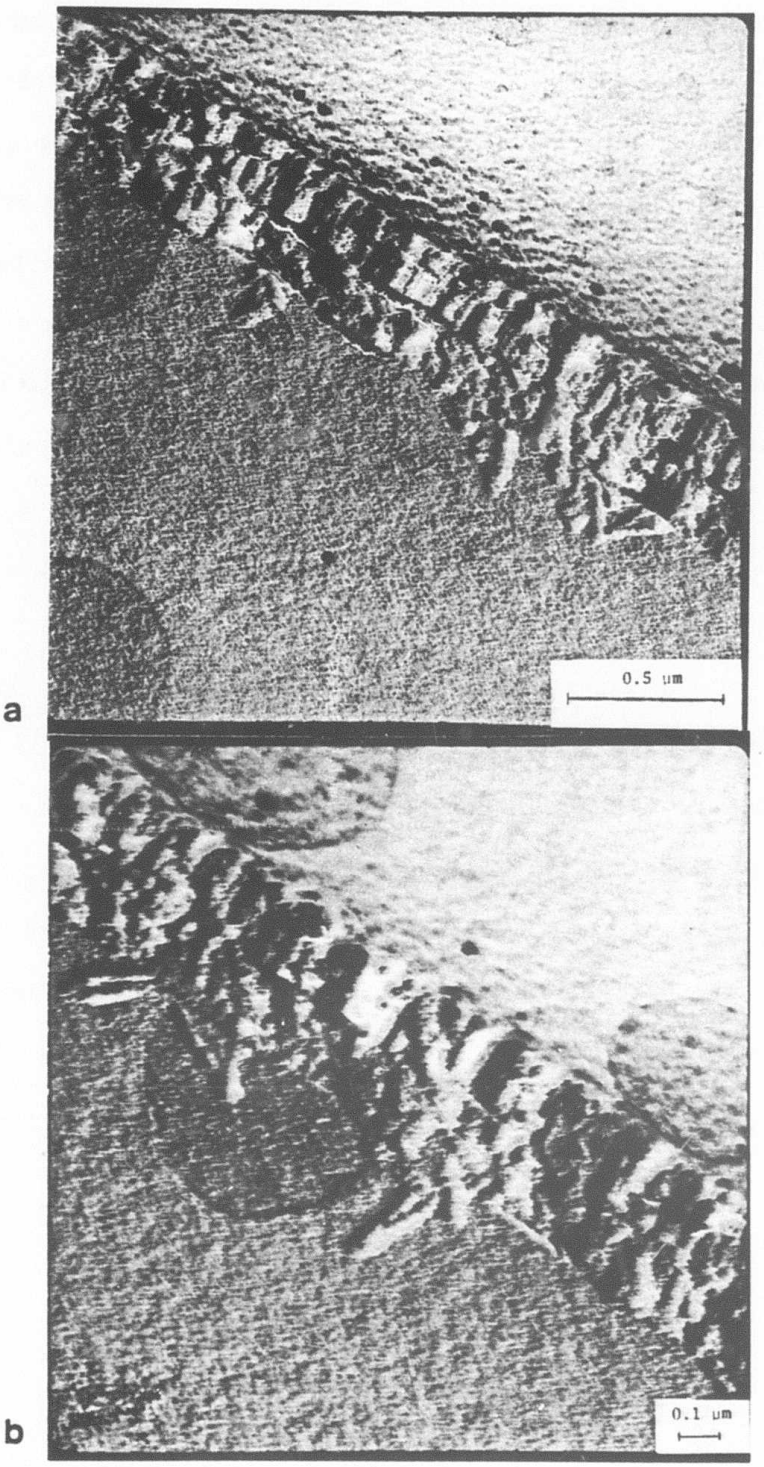


Figure 2.2. TEM photograph of glass/ZnS($3/4\lambda_o$) cryolite ($1/2\lambda_o$)/air, λ_o = 500 nm. Lower half of each photograph is glass.

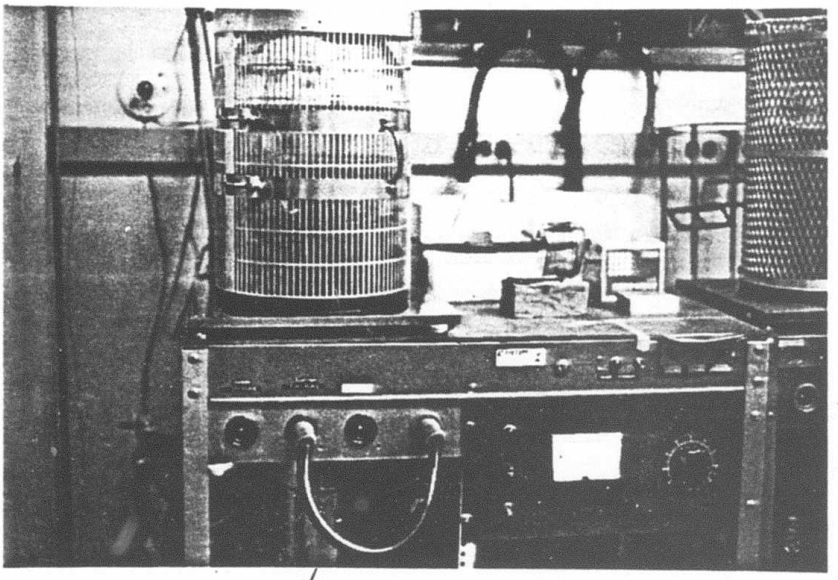
(a) x42800
(b) x66000

diameter coater shown in Fig. 2.3 following the P_t-preshadow techniques given by Pearson (1970) and Guenther and Pulker (1976). The photograph shows clearly that the optical coating films are columnar in structure with pores in between.

The columnar structure of the films has a profound influence on their properties, both optical and mechanical. Large intrinsic stresses, and hence strain energy, due to the forces of attraction between columns, can sometimes exist, the stress being more pronounced in one particular direction. The typical mode of mechanical failure is a peeling of the films at least partly driven by the internal strain energy. Figure 2.4 shows a peel adhesion failure in which parallel strips of coating are becoming detatched from the substrate, the unidirectional peeling probably being a consequence of a directional stress. These films were grown by a very fast evaporation rate of cryolite from a tantalum boat in an Edwards 18 inch coater (Fig. 2.5).

The pores in between the columns are of considerable importance. A film with columnar structure acts as a porous adsorbent. In normal circumstances, those pores have a tendency to adsorb water vapor, the polar nature and capillary condensation behavior of the water playing important roles. Such adsorption of water in the films changes their optical constants, their optical thicknesses and, therefore, the optical performance.

The changes of optical constants of the vacuum deposited films have been observed previously. Schulz (1949) measured the refractive index of LiF coatings by the Abbe refractometer and found



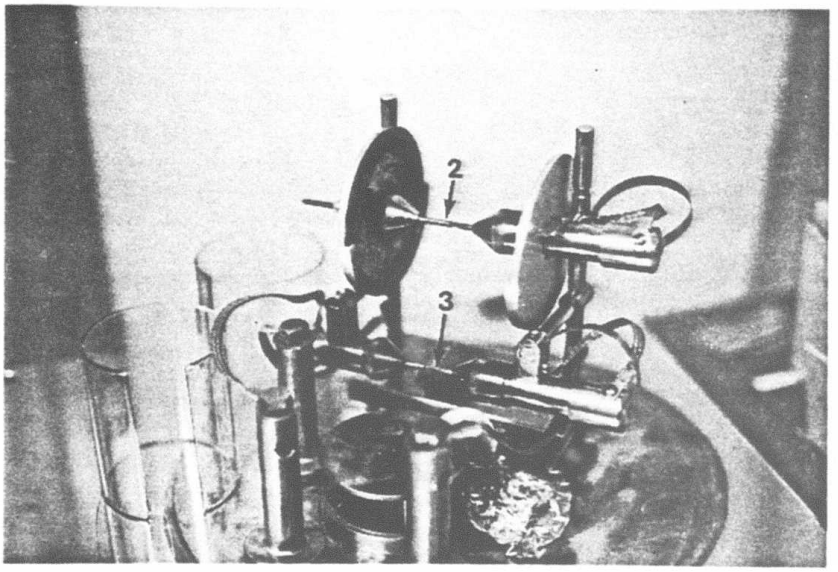


Figure 2.3. Two-inch coating unit for making TEM replicas.

(1) Oil diffusion pump
(2) Carbon rod source
(3) Carbon + platinum point source

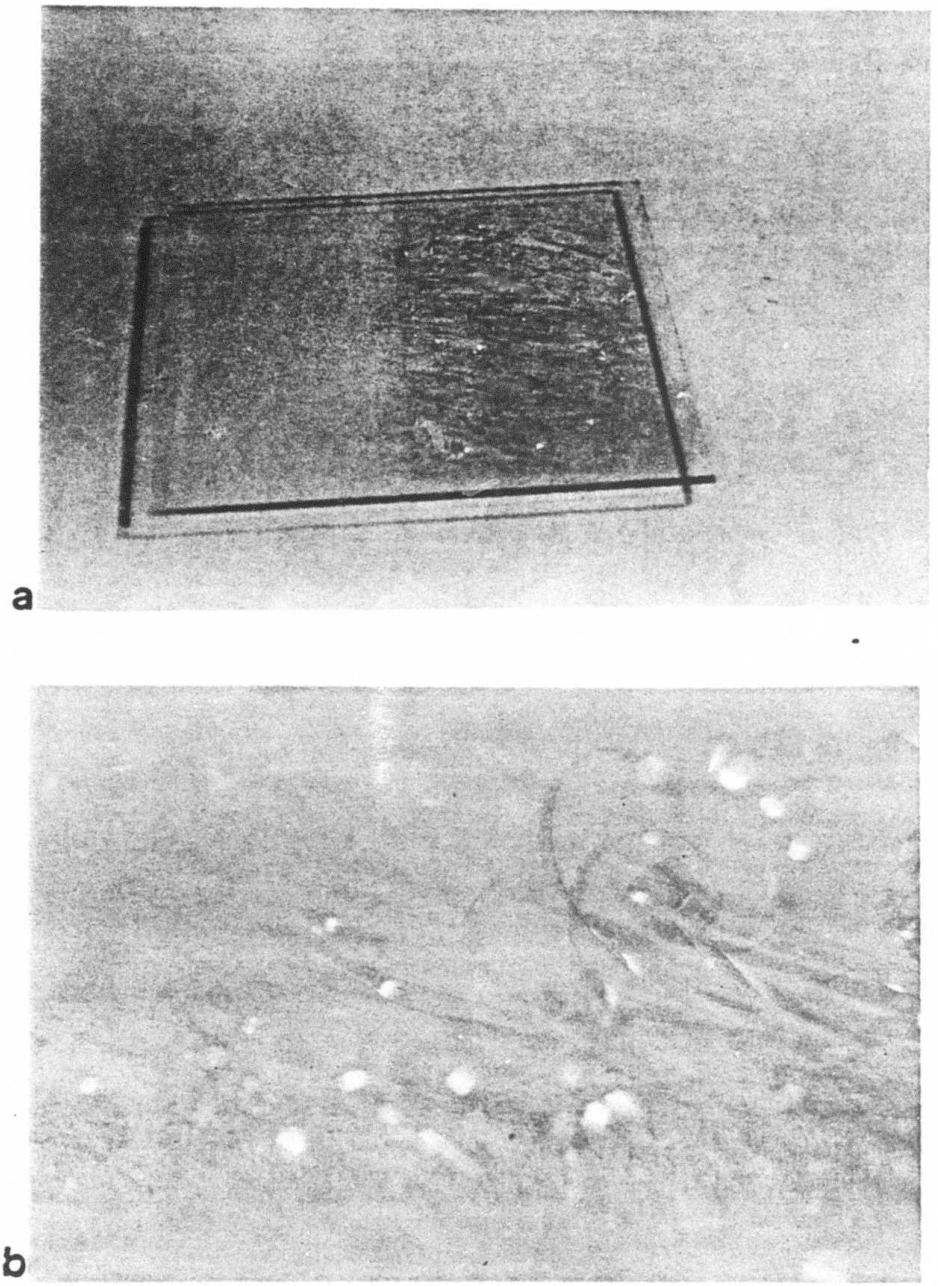


Figure 2.4. Fiber-like appearance of thin film coating.

(a) 1X, (b) 18X.

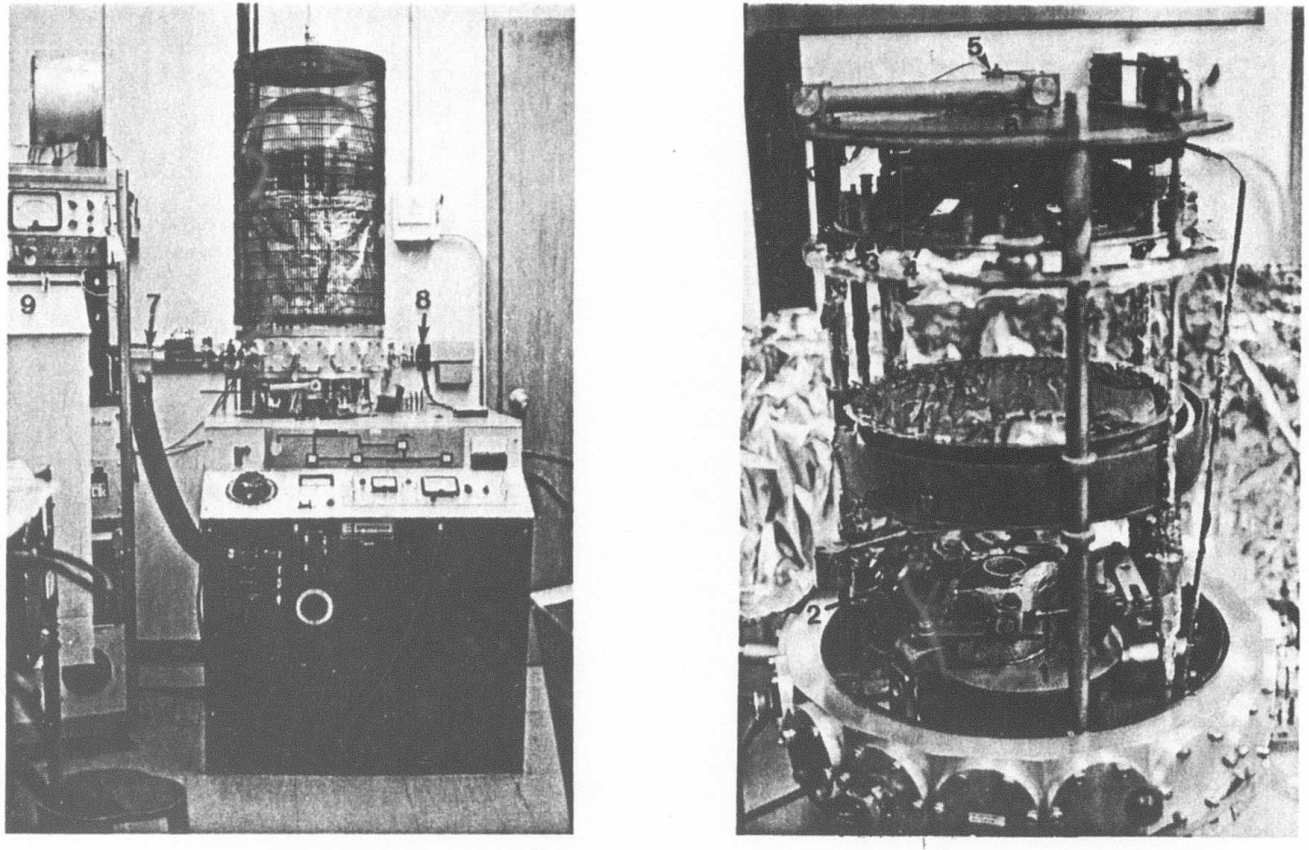


Figure 2.5. Edwards 18-inch coating plant.

(1, 2) evaporation sources (3) substrate holder (4) substrate (5) quartz crystal (6) optical monitor plate (7) light source (8) photomultiplier (9) chart recorder

that the refractive index increased with the refractive index of the contact liquid. He concluded that there was over 6% of accessible voids inside the film. Abelès (1950) detected an increase in the refractive index of cryolite of 1% in five days. Hall and Ferguson (1955) and Gonella and Robrieux (1962) observed a shift towards longer wavelengths in a reflectance curve for magnesium fluoride and calcium fluoride films, respectively. J. Meaburn (1966) observed the drifts of passbands of interference filters. He explained these drifts as thermal effects but did not realize they were due to water adsorption in the filters. Edgar E. Barr (1974) tried to explain the reduction in transmittance of a narrowband filter after coating by crystallization of the spacer layer. He was not aware that in some areas of the coating, adsorbed water was shifting the position of maximum transmittance such that the average transmittance of the whole filter was reduced.

The first two quantitative measurements of the effect of water adsorption and hence the resultant change of refractive index of films were reported by Koppelmann, Krebs, and Leyendecken, 1961), and by Koch (1965).

In 1967, Frank E. Jones studied the electrical conduction of a barium fluoride film electric hygrometer with water adsorption and gave an adsorption isotherm. Its conductance increased as the relative humidity increased because of the higher conductance of water adsorbed in the barium fluoride film.

Knowing that thin films have a columnar structure from TEM, Pulker and Jung (1971) made a film model of cylindrical columns in a closed-packed structure, instead of in the spherical aggregates model of Koch. From this model and the frequency change of a quartz crystal after adsorption/desorption of the water vapor, they calculated inner surface areas of MgF_2, Na_3AlF_6, and ZnS films computing 116, 89, and 26 m^2g^{-1}, respectively. The packing density, defined as the ratio of the film volume composed of solid material to the total volume of the film, which is related to the number and size of the pores, is also given. They conclude that the reversible part of water adsorbed is proportional to the number and size of the pores in the films and the irreversible part is proportional to the inner surface area of the films.

However, except in cryolite, the packing density calculated from their model is different from the measured value. This is because the model is too simple to fit all of the features of the structure of real films. According to their model, packing density is 0.9069, and is independent of the material and evaporation conditions. This is not realistic. We know from the experiment that a wide range of values is possible.

In order to fit the experimental results better, S. Ogura (1975) proposed two new models, namely, truncated conical and truncated paraboloidal. The cylindrical one is then a special case of those models. These models allowed him to explain the existence of a wide range of measured values of packing densities.

If one tries to fit his models to a specific material, one will still have difficulties of film-thickness dependence, surface roughness dependence, etc. on packing density. The models are still too simple to fit completely the real film structure. Therefore, in Ogura's research on pore size distribution, he adopted the very simple assumption that the films have cylindrical columns.

Before attempting to build a new model for optical thin-film structure, one must look at the water adsorption in the films more closely. Three techniques will be applied in the next three successive chapters. These techniques are sufficiently sensitive to the water adsorption in the films to make possible investigations of the ways water penetrates and spreads in the films.

Control of Relative Humidity

In order to derive an adsorption isotherm, the films must be set in an environment of well-controlled relative humidity. In a limited space, a simple but very accurate way is by means of salt solutions (American Society for Testing Materials, 1971) provided we can control the environment temperature within ±1° C. Saturated solutions of certain salts maintain definite RH at constant temperatures. These solutions should have an undissolved surplus of the salts to ensure saturation at all times.

Some of the salts with the RH maintained by their solution are listed in Table 2.1.

Table 2.1. Relative Humidity Over Saturated-Salt Solutions.

Salts	Temp. (° C)	RH (%)
$K_2CO_3 \cdot 2H_2O$	18.5	44
	20.0	42
	24.5	43
$Ca(NO_3)_2 \cdot 4H_2O$	18.5	56
	24.5	51
$NaNO_3$	20	66
NaCl	20	76
	30	75
	40	75
$(NH_4)_2SO_4$	20	81
	25	81.1
	30	81.1
K_2SO_4	20	96.5
	30	96.5
	40	96.5

CHAPTER 3

SURFACE PLASMONS

One way of looking at the resonance condition of a surface plasmon is by plotting the admittance loci of the films on an Argand diagram which was developed by Macleod (1980). It will be described briefly in the following two sections, followed by experiments. Figures 3.1 through 3.8 were taken from Macleod (1980).

Admittance Loci on an Argand Diagram

The optical admittance is defined as the ratio of the magnitudes of the magnetic and electric fields of the wave, and it is a property of the medium. In optics, we can assume that the relative permeability is unity and it follows that the optical admittance, Y, is proportional to the refractive index, the constant of proportionality being the admittance of free space.

$Y = H/E = Y_0 N = Y_0(n-ik)$, where $N = n-ik$ is the refractive index of the medium, defined as the ratio of velocity of light in free space to velocity of light in the medium. Y_0 is the admittance of free space = 1/377 Siemens in SI units.

The optical admittance can be numerically equal to the refractive index if we measure optical admittance in units of the admittance of free space:

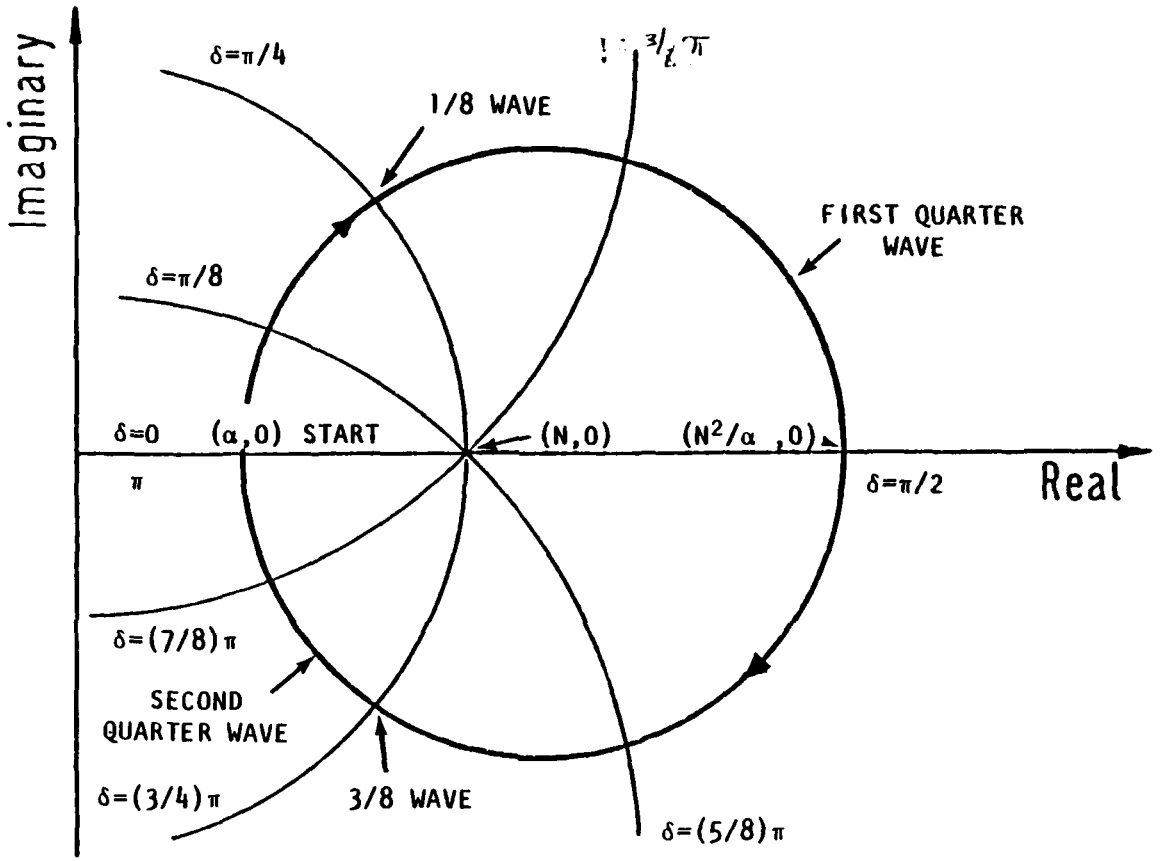


Figure 3.1. Loci of admittance and constant phase thickness (Macleod, 1980).

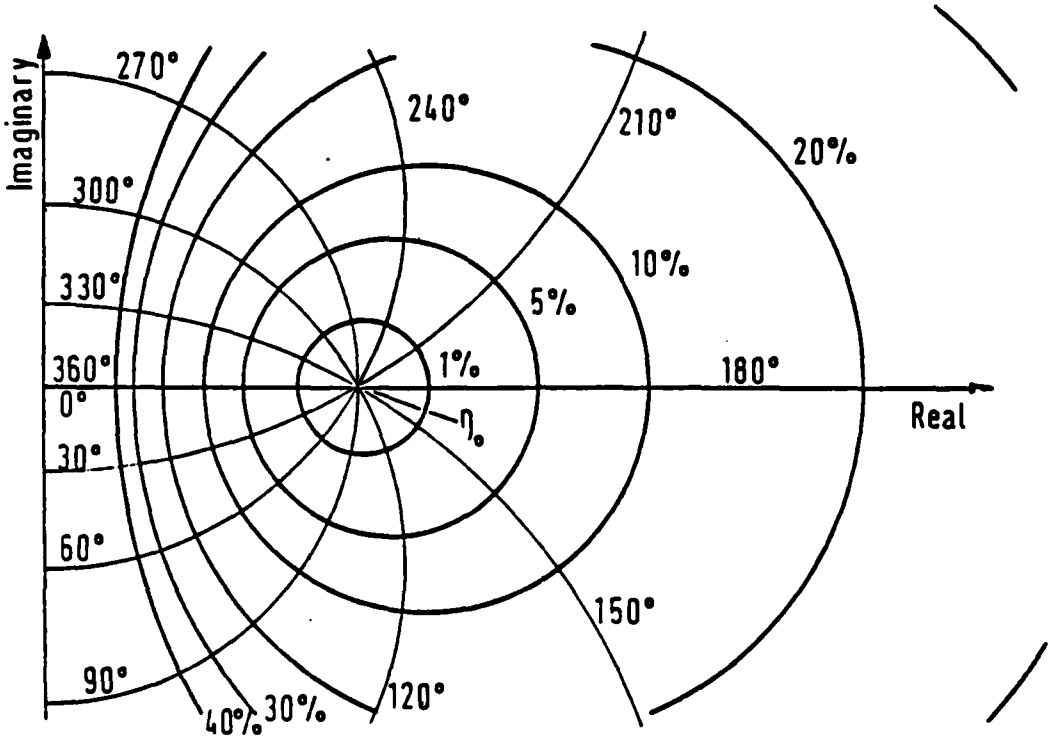
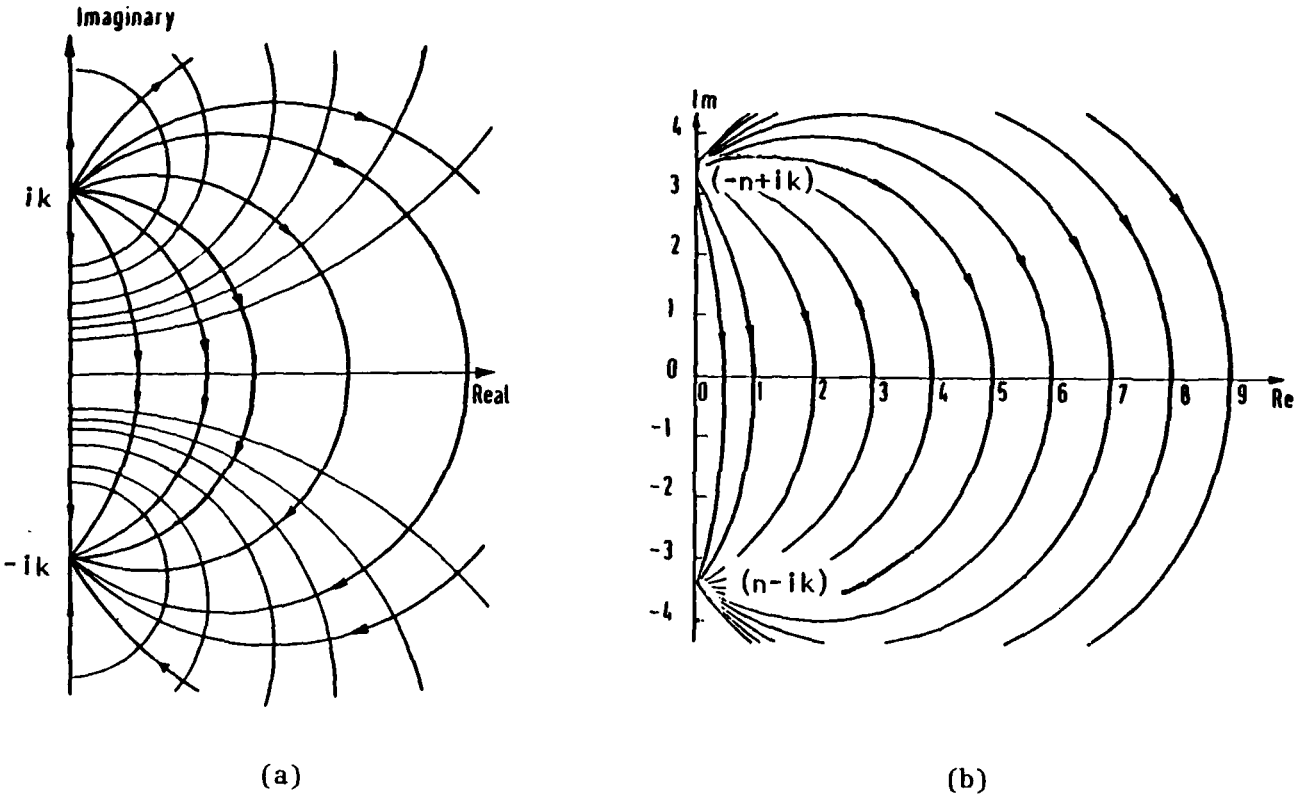


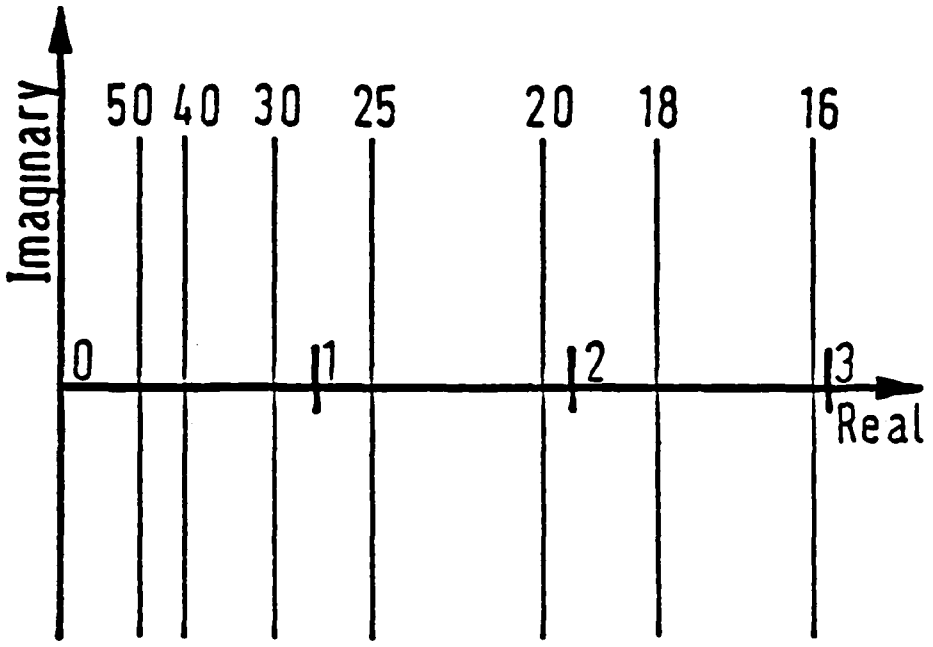
Figure 3.2. Isoreflectance and isophase contours (Macleod, 1980).



(a) (b)

Figure 3.3. Admittance loci for ideal and real metal (Macleod, 1980).

(a) Admittance loci for an ideal metal with admittance -ik. The loci begin at the point ik and terminate on -ik, (b) admittance loci for silver at normal incidence in the visible region.



$$\varepsilon = \frac{27.46\ T^{\frac{1}{2}}}{[R_e(Y)]^{\frac{1}{2}}} \quad \text{(VOLTS/METER)}$$

Figure 3.4. Electric field distribution in Argand diagram (Macleod, 1980).

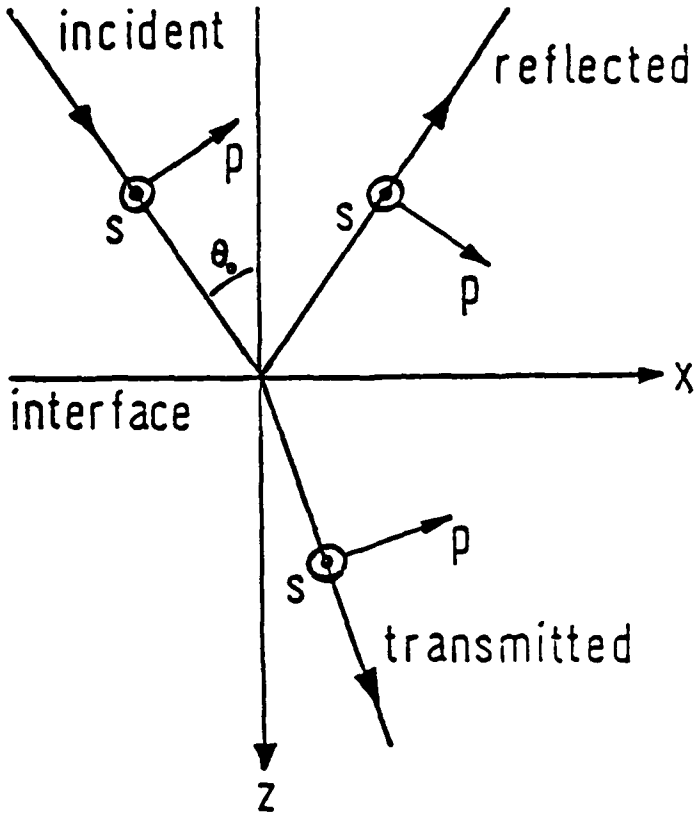


Figure 3.5. Sign convention for positive direction of electric field.

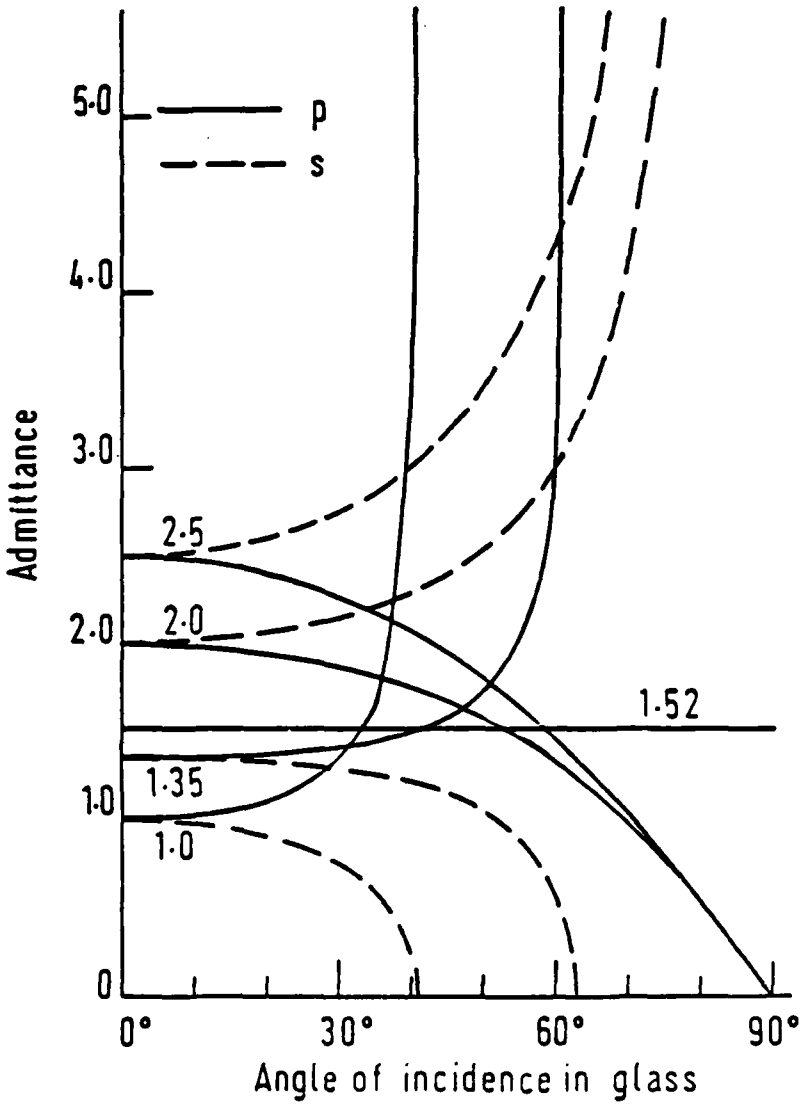


Figure 3.6. Modified p- and s-admittance, η, of materials of indices 1Ω, 1.35, 1.52, 2.0, and 2.5 for an incident medium of index 1.52 (Macleod, 1980).

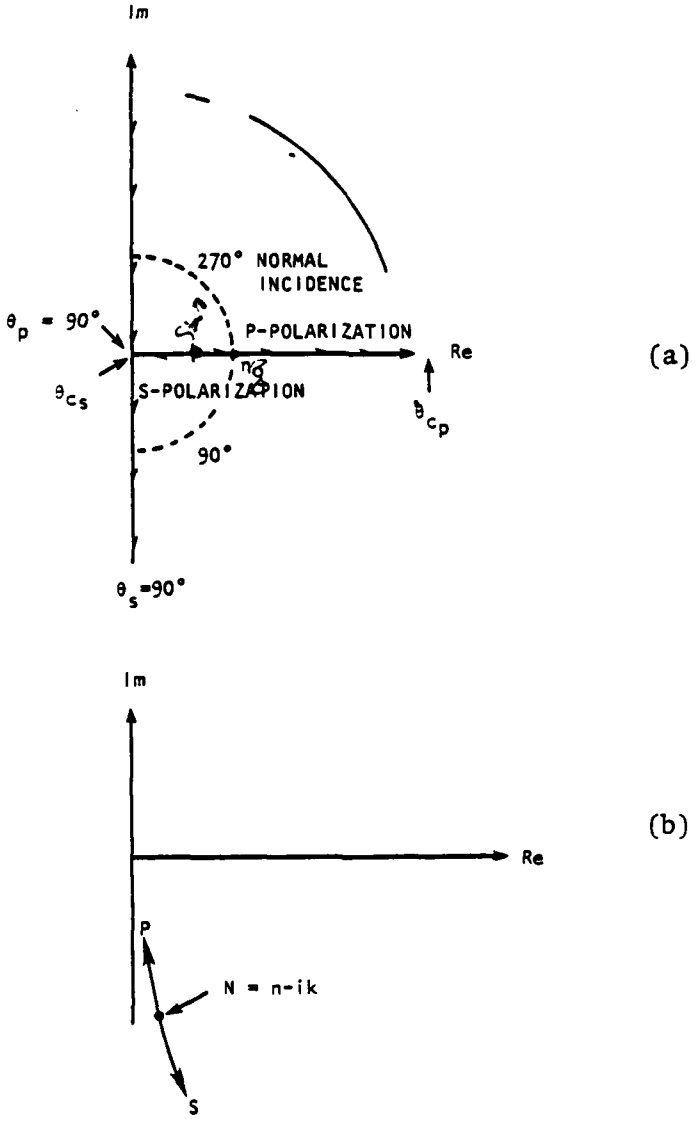
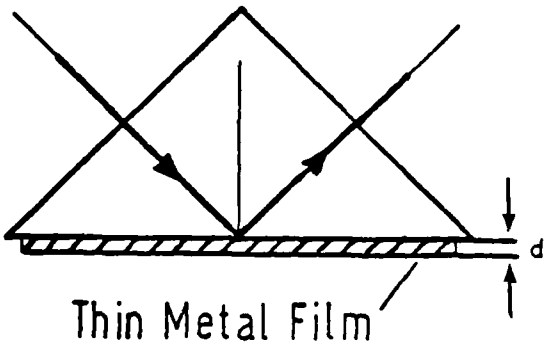
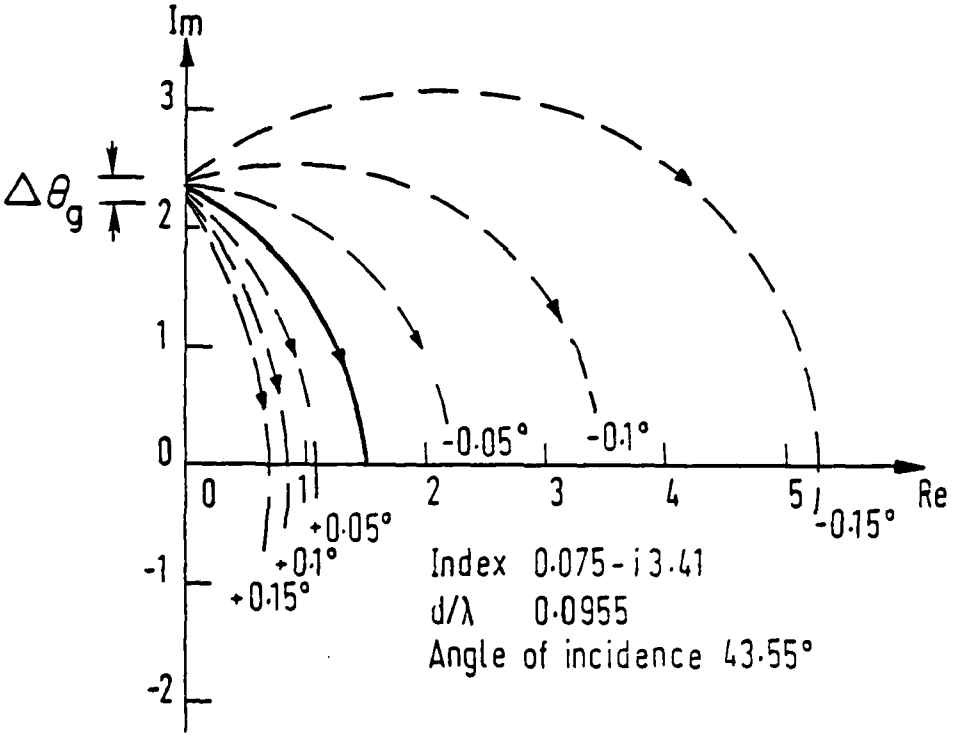


Figure 3.7. The variation of a s- and p-polarized modified admittance (Macleod, 1980).

(a) Dielectric layer, and (b) metallic layer.



(a)



(b)

Figure 3.8. Angular sensitivity of surface plasmon (Macleod, 1980).

(a) Coupling to a surface plasmon wave after Kretschmann and Raether (1968), (b) p-polarized admittance locus locus corresponding to the arrangement in (a). The solid line corresponds to the angle at resonance.

$$Y = n - ik \quad \text{(free space units)}.$$

The characteristic matrix for normal incidence for each layer of the coating is given by

$$\begin{bmatrix} \cos\delta & i\sin\delta/(n-ik) \\ i(n-ik)\sin\delta & \cos\delta \end{bmatrix},$$

where $\delta = 2\pi(n-ik)d/\lambda$ is the phase thickness of the layer and d is the physical thickness of the layer.

The performance of the multilayer is then given by

$$\begin{bmatrix} B \\ C \end{bmatrix} = \left\{ \prod_{r=1}^{q} \begin{bmatrix} \cos\delta_r & i\sin\delta_r/(n_r-ik_r) \\ i(n_r-ik_r)\sin\delta_r & \cos\delta_r \end{bmatrix} \right\} \begin{bmatrix} 1 \\ N_{sub} \end{bmatrix} \quad (3.1)$$

where N_{sub} is the index of the substrate. The equivalent optical admittance of the multilayer is $Y = C/B$, where B is proportional to the electric field while C is proportional to the magnetic field. The amplitude reflection coefficient is

$$\rho = \frac{Y_m - Y}{Y_m + Y} = \frac{n_m - n + ik}{n_m + n - ik} = |\rho|\, e^{i\phi}, \quad (3.2)$$

where Y_m is the admittance of the incident medium and must be real, and ϕ is the phase change on reflection given by

$$\phi = \tan^{-1} \frac{2n_m k}{n_m^2 - n^2 - k^2} . \tag{3.3}$$

The amplitude transmission coefficient is

$$\tau = \frac{2Y_m}{Y+Y_m} = \frac{2n_m}{n_m+n-ik} . \tag{3.4}$$

The reflectance, defined as the ratio of the intensities of the reflected and incident beams, is given by

$$R = \rho\rho^* = \frac{(n_m-n)^2 + k^2}{(n_m+n)^2 + k^2} \tag{3.5}$$

and the transmittance, the ratio of transmitted and incident intensities, by

$$T = \frac{Re(Y)}{Y_m} \tau\tau^* = \frac{4n_m n}{(n_m+n)^2 + k^2} . \tag{3.6}$$

The material already present at any stage in the deposition of the coating can be replaced by an equivalent admittance Y, given by the ratio of C/B at that stage, and subsequent material then behaves as if it were being deposited on a substrate of characteristic admittance Y. This admittance Y will be complex and its locus during the entire

deposition can be plotted on an Argand diagram, starting at the substrate and ending at the front surface.

For any particular layer of index N, the locus of Y on the Argand diagram can be shown to be a circle with center $([N^2 + \alpha^2 + \beta^2]/2\alpha, 0)$ passing through the point (α, β) where $\alpha+i\beta$ is the equivalent optical admittance of the multilayer already deposited when the current layer is started. The scale of phase thickness δ may also be plotted if the film's index N is known. This produces the equation of a circle with center $(0, N/2[\tan\delta-\cot\delta])$, that is on the imaginary axis, passing through the point (N,0).

The admittance circle is traced out clockwise. If the starting point is on the real axis, then a semicircle corresponds to a quarter wave. Drawing the circle becomes easy if we note that, if one point of intersection with the real axis is given by α, then the other point of intersection will be N^2/α. The reflectance is zero only at the point $(n_m, 0)$ where n_m is the admittance of the incident medium, and for the reflectance of a multilayer to be zero, its locus must terminate at that point. Figure 3.1 shows the locus of admittance and locus of constant δ.

It is also possible to plot isoreflectance contours. These are circles with centers $(n_m[1+R]/[1-R], 0)$, i.e., on the real axis and with radii $2\ n_m R^{1/2}/[1-R]$. Isophase contours, that is contours of constant phase changes on reflection, can also be added. They are circles with centers at $(0, n_m \cot\phi)$ i.e., on the imaginary axis, and

with radii $n_m \csc\phi$, where ϕ is the phase change on reflection, and passing through the point $(n_m, 0)$. Figure 3.2 gives the scheme of isoreflectance contours and isophase contours.

Metal layers, or other absorbing layers can also be included although the calculation requires the assistance of a computer. For a lossless metal in which the refractive index, and hence optical admittance, is purely imaginary, ~~and~~ given by -ik, which are on the imaginary axis. Figure 3.3(a) shows the typical form. Real metallic layers depart somewhat from this ideal model, but if the metal is of high performance, i.e., if the ratio k/n is high, then the loci are similar to the perfect case. It is as if the diagram were rotated slightly about the origin so that the points where all circles intersect are (n,-k) and (-n,k), respectively. Figure 3.3(b) shows a set of optical admittance loci calculated for silver, n-ik = 0.075 - i3.41, which shows this typical behavior. If the locus of a metallic layer ends on the point $(n_m,0)$ on the real axis, the reflectance will be zero.

The above graphical technique is used a great deal in understanding the basis of designs and in visualization of coating performance, and in the selection of designs for subsequent computer refinement. Besides, this diagram has an advantage that contours of electric field amplitude are very simple in form, and can readily be added when all the layers are dielectric.

The net intensity passing into multilayer can be written as

$$I = \frac{1}{2} Y_0 \, \mathrm{Re}(BC^*) = \frac{1}{2} Y_0 \, \mathrm{Re}[YBB^*] = \frac{1}{2} Y_o \, BB^* \, \mathrm{Re}(Y) \quad (3.7)$$

where $BB^* = \varepsilon^2 =$ (electric field amplitude)^2.

If the layers are dielectric, then the net intensity actually entering the assembly is the same as that which emerges. Let unit intensity emerge from the multilayer system, then

$$\varepsilon = (BB^*)^{1/2} = \left[\frac{1}{\frac{1}{2} Y_0 \, \mathrm{Re}(Y)}\right]^{1/2} = \frac{27.46}{[\mathrm{Re}(Y)]^{1/2}}.$$

If the incident intensity is unity, then

$$\varepsilon = \frac{27.46 \, T^{1/2}}{[\mathrm{Re}(Y)]^{1/2}}, \quad (3.8)$$

where T is the transmittance, ε is in Volts/meter provided that Y is in free space unit[5], i.e., if Y is numerically equal to refractive index. Figure 3.4 gives the electric field distribution in the Argrand diagram.

Tilted Films

As thin film coatings are gradually tilted with respect to the direction of incident light, their behavior departs increasingly from

that at normal incidence, and the changes can be substantial. For light which is incident other than normally, we therefore must redefine the optical admittance as the ratio of the components of magnetic and electric field parallel to, and intensities normal to the interfaces.

With a sign convention as shown in Fig. 3.5, we then have optical admittance for S- and P-polarized components

$$y_s = (n - ik)\cos\theta \tag{3.9}$$

$$y_p = (n - ik)/\cos\theta \tag{3.10}$$

these admittance being measured in free space units. θ is given by Snell's law:

$$n_m \sin\theta_m = (n-ik)\sin\theta$$

and the z-part of the phase factor by

$$\exp\ -i\ \frac{2\pi}{\lambda}\ (n - ik)\cos\theta \cdot z\ .$$

An alternative scheme which avoids some computing difficulties, because of ambiguities of the inverse trigonometric functions, is the replacement of $(n-ik)\cos\theta$ by

$$(n^2 - k^2 - n_m{}^2\sin^2\theta_m - 2ink)^{1/2}$$

with the correct root being in the fourth quadrant. The phase factor then becomes

$$\exp\ -i\ \frac{2\pi}{\lambda}\ (n^2 - k^2 - n_m{}^2\sin^2\theta_m - 2ink)^{1/2} \cdot z$$

and the admittances

$$y_s = (n^2 - k^2 - n_m{}^2\sin^2\theta_m - 2ink)^{1/2} \tag{3.11}$$

in the fourth quadrant, and

$$y_p = (n - ik)^2/y_s. \tag{3.12}$$

The calculation of multilayer properties at an angle of incidence other than normal is then

$$\begin{bmatrix} B \\ C \end{bmatrix} = \left\{ \prod_{r=1}^{q} \begin{bmatrix} \cos\delta_r & i\sin\delta_r/y_r \\ iy_r\sin\delta_r & \cos\delta_r \end{bmatrix} \right\} \begin{bmatrix} 1 \\ Y_{sub} \end{bmatrix} \tag{3.13}$$

with the appropriate S- or P- admittance and the corrected value of phase thickness $\delta = (2\pi d/\lambda)y_s$. The reflectance, transmittance, and phase angle are

$$R = \frac{y_m B - C}{y_m B + C} \cdot \frac{y_m B - C}{y_m B + C}^{*} \tag{3.14}$$

$$T = \frac{4 y_m \, \mathrm{Re}(y_{sub})}{(y_m B + C)\,(y_m B + C)^*} \tag{3.15}$$

$$\phi = \tan^{-1} \frac{i\, y_m (CB^* - BC^*)}{y_m^2 BB^* - CC^*} \, . \tag{3.16}$$

In order to preserve, for both S- and P-polarization, the normal incidence admittance for the incident medium which simplifies the Argand diagram construction for illustrating tilted thin film performance, Macleod (1980) proposed modified admittances

$$\eta_s = (n - ik)\cos\theta / \cos\theta_m$$

or

$$\eta_s = \frac{(n^2 - k^2 - n_m^2 \sin^2\theta_m - 2ink)^{1/2}}{\cos\theta_m} \tag{3.17}$$

in fourth quadrant, and

$$\eta_p = \frac{(n - ik)^2}{\eta_s} . \tag{3.18}$$

Figure 3.6 shows the behavior of dielectric materials when the incident medium is glass of index 1.52. There is a splitting of the S- and P-polarized admittances which increases with angle of incidence. For indices which are lower than that of the glass, it is possible to reach the critical angle and at that point, the admittance reaches either zero or infinity and disappears from the diagram. A particularly interesting case is the free space admittance when a beam of light is incident on the hypotenuse of a prism. Here, free space is acting as a substrate. Figure 3.7(a) shows the variation of the S- and P-polarized modified admittance of free space. η_g is the incident admittance. The S-admittance falls along the real axis until zero at the critical angle (θ_c) and then it turns along the negative direction of the imaginary axis tending to negative imaginary infinity as the angle of incidence tends to 90°. The P-admittance rises along the real axis, passing the point η_g at the Brewster angle, becoming infinity at θ_c, switching over to positive imaginary infinity and then sliding down the imaginary axis tending to zero as the angle of incidence tends to 90°.

For the metallic layer, the change in the modified admittance is mainly due to the $\cos\theta_m$ term. The P-admittance simply moves towards the origin and S-admittance away from the origin, as shown in Fig. 3.7(b). Thus, the principal effect for high performance metal layers with tilt is an expansion of the circular loci for S-polarization and a contraction for P-polarization. The basic form remains the same.

Surface Plasmon Resonance in Single Layers

For an uncoated hypotenuse, the second medium is air of refractive index unity. As one can see from Fig. 3.7(a), for θ_m greater than θ_c, the modified admittance for P-polarized light is positive imaginary and the reflectance is unity. Now let a thin absorbing, e.g., metallic layer be added to the hypotenuse, the admittance will then leave the imaginary axis. Figure 3.8(a) shows the illuminating arrangement and Fig. 3.8(b) the loci. For a very narrow range of starting values, the metal locus cuts the real axis in the vicinity of the incident admittance, and if the metal thickness is such that the locus terminates there, then the reflectance of the combination will be low. For one particular angle of incidence and metal thickness, shown in Fig. 3.8(b), the reflectance will be zero. This condition is very sensitive to angle of incidence which corresponds to the very small value of $\Delta\theta_g$ in Fig. 3.8(b). Since the admittance of the metal varies much more slowly than the air substrate, the zero reflectance condition will no longer hold, even for quite small tilts. This very narrow drop in reflectance to a very low value, which has all the hallmarks of a sharp resonance, can be interpreted as the generation of a surface plasma wave on the metal film (Kretschmann and Raether, 1968; Raether, 1977). Because of the opposite sign of the S-admittance for the metal, the effect exists only for P-polarization.

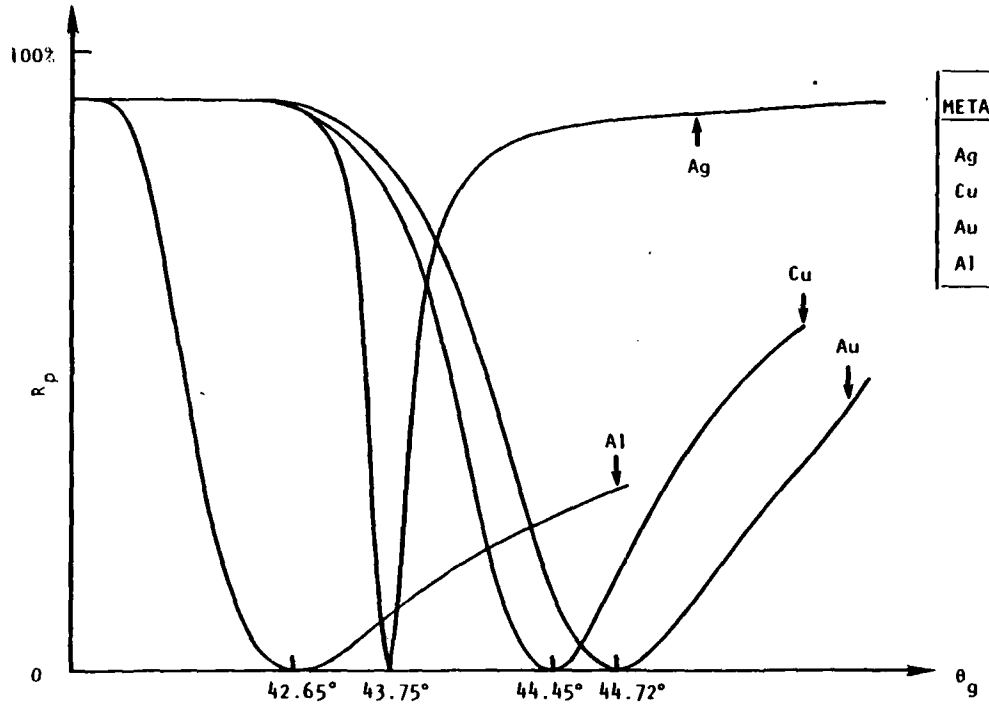
For a poor metal, n is large and the intersection of the admittance loci for different tilt angles is away from the imaginary axis. Therefore the $\Delta\theta_g$ is large, which implies that the half width

of resonance angle, $\Delta\theta_h$, will be large. In other words, the larger the n of the metal, the less sensitive will be the resonance.

For a metal with larger value of k, the starting point on the imaginary axis is higher, and therefore a smaller tilt angle is needed for the metal locus to reach the incident admittance, as shown in Fig. 3.9.

Figure 3.9 gives the characteristics of reflectances as a function of incident angle for different metals with given refractive indices. Alternatively, by knowing the reflectance as a function of incident angle, one can calculate the refractive index of that metal. One can see from the figure that the larger k/n of the metal is, the narrower the $\Delta\theta_h$ will be. Silver is then the best candidate for surface plasma wave observations.

When a thin dielectric layer is deposited over the metal next to the surrounding air, the starting point for the metal locus will be shifted along the imaginary axis. Because the metal loci at the imaginary axis are clustered closely together (almost intersecting), a small change in starting point produces an enormous change in the locus and hence in the point at which it cuts the real axis, leading to a substantial change in reflectance. This very large change which a thin external dielectric film makes to the internal reflectance of the metal film, has been used in the study of contaminant films adsorbed on metal surfaces. Film thickness of a few Ångstroms have been detected in this way. Provided that the film is very thin, then an additional tilt of the system will be sufficient to pull the



METAL	k	$\frac{k}{n}$	$\Delta\theta_h$	d
Ag	3.75	62.5	0.28°	58 nm
Cu	3.07	18.06	1.43°	52 nm
Au	2.97	12.91	2°	52 nm
Al	6	6.19	3.23°	15 nm

Figure 3.9. Reflectance as a function of incident angle for system of Fig. 3.8(a).

intersection of the metal locus with the real axis back to the incident admittance, and so the effect can be interpreted as a shift in the resonance rather than a damping.

Figure 3.10 shows the reflectance versus incident angle from which the refractive index of silver was calculated to be 0.0569 - i4.1985 at wavelength of 0.6328 μm by using Eqs. (3.13) to (3.18) and the statistical testing approach (Tang and Zheng, 1982). The apparatus used for this study is shown in Fig. 3.11. Figure 3.10 also shows the small shift in resonance position due to water adsorption. The lack of change in $\Delta\theta_h$ suggests high packing density for the silver film. The small shift in resonance angle, 0.07°, tells us that there is a thin water layer, 12 Å, adsorbed on top of the silver film. A small shift of resonance angle while the Ag film was exposed to air for a few days has also been detected, which can be explained as a sulfiding of the silver, indicating that a very thin dielectric film, Ag_2S, formed on top of the metal next to the surrounding air.

Surface Plasmon Resonance in Multilayers

The great sensitivity in incident angle of the surface plasmon allows us to calculate the optical constants of a coated metal, as already shown in the last section. One can then also apply this technique to calculate the optical constants of a dielectric film provided that the film is homogeneous. The dielectric film must be coated over the metal film. Figure 3.12 shows such a configuration. The addition of the dielectric layer between the metal surface and the surrounding air can move the starting point, Fig. 3.8(b), for the metal

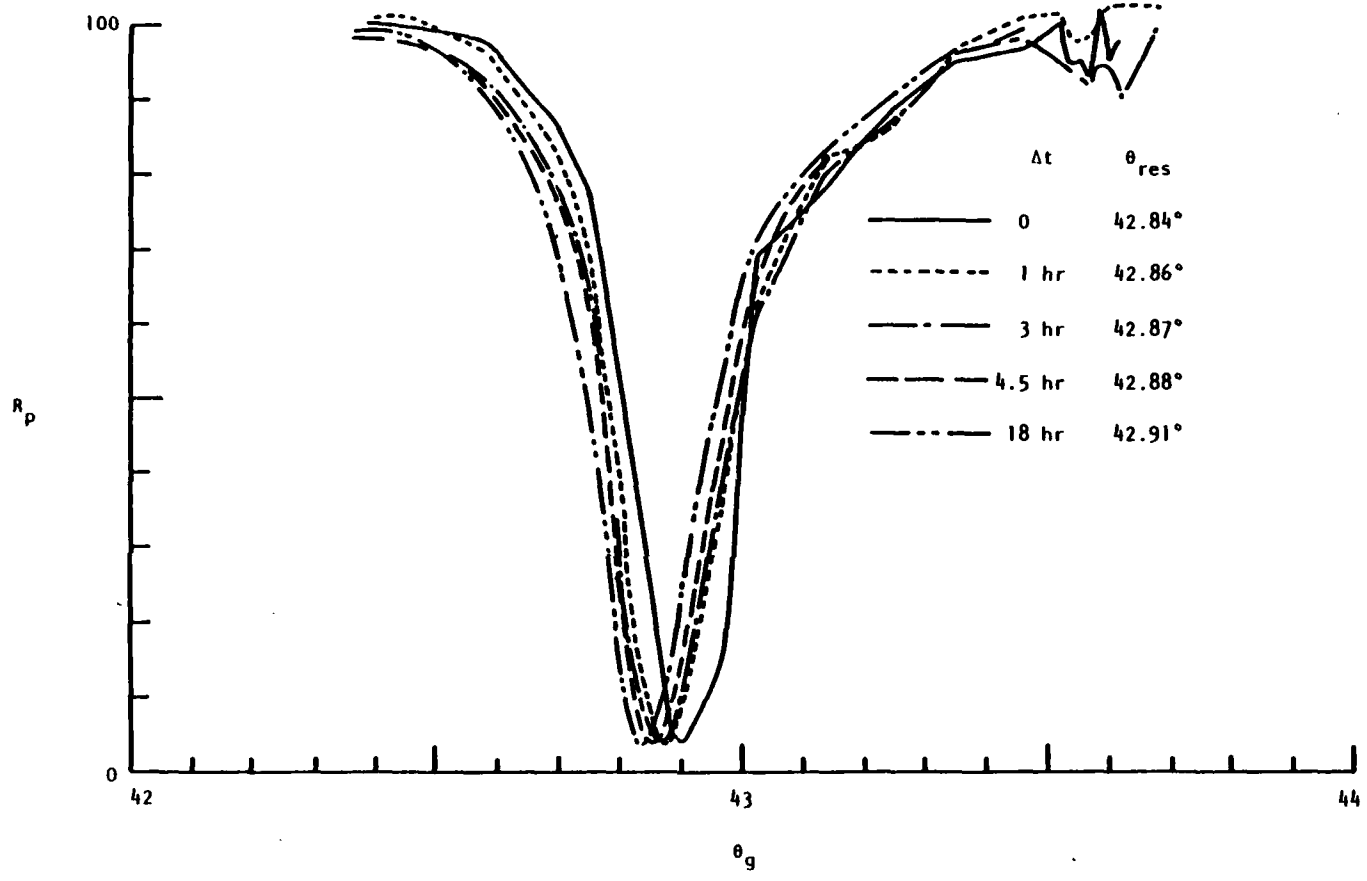
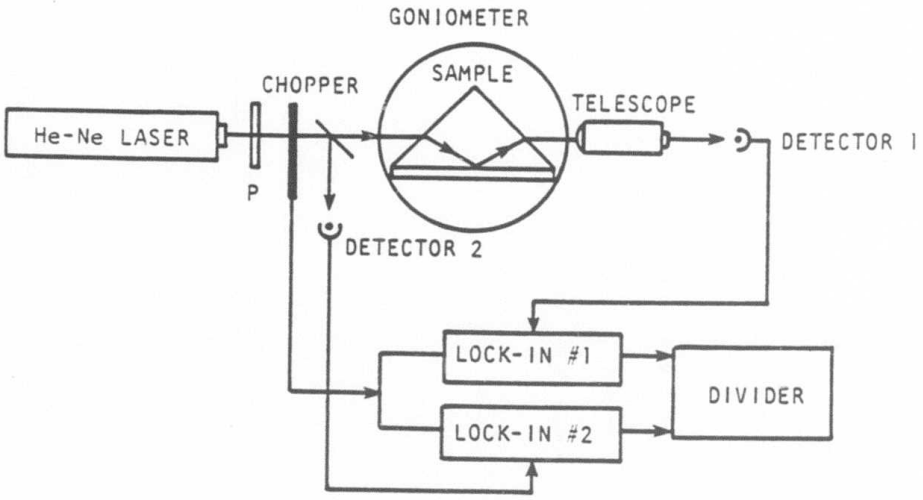


Figure 3.10. Experimental measurements of the shift in resonance angle due to water adsorption for a system similar to Fig. 3.8(a) subjected to RH 100%. N=0.0569-i4.1985, d=50 nm calculated from the Δt=0 curve.



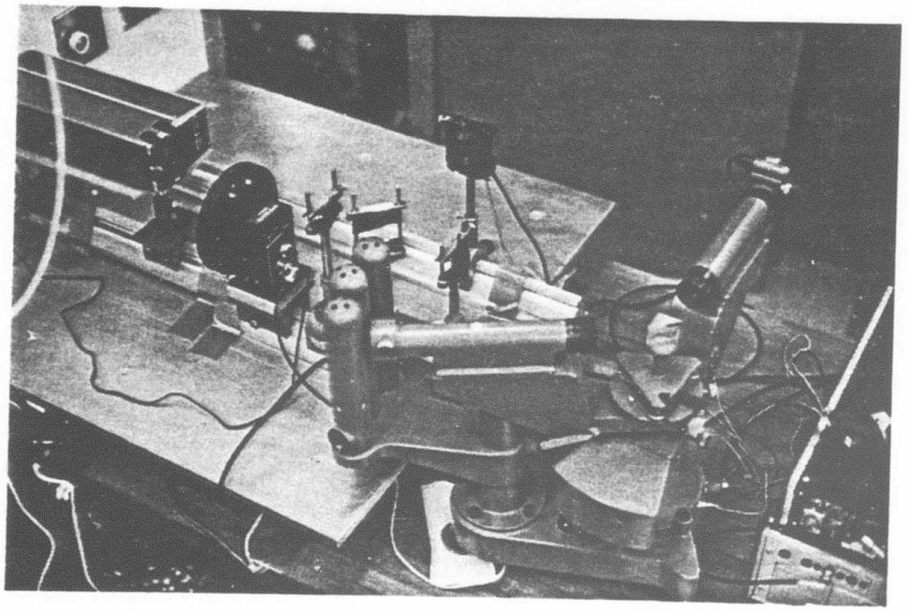


Figure 3.11. Apparatus used for measuring surface plasmon.

(a) schematic drawing
(b) actual machine

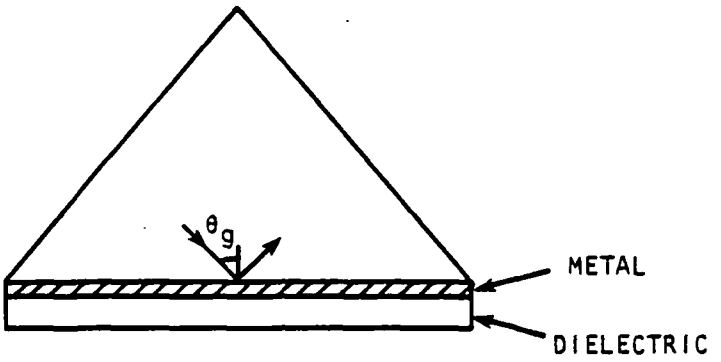


Figure 3.12. Schematic of a dielectric overcoat on a metal for observing the surface plasmon, halfwave thickness for p-polarized light and quarterwave thickness for s-polarized light.

on the imaginary axis. For S-polarized light, a quarter wave thickness of dielectric moves the starting point from the negative part of the imaginary axis to a position from which the metal locus can cut the real axis in just the same way as in the case of uncoated metal in P-polarized light. For P-polarized light, the low reflectance will be repeated for each additional half wave dielectric layer which is added. Figure 3.13 shows an experimental result where the dielectric is cryolite. Here the refractive index was calculated to be 1.315, again, by using Eqs. (13) through (18) and the statistical testing approach.

At resonance, the electromagnetic wave is guided from the prism through the silver layer and down to the dielectric layer where the electric field is a maximum. Figure 3.14 shows the theoretical electric field distribution for a P-polarized surface plasmon in the multilayer system. In practice, the wave tends to be scattered isotropically inside the layer where the field is large, and often a scattering contour, as shown in Fig. 3.15, appears in the light reflected from this system.

Adsorption Isotherms

Since coating films are porous in general, they will adsorb water vapor when set in a humid atmosphere. Therefore, the resonance in Fig. 3.13 will shift to the right if the sample is set in 100% RH. In order to verify that such a shifting is due to water adsorption, the sample can then be returned to normal air when the moisture should desorb and the resonance shift back. This experiment shows that the

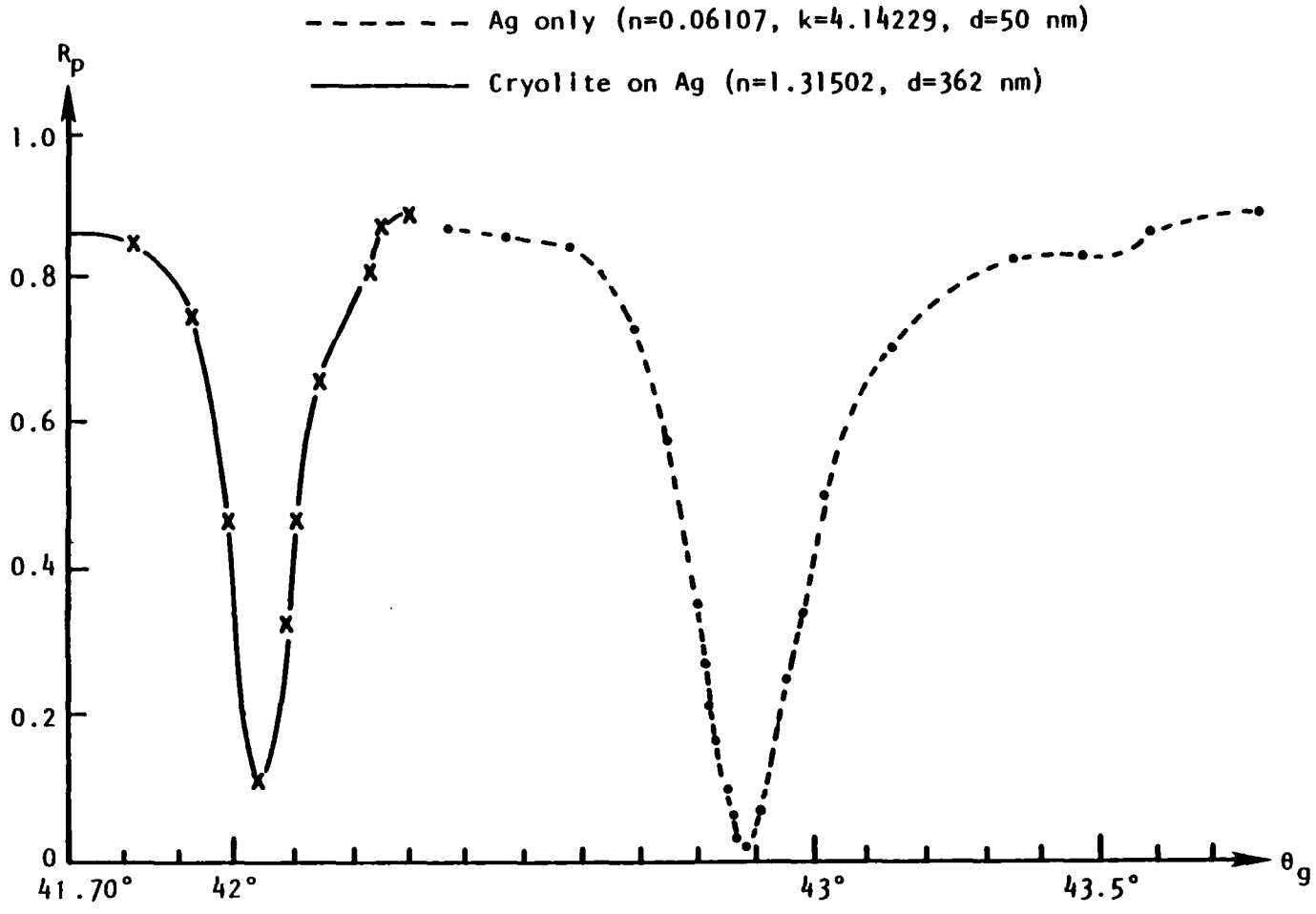


Figure 3.13. Reflectance as a function of an angle of incidence for system of Fig. 3.12.

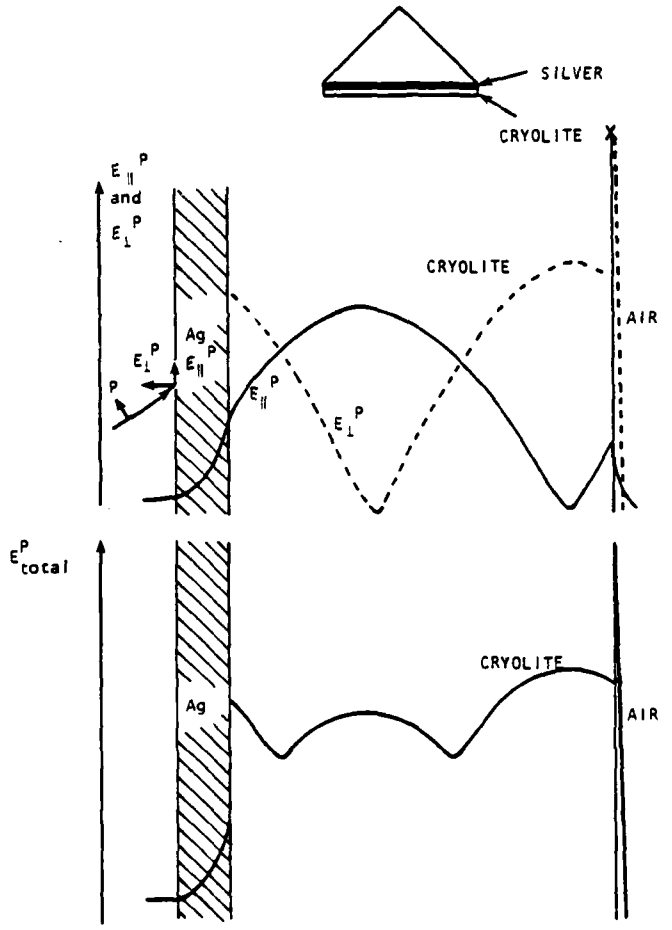
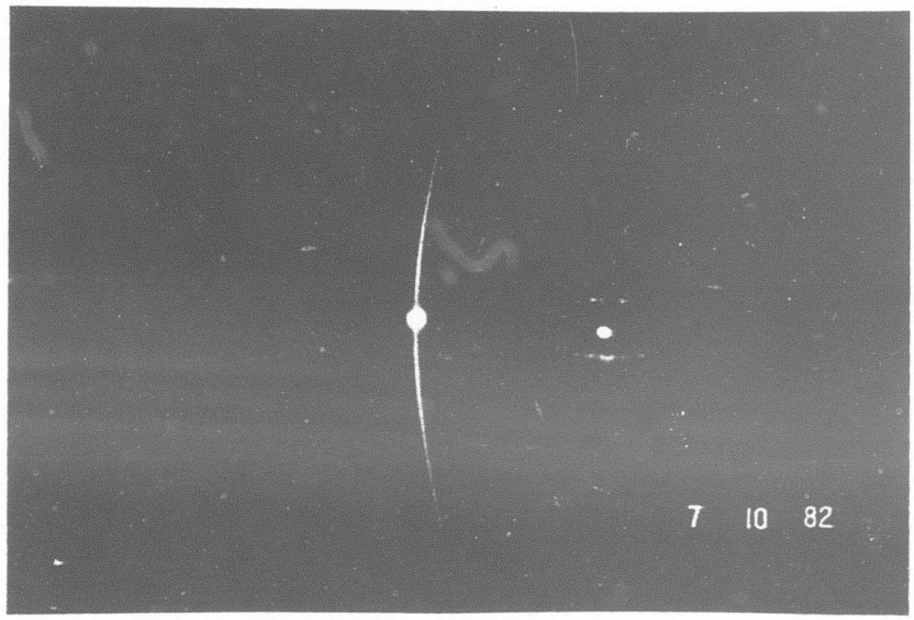
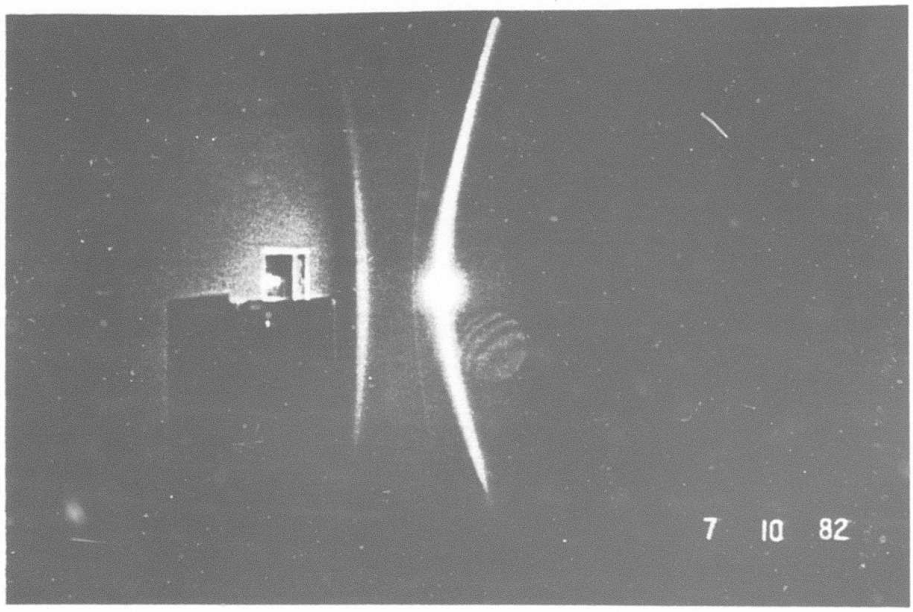


Figure 3.14. Electric field distribution of p-polarized surface plasmon in multilayer system.



(a)



(b)

Figure 3.15. Photographs of the illumination of a screen by the light reflected from the films at resonance. The electromagnetic wave is scattered mainly in the dielectric layer of Fig. 3.14 and emerges as part of a cone of light.

(a) Fresh films, (b) films degraded by environmental attack.

resonance angle does drift back, but not necessarily to the starting value. The moisture which does not desorb is sometimes referred to as "irreversible water" (Pulker and Jung, 1971). The adsorption and desorption of cryolite as a function of time is shown in Fig. 3.16. The abnormally large values of refractive index and of irreversible change suggest that a chemical reaction has taken place.

Figure 3.17 shows the adsorption isotherm. In the calculation, a simple assumption was made that the index of silver was unchanged during the whole process. The enormous shift of resonance angle after 81% RH appears due to a chemical reaction between cryolite and water, which changes the refractive index to a very large value. The effect of the increase in the refractive index on the resonance angle can be understood by considering the admittance at the interface between silver and cryolite is displaced to a higher value on the imaginary axis, as shown in Fig. 3.8(b). After water adsorption in RH greater than 81%, the refractive index is greater than 1.35, as shown in Fig. 3.17, which is a very abnormal value. It is suspected that $AlF_3 \cdot H_2O$, which has a refractive index 1.51 (Weast, 1972), was formed after a chemical reaction.

The reason why 81% relative humidity is critical is not understood. The distribution of pore sizes in the film can, in principle, be derived from an adsorption patterns, although in this case it may be disturbed by a reaction. However, we might assume it is current up to levels of around 81% humidity and its lack of change then implies an absence of porosity in the appropriate size range. The

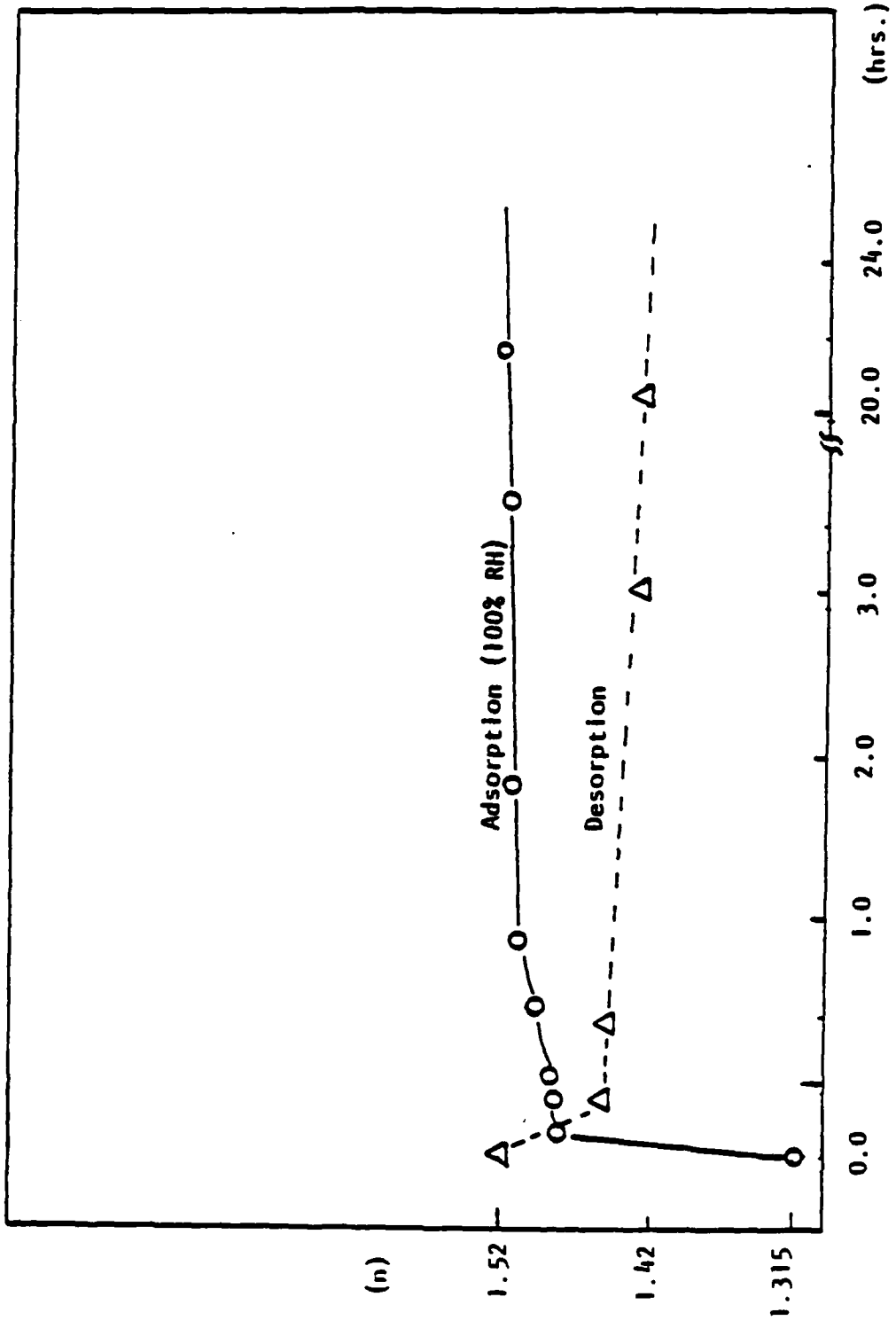


Figure 3.16. Adsorption and desorption in cryolite.

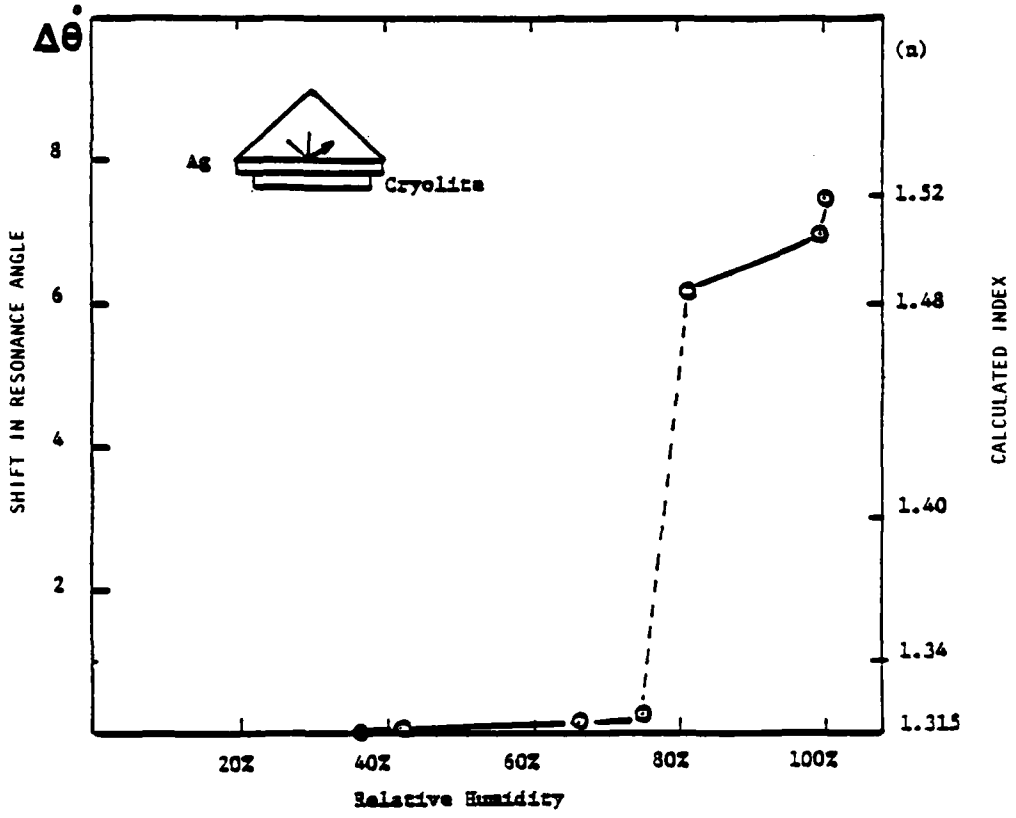


Figure 3.17. Adsorption isotherm of cryolite.

shift at RH 81% could be due to the presence of pores of radius 50 Å (Adamson, 1976), which fill with liquid water at that point. The liquid water could then take part in a chemical reaction in a way impossible for the tightly bound surface monolayer which may be all that is present up to that point.

In order to make sure that the abnormal change in resonance angle is due to changes in the cryolite index rather than that of silver, a single cryolite layer was set in 100% RH and then measured in an Abelés refractometer. The result is shown in Fig. 3.18. After half an hour of water adsorption, the index was already greater than 1.35, the bulk cryolite index. This result tells us that it is the cryolite which produced the enormous shift in resonance angle, not the silver. Comparison of the indices shown in Figs. 3.17 and 3.18 at first suggests an inconsistency in the maximum values of 1.51 to 1.42. But Fig. 3.16 shows that the desorption rate, when the sample was removed from the humidity chamber, was extremely rapid and the difference between 1.51 and 1.42 then becomes more acceptable.

Figure 3.19 gives a visible evidence that the cryolite film was corroded by moisture which changed the refractive index. The randomly distributed patches correspond to the defect centers where water penetrated. This effect will be demonstrated more clearly in the next two chapters.

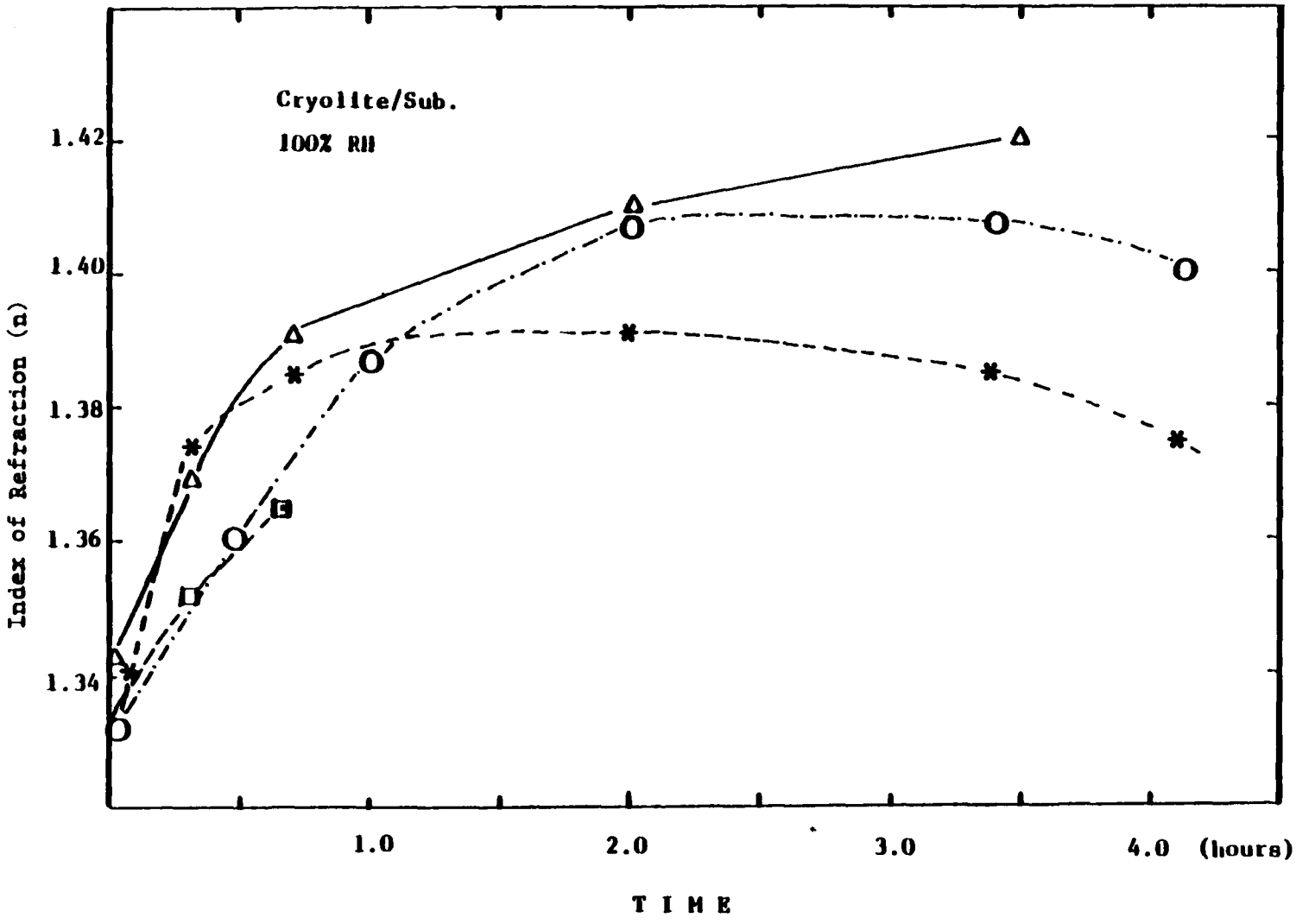
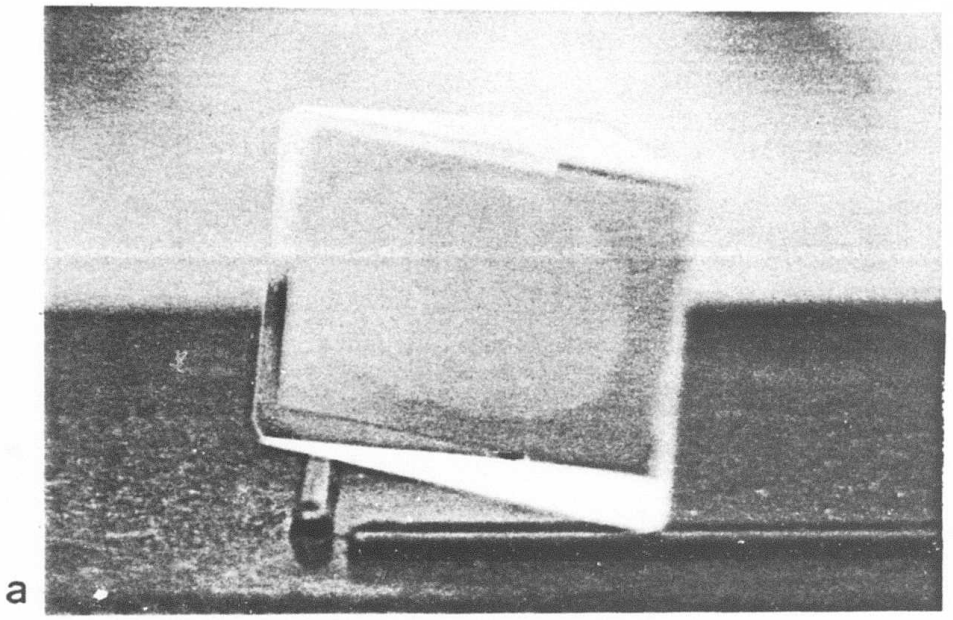
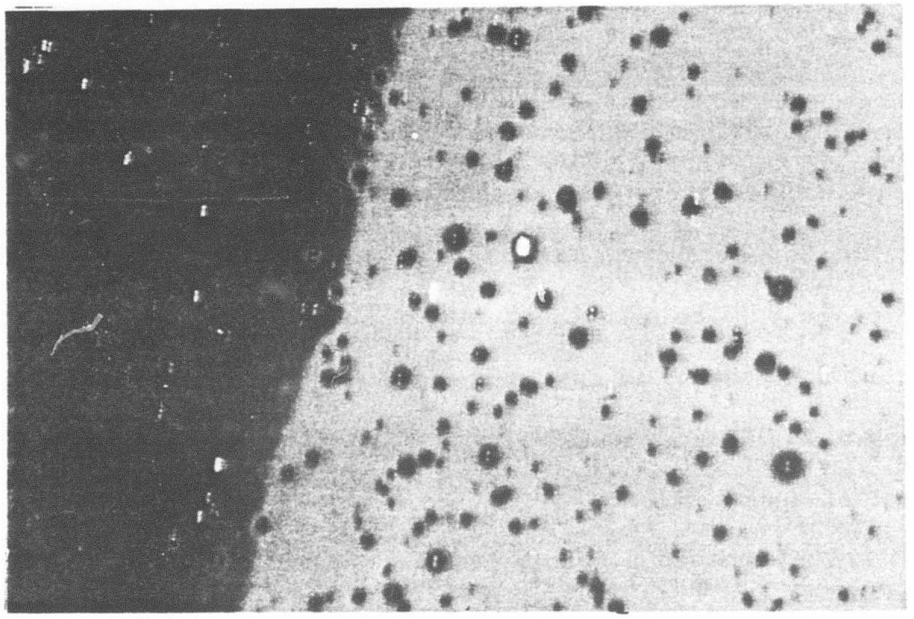


Figure 3.18. Change of refractive index measured in an Abelés refractometer after water adsorption.



a



b

Figure 3.19. Degradation of cryolite film in humid atmosphere above NaCl solution.

(a) ≈1 x.
(b) ≈140 x. Patches are the defect centers.

CHAPTER 4

MOISTURE ADSORPTION IN METAL-DIELECTRIC NARROWBAND FILTERS

As mentioned in the previous chapters, moisture adsorption is the main cause of changes in the optical properties of thin-film coatings. An alternative technique that has been used (Title, Pope, and Andelin, 1974; Macleod and Richmond, 1976; Macleod, 1976; Richmond, 1976; Lissberger, 1978) for detection of very slight changes in optical thin films is to construct a narrowband filter using the material.

Metal-Dielectric Narrowband Filter

The simplest narrowband filters are constructed from metal and dielectric layers and are therefore known as metal-dielectric filters. The metal used here is silver, which has quite high packing density, as will be seen later in this chapter, and is a very stable in a humid atmosphere, as can be seen by the surface plasmon technique (Chapter 3). The material we want to investigate is then made the spacer of such a filter.

The schematic structure of a metal-dielectric narrowband filter is shown in Fig. 4.1, where d_a and d_b are the thicknesses of the two silver layers with index n_{Ag}, and ϕ_a, ϕ_b are the phase changes upon reflection at the mirror-spacer interfaces. The thickness of the spacer layer with index n is d. The transmittance is

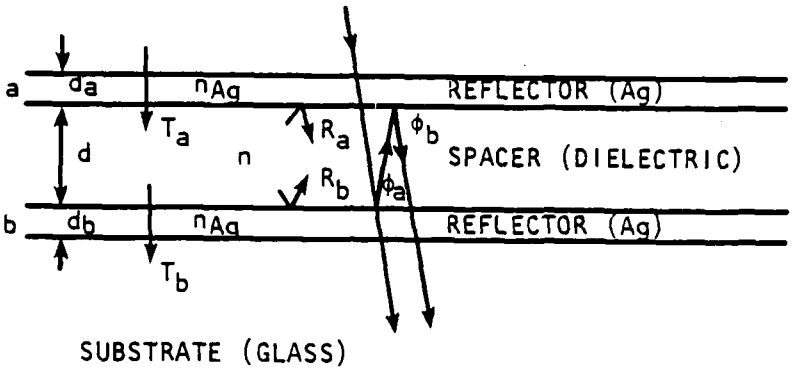


Figure 4.1. The schematic structure of a metal-dielectric narrowband filter.

$$T = \frac{T_a T_b}{[1-(R_a R_b)^{1/2}]^2} \cdot \frac{1}{1+F \sin^2[\delta - (\varphi_a+\varphi_b)/2]}$$

where

$$F = \frac{4\sqrt{R_a R_b}}{(1-\sqrt{R_a R_b})^2},$$

$$\delta = \frac{2\pi nd\cos\theta}{\lambda_0},$$

and R_a and R_b are the reflectances of the silver layers measured from within the spacer layer.

The half-width is then

$$\Delta\lambda_H = \frac{2\lambda_0}{\left[\pi\sqrt{F}\ |m - (\varphi_a+\varphi_b)/2\pi|\right]},$$

where m is the order number.

In order to attain maximum transmittance, R_a should be equal to R_b, i.e., the thicknesses of the silver layer, d_a and d_b, shall be of the correct values. Also, in order to obtain the correct peak wavelength, i.e., position of the transmission maximum, the optical thickness of the spacer (nd) must include a correction for the phase changes φ_a and φ_b. That is to say

$$\delta - \frac{\phi_a+\phi_b}{2} = m\pi$$

or

$$\frac{nd}{\lambda} = \frac{m\pi + (\phi_a + \phi_b)/2}{2\pi} .$$

For n_{Ag} given by n-ik = 0.05-i2.87 at λ = 500 nm, and for $R_a = R_b$ = 90.54%, the thicknesses of silver then will be d_a = 46.8 nm and d_b = 50 nm. The corresponding phase changes are ϕ_a = 127.4° and ϕ_b = 128.5°. Therefore, to achieve a correct peak wavelength, the optical thickness of the spacer shall be

$$\frac{nd}{\lambda} = \frac{m180°+128°}{360°} ,$$

and for the second order, m = 2,

$$\frac{nd}{\lambda} = 1.36. \qquad (4.1)$$

During manufacture, the optical monitoring system measures the transmittance of the growing filter. This is shown in Fig. 4.2. $\overline{AB}$ corresponds to d_b of the silver layer, and $\overline{BC}$ and $\overline{DE}$ are the thicknesses of dielectric corresponding to the compensation of phase

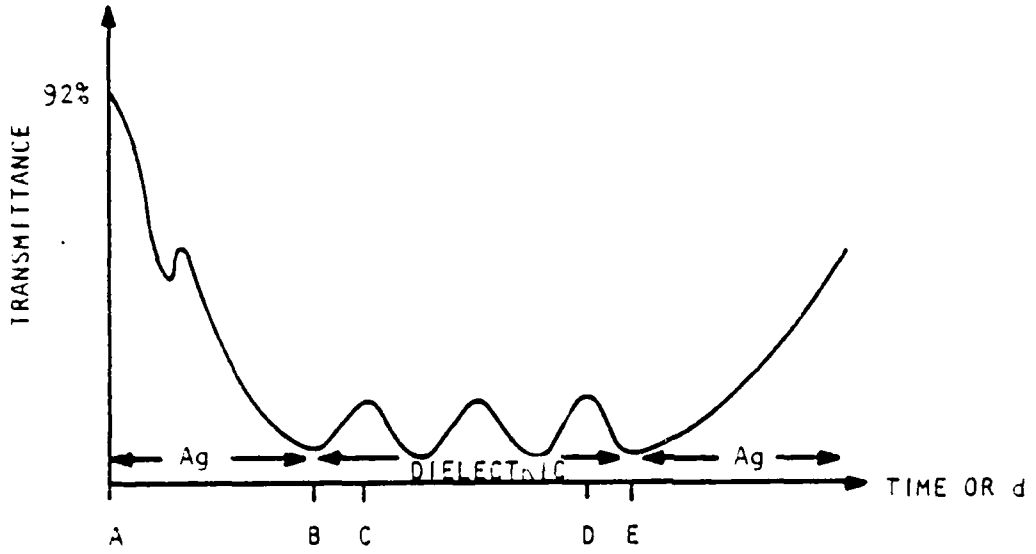


Figure 4.2. Measurement of transmittance of a growing filter.

changes (Arsenault and Boivin, 1977). Filters were prepared in a vacuum system (Fig. 2.5) at a pressure in the range of $1\text{-}5\times10^{-5}$ torr, using indirect monitoring with the substrate holder rotating. The spacer material is cryolite which is evaporated from a tantalum canoe. The silver was evaporated from a tantalum dimple.

Wavelength Shift due to Water Adsorption

Immediately after coating, the filter characteristic will be similar to the left side of Fig. 4.3. When the filter is exposed to atmospheric humidity, the optical constant of the spacer will change where water adsorption occurs. Therefore, as shown in the right side of Fig. 4.3, the position of maximum transmission is shifted to a longer wavelength. That part of the spacer which is affected in this way therefore has different optical characteristics from the surrounding unaffected material, and under certain illuminating conditions, shows up as a patch.

The apparatus for observing moisture adsorption consists of a cell in which coatings can be subjected to a controlled relative humidity while they are examined in collimated monochromatic light, as shown in Fig. 4.4. Figure 4.5 is a photograph of the patches. The filter cell is mounted on a micrometer-driven x-y stage that can be manually adjusted.

Measurements using a vibrating quartz crystal give a packing density for silver of 0.99; therefore, the optical constant changes in the silver are negligibly small when compared with changes in the spacer layer. The packing density of the spacer layer can be as low

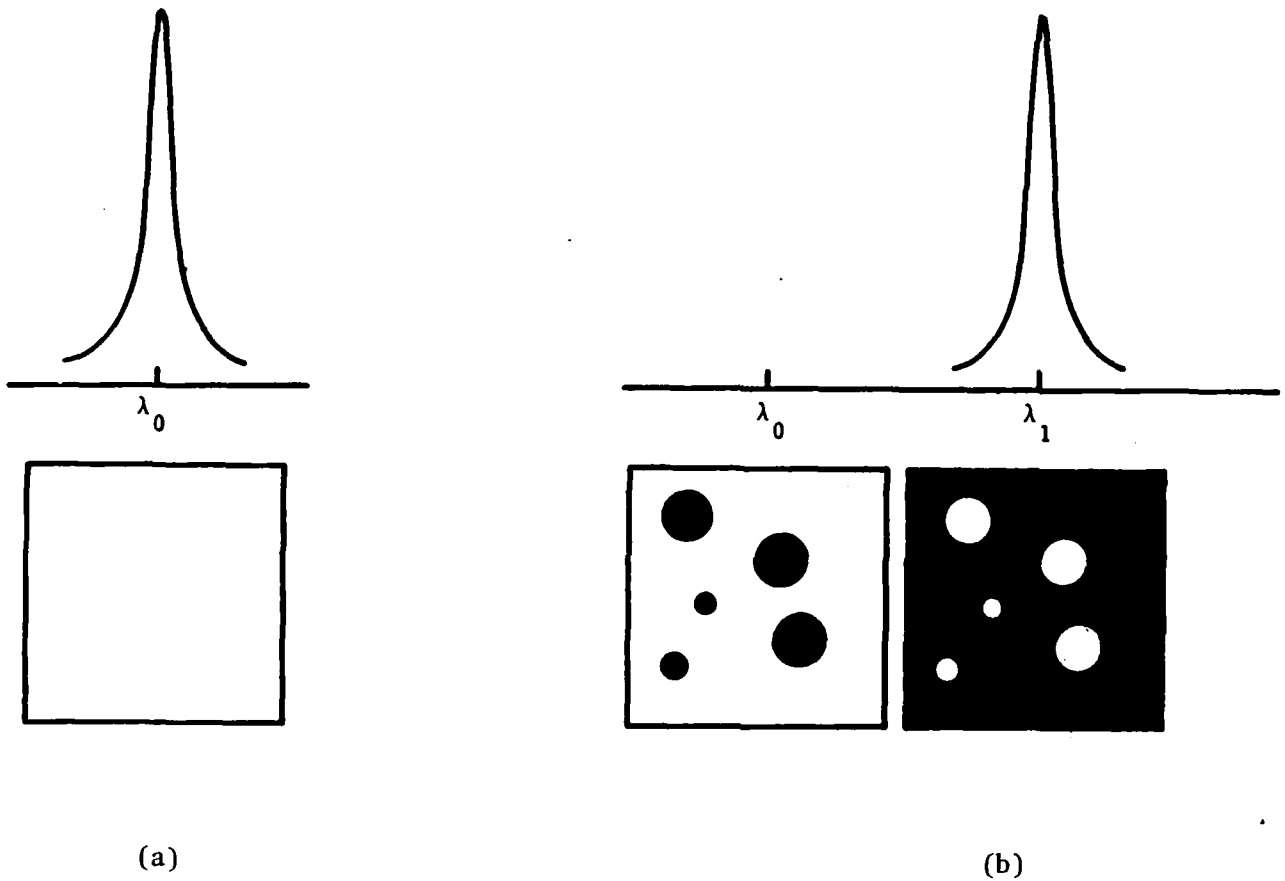


Figure 4.3. Schematic showing peak wavelength shift.

(a) Immediately after coating, (b) the result of any changes of optical constant in layer.

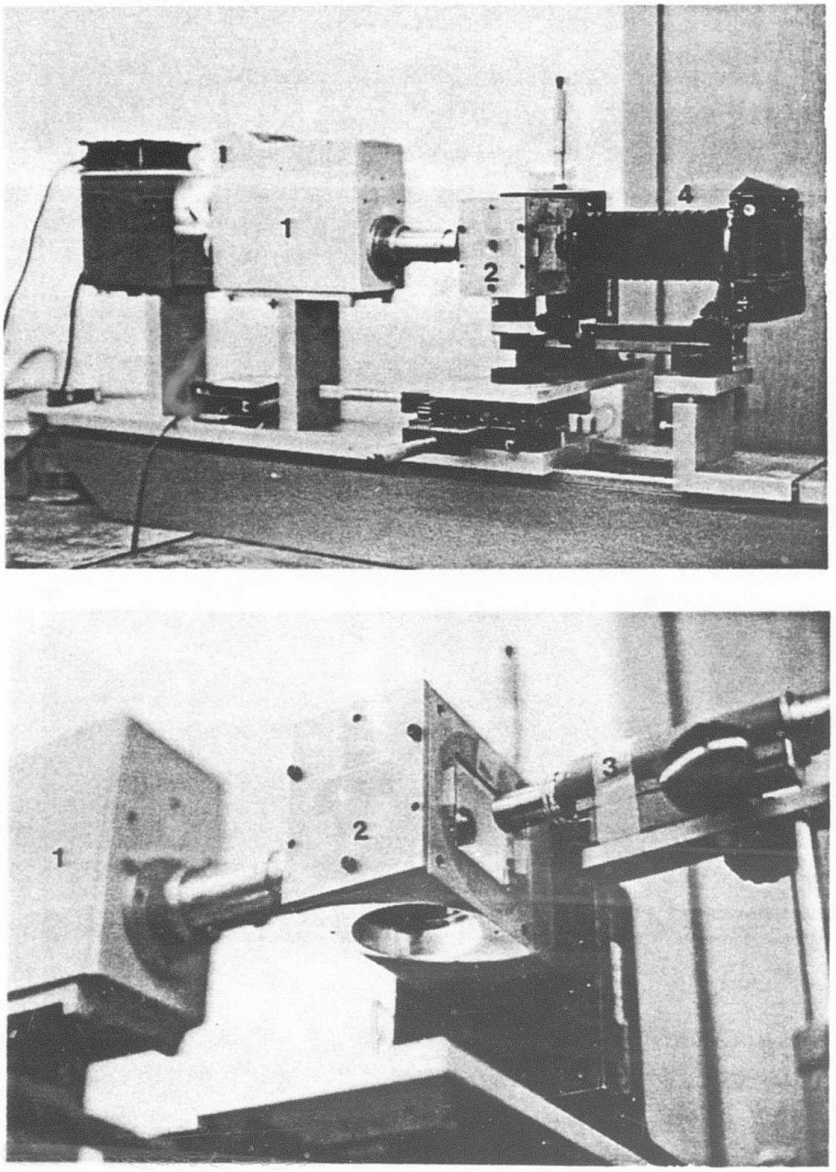


Figure 4.4. Apparatus for observing water adsorption in the coating filter. (1) Monochromator, (2) cell in which relative humidity can be controlled, (3) microscope, (4) camera.

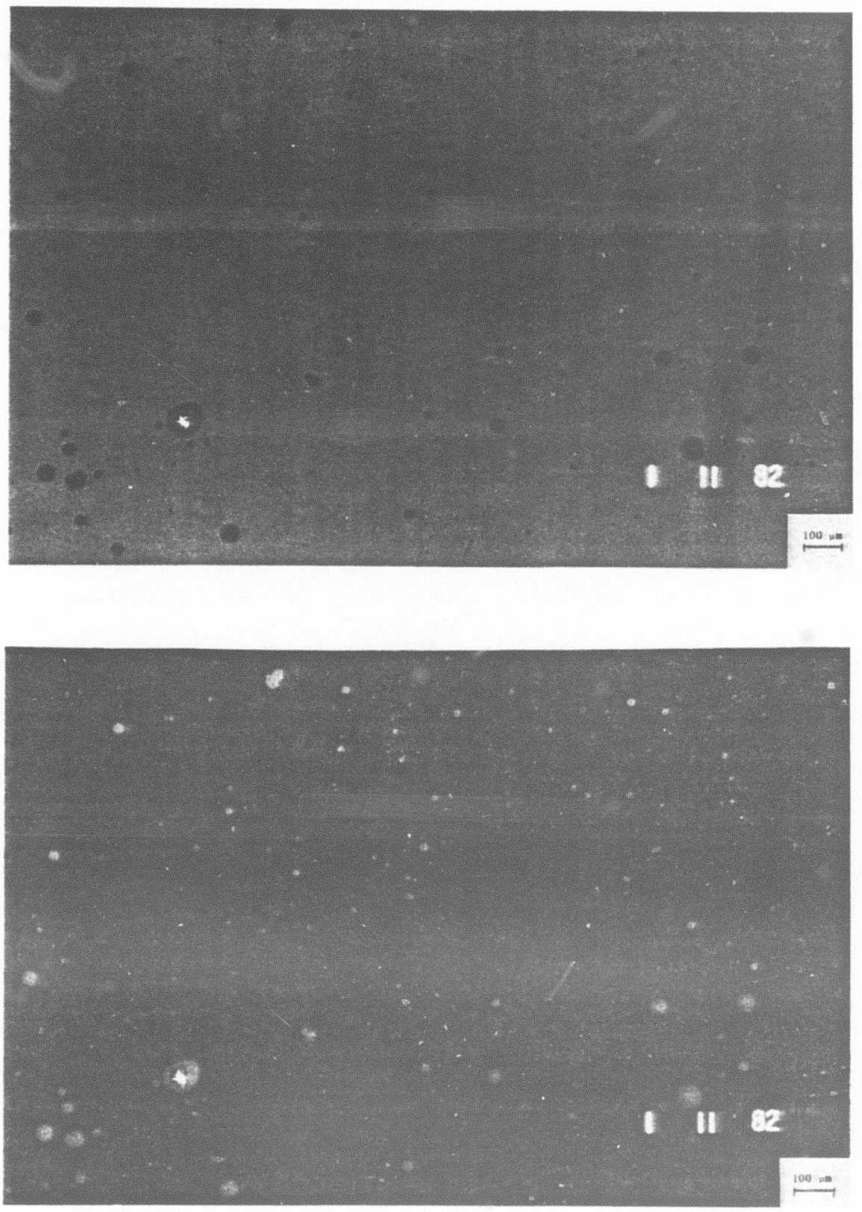


Figure 4.5. Water adsorption in silver/cryolite filter.

ML-11-3 stored in desiccator for 3 days. RH in air = 35%. (a) λ = 543 nm. (b) λ = 549 nm.

as 0.80 for cryolite (Ogura, 1975). Figure 4.6 shows a computer simulation of the shifts in the maximum transmission. The reflectors, i.e., the silver layers, were assumed unchanged under water adsorption. Further, the geometric thickness of the spacer was unchanged. The only parameter changed was the refractive index of the cryolite. Before water adsorption, it was $n = n_b p + n_0(1-p)$. After water adsorption it became $n = n_b p + n_w(1-p)$, where $n_b = 1.36$ is the refractive index of bulk cryolite, $n_0 = 1$, $n_w = 1.33$ are indices of air and water, and p is the packing density.

Figure 4.7 gives actual spectrometer measurements and shows the optical performance of a filter and the wavelength shift and water adsorption in an atmosphere of 36% relative humidity.

Adsorption Isotherm

As time goes on, the patches shown in Fig. 4.5 will grow as long as exposure to humidity continues. The rate at which the patches grow is quite dependent on the RH to which the filter is exposed. Figure 4.8 plots some typical growth rates.

Figure 4.9 gives an adsorption isotherm in which the growth rate of the patches is shown. The wavelength shift also depends on the relative humidity. Figure 4.10 gives an adsorption isotherm in terms of wavelength shift. When the clean surface of a coating is exposed to the atmosphere, it adsorbs moisture in the form of a thin sheet of liquid. At low values of RH, below 75% here, the sheet is approximately a monolayer. As RH increases, a multilayer of water vapor is adsorbed, and the pores in the films become filled in the

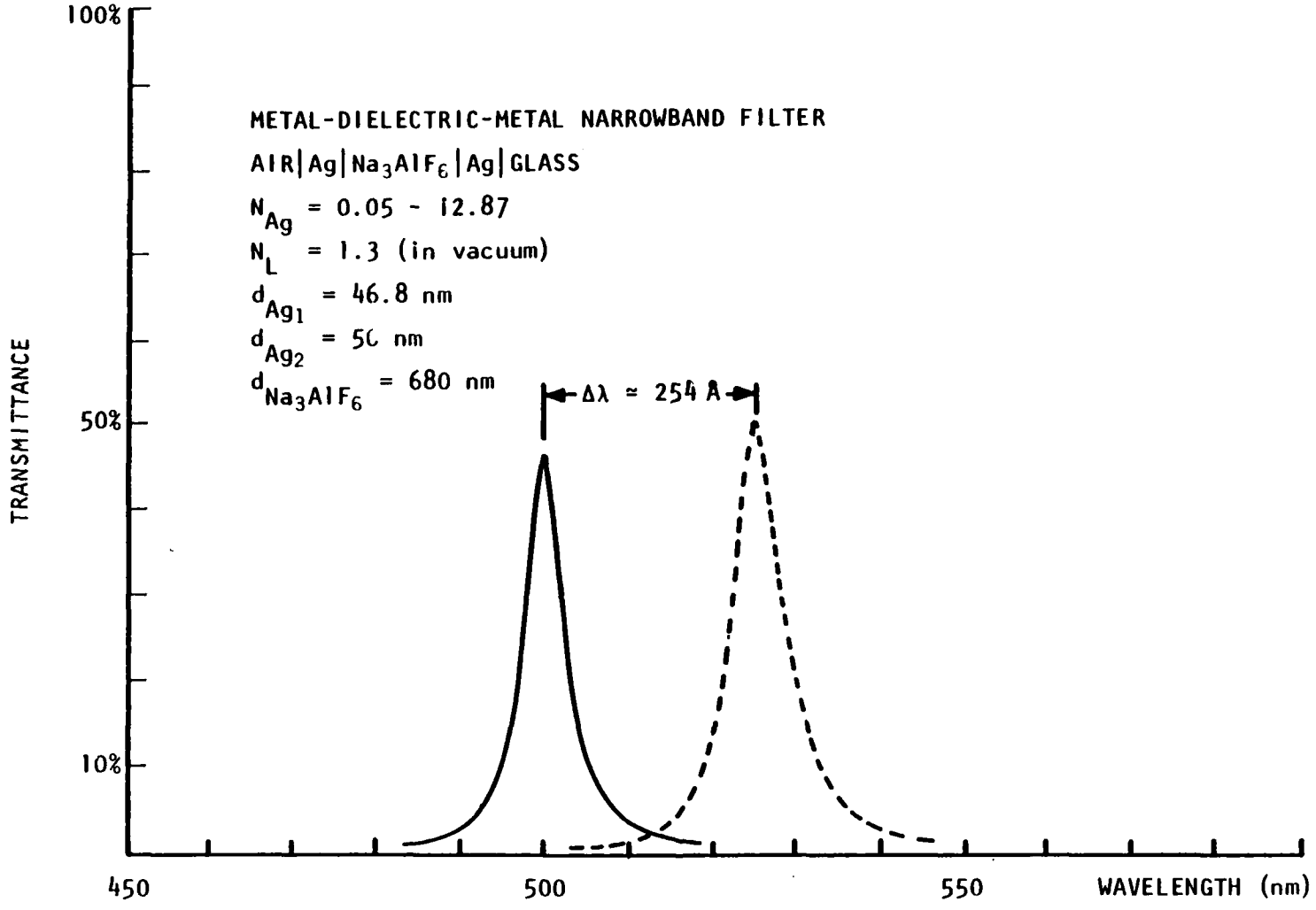


Figure 4.6. Computer simulation of water adsorption in metal-dielectric-metal narrowband filter, assuming a packing density of Na_3AlF_6 is 0.82.

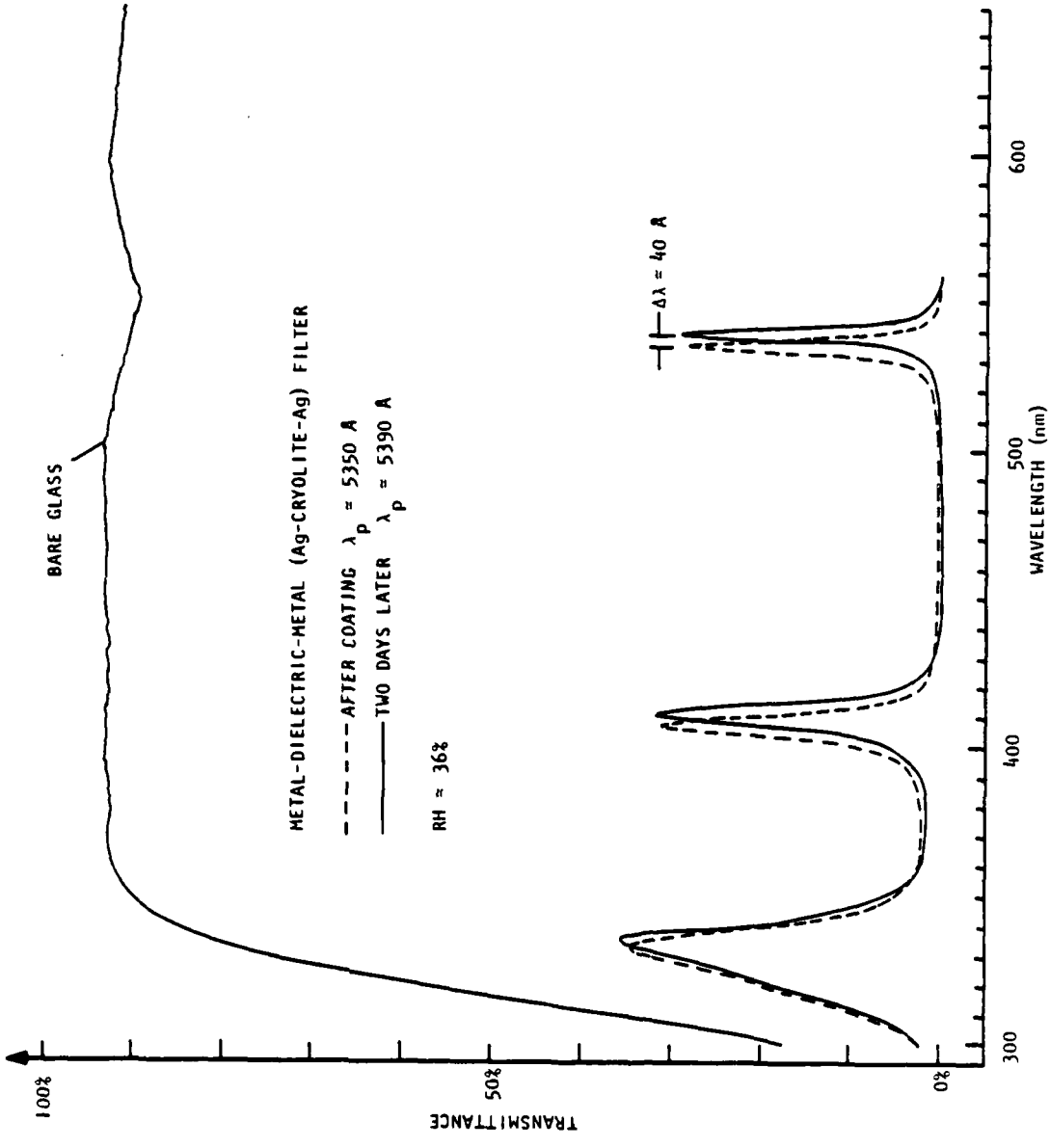


Figure 4.7. Measured shifts due to water adsorption.

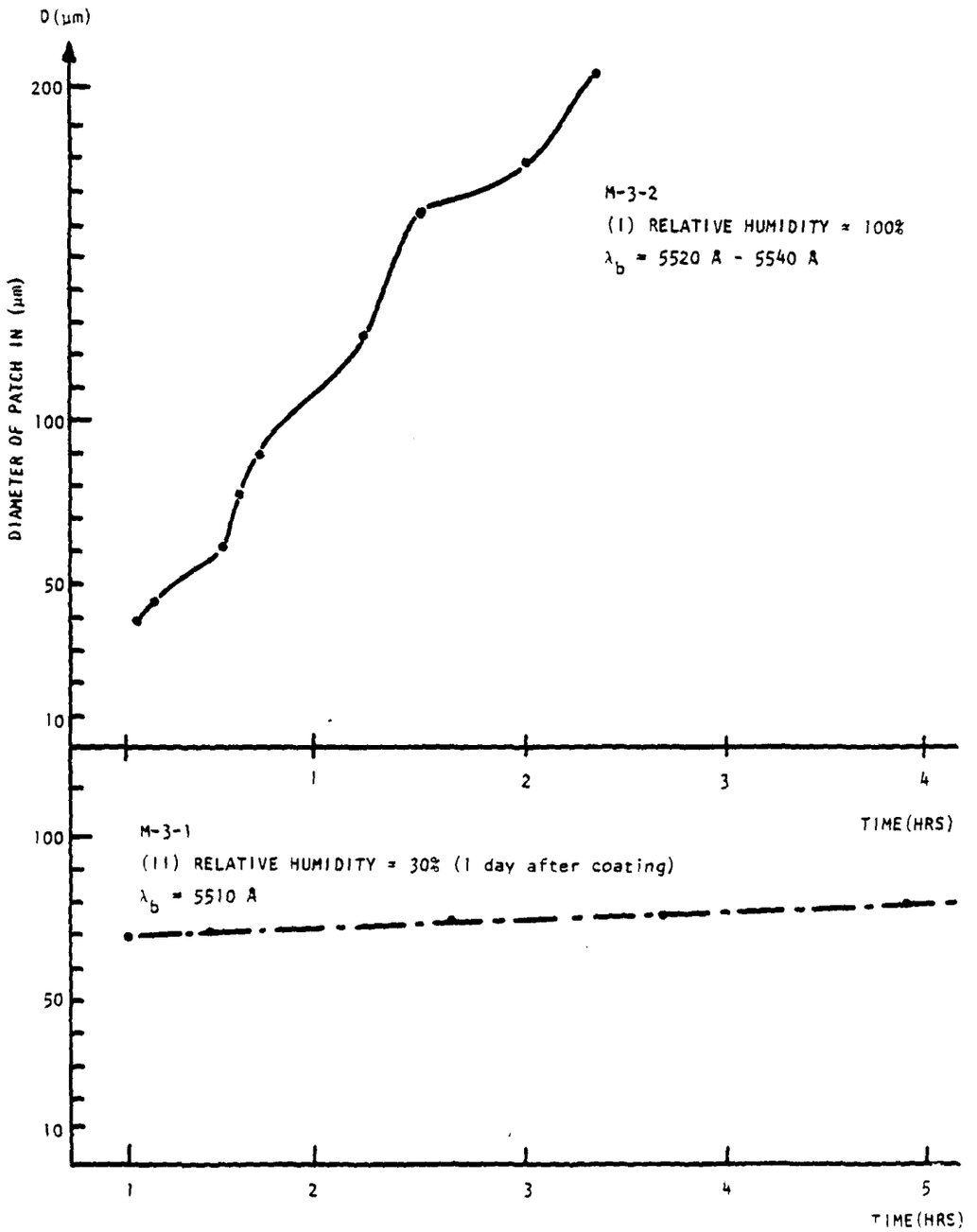


Figure 4.8. Water adsorption of metal-dielectric-metal narrowband filter air/Ag/Na_3AlF_6/Ag/glass.

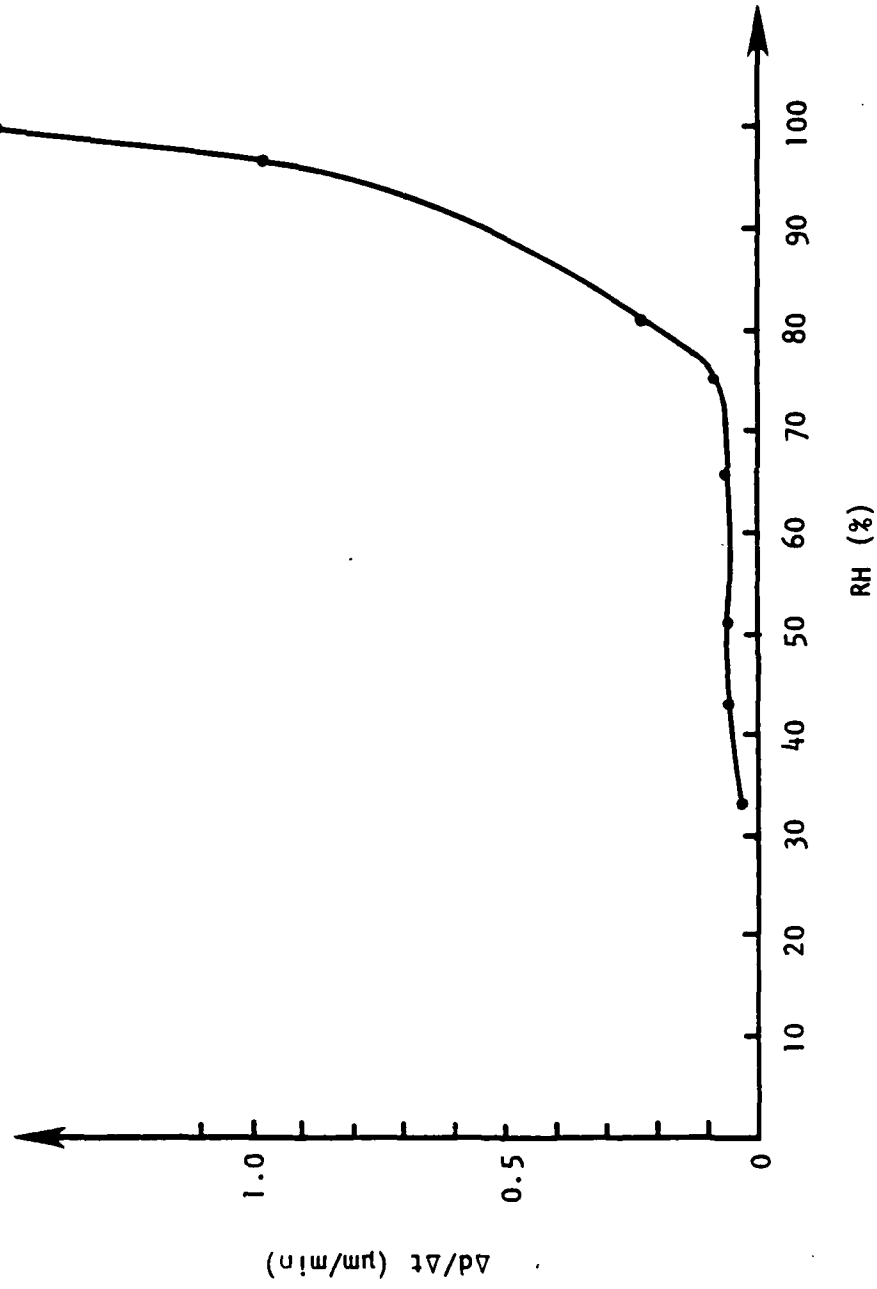


Figure 4.9. Adsorption isotherm giving the growth rate of patches. (Sample M1-11, silver-cryolite filter.)

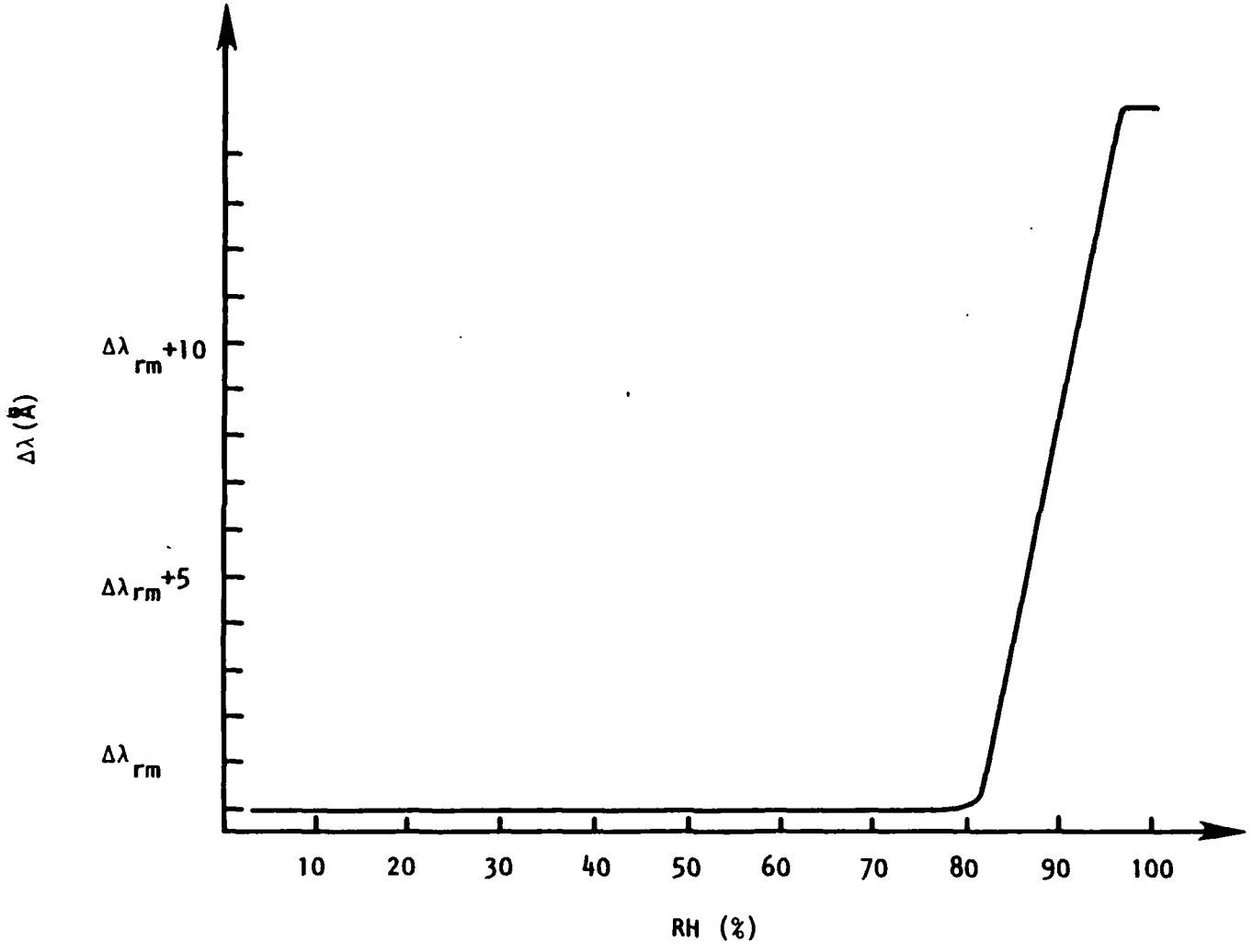


Figure 4.10. Wavelength shift due to water adsorption within four hours, where $\Delta\lambda_{rm}$ is the wavelength shift when the filter is exposed to air after opening the coater. (Sample ML-11, silver-cryolite filter.)

order of smallest to largest. Finally, there is a chemical reaction between the cryolite and water, which causes a dramatic increase in the growth rate and the wavelength shift above 81% RH. This result is consistent with the discussion in Chapter 3.

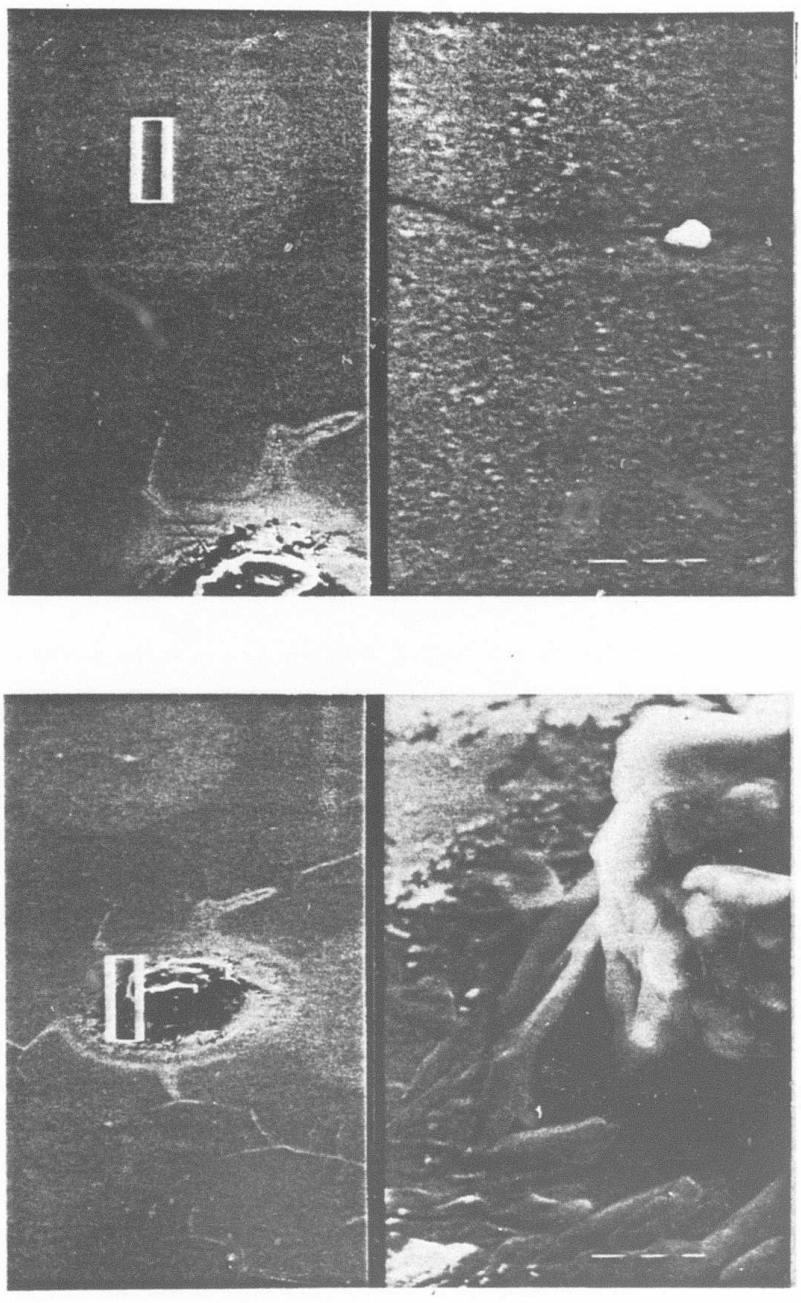
The recrystallization of cryolite after it reacts with water is shown by the scanning electron microscope (SEM) in Fig. 4.11. The crystal is suspected to be $AlF_3 \cdot H_2O$ which has a refractive index of 1.51 (Weast, 1972). This abnormally large index can then explain the dramatic change in the wavelength shift. In Fig. 4.11 one still can see traces of the patch around the defective center.

It is assumed that water seeped from some pores and spread laterally. One can even see how the water passes from place to place in Fig. 4.12. One can see that the size of the network is around 20-50 μm, which tells us that the grain size of the films can not be greater than that.

Packing Density

Because of the simple structure of the metal-dielectric narrowband filter, one can calculate the packing density of the spacer layer from the wavelength shift. For example, immediately after coating, the position of the transmission maximum was at $\lambda_1 = 525$ nm. After the water adsorption process was saturated, it became $\lambda_2 = 550$ nm. If we assume no chemical reaction at that stage, then the indices are

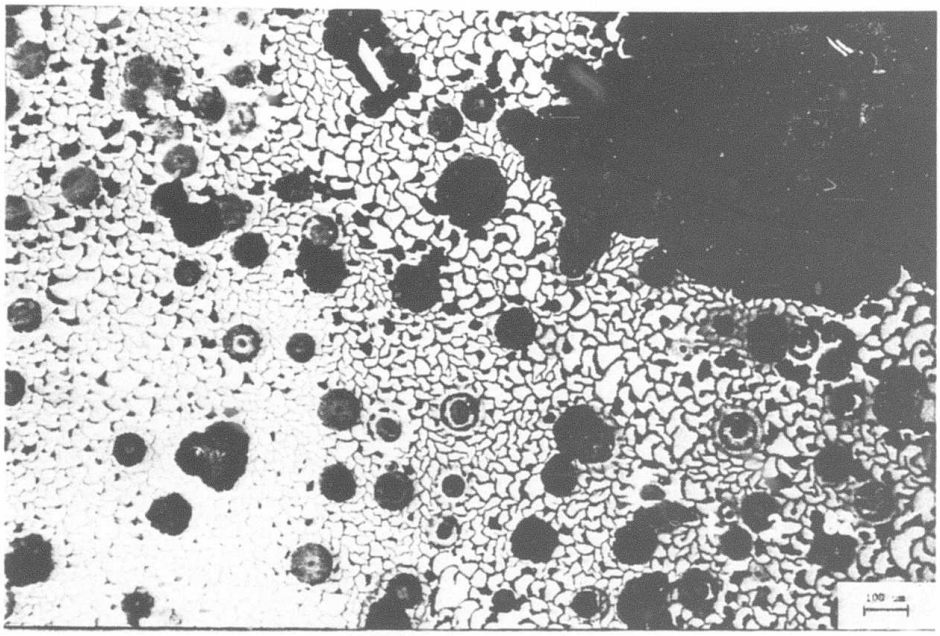
$$n_1 = n_b p + n_0(1-p)$$



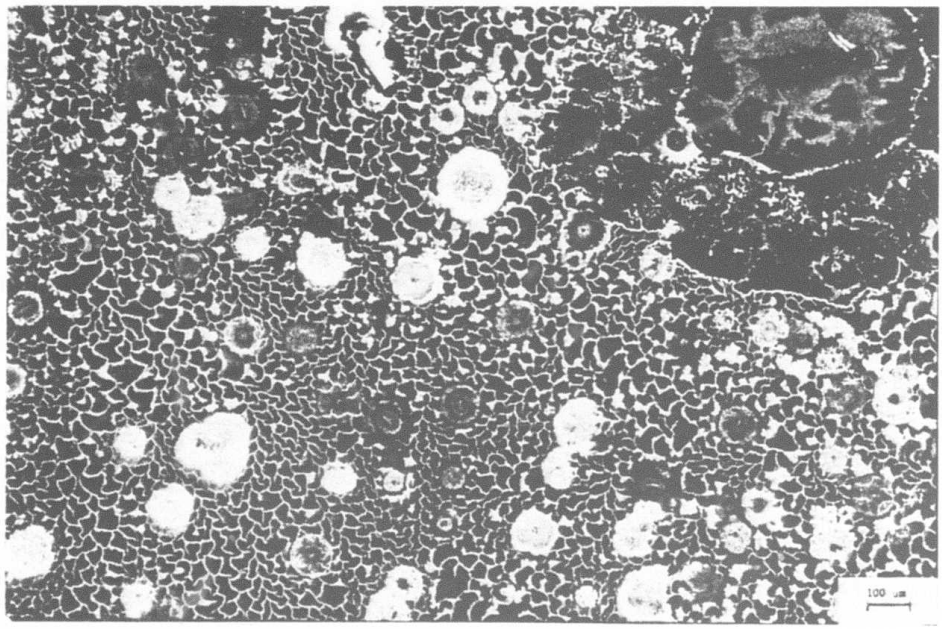
(a)

(b)

Figure 4.11. Texture of the filter surface by scanning electron microscope; water adsorption in Ag-Na_3AlF_6-Ag filter. (a) Tilt 250°, x400/x4000, (b) Tilt 55°, x370/3700.



(a) λ_d = 573 nm



(b) λ_b = 538 nm.

Figure 4.12. Network of channels in a metal-dielectric-metal filter.

Note that the channels are shifted in wavelength but are not fissures through the filter.

$$n_2 = n_b p + n_w(1-p),$$

where n_b is the refractive index of bulk cryolite, which is 1.35, p is the packing density of the cryolite, and n_w and n_0 are the indices of water (1.33) and air (1.0), respectively. From Eq. (4.1), nd = 1.36 λ. If there is no chemical reaction, it is reasonable to assume that the geometric thickness of the spacer does not change, then

$$\frac{n_1}{n_2} = \frac{\lambda_1}{\lambda_2} = \frac{n_b p + 1.0(1-p)}{n_b p + 1.33(1-p)}.$$

This gives p = 0.81 with the index of cryolite being 1.3 in vacuum.

This figure is quite reasonable when compared with the value obtained from the quartz crystal microbalance. However, two things are unknown. First, while the coater was opened and the filter taken to the spectrometer, it had already adsorbed some moisture. Therefore the initial value of maximum transmission was actually smaller than λ_1. However the exact extent is unknown, unless we are able to measure it in the chamber immediately after coating. Second, as mentioned earlier, cryolite reacts with water and its index increases by chemical reaction. Therefore, the true saturated value is smaller than λ_2. This effect perturbs the saturated optical constants of the cryolite to a largely unknown extent and creates difficulties in the measurement of simple adsorption.

The first problem can be solved by using direct monitoring in manufacturing the filter so that the position of maximum transmission is the monitoring wavelength.

The second problem may be solved by using different adsorbates which are chemically inert with respect to the material in the spacer. To find such an inert adsorbate which still has adequate vapor pressure at room temperature is not easy.

Baking Effect

If the wavelength shift is due to water adsorption, one can evacuate the water by a baking process. Figure 4.13 shows the position of maximum transmission which drifted back, as measured in the spectrometer, after two hours baking at 120° C.

Figure 4.14 shows the patches photographed before the baking. After baking, the patches were as shown in Fig. 4.15. One can see that the pattern did not shrink back, even more, new small patches occurred inside old patches, although the position of maximum transmission did shift back about 180 Å. All of those phenomena tell us that there is a chemical reaction during the adsorption process.

Because of the microsize of the pores, the water can be desorbed only very slowly. Baking the film too fast will cause cracks because of the pressure which is exerted by the expanding water vapor. Baking rates below 3° C/min will be safe.

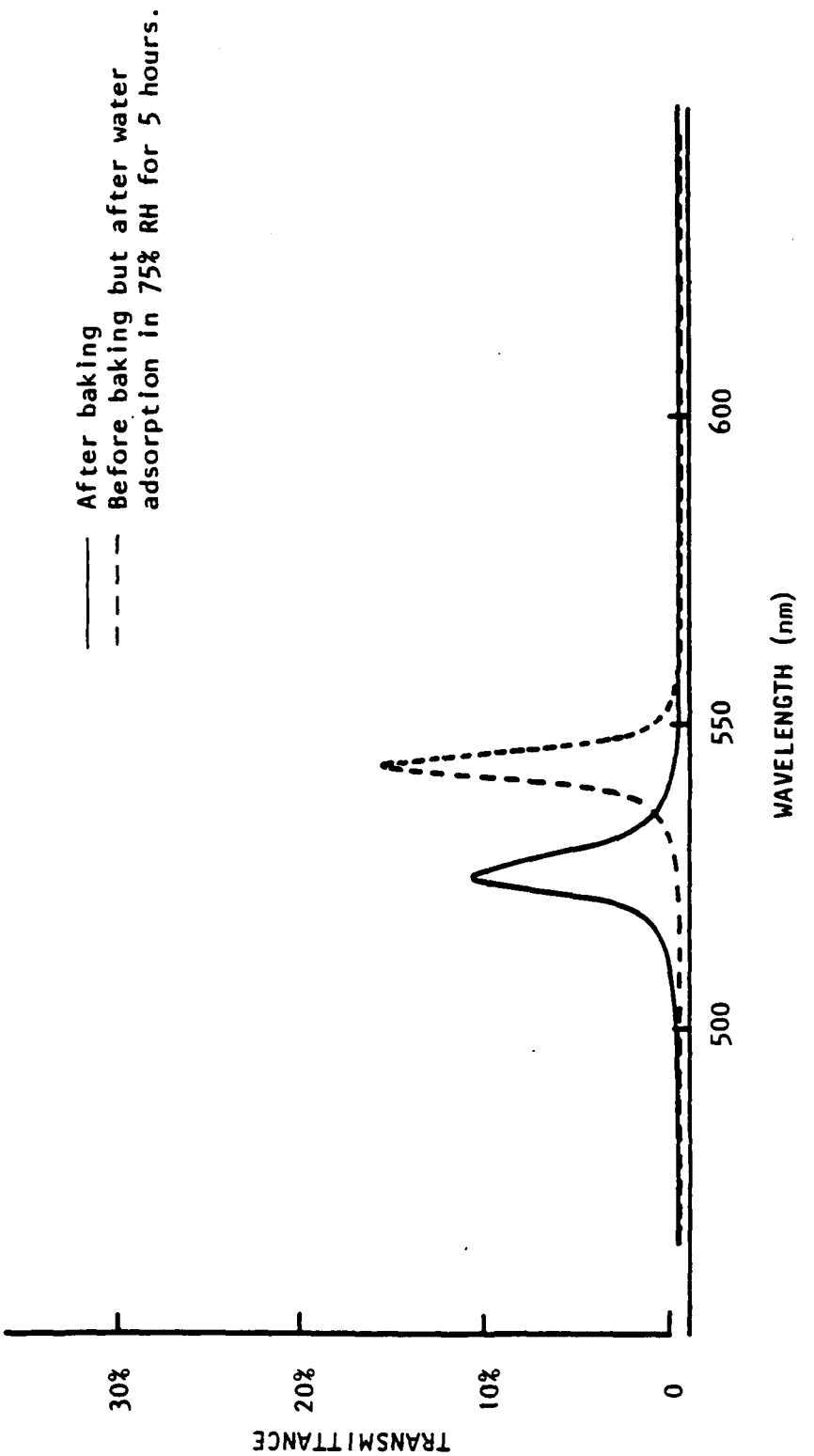


Figure 4.13. Baking effect of silver-cryolite filter baked at 120° C for two hours.

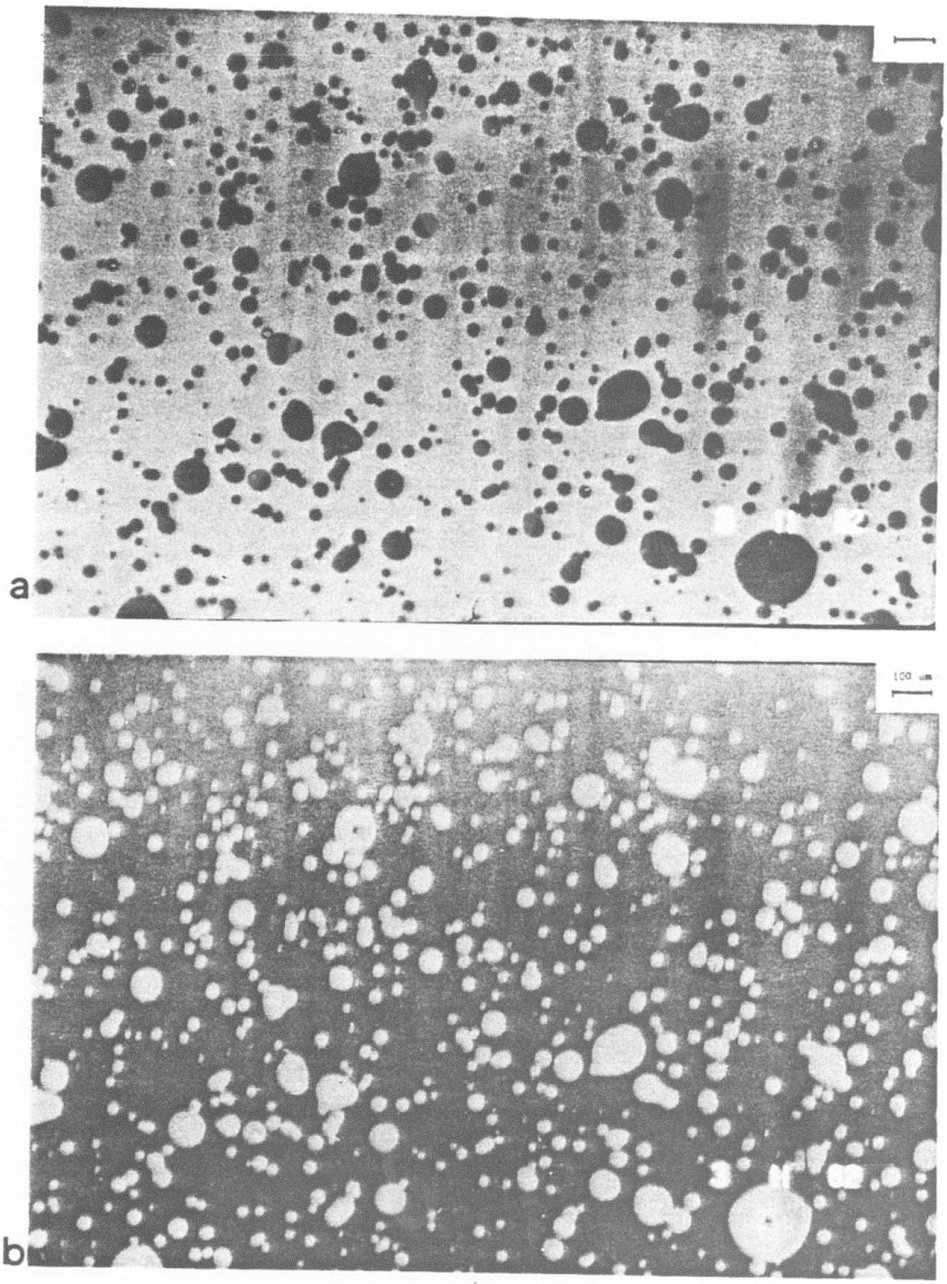


Figure 4.14. Water adsorption in Ag/Na_3AlF_6 filter. Sample ML-11-6, set in RH = 75% for 5 hr. (a) λ = 543 nm. (b) λ = 547 nm.

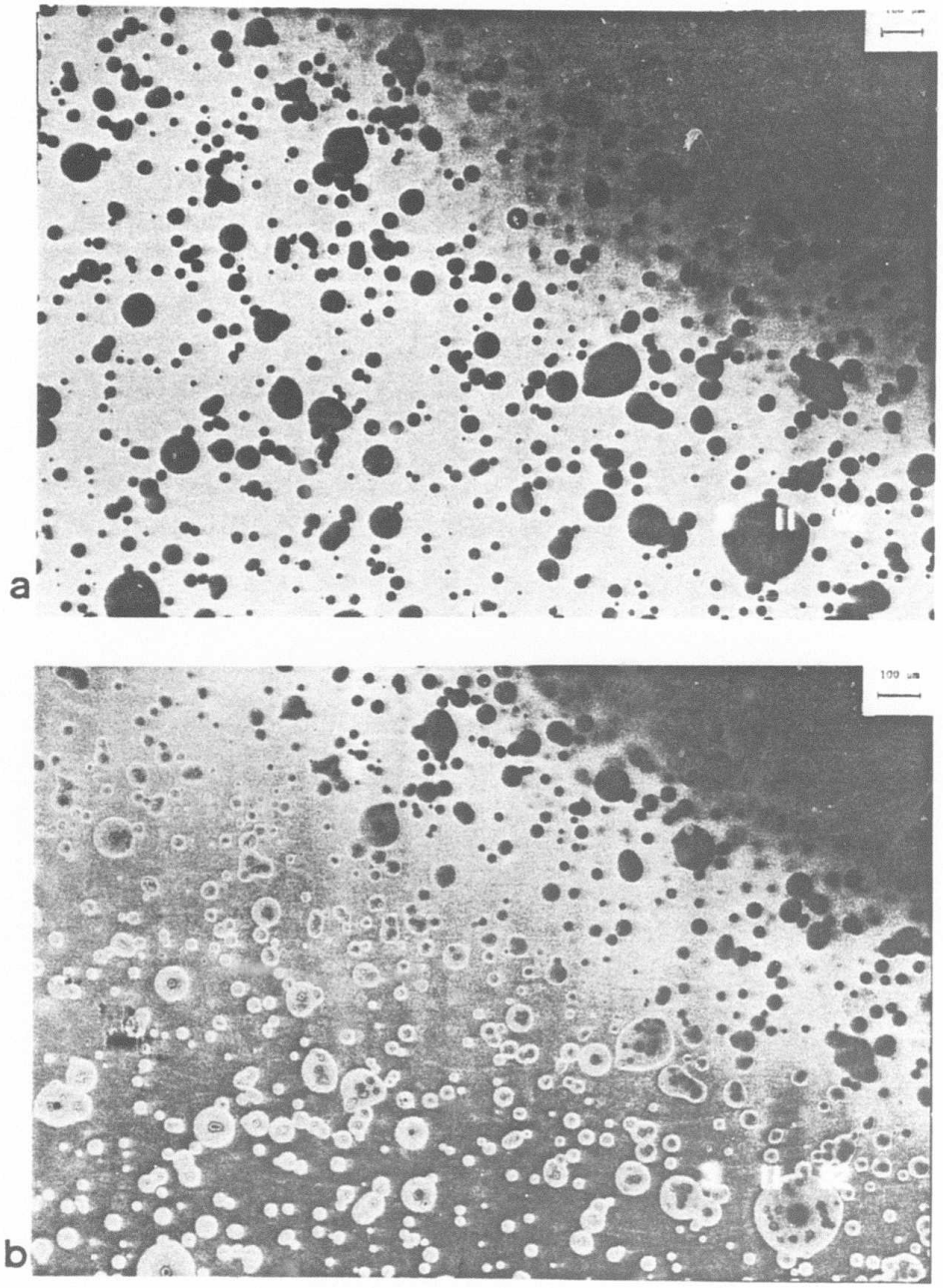


Figure 4.15. Result of baking Ag/Na_3AlF_6 filter. Sample ML-11-6 baked at 120°C for 2 hr after water adsorption in RH = 75%, $\Delta\lambda_{BK}$ = -185Å. New sub-patches can be seen in the original patches. (a) λ = 525 nm. (b) λ = 528.5 nm.

Moisture and Adhesion Failure

The nature of the forces which attach thin films to each other and to the substrate can range from van der Waals forces, when there is no chemical affinity between the materials, to strong chemical bonding such as ionic or covalent bonds. Van der Waals forces are the weakest of these. The strong hydrogen bond plays an important role in adhesion failure that is due to the water adsorption.

Peeling is an adhesion failure typical of thin films. This peeling may be a simple lifting of the coating, or blistering, but it is always characterized by progressive delamination rather than by the simultaneous detachment of a large area. Shear occurs in the weak boundary layer, which is a thin layer at the interface of different materials. The mechanical strength is weaker at the boundary of the grains than inside the grains.

The adsorption of water will make the weak boundary layer and weak grain boundaries even weaker because of the hydrogen bonding with the monolayer of water formed on the boundaries. There are a number of places where a bond transfer is favored, for instance, at the edge of the films, at places where there are scratches or pin holes, and more important, at the penetration pores.

In the case of the silver-cryolite filter here, the situation is even worse. There are two reasons for this. The first is that the water passes easily between silver and glass, as mentioned by Holland

(1956). Second, the cryolite chemically reacts with water. Once these happen, the adhesion is liable to fail and delamination, often in the form of a blister, is liable to take place. Figure 4.11 shows the cracking typical of such failures. In the case of Fig. 4.12, blistering of the films is imminent.

Most of the films can not pass the Scotch tape test after water adsorption, except at low relative humidity. The top silver film can be peeled off quite easily. If RH is greater than 75%, the entire multilayer can be peeled off easily.

CHAPTER 5

MOISTURE ADSORPTION IN ALL-DIELECTRIC NARROWBAND FILTERS

The disadvantages of metal-dielectric narrowband filters are their low transmittance and the difficulty of obtaining the correct peak wavelength in manufacture. In order to observe the patches clearly, the half-band width of the filter should be less than 70 Å, which implies a transmittance as low as 20% for a metal-dielectric narrowband filter. Also, due to the phase shift at the interface between mirror and spacer, which is sensitive to both wavelength and metal thickness, the wavelength of maximum transmission is hard to control. This can be shown by computer calculations as in Fig. 5.1 with standard deviations of only 1%.

All-dielectric Narrowband Filters

All-dielectric narrowband filters have no such problems. The narrower the bandwidth of the filter one can make, the more detail of water penetration through the filter can be seen.

Figure 5.2 gives a schematic structure model of the water penetration process in a 19 layer all-dielectric narrowband filter. The H and L stand for quarterwave optical thicknesses of high and low indices, respectively. In this case, ZnS is the high index material and cryolite is the low index material.

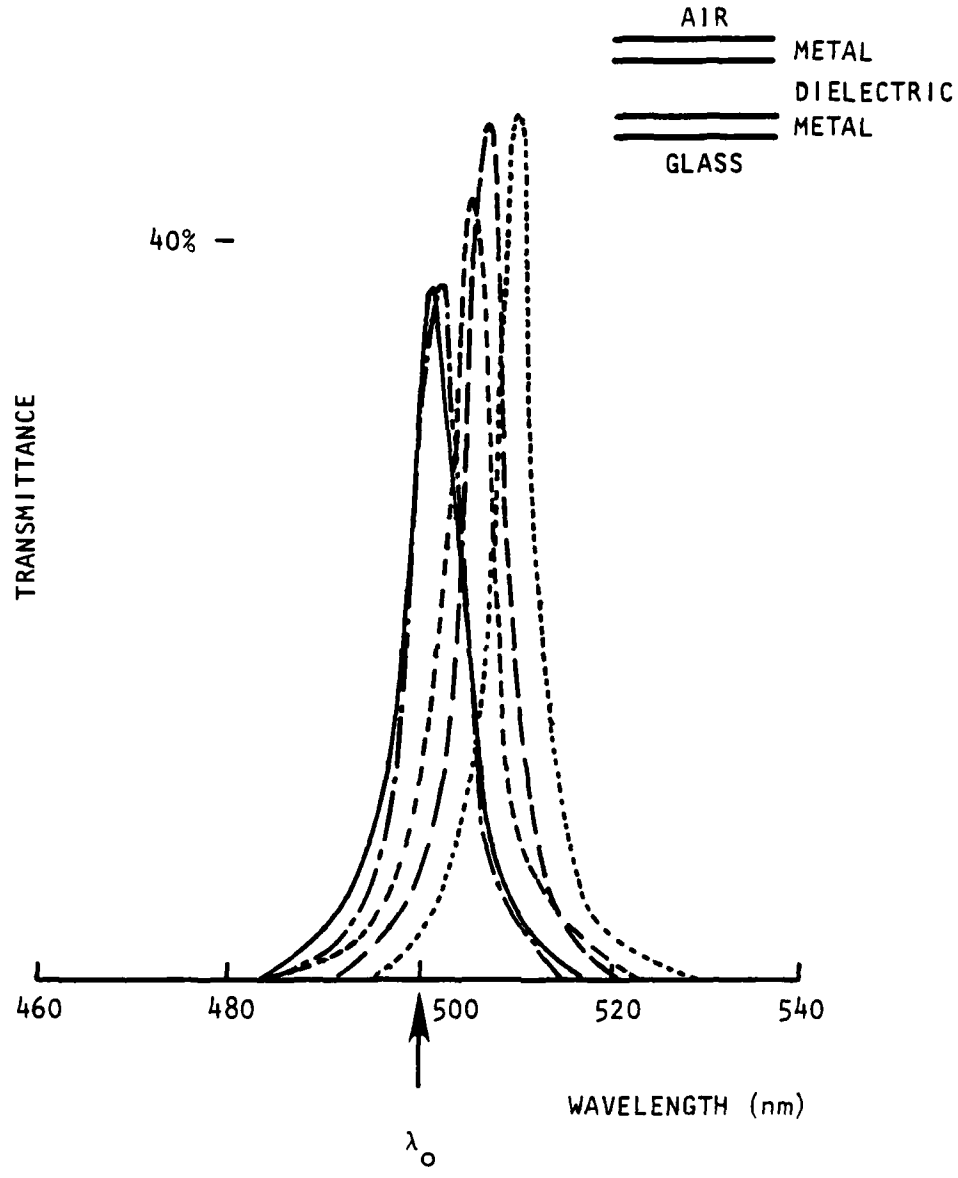


Figure 5.1. Calculated performance of silver-cryolite narrowband filters with thickness errors. Mean = 1%, standard deviation = 1%.

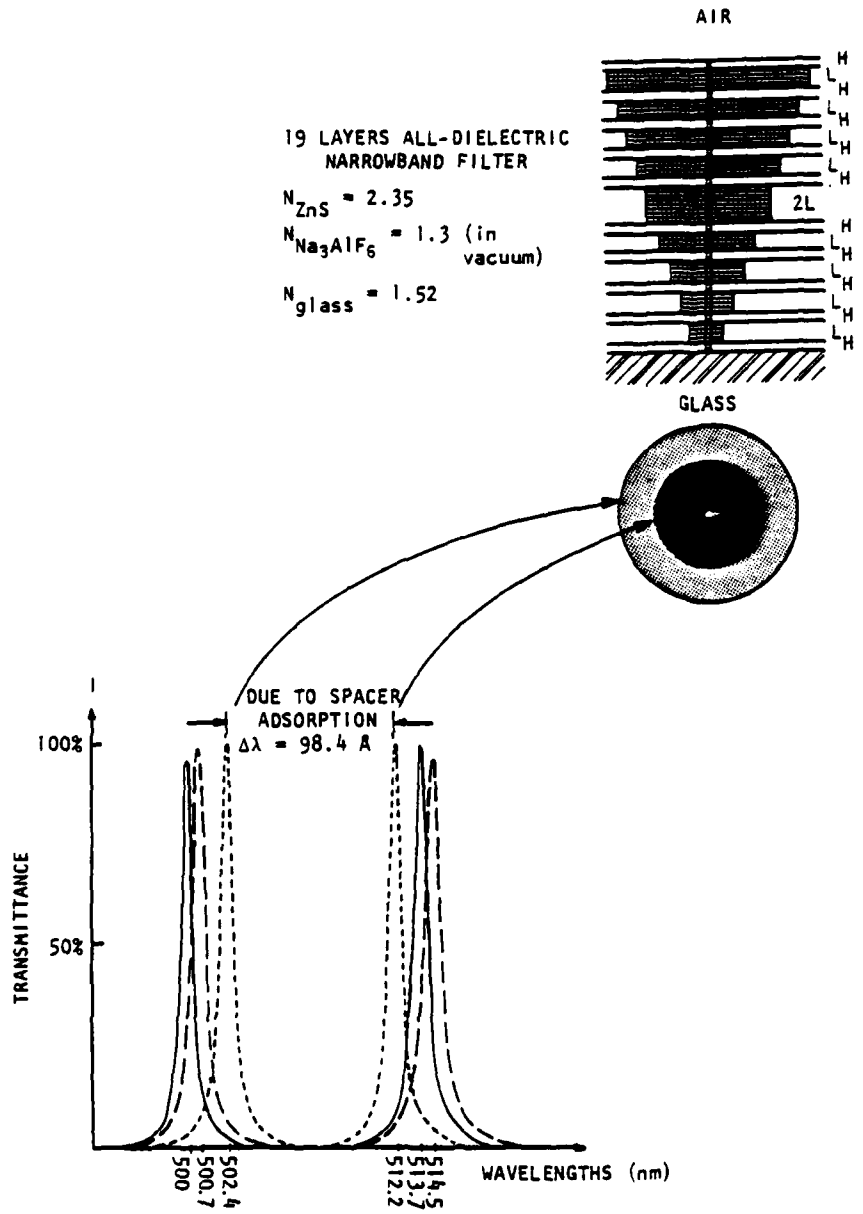


Figure 5.2. Computer simulation of water adsorption in all-dielectric narrowband filter. Assume that packing density of Na_3AlF_6 is 0.82 and that packing density of ZnS is 1.0.

The water enters through a central pore, and penetrates to the substrate, and spreads laterally through the layers.

The corresponding shift in peak wavelength is also shown in the lower left. The most significant shift is due to the water adsorption in the spacer layer. Therefore, it is the spacer where the material to be examined is put.

Again, the filters were manufactured by thermal evaporation in a vacuum of $1\text{-}5\times10^{-5}$ torr, in the 18 inch Edwards coater (Fig. 2.6), monitoring indirectly with substrate holder rotating. Evaporation rates for each material were kept constant. The theoretical bandwidth $\Delta\lambda_H$, is given for a low index spacer by

$$\Delta\lambda_H = \lambda_0 \frac{4n_s n_L^{2x-1}}{\pi n_H^{2x}} \cdot \frac{n_H - n_L}{n_H}$$

and for a high index spacer by

$$\Delta\lambda_H = \lambda_0 \frac{4n_s n_L^{2x}}{\pi n_H^{2x+1}} \cdot \frac{n_H - n_L}{n_H} .$$

Figure 5.3 shows the performance of a narrowband filter and its shift in wavelength due to water adsorption measured by a spectrometer.

Adsorption Isotherm

When a filter is set in the apparatus shown in Fig. 4.4, one sees patches in the filter like Fig. 5.4 (Macleod, 1976; Macleod and

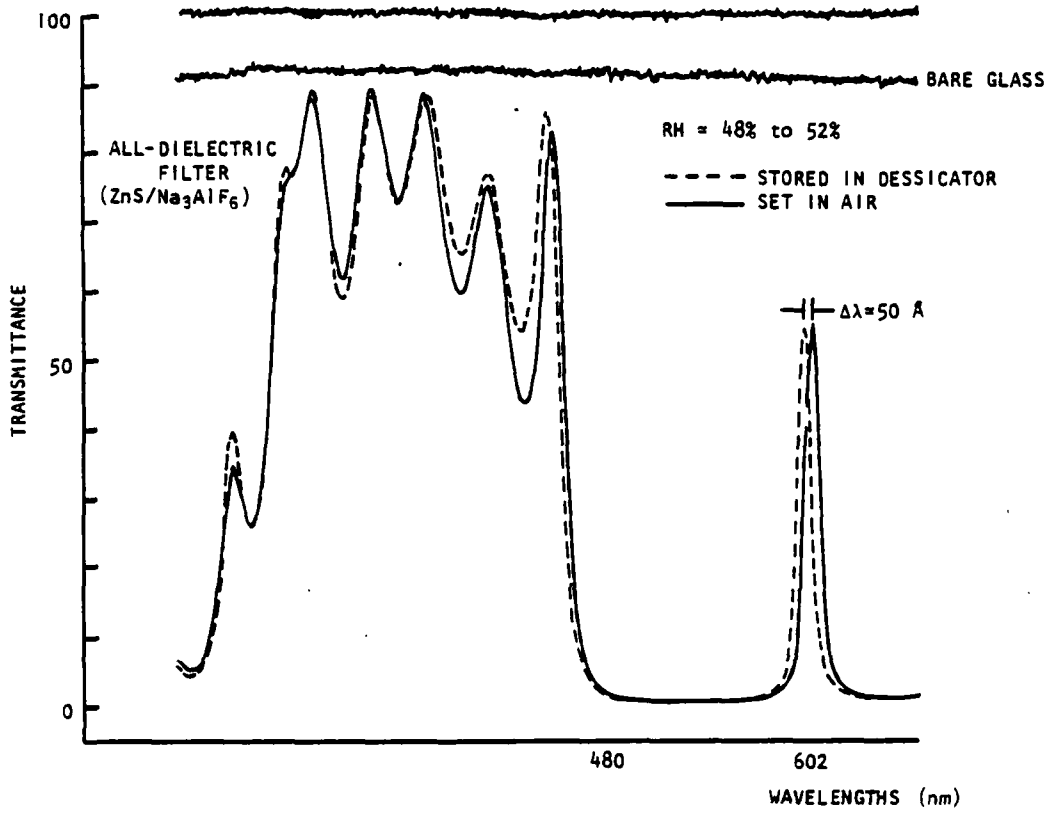


Figure 5.3. Shift of characteristic of narrowband filter due to moisture adsorption.

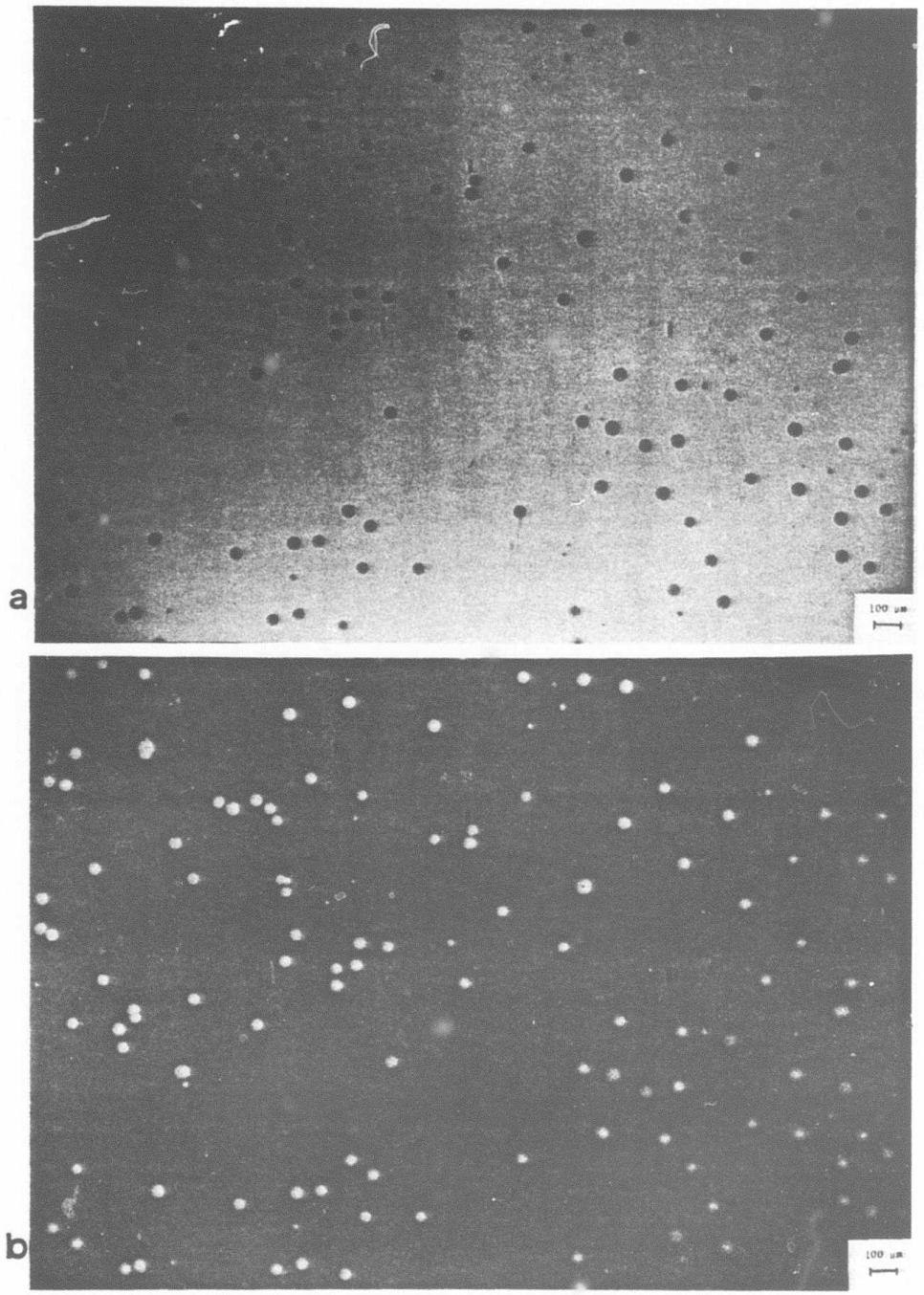


Figure 5.4. Water adsorption in ZnS/Na_3AlF_6 filter 4 days after coating, RH = 47%. (a) λ = 484 nm. (b) λ = 509 nm.

Richmond, 1976; Richmond, 1976; Lissberger, 1978). The normal measuring technique consists of adjusting the monochromator to give the best contrast and then carrying out the measurements by moving the micrometer stage on which the filter cell is mounted.

The patches in zinc sulfide/cryolite multilayers are usually clearly defined with sharp boundaries, as can be seen in the photograph. There are several circles in each patch which vary in peak wavelengths and correspond to moisture at different depths in the filter.

As time goes on, the patch size grows as in Figs. 5.5 through 5.8. This growth in patch size is the main feature of the adsorption process. The growth rate depends on the relative humidity and also depends on the size of central pore, as shown in Fig. 5.9.

Figures 5.10 and 5.11 show the isothermal growth rate as a function of relative humidity. The shape can be classified as a type IV adsorption isotherm that corresponds to multilayer water adsorption in a porous adsorbent.

Adsorption in Different Layers

The inner circles of the patch, (D',D"), show the same type of adsorption behavior implying the same adsorption mechanism inside the inner layers of the filter as the outer layers, except at a slower rate.

The wavelength shifts in different layers are shown in Figs. 5.12 and 5.13. The dashed line corresponds to the spacer layer. The

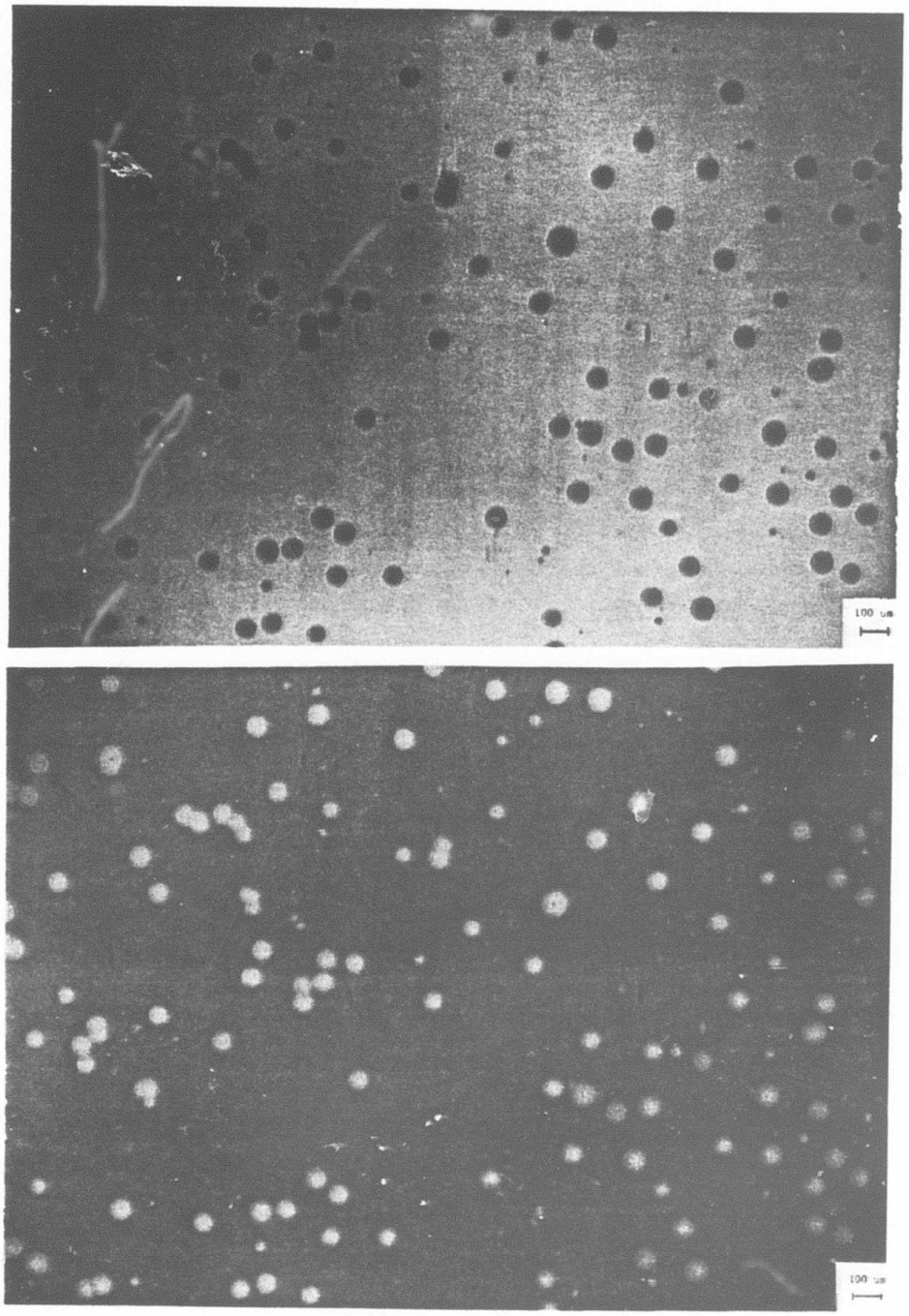
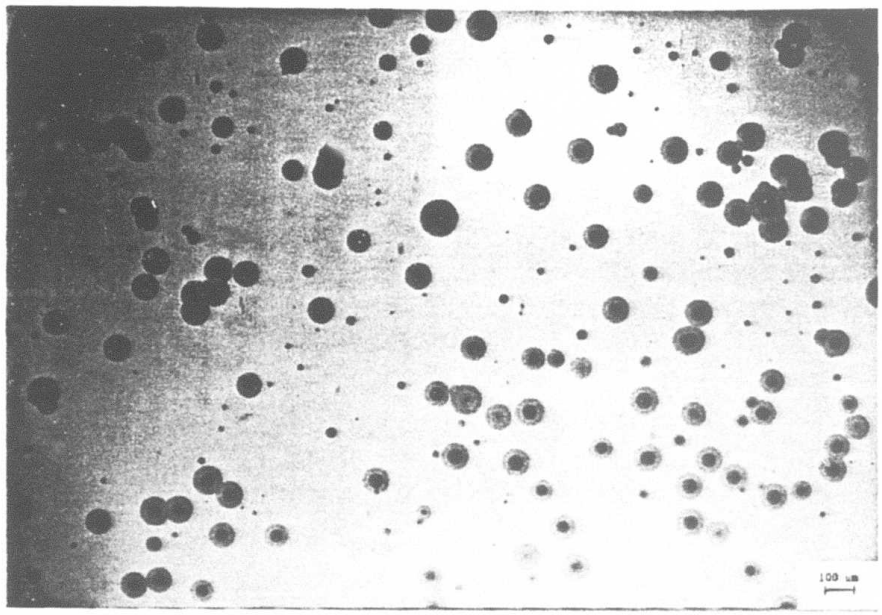
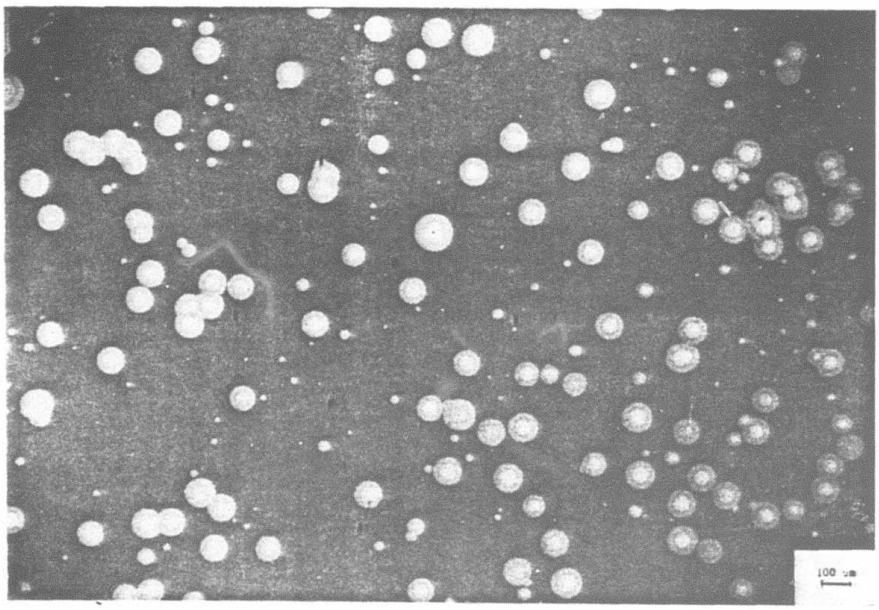


Figure 5.5. Water adsorption in ZnS/Na_3AlF_6 filter 5 days after coating, RH = 47%. (a) λ = 484 nm. (b) λ = 508 nm.

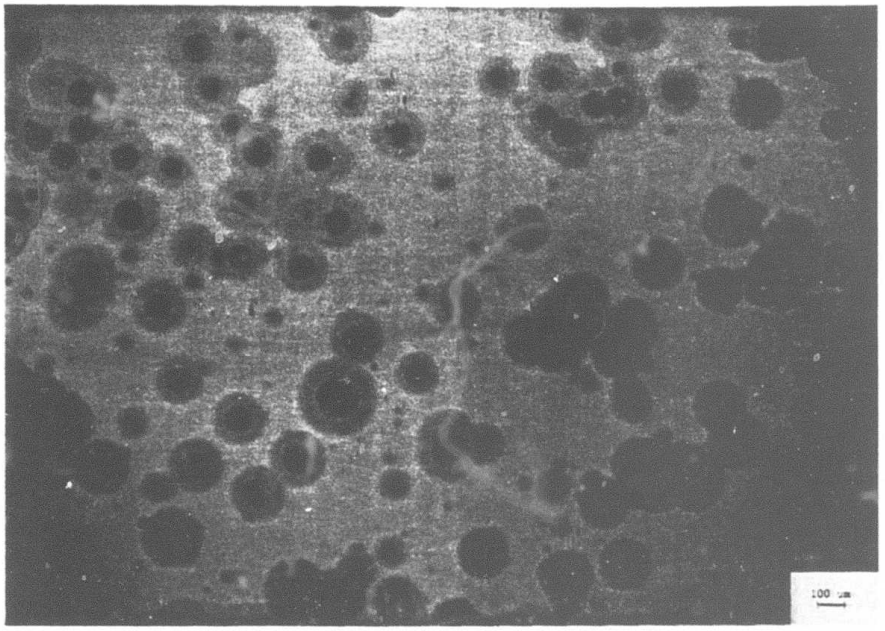


(a)

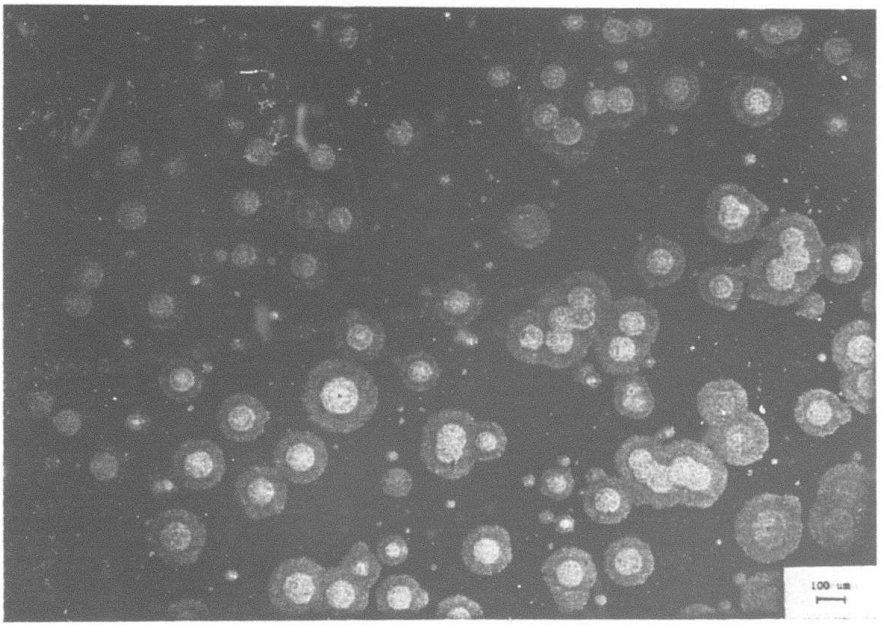


(b)

Figure 5.6. Water adsorption in ZnS/Na_3AlF_6 filter six days after coating. RH = 46%. (a) λ = 484 nm. (b) λ = 507 nm.



(a)



(b)

Figure 5.7. Water adsorption in ZnS/Na_3AlF_6 filter eight days after coating. RH = 50%. (a) λ = 485 nm. (b) λ = 508 nm.

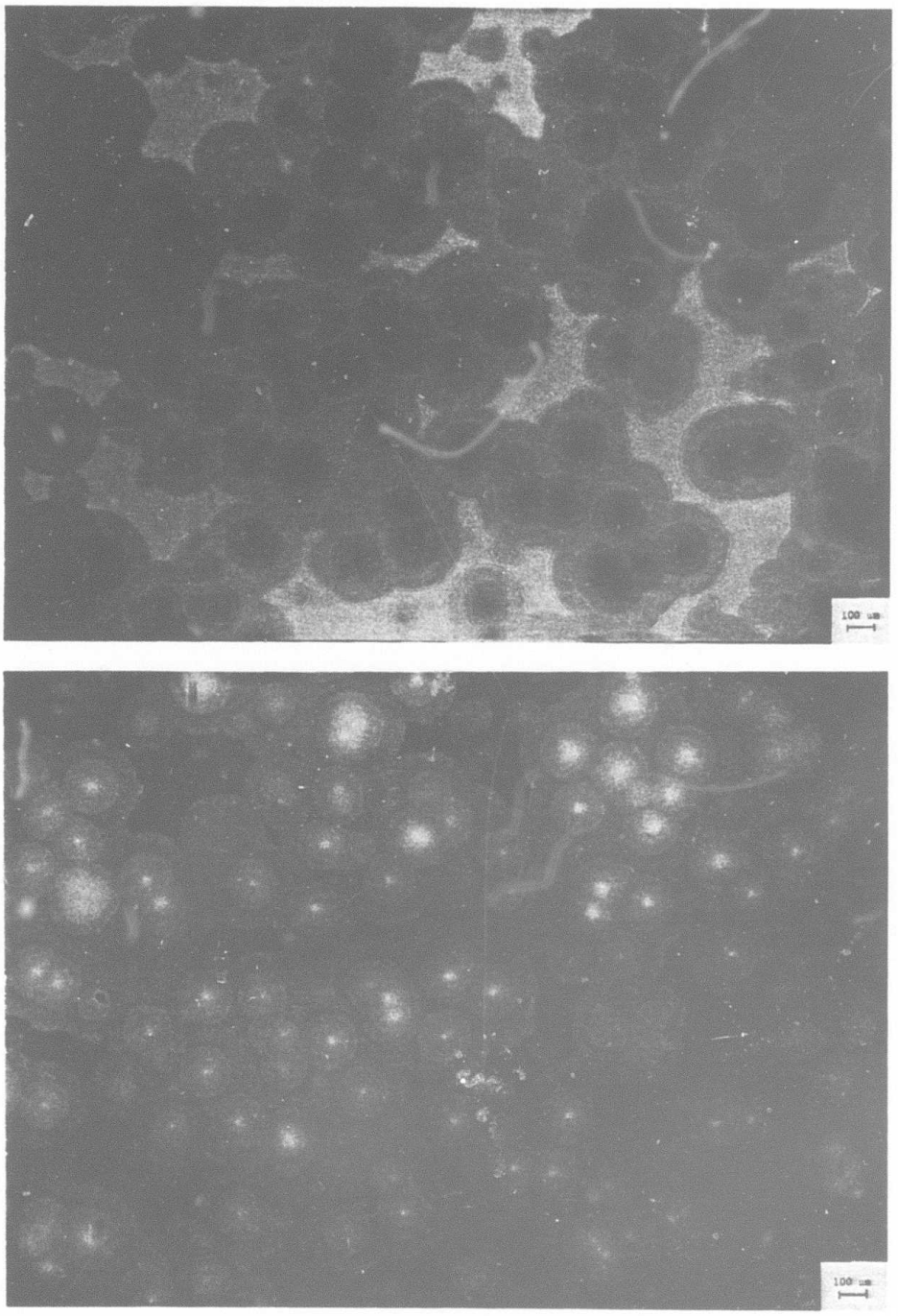


Figure 5.8. The filter of Fig. 5.7 a few days later. The first circles are linked together. (a) λ = 488.5 nm. (b) λ = 512.8 nm.

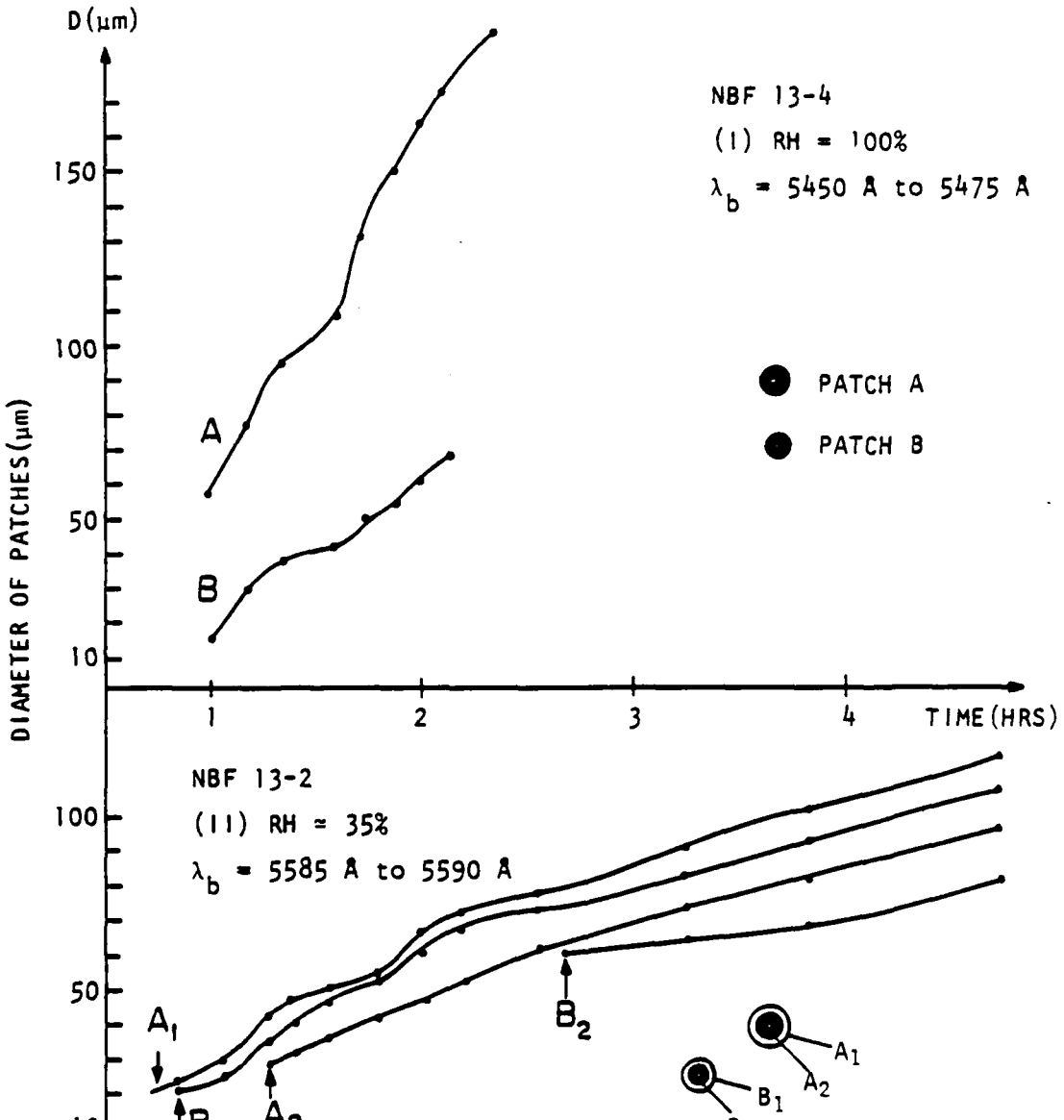


Figure 5.9. Water adsorption of all-dielectric narrowband filter (ZnS/Na_3AlF_6). Growth rate of patches.

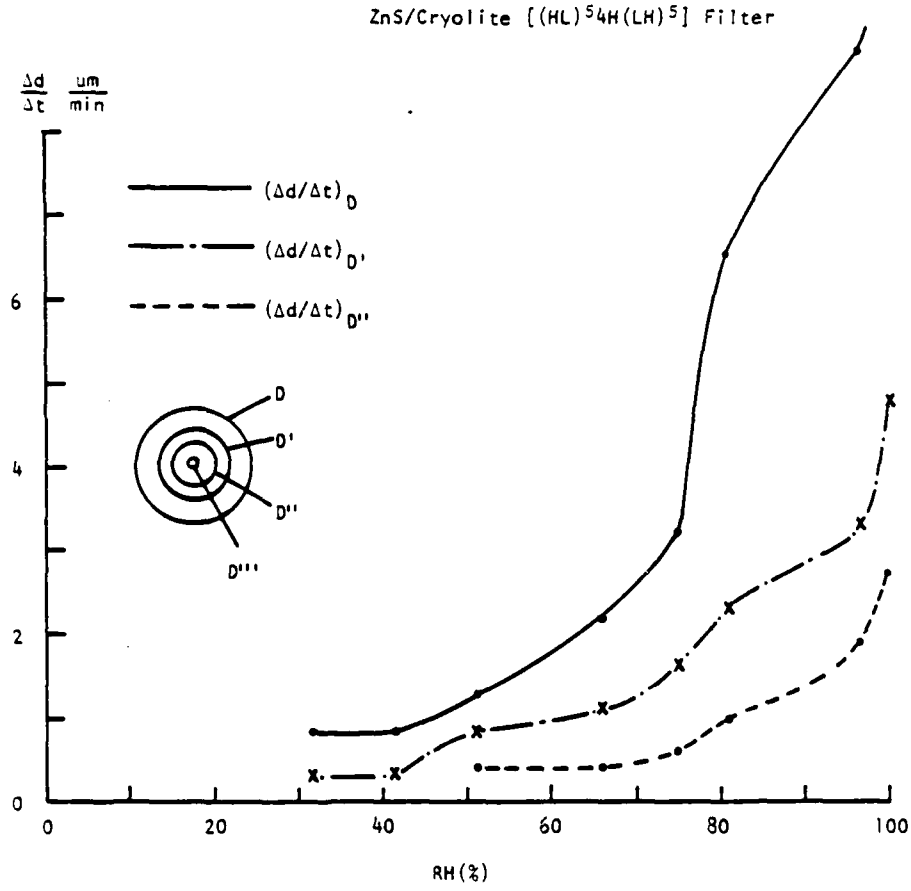


Figure 5.10. The patch growth rate in ZnS/Cryolite $[(HL)^5 4H(LH)^5]$ filter versus relative humidity.

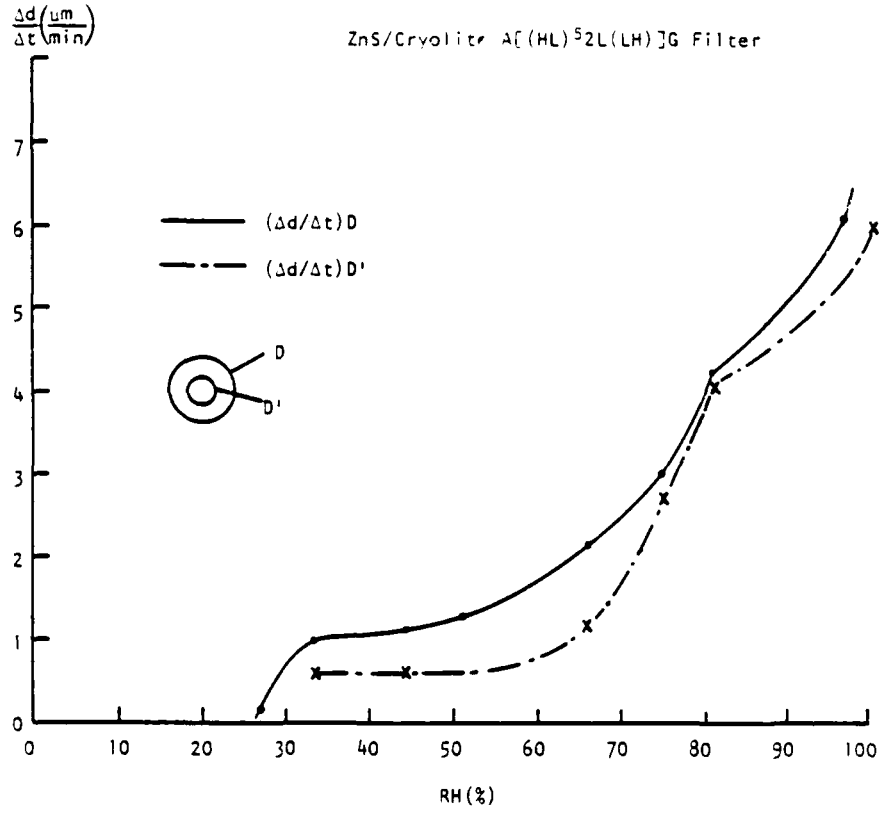


Figure 5.11. The patch growth rate in ZnS/Cryolite A[(HL)^{5}2L(LH)^5]G filter versus relative humidity.

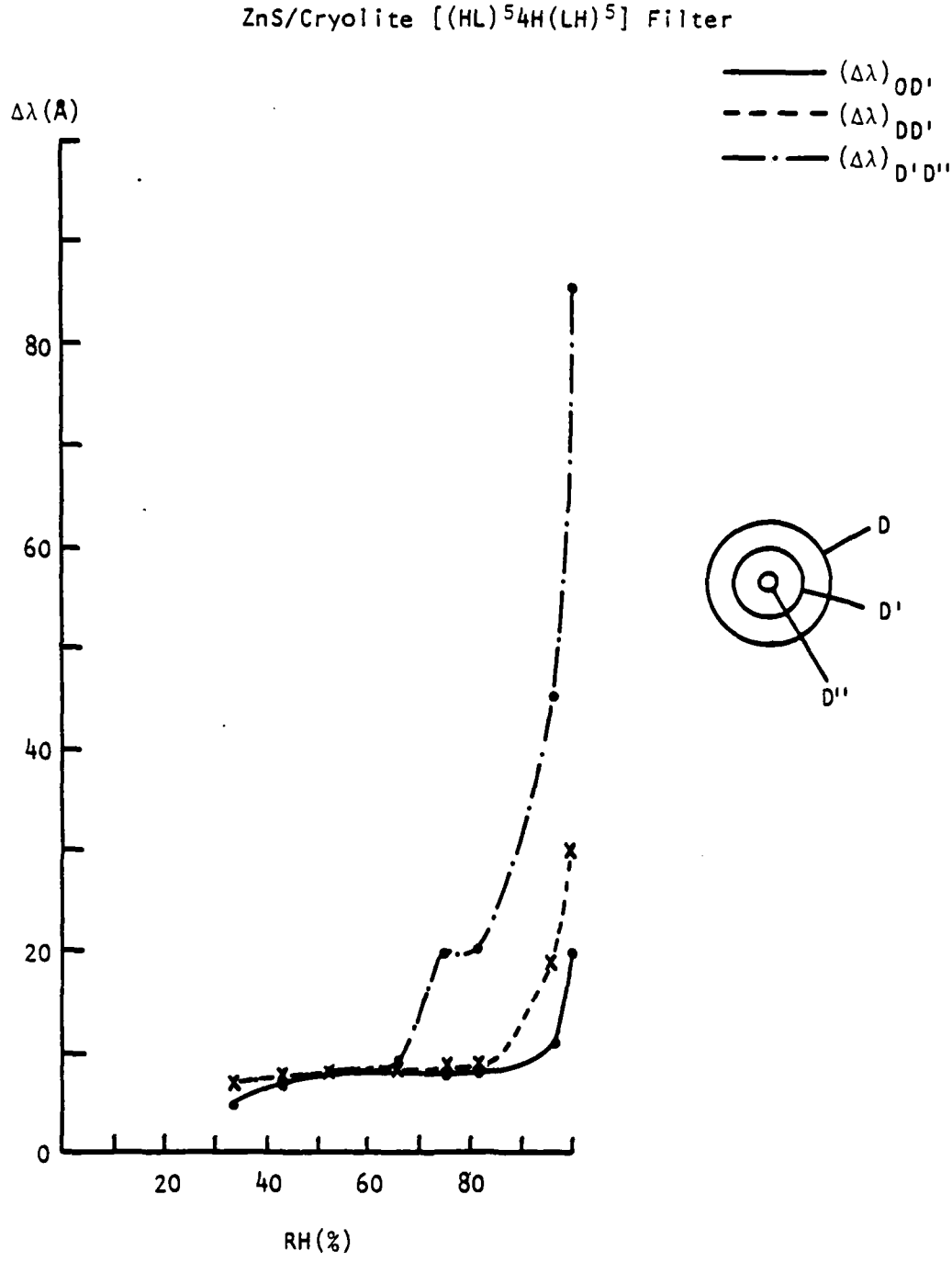


Figure 5.12. The wavelength difference between different circles in the same patch of ZnS/Cryolite $[(HL)^5 4H(LH)^5]$ versus relative humidity.

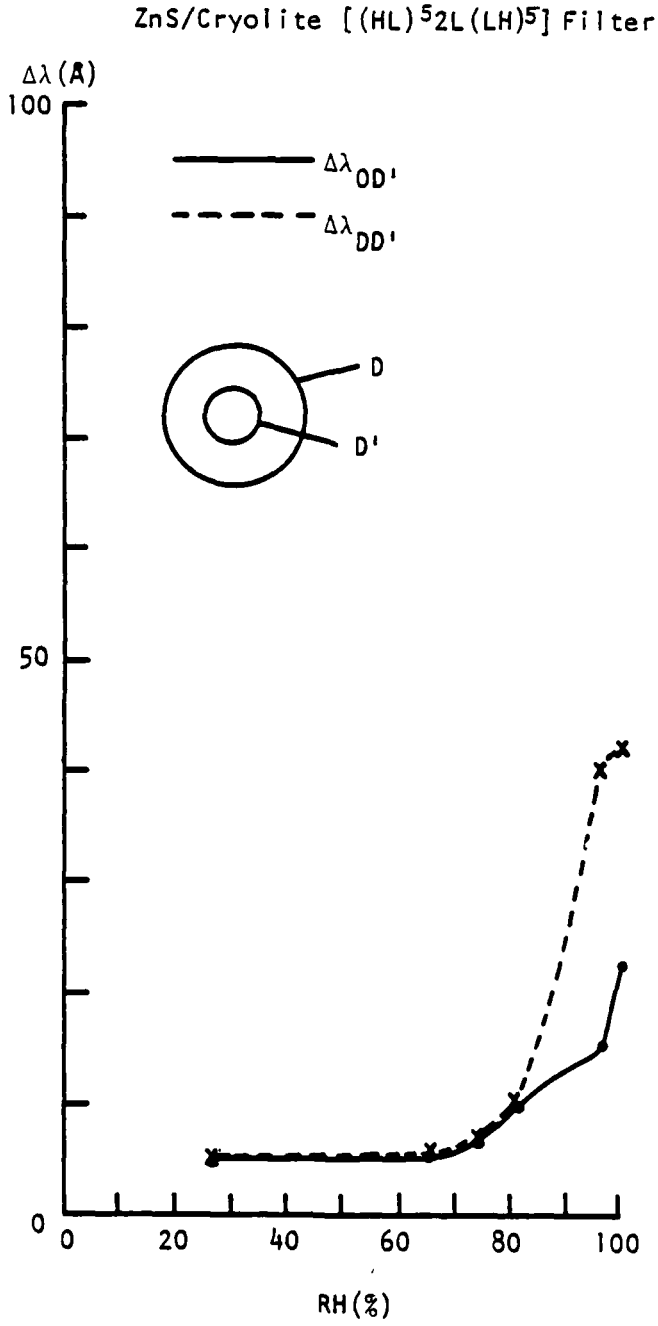


Figure 5.13. The wavelength difference between different circles in the same patch of ZnS/Cryolite $[(HL)^5 2L(LH)^5]$ versus relative humidity.

dramatic shift after 80% RH is due to a filling of the pores with water and a chemical reaction that occurs at that time.

High Index Spacer and Low Index Spacer

The water adsorption process occurs very slowly at low RH and it takes a long time for water to go through the layers. Figures 5.14 and 5.15 give an idea of how the wavelength shift relates to the RH and to the time. Comparing the zinc sulfide spacer and cryolite spacer, one observes that the latter one has a much greater shift, especially at high RH. There are two implications. First, the cryolite is more porous than zinc sulfide, which is actually known to have high packing density (Ogura, 1975; Pulker and Jung, 1976; Macleod and Richmond, 1976; Richmond, 1976; Lissberger, 1978) and to act as a barrier that slows down or even stops the water penetration deeper into the layers of the filter. Second, the cryolite reacts with water chemically which increases its refractive index even more, while the zinc sulfide does not.

The time that the water needs to spread away from the central pore is not only RH dependent, but also depth-of-layers dependent as shown in Fig. 5.16.

Tables 5.1 and 5.2 summarize the results. The last column lists the growth rate of patches associated with the smallest defects, too small to be seen with the microscope. Here the growth rate is very slow. This is shown in Fig. 5.17, where the small defect produces one circle at a lower rate of spreading than the multiple circles

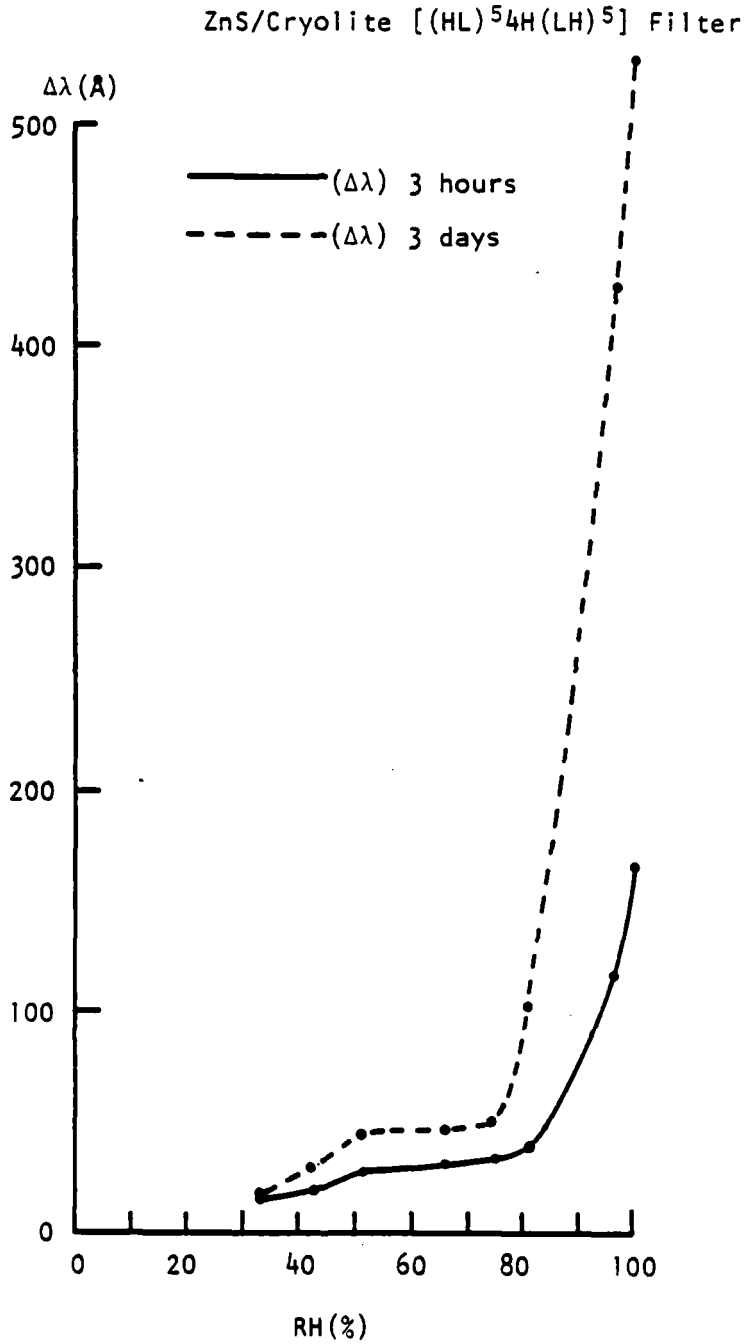


Figure 5.14. The wavelength shift of ZnS/Cryolite [(HL)^{5}4H(LH)^5] filters due to water adsorption in different relative humidities.

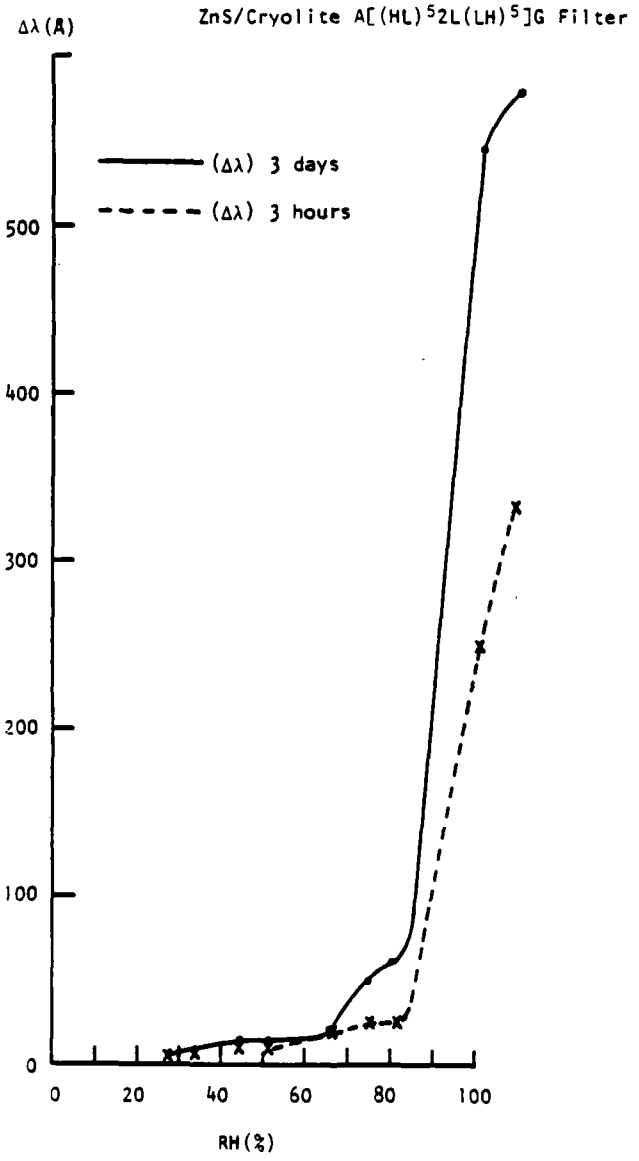


Figure 5.15. The wavelength shift of ZnS/Cryolite A[(HL)^{5}2L(LH)^5]G filters due to water adsorption in different relative humidities.

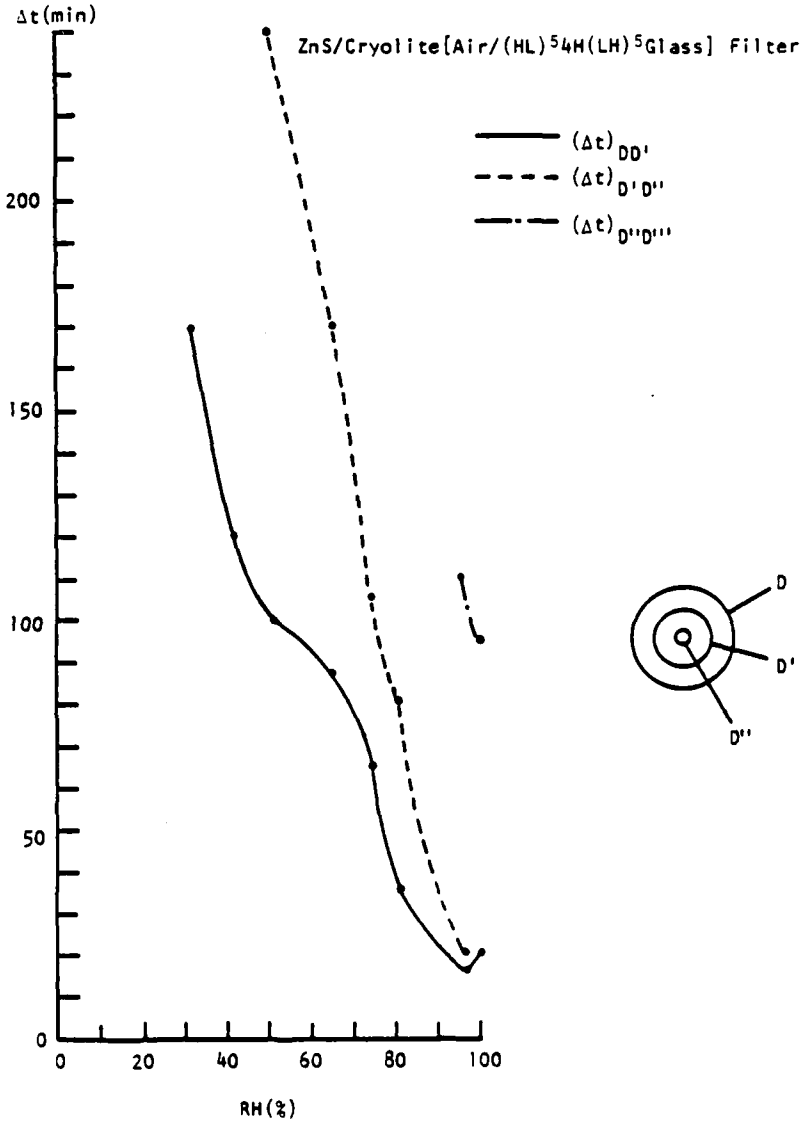


Figure 5.16. The time taken for the circles in the same patch to reach a given size versus relative humidity.

Table 5.1. Multilayer Water Adsorption of $A|(HL)^5 4H(LH)^5|G$.

Sample Defect size	R.H. RH_{rm}	$\frac{\Delta\lambda_{OD}}{\Delta t_{OD}}$	$\frac{\Delta\lambda_{DD'}}{\Delta t_{DD'}}$	$\frac{\Delta\lambda_{D'D''}}{\Delta t_{D'D''}}$	$\frac{\Delta\lambda_{D''D'''}}{\Delta t_{D''D'''}}$	$\frac{\Sigma\Delta\lambda}{3\ hr}$	$\frac{\Sigma\Delta\lambda}{3\ days}$	$\frac{\Delta\lambda_{BA}}{30\ min}$	$\frac{\Delta\lambda_{BK}}{130^oC}$	$\frac{\Delta d}{\Delta t_D}$	$\frac{\Delta d}{\Delta t_{D'}}$	$\frac{\Delta d}{\Delta t_{D''}}$	$\frac{\Delta d}{\Delta t_{D'''}}$	$\frac{\Delta d}{\Delta t_{ND}}$
H-2-6 10 μm	100% 40%	20Å instantly	30Å 20 min	85Å 20 min	33Å 95 min	168Å	528Å	-110Å	-225Å	14	5.3	2.7	2.2	
H-2-1 8 μm	96.5% 41%	11Å instantly	9Å 16 min	45Å 20 min	40Å 115 min	115Å	425Å	-80Å	-125Å	8.9	3.33	1.88	0.5	3.7
H-2-5 10 μm	81% 43%	8Å few sec	8Å 36 min	20Å 81 min		36Å	100Å	-10Å	-45Å	6.5	2.3	0.97		3
H-2-2 8 μm	75% 41%	8Å few sec	8Å 65 min	20Å 105 min		33Å	50Å	-8Å	-20Å	3.25	1.63	0.6		
H-2-4 10 μm	66% 44%	8Å few sec	8Å 88 min	9Å 170 min		30Å	46Å	-6Å	-18Å	2.2	1.1	0.39		
H-2-3 10 μm	51% 44%	8Å few sec	8Å 100 min	8Å 240 min		26Å	45Å	-3Å	-7Å	1.28	0.86	0.4		
H-3-4 10 μm	43% 49.5%	7Å few sec	8Å 120 min			18Å	30Å	+2Å	-2Å	0.82	0.3			
H-3-6 8 μm	33% 52-54%	5Å few sec	7Å 170 min			14Å	17Å	+3Å	-2Å	0.85	0.28			0.16

$\Delta\lambda_{OD}$ = λ shift from filter as produced to 1st patch appearing

$\Delta\lambda_{DD'}$ = λ shift from 1st patch to 2nd patch

$\Delta\lambda_{DD''}$ = λ shift from 2nd patch to 3rd patch

$\Delta\lambda_{BA}$ = λ shift from saturated back to air

$\Delta\lambda_{BK}$ = λ shift due to baking for 2 hr

$\Delta d/\Delta t$ = patch growth rate in μm/min

$\Delta d/\Delta t_{ND}$ = patch growth rate with no visible defect in patch center

RH_{rm} = relative humidity in room

* Only two circles in patch

** Only one circle in patch

Table 5.2. Multilayer Water Adsorption of $A|(HL)^5 2L(LH)^5|G$.

Sample Defect size	R.H. RH_{rm}	$\frac{\Delta\lambda_{OD}}{\Delta t_{OD}}$	$\frac{\Delta\lambda_{DD'}}{\Delta t_{DD'}}$	$\frac{\Delta\lambda_{D'D''}}{\Delta t_{D'D''}}$	$\frac{\Delta\lambda_{D''D'''}}{\Delta t_{D''D'''}}$	$\frac{\Sigma\Delta\lambda}{3\ hr}$	$\frac{\Sigma\Delta\lambda}{3\ days}$	$\frac{\Delta\lambda_{BA}}{30\ min}$	$\frac{\Delta\lambda_{BK}}{130^{o}C}$	$\frac{\Delta d}{\Delta t_{D}}$	$\frac{\Delta d}{\Delta t_{D'}}$	$\frac{\Delta d}{\Delta t_{D''}}$	$\frac{\Delta d}{\Delta t_{D'''}}$	$\frac{\Delta d}{\Delta t_{ND}}$
L-34-1 10 μm	100% 28%	22Å instantly	42Å	41Å 20 min	33Å 35 min	332Å	572Å	-70Å	-140Å	8.2	6.0	3	1.2	
L-34-2 10 μm	96.5% 42%	15Å instantly	40Å 9 min	50Å 63 min		150Å	545Å	-40Å	-105Å	6	5.6			1.9*
L-34-3 9 μm	81% 35%	10Å few sec	10Å 18 min			25Å	60Å	0	-55Å	4.2	4.0			
L-34-4 9 μm	75% 33%		7Å 25 min			25Å	50Å	0	-30Å	3	2.7			3*
L-34-5 10 μm	66% 35%	5Å few sec	5Å 35 min			20Å	20Å	0	-25Å	2.3	1.2			
67-2-3 10 μm	51% 35%		5Å 65 min			10Å	14Å		-15Å	1.27	0.6			
L-36-6 10 μm	44% 44%		5Å			10Å	14Å		-15Å	1.1	0.6			0.55**
L-36-3 15 μm	33% 44%		5Å			9Å	10Å	0	-15Å	1	0.6			0.13**
L-34-6 10 μm	27%	5Å				5Å	5Å		-15Å	0.33				

$\Delta\lambda_{OD}$ = λ shift from filter as produced to 1st patch appearing

$\Delta\lambda_{DD'}$ = λ shift from 1st patch to 2nd patch

$\Delta\lambda_{DD''}$ = λ shift from 2nd patch to 3rd patch

$\Delta\lambda_{BA}$ = λ shift from saturated back to air

$\Delta\lambda_{BK}$ = λ shift due to baking for 2 hr

$\Delta d/\Delta t$ = patch growth rate in μm/min

$\Delta d/\Delta t_{ND}$ = patch growth rate with no visible defect in patch center

RH_{rm} = relative humidity in room

* Only two circles in patch

** Only one circle in patch

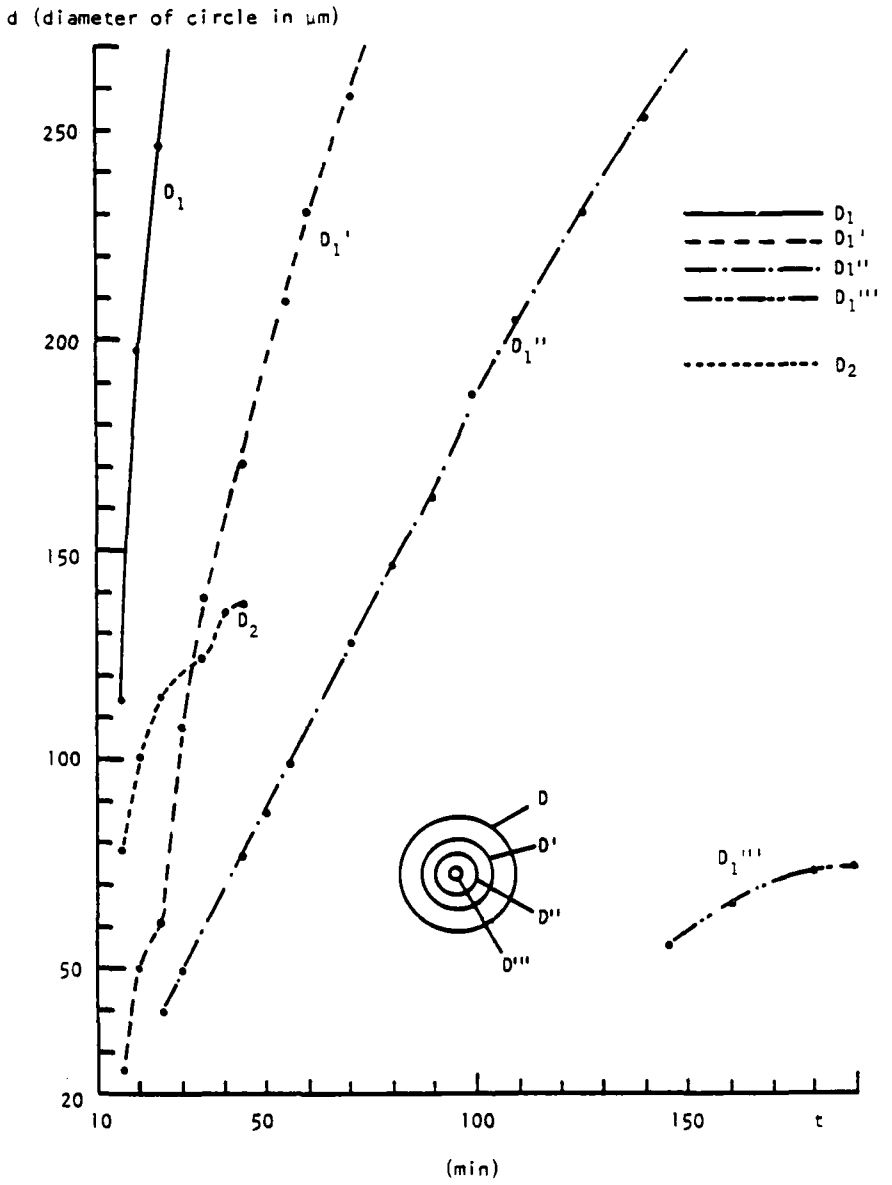


Figure 5.17. The growth of patch size in filter due to water adsorption (100% RH). (Defect center size of patch 1 is ≈ 12 μm. Defect center size of patch 2 is less than 1 μm.)

associated with the larger defect, which indicates that the larger defect causes a penetration deeper into the coating at a greater rate.

Desorption

The ninth column of the tables indicates that the water will be desorbed from the films if the humidity of the environment is less than it was when the water was adsorbed.

An important question is whether the desorption can be complete. The tenth column of the tables shows some effects of baking. Baking can remove some of the water from the film, but not all of it. The reason is the strong bonding of the initial monolayer of water to the inner surface of the voids as explained in Chapter 2. This phenomenon is referred to as the irreversible part of the adsorption by Pulker and Jung (1971). Yet, the more water adsorbed by the films, the more water can be baked out, as shown by Figs. 5.18 and 5.19.

Another reason for only a limited recovery of wavelength due to baking, as one can check in the eighth to tenth columns of the tables, is due to the fact that one of the materials used, cryolite, undergoes some chemical reaction with the water. In Table 5.1, which deals with a high-index spacer, the difference between wavelength shift on adsorption and wavelength shift on desorption is considerable at all levels of humidity. In Table 5.2, which lists the results for a low-index spacer, the difference becomes very significant at values of humidity greater than 75% RH. In many of the earlier results we recall a sharp increase in the effects of adsorption in cryolite at

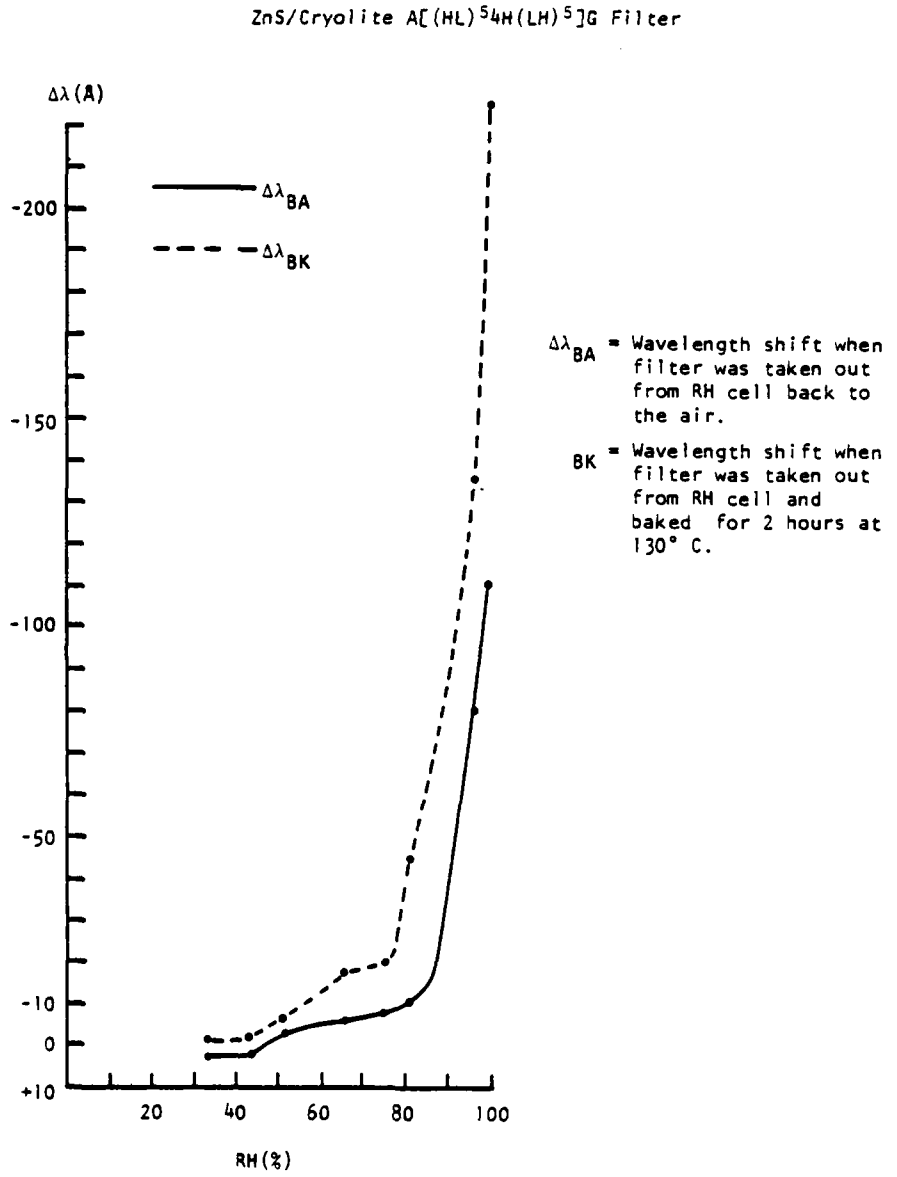


Figure 5.18. The wavelength shift of filter due to water desorption after being taken out of the cell at different relative humidities. (The RH in the air is 48% to 52% during desorption.)

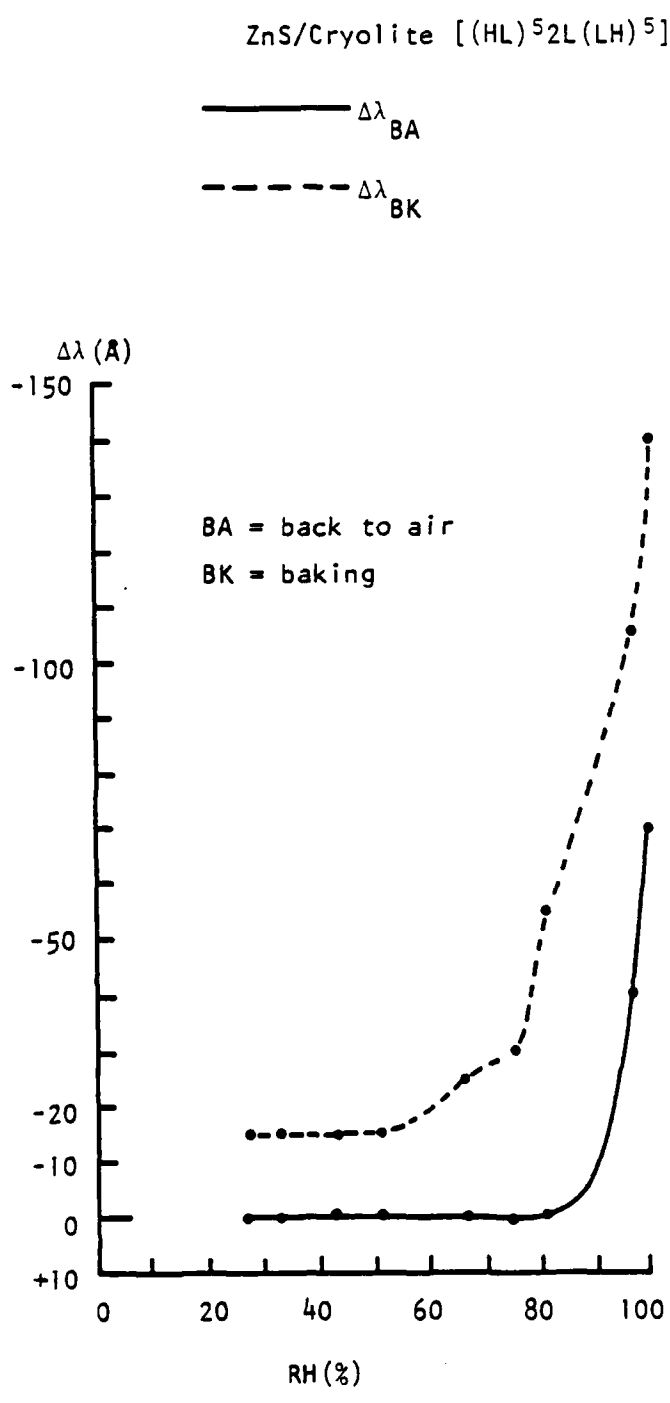


Figure 5.19. The wavelength shift of filter due to water desorption after being taken out of the cell at different relative humidities. (The RH in the air is 48 to 52% during desorption.)

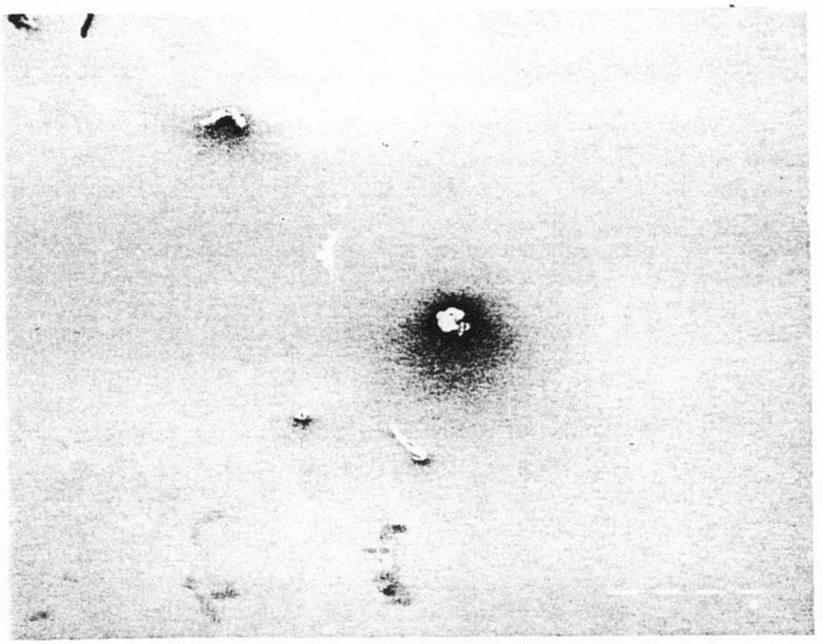
relative humidities of around 80% which we have attributed to a chemical reaction. The cryolite is somewhat soluble in the water. Figures 5.20 and 4.11 show recrystallization of dissolved material.

Table 5.3 summarizes the water adsorption in filters at different relative humidities and the water desorption due to baking. It is interesting to note from the table that the half-peak widths, $\Delta\lambda_H$, become broader after water adsorption for all the filters except sample L-36-4 at the lowest relative humidity, and become narrower after water desorption for most of the filters. The peak transmittance (T_p) decreased after water adsorption and increased after water desorption. These are illustrated by the spectrometer traces in Fig. 5.21.

The reason for broadening of $\Delta\lambda_H$ after water adsorption is the nonuniformity of T_p over the surface. If the field of view of the spectrometer includes both wet material in a patch and dry material, then there will be two peaks as shown in Figs. 5.22 and 5.23.

Narrowband Filters of Oxide Materials

All the narrowband filters constructed from oxide materials suffered a shift of peak transmission to longer wavelengths because of moisture adsorption. However, none of them exhibited clear, sharp patches. A narrowband filter made from ZrO_2/SiO_2, for example, gave patches with very blurred boundaries as shown in Fig. 5.24. This filter was made in the Balzers BAK760 with electron-beam sources (see Fig. 5.25). Oxygen was introduced at a constant partial pressure of



(a)

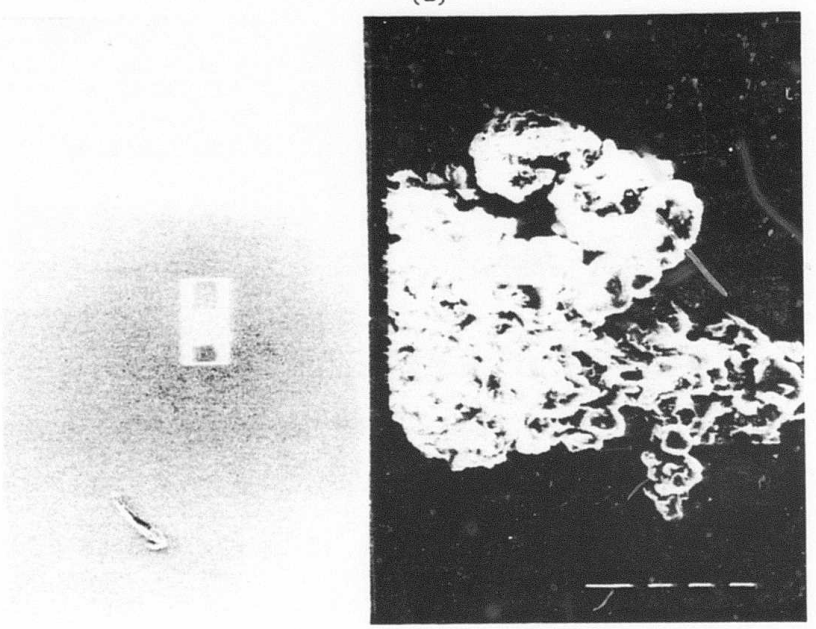


Figure 5.20. Dust, defect and patch on filter shown by scanning electron microscope at different magnification. (a) 30x. (b) 45x. (c) 450x.

Table 5.3. Water Adsorption and Baking Effect of ZnS/Cryolite Filter.

Sample		RH (%)	$\Delta\lambda_{RH}$ (Å)	$\left.\frac{\Delta\lambda_{RH}}{\Delta\lambda_0}\right\|_H$	$\left.\frac{T_{RH}}{T_0}\right\|_H$	$\Delta\lambda_{BK}$ (Å)	$\left.\frac{\Delta\lambda_{BK}}{\Delta\lambda_{RH}}\right\|_H$	$\left.\frac{T_{BK}}{T_{RH}}\right\|_P$
$(HL)^5 4H (LH)^5$	H-3-1	100	550	2.25	0.3	-225	0.98	1.22*
	H-2-1	96.5	425	1.4	0.5	-125	1.0	0.55*
	H-2-5	81	100	1.1	0.97	-45	0.98	1.03
	H-2-2	75	50	1.1	0.75	-20	0.95	1.02
	H-3-2	66	48	1.2	0.76	-18	0.99	0.98
	H-2-3	51	45	1.08	0.8	-7	0.99	1.02
	H-3-4	43	30	1.2	0.8	-2	1.0	0.99
	H-3-6	33	17	1.06	0.9	-2	1.0	0.99
$(HL)^5 2L (LH)^5$	L-34-1	100	572	2.2	0.7	-140	PEELING	
	L-34-2	96.5	545	1.35	0.85	-105	0.75	1.18*
	L-34-3	81	60	1.06	0.87	-55	0.94	1.15
	L-34-4	75	50	1.06	0.87	-30	0.98	1.02
	L-34-5	66	20	1.02	0.88	-25	0.99	1.02
	UT-2-3	51	14	1.21	0.88	-15	1.0	0.97
	L-36-6	43	14	1.0	0.90	-15	0.99	1.02
	L-34-6	33	10	1.02	0.93	-15	1.0	1.01
	L-36-4	27	5	0.51	1.38	-15	1.0	1.0

*Easily peeled off

RH = relative humidity

λ_0 = wavelength of peak transmittance of new filter

λ_{RH} = wavelength of peak transmittance at stated RH

λ_{BK} = wavelength of peak transmittance after baking

$\Delta\lambda_{RH} = \lambda_{RH} - \lambda_0$

$\Delta\lambda_{BK} = \lambda_{BK} - \lambda_{RH}$

$(\Delta\lambda_{RH}/\Delta\lambda_0)|_H$ = ratio of half-peak width of λ_{RH} to that of λ_0

$(\Delta\lambda_{BK}/\Delta\lambda_{RH})|_H$ = ratio of half-peak width of λ_{BK} to that of λ_{RH}

$(T_{RH}/T_0)|_P$ = ratio of peak transmittance at λ_{BK} to that of λ_{RH}

$(T_{BK}/T_{RH})|_P$ = ratio of peak transmittance at λ_{BK} to that at λ_{RH}

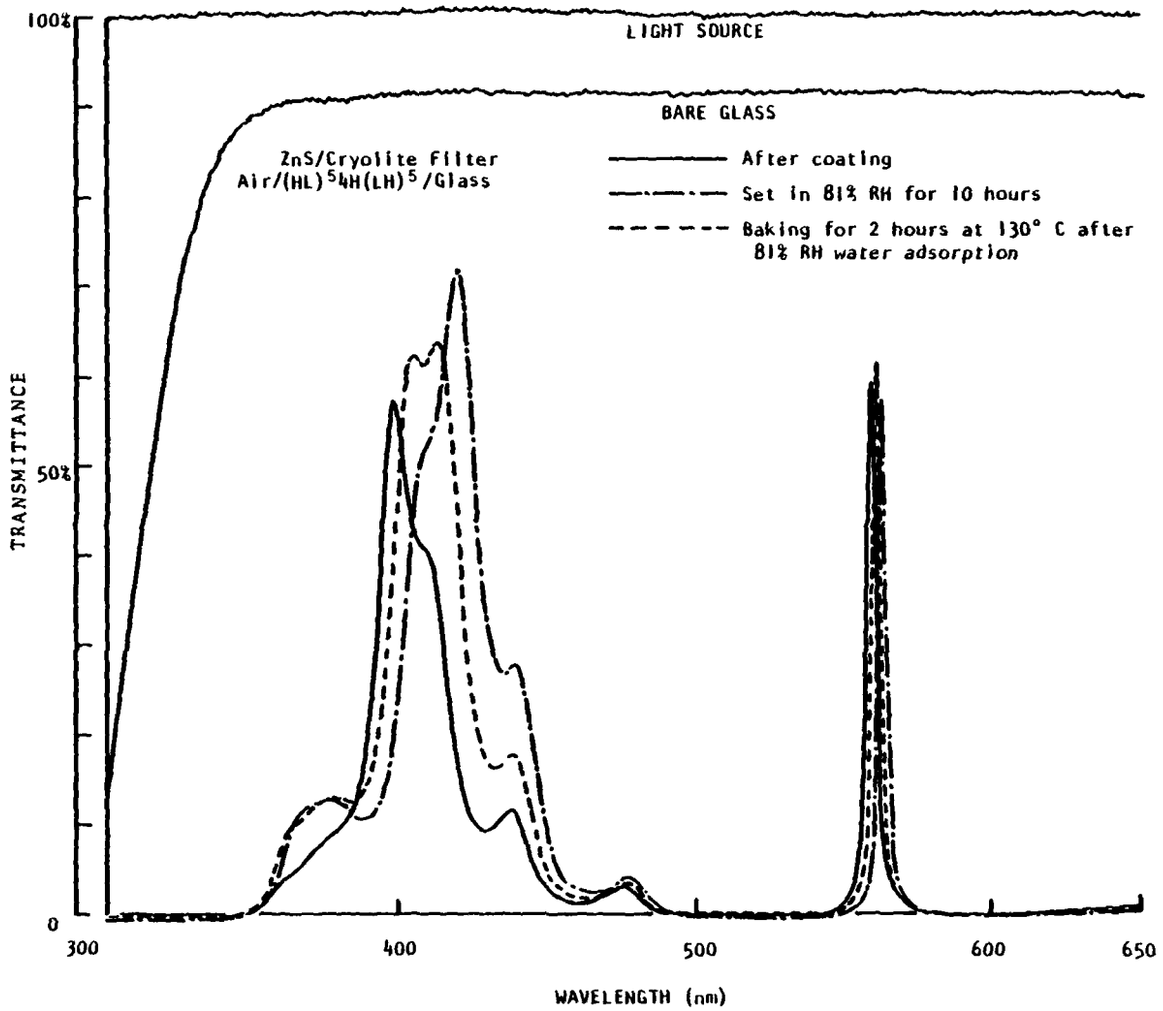


Figure 5.21. Shift of characteristics of narrowband filter after exposure to 81% RH for 10 hours and after baking.

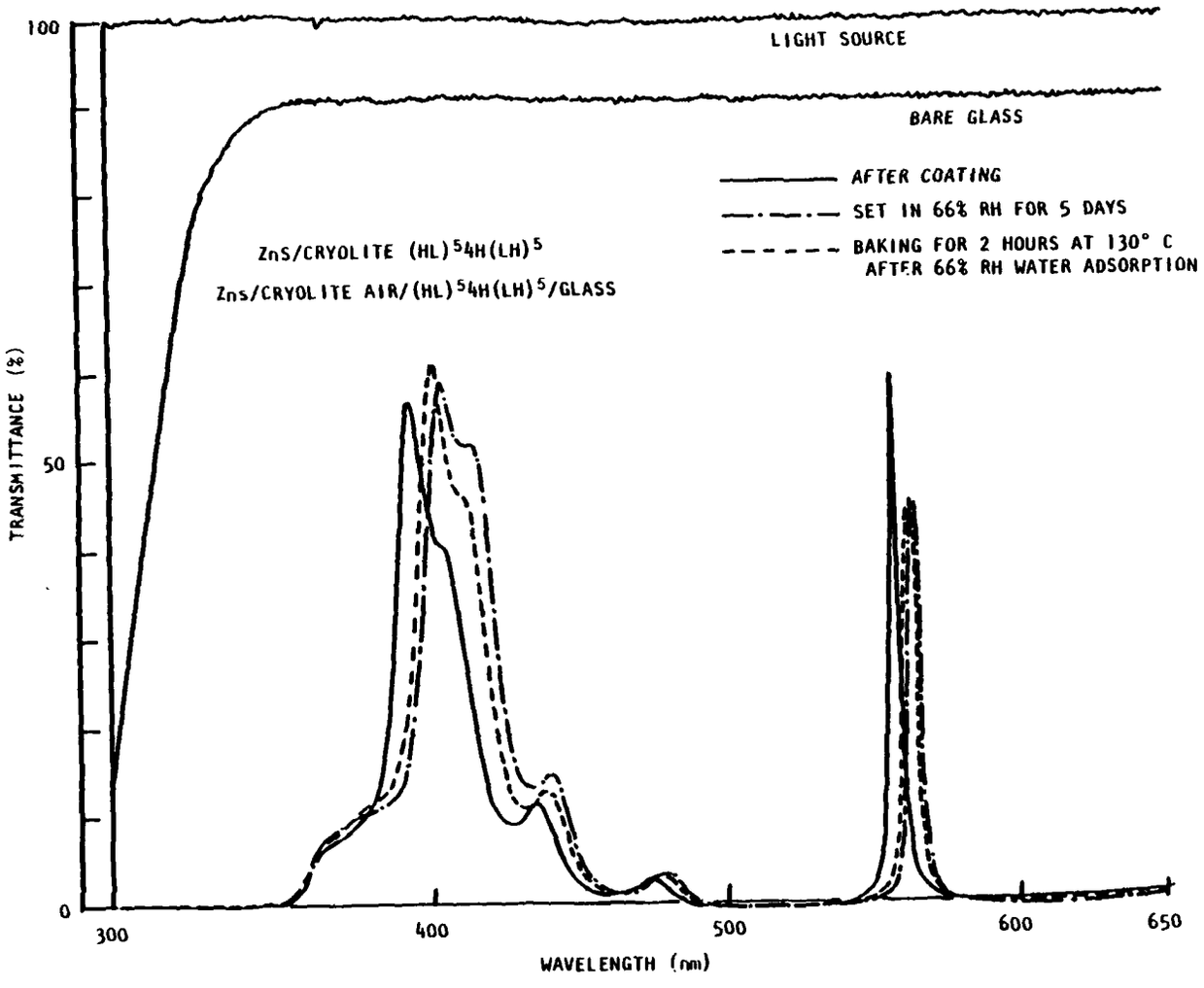


Figure 5.22. Shift of characteristics of narrowband filter after exposure to 66% RH for five days and after baking. Note the appearance of a slight double peak after moisture adsorption.

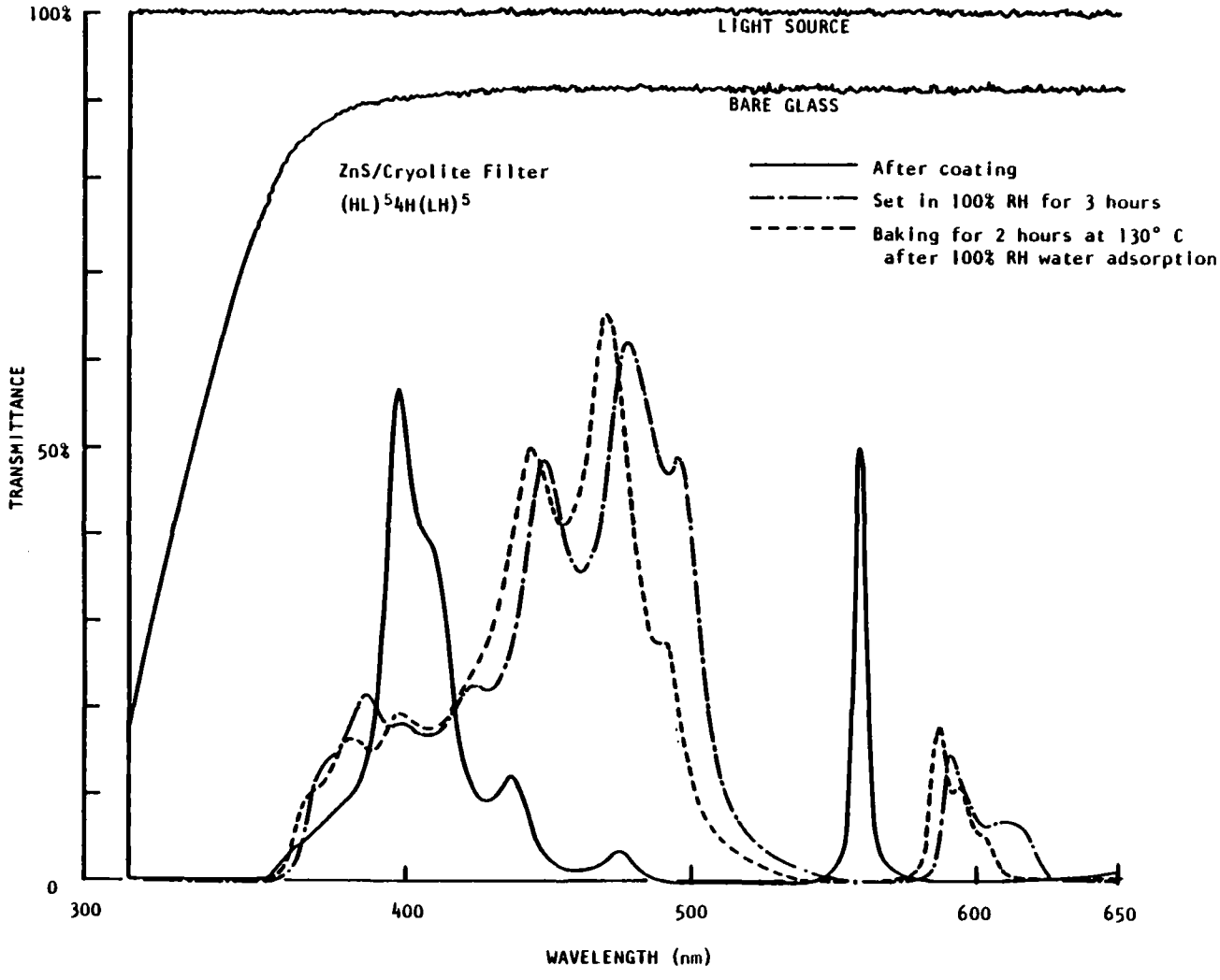


Figure 5.23. Shift of characteristics of narrowband filter after exposure to 100% RH for three hours and after baking. Note the very distorted peak shapes which result.

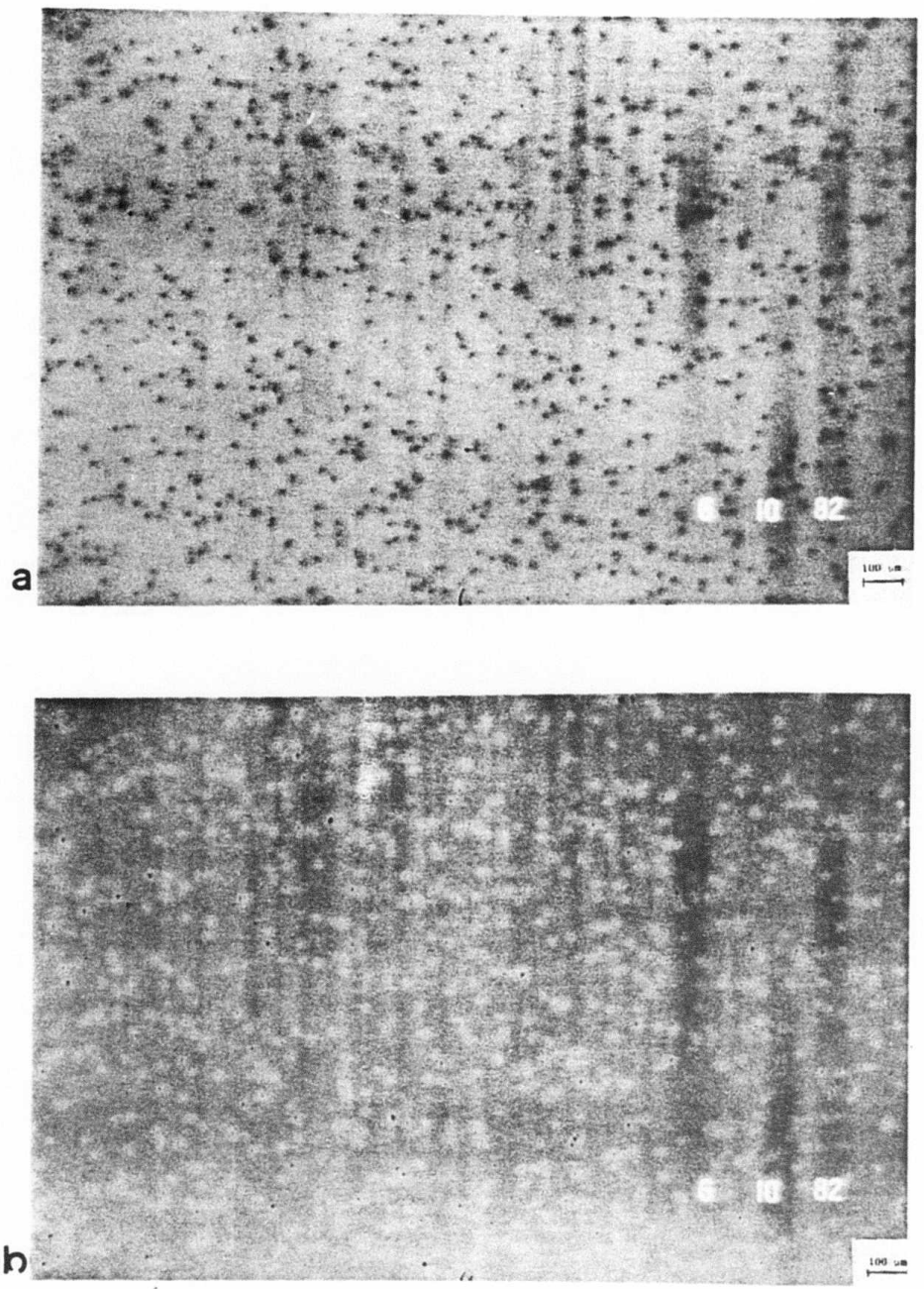


Figure 5.24. Water adsorption in ZrO_2/SiO_2 filter. Sample 760-17-3 immediately after removal from the coater. (a) λ = 543 nm. (b) λ = 553 nm.

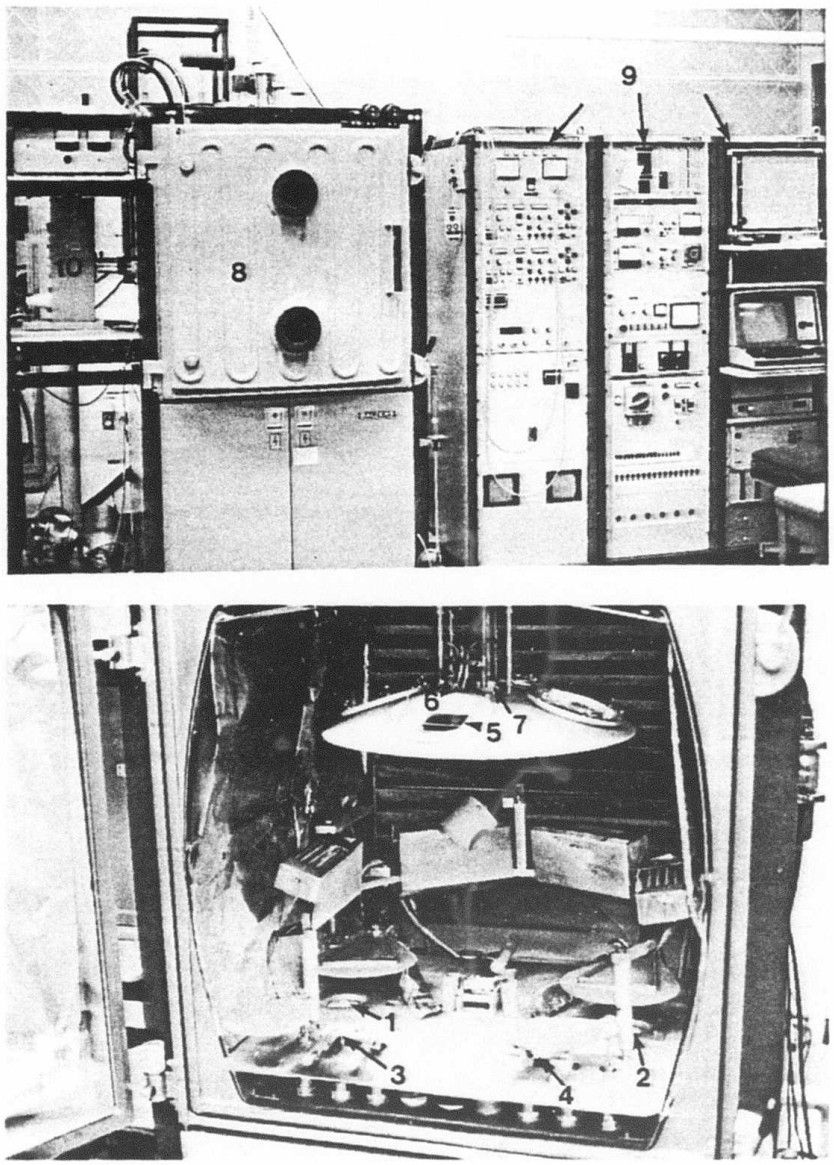


Figure 5.25. Balzers BAK 760 coating plant.
(1, 2) electron beam evaporation sources
(3, 4) thermal evaporation sources (5) substrate
(6) quartz crystal (7) optical monitor plate
(8) BAK 760 chamber (9) control panel
(10) UV light source (not used in this investigation)

$1^{\times}10^{-4}$ torr throughout the coating processes. The substrate was heated to 300° C.

Because of the high melting point of ZrO_2, it is harder to control its evaporation rate than that of the SiO_2. ZrO_2 also exhibits negative inhomogeneity, meaning that the index of refraction of the layer decreases as a function of its thickness. This can be seen from the optical monitoring signal during deposition. The inhomogeneity can be explained as a structural effect (Feldman, Friz, and Stetter, 1976): ZrO_2 has two crystalline forms--monoclinic, stable at low temperatures, and tetragonal, stable at high temperatures--and the inhomogeneity probably results from inhibition of the transformation from the latter to the former during condensation of the film. The result is that ZrO_2 has a very porous structure (Figs. 5.26 and 5.27) with very low packing density. ZrO_2 films are therefore very adsorptive. On the other hand, SiO_2 is in a glass-like structure, very less porous, which can slow down the water penetration into the deeper layers of the films. This is indeed what was observed by watching the growth of the patches in the filter. Within a few minutes the patches expanded, although with blurred boundaries, then extended over the whole surface and then disappeared. This shows that the outermost ZrO_2 layer or layers were filled up with water, which could not penetrate further because of SiO_2 as a barrier layer. One month later, however, new patches appeared as shown in Fig. 5.28. These patches must correspond to water adsorption in the deeper

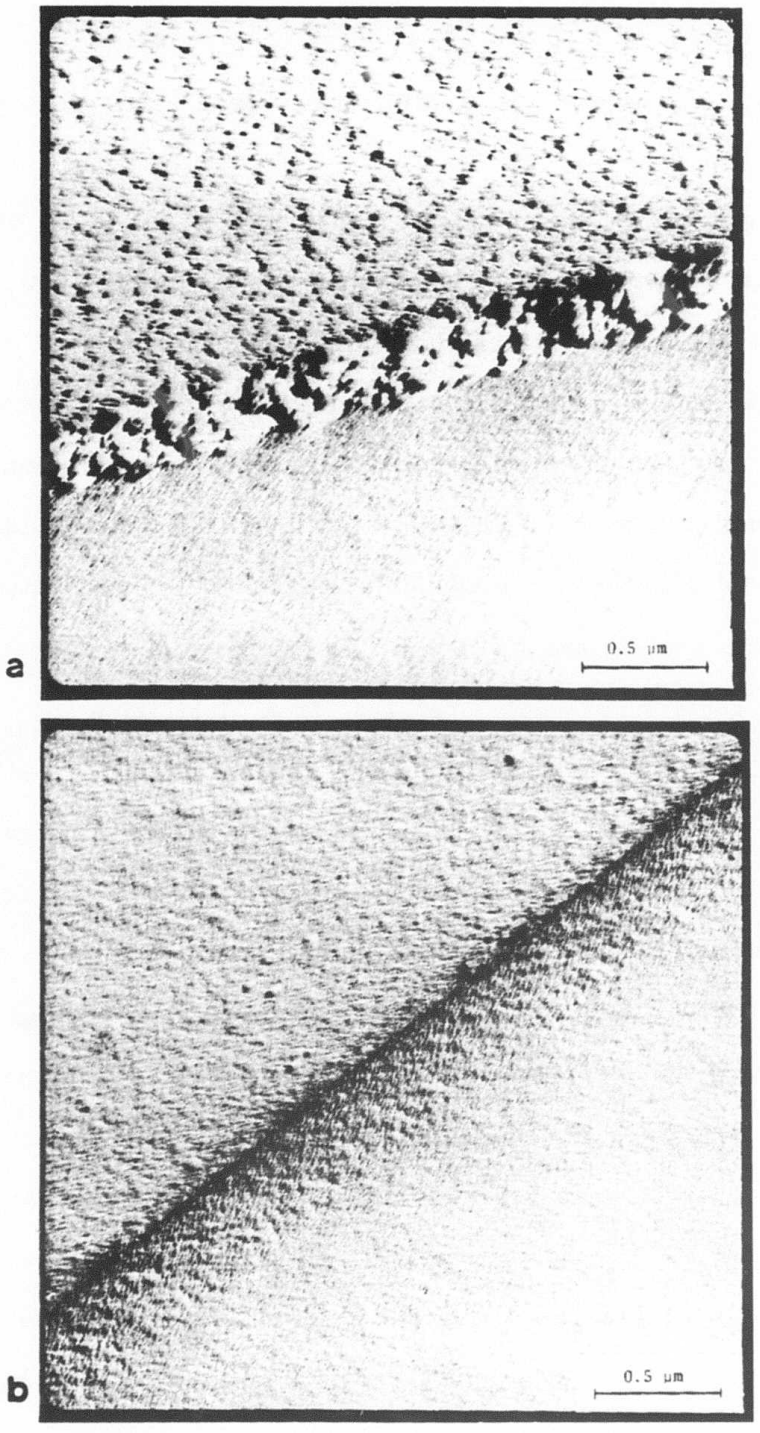


Figure 5.26. Micrograph (TEM) of single-layer film. Lower portion of photographs is glass.
(a) ZrO_2, (b) SiO_2.

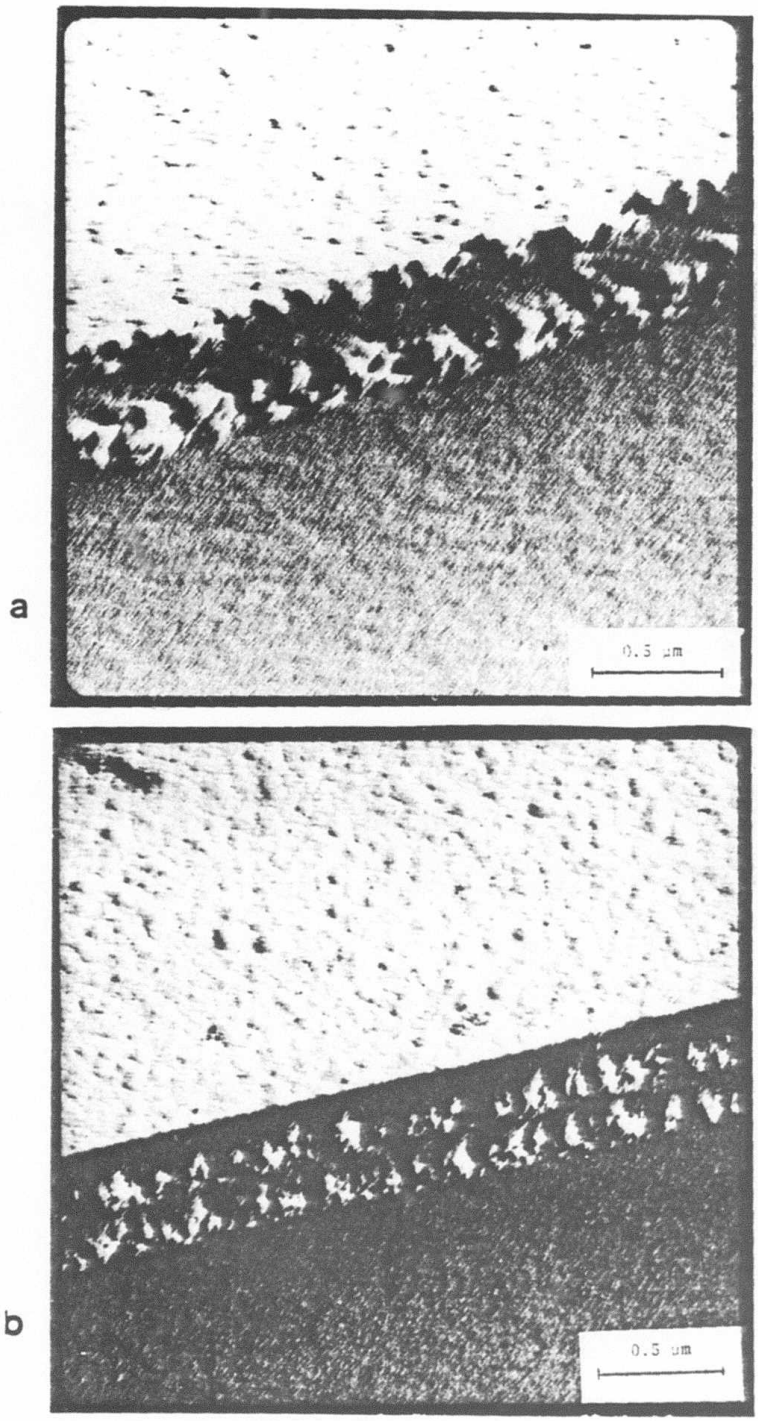


Figure 5.27. Micrograph (TEM) of thin-film multilayer of ZrO_2(H) and SiO_2(L). Lower half of photograph is glass.

(a) Air/2H/3L/3H/Glass, (b) Air/5L/3H/3L/3H/Glass.

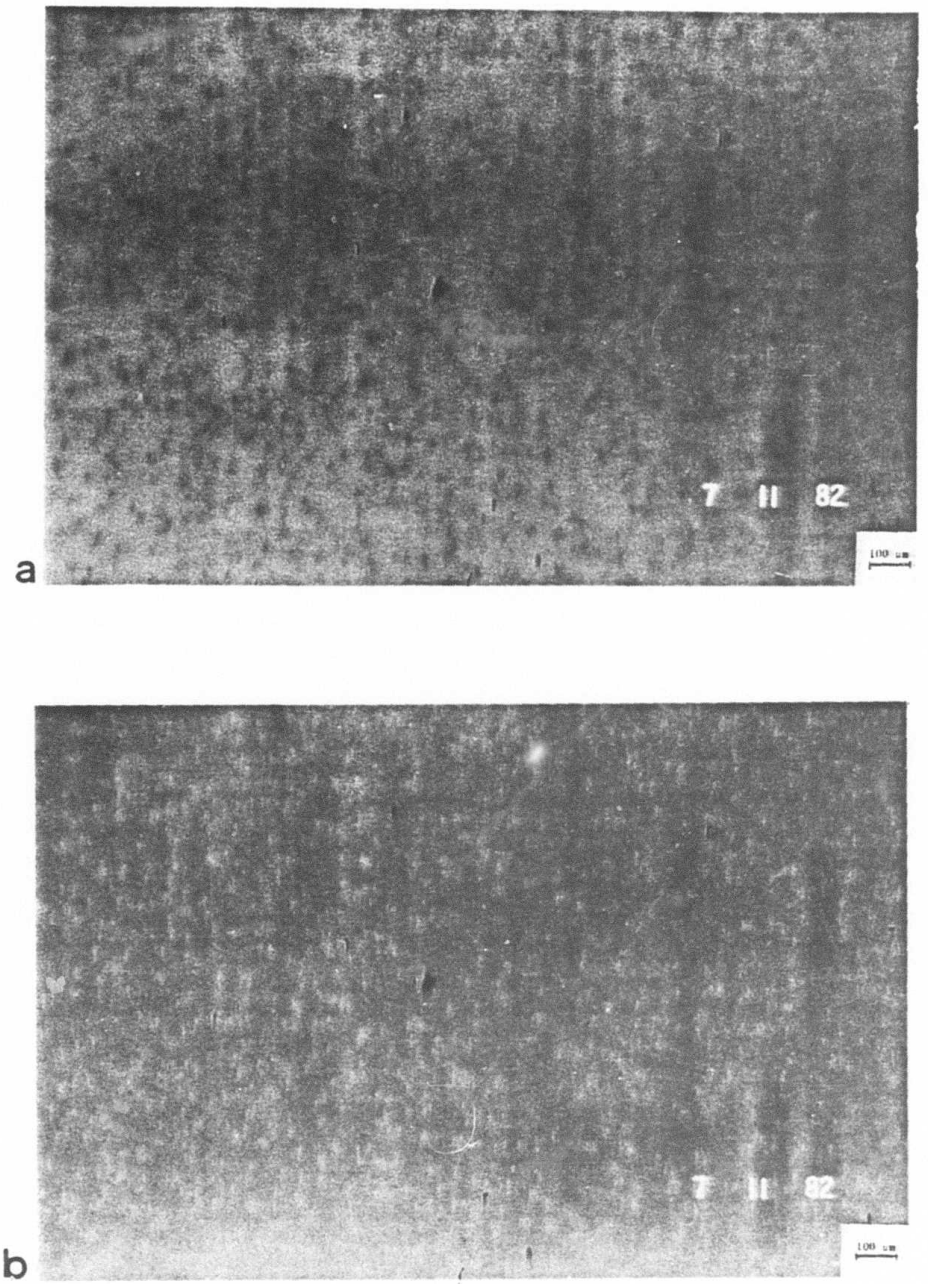


Figure 5.28. Water adsorption in ZrO_2/SiO_2 filter. Sample 760-17-3. New patches appeared one month after the first patches appeared and then disappeared. (a) λ = 547 nm. (b) λ = 554 nm.

layers of the filter. Figure 5.29 shows the wavelength shift measured by spectrometer. The shift again depends on the RH. The adsorption isotherm is of Type IV, as shown in Fig. 5.30, typical of a porous adsorbent adsorbing multilayer of water vapor. The hysteresis shown in Fig. 5.30 is also a typical characteristic of such adsorption systems; the desorption branch lies to the left of the adsorption branch. This may be due to the presence of pores with irregular diameters, for example "ink-bottle pores." In addition, the isotherms may tend to flatten as RH approaches unity.

Since the ZrO_2 and SiO_2 are very chemically stable and high-melting-point materials, the filters can be baked at very high temperature (370° C) in vacuum. Under such treatment, the water was found to desorb but readsorption occurred rapidly when the filters were exposed once again to the air as shown in Fig. 5.31. The patches at this stage were even more blurred than before, indicating that the film structure may be changed during the baking process. This does not happen always as shown by Figs. 5.32 and 5.33, where the wavelength shifted back, and the patch size shrank, after 370° C baking in vacuum. Then, the nonuniform patches in Fig. 5.34 indicate that the optical thickness has now become nonuniform again because the film structure was changed by the baking. Further, the linking of patches after baking, shown in Figs. 5.35 and 5.36 also indicate that the film structure was changed after the baking. Whether the changes are in the ZrO_2 layers or in the SiO_2 layers or inside both is unknown. All one can say is that the baking effect does desorb the water and

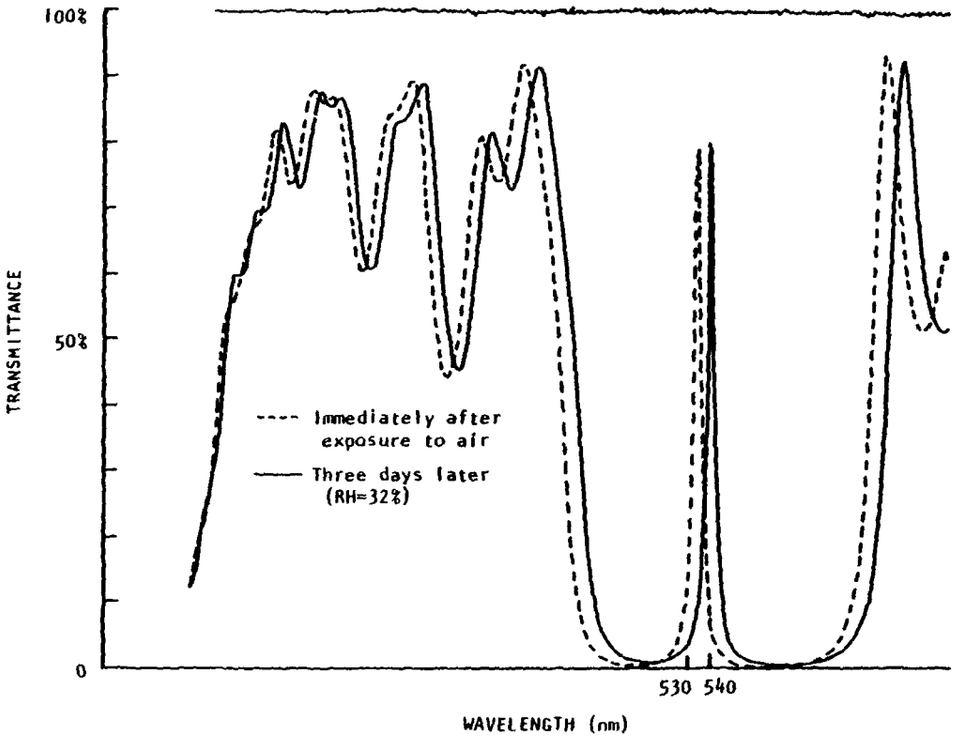


Figure 5.29. The wavelength shift of ZrO_2/SiO_2 filter due to water adsorption (sample 760-21-4, Air/$(HL)^5(6H)(LH)^5$/Glass).

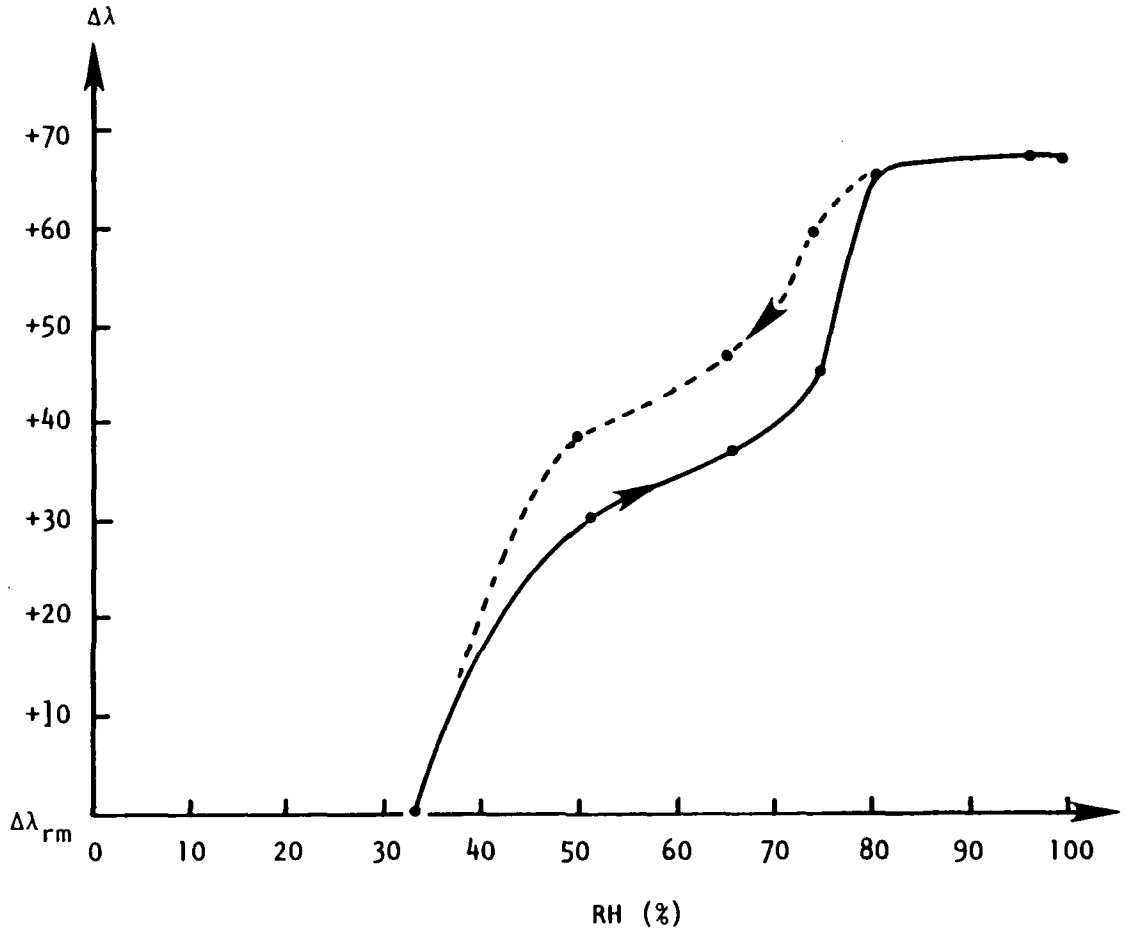


Figure 5.30. Adsorption (——) and desorption (---) isotherms of ZrO_2/SiO_2 narrowband filter of design Air/$(HL)^5 6H(LH)^5$/Glass.

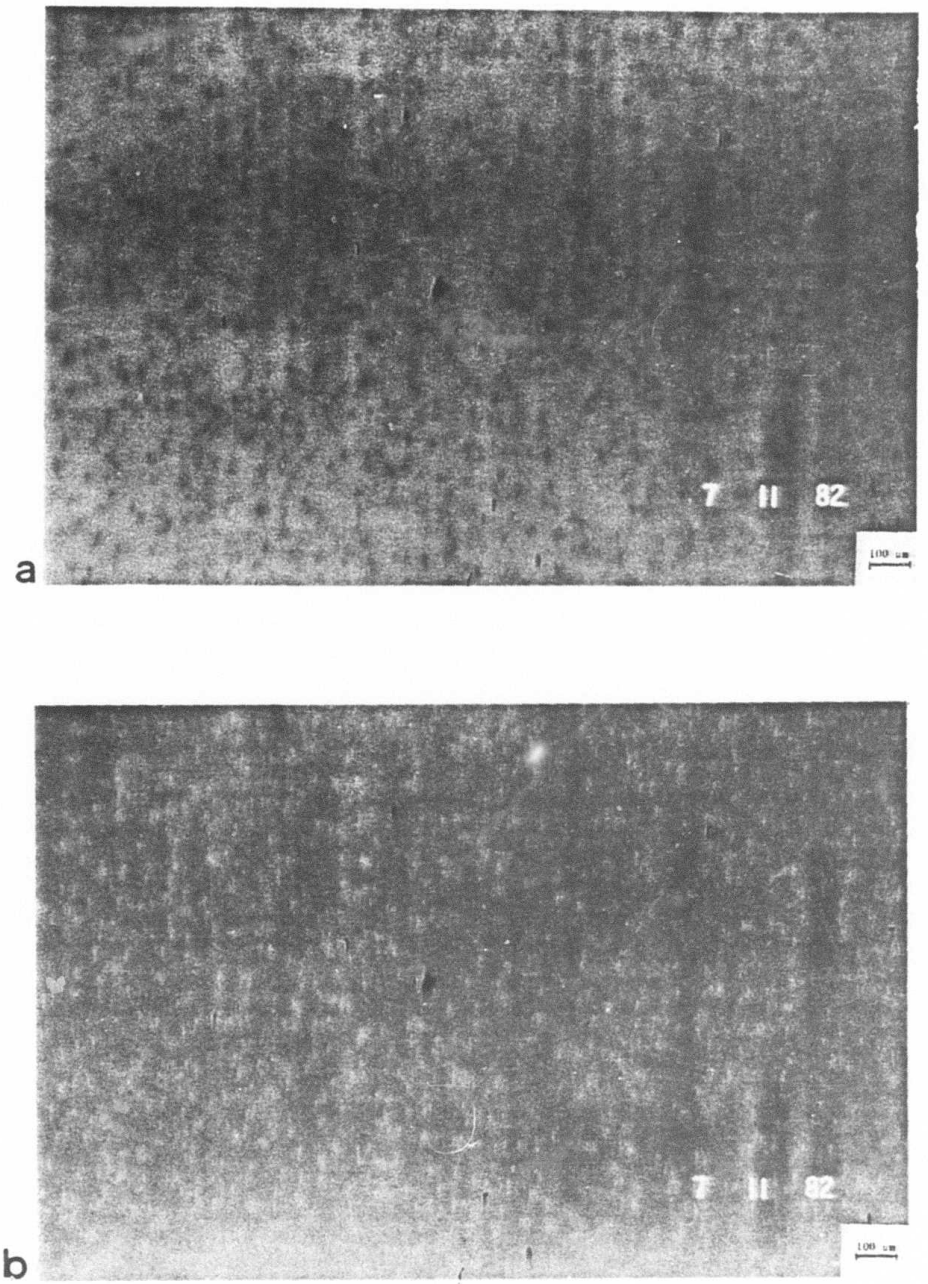


Figure 5.28. Water adsorption in ZrO_2/SiO_2 filter. Sample 760-17-3. New patches appeared one month after the first patches appeared and then disappeared. (a) λ = 547 nm. (b) λ = 554 nm.

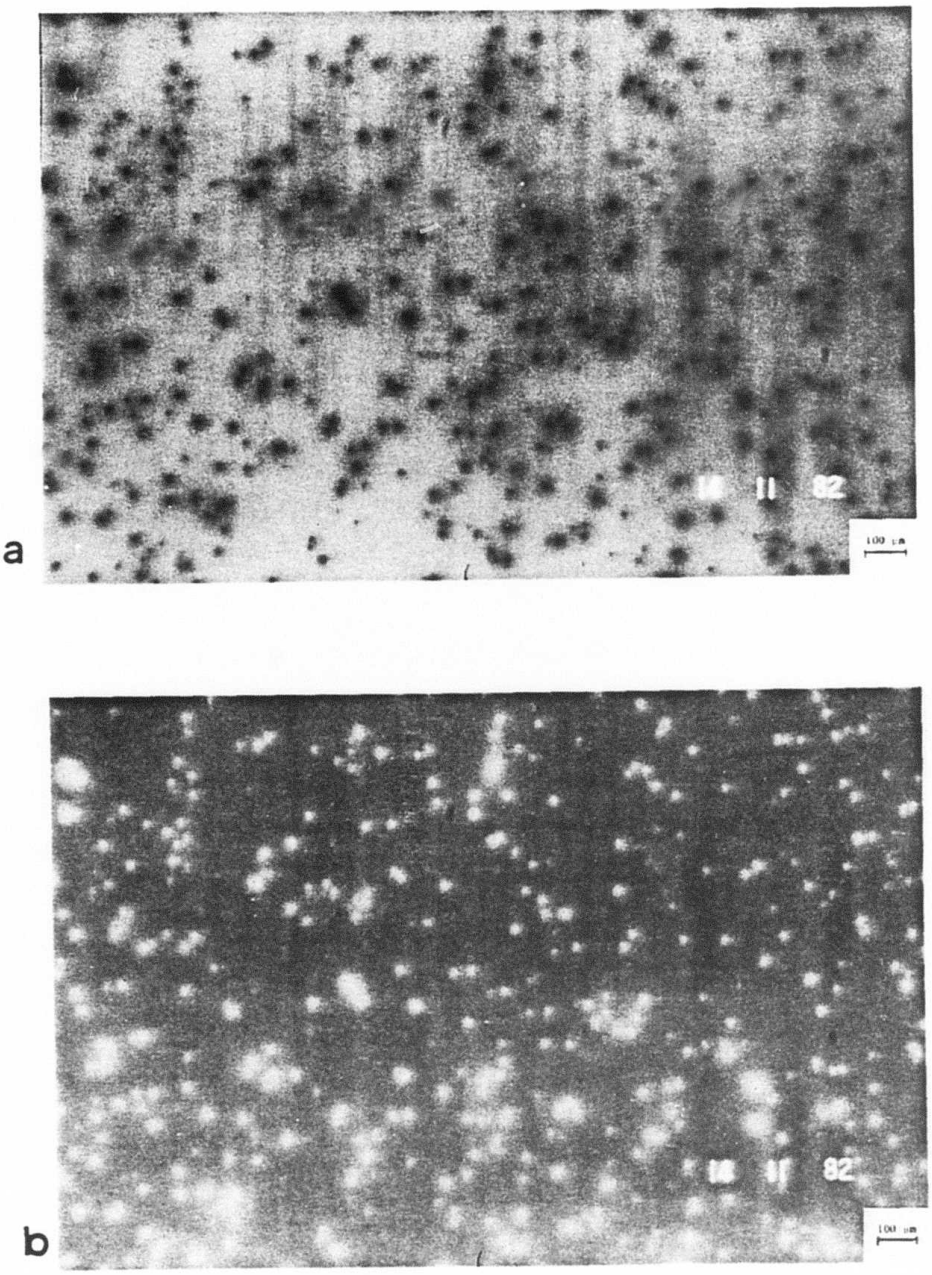


Figure 5.32. Water adsorption in ZrO_2/SiO_2 filter. Sample 760-23-9 a few days after coating and baking. (a) λ = 542.5 nm. (b) λ = 550.5 nm.

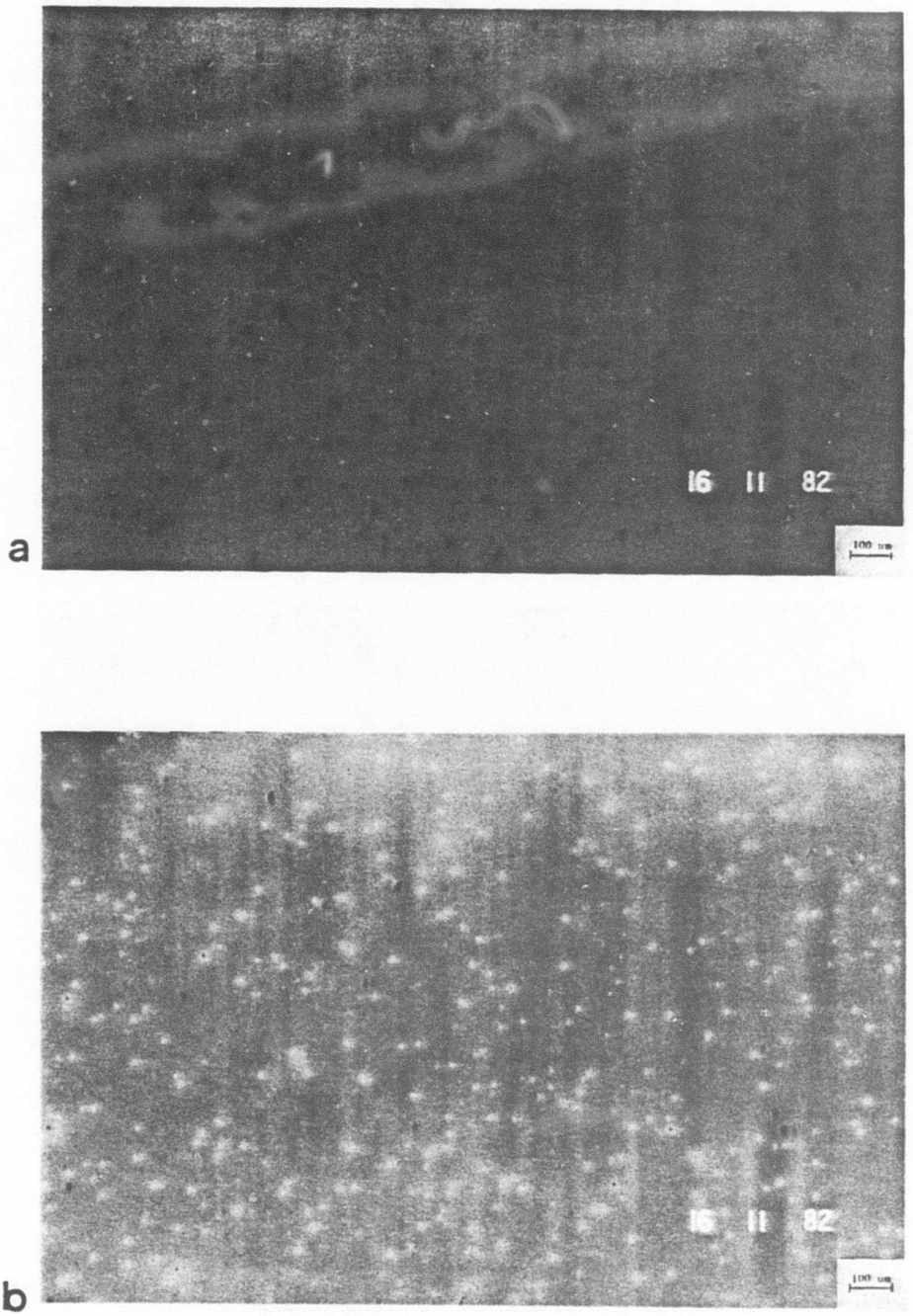


Figure 5.33. Baking of water-adsorbed filter.
Sample 760-23-9 after baking at 370°C for 1.5 hr in vacuum. $\Delta\lambda_{ad}$ = 40Å. $\Delta\lambda_{bk}$ = -20Å.
(a) λ = 539.5 nm. (b) λ = 545.5 nm.

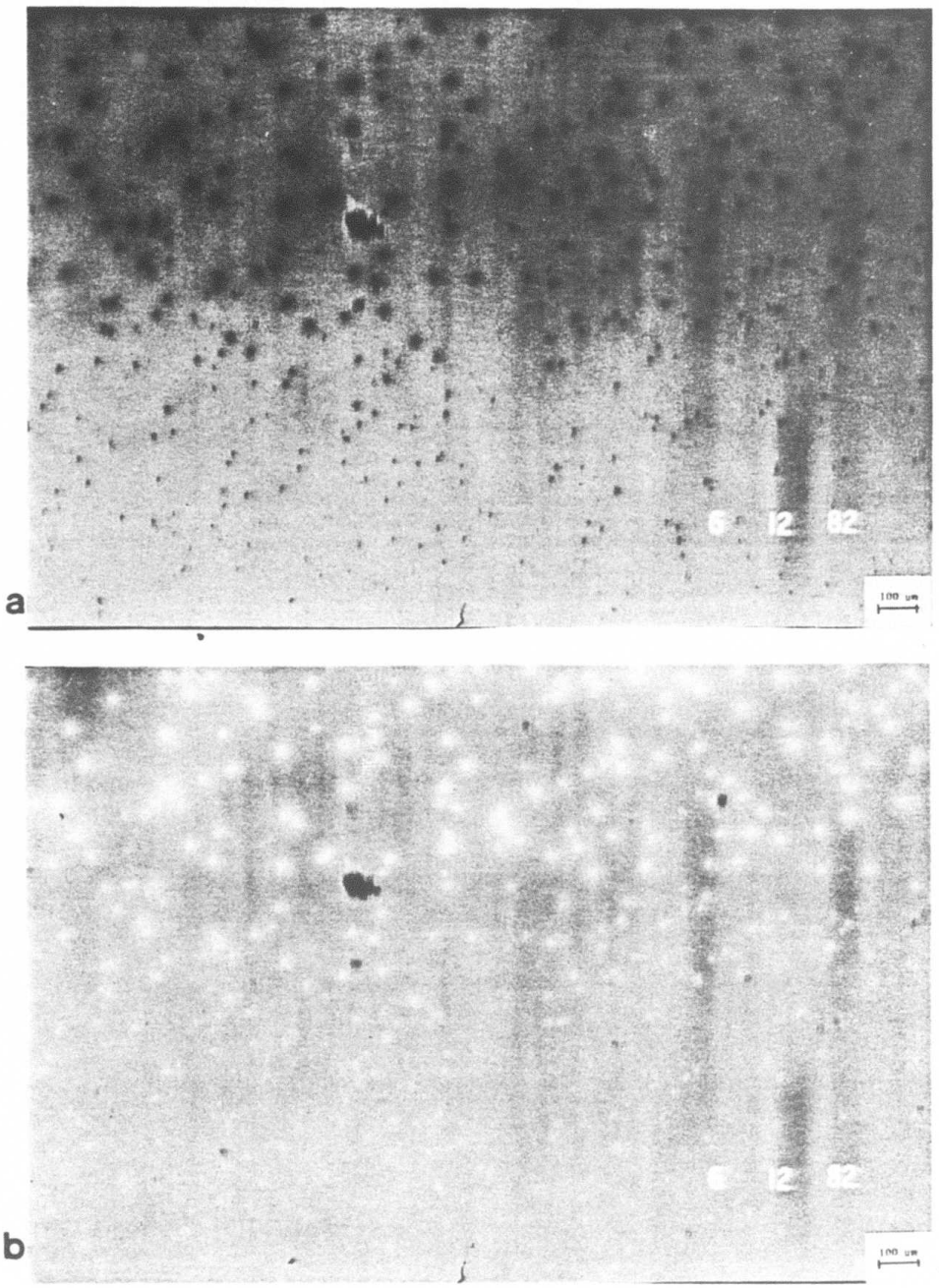
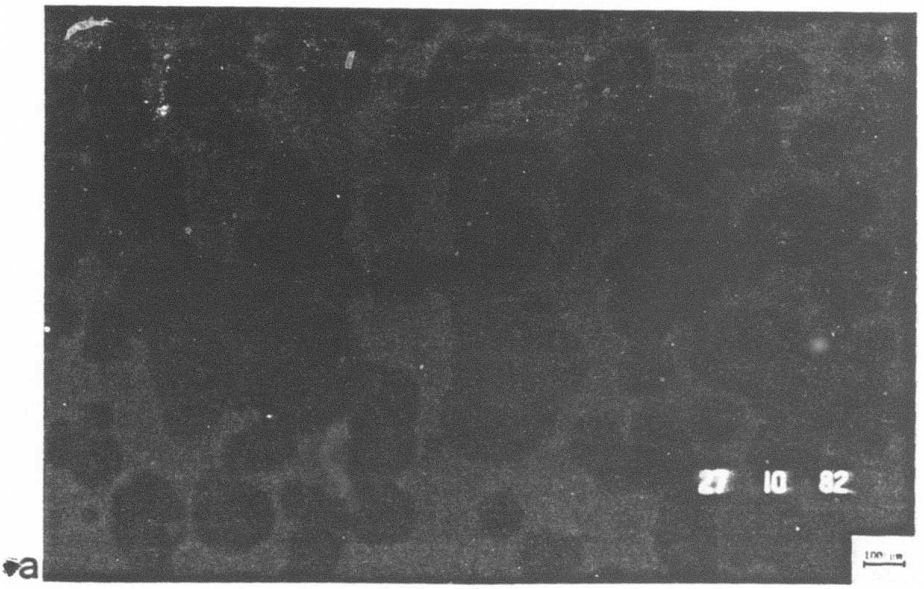
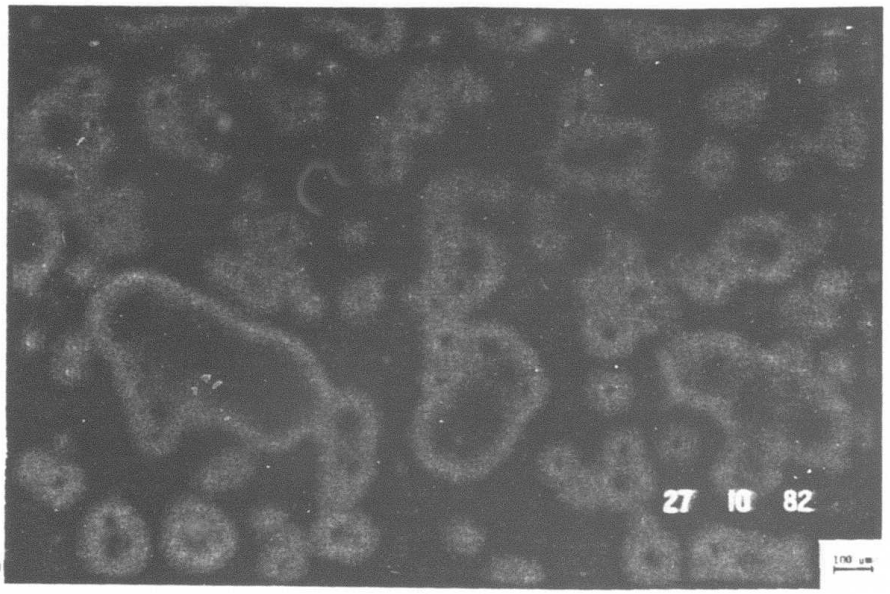


Figure 5.34. Effect of baking on filter. Sample 76-26-1B shows a nonuniformity after baking at 370°C for 1.6 hr in vacuum. (a) λ = 557.5 nm. (b) λ = 565.5 nm.



a



b

Figure 5.35. Effect of baking on filter. Sample 760-21-5 after sitting in 66% RH for 45 hr, $\Delta\lambda_{ad}$ = 25Å. After baking at 370°C for 1.5 hr in vacuum, $\Delta\lambda_{bk}$ = -337Å. After the baking the patches grew much faster. RH_{air} = 41%.
(a) λ = 515 nm, 10 min after coating.
(b) λ = 522 nm, 12 min after baking.

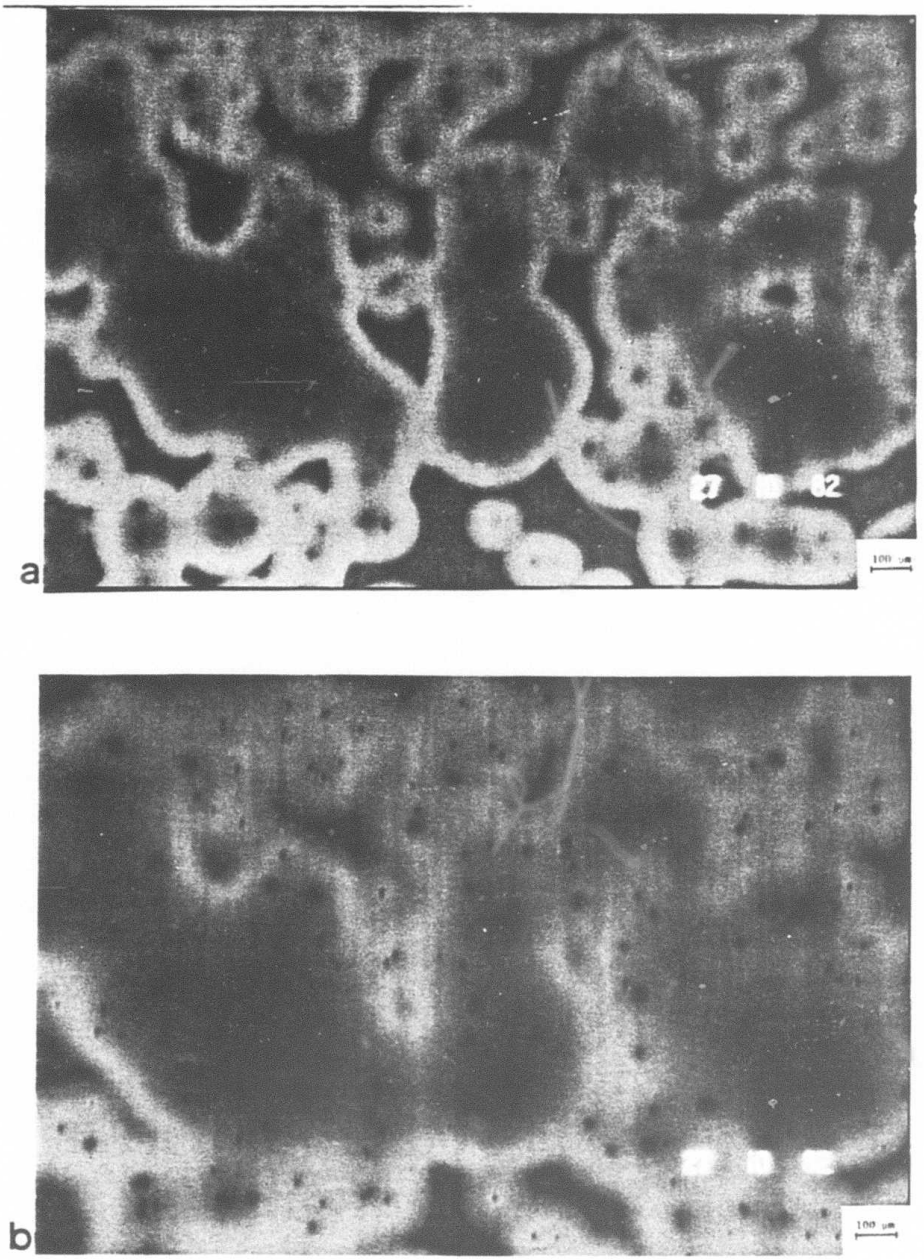


Figure 5.36. Effect of baking on filter. (a) λ = 421.2 nm, 20 min after baking. (b) λ = 522.8 nm, 25 min after baking. Note the increased rate of spreading of patches after baking.

sometimes will change the state of mechanical equilibrium of the film column (Macleod, 1981; Macleod, 1978).

Moisture and Adhesion Failure

Most of the zinc sulfide/cryolite filters showed peeling during the Scotch tape test after water adsorption, except at low RH. The reason is the chemical reaction between cryolite and water, which reduces the mechanical strength across the interface. Films usually peeled off only a few layers at a time. Cracks were also found after water adsorption at RH greater than 81% (Fig. 5.37). This is due to the recrystallization of cryolite which introduces new stresses.

No adhesion failures were found for ZrO_2/SiO_2 filters, because when metals which form oxides are deposited on glass, a transition region of oxides is established between the substrate and the film which greatly enhances the adhesion (Chopra, 1969; Eckertova, 1977).

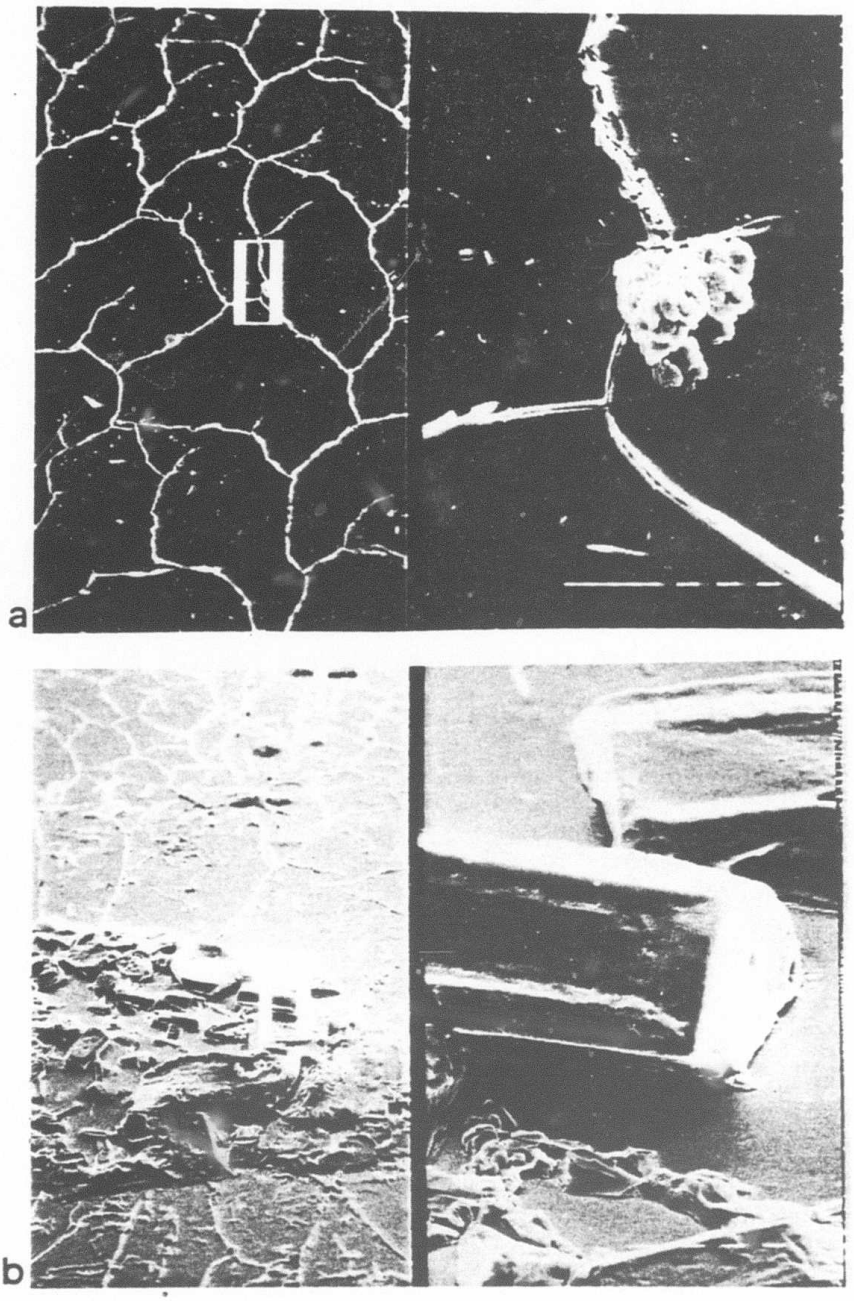


Figure 5.37. Cracking and recrystallization of ZnS/Na_3AlF_6 filter. (a) After strong adsorption of water vapor (100% RH), 120X/1200X, tilt 50°. (b) Corroded by NaCl, 40X/400X, tilt 50°.

CHAPTER 6

PREVENTION OF ADSORPTION IN COATING FILMS

One can stop the coating film from adsorbing water by putting a protective layer or cover plate over the coating. This is a passive cure and will be discussed at the end of this chapter.

The active cure for water adsorption in films is to make the films less porous, or in other words, to increase high packing density. Before discussing how to make high packing density films, it is useful to look at the factors which may cause films to be porous. The technique used in the previous chapters is a good method for investigation. The appearance of the patches indicates where there is water adsorption in the films and shows where the films are more porous, or where there are defects.

Dust, Substrate Surface Defects, and Adsorption

In the previous chapters, much of the investigation has centered on the precise nature of the sites through which moisture enters the multilayer. The distribution of patches is nonuniform and the number is sufficiently small when compared with the size range of the grains of the coating (20 to 60 nm) that we can be certain that the normal microstructure of the coating is not the primary cause. The most likely cause is some type of defect. Therefore, defects of different kinds were deliberately introduced and their effect on the

incidence of penetration sites was assessed. Deliberately roughened substrates were made either by sandblasting (Figs. 6.1 to 6.3 with details of the sandblasted surfaces in Figs. 6.4 and 6.5) or by simple scratching (Fig. 6.6). Both showed greatly increased incidence of patches. Aluminum oxide dust was deliberately introduced on a substrate and showed similar effects (Fig. 6.7). In this case, simultaneous dark field illumination of the filter surface in reflection and normal monochromatic illumination in transmission show the dust particles in the center of the patch which must therefore play an important part in creating defects (Fig. 6.8). Some micrographs of the dust are shown in Fig. 6.9.

On the other hand, Fig. 6.10 shows that the patch density is much less for a superpolished substrate when compared with the regular substrate with more surface defects. Figures 6.11 and 6.12 show how such a filter adsorbs moisture. In Fig. 6.12 one observes that the texture of the patches is finer and the boundary of the patches is rounder compared with the regular substrate filter (Fig. 6.13).

Computer Simulation of Film Growth

Much has been learned about layer microstructure from simple computer simulations of film growth. A successful model that reproduces many of the features of the microstructure uses a two-dimensional approximation in which the condensing molecules are represented by circles arriving randomly at a fixed angle of incidence corresponding to the source direction (Dirks and Leamy, 1977). The

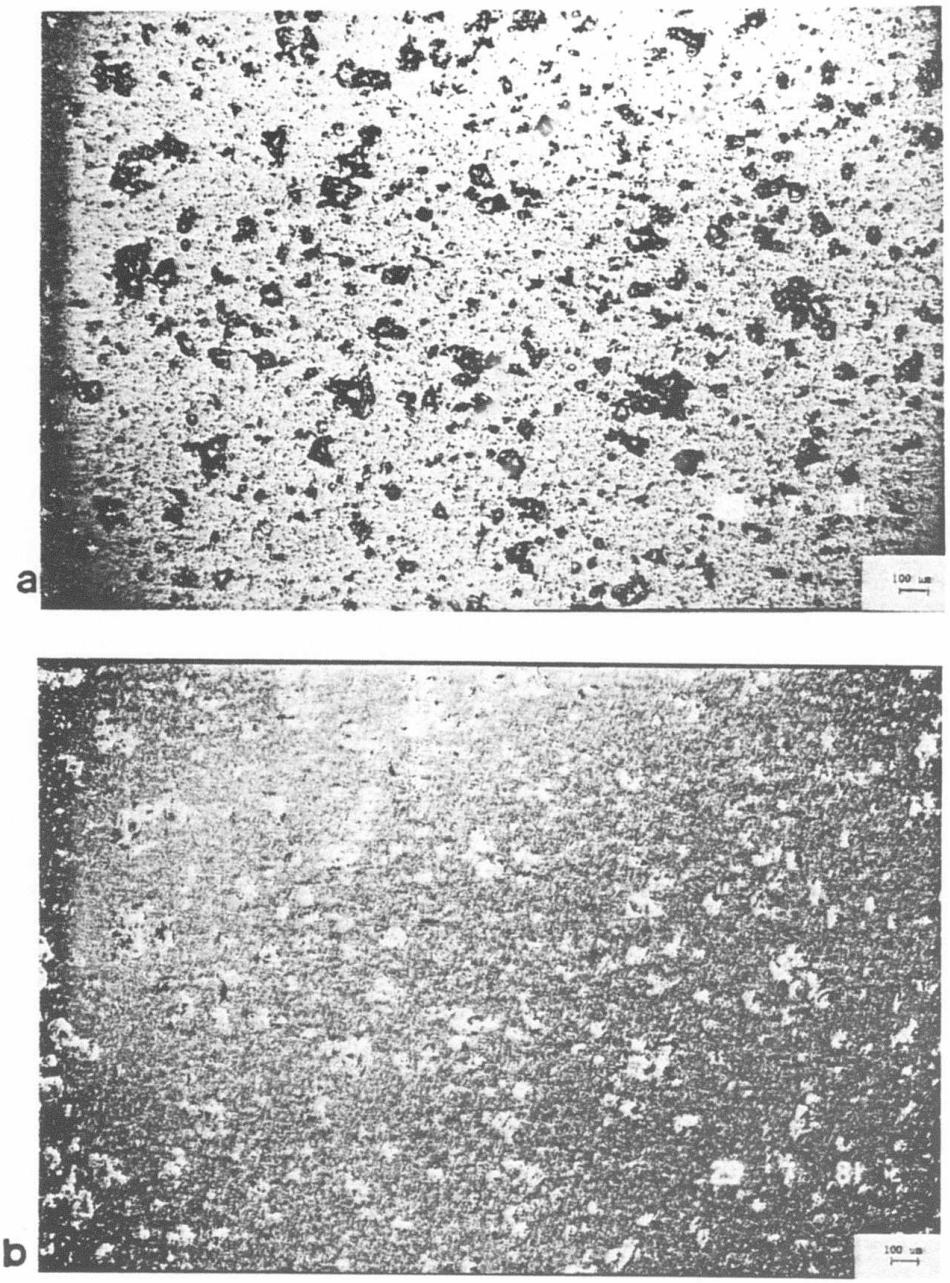


Figure 6.1. Water adsorption in ZnS/Na_3AlF_6 filter with sandblasted substrate (very rough surface). (a) λ_d = 440 nm, (b) λ_b = 540 nm.

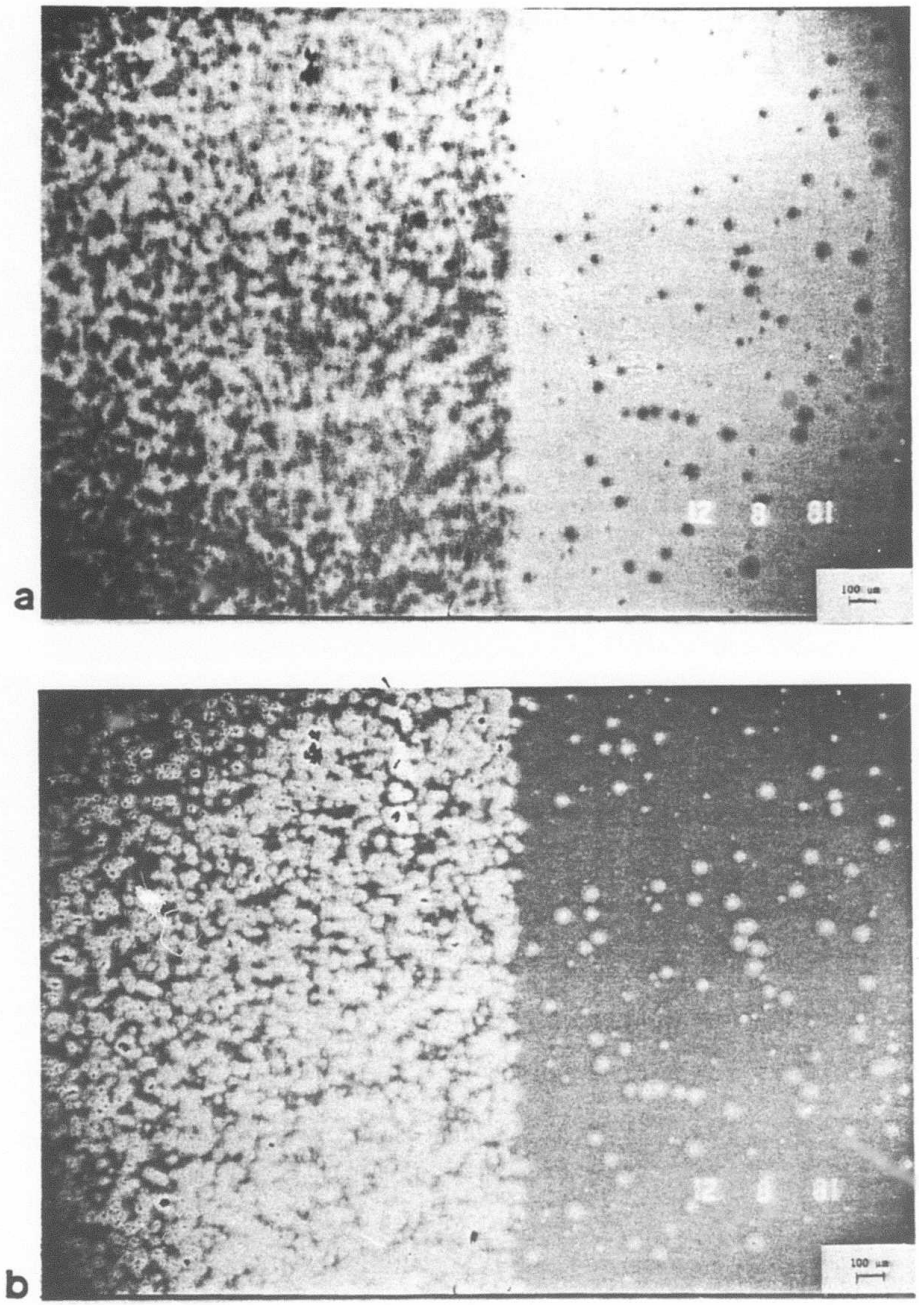


Figure 6.2. Water adsorption in ZnS/Na_3AlF_6 filter. Left side of photos is with sandblasted substrate, right side is without sandblasting.
(a) λ_d = 471 nm, (b) λ_b = 494 nm.

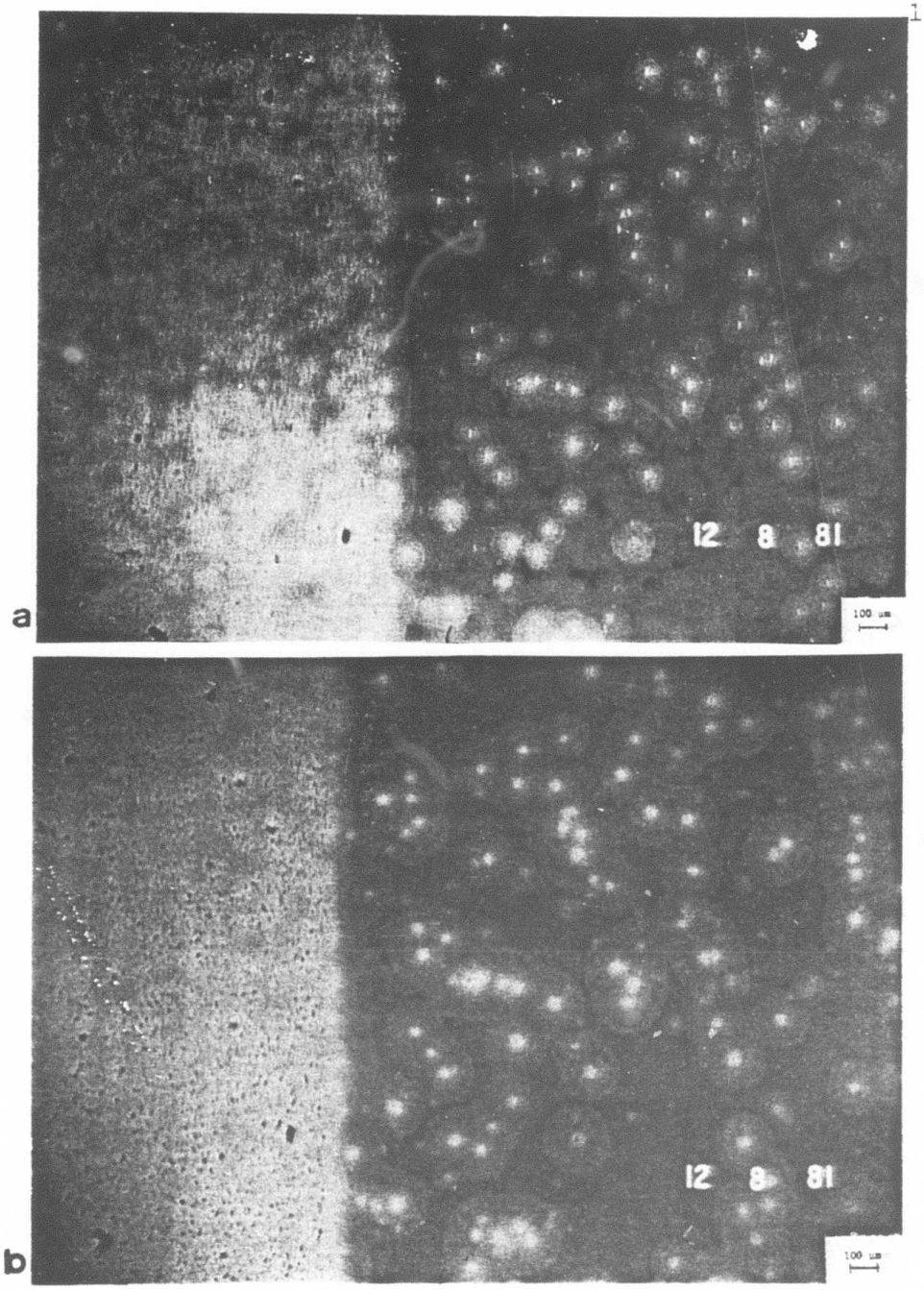


Figure 6.3. Water adsorption in ZnS/Aa$_3$AlF$_6$ filter. Left side of photographs is with sandblasted substrate and right side is without sandblasting. (a) After 50 minutes, (b) after 150 minutes.

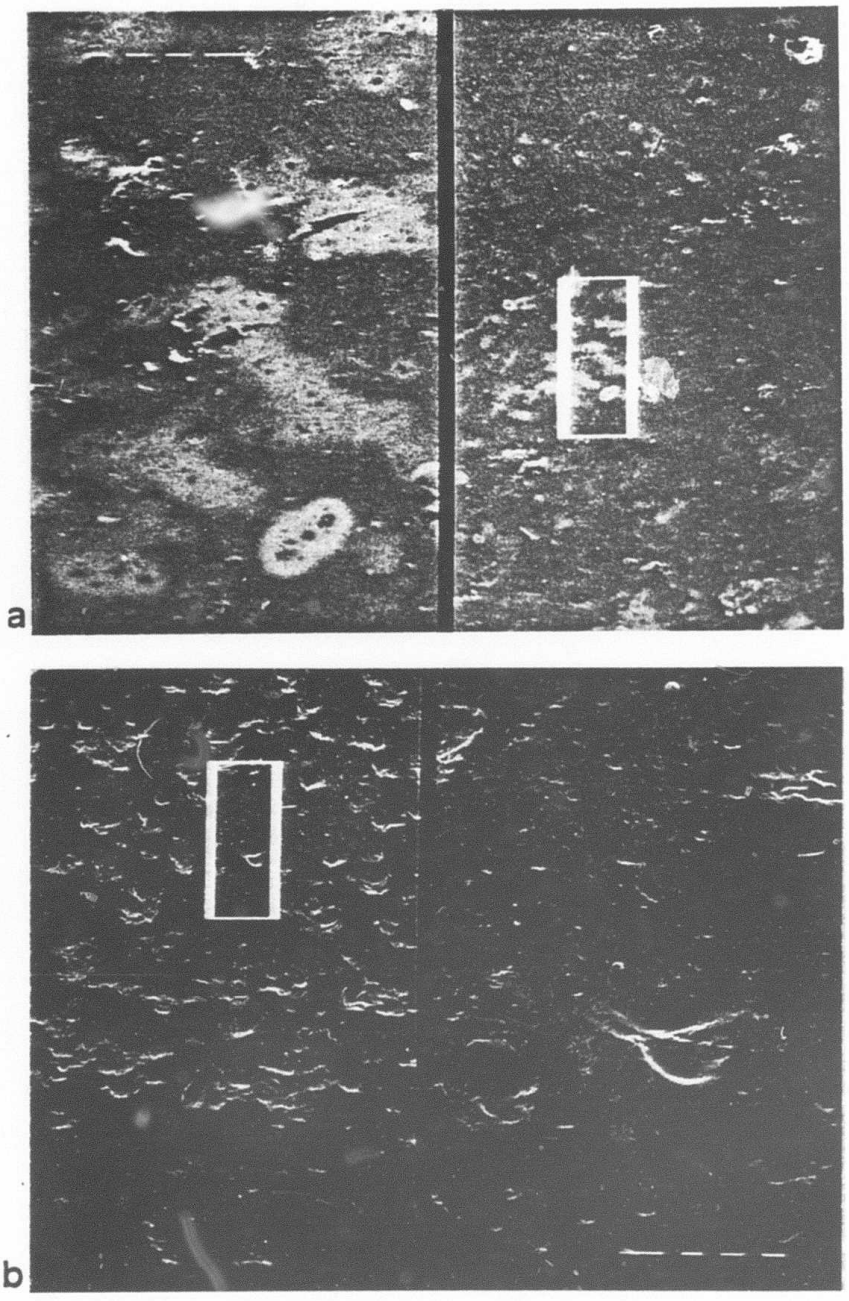


Figure 6.4. SEM photograph of sandblasted substrate.

(a) Water adsorption of film on substrate, tilt 40°, 50X/250X. (b) Very rough surface, tilt 40°, 50X/250X

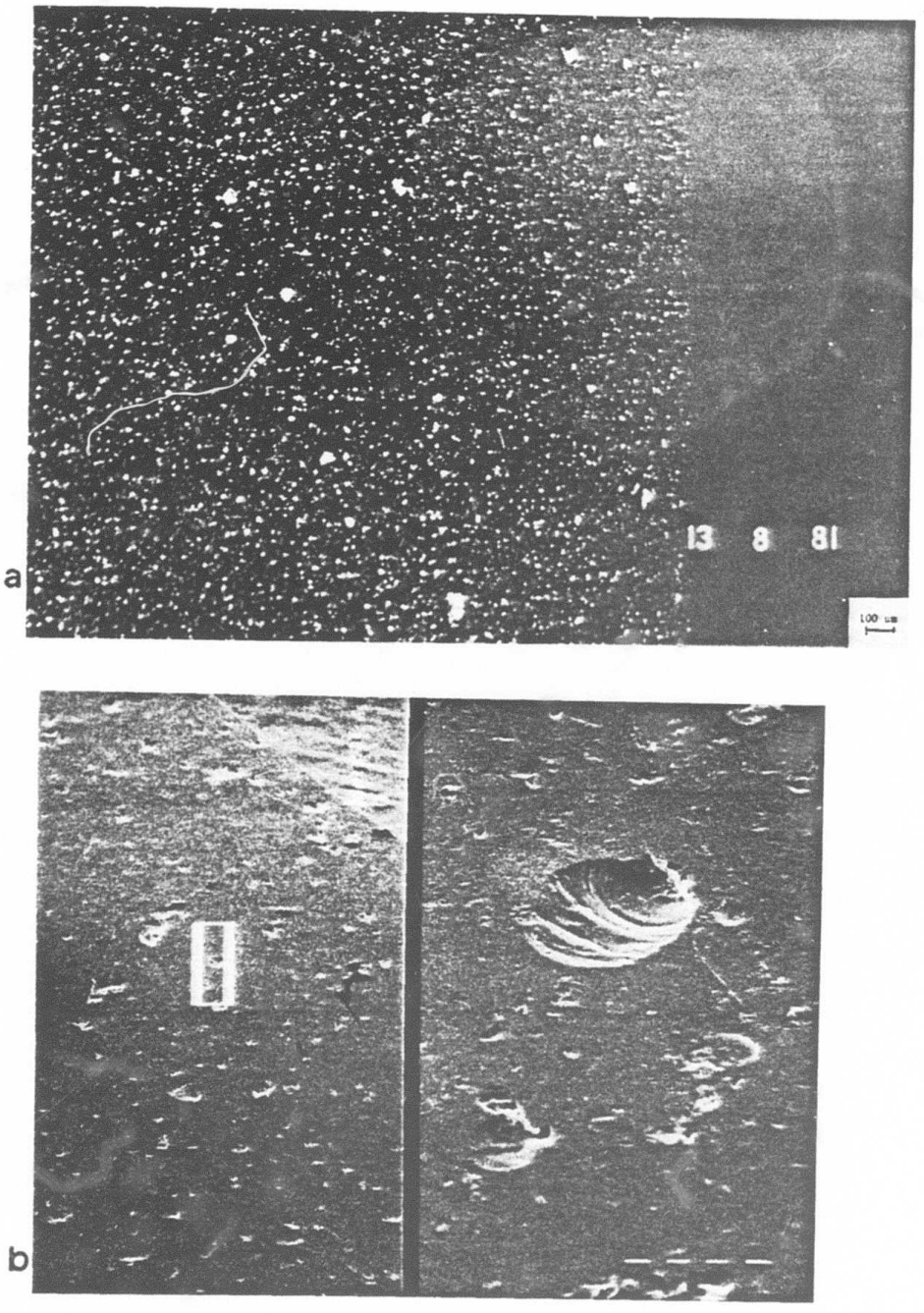


Figure 6.5. Sandblasted substrate.
(a) Light scattering from surface, (b) SEM of substrate, tilt 40°, 25X/250X.

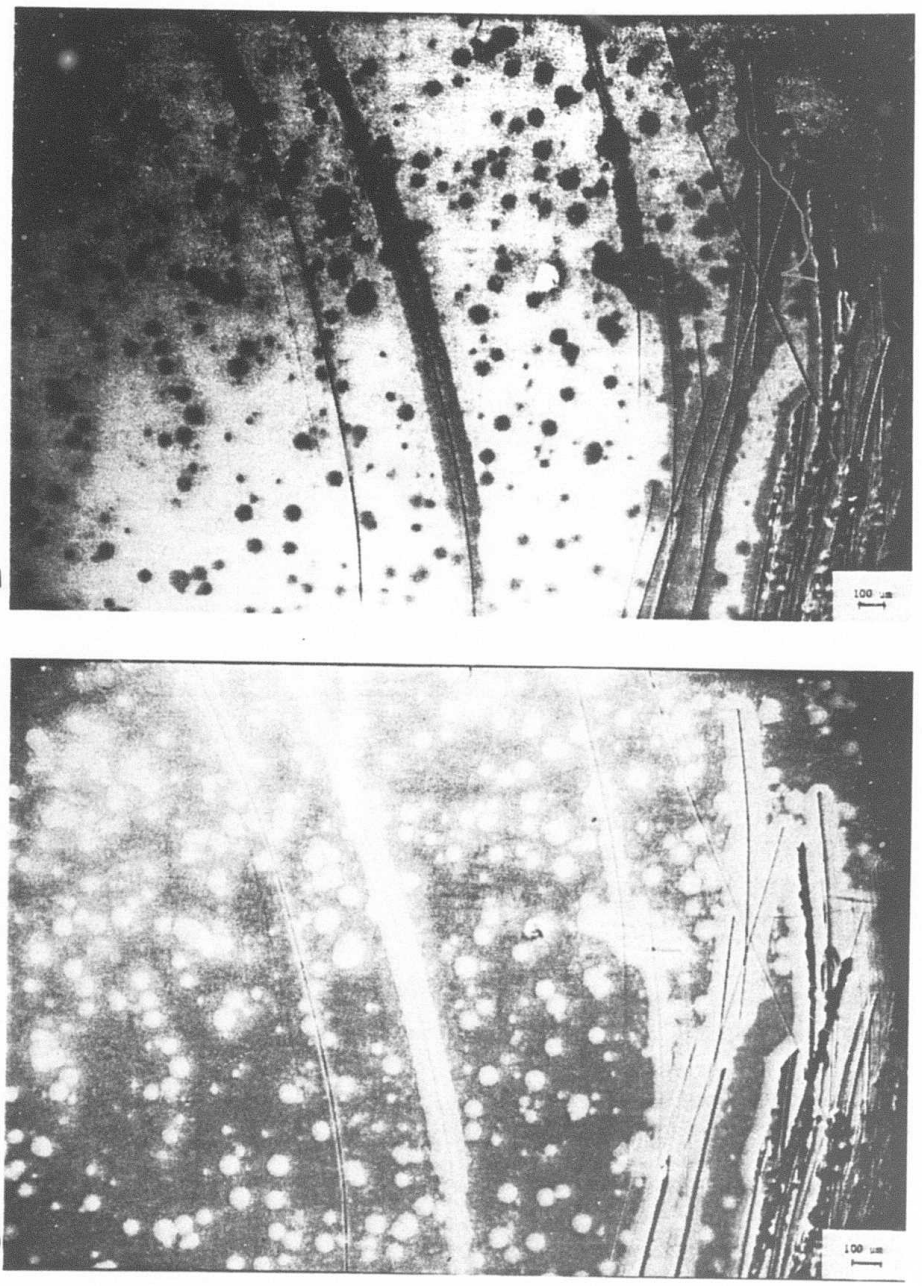


Figure 6.6. Water adsorption in ZnS/Na_3AlF_6 filter. Substrate scratched by sandpaper before coating. Any defect in the substrate will appear at the center of the patch.

RH = 100%. (a) λ_d = 472 nm, (b) λ_b = 497.5 nm.

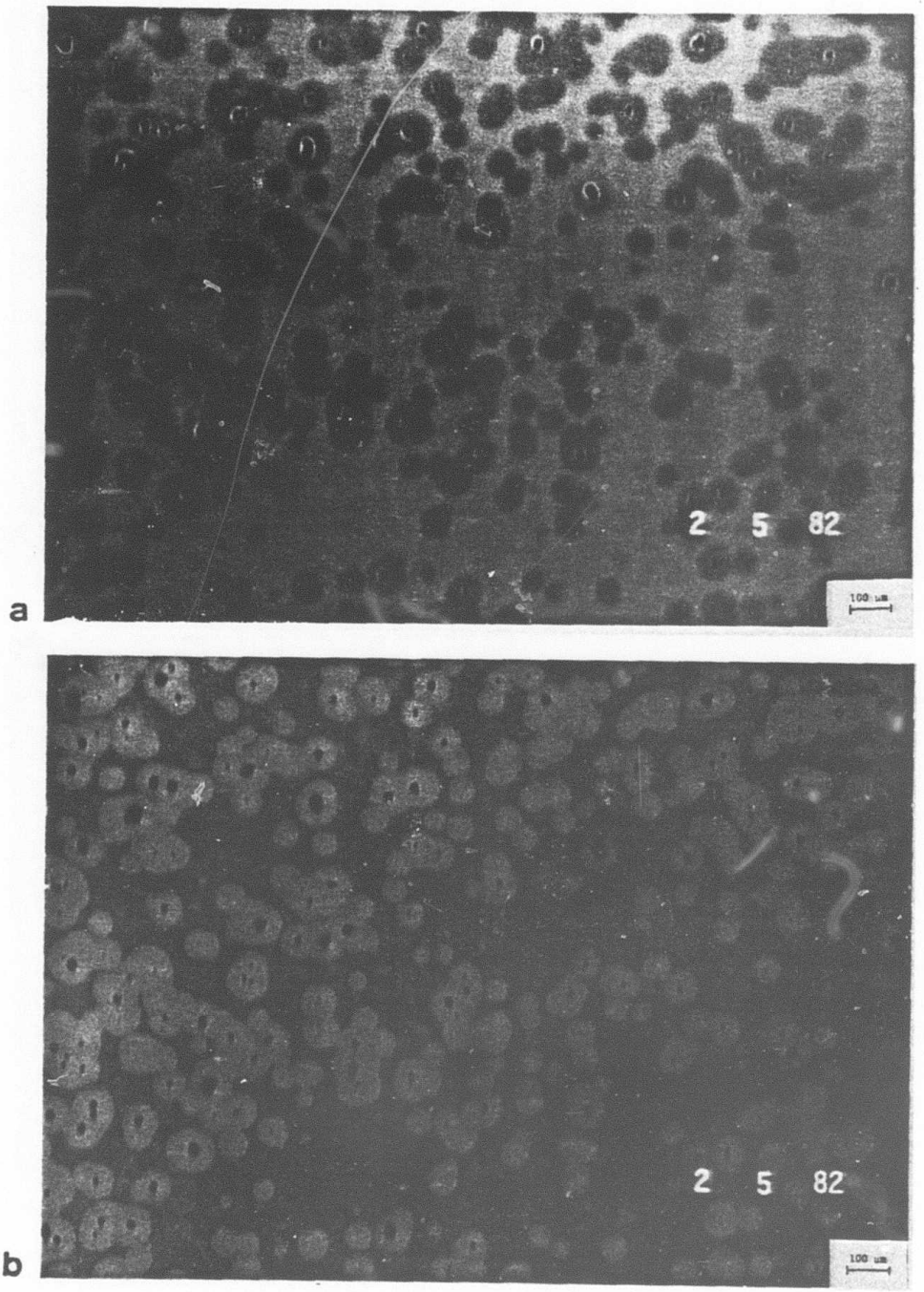


Figure 6.7. Water adsorption in filter, RH = 43%. Aluminum oxide dust intentionally put on substrate.
(a) λ_d = 505.6 nm, (b) λ_b = 510.2 nm.

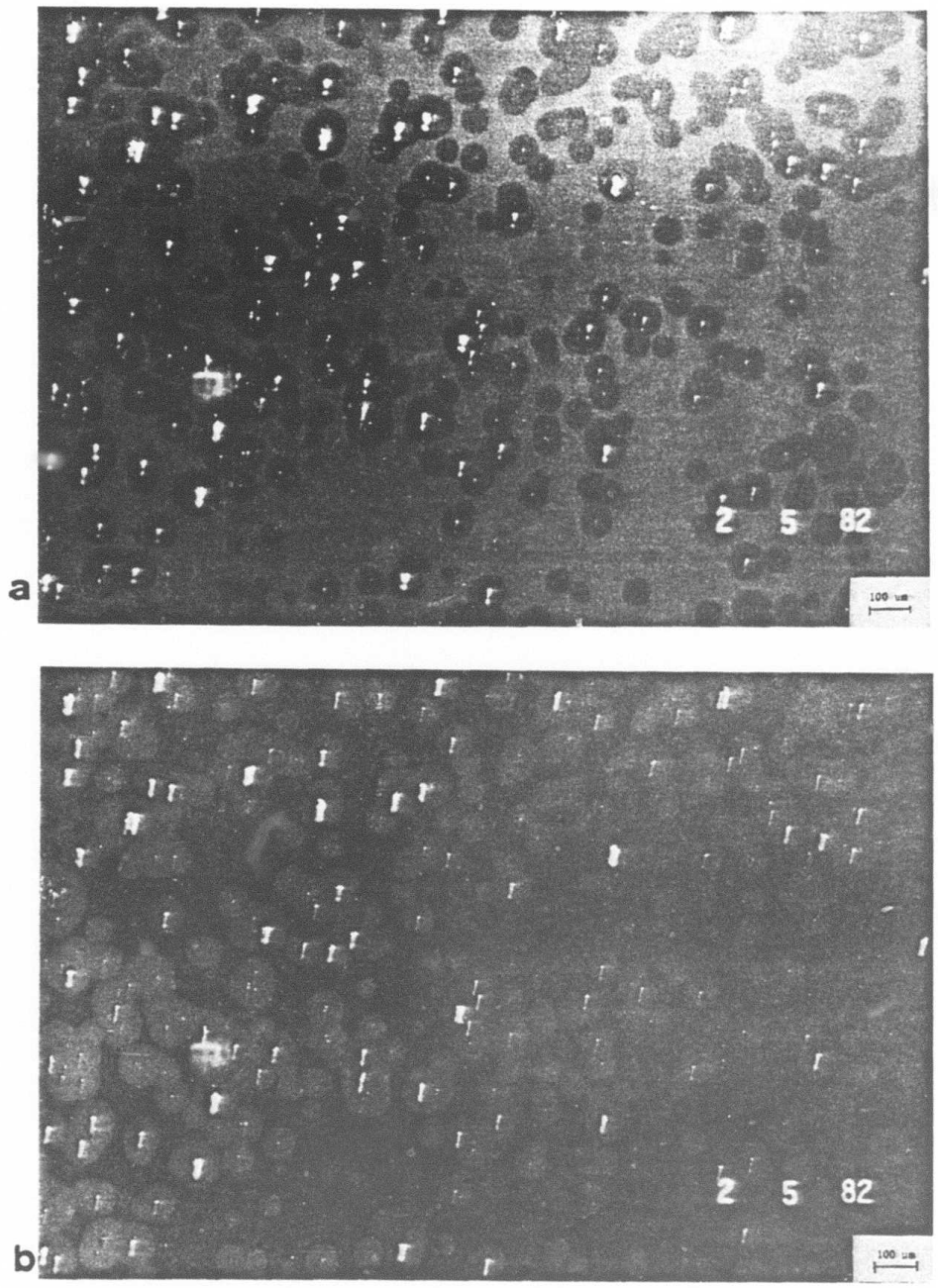


Figure 6.8. Scattered light shows the positional relation between dust and patch. Back shining light of wavelength λ plus 60° front scattering light.

(a) λ = 505.6 nm, (b) λ = 510.1 nm.

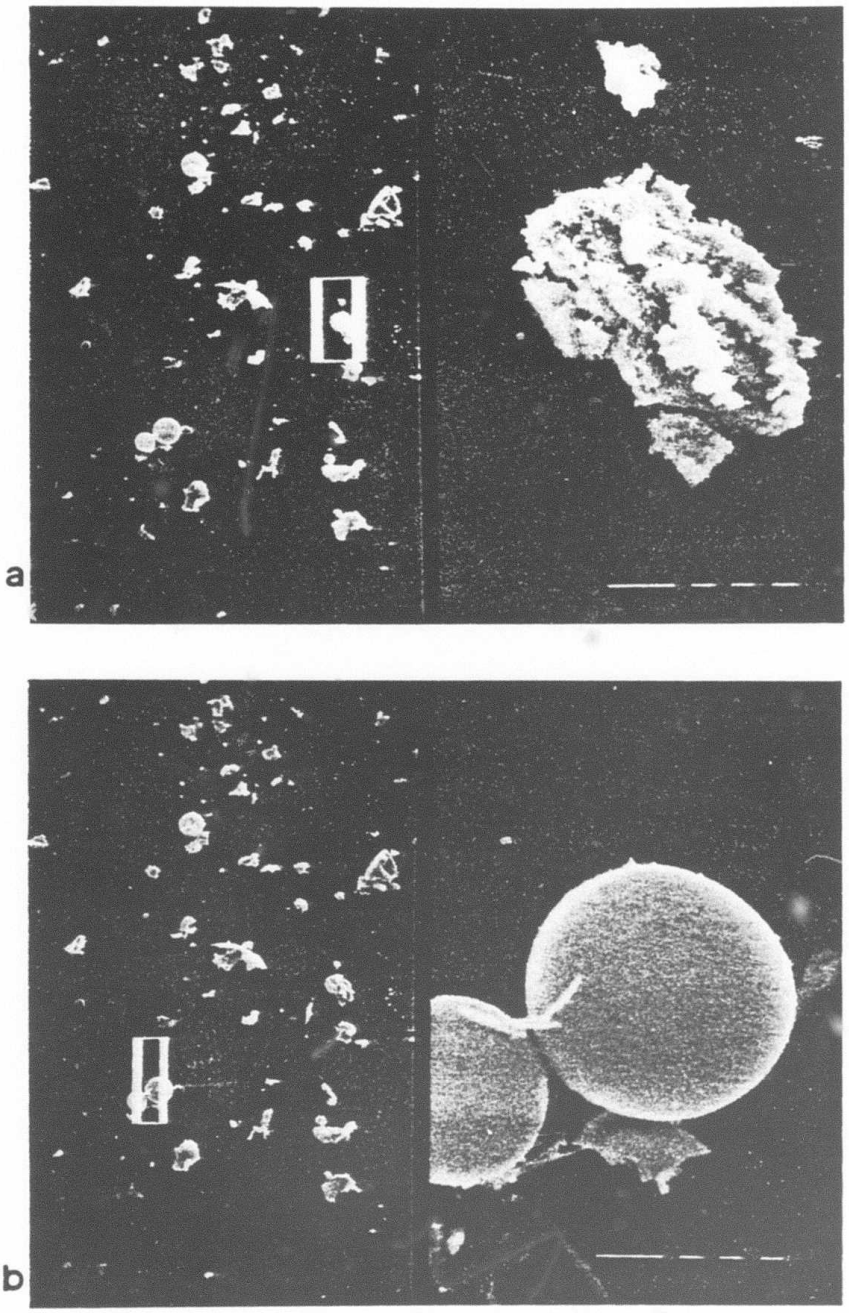


Figure 6.9. Aluminum oxide intentionally dusted on substrate (by scanning electron microscope, tilt 30°, 80X/800X).

(a) Irregular particle, (b) spherical particle.

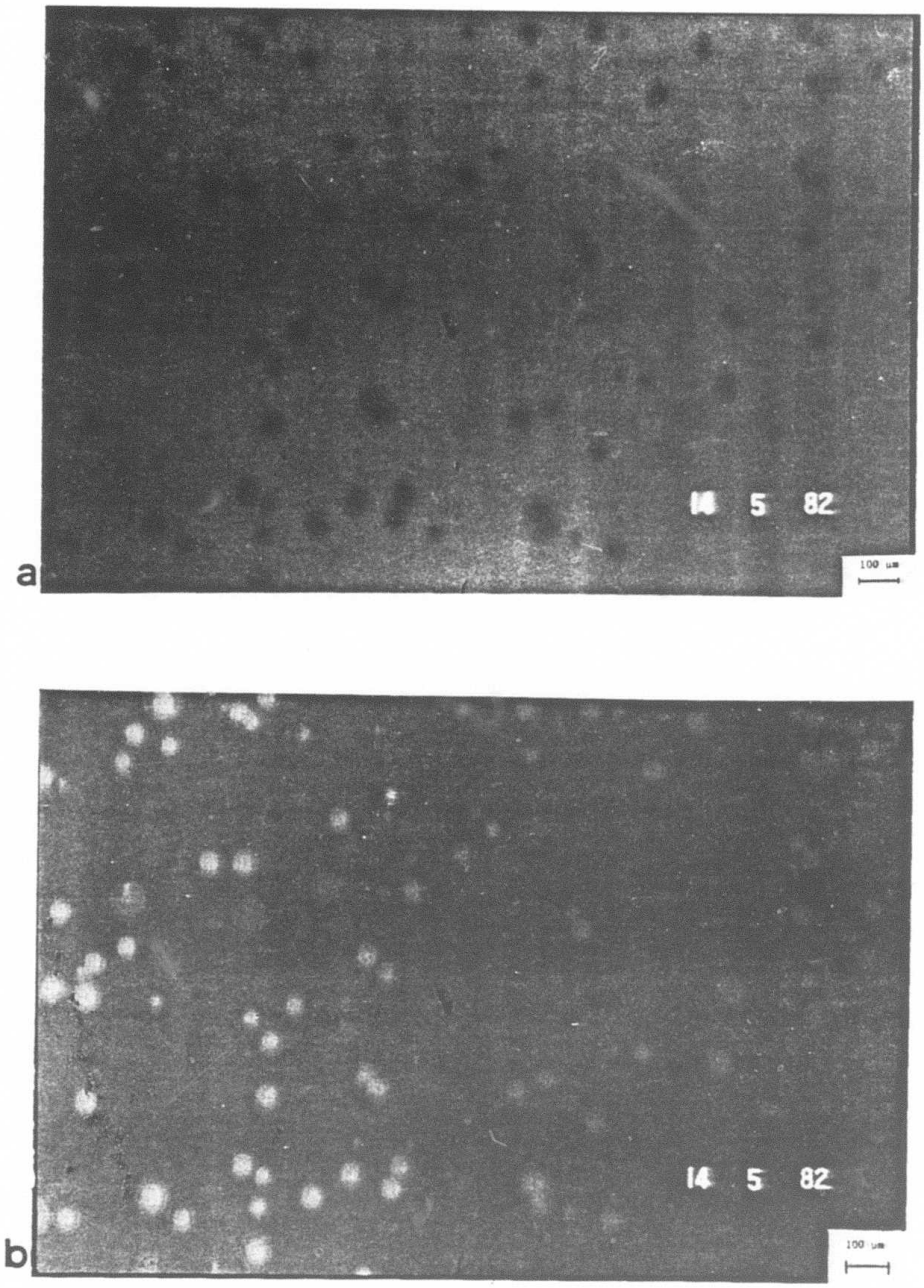
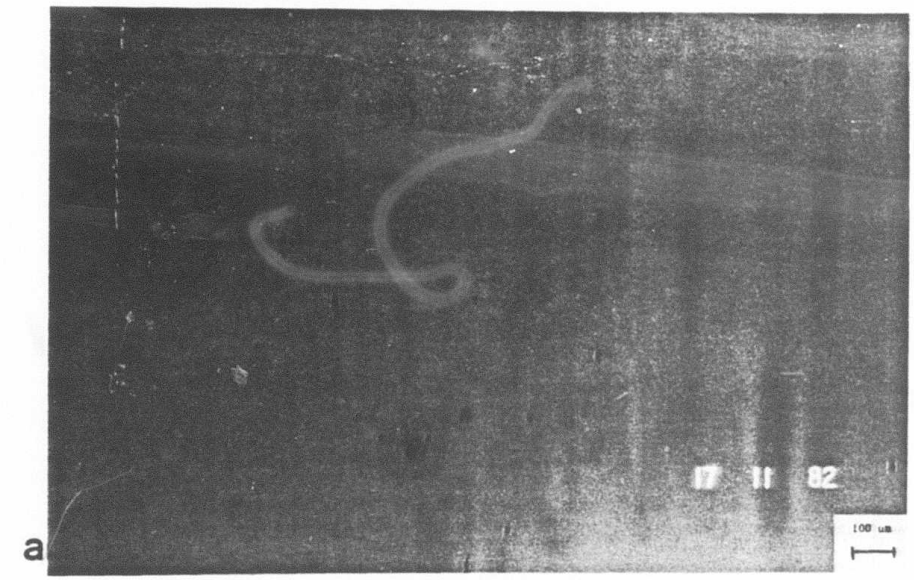
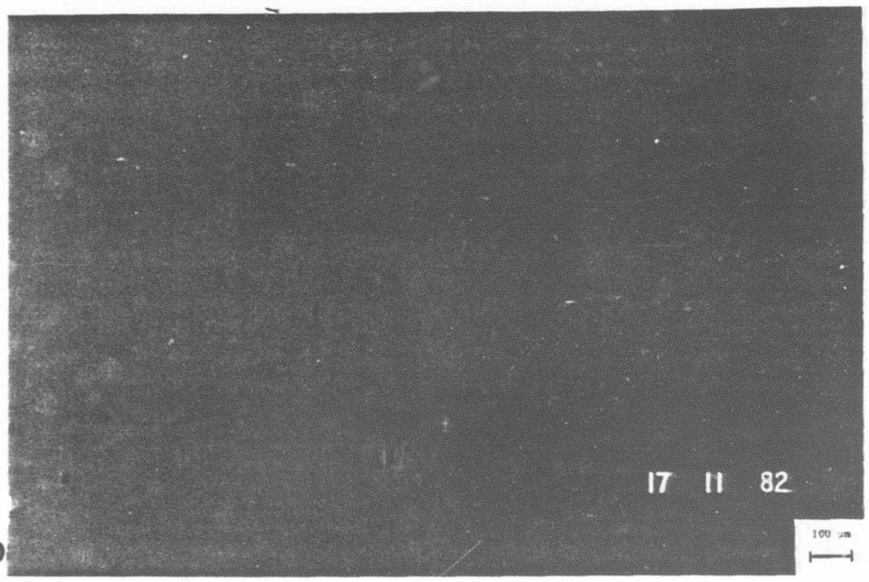


Figure 6.10. Sample D-23-1. Superpolished substrate. Note reduced density of patches when compared with a regular substrate. RH = 51%. (a) λ = 516.5 nm. (b) λ = 510.5 nm.



a



b

Figure 6.11. Sample D-23-3. Superpolished substrate. The sample was stored in desiccator for 6 months. (a) λ = 507 nm. (b) λ = 511 nm.

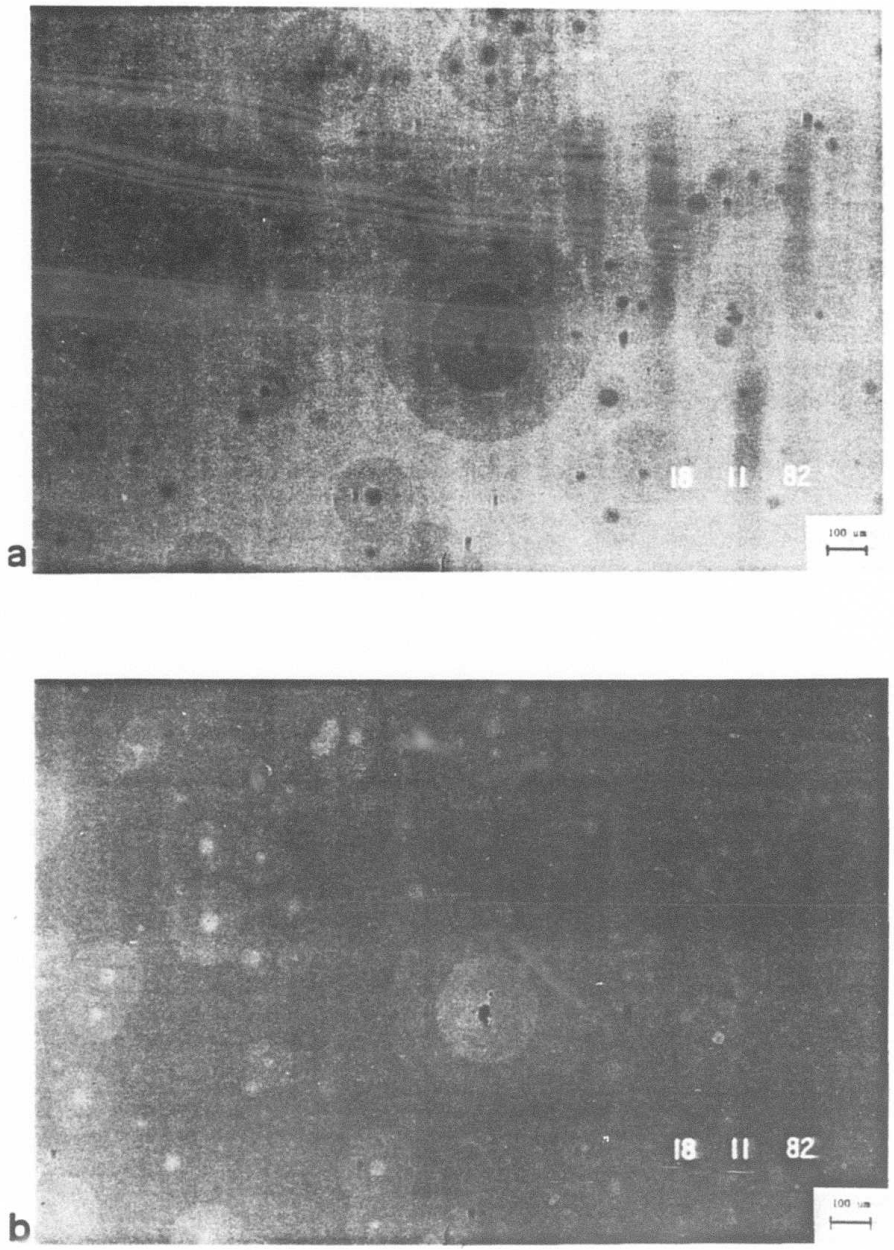


Figure 6.12. Sample D-23-3. Superpolished substrate 1 day after removal from the desiccator where the sample was stored for 6 months. (a) λ = 514 nm. (b) λ = 517 nm.

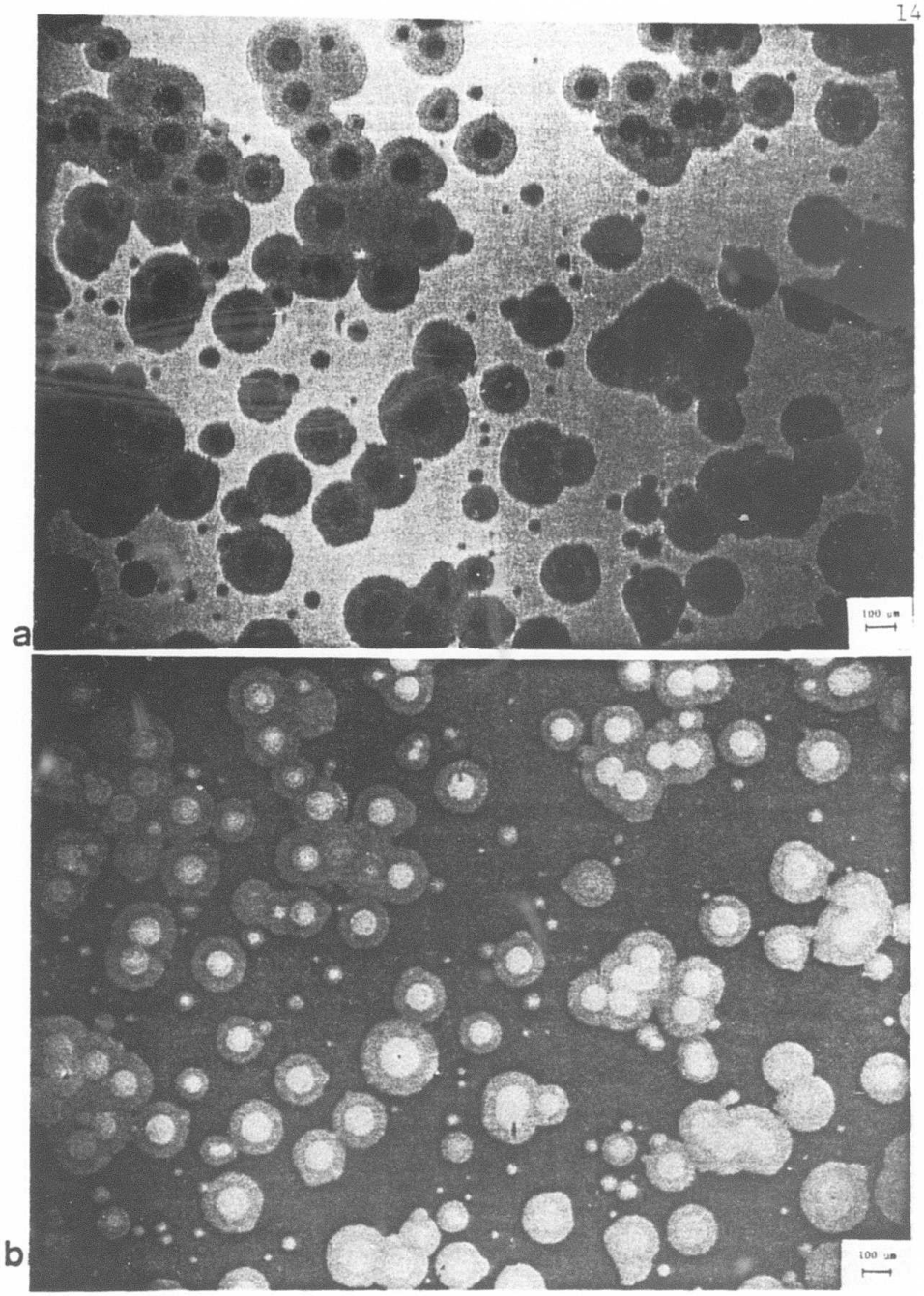


Figure 6.13. Sample D-3-1. Moisture adsorption in a filter on a regular microscope slide substrate. (a) λ = 484 nm. (b) λ = 508 nm.

molecules either have zero mobility, so that they stick where they land, or limited mobility in which case they roll into the nearest position where they are supported on two points (three if they were spherical). The results support the theory that the columnar structure of the films is due to self-shadowing within the growing film (a molecule being unable to reach the area shadowed from the evaporation source by previously deposited molecules) combined with the limited mobility of the condensing evaporant on the substrate, which prevents later molecules from migrating into the shadows of previous ones. The zero-mobility case produces long thread-like growths with low packing density, but the limited-mobility case reproduces a dendritic growth that is similar to what is seen in practice. Some of these features have been reviewed recently (Macleod, 1982; Guenther, 1982). Guenther has produced simple models of nodular growth using the zero mobility model (Guenther, 1982). Small projections on the surface of the substrate cause a local increase in the number of thread-like fibers, which propagate upward in the typical nodular form.

All the published models to date use a fixed direction of incidence that is unlike the conditions in an optical thin-film coating plant where rotating substrates are subjected to a range of angles of incidence. It is not immediately obvious that shadowing should be as effective in the presence of varying incidence. Variable angle of incidence requires a more complex program using more computer time because of a coordinate transformation that is necessary. It also

seemed useful to repeat Guenther's calculations with the more realistic limited model.

Results are shown in Figs. 6.14 and 6.15. For speed and convenience, the output was displayed on a line printer and the circles on the diagram were traced from it. This gives a digitized appearance to the drawings. In Fig. 6.14 there is no rotation. The source is considered to be at a fixed direction of 20° from normal. The ideal surface shows the typical dendritic appearance of the film, which includes considerable void volume. Also shown in the diagram is the effect of dust or a projection of the substrate surface, and of a depression or scratch. The same set of random numbers were used for all three cases to highlight the differences. The experimental evidence has been given in the previous section (see Figs. 6.1, 6.2, 6.6, 6.7 and 6.10).

Glow-Discharge Cleaning

Since dust will cause the incidence of patches as discussed in previous sections, cleaning the substrate is necessary before deposition. Glow-discharge cleaning is usually used. Coating without glow-discharge leaves more dust on the substrate and therefore creates denser patches as shown in Fig. 6.16. In Fig. 6.17, the nonuniform distribution of maximum transmission wavelength over the area of the filter indicates that diffusion pump oil has formed a nonuniform layer on the substrate. This additional oil layer also reduces the adhesion of the coating to the substrate. One can also use a non-oil pump, such as a cryogenic pump, to eliminate

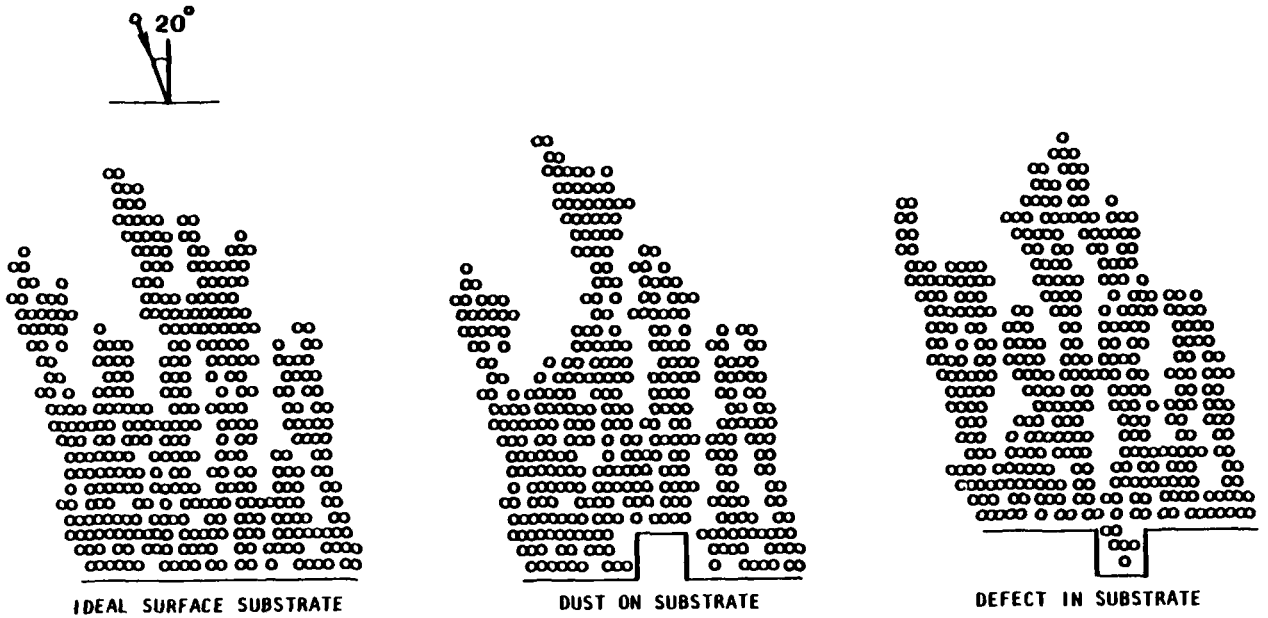


Figure 6.14. Computer simulation of thin film growth on different types of substrate (evaporation angle = 20°, with substrate holder not rotating).

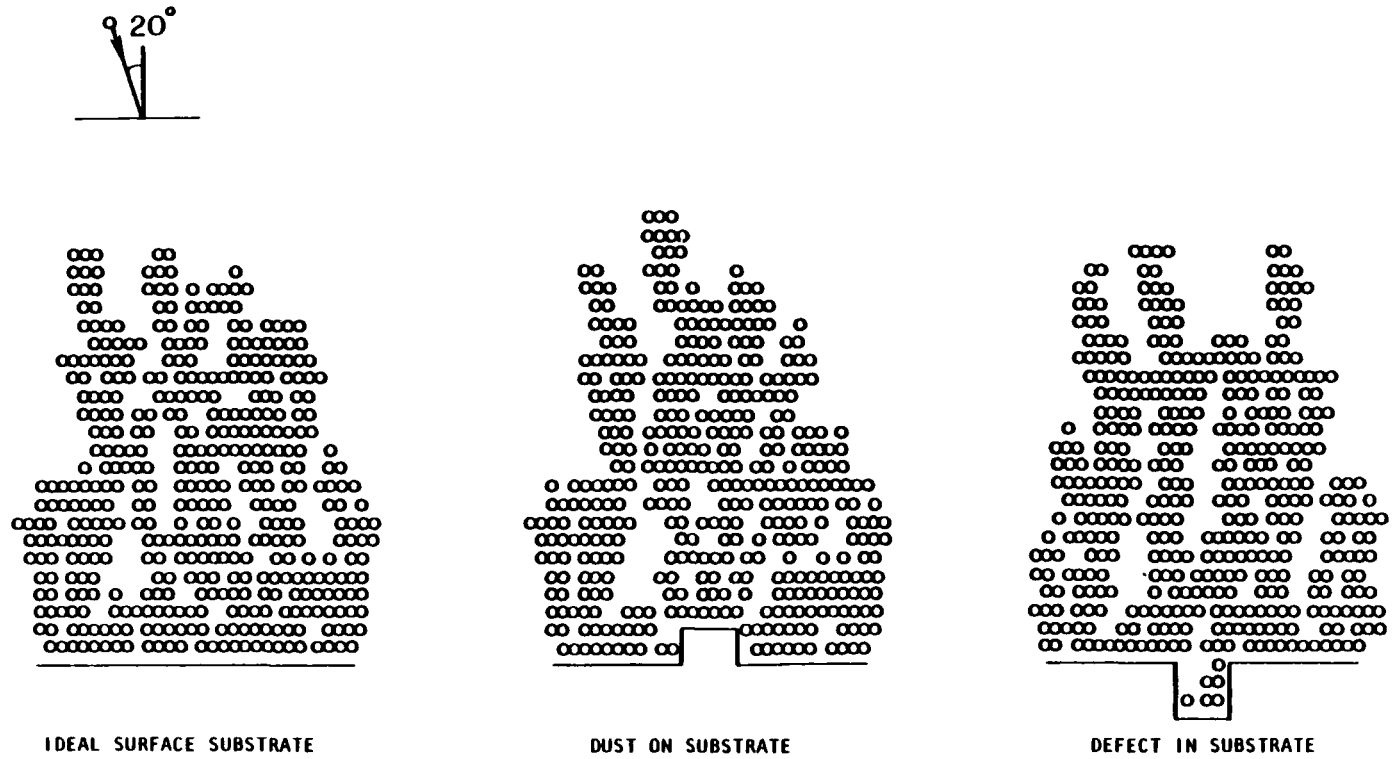


Figure 6.15. Computer simulation of thin film growth on different types of substrate (evaporation angle = 20°, with substrate holder rotating).

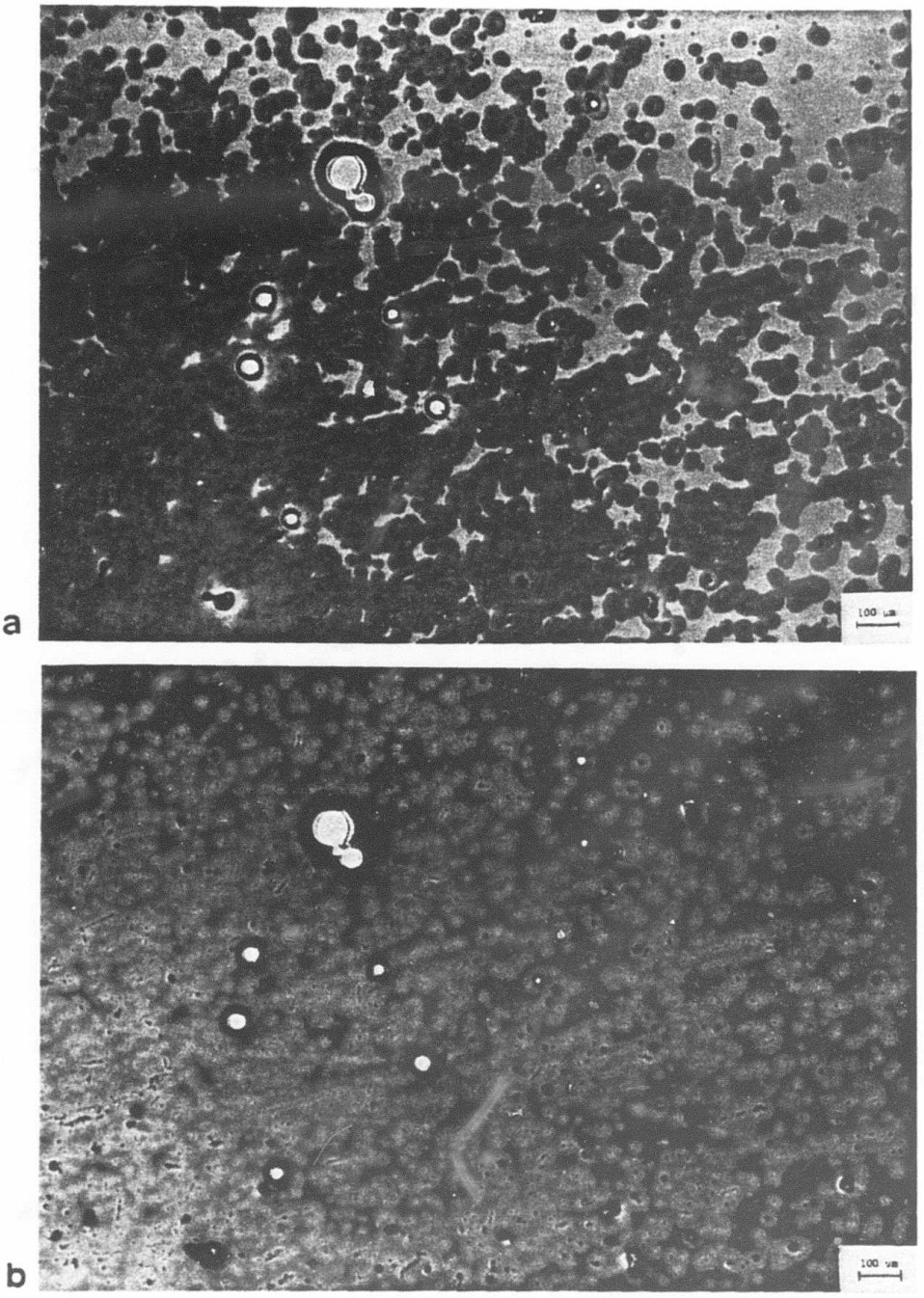


Figure 6.16. Water adsorption in filter in air without glow discharge. Coating shows more dust resting on substrate and therefore creates denser patches.

(a) = 508.5 nm, (b) = 514.5 nm.

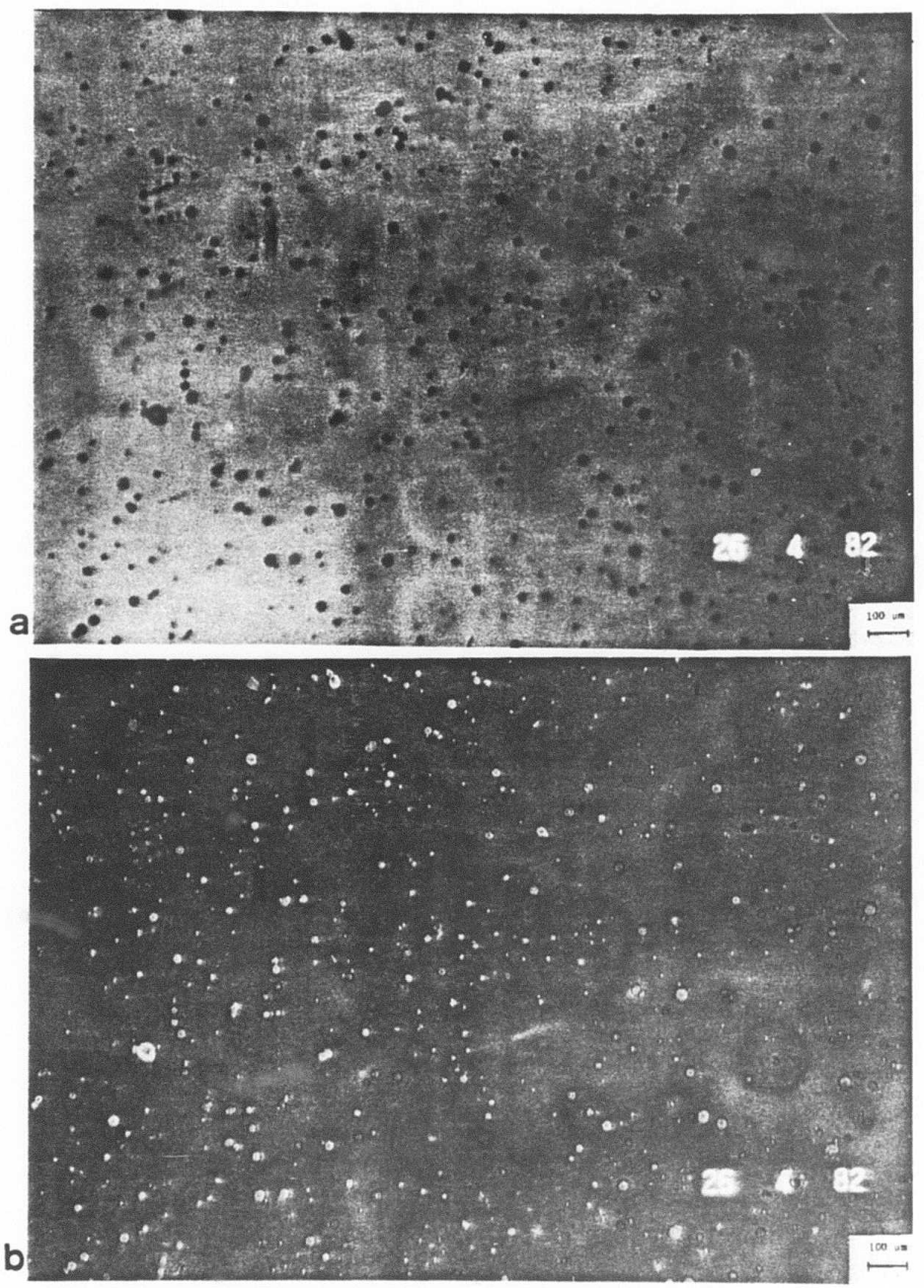


Figure 6.17. Sample ML-12-3 without glow-discharge cleaning before coating. The nonuniform distribution of patches is due to diffusion pump oil deposited on the substrate before the films were deposited. (a) λ = 547 nm. (b) λ = 552 nm.

predeposition of the oil layer before coating. The cryogenic pump used on our BAK-760 (Fig. 5.25) can meet this requirement (Fig. 6.18).

The glow-discharge will heat up the substrate and desorb the adsorbed water. It will also give the condensed molecules more mobility, leading to higher packing density and more interface diffusion between condensed molecules and substrate, increasing the adhesion. However, if the inside of the coating plant is not very clean, the glow discharge can increase the incidence of dust particles on the substrate surface. This should be avoided when coatings of the highest performance are required (Perry, 1965).

Energy Activation for Condensing Molecules

Since the voids in the films are mainly due to the limited mobility of the condensing molecules, it is feasible to search for ways to increase the mobility of the condensing molecules in order to produce non-porous films.

The simplest way is to heat the substrate during deposition, provided that the temperature is not so high as to reevaporate or dissociate the condensed molecules. A well-known example is MgF_2. Its packing density increases from 0.80 to 0.95 with an increase of substrate temperature from 40° to 365° C (Ritter and Hoffmann, 1969). The refractive index of the MgF_2 films increases with increasing substrate temperature. For 5000 Å thick films, these figures are 1.35 for 190° C, 1.37 for 280° C, and 1.38 for 340° C. These values correspond to packing densities of 0.895, 0.934, and 0.955, as reported by Ritter and Hoffman (1969).

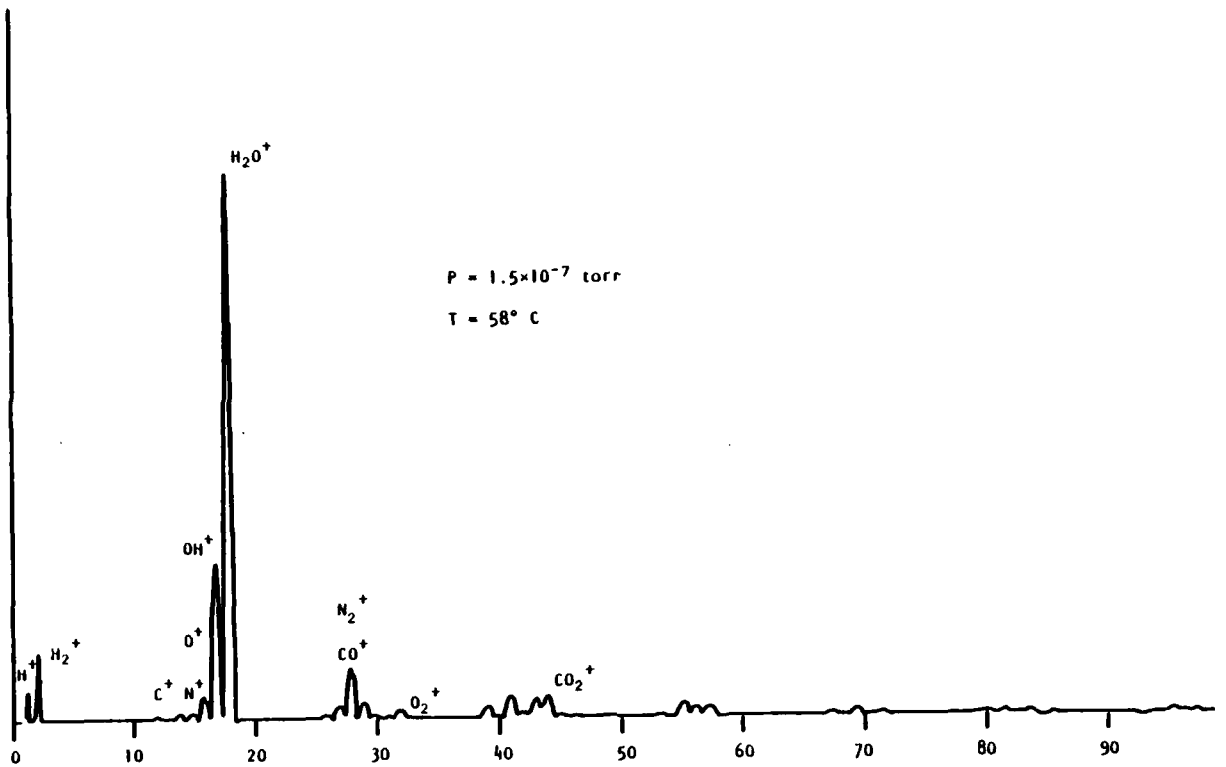


Figure 6.18. The mass spectrum of the residual gas in the BAK-760 coating plant. The cryogenic pump (oil-free) with Roots pump for roughing, leaves us no detectable hydrocarbons. The dominant residual gas is water (6%).

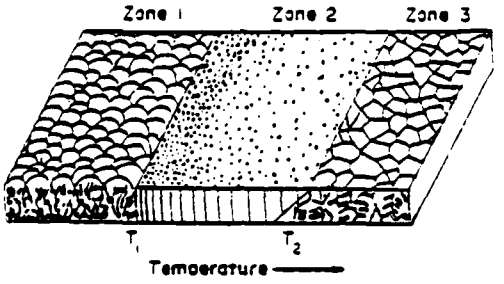
Another example of an increase in refractive index accompanying increased substrate temperature and increased packing density is silicon oxide films, as reported by Bradford et al. (1977). The ZrO_2 used for making narrowband filters in Chapter 5 also shows an increase in refractive index with an increasing substrate temperature from 1.85 at room temperature to 2.00 at 300° C.

Packing density and refractive index are interrelated by the Clausius-Mosotti formula:

$$p = \frac{\rho_f}{\rho_b} = \frac{n_f^2-1}{n_f^2+2} \cdot \frac{n_b^2+2}{n_b^2-1},$$

where n_f and n_b are the refractive indices of the film and the solid bulk material, respectively. The packing densities of ZrO_2 are then 0.78 and 0.88 at substrate temperatures of nominal room temperature and 300° C, respectively, under the assumption that n_b is 2.23 (Ritter, 1976).

The increase in packing density with increasing substrate temperature can be explained by the greater surface mobility of impinging atoms or molecules which favor the formation of larger and more closely packed crystals. The temperature-dependent film structure model was first proposed by Movchan and Demchishin (1969) (see Fig. 6.19), and was subsequently modified by Thornton (1974), as shown in Fig. 6.20.



	Zone 1	Zone 2	Zone 3
Metals	$<0.3\ T'_m$	$0.3\text{-}0.45\ T'_m$	$>0.45\ T'_m$
Oxides	$<0.26\ T'_m$	$0.26\text{-}0.45\ T'_m$	$>0.45\ T'_m$

Figure 6.19. Structural zones in condensates (after Movchan and Demchishin).

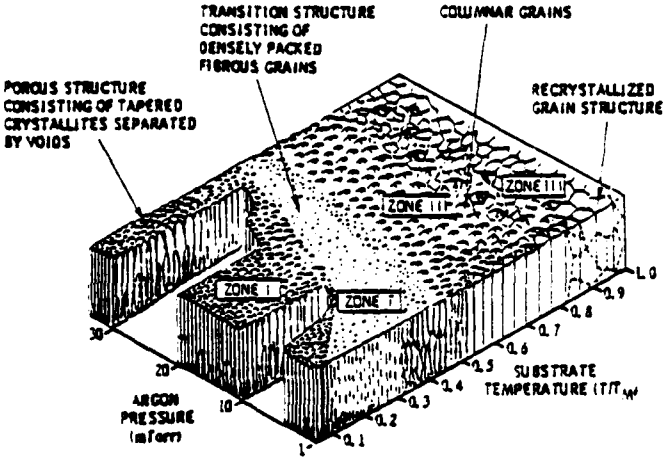


Figure 6.20. Structural zones in condensates (after Thornton).

At low temperatures, the structure grows as tapered crystallites form a limited number of nuclei. As the substrate temperature increases, the surface mobility of the atoms increases. The structure morphology first transforms to that of tightly-packed fibrous grains with weak grain boundaries, and then to a full density columnar morphology. The size of the columnar grains increases as the condensation temperature increases. Finally, at much higher temperatures, the structure shows an equiaxed grain morphology. The break between columnar and solid structure commonly occurs at a substrate temperature of 0.45 times the melting temperature.

There are problems in heating refractory materials, such as oxides, to a sufficiently high temperature by normal means, because of their high melting points, and adding another type of energy to the impinging atoms is necessary. There are several ways to meet this requirement, such as biased sputtering, electron bombardment, ion bombardment, UV radiation, laser annealing, ultrasonic agitation, etc.

In sputtering, some of the kinetic energy of the bombarding ions is transferred to the target atoms. If the sputtered target molecule does not collide repeatedly with the argon ions before arriving at the substrate, the surface mobility of the coating will increase, and will assist in increasing the packing density of the coating films.

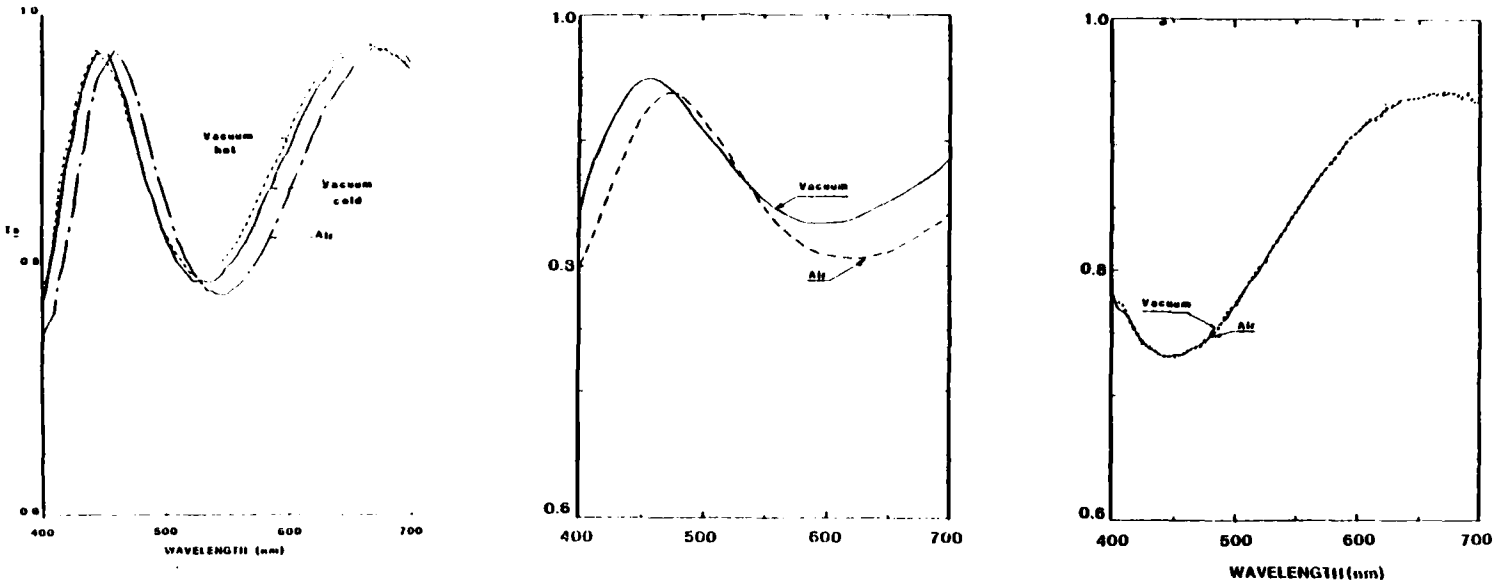
Mattox and Kominiak (1972) used biased-assisted sputtering to densify metal films such as tantalum, chromium, etc., which resulted in a less columnar appearance. Ivanova and Motovilov (1977) reported

that their filter parameters remained unchanged after five days' exposure to 80-100% relative humidity. The filters were obtained by reactive cathodic sputtering of titanium and silicon in oxygen. Donovan et al. (1981) showed that sputtered Si films are optically superior to evaporated Si films. The sputtered films have higher laser damage threshold than evaporated ones because of higher density and greater homogeneity.

Recently, Burleigh Northwest (1982) announced that by using RF sputtering they had achieved nearly bulk density in thin coating films. Shifts of the passband of their sputtered polarizer were between -5 Å and +10 Å, which when compared with shifts in evaporated coatings of 100Å to 120 Å, were negligibly small. By using RF-biased RF sputtering, Holm and Christensen (1981) made very tough SiO_2/TiO_2 films. They found no detectable wavelength drift when the filter was exposed to 100% RH for more than 340 hours.

Electron bombardment during deposition has been carried out by S. Browning (1982). Higher packing density of electron bombarded films compared to unbombarded films has been observed, for example, on $2KF{\cdot}ZrF_4$ and Sb_2O_3.

Noticeable effects of ion bombardment on coating films were reported by P. J. Martin et al. (1982). Films of ZrO_2 and SiO_2 grown on substrates nominally at room temperature under 16 $\mu A/cm^2$ 600 V argon-ion bombardment showed virtually no drift when exposed to a humid atmosphere (Figs. 6.21 to 6.23).



(a) (b) (c)

Figure 6.21. The increased packing density of $Zr O_2$ films produced by ion bombardment during deposition is indicated by the absence of a wavelength shift on exposure to atmospheric humidity. (After Martin et al.)

(a) $Zr O_2$, substrate temperature 300° C, (b) $Zr O_2$ cold substrate, no ions, (b) $Zr O_2$ cold substrate with ion bombardment.

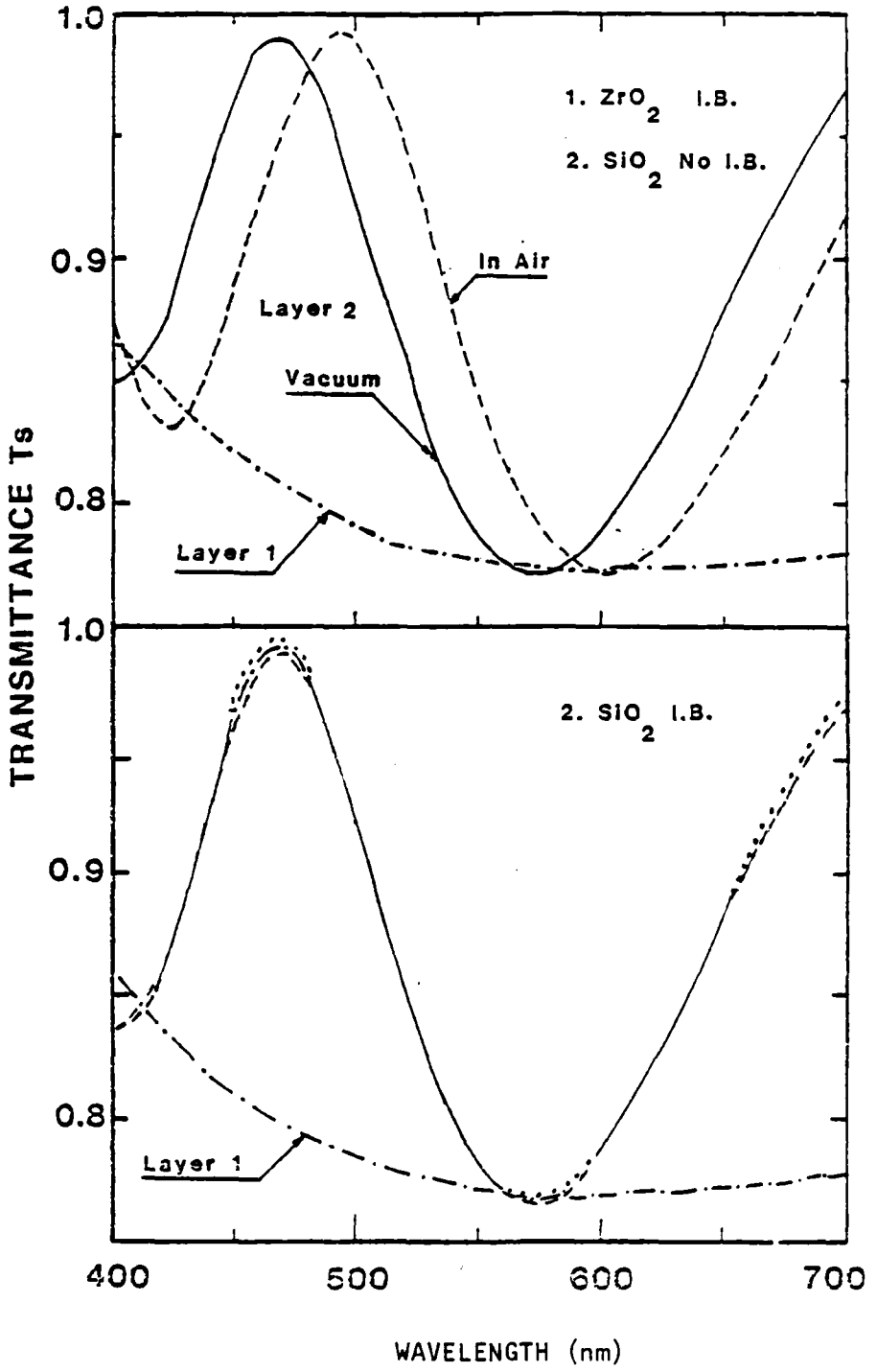


Figure 6.22. Silicon oxide films deposited over an ion-bombarded zirconium oxide film to increase fringe contrast. Upper graph is without ion bombardment and lower is with ion bombardment. Note the lack of sensitivity to atmospheric moisture of bombarded film. (After Martin et al.)

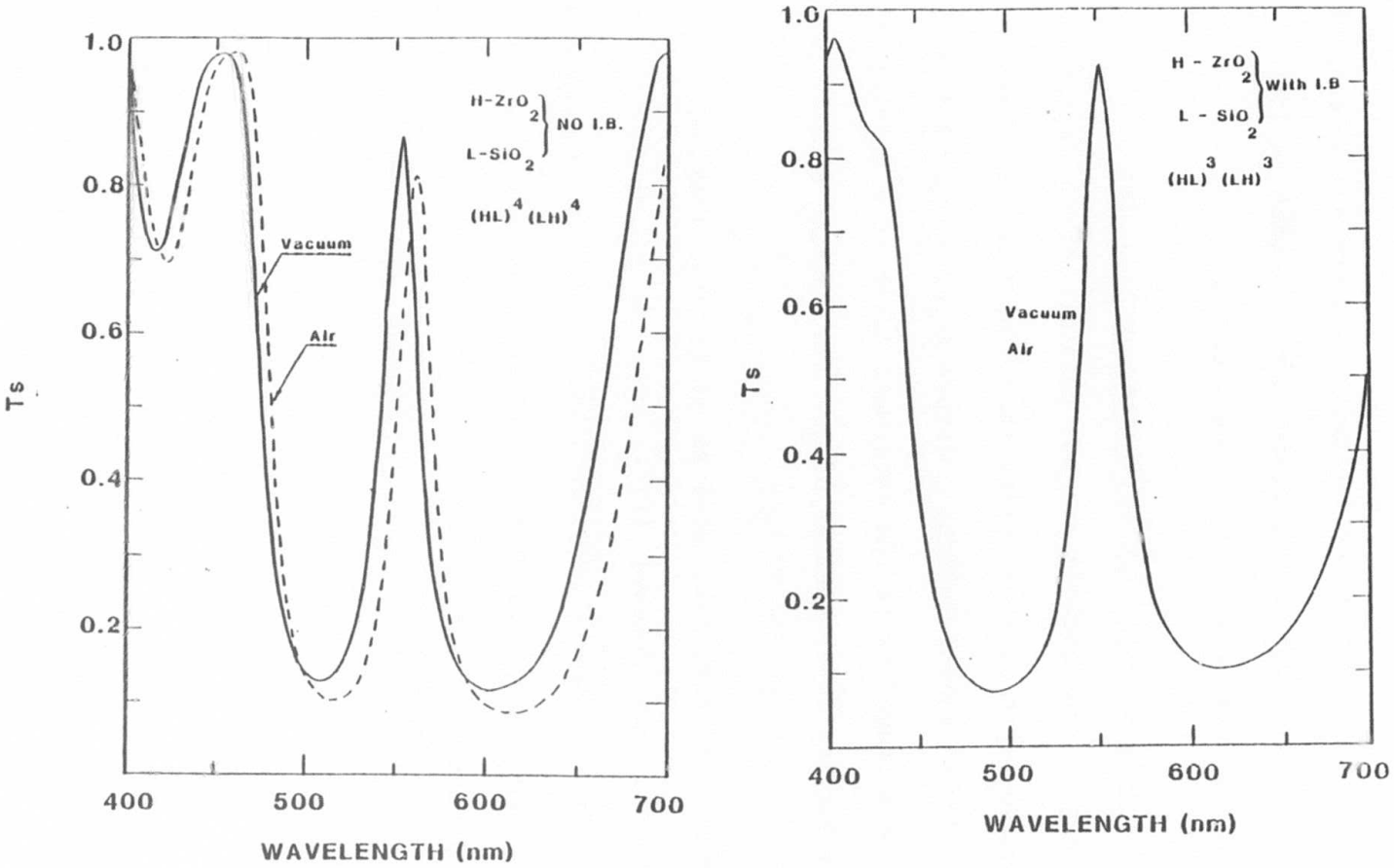


Figure 6.23. Comparison of sensitivity to moisture of narrowband filters constructed from ion-bombarded films (right) and conventionally deposited (left). The ion-bombarded filter shows no detectable drift. (After Martin et al.)

Other types of energy-adding to the film during the deposition are also possible; for example, UV radiation, laser illumination, etc. However, the optical systems for those techniques are not as easy to implement as the systems of electrodes for electron or ion bombardment, except when coating very small areas.

Protective Layer or Cover Plates over Coating

If energy-adding methods are not possible during deposition, then a protective layer or cover plate should be cemented over the top and edge of the coating to stop moisture penetration. ZnS, for example, can be arranged to be the outermost layer of a multilayer, and acts as a barrier layer because of its high packing density (Fig. 6.24).

Organic films have been used as protective coatings, e.g., Hollahan, Wydeven, and Johnson (1974) used a polychlorotrifluoroethylene film deposited by RF diode sputtering. The coating provides protection against humidity (744 hours exposure to 88.8% RH) and has some antireflection effect.

Cementing a glass cover over a coating immediately after manufacture can also slow down and even stop the penetration of moisture, provided that the edges are well sealed and that no water is in the cement (Levina and Furman, 1973). However, not all epoxy resins can stop water penetration. Balsam optical cement plus edge protection with VG-1 Sealer has been suggested. Epo-tek 301-2 has also been used successfully (Netterfield, 1982).

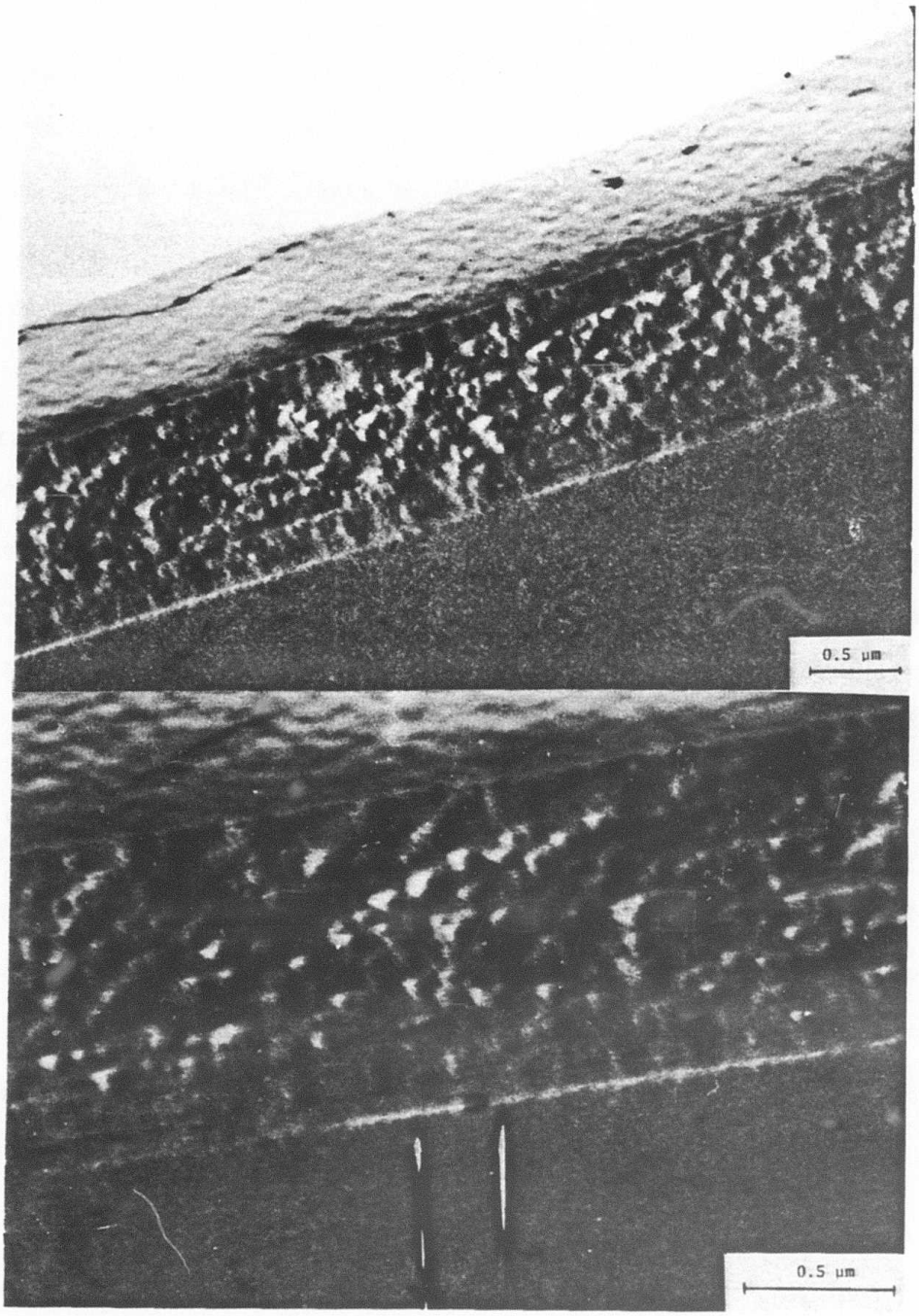


Figure 6.24. TEM photograph of G/ZnS($3/4\lambda_o$)/cryolite ($7/4\lambda_o$)/A λ_o = 500 nm. Less porous ZnS film can be used as a protective layer against water adsorption. Lower portion of photographs is glass.

Although cementing will protect the coating from water adsorption, abrasion, etc., it is still a passive way to cure the problem. It is preferable to find an active way of giving the condensing atoms or molecules kinetic energy so that a nonporous film will result. Nowadays, many systems involve high power lasers. Cemented filters usually cannot sustain such irradiation because of absorption and resultant heating. The absorption may occur in the cement or inside the film itself. Figure 6.25 shows a filter damaged by an argon-ion laser (sample given by D. Weinberger). The instant a coating is finished, it begins to adsorb water. Therefore, there is always a certain amount of adsorbed water in the films no matter how fast they are cemented. The damage trace shown in the filter indicates where adsorbed water was reevaporated by the scanning laser.

There is also strong evidence that heat treatment after deposition at temperatures around 100° C will stabilize a filter (Macleod, 1976; Meaburn, 1966; Title et al., 1974). Such treatment increases the resistance to moisture penetration and also drives out moisture already in the layers. One problem is that the heat treatment usually produces a shift toward shorter wavelengths.

Summary

Curing water adsorption in the coating films can be done in two ways: actively and passively. The active ways exclude defects and give more mobility to the condensing molecules to produce higher packing density of the films. Remedying defects, covering the porous

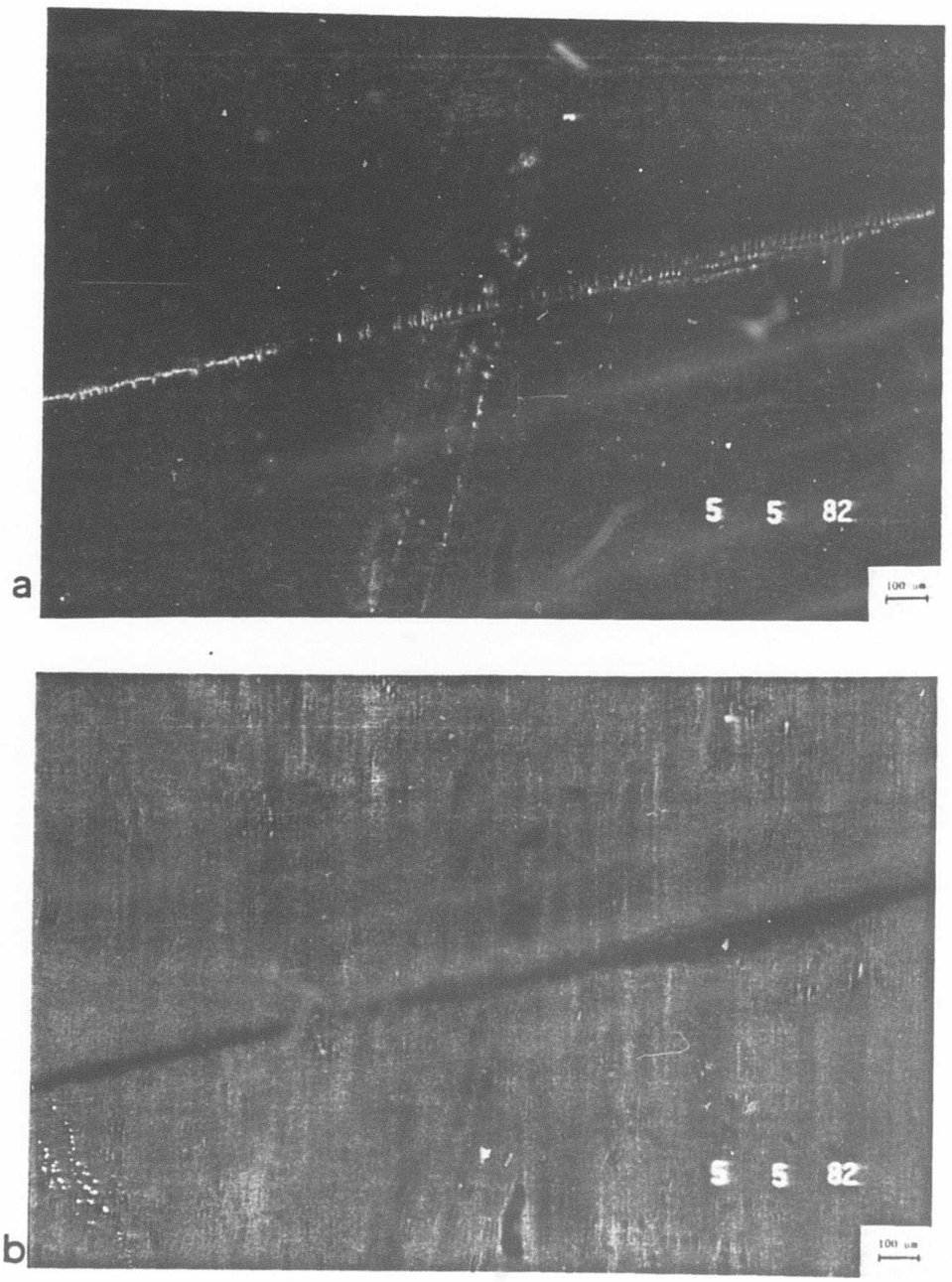


Figure 6.25. Filter damaged by an argon ion laser beam. The adsorbed water was reevaporated by the irradiation and the films were then damaged as the laser scanned over them. (a) = 513 nm. (b) = 514.5 nm.

lms with protective layers or cover plates, and heat treatment are ssive methods.

In order to exclude defects, one should first choose a good bstrate which is as smooth as possible and which has no surface fects, pin holes, scratches or dust. Second, one should perform ow-discharge cleaning prior to deposition to clean the substrate, move predeposited oil, and desorb the adsorbed water. Third, one ould choose high-purity materials and evaporate carefully so that no itting of even the smallest particles of coating material larger an atoms or molecules will be introduced.

Greater mobility of the condensing atoms or molecules can be hieved by heating the substrate, sputtering, electron bombardment, n bombardment, UV radiation or laser illumination so that a non- rous film will be produced.

Passive techniques involve remedying the defects after position. For instance, covering the coating with organic films, menting with cover plates or heat treatments have all been ccessful, but this changes the optical performance.

CHAPTER 7

MODELS FOR WATER PENETRATION IN THIN FILMS

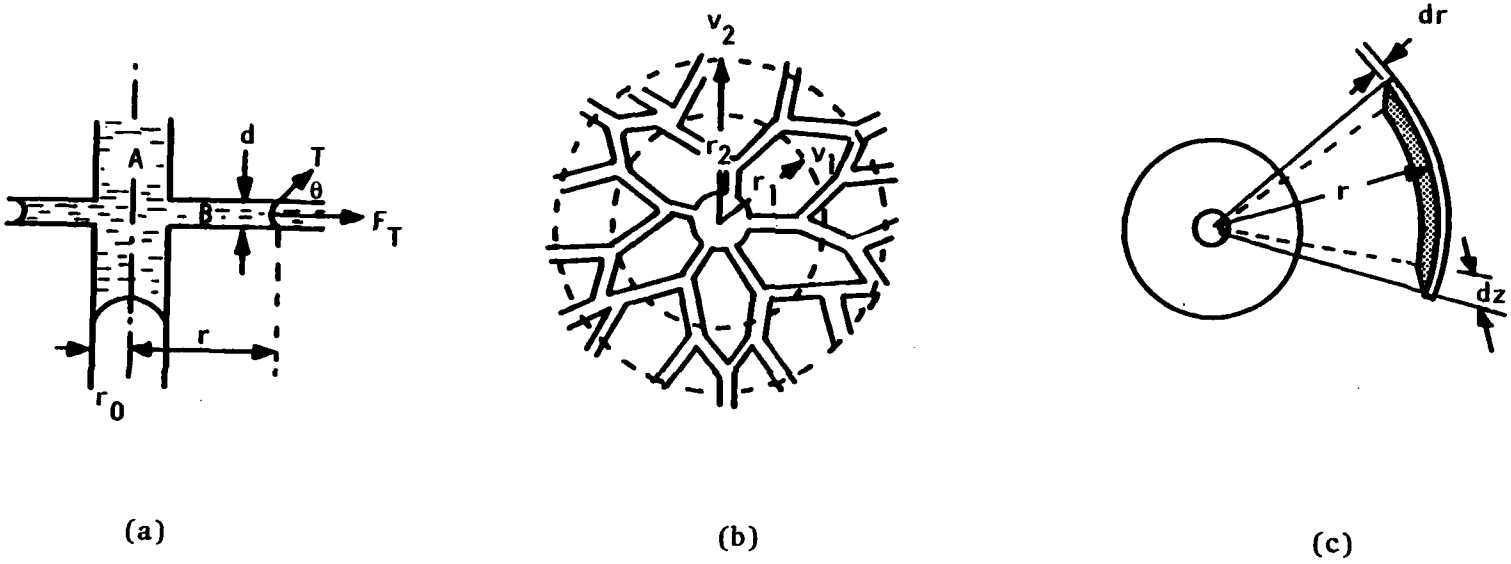
From the results in Chapter 3 through Chapter 5 we know that coating films are porous in general and we may to make the assumption that water penetrates the multilayer through some of these pores and then spreads laterally, as shown in Fig. 5.2. Figure 4.10 also gave us some ideas of how water goes through a film laterally. Based on these concepts, three models are presented in the following sections to describe water penetration inside a film.

Single Pore

Water is assumed to pass via capillary flow through a central pore A and then spread to a side pore B, as in Fig. 7.1(a). This single pore model can describe how water passes through both pores A and B. The following derivation deals with the side pore B as an example, but is also applicable to pore A.

Assume that d is the diameter of the side pore, r_0 is the radius of the central pore, r is the distance water has reached, and T is the surface tension of water. There are three forces which must remain in balance:

(1) Force due to surface tension: $F_s = 2\pi(d/2)T\cos\theta = Ad$, for slow motion, θ and T are constants, and $A = 72.14$ dyne/cm for water (Adamson, 1976). Therefore, $A = \pi T\cos\theta$ is a constant.



(a) (b) (c)

Figure 7.1. Three possible models for porous films.

(ii) Friction force: $F_f = k\eta rv$, where v is the velocity = d(r)/dt, η is viscosity, and k is proportionality constant.

(iii) Change of momentum, i.e., net force: $F_{net} = d(mv)/dt$, where mass $m = \pi(d/2)^2 \cdot rD = \pi/4\ d^2 r$ (for water, density D = 1).

Therefore, we can write the differential equation:

$$Ad - k\eta rv = \frac{\pi}{4} d^2 \, d(rv)/dt, \tag{7.1}$$

and the solution is

$$Ad - k\eta rv = C\, e^{-(4k\eta)/(\pi d^2)}, \tag{7.2}$$

where C = Ad if v = 0 at t = 0.

Since v = d(r)/dt, we can write the travel distance, r, as a function of time, t:

$$r = \left\{[r_0^2 - Kt_0 - B] + Kt + Be^{-E(t-t_0)}\right\}^{1/2}, \tag{7.3}$$

where $K = 2Ad/k\eta = 2\pi T\cos\theta d/k\eta$,

$$B = \frac{\pi d^2}{2(k\eta)^2} Ce - \frac{4k\eta}{\pi d^2} t_0$$

$$E = \frac{4k\eta}{\pi d^2}.$$

In Eq. (7.3), the fourth term of the right side, Kt, is dominant. Therefore, the length of penetration is proportional to the square

root of the time. This result is consistent with the results of Stone and Earl (1973).

Since K is proportional to the diameter of the pore, the larger pore will have a higher rate of penetration. Figure 5.17 illustrates the point that the larger the defect size, the faster the growth rate of the patch.

Multipores with Assumption of Constant Rate of Supply from the Central Pore

This model, as shown in Fig. 7.1(b), attempts to describe how water spreads laterally. The flow rate is assumed to be limited by a central pore such that the flux is a constant in time. The flux is given by

$$Q = 2\pi r v \rho(r), \tag{7.4}$$

where $\rho(r)$ is the distribution density of side pores and v is the velocity at distance r. Since $Q_1 = Q_2 = Q_3 = \ldots$, for $r > r_1$,

$$t = \int_{r_1}^{r} \frac{dr}{v} = \int_{r_1}^{r} \frac{dr\, r\rho(r)}{r_1 v_1 \rho(r_1)}$$

$$= \frac{1}{r_1 v_1 \rho(r_1)} \int_{r_1}^{r} r\rho(r)\, dr. \tag{7.5}$$

It is obvious that spread rate is dependent on the side pore distribution, $\rho(r)$.

If $\rho(r)$ is constant in r, then $\rho(r)/\rho(r_1) = 1$, and

$$t = \frac{1}{2r_1 v_1} (r^2 - r_1^2) \tag{7.6}$$

or

$$r = \left(r_1^2 + 2r_1 v_1 t \right)^{1/2} \tag{7.7}$$

If $\rho(r) \propto \frac{1}{r}$, then

$$t = \frac{1}{v_1} (r - r_1)$$

and

$$r = r_1 + v_1 t. \tag{7.8}$$

If $\rho(r) \propto 1/r^2$, then

$$t = \frac{r_1}{v_1} \ln \frac{r}{r_1} \quad ,$$

and

$$r = r_1 \, e^{(v_1/r_1)t}. \tag{7.9}$$

Analysis of the experimental results of Figs. 4.6 and 5.9, indicate that in the early stage of water spreading, r is a function of t in the form of Eq. (7.7) The behavior at a later stage of spreading depends on the RH. At low RH, r becomes proportional to t, i.e., Eq. (7.8) applies. This is the capillary flow predicted by Summ, Raud and Goryunov (1979). At higher RH, the flow becomes a combination of Eqs. (7.7) through (7.9). These results indicate that the distribution density for the pores, $\rho(r)$, is a constant when r is close to the central pore and falls in magnitude when r is further away from the central pore.

Multipores with Capillary Forces

In this model we assume capillary flow in both the central pore and in each side pore. Let the density of fluid at (x, y, z; t) be $\rho(r_1 t)$, then the continuity equation gives us

$$\frac{\partial}{\partial t} \rho + \nabla \cdot \rho v = 0.$$

For incompressible pores, ρ is proportional to the density of pores and is constant in time. Therefore, $\nabla \rho v = 0$, or $1/r \, \partial(r\rho v)/\partial r = 0$, i.e., $r\rho v = C(t)$, where $C(t)$ is a constant in r.

The drag force involved in the water flow, Fig. 7.1(c), is given over the small distance dr by

$$f_d = Q\eta(d)dr,$$

where Q is the flow flux given by $2\pi rv\ dz$, dz is the thickness of fluid, η is the viscosity, and d is the size of pores. The total drag force is then

$$F_d = \int f_d = 2\pi dz\ \eta(d) \int rv\rho(r)dr$$

$$= 2\pi\ dz\ \eta(d)\ C(t) \int dr$$

$$= 2\pi\ dz\ \eta(d)\ C(t)r \quad . \tag{7.10}$$

The capillary force per pore is given by

$$f_c = 2\pi\ \frac{d}{2}\ T\cos\theta = \pi d\ T\ \cos\theta,$$

and the total capillary force is then

$$F_c = \int f_c = 2\pi r\ f_c\ \frac{\rho}{d}\ dz$$

$$= 2\pi^2\ T\ \cos\theta\ \rho r\ dz, \tag{7.11}$$

where ρ/d is the number of pores in unit area of flow cross section.

The mass of the fluid within dr and dz is

$$m = 2\pi r\ dr\ \rho\ dz \cdot D,$$

where D is the density (which is one for water). Momentum is $p = mv = 2\pi r\ dr\ \rho dz\ dr/dt$, and the total momentum is $P = \int p = 2\pi dz \int r\ \rho v\ dr = 2\pi\ dzC(t) \cdot r$. Therefore, the change of momentum is

$$\dot{P} = d[(2\pi dz\ C(t)r])/dt. \tag{7.12}$$

Combining Eqs. (7.10) through (7.12), we then have a differential equation for the flowing water

$$\frac{d}{dt}\ [2\pi dz\ C(t)r] = 2\pi^2\ T\cos\theta\ \rho\ rdz - 2\pi\ dz\eta r\ C(t). \tag{7.13}$$

If the pore sizes do not change with time, the thickness of fluid dz is a constant. Equation (7.13) is then simplified to

$$\frac{d}{dt}\ [C(t)r] = A\rho r - \eta r\ C(t). \tag{7.14}$$

Since $\rho(r)$ is not a function of time, Eq. (7.14) can be written as

$$\frac{d}{dt}\ [r^2 v] = Ar - \eta r^2 v. \tag{7.15}$$

This equation tells us that the behavior of r is independent of $\rho(r)$, during the whole spreading process away from the central pore. This is not quite consistent with the experimental results except for a very low RH.

From the above discussion we might conclude that the mechanism of water penetration inside the films at an early stage is due to capillary flow in the central pore and in the side pores. At low relative humidity the flow appears to be characteristic of a capillary flow both in the central and in the side pores. That is, both are involved in the determination of flow rather than the central pore dominating the supply of water to the side pores. At high relative humidity, the spreading of the water farther away from the central pore is limited by the central pore itself. The distribution density of the pores decreases as the distance from the central pore increases.

The decrease in the value of $\rho(r)$, the distribution density, as a function of distance from the central pore is consistent with a defect from which might radiate a series of fissures or cracks. This suggests that the central defect has considerable influence on the surrounding film, and that its influence stretches farther than might previously have been suspected. The total defect is more than a simple crack or hole in otherwise normal film material. The nature of the defect can vary and we have shown how it can be associated with

objects such as dust particles within the film or substrate defects such as asperities or cracks.

CHAPTER 8

CONCLUSION

Vapor deposited thin films have a columnar structure with voids or pores in between the columns. The effect of this microstructure is to make optical and mechanical properties of the layers differ significantly from those of bulk materials. The columnar nature of the structure has been verified by TEM micrographs and computer simulation of film growth and supports the view that the origins of the structure lie in the limited mobility of the condensing atoms (molecules) and the self-shadowing effect of material already deposited.

The pores have a major influence on the water adsorption behavior of films. It is because of this adsorption that the refractive index of the film increases or decreases when environmental conditions change. The optical performance of the complete coating varies according to the amount of water it has adsorbed or desorbed. The three techniques, given in Chapters 3, 4, and 5, allow us to observe small instabilities in a film, which are due to water adsorption. From the shift of resonance angle or from the growth rate of patch size and/or the peak wavelength shift, we are able to deduce how porous a film is. The knee of an adsorption isotherm indicates the pore size. The knee at 81% RH for cryolite, for

example, implies that most of the pores have radii greater than 50 Å. If a film is given a higher packing density by, for example, substrate heating, ion bombardment, electron bombardment, sputtering, UV radiation, etc., the shift in resonance angle or in peak wavelength is reduced. This implies that less water is adsorbed and that a smaller value of RH corresponding to the knee of the adsorption isotherm would be expected because of a reduction in pore size.

While the surface plasmon technique given in Chapter 3 is a very simple device that provides a good sense of small optical instabilities in a thin film and also allows us to measure a packing density of the film, three things must be noted. First, the coating procedure is a two-step process, since we need to open the coater to measure the optical constants and thickness of the silver layer before depositing the dielectric layer in which we are interested. Therefore, any extra layers on top of the silver, which this process induces, will introduce an error in the result unless we are able to measure the optical constants and thickness of the silver without opening the coater. Second, the dielectric layer is assumed lossless in the calculation. Any loss due to absorption or scattering will then affect the result unless we account for the losses in the calculation. Third, the film is assumed homogeneous and isotropic. But unfortunately, most films have some inhomogeneity and the columnar structure of the films indicates that they are anisotropic.

The three problems mentioned above also happen in the narrowband filter techniques (Chapters 4 and 5). However, the first

problem can be solved easily by using direct monitoring during manufacture. The second problem does not have an excessively harmful effect on the porosity or the packing density of the films. The packing density can be calculated if the material we used has no chemical reaction with water. The third problem forces us to recognize that the films we are measuring are anisotropic but, since our measurements are principally at normal incidence, the influence of the anisotropy is minimized.

The narrowband filter techniques have another advantage of giving information about the water penetration mechanism, which assists us in constructing the models of Chapter 7.

Through the narrowband filter techniques, we also verified that surface defects of the substrate, dust, spitting of sources, and impurities do affect the nature of the films and exaggerate its porosity, because they create the central pores for water to penetrate. By looking at water adsorption in different materials, we confirm that the higher the packing density, the less water is adsorbed.

Knowing the above facts, we can conclude that to prevent water adsorption we must choose substrates with no defects, avoid dust problems, know that glow discharge can help, use high purity material, and evaporate properly. Most important is to attempt to achieve high packing density in the films.

In order to have high packing density films, we must give the condensing atoms (molecules) more mobility. This can be done by

heating the substrate, and/or by using ion bombardment, electron bombardment, UV radiation, sputtering, etc.

An alternative way of preventing water adsorption in films is the use of a protective layer or cover plate. Although this is not as effective as removing the sensitivity of the layers themselves, it is easy and cheap.

What of the mechanism of moisture penetration and spreading? In single films, where the pores are linked directly to the atmosphere, the mechanism is one of surface adsorption followed by capillary condensation. Adsorption isotherms obtained by Ogura (1975) clearly show these two features.

In multilayers, the process is much more complex. Some of the layers are less permeable than others and the total thickness of the film assemblies is very much greater than that of a single film. The first direct and obvious consequence of this is that the whole process of moisture adsorption is very much slower than in single layers. However, there is also a less immediately obvious consequence. This is that the moisture enters unevenly in patches which are circular in shape. This behavior is not simply that there is a slow variation of permeability over the surface, which might be expected. Such a mechanism would be likely to give a slow radial variation of wavelength with an eventual change over the whole area of the patch. The patches are, rather, composed of areas of constant wavelength which gradually enlarge with time. There are patches within patches with the same center, and expanding also, often at a slower rate than

the outer patch. The wavelength shift within the patch remains substantially constant as long as the relative humidity does not change. Thus the results are consistent with the penetration of the moisture through a central pore and the spreading laterally across the layers.

Why does moisture not pass directly through the layers? The first reason is that some materials are of very low permeability. Zinc sulfide is one such material. Silicon dioxide appears to be another. Second, there is no continuity of the pores from one layer to the next. In fact, the micrographs always show a marked discontinuity between one layer and the next. Even discontinuities in deposition of a single layer can cause an interruption in the continuity of the pores. Lissberger and Pearson (1976) noted the existence of pseudoboundaries in thick single films, which were attributed to variations in deposition. Ogura (1975) found that the deposition of one layer over another, even with no change in material, resulted in the creation of trapped pores. Also, the adsorption isotherms obtained were quite inconsistent with continuity in the pore structure. Thus the boundaries of the layers can and probably do act as at least partial moisture barriers. Gibson and Lissberger (1983) question this view and cite evidence from adsorption studies on cryolite and zinc sulfide multilayers. Irregular patches within the regular circular ones are attributed by them to the adsorption of moisture in the zinc sulfide layers. They believe that the boundaries between the layers are the very routes by which moisture propagates.

This, however, is inconsistent with Ogura's observations and it is difficult to see how delamination could be prevented if it were true. Of course such an effect can occur at a rather late stage of the process when delamination is indeed taking place with the formation of blisters. Furthermore, although the text of Gibson and Lissberger's paper asserts the boundary propagation model, yet the diagram accompanying it shows penetration within the cryolite layers. There can be greater concentrations of water in the vicinity of layer boundaries. The nuclear reaction technique of Donovan et al. (1980) and the calorimetric measurements of Temple (1979) demonstrate this. However, we consider this to be more a consequence of the void shape rather than a result of moisture propagation along the boundaries. Finally, if moisture propagated along the boundaries and then into the layers, this should be visible as a gradual wavelength shift in the patches. If it were not so then moisture would be propagating instantaneously across the layers from the boundaries. This, in turn, would imply rapid propagation from front to back of the multilayer, which contradicts the observations that propagation is lateral. We recall Ogura's observation of the impeding effect of a boundary even in the same layer material. Thus, we conclude that the propagation across the layers is within the layers and is not simply a regular feature of the boundaries. Thus, our model of moisture penetration is that it enters at isolated sites from which it spreads out within the layers.

It is interesting to examine the photograph of patterns presented by Gibson and Lissberger to support their ideas of penetration in zinc sulfide. The irregular patches in question look very similar to those in the baked metal-dielectric filter containing only cryolite as dielectric material (see Fig. 4.15). In this latter case, we know that there is no zinc sulfide present and it is therefore more likely that a chemical reaction in cryolite is responsible. Could this also be the case with the Gibson and Lissberger results?

What permits the moisture to enter? The central penetration pores cannot be simply a statistical consequence of the intrinsic pores with various layers coinciding from time to time. If this were all, then we would not be able to reduce or increase their incidence in the way we did in Chapter 6. We find, rather, that the introduction of perturbations of some description, dust particles, pieces of source material, or roughened substrates all contribute markedly to an increase in the incidence of penetration sites. Superpolishing substrates, on the other hand, reduces their incidence. Computer simulation of film growth over substrate defects showed the development of large fissures over the defect. Such large cracks or voids would be ideal penetration sites. Guenther (1982) has studied the development of nodular growth and has shown that they can be created by substrate asperities. Thus, nodules may be associated with central pores.

Water appears to spread from the central pore via capillary action. At values of relative humidity from low to medium the condensation in the central pore is sufficient to supply all the water that is required. The spreading is limited by the secondary channels away from the pore. This suggests a central pore that has a large surface area yet low critical relative humidity. Narrow cracks which are long but narrow might be a possibility. The ring-like crack around a nodule could well be the type of pore which would give the observed behavior. Then the supply at high relative humidity is limited by the central pore. Again, this would agree with long, narrow fissures. It is possible that the inherent structure of the layers is responsible. The gaps between the columns could be the capillaries which transmit the water. The layers might act, then, much as a sheet of blotting paper. We might imagine the central pore as an isolated defect in a matrix of otherwise undisturbed material. This, however, does not fit the experimental evidence. The rate of spreading at intermediate values of relative humidity show that there is a radial fall in the distribution of capillary channels, in agreement with a set of channels of constant number and size radiating out from the central pore. They could well be radial fissures or cracks. This model helps us to understand that the strange way in which the rate of spreading and time to reach equilibrium is not simply a function of packing density. Richmond (1976) found that multilayers of zinc sulfide and magnesium fluoride reached equilibrium much more rapidly than zinc sulfide and cryolite, although packing density seemed

similar. However, magnesium fluoride has high tensile stress which might be expected to encourage the formation of radial cracks around a weak defect. Thus, the structure model consists of a disturbed region around the central defects which is much greater in size than the defect itself. This could have implications for laser damage studies.

Further Questions and Suggestions for Future Work

1. Further work is needed on the precise nature of the particular aspect of the defects which allows water to penetrate, especially in metals.

2. The influence of deposition conditions on the porous nature of the moisture adsorption requires further study.

3. Baking desorbs water, but the possibility that structural changes accompany the desorption should be investigated.

4. A more quantitative relationship between microstructure and refractive index is required.

5. Other techniques such as IR spectroscopy, laser Raman spectroscopy would be valuable.

6. The work should be extended to still more materials, especially the refractory oxides.

7. Does the moisture penetration have any relationship with variations in laser damage threshold? We know that it has a major effect when the laser wavelength coincides with a water adsorption band, but is there any effect for laser lines which do not coincide with the absorption bounds?

8. Ways of improving film solidity and reducing susceptibility to moisture should be investigated.

REFERENCES

Abelès, F., "The determination of the index and of the thickness of thin transparent films," J. Phys. Radium 11, 310, 1950.

Adamson, A. W., Physical Chemistry of Surfaces, 3rd Edition, (John Wiley and Sons, New York, 1976).

Adamson, A. W., and L. M. Dormant, "Adsorption of nitrogen on ice at 78° K," J. Am. Chem. Soc. 88, 2055, 1966.

American Society for Testing Materials, Standard E104-51 (reapproved 1971), "Maintaining constant relative humidity by means of aqueous solutions," R. P. Lukens, ed. (Annual Book of ASTM Standards, Philadelphia, Pennsylvania, 1982).

Aresenault, R., and G. Boivin, "Fabrication of metal-dielectric interference filters," Appl. Opt. 16, 1890, 1977.

Barr, E. E., "Visible and ultraviolet bandpass filters," Proc. SPIE 50, 87, 1974.

Bradford, A. P., G. Hass, M. McFarland and E. Ritter, "The effect of the substrate temperature on the optical properties of reactively evaporated silicon oxide films," Thin Solid Films 42, 361, 1977.

Browning, S., Optical Sciences Center, University of Arizona, Tucson, Arizona, private communication, 1982.

Brunauer, S., L. S. Deming, W. E. Deming, and E. Teller, "A theory of the Van der Walls adsorption of gases," J. Am. Chem. Soc. 62, 1723, 1940.

Burleigh Northwest, "New sputterings--thin film polarizers that stay put!" Lasers and Applications, p. 14, Sept. 1982.

Chopra, K. L., Thin Film Phenomena, (McGraw-Hill Book Co., New York, 1969), p. 321.

Dirks, A. G., and H. J. Leamy, "Columnar microstructure in vapor-deposited thin films," Thin Solid Films 47, 219, 1977.

Donovan, T. M., E. J. Ashley, J. B. Franck, and J. O. Porteus, "Hydrogenated amorphous silicon films: preparation, characterization, absorption and laser-damage resistance," 13th Annual Symposium on Optical Materials for High Power Lasers, Boulder, Colorado, 17-18 November 1981.

Donovan, T. M., P. A. Temple, S.-C. Wu, and T. A. Tombrello, "The relative importance of interface and volume absorption by water in evaporated films," in Laser Induced Damage in Optical Materials: 1979, A. J. Glass, A. H. Guenther, and B. E. Newnam, eds., (National Bureau of Standards, Special Publication 568, 1980), p. 237.

Eckertova, L., Physics of Thin Films, (Plenum Press, New York, 1977), p. 159.

Feldman, J., M. Friz, and F. Stetter, "Materials for evaporation," Vacuum Tech. Res. and Dev., 44, 49, December 1976

Gibson, D. R., and P. H. Lissberger, "Optical properties of narrowband spectral filter coatings related to layer structure and preparation," Appl. Opt. 22, 269, 1983.

Gonella, J. R., and B. Robrieux, "Evolution of thin films of calcium fluoride," Opt. Acta 9, 101, 1962.

Gregg, S. J., and K. S. W. Sing, Adsorption, Surface Area and Porosity (Academic Press, London, 1967).

Guenther, K. H., "Columnar and nodular growth of thin film," Proc. SPIE 346, 9, 1982.

Guenther, K. H., and H. K. Pulker, "Electron microscopic investigation of cross sections of optical thin films," Appl. Opt. 15, 2992, 1976.

Ivanova, L. A., and O. A. Motovilov, "Stable narrow-band interference filters for the 0.7-1.5 μm region of the spectrum," Sov. J. Opt. Technol. 44, 739, 1977.

Hall, J. F., and W. F. C. Ferguson, "Dispersion of ZnS and MgF_2 films in the visible spectrum," J. Opt. Soc. Am. 45, 74, 1955.

Hollahan, J. R., T. Wydeven, and C. C. Johnson, "Combination moisture resistant and antireflection plasma polymerized thin films for optical coatings," Appl. Opt. 13, 1844, 1974.

Holland, L., Vacuum Deposition of Thin Films (Chapman and Hall, Ltd., London, 1956), pp. 98-103.

Holm, N. E., and O. Christensen, "Humidity sensitivity of optical structures prepared by RF-biased RF sputtering," Thin Solid Films 85, 71, 1981.

Jones, F. E., "Study of the storage stability of the BaF_2 film electric hygrometer element," J. Res. of NBS 71c, 199, 1967.

Koch, H., "Optical investigations of the water vapor sorption by evaporated films (especially on MgF_2 film)," Phys. Stat. Sol. 12, 553, 1965.

Koppelmann, G., K. Krebs, and H. Leyendecken," Optical investigation of the structure of cryolite films," Z. Phys. 163, 557, 1961.

Kretschmann, E., and H. Raether, "Radiative decay of non-radiative surface plasmons excited by light," Z. Naturforsch, 23A, 2135, 1968.

Levina, M. D., and S. A. Furman, "A factor defining the aging of cemented narrow-band interference filters," Sov. J. Opt. Tech. 40, 264, 1973.

Lissberger, P. H., "Basic developments in optical coatings," Thin Solid Films 50, 241, 1978.

Lissberger, P. H., and Pearson, "The performance and structural properties of multilayer optical filters," Thin Solid Films 34, 349, 1976.

Meaburn, J., "The stability of interference filters," Appl. Opt. 5, 1757, 1966.

Macleod, H. A., "Thin film narrowband optical filters," Thin Solid Films 34, 335, 1976.

Macleod, H. A., "Why are optical coatings so awkward?" paper presented at Optical Coating Laboratory Inc., Santa Rosa, California, November 1978.

Macleod, H. A., "Tilted films," paper presented at the Meeting of the Optical Society of America, Chicago, Illinois, October 1980.

Macleod, H. A., "Performance-limiting factors in optical coatings." Proc. SPIE 288, 580, 1981.

Macleod, H. A., "Microstructure of optical thin films," Proc. SPIE 325, 21-28, 1982.

Macleod, H. A., and D. Richmond, "Moisture penetration patterns in thin films," Thin Solid Films 37, 163, 1976.

Martin, P. J., H. A. Macleod, R. P. Netterfield, C. G. Pacey, and W. G. Sainty, "Ion-beam-assisted deposition of thin films," Appl. Opt. 22, 178, 1982.

Mattox, D. M., and G. J. Kominiak, "Structure and modification by ion bombardment during deposition," J. Vac. Sci. Tech. 9, 528, 1972.

Meaburn, J., "The stability of interference filters," Appl. Opt. 5, 1757, 1966.

Movchan, B. A., and A. V. Demchishin, "Investigation of the structure and properties of thick vacuum-deposited films of nickel, titanium, tungsten, alumina and zirconium dioxide," Fizika Metall 28, 83, 1969.

Netterfield, R. P., CSIRO Division of Applied Physics, Sydney, Australia, private communication, 1982.

Ogura, S., "Some features of the behaviour of optical thin films," PhD Thesis, Newcastle upon Tyne Polytechnic, U. K., 1975.

Pearson, J. M., "Electron microscopy of multilayer thin films," Thin Solid Films 6, 349, 1970.

Perry, D. L., "Low-loss multilayer dielectric mirrors," Appl. Opt. 4, 987, 1965.

Pulker, H. K., and K. K. Haye, "Causes of pinhole formation in vapor-deposited films," in Proceedings of the International Symposium of Basic Problems in Thin Film Physics, (German) R. Niedermayer, et al., eds., p. 204-206, 1966.

Pulker, H. K., and E. Jung, "Correlation between film structure and sorption behavior of vapor deposited ZnS, cryolite and MgF_2 films," Thin Solid Films 9, 57, 1971.

Raether, H., "Surface plasma oscillations and their applications," in Physics of Thin Films, Vol. 9, pp. 145-261, G. Hass, M. H. Francombe and R. W. Hoffman, eds. (Academic Press, New York, 1977).

Richmond, D., "Thin film narrowband optical filters," PhD Thesis, Newcastle upon Tyne Polytechnic, U. K., 1976.

Ritter, E., "Optical film materials and their applications," Appl. Opt. 15, 2318, 1976.

Ritter, E., and R. Hoffmann, "Influence of substrate temperature on the condensation of vacuum evaporated films of MgF_2 and ZnS," J. Vac. Sci. and Tech. 6, 733, 1969.

Schulz, L. G., "The structure and growth of evaporation LiF and NaCl films on amorphous substrates," J. Chem. Phys. 17, 1153, 1949.

Stone, J., and H. E. Earl, "Filling rates of long liquid-filled capillaries," J. Appl. Phys. 44, 5642, 1973.

Summ, B. D., E. A. Raud, and Y. V. Goryunov, "Initial stage of capillary flow," Colloid J. 41, 518, 1979.

Tadros, M. E., P. Hu, and A. W. Adamson," Adsorption and contact angle studies," J. Colloid Interface Sci. 49, 184, 1974.

Tang, J. F., and Q. Zheng, "Automatic design of optical thin-film system," J. Opt. Soc. Am. 72, 1522, 1982.

Temple, P. A., "Measurement of thin-film optical absorption at the air-film interface, within the film, and at the film-substrate interface," Appl. Phys. Lett. 34, 677, 1979.

Title, A. M., T. P. Pope, and J. P. Andelin, Jr., "Drift in interference filters, Part I," Appl. Opt. 13, 2675, 1974.

Thornton, J. A., "Influence of apparatus geometry and deposition conditions on the structure and topography of thick sputtered coatings," J. Vac. Sci. Tech. 11, 666, 1974.

Weast, R. C., Handbook of Chemistry and Physics, 52nd Edition, p. B-63, (The Chemical Rubber Co., 1972).

Wade, W. H., and J. W. Whalen, "Pendular-ring condensation on teflon powders," J. Phys, Chem. 72, 2898, 1968.

APPENDIX C

ION BOMBARDMENT-INDUCED RETARDED MOISTURE ADSORPTION IN OPTICAL THIN FILMS

Reprinted from Applied Optics, Vol. 23, page 3633, October 15, 1984
Copyright © 1984 by the Optical Society of America and reprinted by permission of the copyright owner.

Ion bombardment-induced retarded moisture adsorption in optical thin films

Steven G. Saxe, M. J. Messerly, Bertrand Bovard, Lewis DeSandre, Fred J. Van Milligen, and H. A. Macleod

Moisture adsorption and desorption in optical filters made of TiO_2 and SiO_2 can be retarded by bombarding the completed films with 3-keV oxygen ions. This effect is not seen in filters made of ZrO_2 and SiO_2. We propose that retardation is due primarily to a swelling of the TiO_2 surface as material is converted from crystalline to amorphous. In ZrO_2, bombardment induces a transition toward more crystalline order, and the effect is not observed. This paper describes our experiments and results and discusses alternate explanations of the retardation effect.

I. Introduction

The performance of thin-film optical filters is unstable due largely to the porosity of the films and their consequent tendency to adsorb moisture. The adsorbed moisture displaces air in the coating volume and thereby raises the effective refractive index of the film. This in turn increases the optical thickness and the wavelength at which the filter operates. As a result, the filter wavelength shifts away from that for which it was manufactured. Furthermore, the shift is dependent on the amount of moisture adsorbed into the film, which can vary with the temperature and relative humidity of the environment.

Moisture adsorption is a consequence of film microstructure. The structure of an evaporated thin film is primarily columnar[1] with the axis of the columns approximately parallel to the vapor angle of incidence and perpendicular to the substrate surface. The surface of the film is a rough terrain of column tops and intercolumn voids. Water fills the open volume of the film by migrating down the intercolumn voids.

Much work has been done to reduce the porosity of an evaporated film by bombarding the growing film with ions.[2-4] Ion-assisted deposition (IAD) can increase the film packing density to the degree that no measurable change in performance is observed on exposure to atmospheric moisture.[5,6]

While much work is done on bombardment during deposition, we have investigated the effect of bombarding completed films. We have found that certain films adsorb and desorb moisture much more slowly after bombardment than before. This phenomenon could be important in developing a postdeposition technique for creating impermeable sealing layers on coatings. A postdeposition process obviates the need for large scale ion bombardment during deposition and the consequent uniformity and manufacturing problems. Furthermore, an explanation of the retardation effect throws light on a subject of immense current interest: the microstructure of thin films.

The next two sections of this paper present the details of our experiments and the effects of bombarding completed films. The following section discusses possible mechanisms for the retardation effect and proposes the most probable explanation.

II. Experimental

The experiments were performed in a Balzers 760 evaporation plant equipped with a water-cooled cold cathode ion source[7] and a wideband scanning monochromator monitor system. The geometrical relationship among the ion source, test sample, and monitor beam is shown in Fig. 1. Table I summarizes the parameters used in these experiments.

The bombardment subjects were Fabry-Perot-type narrowband filters (NBFs) made with TiO_2/SiO_2 (titania/silica) and also with ZrO_2/SiO_2 (zirconia/silica). The top layer of filters with this design is a high index layer, i.e., TiO_2 or ZrO_2. In each trial, two identical samples, one test and one control, were placed in a rotating turret sample holder. Both the test sample and the control sample could be rotated into the monitor beam and observed. A typical trial of the experiment

The authors are with University of Arizona, Optical Sciences Center, Tucson, Arizona 85721.
Received 1 June 1984.
0003-6935/84/203633-05$02.00/0.
© 1984 Optical Society of America.

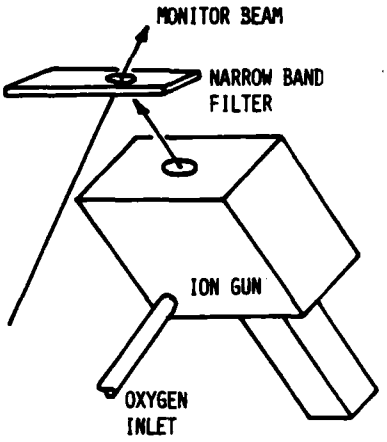


Fig. 1. Relationship among ion gun, test sample, and monitor beam. Monitor is external to vacuum chamber but is operable even during ion bombardment.

consisted of measuring the samples in atmosphere, pumping them down, bombarding the test sample, and then venting them to atmosphere, all while monitoring the transmittance spectra of both samples. Thus we were able to follow the history of both bombarded and unbombarded samples and to compare their differences under controlled conditions.

The transmittance of the samples was monitored *in situ* by a wideband scanning monochromator. Details of this system are presented elsewhere.[8] The transmittance spectrum of an NBF is a sensitive indicator of the relative amount of moisture adsorbed into the film. The performance of a freshly evaporated filter changes radically as soon as it is exposed to the atmosphere. The filter reflectance band widens, deepens, and shifts toward longer wavelengths. These changes are consistent with the expectation that the layers' refractive indices increase with adsorbed moisture.

When a completed filter is returned to the vacuum chamber and pumped down, the filter transmittance characteristics move *in toto* toward shorter wavelengths, showing that the filter is giving up adsorbed moisture. When the chamber is vented to atmosphere, the filter performance returns to its previous (in air) position. A typical change is shown in Fig. 2. We have used the degree and rate of wavelength shift to measure the degree and rate of moisture adsorption and desorption in optical filters.

A. Bombardment-Induced Changes

During bombardment, the test sample shows changes not seen in the unbombarded control sample. The most notable change is in the shape and height of the transmittance curve. Figure 3 shows typical transmittance curves for a titania/silica NBF before and after bombardment. The change in curve shape can be explained as a thinning of the top layer of coating by a fraction of its thickness. This is not unexpected since the ion energy is large enough to cause appreciable sputtering. Only a fraction of the layer is removed because the ion flux is small and bombardment times are relatively

Table I. Parameters Used in Ion Bombardment Experiments

Ion species	O_2^+
Ion energy	3 keV
Ion flux[a]	$\sim 1\ \mu_A \cdot cm^{-2}$
Ion angle of incidence	45°
Bombardment duration	5 min
Filter design	$(HL)^4\ 6H\ (LH)^4$
Low index material	SiO_2
High index materials	ZrO_2, TiO_2

[a] Ion flux proved difficult to measure and was estimated from sputtering rate.

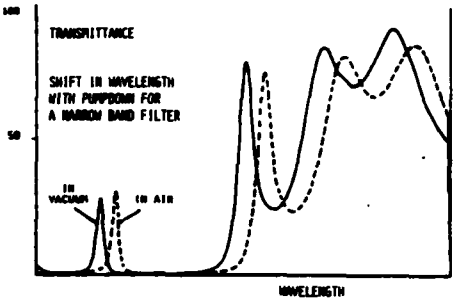


Fig. 2. Typical change in narrowband filter transmittance from air to vacuum. The curve moves *in toto* toward shorter wavelengths under vacuum, showing that moisture is removed from the entire volume of the coating and not simply from a surface layer. Note that the filter is not a very good one; the in-band transmittance is quite low.

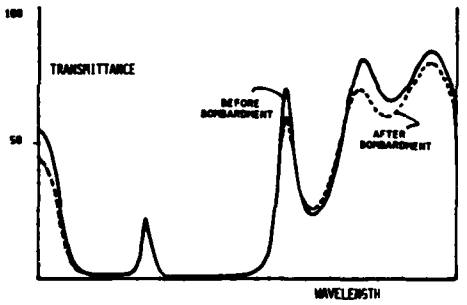


Fig. 3. Transmittance spectra for a titania/silica narrowband filter before and after bombardment. The difference is consistent with bombardment-induced decrease in thickness and increase in optical absorption for top layer only.

short. The overall decrease in transmittance is seen in titania films but not in zirconia. The decrease is almost certainly due to preferential sputtering of oxygen out of the film. The oxygen-depleted (reduced) surface layer is then absorbing, and the transmittance decreases. The transmittance of a bombarded sample increases slowly with time as the top layer reoxidizes in air. Both of these changes have been successfully simulated with a thin-film design program by manipulating the specification of the top layer. The imaginary index of refraction k was increased from zero, and the thickness was decreased.

From Fig. 2 we may deduce that moisture is adsorbed and desorbed throughout the volume of the coating. The position of the transmittance spike is dependent

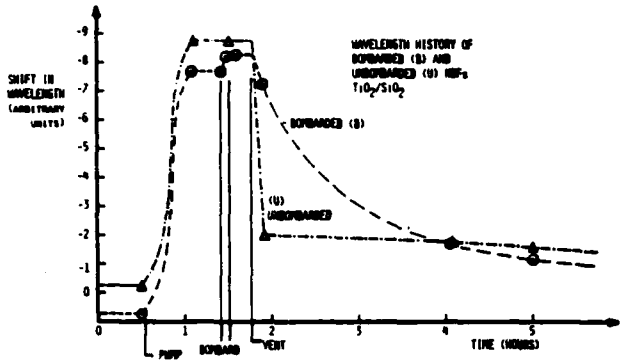


Fig. 4. Wavelength position vs time for initial bombardment of titania/silica narrowband filter. After bombardment the test sample readsorbs moisture only slowly while the unbombarded control sample returns rapidly.

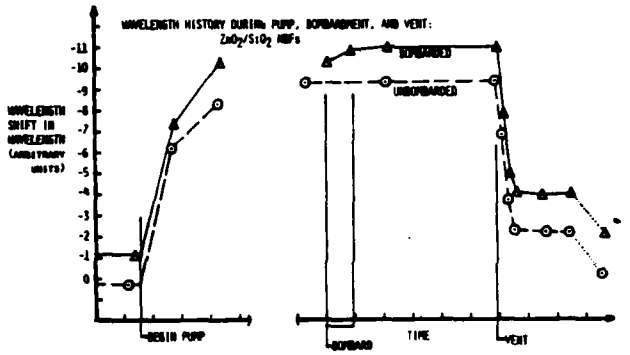


Fig. 5. Wavelength position vs time for initial bombardment of zirconia/silica narrowband filter. No difference is seen between the behaviors of the bombarded and unbombarded samples.

primarily on the optical thickness of the spacer layer which is buried deep in the center of the layer system. Since the spike position changes with moisture content, we must conclude that water penetrates deep into the film. From the bombardment-induced changes, we may conclude that the effect of ion bombardment is restricted to the top layer or more strictly to some fraction of it. This is not inconsistent with predictions of ion penetration depth based on physical models.[9]

III. Results

The experiment described above was carried out on NBFs made of titania/silica and of zirconia/silica. The wavelength position of the transmittance curve was plotted vs time for each sample to give a history of wavelength under varying conditions. Figure 4 shows the history for the initial bombardment run on a titania/silica filter. During pumpdown, both test and control samples followed the same curve. The test sample showed a small shift during bombardment and then stabilized again. The most remarkable difference appeared after the chamber was vented. The unbombarded control sample returned rapidly to a position near its beginning state, but the bombarded test sample moved only slightly from its vacuum state. Two hours later, the samples were more similar, and by extrapolation we expect that both returned to their initial states within hours.

The same experiment on zirconia/silica samples yields substantially different results. The history of the zirconia test is shown in Fig. 5. The history was much the same as the titania up to the point where the chamber was vented to atmosphere. At this point, both test and control samples behaved identically. That is, where bombardment induced a change in titania, it did not in zirconia. Since the only difference between the filters is the material used for the high index (including the top layer), the observed difference in the adsorption behaviors is attributable to differences between these materials.

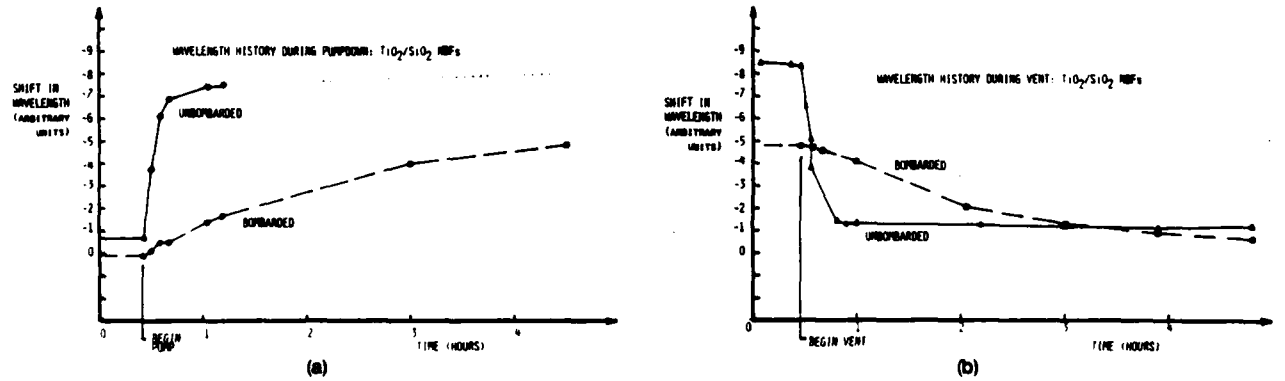


Fig. 6. (a) Wavelength position vs time during pumpdown for a previously bombarded titania/silica NBF and an unbombarded control sample. Moisture desorption in the bombarded sample is still much slower than in the unbombarded control. (b) Similar plot before, during, and after vent to atmosphere. Under vacuum, the bombarded sample did not desorb as much moisture as the unbombarded control. After vent, moisture adsorption is still retarded.

To investigate whether the induced change in titania was permanent, we repeated the pumpdown cycle on a pair of samples which had been bombarded weeks before. The history of this experiment is shown in Fig. 6. Figure 6(a) records the pumpdown phase. The bombarded sample was seen to shift much more slowly than the unbombarded, indicating that it was desorbing moisture more slowly. Figure 6(b) shows the history before and during vent. During the period before vent, it is apparent that the bombarded sample did not shift as far as did the unbombarded. This means that it did not give up as much adsorbed moisture to the vacuum. Upon venting, the unbombarded sample returned immediately to its initial position while the bombarded sample returned much more slowly. The changes induced by bombardment are, therefore, permanent (permanent for several weeks or more).

IV. Discussion

A suitable physical model for this ion bombardment remains to be found. The successful model must explain the retarded moisture adsorption and the difference between the behaviors of titania and zirconia.

Lo *et al.* have shown that fully oxidized titania (TiO_2) surfaces bombarded with argon ions reduce to suboxide forms. The resulting surfaces are chemically and electronically equivalent to TiO_2 surfaces on which a monolayer of Ti metal has been deposited. The valence state of titanium on these surfaces is primarily Ti^{3+}. It has also been shown that water adsorbed on the reduced titania (Ti_2O_3) surface will dissociate into hydroxyl groups OH, which remain adsorbed on the surface.[10]

This suggests a possible mechanism for the retarded moisture adsorption seen in titania films. We suppose that the titania is reduced by the bombardment and that atmospheric water on its way into the volume of the film is being dissociated and adsorbed as OH at the surface. Consequently moisture is not allowed to fill the film at the expected rate. Once the adsorbed OH groups fill all the vacancies on the reduced surface, we expect normal volume adsorption processes to resume.

This view is at odds with the experimental results in two details. First, we do not see the normal adsorption processes resume. What we do see are permanent changes in the moisture adsorption and desorption behavior of the entire film volume. Bombardment is a surface effect and is presumed incapable of affecting the chemistry of the interior of the film. The second discrepancy concerns the long-term behavior of the moisture adsorption. The optical absorption induced by the bombardment is an indicator of the reduced titania. This absorption decreases with time as the surface of the film reoxidizes in air. The film surface should thereby lose its ability to dissociate water. However, experiments done weeks after bombardment show that retarded moisture adsorption persists longer than the reduced titania.

Another explanation is possible. As stated above, the incident ions are energetic enough to cause sputtering (removal) of coating material. From this we may postulate that retarded moisture adsorption is due to a film surface modified by sputtering and redeposition. In this view, material is removed from the solid part of the top surface of the coating and is redeposited in the coating voids. (Sputtering and redeposition is not unlike compaction or smashing in its overall result.) This occludes the passages into the film and slows the transport of moisture into the film volume. Furthermore, if enough material is deposited in the voids, the total amount of moisture adsorbable may be reduced. This view is consistent with the results presented above, but one remaining fact must be explained: the effect is not seen in zirconia. Can such a simple physical model explain the difference between the behaviors of the two materials?

To explain the large difference in behaviors, there must be a significant difference in the rate at which the two materials sputter. The sputtering or milling rate is related to the lattice bond energy,[11] to the relative masses of the bombarded and bombarding particles, and to the electronic configurations of the particles.[12] We may avoid the need to delve into a model of ion milling by referring directly to experimental values for the sputtering yields of zirconia and titania. We find that the yields for 600-eV argon ions are 0.96 for titania and 0.32 for zirconia.[13] While we are not concerned here with 600-eV argon ions, these values do tell that the sputtering yields are of the same order of magnitude.

We may lend confidence to these reported values by referring to the results of our computer simulations of changes in transmittance spectra due to top layer milling. By comparing our simulated spectral changes with those obtained experimentally, we were able to estimate the amount of material removed. Our estimate for zirconia was much the same as that for titania, in agreement with the above report. In both cases the amount was some tens of angstroms, a few percent of the total layer thickness.

There is, therefore, not a large difference between zirconia and titania in the amount of material sputtered. There is also no reason to expect the two would differ appreciably in the amount of sputtered material redeposited in the coating voids. We may suppose that there are geometrical differences between the surface topographies of titania and zirconia which affect the result of sputtering and redeposition. If, for example, the intercolumn voids in zirconia are comparatively large, the redeposited material may not be sufficient to occlude the passageways. Unfortunately, there is also no reason to expect significant geometrical differences between the materials. We are still without an explanation for the lack of an effect in zirconia.

Information gained from ion-assisted deposition experiments offers yet another explanation. When zirconia and titania are deposited thermally without the aid of ions, x-ray diffraction measurements of the films show weak crystalline order. When the evaporation is accompanied by ion bombardment, the degree of crys-

tallinity is changed.[14] In the case of titania, the films become less ordered and more amorphous.[15] Zirconia, however, becomes more crystalline when ion-assisted.[4]

It is conceivable that bombardment induces crystalline reordering as well as sputtering and redeposition. We extend the IAD results and presume that zirconia crystallizes while titania becomes more amorphous. Since a crystalline material occupies less volume than the same amount of an amorphous one, we may say that the surface of the titania swells while that of zirconia shrinks. The surface pores in titania close up while those in zirconia widen. The constricted pores present the same impediment to moisture that we predicted for the sputtering and redeposition model. We now have an explanation which encompasses both the retardation effect and the observed difference between the two materials.

V. Conclusions

This last explanation is the only one which adequately explains the observed difference between zirconia and titania films. Changes in valence state or differences in milling rate as outlined earlier may contribute to the experimental observations, but we propose that this last mechanism is the primary one.

The crystallization/decrystallization hypothesis is not easy to test. The thickness of the modified surface layer is at most 300 Å, a thickness far too small to yield useful x-ray diffraction results. Further work could test the hypothesis by repeatedly evaporating then bombarding a material to build up a thick layer of the modified structure. The thick layer could be analyzed by x-ray diffraction.

References

1. H. A. Macleod, "Microstructure of Optical Thin Films," Proc. Soc. Photo-Opt. Instrum. Eng. **325**, 21 (1982).
2. T. H. Allen, in *Proceedings, International Ion Engineering Congress—ISIAT '83 and IPAT '83* (Kyoto, 1983), pp. 1305–1310.
3. W. G. Sainty, R. P. Netterfield, and P. J. Martin, "Protective Dielectric Coatings Produced by Ion-Assisted Deposition," Appl. Opt. **23**, 1116 (1984).
4. P. J. Martin, R. P. Netterfield, and W. G. Sainty, "Modification of the Optical and Structural Properties of Dielectric ZrO_2 Films by Ion-Assisted Deposition," J. Appl. Phys. **55**, 235 (1984).
5. N. A. Holm and O. Christensen, "Humidity Sensitivity of Optical Structures Prepared by R. F.-Biased R. F. Sputtering," Thin Solid Films **85**, 71 (1981).
6. P. J. Martin, H. A. Macleod, R. P. Netterfield, C. G. Pacey, and W. G. Sainty, "Ion-Beam-Assisted Deposition of Thin Films," Appl. Opt. **22**, 178 (1983).
7. This source was manufactured by Denton Vacuum, Inc., Cherry Hill, N.J. 08003-4072.
8. F. J. Van Milligen, to be presented at Optical Society of America Annual Meeting, San Diego (1984).
9. O. Almen and G. Bruce, "Collection and Sputtering Experiments with Noble Gas Ions," *Nucl. Instrum. Methods* **11**, 257 (1961).
10. W. J. Lo, Y. W. Chung, and G. A. Somorjai, "Electron Spectroscopy Studies of the Chemisorption of O_2, H_2 and H_2O on the TiO_2 (100) Surfaces with Varied Stoichiometry: Evidence for the Photogeneration of Ti^{3+} and for its Importance in Chemisorption," Surf. Sci. **71**, 199 (1978).
11. P. Sigmund, "Theory of Sputtering. I. Sputtering Yield of Amorphous and Polycrystalline Targets," Phys. Rev. **184**, 383 (1969).
12. E. G. Spencer and P. H. Schmidt, "Ion-Beam Techniques for Device Fabrication," J. Vac. Sci. Technol. **8**, S52 (1971).
13. B. Chapman, *Glow Discharge Processes* (Wiley-Interscience, New York, 1980), p. 396.
14. J. J. Wharton, Ph.D. Dissertation, U. Arizona (1983).
15. W. T. Pawlewicz, P. M. Martin, D. D. Hays, and I. B. Mann, "Recent Developments in Reactively Sputtered Optical Thin Films," Proc. Soc. Photo-Opt. Instrum. Eng. **325**, 105 (1982).

The first notice of a moisture adsorption effect after ion bombardment was made by J. J. Wharton, I. J. Hodgkinson, and H. A. Macleod at the University of Arizona. This work was supported by a contract with China Lake Naval Weapons Center—Defence Advanced Research Projects Agency. Additional support for a postdoctoral position was provided by the U.S. Air Force Office of Scientific Research and for a fellowship by the U.S. Army Research Office. We wish to thank Tim Reith and Kent Howard of IBM for the sputtering yield information, Ross Potoff and R. W. Sprague for their expertise and invaluable help with hardware and lab work, and U. J. Gibson for many fruitful discussions.

This paper is based on a presentation made at the third topical meeting on Optical Interference Coatings, Monterey, Calif., 17–19 Apr. 1984.

REPORT DOCUMENTATION PAGE

1a. REPORT SECURITY CLASSIFICATION UNCLASSIFIED	1b. RESTRICTIVE MARKINGS
2a. SECURITY CLASSIFICATION AUTHORITY	3. DISTRIBUTION/AVAILABILITY OF REPORT Approved for public release; distribution unlimited.
2b. DECLASSIFICATION/DOWNGRADING SCHEDULE	
4. PERFORMING ORGANIZATION REPORT NUMBER(S)	5. MONITORING ORGANIZATION REPORT NUMBER(S)
6a. NAME OF PERFORMING ORGANIZATION Optical Sciences Center University of Arizona 6b. OFFICE SYMBOL (If applicable)	7a. NAME OF MONITORING ORGANIZATION Naval Weapons Center
6c. ADDRESS (City, State and ZIP Code) Optical Sciences Center University of Arizona Tucson, AZ 85721	7b. ADDRESS (City, State and ZIP Code) China Lake, California 93555
8a. NAME OF FUNDING/SPONSORING ORGANIZATION DARPA 8b. OFFICE SYMBOL (If applicable)	9. PROCUREMENT INSTRUMENT IDENTIFICATION NUMBER N60530-81-C-0158
8c. ADDRESS (City, State and ZIP Code) 1400 Wilson Blvd Arlington, Virginia 22204	10. SOURCE OF FUNDING NOS. PROGRAM ELEMENT NO. / PROJECT NO. / TASK NO. / WORK UNIT NO.
11. TITLE (Include Security Classification) Thin Film Research, Vols. 1 and 2	
12. PERSONAL AUTHOR(S) H. Angus Macleod	
13a. TYPE OF REPORT Final	13b. TIME COVERED FROM 1/8/81 TO 7/31/84
14. DATE OF REPORT (Yr., Mo., Day) May 30, 1985	15. PAGE COUNT 77 + Appendices
16. SUPPLEMENTARY NOTATION	

17 COSATI CODES		
FIELD	GROUP	SUB. GR.

18. SUBJECT TERMS (Continue on reverse if necessary and identify by block number)
Thin films, coatings, physical vapor deposition, PVD, ion-assisted deposition, IAD, ion bombardment, electron-assisted deposition, electron bombardment, optical thickness monitor,

19. ABSTRACT (Continue on reverse if necessary and identify by block number)

Optical thin films are critical components in a broad range of technologies, ranging from energy conversion to information storage. In response to the demand for increasingly specialized and durable coatings, enquiry into the basic nature of these coatings has intensified. Such efforts are necessary because assumptions that thin films were similar to nominally identical bulk materials have proven unreliable. For example, while most bulk materials show a high degree of isotropy, thin films display pronounced anisotropy. Another distinction between bulk and thin film materials is the lower density of the latter, with the resulting porosity. Both anisotropy and porosity often contribute to the unpredictable performance and durability of optical coatings. This report covers three years of fruitful research aimed at better understanding and modifying film microstructure in the direction of greater isotropy and density through novel deposition techniques. We have supported this effort with an array of analysis techniques and with a major effort in film growth simulation and in the theoretical description of anisotropic films. Our

20. DISTRIBUTION/AVAILABILITY OF ABSTRACT UNCLASSIFIED/UNLIMITED ☒ SAME AS RPT ☐ DTIC USERS ☐	21 ABSTRACT SECURITY CLASSIFICATION Unclassified
22a. NAME OF RESPONSIBLE INDIVIDUAL H. Angus Macleod	22b TELEPHONE NUMBER (Include Area Code) (602) 621-2449 / 22c OFFICE SYMBOL

DD FORM 1473, 83 APR EDITION OF 1 JAN 73 IS OBSOLETE.

18. Subject Terms (Continued)

scanning optical monitor, surface plasmons, narrowband filters, moisture adsorption, columnar growth, anisotropic structure, optical constants, inhomogeneities.

19. Abstract (Continued)

program also included development of a scanning monochromator for our Balzers 760 evaporation system, which covers a 400 to 800 nm bandwidth by dispersing the beam with a holographic grating and detecting it with a linear array.

Accession For
NTIS GRA&I
DTIC TAB
Unannounced
Justification
By
Distribution/
Availability Codes
Dist | Avail and/or Special
A-1

